Volume 130
2005

Progress in Colloid and Polymer Science

EDITORS
F. Kremer
W. Richtering

Scattering Methods and the Properties of Polymer Materials

VOLUME EDITORS
N. Stribeck
B. Smarsly

Springer

Progress in Colloid and Polymer Science

Recently Published and Forthcoming Volumes

Scattering Methods and the Properties of Polymer Materials
Volume Editors: Stribeck, N., Smarsly, B.
Vol. 130, 2005

Mesophases, Polymers, and Particles
Volume Editors: Lagaly, G., Richtering W.
Vol. 129, 2004

Surface and Colloid Science
Volume Editor: Galembeck, F.
Vol. 128, 2004

Analytical Ultracentrifugation VII
Volume Editors: Lechner, M. D., Börger, L.
Vol. 127, 2004

Trends in Colloid and Interface Science XVII
Volume Editors: Cabuil, V., Levitz, P., Treiner, C.
Vol. 126, 2004

From Colloids to Nanotechnology
Volume Editors: Zrinyi, M., Hórvölgyi, Z. D.
Vol. 125, 2004

Aqueous Polymer Dispersions
Volume Editor: Tauer, K.
Vol. 124, 2004

Trends in Colloid and Interface Science XVI
Volume Editors: Miguel, M., Burrows, H. D.
Vol. 123, 2004

Aqueous Polymer–Cosolute Systems
Volume Editor: Anghel, D. F.
Vol. 122, 2002

Molecular Organisation on Interfaces
Volume Editor: Lagaly, G.
Vol. 121, 2002

Lipid and Polymer-Lipid Systems
Volume Editor: Nylander, T.
Vol. 120, 2002

Progress in Colloid and Polymer Science
Editors: F. Kremer, Leipzig and W. Richtering, Aachen

Volume 130 · 2005

Scattering Methods and the Properties of Polymer Materials

Volume Editors:
Norbert Stribeck, Bernd Smarsly

Springer

ISSN 0340-255X
ISBN-10 3-540-25323-8
ISBN-13 978-3-540-25323-5
DOI 10.1007/b96538
Springer Berlin, Heidelberg, New York

Springer is a part of
Springer Science + Business Media

springeronline.com

Printed in Germany

Editor: Dr. Marion Hertel,
Springer-Verlag Heidelberg

Desk editor: Beate Siek,
Springer-Verlag Heidelberg

Production: ProEdit GmbH,
Elke Beul-Göhringer, Heidelberg

Cover design: Estudio Calamar,
F. Steinen-Broo, Pau/Girona, Spain

Typesetting: SPS, Chennai, India

Printing and Binding:
Mercedes-Druck, Berlin

Printed on acid-free paper

2/3141 beu-göh 5 4 3 2 1 0

Progr Colloid Polym Sci (2005) 130: V–VI

Professor Wilhelm Ruland on the occasion of his 80th anniversary

It is a rare event in the scientific community that one of its distinguished members keeps working in the daily business of research at the age of 80. In this respect and for the polymer community the year 2005 is a very special year, since with Richard S. Stein and Wilhelm Ruland even two of its esteemed "scatterers" are celebrating their 80th anniversary without showing any indications of being scattered (sorry, Dick) for varying your bonmot). Thus a cordial salutation is additionally conveyed to Dick Stein in Amherst as we are commemorating the birthday of Wilhelm Ruland with this special issue of "Progress in Colloid and Polymer Science"

Born in October 1925 in Stolberg in the border triangle between Belgium, The Netherlands and Germany Wilhelm Ruland found ideal "starting values" to become a Francophile European. After finishing his studies of Chemistry at the RWTH in Aachen in 1957, he started to work as an industry researcher in Belgium, joining the European Research Center of the Union Carbide Corporation, where he cooperated with Hans Tompa and published a series of outstanding scientific papers. The most prominent of these papers appears to be the "Ruland method" for the determination of crystallinity of polymers. During this period he climbed to the position of the research director of his institution. When Union Carbide moved their research to America, even a generous offer could not motivate him to leave Europe. So in 1972 he became a professor at the University of Marburg. There he reinforced the lively polymer institute of F.H. Müller that was just moving and extending on new premises. With the staff completed by the chemist Professor Walter Heitz ("colleague Ruland is hanging out in reciprocal space"), the second not less fruitful and still lasting research period began for Wilhelm Ruland. Here, on top of everything, he was allowed to demonstrate his teaching qualities. His concise and precise lecturing is breathing the spirit of modern French mathematics (Laurent Schwartz – dual spaces), the tools of which he is virtuosically mastering in order to advance his research. Presumably in the philosophical background of this branch of mathematics lies a substantial impulse for his life as a researcher: Beneath the German motto of the experimentalist "Versuch macht klug" he puts the pursuit of the enlightened scientist to both found the fields of polymer physics in an axiomatic manner and then to enter into working them out in commensurable strictness. In this context "enlightenment" as well means, less to rely on the deceptive senses but more on the strictness of human intellect.

With respect to Professor Ruland's high profile in the field of structure investigation, one of his "trademarks" is the development of unparalleled strategies to create elegant mathematical solutions for scattering problems. In his various contributions in this field one can clearly feel his strong striving towards the most elegant theoretical solution of a mathematical problem, in particular to obtain fully analytical expressions. It can not be emphasized enough that his clarity and conciseness in the mathematical description of complex aspects, for instance on the generalisation of the evaluation of the asymptotic behavior of scattering curves following Kirste and Porod, has significantly contributed to the progress in the field of small-angle scattering – Professor Ruland is certainly "un bon vivant", filling abstract science with joy and creativity, which is best described by his own motto "Nothing is more practical than a good theory!".

In this way Wilhelm Ruland is adding to scientific progress since several decades with a long sequence of methodological contributions. No matter if today he is pointing out the narrow validity ranges for the fractal concept, if he is focusing on the neglected absorption correction as scattering geometries are changed, or if he is computing theoretical scattering patterns of modern highly ordered nanostructures: Upon reading his papers it becomes obvious how motivating (sorry, we find no English equivalent to the German word ''beglückend'') it can be ''to search the exit of self-inflicted immaturity'' (Immanuel Kant). Curiosity and conciseness as the basis of scientific work, beneath that placidity in material matters (''As scientists we belong to the small group of humans who are allowed to pursue their hobby in their professional life. This means that we cannot expect more than an alimentation'' (W. Ruland)) – these components appear to be a proper basis for a satisfying life as a scientist.

Only after years of dictatorship the political conditions for an enlightened progress were created in Germany. That is the reason why the scientific life of Wilhelm Ruland started at a relatively late age. Let us be aware of the fact, that the climate of liberality is never guaranteed. In order to fully concentrate on his work for humanism and liberality, Dick Stein has withdrawn his promised contributions for this issue. He writes: ''I am truely sorry, but I think you can realize the importance of my task. If the politics of the US continues to decline, the science will not be immortal. Science best occurs in a free society, and it is my hope that the spirit of cooperation and understanding among scientists throughtout the world, so well shown by Professor Ruland, may serve as a model for the behaviour of our politicians and citizens.''

Chapeau!
Norbert Stribeck
Bernd Smarsly

Progr Colloid Polym Sci (2005) 130: VII

PREFACE

In this special issue on the occasion of Wilhelm Ruland's 80th anniversary a collection of original studies from colleagues and companions is presented. In this way the issue does not only reflect the esteem of an outstanding scientist, but also represents a profile of current research activities. In many of the contributions the application and progress of scattering methods plays an important role in an effort to understand the nanostructures which today are in the focus of scientific interest. In this connexion polymer materials are frequently studied, the natural coil dimensions of which are in the order of several nanometres.

Thus two preparative papers on the making of advanced polymer materials are found in the beginning of this issue. In the second section two studies are presented that focus on scattering theory. In the third and last section the majority of the contributions is found. The corresponding papers are focusing on concepts for the study of structure and of its evolution. The first subsection presents investigations of isotropic materials and solutions. The second subsection collects work on anisotropic materials. Even if all the papers of this section contain experimental work, some of them exhibit a considerable degree of theoretical penetration by modification of classical concepts of scattering theory or even by the presentation of novel ideas. The materials studied cover the whole spectrum of nanostructures from the classical to the modern ones.

Although several colleagues have withdrawn their earlier promise to contribute, the initial enthusiasm to celebrate Wilhelm Ruland was big enough to finally accomplish this nice bouquet. Thus the guest editors gratefully express their appreciation to all the scientists who made this effort become a success.

May 2005

Norbert Stribeck
Bernd Smarsly

Progr Colloid Polym Sci (2005) 130: VIII–IX

CONTENTS

Progr Colloid Polym Sci (2005) 130: 1–14
DOI 10.1007/b107336
Published online: 3 June 2005

Ulrich Siemann

Solvent cast technology – a versatile tool for thin film production

Abstract The oldest technology in plastic films manufacturing, the continuous solvent cast process, was developed more than hundred years ago driven by the needs of the emerging photographic industry. In the years after 1950, new film extrusion techniques of thermoplastic polymers became the dominant production method for plastic films and the importance of solvent cast technology has declined. Nowadays, the solvent cast technology is becoming increasingly attractive for the production of films with extremely high quality requirements. The advantages of this technology include uniform thickness distribution, maximum optical purity and extremely low haze. The optical orientation is virtually isotropic and the films have excellent flatness and dimensional stability. The cast film can be processed in-line with an optical coating design. The tremendous growth of new liquid crystal display applications has incited the development of new materials and improved processes for solvent casting and coating techniques. The key elements of cast film manufacturing are explained, and technological details are discussed for dope preparation, die design, casting support, film drying and solvent recovery. Main applications of films made by different polymer/solvent combinations are described.

U. Siemann
LOFO High Tech Film GmbH,
Weidstr. 2, 79576 Weil am Rhein,
Germany
e-mail: dr.u.Siemann@lofo.com
Tel.: +49-7621-703-114
Fax: +49-7621-703-313

Introduction

From the end of the 19th century, the development of a process for manufacturing thin plastic films was tightly linked to the emerging industry for movies and photographic films. 5 mil (125 micron) film was produced using a discontinuous device with a caster moving over 200 feet long glass plates at Eastman KODAK [1]. Soon, first patents were issued to cast celluloid films on a moving surface by the ''Celluloid Company'' in the United States and patented in 1896 [2]. For economic reasons, Eastman KODAK developed a continuous casting process parallel to the Celluloid Company, resulting in a patent infringement. KODAK switched over from the discontinuous to the continuous casting process about 5 years later. At that time, photographic film base was produced from cellulose nitrate and campher as a plasticizer from solutions in solvents such as acetone, ether and alcohol on wheels with diameters of 9 feet (~2½ meters) at a maximum speed of approx. 150 feet/h (50 m/h). That translates into about 50 square meters / hour. The know-how required to manufacture highly stable huge steel wheels with perfectly polished surfaces was perfected by the Eastman KODAK Company over the next 100 years. It was an interesting ''switch'' in industrial history, that the competing European film companies started some years later with belt casting technology and even now both manufacturing processes still run parallel in the US and elsewhere. The use of an endless flexible belt seemed to offer certain advantages in terms of process speed. On the other hand, the technology needed to produce belts with a uniform thickness, invisible joints and polished surface was not very far developed in the early 20th century.

From 1907 onwards, the first belt machines with copper belts of 1 m width and 35 to 50 feet (12... 14 m) length were installed by AGFA in Berlin [3]. The development of this type of technology was triggered by the difficulty of drying the film fast enough on a wheel whose circumference was at that time restricted to about 9 m. But casting speed is not necessarily a direct function only of drying length at the casting support. Initially, the belt machines did not run faster than the wheel machines, because of Eastman KODAK's more advanced technology. It should be mentioned that back then, the cast film production process did not include solvent recovery! Because of the highly flammable nature of nitrocellulose films, other materials were screened for photographical use. In the early 20th century, cellulose triacetate in combination with the plasticizer triphenylphosphate was identified by Eastman as "safety film", but it took many years to achieve a mass production because methylene chloride as the most suitable solvent was not available at low cost at that time. Since the mid 20th century, cellulose triacetate turned out to be the most important material to produce photographical films and movies [4]. It has taken many years for the solvent casting manufacturing process to develop into a high precision technique [5]. Today, it is used for the production of engineering plastics, optical films, medical films and sheet forming for electronic applications. A sketch of the entire solvent cast process on a belt line is shown in Figure 1.

Key elements of solvent cast technology

Raw materials

For the raw materials of the dope making process there are some obvious prerequisites.

- The polymer must be soluble in a volatile solvent or water
- A stable solution with a reasonable minimum solid content and viscosity should be formed
- Formation of a homogeneous film and release from the casting support must be possible.

To provide these properties many process tricks are used such as co-solvent systems, dissolution at overpressure, use of special molecular weight distributions of polymers or co-polymers, additives such as plasticizers, release agents etc. Examples of dope composition for cast film products are shown in Table 1. Starting with the cellulose derivatives used from the historical beginning of this technique, processes for other high performance materials have been developed over the last 40 years. Water is still a common solvent for food-grade films made of biopolymers or polyvinylalcohol. Typical additives used to provide specific film properties are antiblocking and antistatic compounds, chelating agents, colours, electrical conductive substances, pigments etc. When adding solid substances that can be processed as highly loaded

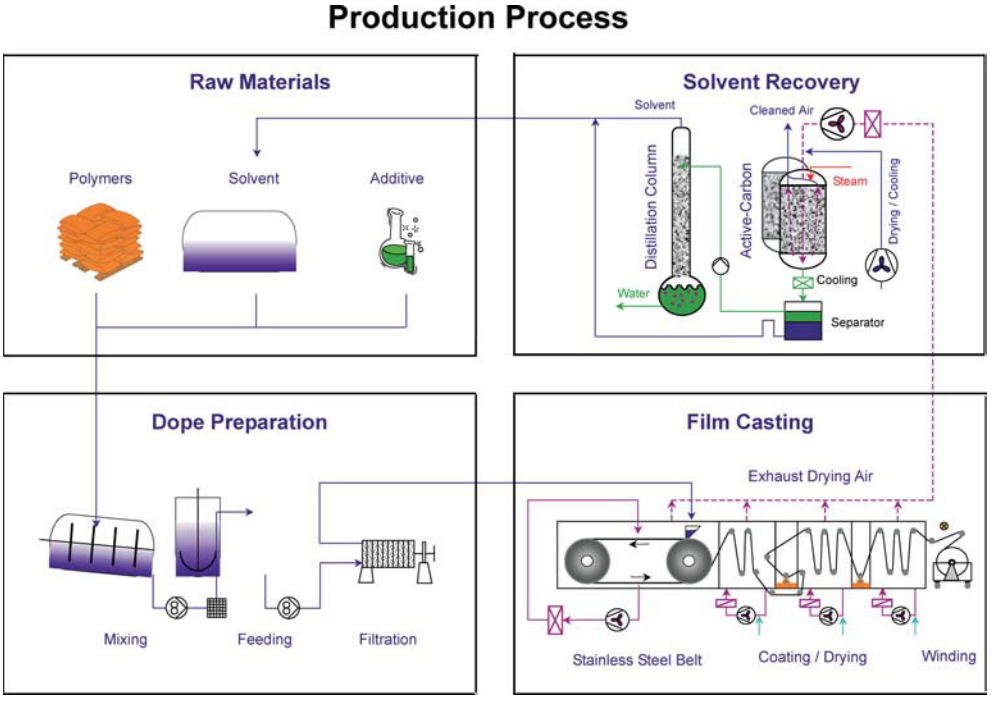

Fig. 1 Production of solvent cast films

Table 1 Polymers and Typical Solvents for Casting Processes

Cellulose Nitrate	Ether, Esters	Polyimides	Dimethylformamide
Cellulose Diacetate	Acetone, Methanol		
Cellulose Triacetate (TAC)	Methylene Chloride, Alcohols	Polyvinylalcohol	Water, Methanol
		Methyl Cellulose	Water
		Starch derivatives	Water
Polycarbonates	Methylene Chloride	Gelatine	Water, Methanol
Polyethersulfon	Methylene Chloride		
Polyetherimide	Methylene Chloride		
Polyvinylidene fluoride	Acetone		
PVC (Polyvinyl chloride)	Tetrahydrofuran		
	Methyl-ethylketon		

dispersions, the rheological implications have to be carefully monitored. Particle size distribution and filter mesh size should be adjusted during handling. When adding soluble solid or liquid compounds such as plasticizers, the assumptions are the same as for bulk polymers: solubility and stability in solution and in film formation process. It should be noted here that cast films can in most cases be re-dissolved and reused as raw material. The solution or polymer film is exposed to relatively low thermal or mechanical stress throughout the entire production process. As a result, degradation or adverse side reactions are insignificant.

Dope preparation

During this step, the solid polymer in various geometrical shapes such as flakes, granules chips or powder is dissolved in pure solvents or mixtures. In principle, standard types of chemical process mixers can be used.

Due to the large difference in viscosity – from pure solvents to highly viscous solutions – the geometry of the stirrer or paddle elements has to be carefully selected. Horizontal and vertical mixing vessels can be used, and the mixer elements may typically take the form of blades, anchors, spirals etc. Heating and cooling management by thermal jackets is generally required. Mechanical shear rate and dope temperature has to be carefully controlled. It influences the quality of the dissolution process, the formation of gel particles, solvent evaporation, skin formation and the degradation of polymer chains. The addition of plasticizer, additives, co-solvents, non solvents, pigments and similar substances should be considered, as should the subsequent dispersion or dissolution step. Typically, viscosities change from 1500 mPas to 80.000 mPas during the dissolution process, solids concentration ranges between 5% and 40% and temperatures can vary between room temperature and the boiling point of the solvents. A dissolution process at some bar overpressure and elevated temperature can be used for polymers with difficult dissolution properties, e.g. PVC in THF. Dissolution time is normally several hours. Depending on the specific process, the de-aeration step can be done batch wise by boiling in the mixing vessel or holding tank, by degassing continuously in heat exchangers or by vacuum equipment. Dope degassing is required in many cases to prevent air bubbles during the film forming process. The next step after dope preparation is solution clarification. Depending on the handling system, a 2 or 3 step filtration process and solution ripening in holding tanks are used. Several processes run at slight over-pressure in the vessels to avoid skin formation and loss of solvents, others at slight under-pressure and with an exhaust system to avoid solvent emissions during the heating and cooling steps. The entire dope line, including tanks, pipes, filters etc., needs precision temperature control. In specific dope making processes, further additives such as colour master-batches can be injected just before the casting step to prevent the colour contaminating the dope line.

Special attention should be given to the filtration processes. Frame and plate, candle type and back-flash type filters are used. One of the big advantages of the solvent cast technology is that fine filtration processes with very small mesh sizes, e.g. metal screens, can be used when films without particle type defects are required. Usually several filtration steps are subsequently used, ranging from coarse to fine filtration. Pressure difference during the build-up of residues on the filter pads, which are usually made of textiles, fabrics etc., has to be checked. Dope clarity can be checked with in-line instruments employing light diffraction principles. Some producers use filter aids to improve gel particle separation. The advantage of the plate and frame filters is that they offer large surface areas, the disadvantage is handling during make-up, cleaning and the removal of waste from the contaminated filter pads. For safety and environmental reasons, in line filter washing and back-flash cleaning operations have been introduced over recent years. The dope pumps also need special care. Aggressive solvents or compounds at an elevated temperature and pressure, abrasion by particles, pulse-free feeding of dope even at elevated pressures are key factors in selecting suitable pump types.

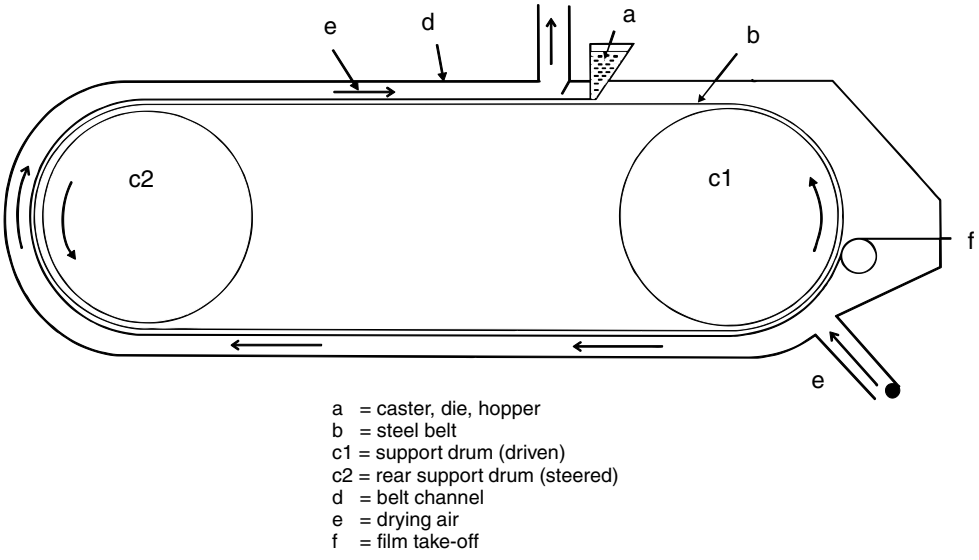

Fig. 2 Cross-section of a Belt Machine

Casting process – casting support

A cross-section of a belt machine is shown in Figure 2. Typically, supporting belts are 1.0 to 2.0 m wide and 10 to 100 m long. Stainless steel belts are between 1.0 and 2.0 mm thick. The belt channel allows a stream of air to flow in machine direction or counter direction. One of the two pulleys or drums is connected to a drive that requires extremely accurate speed control to avoid even slight speed variations. One drum is connected to a servo system that adjusts belt tension in order to ensure constant flatness and "absence" of belt movements (vibrations) in the critical area just behind the caster. Another important reason for tension control is the expansion and dilatation of the belt length caused by temperature changes. Belt machines need a guide system because the belt tends to shift during operation. The belt is guided by horizontal movements of the support drums. Optical or inductive sensors provide signals proportional to the belt edge offset. The signals are fed into the tension/guide control system. The two bearings of the 2nd support drum are moved equal distances in opposite directions to simulate centre pivoting. Many different support materials have been used for belts: Copper, silver-plated copper, chromium-plated steel, stainless steel, metal coated with polyvinylalcohol or gelatin, polyester film, PTFE film and other polymer films. At present the commonest support materials are stainless steel and chromium-plated surfaces. Important items for belt and drum machines are the material's heat conductivity, the technical processes used to create the required surface finish and the options for repairing small surface defects. The release behaviour of the semi-finished cast film from the support is pivotal to the process. Moreover, the supporting belts and their welded joints must be flexible enough to ensure long-term operation. Manufacturing a highly glossy belt surface is a tedious process lasting several weeks. There are not many suppliers of belts in the world. Typical geometrical specifications for the surfaces of stainless steel bands are: stainless steel NC 22V, thickness 1.4 mm, thickness tolerance 20 microns, surface finish Ra = 0.02 microns, Rt = 0,1 micron. Further, the specification of the thickness variation of the welding seam is very important and usually customer-specific. The cast technique permits simple production of films with structured surfaces. The belt surface is clearly and accurately replicated on one surface of the film. The techniques used to adapt the surface of the drums or belts to highly glossy, structured or matt film finishes are proprietary methods that have been developed over many years.

A cross-section of a drum casting line is shown in Figure 3. Nowadays drums are typically 4 to 8 m in diameter and 1.20 m to 1.50 m wide. The drum is tightly sealed to prevent vapour emissions and to direct the air stream against the direction of drum movement. There are separate temperature zones to provide fast drying and to facilitate strip-off from the drum. The drum surface are usually made from stainless steel or chromium plated steel.

A third type of casting support is a moving plastic film with a defined surface structure and special release properties, see Figure 4. The support films are generally PTFE or siliconized PET. The support film length is limited, but automated splicing devices are used to avoid interruptions of the continuous film casting.

Each of the three solvent cast production methods has advantages and disadvantages in terms of investment cost, production speed, production cost, film quality etc. The first preference for the selection of a process is the feasibility to produce a film from a specific raw material

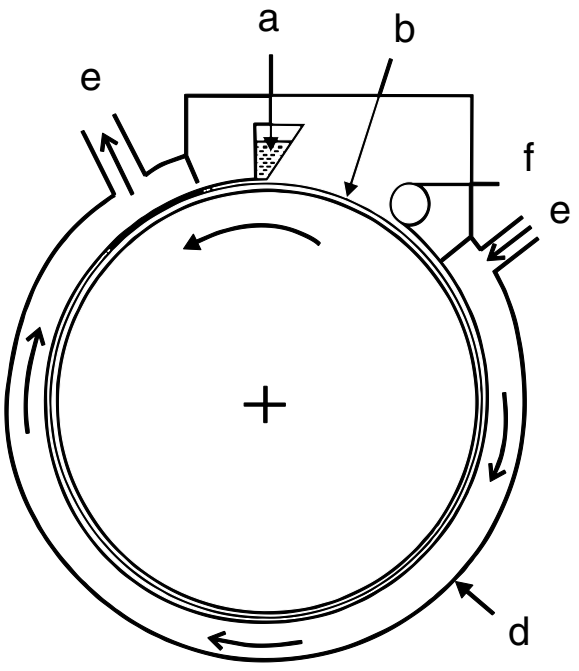

a = caster, die, hopper
b = drum surface
d = drum channel
e = drying air
f = film take-off

Fig. 3 Cross-section of a Drum Casting Machine

combination with the intended thickness and the other specified quality requirements.

Caster

This device (caster, spreader, die, hopper) is an important key element of cast technology. The dope is pumped by a special pump through heat exchangers into the spreader. The function of the spreader is to distribute the liquid homogeneously over a span of 1 to 2 meters. The thickness profile of the resulting liquid film should be as accurate as possible. The hydrostatic pressure between the centre and edges of the caster slot has to be equilibrated by mechanical design as shown in Figure 5 [6]. It is essential to keep the temperature of the liquid in the caster constant because the resulting viscosity changes result in inhomogeneous thickness distribution. Various types of die systems are used, only two examples are shown in Figure 6. There are many different caster constructions designed for the various processes [7].

In any case, the following principles have to be considered.

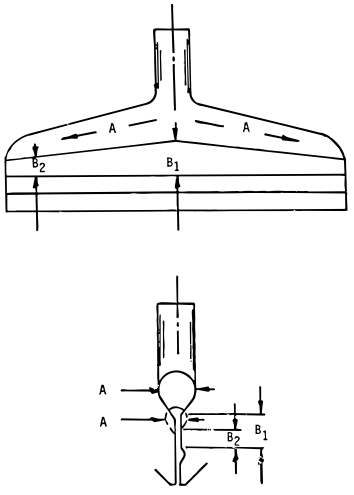

A = manifold of coathanger die
B1/B2 = preland sections

Fig. 5 Caster Lay-out for Solvent Casting

Fig. 4 Cross-section of a Support Film Casting Line

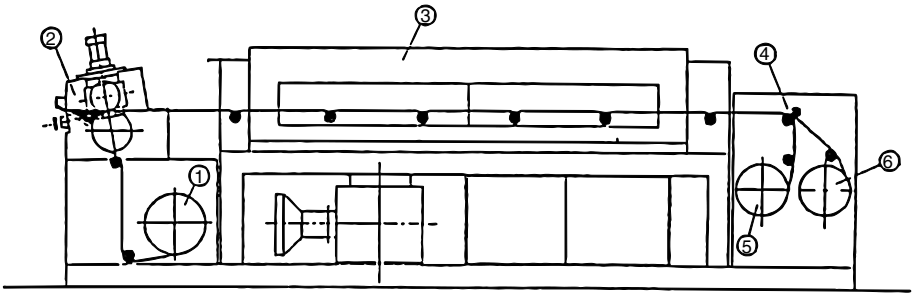

1 = support film unwinder
2 = T-die
3 = flat bed dryer
4 = separation point
5 = support film winder
6 = product film winder

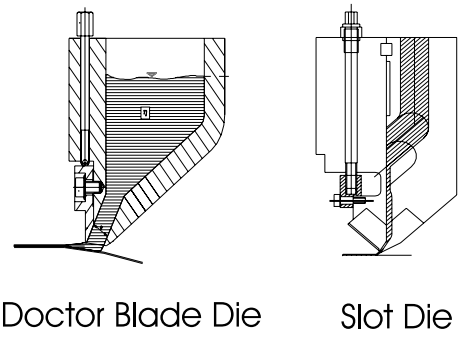

Fig. 6 Cross-section of dies for Solvent Casting

- The rheological situation in governed by laminar flow
- Pressure differences across the profile have to be equilibrated
- Small internal mechanical defects such as thickness variations in the slot or changes in surface roughness can cause film profile defects
- The appearance of transverse lines in the film product can be avoided by adjusting geometry, support speed, viscosity and flow parameters

More detailed evaluation of process parameters for slot coaters by means of computational fluid dynamics is described elsewhere [8].

Drying process

First drying step

The drying assemblies for casting-on-film lines, belt machines and drum machines are constructed quite differently to achieve optimum results. The various methods include indirect heating, heating by radiation and air-stream drying. They can be separated or combined in different zones to increase the accuracy of control over film formation and film drying at the support surface. Heated air with no solvent or a low solvent concentration is blown in, the solvent-loaded air is exhausted by fans and directed to the solvent recovery unit.

The treatment of the first liquid film in the machine with solvent loaded air is state-of-the-art for preventing surface distortions during the film formation process. Controlled air flow, e.g. for avoiding vortices is also important. Maintaining a temperature balance between the dope, support surface temperature and air temperature during the very first continuous evaporation of the solvent out of the liquid film is one of the most difficult jobs of the film casting process, see Figure 7. In addition, the film take-off from the support needs precision adjustment of process conditions. Usually, the film is cooled down during the last step to reduce tackiness. If the tackiness is too low, the film detaches from the downside of the belt or drum and the process has to be stopped immediately. In the first step, film formation on the belt or drum typically yields films with a relatively high residual solvent content. In this step, there is only one open surface. Both open surfaces of the film are subsequently dried using more effective drying equipment. The drying process is separated into two steps for a special reason. Thermoplastic polymer-solvent systems display different diffusion regimes. When solvent concentrations are high, the glass transition temperature falls below the process temperature. As a result, the diffusion coefficient of the solvent in the film is high and rapid evaporation takes place. Below a certain concentration limit and depending on the chemical nature of the combination, e.g. near 3 to 6% residual solvent, the glass transition temperature rises to a temperature higher than

Fig. 7 Temperature Balance in Film Formation Process

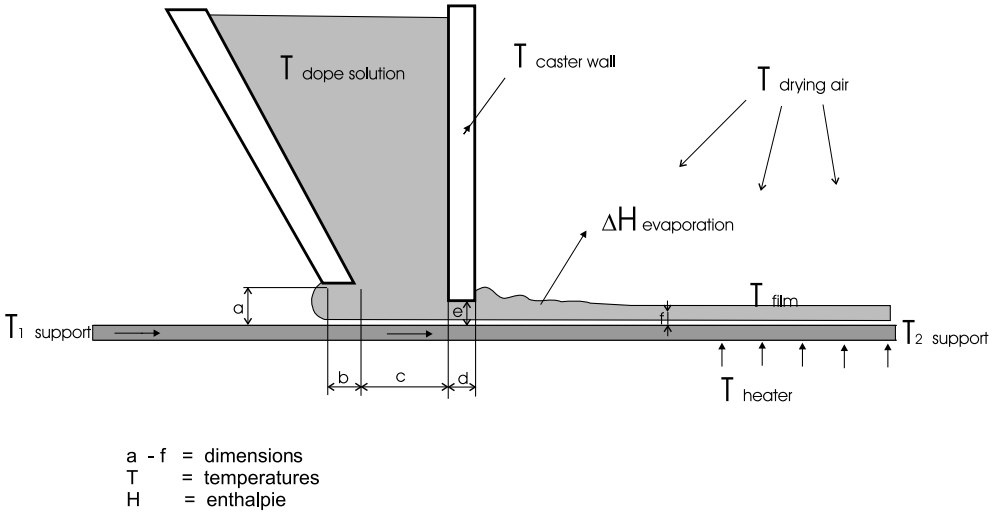

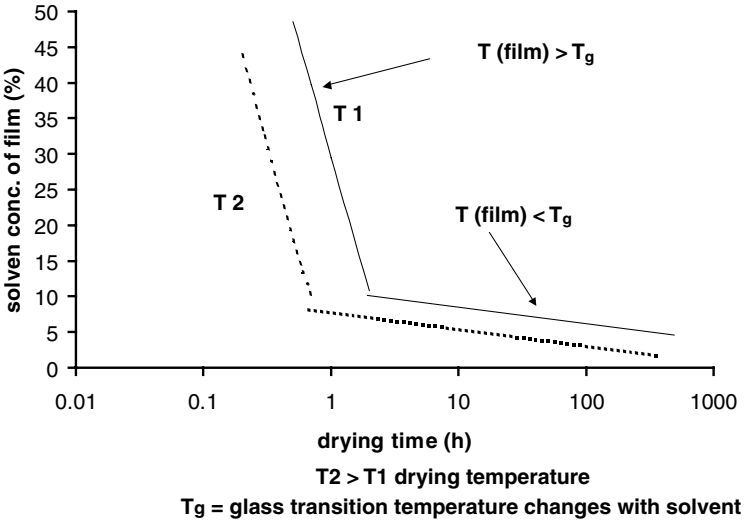

Fig. 8 Drying Conditions – Two Different Diffusion Regimes

process temperature. The resulting diffusion coefficient can be 1000 × lower than before, see Figure 8. Therefore, the process conditions are adjusted to avoid early solidification of the surface – i.e. to avoid a low diffusion coefficient and slow drying. Occasionally, chilling is necessary as a first process step. Depending on dope type, temperature and machine construction, the residence time of films on a belt or drum is between 0.2 and 20 minutes. Residual solvent at strip-off can vary between 3% and 40%. The available process condition options are governed to a very large extent by the type of material combination. Detailed mathematical modeling of the film drying process was investigated by several groups [9].

Second drying step

As explained before, primary and secondary drying are generally necessary before and after strip-off in each case. The film at the end of the support is in some cases cooled down by cooling rollers or chilled air. This reduces its sensitivity to mechanical surface defects and increases its mechanical strength. Different dryer systems exist and a combination is often used. A floating bed dryer or a clamp process is used by some companies to avoid surface scratches resulting from contact with rollers, see Figure 9. [10]

Efficient drying requires air streams from both sides. This can be achieved for instance by looping the film around a series of polished rollers in drying cabinets employing jet streams of filtered clean air, see Figure 10. The exhaust air from the dryers goes to solvent recovery as well. Heated rollers can be used for special high-efficiency drying and IR radiators are used sometimes in the last part of the drying process. Depending on the length of the drying track, a puller roller system consisting of several electrically connected and controlled puller motors is required.

At the end of the drying process, edge slitting knifes and knurling equipment are installed. Knurled edges or, as an alternative, protective film are needed to prevent the surfaces of the single laps from blocking during wind-up. Web tension control and side edge control for the product rolls is standard in the film industry. Even after a drying process with residual solvent contents of less than 0.5%, the film still has different properties at its air-side and support-side surfaces, according to the film formation process. The solvent diffusion coefficient of a given polymer-solvent combination is the crucial parameter governing production speed. Nowadays, the typical production speed for casting lines is 10 ... 60 m/min, or in area terms depending on the film width > 600 to 6000 square meters/h.

In-line coating

It is possible to apply coatings to the film during the drying process, but it will not explained in detail here. In-line coating should be mentioned because it is a standard process in the photo film industry and consumes a vast amount of solvent cast films. Coating equipment is integrated into the middle of the drying track. Both surfaces can then be coated and several layers subsequent applied. Organic solvent- or water-based coatings are dried on the film surface before it comes into contact with the next roller. Air jets and infrared devices are used to enhance drying speed and sometimes the coatings require a UV- or heat-curing step (hard coat, anti-glare coating). Roll coating or slot coating techniques are used to apply curl correction, gelatine substrate, antistatic, slip agent, a

Fig. 9 Clamp or Tenter Dryer

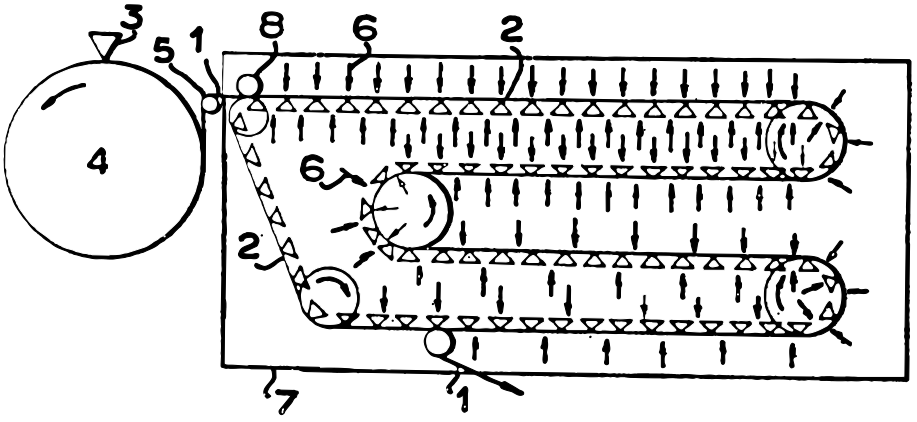

1 = film
2 = pin tenter
3 = casting die
4 = support drum
5 = stripping roll
6 = hot air
7 = drying chamber
8 = grooved roll

colored layer, diffusion barriers, optically active liquid crystal layers, magnetically active layers and others.

Solvent recovery and handling

Legislative conditions

Obviously, solvent casting cannot be mastered without detailed know-how and experience in handling organic solvents. Some of the most commonly used solvents for casting purposes are methylene chloride, methanol and acetone. Use of these solvents is subject to numerous restrictions. The table of limit concentrations for exposure illustrates German regulations is shown in Table 2. There are many more regulations governing the construction and operation of casting facilities as well as discharging. In Germany, for instance, more than 400 laws and regulations on environmental issues and healthcare have to be taken on board. Extra tight

Fig. 10 Air Flotation Dryer – Roller cabinet

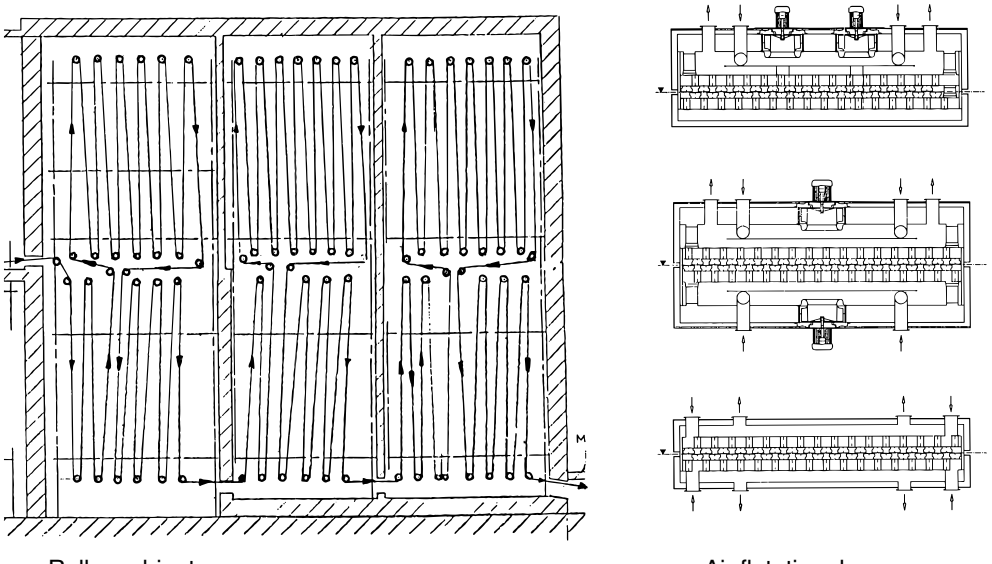

Roller cabinet

Air flotation dryers

Table 2 Environmental, Safety and Occupational Exposure of Solvents

Regulations in Germany Solvent	Typical use of solvent	* 8 h- TWA limits [mg/m^3]	** STEL [mg/m^3]	Max. exhaust air concentration [mg/m^3]	Max. wastewater concentration [mg/l]	*** LEL * 0.5 [g/l]
Acetone	Solvent for PVDF, Coating solutions	1200	4800	150	2	30
Methanol	Solvent for TAC, coating solutions	260	1040	150	10	36
Methylene chloride	Solvent for PC, PES, PEI, TAC	360	1440	20	0,1	230

*8 h-TWA = 8 hours time weighted average
**STEL = Short time exposure limit
***LEL = Lower explosion limit

casings, fittings, seals, double-shell tanks with automatic leakage monitors, extra retention basins for incidents, explosion-proof equipment, automatic fire detectors and sprinklers, automatic in-line measurements of exhaust air from the recovery process, solvent detectors for waste water etc. are part of the established standards for newly constructed lines. In several companies, the air in working zones is monitored continuously, in others it is monitored specifically during critical processes such as dope filter changes. No more details will be discussed here on this item because there are many differences in legislation, not only between countries, but also between states and even local authorities.

Recovery and incineration

Table 3 shows a summary of suitable recovery and decomposition processes for solvents [11].

Adsorption process

The most effective and flexible recovery process in terms of reducing solvent concentrations to very low levels is the adsorption process using activated charcoal. Other adsorbents such as silica gels, zeolites and polymer beads have also been tested [12]. The standard adsorption process runs discontinuously and alternatively in two or more columns, see Figure 11.

Table 3 Solvent Recovery and Combustion – Optimum Process Feed Concentration

Indirect Condensation	> 50 g/m^3
Adsorption process	1–100 g/m^3
Absorption process	1–50 g/m^3
Direct condensation	> 25 g/m^3
Membrane process	> 20 g/m^3
Thermal oxidation	> 10 g/m^3
Catalytic oxidation	3 ... 10 g/m^3
Bio filter	0.2–3 g/m^3

De-sorption is performed by means of a hot nitrogen stream or by steam. The charcoal bead has to be dried and cooled before the start of the next adsorption cycle, see Figure 12. After steaming out, the solvent-water mixture is condensed and distilled. If a binary or ternary solvent was used, a series of columns is needed for purification. Typical performance data for activated charcoal absorbers are: 5 tons of activated charcoal can

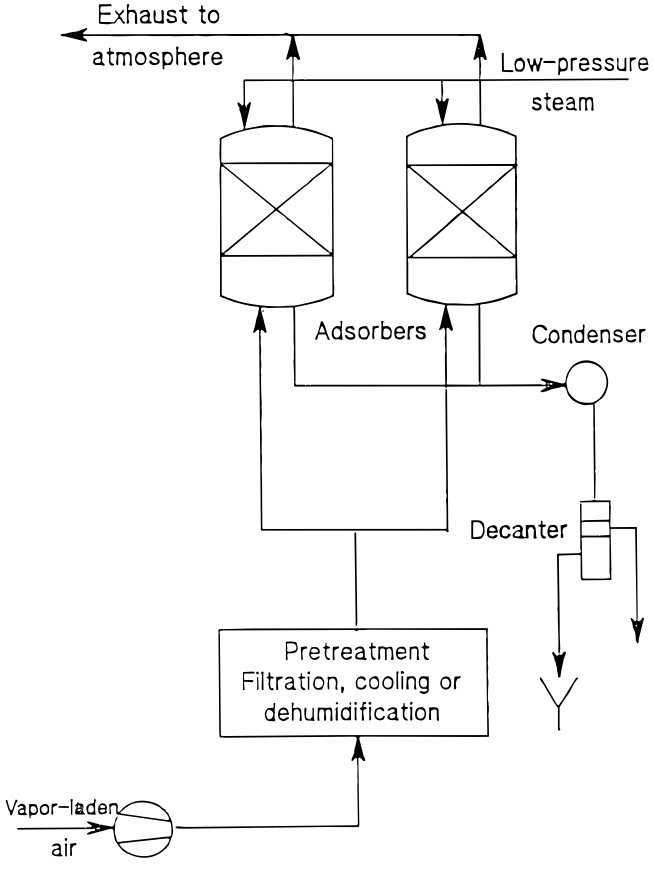

Fig. 11 Solvent Recovery Process by Adsorption

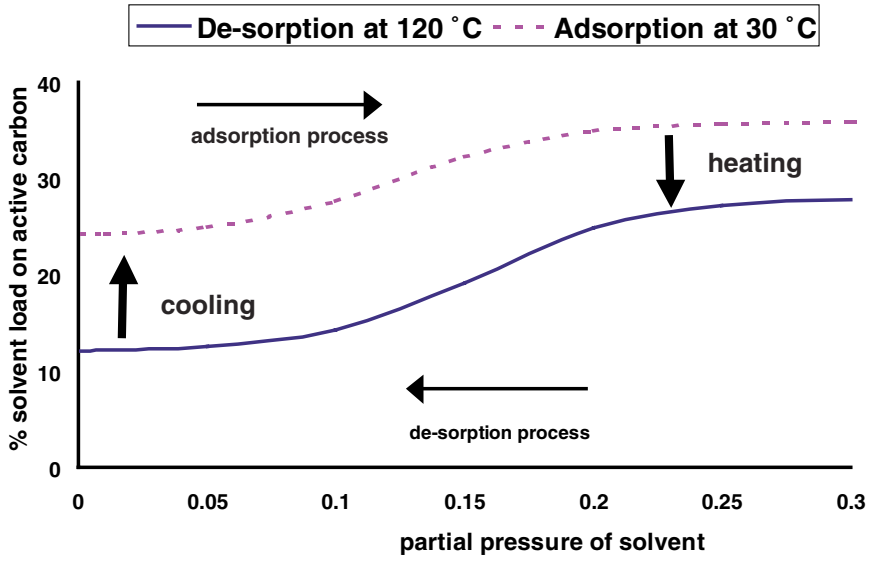

Fig. 12 Adsorption / Desorption Isotherms of Active Carbon

adsorb a differential load of about 600 kg of methylene chloride. Depending on volume flow, feed gas concentration and bead diameter, one loading cycle can vary between 3/4 of an hour and 3 hours. The purified gas contains only 1 – 5 ppm solvent and reaches 20 ppm at the end of the loading process according to the legal regulations. About 0.8 kg steam of steam is required to recover 1 kg of solvent – i.e. steam consumption is an important cost factor in solvent recovery by this method. Other adsorptive substances have been tried, but they are either ineffective or too expensive for organic solvents. A system of continuous adsorption using a system of circulating activated charcoal pellets has been put forward. In practice, however, adsorber charcoal debris levels were too high, resulting in valve pollution etc. and in higher adsorber material consumption costs. The "wheel process" is another attempt to continuously run the adsorption process with activated charcoal instead of using columns.

Absorption process

In the search for other continuously operating recovery principles, the absorption into liquid carrier was adopted and plants of this type set up in several sites, diagram in Figure 13. The most important parameter governing this process is the partition coefficient of a specific solvent to a specific liquid carrier. The temperature dependency of this coefficient is used to absorb and desorb the solvent in a similar way to the adsorption process. Unfortunately, to run the process effectively many solvents need cooling in the absorption step. This increases recovery costs substantially. The carrier liquid should be stable over many years without significant degradation. Substances with low vapour pressure and high boiling points are preferred to permit solvent recovery by a simple stripping process. For instance diethyleneglycolmethylether was used in a recovery plant for a mixture of the solvents ethanol and trichloroethylene [13]. Table 4 shows a comparison of both recovery methods. Unfortunately, it is impossible to achieve a very low exhaust air solvent concentration as legally required for solvents with high vapour pressures, such as methylene chloride.

Cooling-out

Cooling can be a very effective way of cleaning the process air, depending on the boiling point of the solvent.

In the case of commonly used solvents, large amounts of energy have to be consumed to achieve the required low concentration in clean air. On the other hand, continuously operating condensers are compact and low-maintenance. As a result, cooling devices are used to recover solvents for the make-up of the process air in the casting line, Figure 14. Given the vapour pressure curve, the high solvent concentration in air can be reduced to the equilibrium concentration at a given temperature with only moderate power consumption.

Incineration – thermal or catalytic

These are not really solvent recovery methods so much as ways of recovering thermal energy [14]. Thermal incineration is generally required for complex mixtures of solvents if separation by distillation is too expensive. A similar reason is the use for production lines which use various solvents at different times. The flexibility to switch over to another solvent in a short time cannot be achieved in the recovery systems discussed before.

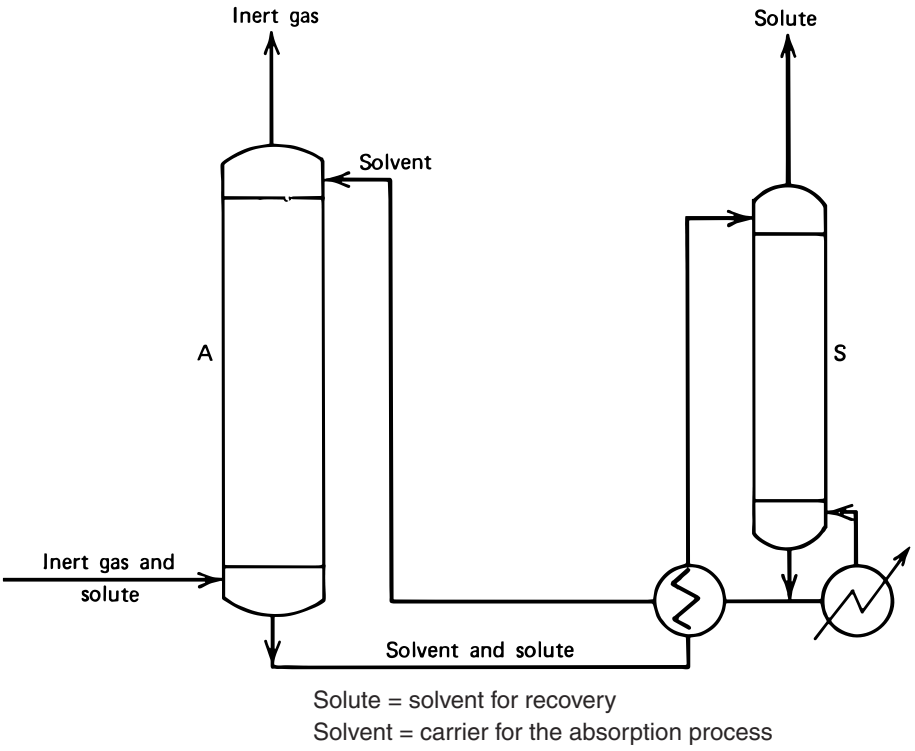

Fig. 13 Solvent Recovery Process by Absorption

Table 4 Comparison of Adsorption and Absorption for Solvent Recovery Process

	Adsorption (Active Carbon)	Absorption (Liquid)
Use of energy	> 10 kW/kg solvent	> 6 kW/kg solvent
Process	Discontinuous, many mechanical parts	Continuous, few mechanical parts
Technical experience	> 80 years	> 20 years
Feed concentration	A wide range of concentrations possible	Mainly for concentrations > 20 g/m^3
Concentration in cleaned air	Low, < 20 ppm (for Methylene Chloride)	Medium for solvents with low boiling points
Corrosion	Corrosive products by catalytic degradation	Negligible
Probability of incidents	Medium (active carbon)	Low
Purity of recovered solvent	Solvent – water mixture, degradation products	High purity without additional purification steps

Products and Markets

Principal advantages and drawbacks of solvent cast films

The main advantage of solvent cast technology is caused by the unique process drying a liquid on a surface without applying further mechanical or thermal stress. Additionally, dope handling and filtration offer a variety of specific features for the final product. Advantages are:

- Homogeneous thickness distribution
- Highest optical purity, free of gels or specks
- Excellent transparency, low haze
- Isotropic orientation, low optical retardation, excellent flatness
- Processing of thermally or mechanically sensitive components is feasible
- Possibility of production of high-temperature resistant films from non-melting but soluble raw materials

There are constraints on the types of polymer films for which solvent casting technology must or cannot be used. Relatively few materials can be processed into films by both methods – slot extrusion and solvent casting. In these cases, a cost-performance comparison decides. Very thin films cannot be produced by extrusion without stretching, very thick films are very costly to produce by solvent casting and lamination. In general, solvent-cast products are more expensive than extruded film to manufacture for several reasons:

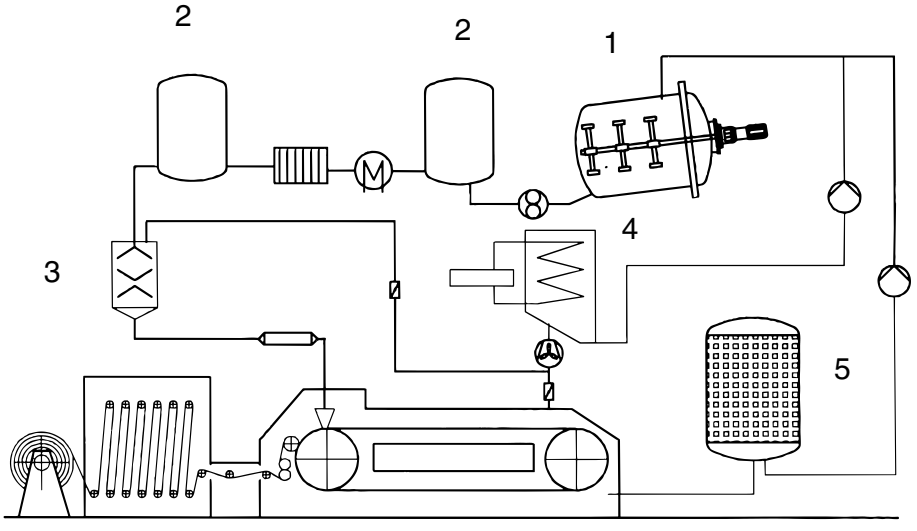

Fig. 14 Internal Solvent Recovery by Cooling

- Slow production speed depending on a slow solvent diffusion process
- Extra energy costs of solvent recovery
- Investments in facilities for handling solvents and dope solutions

On the other hand, the performance and, more specifically, the high quality of solvent cast films cannot be achieved using other processes. This will described in the next chapter.

Examples for solvent cast films

Photographic application

The largest areas of solvent cast films are produced for photographic use. About ~ 300 million square meters of cellulose triacetate film base are used every year for 35 mm amateur films, movie films and other film types. The market is rapidly declining since 2002 because of the fierce competition of digital photography.

LCD applications

Optical polarizers are based on polyvinylalcohol films cast from an aqueous solution. This film is stretched and doped with iodine or organic dyes to provide the polarizing function. The polyvinylalcohol polarizing layer is usually protected against mechanical and other environmental effects by two cellulose triacetate films with highest optical properties and very low birefringence, see Figure 15 [5]. Each LC display needs two polarizers by virtue of the physical principles governing the electro-optical effect of the liquid crystals.

The fastest-growing area of solvent cast films with more than 20% growth per year is the production of optical cellulose triacetate film for manufacturing polarizers for LC displays. The quality requirements are much

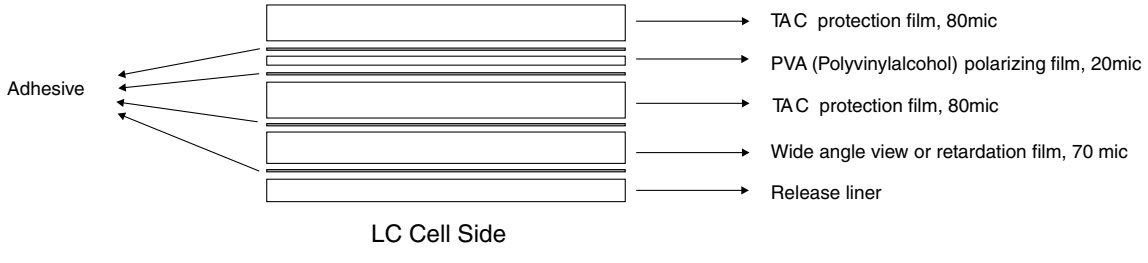

Fig. 15 Cross-section of a LCD polarizer

higher than for photographic TAC film base. The actual consumption in 2004 was about 200 Mio square meters / year. A recent application is the use of LC displays for TVs (up to 62 inch screen). This will rapidly increase the use of cellulose triacetate based solvent cast film in the near future.

Polycarbonate is used for several specialty films, some of them designed for optical purposes. Compensation or retardation film is required in STN LCD displays to correct the color appearance, increase contrast and viewing angle [15]. Recently, a new type of cyclic olefinic polymer ARTON ^{R} was introduced for the application wide view angle enhancement in TFT LCD [16]. The ARTON ^{R} film is produced by solvent casting in volumes of several million square meters per year [17]. It allows a viewing angle of more than 170° and is mainly used in LCD TV sets.

Other optical applications

Cellulose diacetate, soluble in acetone, is converted to films by means of solvent coating mainly in thicknesses between 14 and 200 microns. Since about 1950, big volumes have been used for applications such as print lamination, graphic arts, windows in food stuff boxes, photographical sleeves, googles and visors. The advantages of this film type are high gloss levels, excellent transparency and a good balance between moisture resistance and water permeability. That makes it an ideal film especially for the combination together with paper or carton. The actual consumption of the cellulose diacetate films is about 4000 to 4500 tons/ year [18].

Another optical application is a solvent cast film made from polycarbonate for the use in a new type of optical storage media "blue ray disc" [19].

Electrical and Electronic applications

Other advantages of cast film technology are important for electrical and electronic applications. Electrical properties that are stable at high temperatures over the long term can only be achieved with polymers with high or no melting temperatures. Processing of highly purified and filtered polymers with high glass transition temperatures, high bulk resistivity and a low dissipation factor is possible. It is often not feasible to produce these films using thermoplastic manufacturing methods. In some cases, a soluble polymer such as poly (amide carboxylic) is cast from solutions in dimethylacetamide to form a film which is subsequently cross-linked with acetic anhydride during the casting process. Typical products are base materials for flexible printed circuits, insulation films, wrappings, capacitors etc.

Polymers such as polycarbonates, polyimides, etc. are used for these purposes. Consumption of this type of film is increasing with the growth of the electronic industry and the development of new, more sophisticated electronic devices. The sales forecast for just one type of polyimide film (KAPTON ^{R}) for 2004 is about 3000 tons with high added value.

High-temperature applications

Some of the high-temperature applications are identical to the list shown above for electrical / electronic use. Depending on the temperature requirements and the chemical composition of the polymer, cast film techniques can be used for release films. Polyimides, cellulose triacetate and others are the typical raw materials.

Another emerging area is the application of high-temperature resistive films for LCDs, as already mentioned, and as substrate materials for OLED displays [20]. Feasible trial films have been made on the basis of polyether sulfone, polycarbonate, cyclic polyolefins, polyarylates and polyimides.

Diverse Applications

There are various film applications which require the specific advantages of the solvent cast film process:

- Very high load of filler or functional compounds
- Homogeneous thickness distribution
- Gauges of 100 mic or below
- Low shrinkage

The products have a variety of specific properties:

High electrical or thermal conductivity, high magnetic coercivity, conductivity of protons for fuel cell membranes, substrate for diagnostic films with a defined optical remission, highly filled films for tamper-proof labels, weather-proof labels etc.

Acoustic membranes produced from solvent cast films have to possess:

- Very thin gauges and a matt surface
- Isotropic mechanical properties before and after thermoforming
- Long-term stability under mechanical stress

These membranes are used in normal-sized and miniature loudspeakers, e.g. for mobile phones. Typical raw materials are polycarbonate and polyarylate [21].

To achieve a controlled pore structure, another inherent advantage of solvent casting is used [22]:

- Solubility, partial solubility in solvents and in-line precipitation and extraction process

Products based on proprietary processes have been used for diuresis membranes, desalination membranes, waste water purification and other membrane processes for many years. Cellulose derivates, polysulfones and polyimides have been used for these purposes.

Conclusion

The oldest technology for the production of thin polymer films is nowadays used for niche products with high quality requirements such as photographical film base, flexible printed circuits, high-temperature resistive films, loudspeaker membranes etc. In recent years, mainly new optical applications needed new amorphous films with highest clarity and specific optical birefringence properties. In most cases, these amorphous films are not easily accessible by Ruland's structural investigation methods, because the absence of microdomains or crystallinity is one of the assumptions to provide good solubility in organic solvents and in particular a perfect glass-like appearance after the film formation process. The future of solvent cast technology will be closely linked to the need of optical films by the emerging liquid crystal display industry or other new optical applications which require polymer films with outstanding properties.

Acknowledgement I am most honoured to have the opportunity to proffer my profound gratitude to Professor Ruland, who was able, during my thesis work, to explicate the mysteries of the reciprocal room ... even to a chemist.

References

1. Collins D (1990) The story of Kodak. HN Abrams Inc, New York
2. Steven, Lefferts (1896) USP 573928
3. Couzens EG (1968) A short history of the film casting process and its products. Bexford Ltd, Essex
4. Adelstein PZ et al (1972) Manufacture and physical properties of film. Paper and plates. 127 ff, Neblette's handbook of photography and reprography
5. Sata H, Murayama M, Shimamoto S (2004) Properties and application of cellulose triacetate film. p 323–333, Macromol. Symp. 208 (2004)
6. Lippert HG (1987) Polymers, lamination and coatings conference. 193 ff
7. Durst F et al (1989) Coating, 434 ff
8. Müller C et al (1997) Sensitivity analysis of slot coaters, p 1–15, University of Erlangen-Nürnberg, von Karman Institute for fluid dynamics. Lecture series 1997–6
9. Alleborn et al (1997) Analysis of film drying. Lecture series 1997–06, University Erlangen-Nürnberg: Thin liquid and coating processes
10. Takeda R et al (1992) USP 5 152 947 Fuji Photofilm
11. Nitsche M (1991) Technische Mitteilungen 84: 72
12. Mathews W (1991) Technische Mitteilungen 84: 78
13. Lerch H (1991)Technische Mitteilungen 84: 87
14. Calowitz O (1991) Technische Mitteilungen 84: 94
15. Nagoshi T (1998) Optical films and methods for producing the same, EP 0992331 A1
16. Fukuda T Kagaku kogaku 61, 405–407
17. EP 1342 745 A1
18. Law PW, Longdon A, Willins GG (2004) Macromol. Symp. 208: 293–323
19. EP 1 195 758 A
20. Angiolini S (2002) Eurodisplay 22, Le Club Visu-SID France p 907–910
21. EP 0306905
22. Melzner D (2002) Funktionspolymere für Systemlösungen, GDCh Fachgruppe Makromolekulare Chemie, Vortragstagung Darmstadt:59

Progr Colloid Polym Sci (2005) 130: 15–19
DOI 10.1007/b107393
Published online: 3 June 2005

Zaicheng Sun
Jun Zeng
Haoqing Hou
Holger Wickel
Joachim H. Wendorff
Andreas Greiner

Preparation of poly(p-xylylene) TUFT-tubes containing Palladium, Silver, or Copper Nanoparticles

Abstract Poly(p-xylylene) (PPX) tubes with palladium nanoparticles were prepared by the so-called TUFT process (tubes by fiber templates process) and subsequent heating steps. Poly(L-lactide) (PLA) with palladium diacetate ($Pd(OAc)_2$ as soluble precursor for Pd was electrospun to form composite fibers. The Pd precursor loaded PLA fibers were coated by PPX via chemical vapor deposition (CVD). Two annealing procedures were applied to these electrospun composite fibers. Firstly, electrospun PPX/$Pd(OAc)_2$ fibers were annealed at 170 °C for 4 hours under argon atmosphere for the conversion of $Pd(OAc)_2$ to Pd nanoparticles. Subsequently, the PLA template fibers were removed by annealing at 360°C for 4 hours under vacuum. The resulting PPX tubes were doped by Pd nanoparticles distributed along the inside of the PPX tubes. However, deposition of Pd nanoparticles on the outside of the PPX nanotubes was observed when the otherwise infinitely long composite precursor PPX/Pd/PLA tubes were cut at the ends prior to annealing. Following the same concept PPX/Ag and PPX/Cu tubes were prepared.

Keywords PPX · Nanoparticles · Electrospinning

Dedicated to Professor Dr. W. Ruland on the occasion of his 80th birthday

Z. Sun · J. Zeng · H. Hou · H. Wickel
J. H. Wendorff · A. Greiner (✉)
Department of Chemistry and Scientific Center of Materials Science, Philipps University of Marburg,
Hans-Meerwein-Strasse,
35042 Marburg, Germany
e-mail: greiner@staff.uni-marburg.de
Tel.: +49-6421-2825573
Fax: +49-6421-2825785

Metal nanoparticles are of great interest for a variety of applications in catalysis, optics, biomedics just to name a few [1]. Numerous systems such as diblock copolymers micelles [3,2], diblock copolymer film [3], dendrimers [4], zeolites [5], nanoporous carbon [6], phospholipid membranes [7], and inverse microemulsions [8] were used for the synthesis of nanoparticles and their immobilization on confined geometries. For the synthesis of metal nanoparticles, the key step is to stabilize the particles in nanometer size and prevent their aggregation to form bigger particles. To date, a large number of methods have been explored to synthesize metal nanoparticles. Normally, acid or amino groups are used as sites to adsorb the metal salt by ionic bonds. Then the reductant is added into the system in order to transform the salt to metal. In order to stabilize the metal nanoparticle suspension, long chain alkylsulfhydrate, surfactants or polymer with thiol group have been employed [9,10,11,12].

Our group has accomplished the preparation of PPX tubes containing Pd by the so-called TUFT-process (TUFT = tubes by fiber templates) [13]. According to the TUFT process degradable polymer template nanofibers obtained by electrospinning [14] were coated by other materials (polymer or metal). Tubes from polymers were developed by selective removal of the core template fibers. Metal loaded TUFT-tubes were obtained either by sequential coating of the template fibers, by physical vapor deposition, or by processing of the template fibers in the presence of metal precursor compounds which were converted to elemental metals by annealing resulting in PPX nanotubes with a Pd core layer.

Topic of this work is the more detailed exploration of Pd containing PPX TUFT-tubes and the transfer of the synthetic concept to other metals.

Results and discussion

PPX nanotubes with Pd nanoparticles were prepared by coating of PLA/$Pd(OAc)_2$ template fibers and subsequent annealing as schematically shown in Fig. 1. PLA/$Pd(OAc)_2$ template nanofibers with diameters in the range of 100 – 500 nm were obtained by electrospinning of solutions of PLA (1–2 w/w%) and $Pd(OAc)_2$ (5 – 20% related to PLA) in dichloromethane (Fig. 2). It should be mentioned here that electrospun fibers are practically endless but were limited here by the width of the frames shown in Fig. 1 (1 cm).

The PLA/$Pd(OAc)_2$ template nanofibers were coated by CVD with PPX according to the procedure of Gorham [15]. The thickness of the PPX coating was controlled by the amount of the PPX-precursor [2.2]paracyclophane and was adjusted to 200–500 nm. Subsequently, the fibers were heated to 170 °C for 4 hours under argon atmosphere for conversion of $Pd(OAc)_2$ to Pd nanoparticles. Wide angle X-diffraction pattern (WAXS) of PLA/$Pd(OAc)_2$/PPX composite fibers showed prior to annealing at 170 °C no peaks in the range of $2\theta = 30° - 50°$, however, after annealing broad peaks were observed at $2\theta = 40°$ and $2\theta = 46.5°$, which indicated the formation of crystalline Pd (Fig. 3).

Finally, heating to 360 °C for 4 hours in vacuum (10^{-2} mbar) resulted in quantitative degradation of PLA to volatile products (dilactide). The WAXS pattern in the region between $2\theta = 40 - 46.5$ remained unchanged as obvious from Fig. 3. The conversion of $Pd(OAc)_2$ and the degradation of PLA was also confirmed by the comparison of the IR-spectra of as prepared and heated samples. After heating to 170 °C and 360 °C signals for acetate moieties of $Pd(OAc)_2$ and PLA disappeared whereas the peaks characteristic for PPX remained.

In contrast to our previous report individual Pd nanoparticles are now clearly visible inside the PPX nanotubes (Fig. 4). The diameters of the Pd nanoparticles were centered on 10 nm and are not agglomerated. The Pd nanoparticles obviously did not penetrate the PPX layer, which also indicates that the precursor $Pd(OAC)_2$ does not penetrate into the PPX layer upon heating.

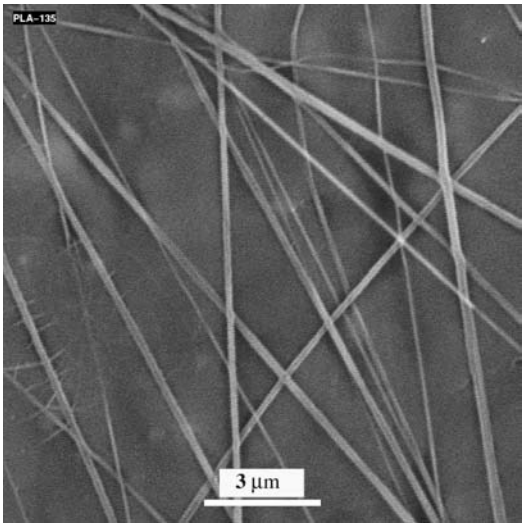

Fig. 2 SEM micrograph of electrospun PLA / $Pd(OAc)_2$ composite nanofibers

Interestingly, PPX tubes can be also prepared with Pd nanoparticles on the outside wall of the PPX tubes. PLA / $Pd(OAc)_2$ composite fibers were obtained by electrospinning from a 3 weight % PLA/$Pd(OAc)_2$ solution in dichloromethane (w% PLA/w% $Pd(OAc)_2$ = 1 : 1) and coated subsequently by PPX via CVD as previously described resulting in PLA/$Pd(OAc)_2$/PPX composites. Cutting of these composite fibers with a scalpel resulted in tubes with open ends as shown for PPX tubes (Fig. 5)

PPX tubes with Pd nanoparticles on the outside of the tubes were obtained by annealing of the cut PLA/$Pd(OAc)_2$/PPX composite fibers (Fig. 6). The size of the Pd particles were centered around 50 nm. The factors governing the sizes and shapes of the particles and the

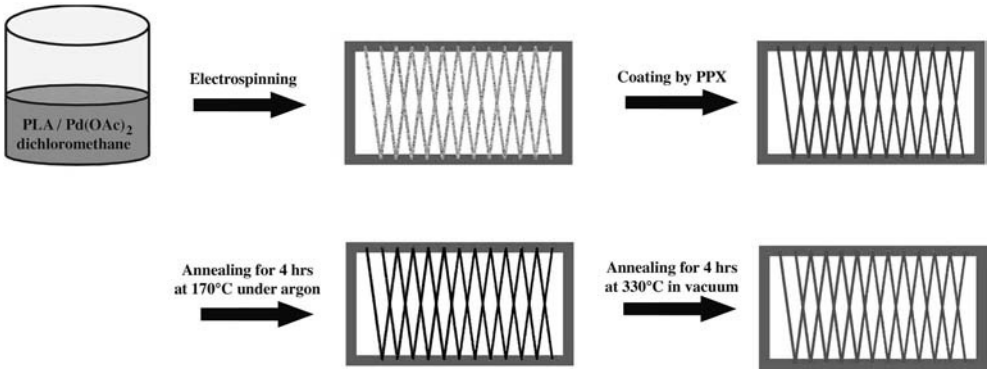

Fig 1. Schematic graph for the preparation process of Pd-doped PPX nanotubes

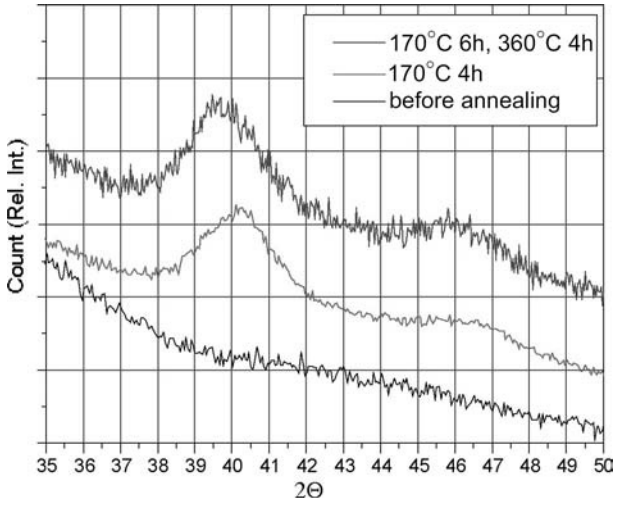

Fig. 3 WAXS pattern of PLA-$Pd(OAc)_2$-PPX composite fibers (20 % $Pd(OAc)_2$) between $2\theta = 35° - 50°$ as prepared, after heating to170 °C for 4 hours and after heating to 360 °C for 4 hours

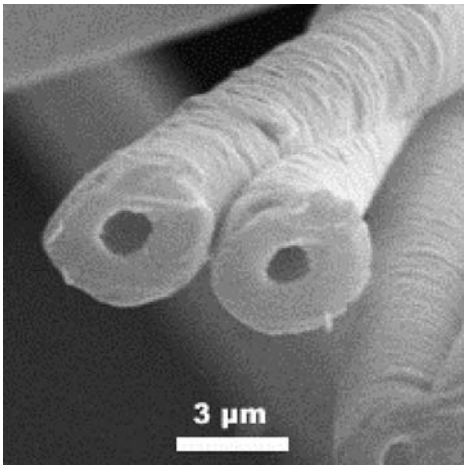

Fig. 5. SEM micrograph of PPX tubes with open ends obtained by cutting of the PPX tubes with a scalpel (just one end of the tubes was cutted)

mechanism of the process of Pd formation on the outside of the tubes remained till now unclear. However, it is obvious that Pd nanoparticles are inside as well as outside of the PPX tubes after annealing of cut tubes.

Following the same procedure but with $Pd(OAc)_2$ replaced by silver acetate or copper acetate in the PLA template fibers and no cutting of the tube ends prior to annealing resulted in PPX tubes with silver or copper nanoparticles inside the PPX tubes (Fig. 7).

Experimental

Materials and methods

Poly(L-lactide) (PLA, Boehringer/Ingelheim, M_n = 420.000 M_w = 670.000, M_w/M_n = 1.60 obtained by gel permeation chromatography versus polystyrene standards with a set of three columns with chloroform as solvent (300 × 8 mm, type SDV, 10 μm from PSS) using a differential refractometer as detector at 25 °C), $Pd(OAc)_2$, Ag(OAc), and $Cu(OAc)_2$ (Aldrich), and

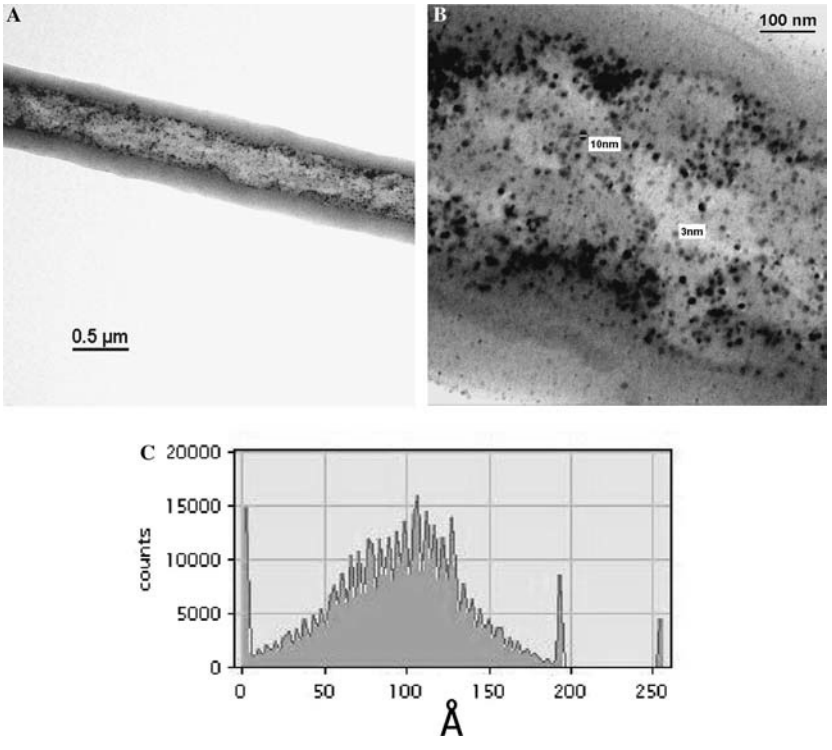

Fig. 4 TEM micrograph of unstained PPX nanotubes containing Pd nanoparticles at different magnifications (A, B) and size distribution of the Pd nanoparticles (C)

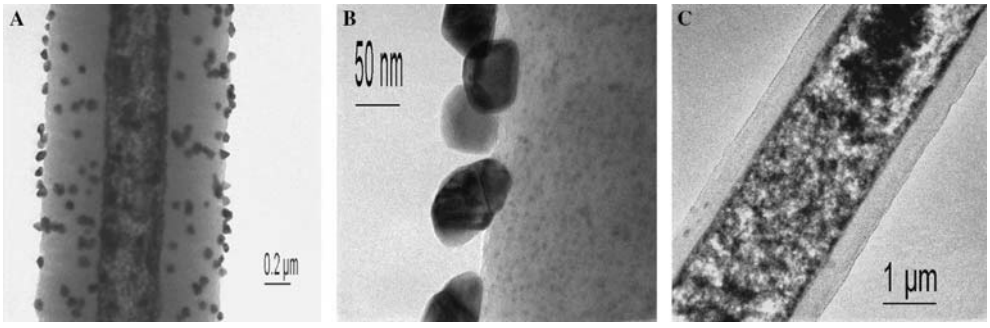

Fig 6 TEM micrograph of cut and annealed (385 °C, 0.01 mbar, 5 hrs) PPX / Pd nanotubes (A, B) and uncut annealed (365 °C, 0.01 mbar, 3 hrs) PPX /Pd nanotubes (C)

[2.2]paracyclophane (Specialty Coating Systems) were used as received.

Wide-angle x-ray scattering (WAXS) was performed with a Siemens D5000 goniometer using Cu-K_α radiation. Scanning electron microscopic (SEM) images of the nanotubes were obtained using a Cam Scan 4 microscope operated at an accelerating voltage of 15 kV. The SEM samples were prepared by attaching a small piece of the nanotube mat to a SEM sample holder via a conductive sticking tape. A thin film of Au amounting to a thickness of about 5 nm was coated onto the sample surface using the Edwards AUTO 306 coating system. Transmission electron microscopic (TEM) images were obtained using a JEM 3010 microscope operated at 300 kV.

General procedure for the preparation of PPX tubes containing Pd nanoparticles

PPX nanotubes with Pd nanoparticles were prepared by coating of PLA/$Pd(OAc)_2$ template fibers and subsequent annealing as schematically shown in Fig. 1. For the preparation of PLA/$Pd(OAc)_2$ nanofibers homogeneous solutions of 1–2 wt% of PLA with 5 – 20 w-% $Pd(OAc)_2$ (related to PLA) was prepared. Electrospinning of these solutions was done by an electrospinning apparatus described earlier[13b]. The voltage was set to 40–60 kV. The spinning rate was adjusted to 2 ml/hour. The distance of the electrodes was adjusted to 10 cm. The fibers were collected using an aluminum frame with 1 cm width of the bars as described earlier [16]. The nanofibers collected on the aluminum frame were coated by PPX following the Gorham procedure [17] in a Lab Coater (Specialty Coating Systems) using [2,2] paracyclophane (200 mg) as precursor resulting in a 200 nm PPX coating.

The PPX/PLA/$Pd(OAc)_2$ composite fibers were subjected to annealing for 4 hours at 170 °C under argon atmosphere and for an additional 4 hours at 330 °C under vacuum resulting in Pd doped PPX nanotubes.

Conclusions

PPX TUFT-tubes loaded with metal nanoparticles such as Pd-, Ag-, or Cu-nanoparticles can be prepared by processing of PLA/metal acetate composite

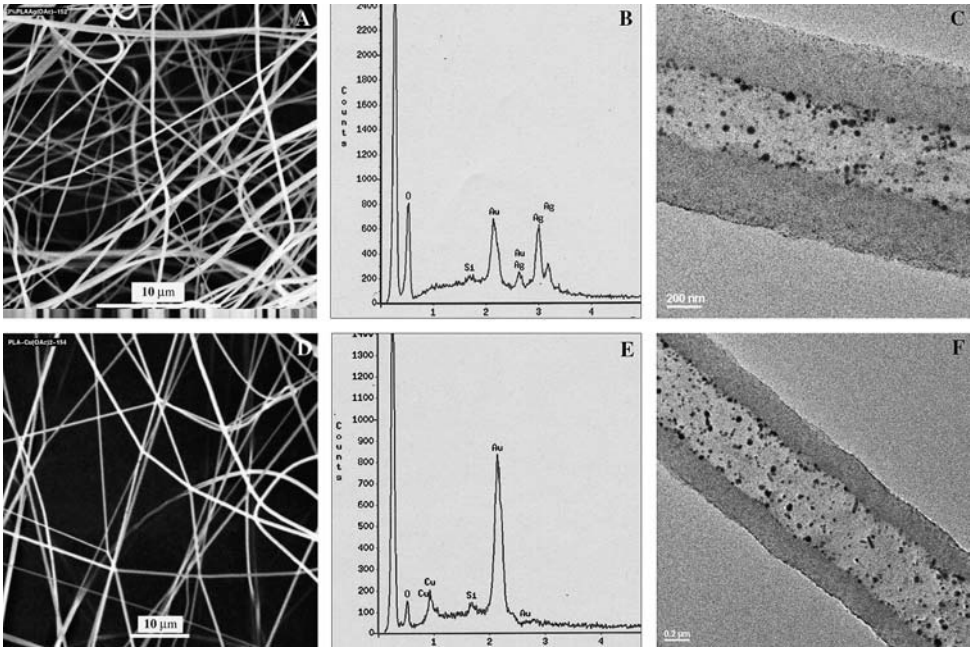

Fig. 7 SEM micrographs and EDX analysis of electrospun PLA/AgOAc (A, B) and PLA/$Cu(OAc)_2$ (D, E) composite nanofibers and TEM micrographs of PPX nanotubes with Ag nanoparticles (C) and Cu nanoparticles (F) obtained from corresponding composite fibers. The presence of Ag and Cu resp. was clearly proved by EDX analysi

nanofibers via electrospinning, followed by coating of these composite fibers by PPX via CVD, and finally by conversion of metal acetate to metal nanoparticles and degradation of PLA. Metal nanoparticles remained on the inside of the PPX nanotubes with uncut tubes where as metal nanoparticles were seeded on the outside of the tubes after cutting tubes. It may be speculated whether low temperature metal-organic vapor deposition as previously observed for other Pd precursors[18] led to Pd nanoparticle formation on the outside of the tubes when cutted composite fibers were used. Research on this issue is ongoing and will be the topic of forthcoming papers.

Acknowledgement Financial support by Alexander von Humboldt Foundation (Z.S.), Deutsche Forschungsgemeinschaft, and Bundesministerium für Bildung und Forschung is greatly appreciated. The authors are thankful for the kind donation of PLA (Boehringer Ingelheim) and [2.2]paracyclophane (Specialty Coating Systems).

References

1. For an overview see: ''Nanoparticles'', ed. Rotello V, Kluwer Acad Plenum Publ, N.Y. 2004.
2. (a) Beecoft LL, Ober CK, (1997) Chem Mater 9: 1302. (b) Spatz JP, Roescher A., Sheiko S, Krausch G, Möller MV (1995) Adv Mater 7: 1000. (c) Corbierre MK, Cameron NS, Sutton M, Mochrie SGJ, Lurio LB, Rühm A. (2001) Lennox RB, J Am Chem Soc 123: 10411
3. Cienien JF, Cohen RE, Duran A (1999) Mater Sci Eng 7: 45
4. (a) Crooks RM, Zhao M, Sun L, Chechik V, Yeung LK (2001) Acc Chem Res 34: 181 and reference therein. (b) Balogh L, Tomalia DA (1998) J Am Chem Soc 120: 7355 (c) Vassilev K, Kreider J, Miller PD, Ford WT (1999) React Funct Polym, 41: 205
5. Wang Y, Herron N (1988) J Phys Chem 92: 4988
6. Joo SH, Chol SJ, Oh L, Kwak J, Liu Z, Terasaki O, Ryoo R (2001) Nature 412: 169
7. Zhao XK, Barai S, Rolandi R, Fendler JH (1988) J Am Chem Soc 110: 1012
8. Dresco PA, Zaitsev VS, Gambino RJ, Chu B, Langmuir (1999) 15: 1945
9. (a) Damle C, Biswas K, Sastry M, Langmuir (2001) 17: 7156 (b) Selvan ST, Spatz JP, Klok HA, Möller M, (1998) Adv Mater 10: 132 (c) Watkins JJ, McCarthy TJ, Chem Mater (1995) 7: 1991
10. (a) Corbierre MK, Cameron NS, Sutton M, Mochrie SG, Lurio LB, Ruehm A, Lennox RB (2001) J Am Chem Soc 123: 10411 (b) Liu Z, Pappacena K, Cerise J, Kim J, During CJ, O'Shaughnessy B, Levicky R (2002) Nano Lett 2: 219
11. Mirkin CA, Letsinger RL, Mucic RC, Storhoff JJ (1996) Nature 382: 607
12. (a) Wuelfing WP, Gross SM, Miles DT, Murray RW (1998) J Am Chem Soc, 120: 12696. (b) Mandal TK, Fleming S, Walt DR, (2002) Nano Lett, 2: 3
13. (a) Hou H, Jun Z, Reuning A, Schaper A, Wendorff JH, Greiner A (2002) Macromolecules 35: 2429 (b) Bognitzki M, Hou H, Ishaque M, Frese T, Hellwig M, Schwarte C, Schaper A, Wendorff JH, Greiner A (2000) Adv Mater 12: 637 (c) Caruso R, Schattka JH, Greiner A (2001) Adv Mater 13: 1577
14. For recent reviews on electrospinning see: (a) Fong H, Reneker DH, In: ''Electrospinning and the formation of nanofibers'' in ''Structure formation of polymeric fibers'', (ed) D.R. Salem, M.V. Sussman, p. 225–246, Hanser 2000. (b) Huang ZM, Zhang YZ, Kotaki M, Ramakrishna S (2003) Comp Sci Techn 63: 2223 (c) Dersch R, Greiner A, Wendorff JH, ''Polymer Nanofibers by Electrospinning'' In: Dekker Encyclopedia of Nanoscience and Nanotechnology, p. 2931, (eds) Schwartz JA, Contescu CI, Putyera K, Marcel Dekker, NY 2004.
15. Gorham WF (1966) J Polym Sci Part A-1 4: 3027
16. Dersch R, Liu T, Schaper AK, Greiner A., Wendorff JH (2003) J Polym Sci: Part A: Polym Chem Ed, 41, 545.
17. Gorham WF (1966) J Polym Sci Part A-1 4: 3027.
18. Hierso JC, Feurer R, Kalck P (2000) Chem Mater 12: 390

Progr Colloid Polym Sci (2005) 130: 20–28
DOI 10.1007/b107337
Published online: 3 June 2005

Salvino Ciccariello

X-ray and neutron scattering: classical versus quantum-statistical relations

Abstract We review the classical as well as the quantum-statistical derivations of the scattering intensities for x-ray and neutron scattering. The comparison of the two expressions show how the electron or the scattering-length classical densities are related to the corresponding quantum-statistical quantities. The further assumptions usually considered in the case of small-angle scattering are also discussed.

S. Ciccariello
Dipartimento di Fisica "G. Galilei" e
unità INFM, via F. Marzolo 8,
35131 Padova, Italy
e-mail: circcariello@pd.infn.it

Classical derivation

The basic formula of x-ray classical crystallography simply states that, for any sample, the observed scattering intensity $I(\mathbf{q})$ is linearly related (through a known quantity) to the square modulus of the Fourier transform (FT) $\tilde{n}(\mathbf{q})$ of the electron density $n(\mathbf{r})$ of the sample. [In the above expressions $\mathbf{q}$ is related to the scattering vectors $\mathbf{q}_{\text{in}}$ and $\mathbf{q}_{\text{out}}$ of the ingoing and outgoing x-rays as $\mathbf{q} = \mathbf{q}_{\text{in}} - \mathbf{q}_{\text{out}}$. The scattering is assumed to be elastic. Thus, $q_{\text{in}} = q_{\text{out}} = 2\pi/\lambda$ and $q = (4\pi/\lambda)\sin(\theta/2)$, where λ denotes the wave-length of the x-ray radiation and θ the scattering angle.] The derivation of this relation can be performed in two apparently different ways based however on the same physical assumptions, as it will appear clear from the following brief review.

a) First derivation

This is that reported by Guinier and Warren [1,2]. The ingoing x-ray beam is described by a plane, monochromatic electromagnetic (e.m.) wave whose electric and magnetic components respectively are $\mathbf{E}_{\text{in}}(\mathbf{r},t) = \mathbf{E}_0 \mathrm{e}^{-i(\omega t - \mathbf{r}\cdot\mathbf{q}_{\text{in}})}$ and $\mathbf{B}_{\text{in}}(\mathbf{r},t) = \hat{\mathbf{q}}_{\text{in}} \times \mathbf{E}_{\text{in}}(\mathbf{r},t)/c$, with $\hat{\mathbf{q}}_{\text{in}} = \mathbf{q}_{\text{in}}/|\mathbf{q}_{\text{in}}|$, $\omega = c|\mathbf{q}_{\text{in}}|$, $\mathbf{E}_0 \cdot \mathbf{q}_{\text{in}} = 0$, $|\mathbf{E}_0|$ simply related to the beam intensity and c denoting the light speed in the vacuum. Consider now a free point-like particle with mass m, electric charge e and velocity $\mathbf{v}$. This particle creates a further e.m. field that is not a "radiating" field as far as the particle's velocity is constant, since both the electric and the magnetic component at a distance R from the charge decrease as R^{-2} instead of R^{-1}, as required for a radiating field. Assume now that the charge set at the point $\mathbf{r}_1$ be invested by the ingoing plane wave. At time t, it will experience Lorentz' force $e\big(\mathbf{E}_{\text{in}}(\mathbf{r}_1,t) + \mathbf{v}(t) \times \mathbf{B}_{\text{in}}(\mathbf{r}_1,t)\big)$. The particle will then acquire an acceleration and, according to Liènard-Wieckert's solutions of the Maxwell equations (see Section 4.1 of Jackson[3]), it generates now an e.m. field that is the sum of a non-radiating and a radiating term. If the velocity of the particle, before this be invested by the ingoing wave, is small in comparison with c, the oscillatory nature of $\mathbf{E}_{\text{in}}(\mathbf{r},t)$ ensures that property $|\mathbf{v}(t)| << c$ holds true throughout the time [and that $\mathbf{r}_1(t)$ does not appreciably change during a short time interval]. In this case, relativistic mechanics reduces to classical mechanics and Liènard-Wieckert's radiating e.m. field created by the accelerated particle at a generic point $\mathbf{r}_0$, in SI units, reads

$$\mathbf{E}_{\text{rad}}(\mathbf{r}_0,t) = -\left[\frac{\mathrm{e}\mathbf{a}_\perp(\mathbf{r}_1,t)}{4\pi\epsilon_0 c^2|\mathbf{r}_1-\mathbf{r}_0|}\right]_{\text{ret}} = -\left[\frac{\mathrm{e}^2\mathbf{E}_{\text{in},\perp}(\mathbf{r}_1,t)}{4\pi\epsilon_0 c^2 m|\mathbf{r}_0-\mathbf{r}_1|}\right]_{\text{ret}}$$
$$= -\left(\frac{\mathrm{e}^2}{4\pi\epsilon_0 mc^2}\right)\left[\frac{\mathbf{E}_{o,\perp}\mathrm{e}^{-i(\omega(t-|\mathbf{r}_0-\mathbf{r}_1|/c)-\mathbf{q}_{\text{in}}\cdot\mathbf{r}_1)}}{|\mathbf{r}_0-\mathbf{r}_1|}\right]_{\text{ret}}, \tag{1a}$$

$$\mathbf{B}_{\rm rad}(\mathbf{r}_0,t) = -\Big(\frac{\mathrm{e}^2}{4\pi\epsilon_0 mc^3}\Big) \times \Big[\frac{(\mathbf{r}_0-\mathbf{r}_1)\times\mathbf{E}_{o,\perp}\mathrm{e}^{-i(\omega(t-|\mathbf{r}_0-\mathbf{r}_1|/c)-\mathbf{q}_{\rm in}\cdot\mathbf{r}_1)}}{|\mathbf{r}_0-\mathbf{r}_1|^2}\Big]_{\rm ret}. \tag{1b}$$

Here $\mathbf{a}_\perp$ ($\mathbf{E}_{{\rm in},\perp}$) is the component of particle's retarted acceleration $\mathbf{a}$ (ingoing electric field) orthogonal to the vector $[\mathbf{r}_0-\mathbf{r}_1]_{ret}$ and $\mathbf{r}_1$ is the particle position at the time t' that, compared with the actual time t, is retarded of the amount $|\mathbf{r}_0-\mathbf{r}_1(t')|/c$ necessary to the light for travelling from the particle position $\mathbf{r}_1(t')$ to the point $\mathbf{r}_0$ where we want to determine the e.m. field of the charge accelerated by the ingoing e.m. plane wave. The approximation of retaining the only radiative terms in (1) increases with $|\mathbf{r}_0-\mathbf{r}_1|$, the accuracy being already $\sim 99\%$ when $|\mathbf{r}_0-\mathbf{r}_1|\approx 100\lambda$. In any scattering experiment set up, the ingoing e.m. field is essentially confined to the region delimited by the slits because the latter sizes are large enough, in comparison to the ingoing beam wave-length, to make diffraction effect negligible for the ingoing beam. Since the detectors are located outside the aforesaid region, the energy going through a detector is only due to the e.m. field generated by the charged particle and given by (1) when $\mathbf{r}_0$ denotes the point where the detector is located. It is convenient to write Eq. (1) in a form that more explicitly accounts for the retard condition. The particle velocity being small in comparison with c, to a first approximation we have that

$$t-|\mathbf{r}_0-\mathbf{r}_1(t')|/c \approx t-|\mathbf{r}_0-\mathbf{r}_1(t)|/c \text{ and } \mathbf{r}_1(t')\approx\mathbf{r}_1(t). \tag{2}$$

Moreover, the particle moves within a box whose size is quite small in comparison with the (mean) distance (denoted by R_0) of the box from the detector. Then, the direction of the vector $\mathbf{r}_0-\mathbf{r}_1(t)$, whatever t, approximately coincides with that of the vector joining a point of the box to the point where the detector is located. The direction of this vector is that of $\hat{\mathbf{q}}_{\rm out}\equiv\mathbf{q}_{\rm out}/|\mathbf{q}_{\rm out}|$. Thus, $\omega|\mathbf{r}_0-\mathbf{r}_1(t)|/c=(2\pi/\lambda)|\mathbf{r}_0-\mathbf{r}_1(t)|=(2\pi/\lambda)\hat{\mathbf{q}}_{\rm out}\cdot(\mathbf{r}_0-\mathbf{r}_1(t))=\mathbf{q}_{\rm out}\cdot(\mathbf{r}_0-\mathbf{r}_1(t))$. In this way, the quantity inside square brackets on the right hand side (rhs) of (1a) becomes

$$\begin{aligned}&\Big[\frac{\mathbf{E}_{0,\perp}\mathrm{e}^{-i(\omega(t-|\mathbf{r}_0-\mathbf{r}_1(t')|/c)-\mathbf{q}_{\rm in}\cdot\mathbf{r}_1(t'))}}{|\mathbf{r}_0-\mathbf{r}_1(t')|}\Big]_{\rm ret}\\ &\quad\approx\frac{\mathbf{E}_{0,\perp}\mathrm{e}^{-i(\omega t-\mathbf{q}_{\rm out}\cdot\mathbf{r}_0)}\mathrm{e}^{i(\mathbf{q}_{\rm in}-\mathbf{q}_{\rm out})\cdot\mathbf{r}_1(t)}}{|\mathbf{r}_0-\mathbf{r}_1(t)|}\\ &\quad\approx\frac{\mathbf{E}_{0,\perp}\mathrm{e}^{-i(\omega t-\mathbf{q}_{\rm out}\cdot\mathbf{r}_0)}\mathrm{e}^{i\mathbf{q}\cdot\mathbf{r}_1(t)}}{R_0},\end{aligned} \tag{3}$$

and the radiative e.m. field is

$$\mathbf{E}_{\rm rad}(\mathbf{r}_0,t)\approx-\Big(\frac{\mathrm{e}^2}{4\pi\epsilon_0 mc^2}\Big)\frac{\mathbf{E}_{0,\perp}\mathrm{e}^{-i(\omega t-\mathbf{q}_{\rm out}\cdot\mathbf{r}_0)}\mathrm{e}^{i\mathbf{q}\cdot\mathbf{r}_1(t)}}{R_0} \tag{4a}$$

$$\mathbf{B}_{\rm rad}(\mathbf{r}_0,t)\approx-\Big(\frac{\mathrm{e}^2}{4\pi\epsilon_0 mc^3}\Big)\frac{\hat{\mathbf{q}}_{\rm out}\times\mathbf{E}_{0,\perp}\mathrm{e}^{-i(\omega t-\mathbf{q}_{\rm out}\cdot\mathbf{r}_0)}\mathrm{e}^{i\mathbf{q}\cdot\mathbf{r}_1(t)}}{R_0}. \tag{4b}$$

It is noted that these fields only depend on the particle position through the phase factor $\mathrm{e}^{i\mathbf{q}\cdot\mathbf{r}_1}$ that involves the scattering vector $\mathbf{q}$.

The differential cross-section is easily obtained as the ratio between the time averaged intensity of the e.m. field (4) within the infinitesimal solid angle $d\Omega$ and the density of the time averaged energy flux of the ingoing beam. Assuming the latter unpolarized and that the polarization of the outgoing x-ray be not detected, one finds the so-called Thomson or classical differential cross-section of a point-like charged particle (see Section 1.1 of Ref. [2] for details)

$$\sigma_{\rm Th}(\theta)\equiv\frac{d\sigma}{d\Omega}=\Big[\frac{\mathrm{e}^2}{4\pi\epsilon_0 mc^2}\Big]^2\ \frac{1+\cos^2\theta}{2}. \tag{5}$$

If we have N particles, with equal mass m and electric charge e, that move within a box whose size is very small in comparison to its distance from the detector and assuming that the velocity of each particle is much smaller than c, by the same reasoning reported above one concludes that the radiating e.m. field is

$$\mathbf{E}_{\rm rad}(\mathbf{r}_0,t)\approx-\Big(\frac{\mathrm{e}^2}{4\pi\epsilon_0 mc^2}\Big)\frac{\mathbf{E}_{0,\perp}\mathrm{e}^{-i(\omega t-\mathbf{q}_{\rm out}\cdot\mathbf{r}_0)}}{R_0}\sum_{j=1}^{N}\mathrm{e}^{i\mathbf{q}\cdot\mathbf{r}_j(t)}, \tag{6a}$$

$$\mathbf{B}_{\rm rad}(\mathbf{r}_0,t)\approx-\Big(\frac{\mathrm{e}^2}{4\pi\epsilon_0 mc^3}\Big)\frac{\mathbf{q}_{\rm out}\times\mathbf{E}_{0,\perp}\mathrm{e}^{-i(\omega t-\mathbf{q}_{\rm out}\cdot\mathbf{r}_0)}}{q_{\rm out}R_0}\sum_{j=1}^{N}e^{i\mathbf{q}\cdot\mathbf{r}_j(t)} \tag{6b}$$

and[1] the differential cross-section for the unpolarized case becomes

$$d\sigma=\sigma_{Th}(\theta)\Big\langle\Big|\sum_{j=1}^{N}e^{i\mathbf{q}\cdot\mathbf{r}_j(t)}\Big|^2\Big\rangle_t d\Omega$$

while the "standard" scattering intensity or differential cross-section is

$$I(\mathbf{q})\equiv\frac{1}{\sigma_{Th}(\theta)}\frac{d\sigma}{d\Omega}=\Big\langle\Big|\sum_{j=1}^{N}e^{i\mathbf{q}\cdot\mathbf{r}_j(t)}\Big|^2\Big\rangle_t. \tag{7}$$

Here, the angular brackets denote a time average over the particle positions. This average is generally required

[1] In writing (6a) and (6b) we use the linearity of Maxwell's equations but we are also assuming that the e.m. field of a particle does not affect the motion of another particle. The last approximation is known as the kinematical one and it is no longer accurate for an intense ingoing field. In this case, the accurate theory is that of dynamical scattering thoroughly described by Authier [4].

owing to the fact that the collection of the scattered signal requires a certain amount of time. This is very large compared to the period of the ingoing e.m. beam to make the use of the time averaged intensities accurate. On the other hand, in some cases, it can be so large to make the variations of $\mathbf{r}_j(t)$ appreciable and, consequently, the time average unavoidable. The number density of the charged particles within the box, at time t, is

$$n(\mathbf{r},t)=\sum_{j=1}^{N}\delta(\mathbf{r}-\mathbf{r}_j(t)), \tag{8a}$$

where $\delta(\cdot)$ denotes the Dirac function, and its FT

$$\tilde{n}(\mathbf{q},t)\equiv\int n(\mathbf{r},t)\mathrm{e}^{i\mathbf{q}\cdot\mathbf{r}}dv=\sum_{j=1}^{N}\mathrm{e}^{i\mathbf{q}\cdot\mathbf{r}_j(t)} \tag{8b}$$

clearly coincides with the expression present within the modulus in Eq. (7). In conclusion, the standard intensity is the time average of the square modulus of the FT of the particle number density of the charged particles present within the box. When the particles are in thermodynamical equilibrium, the time average can be substituted with an ensemble average, on the basis of the ergodic assumption and Eq.(7) takes the well-known classical form

$$I(\mathbf{q})=\langle|\tilde{n}(\mathbf{q})|^2\rangle. \tag{9}$$

This expression is the departure point for further approximations. Before discussing the latter, it is convenient to add some remarks on result (9). First, it is recalled that the energy range considered in condensed matter physics is low enough to consider the matter as made up of atoms' bound states. Hence, the constituent charged particles only are electrons and protons. These have a mass $\sim$2000 times larger than that of electrons and, due to (1), the corresponding radiating e.m. fields are $\sim$2000 times smaller than the electron ones. Thus, in the case of X-ray, one can confine himself to consider only the electrons so that the sum present in Eq. (8) will only consider the electrons of the sample and one simply speaks of electron number density. Second, the derivation of (7) or (9) was based on the assumption of point-like particles that move very slowly and on the use of classical e.m. theory. This theory is accurate for particles that do not move too fast but is unable to explain the atomic structure. This can only be understood in a quantum-mechanical framework. Besides, quantum mechanics tells us that only the electrons lying in the outermost shell have a kinetic energy small enough to make the condition $|\mathbf{v}|<c$ obeyed. To circumvent this difficulty, we observe that a coarse-grain average of (8a) over a small sphere of radius δ centered at $\mathbf{r}$, *i.e.*

$$\bar{n}(\mathbf{r},t)\equiv\int_{|\mathbf{r}'-\mathbf{r}|<\delta}n(\mathbf{r}',t)\mathrm{d}v', \tag{10}$$

leads to a continuous number density function whose FT does not differ from (8b) as far as $q<2\pi/\delta$. This implies that the derivation of (9) holds also true starting from a continuous charge distribution since this can be looked at as the collection of the infinitesimal charges $e\bar{n}(\mathbf{r},t)dv$ located at all possible points $\mathbf{r}$ of the box. Each of these infinitesimal charges can play the role of the point-like charge considered in (1). [By so doing, the mass also must be considered infinitesimal and such that $q/m\rightarrow\mathrm{d}q/\mathrm{d}m=q/m$.] On the basis of this result, one can now use the quantum-mechanical result that the electrons of an atomic structure form a cloud around the nucleus in the sense that, if $\Phi_0(\mathbf{r}_1,\mathbf{r}_2,\ldots,\mathbf{r}_M)$ is the wave function associated to the atom's ground state, $|\Phi_0(\mathbf{r}_1,\mathbf{r}_2,\ldots,\mathbf{r}_M)|^2$ represents the probability density of finding the M constituting electrons in the infinitesimal volume elements $\mathrm{d}v_1,\ldots,\mathrm{d}v_M$ located, respectively, at $\mathbf{r}_1$,..,$\mathbf{r}_M$. Then the particle number density of the electrons around the nucleus set at the origin is simply given by the continuous function

$$n_{at}(\mathbf{r})=\int\ldots\int\left[\sum_{j=1}^{M}\delta(\mathbf{r}-\mathbf{r}_j)\right]|\Phi_0(\mathbf{r}_1,\mathbf{r}_2,..,\mathbf{r}_M)|^2\mathrm{d}v_1..\mathrm{d}v_M. \tag{11}$$

If we have N atoms (each consisting of M electrons, for greater simplicity), located at $\mathbf{r}_1,\ldots,\mathbf{r}_N$, we can apply the same considerations to each atom of the sample (neglecting the interations between particles belonging to different atoms). In this way the particle number density of the sample is

$$n(\mathbf{r},t)=\sum_{j=1}^{N}n_{at}(\mathbf{r}-\mathbf{r}_j(t)), \tag{12}$$

and the (standard) scattering intensity is still given by Eq. (9) owing to the considerations developed between Eqs (10) and (11). In other words, once one assumes that the electron number density around an atomic nucleus is given by Eq. (11), the assumption that the electrons move very slowly is no longer required (see § 97 of Ref. [5]), because the electron motion is accounted for by the eigenfunction $\Phi_0(\mathbf{r}_1,\ldots,\mathbf{r}_M)$.

b) Second derivation

The second way of getting Eq. (9) is that reported by Landau and Lifshitz (see § 97 of Ref. [5]). One considers first the Maxwell equations within the sample invested by an e.m. plane wave with angular velocity ω. The ingoing field will generate a local density current and one has to find the solution of the Maxwell equations in presence of these induced sources. Conceptually, the physics is that of case (a). It is however useful to review this derivation because it can easily be extended to the case of an ingoing neutron beam. As it was already reported, we must only

consider the lightest particles, *i.e.* the electrons. Each of these experiences an acceleration equal to $e\mathbf{E}/m$ and, due to the time oscillatory behaviour of $\mathbf{E}$, the particle velocity is $\mathbf{v} = ie\mathbf{E}(\mathbf{r})e^{-i\omega t}/m\omega$. It has already been explained that the electron number density is given by (12). Moreover, the time dependence of $n(\mathbf{r}, t)$ occurs on a time scale much larger than that of the ingoing beam. Hence, to a first approximation, $n(\mathbf{r}, t)$ can be considered constant with respect to t (at least, on a time scale of $2\pi/\omega$) and the current density is $\mathbf{j}(\mathbf{r}, t) = en(\mathbf{r})\mathbf{v} = ie^2 n(\mathbf{r})\mathbf{E}(\mathbf{r})e^{-i\omega t}/m\omega$. The relevant Maxwell equations are

$$\nabla \times \mathbf{E}(\mathbf{r}) = i\omega\mathbf{B}(\mathbf{r}) = i\mu_0\omega\mathbf{H} \tag{13a}$$

$$\nabla \times \mathbf{B}(\mathbf{r}) = \nabla \times \mu_0\mathbf{H} = -i\mu_0\omega\epsilon_0[1 - e^2 n(\mathbf{r})/m\omega^2\epsilon_0]\mathbf{E}(\mathbf{r}). \tag{13b}$$

Eq. (13b) can be recast in the form

$$\nabla \times \mathbf{H} = -i\omega\mathbf{D} \tag{14a}$$

and the induction field $\mathbf{D}$ is equal

$$\mathbf{D} = \epsilon_0[1 - e^2 n(\mathbf{r})/m\omega^2\epsilon_0]\mathbf{E}. \tag{14b}$$

This expression shows that $e^2 n(\mathbf{r})/m\omega^2\epsilon_0$ can be considered as the perturbation "parameter". Taking the rotor of Eq. (13a), multiplied by ϵ_0, and using (14a) and (14b) we obtain

$$\nabla \times \nabla \times \mathbf{D} + (e^2/m\omega^2)\nabla \times \nabla \times \big(n(\mathbf{r})\mathbf{E}\big) = \omega^2\mu_0\epsilon_0\mathbf{D}$$

Recalling the vectorial identiy $\nabla \times \nabla \times = -\nabla^2 + \nabla(\nabla\cdot\ )$, the previous equation becomes

$$\nabla^2\mathbf{D}(\mathbf{r}) + (\omega^2/c^2)\mathbf{D}(\mathbf{r}) = (e^2/m\omega^2)\nabla \times \nabla \times \big(n(\mathbf{r})\mathbf{E}\big) \tag{15a}$$

The Green function of the equation $\nabla^2\phi(\mathbf{r}) + (\omega^2/c^2)\phi(\mathbf{r}) = \delta(\mathbf{r})$ is $\phi(\mathbf{r}) = e^{ikr}/4\pi r$ with $k^2 = \omega^2/c^2$. Then, the solution of (15a) is

$$\mathbf{D}(\mathbf{r}) = \frac{e^2}{4\pi m\omega^2}\int \frac{e^{ik|\mathbf{r}-\mathbf{r}'|}}{|\mathbf{r}-\mathbf{r}'|}\nabla' \times \nabla' \times \big(n(\mathbf{r}')\mathbf{E}(\mathbf{r}')\big)dv'. \tag{15b}$$

Here $\mathbf{r}'$ varies within the sample. Then, if $\mathbf{r}$ is very large, we have $k|\mathbf{r}-\mathbf{r}'| \approx \mathbf{q}_{\text{out}}\cdot(\mathbf{r}-\mathbf{r}')$. Besides, $\mathbf{E}(\mathbf{r}')$ can be substituted with the ingoing e.m. field $\mathbf{E}_0 e^{i\mathbf{q}_{\text{in}}\cdot\mathbf{r}'}$, because the remaining factor is already linear in the perturbation. Finally, integrating by parts, one gets

$$\mathbf{D}(\mathbf{r}) \approx \left[\frac{e^2}{4\pi m\omega^2}\right](\mathbf{q}_{\text{out}} \times \mathbf{q}_{\text{out}} \times \mathbf{E}_0)\int \frac{e^{i\mathbf{q}_{\text{out}}\cdot(\mathbf{r}-\mathbf{r}')}}{|\mathbf{r}-\mathbf{r}'|}n(\mathbf{r}')e^{i\mathbf{q}_{\text{in}}\cdot\mathbf{r}'}dv' \tag{16}$$

This equation clearly coincides with (6a) after observing that $\mathbf{r}$ corresponds to $\mathbf{r}_0$, that $\mathbf{r}$ lies outside the sample so that $\mathbf{D}(\mathbf{r}) = \epsilon_0\mathbf{E}(\mathbf{r})$, that $(\mathbf{q}_{\text{out}} \times \mathbf{q}_{\text{out}} \times \mathbf{E}_0) = -(\omega^2/c^2)\mathbf{E}_{0,\perp}$ and that, whatever $\mathbf{r}'$ within the sample, one can safely use the approximation $|\mathbf{r}-\mathbf{r}'| \approx R_0$ in the denominator.

Neutron scattering

Feigin and Svergun [6] showed how to use the previous derivation to get the differential cross-section for the scattering of neutrons from a sample. Actually this derivation cannot be considered as purely classical because we must use the quantum-mechanical assumption that neutrons are described by a wave-function that will momentarily be considered scalar. The wave-function of a single free neutron obeys the simplest form of Schrödinger equation, namely

$$i\hbar\frac{\partial\psi(\mathbf{r}, t)}{\partial t} = -\frac{\hbar^2\nabla^2}{2m_{\text{n}}}\psi(\mathbf{r}, t), \tag{17}$$

where m_{n} denotes the neutron mass and $\hbar$ is Planck's constant divided by 2π. Its general solution is $\psi(\mathbf{r}, t) = e^{i(\mathbf{q}\cdot\mathbf{r}-\epsilon_{\mathbf{q}}t/\hbar)}$ with $\epsilon_{\mathbf{q}} = \hbar^2\mathbf{q}\cdot\mathbf{q}/2m_{\text{n}}$. When the beam neutrons interact with the nuclei of the atoms contained in the sample, to a first approximation the neutrons' hamiltonian contains, beside the kinetic term reported in (17), a potential term proportional to the number density n_{at} of the atoms within the sample. Thus, Eq. (17) becomes

$$i\hbar\frac{\partial\psi(\mathbf{r}, t)}{\partial t} = -\frac{\hbar^2\nabla^2}{2m_{\text{n}}}\psi(\mathbf{r}, t) + gn_{\text{at}}(\mathbf{r})\psi(\mathbf{r}, t) \tag{18}$$

where the coupling constant g has dimensions $[\text{ML}^2\text{T}^{-2}\text{L}^3]$ and it is determined by the scattering of neutron from a single atom. Its expression is (see, *e.g.*, chap. 7 of Ref. [7]) $g = 4\pi\hbar^2 a/2M_{\text{red}}$ where a is the so-called scattering-length (see X.11 of Ref. [8]) and $M_{\text{red}} \equiv m_{\text{n}}M_{\text{at}}/(m_{\text{n}} + M_{\text{at}})$ is the reduced mass of the system neutron-atom the latter's mass being M_{at}. Let us now look for a solution of this equation of the kind $\psi(\mathbf{r}, t) = \phi(\mathbf{r})e^{-i\hbar^2\mathbf{q}^2 t/2m_{\text{n}}\hbar}$. The substitution of this expression in (18) yields

$$\nabla^2\phi(\mathbf{r}) + \mathbf{q}^2\phi(\mathbf{r}) = \frac{2m_{\text{n}}g}{\hbar^2}n_{\text{at}}(\mathbf{r})\phi(\mathbf{r}) \tag{19}$$

that is formally identical to (15a). Hence the solution is

$$\phi(\mathbf{r}) = \frac{m_{\text{n}}g}{2\pi\hbar^2}\int \frac{e^{iq|\mathbf{r}-\mathbf{r}'|}}{|\mathbf{r}-\mathbf{r}'|}n_{\text{at}}(\mathbf{r}')\phi(\mathbf{r}')dv'.$$

By the same procedure used for deriving (16) from (15b), we substitute on the rhs of the above equation $\phi(\mathbf{r})$ with $e^{i\mathbf{q}_{\text{in}}\cdot\mathbf{r}}$, i.e. the solution of the Schrödinger free equation that describes a neutron of the ingoing beam. Thus, the solution of (19) is

$$\phi(\mathbf{r}) \approx \frac{m_n g}{2\pi\hbar^2}\int \frac{e^{iq|\mathbf{r}-\mathbf{r}'|}}{|\mathbf{r}-\mathbf{r}'|} n_{at}(\mathbf{r}')e^{i\mathbf{q}_{in}\cdot\mathbf{r}'}dv' \approx \frac{m_n g}{2\pi\hbar^2}\frac{e^{i\mathbf{q}_{out}\cdot\mathbf{r}}}{R_0}\int n_{at}(\mathbf{r}')e^{i(\mathbf{q}_{in}-\mathbf{q}_{out})\cdot\mathbf{r}'}dv',$$

and the expression of the "standard " differential cross-section for neutron scattering is

$$\left[\frac{m_n g}{2\pi\hbar^2}\right]^{-2}\frac{d\sigma}{d\Omega} = \left|\int n_{at}(\mathbf{r})e^{i\mathbf{q}\cdot\mathbf{r}}dv\right|^2. \quad (20)$$

This expression is commonly referred to, in quantum mechanics, as the Born approximation of the differential cross-section. For thermal neutrons, $\hbar^2\mathbf{q}^2/2m \approx 3k_BT/2$ (where k_B is the Boltzmann constant and T the absolute temperature of the nuclear reactor) the frequency of the oscillatory factor present in above expression of $\psi(\mathbf{r},t)$ is $3k_BT/4\pi\hbar \sim 10^{13}s^{-1}$. This justifies the fact that $n_{at}(\mathbf{r})$ was taken time independent in Eqs (18)–(20). Then, similarly to the case of x-ray scattering, if we take into account the fact that the time required for collecting scattering data is considerably larger than 10^{-13}s, instead of (20), the scattering intensity for neutron scattering is related to the instantaneous FT of the instantaneous scattering-length density through the relations

$$I(\mathbf{q}) = \langle|\tilde{n}_{at}(\mathbf{q},t)|^2\rangle_t = \langle|\tilde{n}_{at}(\mathbf{q})|^2\rangle. \quad (21)$$

Quantum mechanical derivation

From a quantum mechanical point of view, a scattering process is a particular transition made by the system under analysis from one of its eigenstates to another eigenstate under the effect of a perturbation. In fact, in the scattering case, the initial eigenstate of the full system corresponds to having a free particle impinging with momentum $\mathbf{p}_{in}$ on the sample that is in one of its eigenstates, while the system final eigenstate corresponds to having an outgoing free particle with momentum $\mathbf{p}_{out}$ and the sample in another eigenstate. Denoting the free Hamiltonian operator of the full system by H_0, the perturbing Hamiltonian by H_1, the initial and final eigenstates of the system by $|\text{intl}\rangle$ and $|\text{finl}\rangle$, Fermi's golden rule states that the probability of transition for unit time is given by the following expression (see 35 of Ref. [9])

$$w_{\text{intl}\to\text{finl}} = \frac{2\pi}{\hbar}\rho(E)\left|\langle\text{finl}|H_1|\text{intl}\rangle\right|^2 \quad (22)$$

where $\rho(E)$ denotes the density of the number of the eigenstates of H_0 with energies contained within the infinitesimal interval $[E, E+dE]$, while $|\text{intl}\rangle$ and $|\text{finl}\rangle$ are eigenstates of H_0 with eigenvalues equal to E. Equation. (22) only accounts for first order perturbative effects. In order to use (22) for describing the scattering of x-rays or neutrons from a sample, we must recall that H_0 is the sum of two Hamiltonians H_m and H_{beam}. The first accounts for the kinetic contributions and for the mutual interactions of the particles contained in the sample, and for eventual further contributions originating from the interaction of the particles with an external classical field. H_{beam} is the Hamiltonian of the beam particles considered as non-interacting. In the case of x-rays, which are photons with wave-length restricted to a particular range, H_{beam} is the Hamiltonian of the quantized electromagnetic field. Its expression, denoted by H_{pht}, in the so-called transverse gauge is (see 1.2 of Ref. [10])

$$H_{pht} = \frac{1}{2}\int(\mathbf{E_T}^2 + \mathbf{B}^2)dv = \sum_{\mathbf{k}}\sum_{s=1}^{2}\hbar\omega_{\mathbf{k}}b^\dagger_{\mathbf{k},s}b_{\mathbf{k},s}, \quad (23)$$

where $\omega_{\mathbf{k}} = c|\mathbf{k}|$, $\mathbf{k} = 2\pi(n_1,n_2,n_3)/L$ with n_1,n_2,n_3 forming a triple of relative integers, and L the size of a very large cubic box enclosing the system. The operators $b^\dagger_{\mathbf{k},s}$ and $b_{\mathbf{k},s}$ on the rhs of Eq. (23) obey to the Bose-Einstein algebra: $[b_{\mathbf{k},s}, b^\dagger_{\mathbf{k}',s'}] = \delta_{\mathbf{k},\mathbf{k}'}\delta_{s,s'}$ and $[b_{\mathbf{k},s}, b_{\mathbf{k}',s'}] = [b^\dagger_{\mathbf{k},s}, b^\dagger_{\mathbf{k}',s'}] = 0$. Hence, $b^\dagger_{\mathbf{k},s}$ ($b_{\mathbf{k},s}$) creates (annihilates) a photon with momentum equal to $\hbar\mathbf{k}$ and polarization s. Since the e.m. field is transverse it can only have two independent polarization states[2]. This appears evident from the following expression of the quantized electromagnetic potential $\mathbf{A}(\mathbf{r},t)$

$$\mathbf{A}(\mathbf{r},t) = \sum_{\mathbf{k}}\sum_{s=1}^{2}\left(\frac{\hbar c^2}{2\omega_{\mathbf{k}}L^3}\right)^{1/2}[\vec{\varepsilon}_s(\mathbf{k})b_{\mathbf{k},s}e^{i(\mathbf{k}\cdot\mathbf{r}-\omega_{\mathbf{k}}t)} + h.c.], \quad (24)$$

where 'h.c." denotes the hermitian conjugate of the first expression present within the square brackets and $\vec{\varepsilon}_s(\mathbf{k})$ denotes the direction of the electric field for the polarization s. We have $\vec{\varepsilon}_s(\mathbf{k})\cdot\mathbf{k} = 0$ and $\vec{\varepsilon}_s(\mathbf{k})\cdot\vec{\varepsilon}_{s'}(\mathbf{k}) = \delta_{s,s'}$.

For the case of a non-relativistic neutron beam, the Hamiltonian is [7]

$$H_n = \int\sum_{\alpha=1}^{2}\psi^\dagger_\alpha(\mathbf{r})\left(-\frac{\hbar^2\nabla^2}{2m_n}\right)\psi_\alpha(\mathbf{r})dv = \sum_{\mathbf{k}}\sum_{s=1}^{2}\epsilon_{\mathbf{k}}a^\dagger_{\mathbf{k},s}a_{\mathbf{k},s}, \quad (25)$$

where $\epsilon_{\mathbf{k}} = \hbar^2\mathbf{k}^2/2m_n$ is the energy of a neutron with momentum $\hbar\mathbf{k}$. Neutrons are described by an operatorial two-component spinorial field $\psi_\alpha(\mathbf{r},t)$ that at time t

[2] More explicitly, the electric and magnetic fields being vectorial fileds, they have spin $|\mathbf{s}| = 1$. But the transversality condition implies that only two components are lineraly independent. This translates in the well known properties that the e.m. field has two independent polarization states and that the eigenvalues of $\mathbf{k}\cdot\mathbf{s}/|\mathbf{k}|$ only are $\pm\hbar$.

destroys a neutron located at $\mathbf{r}$. The field can also be written as

$$\psi_\alpha(\mathbf{r},t)=\frac{1}{L^{3/2}}\sum_{\mathbf{k}}\sum_{s=1}^{2}u^s{}_\alpha a_{\mathbf{k},s}e^{i(\mathbf{k}\cdot\mathbf{r}-\epsilon_{\mathbf{k}}t/\hbar)},\quad \alpha=1,2. \quad (26)$$

Here, u^1 and u^2 are two-component spinors respectively equal to $\begin{pmatrix}1\\0\end{pmatrix}$ and $\begin{pmatrix}0\\1\end{pmatrix}$ that describe a particle with spin up or down. They are each other orthogonal and normalized, *i.e.* $\sum_{\alpha=1}^{2}u^s_\alpha u^{s'}_\alpha=\delta_{s,s'}$. Finally, $a^\dagger_{\mathbf{k},s}$ and $a_{\mathbf{k},s}$ are the creation and annihilation operator of a neutron with momentum $\hbar\mathbf{k}$ and "polarization" s. They obey to the Fermi-Dirac algebra: $\left\{a_{\mathbf{k},s},a^\dagger_{\mathbf{k}',s'}\right\}=\delta_{\mathbf{k},\mathbf{k}'}\delta_{s,s'}$ and $\left\{a_{\mathbf{k},s},a_{\mathbf{k}',s'}\right\}=\left\{a^\dagger_{\mathbf{k},s},a^\dagger_{\mathbf{k}',s'}\right\}=0$, which ensures that one cannot have more than one particle with the same quantum numbers.

We consider now the interaction Hamiltonians. For the case of X-ray, the interactions among the electrons and among the electrons and the nuclei are accounted for in H_0. Thus, in agreement with the assumption made in 1-b, the interaction Hamiltonian only specifies the interaction of the sample electrons with the e.m. field. It will be denoted as $H_{\mathrm{m-e.m.}}$ and is obtained by the so called minimal-coupling [10]. In terms of the quantized e.m. and electron fields it reads

$$\begin{aligned}H_{\mathrm{m-e.m.}}=&\frac{\mathrm{e}}{mc}\int\left[\psi^\dagger_\alpha(\mathbf{r})\frac{\hbar\nabla}{i}\psi_\alpha(\mathbf{r})\right]\cdot\mathbf{A}(\mathbf{r})\mathrm{d}v\\&+\frac{\mathrm{e}^2}{2mc^2}\int\psi^\dagger_\alpha(\mathbf{r})\psi_\alpha(\mathbf{r})\left[\mathbf{A}(\mathbf{r})\cdot\mathbf{A}(\mathbf{r})\right]\mathrm{d}v.\end{aligned} \quad (27)$$

In this relation, e and m denote electron's charge and mass and $\psi_\alpha(\mathbf{r})$ has the same structure of (26) [by so doing electrons also are treated in a non-relativistic approximation] but $\psi_\alpha(\mathbf{r})$ refers now to electrons in the sense that $a_{\mathbf{k},s}$ ($a^\dagger_{\mathbf{k},s}$) destroys (creates) an electron with momentum $\hbar\mathbf{k}$ and polarization s. Moreover, in (27) and in the following we shall adopt the convention that repeated indices denotes a sum. It is also stressed that in writing Eqs (23), (24) and (27) we are using Gaussian CGS units. It is now convenient to introduce the so-called particle number-density operator $\hat{n}(\mathbf{r})$ according to the definition

$$\hat{n}(\mathbf{r})=\psi^\dagger_\alpha(\mathbf{r})\psi_\alpha(\mathbf{r}). \quad (28)$$

This definition makes sense for any matter field. More explicitly, the expectation value $\hat{n}(\mathbf{r})$ over a quantum state gives the number density of the electrons in the considered state if the field considered in (28) is that of the electrons, that of the neutrons if the field is the neutron one, and so on. Operator $\hat{n}(\mathbf{r})$ is simply obtained by the second quantization procedure starting from the classical definition (8a) and its dimensions are L^{-3}. In terms of $\hat{n}_{\mathrm{el}}(\mathbf{r})$ [subscript "el" specifies that $\hat{n}$ refers to electrons], Eq.(27) becomes

$$\begin{aligned}H_{\mathrm{m-e.m.}}=&\frac{\mathrm{e}}{mc}\int\left[\psi^\dagger_\alpha(\mathbf{r})\frac{\hbar\nabla}{i}\psi_\alpha(\mathbf{r})\right]\cdot\mathbf{A}(\mathbf{r})\mathrm{d}v\\&+\frac{\mathrm{e}^2}{2mc^2}\int\hat{n}_{\mathrm{el}}(\mathbf{r})\left[\mathbf{A}(\mathbf{r})\cdot\mathbf{A}(\mathbf{r})\right]\mathrm{d}v.\end{aligned} \quad (29)$$

In the case of neutron scattering, the interaction Hamiltonian H_1 will be denoted by H_{m-n}. It is obtained by introducing, for each atomic species present in the sample, a "pseudopotential" that describes the interaction between a neutron and a nucleus of the jth atomic species present in the sample (see chapter 5 of Ref. [7]). Assuming that a neutron be located at $\mathbf{r}$ and a nucleus of the jth species at $\mathbf{r}_a$, their pseudopotential is $V_j(|\mathbf{r}-\mathbf{r}_a|)=\frac{4\pi a_j\hbar^2}{2M_{\mathrm{red,j}}}\delta(\mathbf{r}-\mathbf{r}_a)$ where $\delta(\cdot)$ is the three-dimensional Dirac function, $M_{\mathrm{red,j}}$ the reduced mass of the considered neutron-nucleus system and a_j is the so-called scattering-length. In the case of elastic scattering a_j is a real quantity that, depending on the atomic species, can be either positive or negative. We denote by $\hat{n}_{\mathrm{at,j}}$ the number density operator for the jth atomic species and by $\hat{n}_{\mathrm{n}}$ the number density operator of neutrons. The interaction Hamiltonian is

$$\begin{aligned}H_{\mathrm{m-n}}&=\sum_{j=1}^{N_s}\int\mathrm{d}v\int\mathrm{d}v_a\hat{n}_{\mathrm{at,j}}(\mathbf{r}_a)V_j(|\mathbf{r}-\mathbf{r}_a|)\hat{n}_{\mathrm{n}}(\mathbf{r})\mathrm{d}v\\&=\sum_{j=1}^{N_s}g_j\int\hat{n}_{\mathrm{at,j}}(\mathbf{r})\hat{n}_{\mathrm{n}}(\mathbf{r})\mathrm{d}v.\end{aligned} \quad (30)$$

The last expression follows from the explicit form of the strictly local pseudopotentials V_j while N_s denotes the number of the atomic species of the sample. Besides, we have put $g_j\equiv\frac{4\pi a_j\hbar^2}{2M_{\mathrm{red,j}}}$ whose dimensions are $(ML^2T^{-2})L^3$.

We sketch now how the transition probability per unit time is evaluated in the cases of x-ray and neutron scattering. Consider the first case. We have $H_0=H_{\mathrm{m}}+H_{\mathrm{pht}}$ and since H_{m} and H_{pht} depend on different field operators, H_{m} and H_{pht} commute. This implies that each eigenstate of H_0 is direct product of an eigenstate of H_{m} and an eigenstate of H_{pht}. Before the sample is invested by the ingoing photon beam, it is in its fundamental state $|\Psi_0\rangle$ characterized by the property $H_{\mathrm{m}}|\Psi_0\rangle=E_0|\Psi_0\rangle$ with E_0 equal to the smallest of the eigenvalues of H_{m}. After the sample has interacted with the beam, it will be in another eigenstate denoted by $|\Psi_n\rangle$ corresponding to the eigenvalue E_n. The ingoing photon has momentum $\mathbf{p}_{\mathrm{in}}=\hbar\mathbf{q}_{\mathrm{in}}$ and polarization s, and it is described by the state $|\mathbf{p}_{\mathrm{in}},s\rangle=b^\dagger_{\mathbf{q}_{\mathrm{in}},s}|0\rangle$, $|0\rangle$ being the state containing no photon. Similarly, if outgoing photons has momentum $\mathbf{p}_{\mathrm{out}}=\hbar\mathbf{q}_{\mathrm{out}}$ and polarization s', its eigenstate is $|\mathbf{p}_{\mathrm{out}},s'\rangle$. Since the scattering is assumed to be elastic,

we have $\omega_{\mathbf{p}_{\rm in}} = \omega_{\mathbf{p}_{\rm out}}$, i.e. $|\mathbf{q}_{\rm in}| = |\mathbf{q}_{\rm out}|$. Then, in (22) we have to put $|{\rm intl}\rangle = |\Psi_0\rangle \otimes |\mathbf{p}_{\rm in}, s\rangle$ and $|{\rm finl}\rangle = |\Psi_n\rangle \otimes |\mathbf{p}_{\rm out}, s'\rangle$ (where $\otimes$ denotes the tensorial product, see VIII.7 of Ref. [8]), and by (22) and (29) we find that

$$\begin{aligned}\langle {\rm finl}|H_1|{\rm intl}\rangle &= \langle {\rm finl}|H_{\rm m-e.m.}|{\rm intl}\rangle \\ &= \frac{e}{mc}\int \langle \Psi_n|\left[\psi_\alpha^\dagger(\mathbf{r})\frac{\hbar\nabla}{i}\psi_\alpha(\mathbf{r})\right]|\Psi_0\rangle \cdot \langle \mathbf{p}_{\rm out}, s'|\mathbf{A}(\mathbf{r})|\mathbf{p}_{\rm in}, s\rangle {\rm d}v \\ &\quad + \frac{e^2}{2mc^2}\int \langle \Psi_n|\hat{n}_{\rm el}(\mathbf{r})|\Psi_0\rangle\langle \mathbf{p}_{\rm out}, s'|\mathbf{A}(\mathbf{r})\cdot\mathbf{A}(\mathbf{r})|\mathbf{p}_{\rm in}, s\rangle {\rm d}v,\end{aligned} \tag{31}$$

where the property that $\psi_\alpha(\mathbf{r})$ and $\mathbf{A}(\mathbf{r})$ commute has been used. The evaluation of the matrix elements $\langle \mathbf{p}_{\rm out}, s'|\mathbf{A}(\mathbf{r})|\mathbf{p}_{\rm in}, s\rangle$ and $\langle \mathbf{p}_{\rm out}, s'|\mathbf{A}(\mathbf{r})\cdot\mathbf{A}(\mathbf{r})|\mathbf{p}_{\rm in}, s\rangle$ is straightforward using decomposition (24) and the Bose-Einstein algebra. One finds that

$$\langle \mathbf{p}_{\rm out}, s'|\mathbf{A}(\mathbf{r})|\mathbf{p}_{\rm in}, s\rangle = 0, \tag{32a}$$

and

$$\begin{aligned}&\langle \mathbf{p}_{\rm out}, s'|\mathbf{A}(\mathbf{r})\cdot\mathbf{A}(\mathbf{r})|\mathbf{p}_{\rm in}, s\rangle \\ &\quad = \left(\frac{\hbar c^2}{\omega_{\mathbf{q}_{\rm in}} L^3}\right)\vec{\varepsilon}_s(\mathbf{q}_{\rm in})\cdot\vec{\varepsilon}_{s'}(\mathbf{q}_{\rm out}){\rm e}^{i\mathbf{r}\cdot(\mathbf{q}_{\rm in}-\mathbf{q}_{\rm out})}.\end{aligned} \tag{32b}$$

The density of states for the photons outgoing within an infinitesimal solid angle dΩ centered along $\mathbf{q}_{\rm out}$ is $[L^3/(2\pi)^3]\mathbf{q}_{\rm out}^2/c\hbar$. The corresponding transition probability per unit time, divided by c/L^3 (the flux of the ingoing particles) is the differential cross-section. Hence

$$\begin{aligned}\frac{d\sigma}{d\Omega}\Big|_{s,s'} &= \frac{2\pi}{\hbar}\frac{L^3\omega_{\mathbf{q}_{\rm out}}^2}{(2\pi c)^3\hbar}\frac{L^3}{c}\left(\frac{\hbar c^2}{\omega_{\mathbf{q}_{\rm in}}L^3}\right)^2\left(\frac{\rm e^2}{2mc^2}\right)^2\left(\vec{\varepsilon}_s(\mathbf{q}_{\rm in})\right. \\ &\quad \left.\cdot\,\vec{\varepsilon}_{s'}(\mathbf{q}_{\rm out})\right)^2\left|\int e^{i\mathbf{r}\cdot\mathbf{q}}\langle\Psi_n|\hat{n}_{\rm el}(\mathbf{r})|\Psi_0\rangle dv\right|^2 \\ &= \left[\frac{\rm e^2}{4\pi mc^2}\right]^2\left(\vec{\varepsilon}_s(\mathbf{q}_{\rm in})\cdot\vec{\varepsilon}_{s'}(\mathbf{q}_{\rm out})\right)^2 \\ &\quad \times\left|\int e^{i\mathbf{r}\cdot\mathbf{q}}\langle\Psi_n|\hat{n}_{\rm el}(\mathbf{r})|\Psi_0\rangle dv\right|^2.\end{aligned} \tag{33}$$

The above expression assumes that both the ingoing and the outgoing photon have a well defined polarization specified by indices s and s'. If the final polarization state is not observed we must sum over s' and, if the ingoing beam is not polarized, we must take the average over the two possible polarizations. It is quite straightforward to show that $(1/2)\sum_{s,s'}\left(\vec{\varepsilon}_s(\mathbf{q}_{\rm in})\cdot\vec{\varepsilon}_{s'}(\mathbf{q}_{\rm out})\right)^2 = (1+\cos^2\theta)/2$. Recalling that e^2 in rationalized Gaussian CGS units converts into e^2/ϵ_0 when SI units are used, one finds that the quantum-mechanical expression of the differential cross-section for unpolarized x-ray scattering, in SI units, is

$$\begin{aligned}\frac{{\rm d}\sigma}{{\rm d}\Omega} &= \left[\frac{\rm e^2}{4\pi\epsilon_0 mc^2}\right]^2\frac{1+\cos^2\theta}{2}\sum_n \delta_{E_n,E_0} \\ &\quad \times\left|\int\langle\Psi_n|\hat{n}_{\rm el}(\mathbf{r})|\Psi_0\rangle {\rm e}^{i\mathbf{r}\cdot\mathbf{q}}{\rm d}v\right|^2.\end{aligned} \tag{34}$$

In writing down this expression, we have considered the more general case where the ground state of the sample is degenerate. Indeed, due to the presence of the Kronecker symbol δ_{E_n,E_0} all the eigenstate $|\Psi_n\rangle$ of $H_{\rm m}$ contributing to the sum must have eigenvalue E_0 as required from the energy conservation understood in (22).

We work out now the expression of the differential cross-section for the case of unpolarized neutrons. To this aim, we go through the same steps described above and perform the appropriate changes. We can again write that $|{\rm intl}\rangle = |\Psi_0\rangle \otimes |\mathbf{p}_{\rm in}, s\rangle$ where $|\Psi_0\rangle$ is the ground state of the relevant $H_{\rm m}$ and $|\mathbf{p}_{\rm in}, s\rangle = a^\dagger_{\mathbf{q}_{\rm in},s}|0\rangle$.

Considering for simplicity the case of a single atomic species, from (22) and (30) one gets

$$\begin{aligned}\langle {\rm finl}|H_1|{\rm intl}\rangle &= \langle {\rm finl}|H_{\rm m-n}|{\rm intl}\rangle \\ &= g\int\langle\Psi_n|\hat{n}_{\rm at}(\mathbf{r})|\Psi_0\rangle\langle\mathbf{p}_{\rm out}, s'|\hat{n}_{\rm n}(\mathbf{r})|\mathbf{p}_{\rm in}, s\rangle dv.\end{aligned} \tag{35}$$

By Eq.s (28) and (26) immediately follows that

$$\langle \mathbf{p}_{\rm out}, s'|\hat{n}_{\rm n}(\mathbf{r})|\mathbf{p}_{\rm in}, s\rangle = \frac{1}{L^3}\delta_{s,s'}e^{i\mathbf{r}\cdot(\mathbf{q}_{rmin}-\mathbf{q}_{\rm out})} = \frac{1}{L^3}\delta_{s,s'}e^{i\mathbf{r}\cdot\mathbf{q}}.$$

The density of states for the neutrons outgoing within the infinitesimal solid angle $d\Omega$, set along $\mathbf{q}_{\rm out}$, is $[L^3/(2\pi)^3]mq_{\rm out}/\hbar^2$. The flux of the ingoing particles is $v_{\rm in}/L^3 = \hbar q_{\rm in}/(mL^3)$. Then, recalling also the previous definition of g, the differential cross-section for unpolarized neutrons is

$$\begin{aligned}&\frac{2\pi}{\hbar}\frac{mL^3}{\hbar q_{\rm in}}\frac{L^3 mq_{\rm out}}{(2\pi)^3\hbar^2}\frac{1}{L^6}\frac{1}{2}\sum_{s,s'}(\delta_{s,s'})^2\left(\frac{4\pi a\hbar^2}{2M_{\rm red}}\right)^2 \\ &\quad\left|\int\langle\Psi_n|\hat{n}_{\rm at}(\mathbf{r})|\Psi_0\rangle e^{i\mathbf{q}\cdot\mathbf{r}}dv\right|^2,\end{aligned}$$

i.e.

$$\frac{{\rm d}\sigma}{{\rm d}\Omega} = \left[\frac{ma}{M_{\rm red}}\right]^2\sum_{\rm n}\left|\int\langle\Psi_{\rm n}|\hat{n}_{\rm at}(\mathbf{r})|\Psi_0\rangle{\rm e}^{i\mathbf{q}\cdot\mathbf{r}}dv\right|^2\delta_{E_n,E_0}, \tag{36}$$

where, similarly to (34), we have considered for greater generality the case of a degenerate ground state. This case is however rather unlikely and the sum over n can generally be omitted both in (34) and (36). It is now worth to remark that both (34) and (36) do not involve $\hbar$ so that they hold also true in classical physics. In fact, the comparison of (34) with (7), (9) and (8) shows that the classical electron number density there used and denoted now,for greater clarity, as $n_{\rm cl,el}(\mathbf{r})$ corresponds to the expectation value $\langle\Psi_0|\hat{n}_{\rm el}(\mathbf{r})|\Psi_0\rangle$, i.e. the expectation value of the electron number density operator over the ground state of the sample, and we can write

$$n_{\rm cl,el}(\mathbf{r}) \leftrightarrow \langle\Psi_0|\hat{n}_{\rm el}(\mathbf{r})|\Psi_0\rangle. \tag{37}$$

It is stressed that the ground state is determined by $H_{\rm m}$ and therefore it depends on the interactions between the electrons, between the electrons and the nuclei, and

between the nuclei. In the same way, we conclude that for neutrons the following correspondence

$$n_{\mathrm{cl,n}}(\mathbf{r}) \leftrightarrow \langle \Psi_0 | \hat{n}_{\mathrm{n}}(\mathbf{r}) | \Psi_0 \rangle \tag{38}$$

holds true. One might wonder on the reason why in Eqs (7) or (9) we have a time or an ensemble average, while Eq. (37) involve no time dependece. The answer is related to the fact that the quantum-mechanical calculation of the differential cross-section refers to a particular initial state of the sample, i.e. the ground state. The assumption that the quantum state of the sample, before it is invested by the beam particles, be the ground state is correct only if one assumes that the absolute temeperature of the sample be equal to zero . Oppositely, if the sample is in thermal equilibrium at the temperature T, quantum statistical mechanics tells us that the sample can be in any eigenstate $|\Psi_n\rangle$ of H_{m} with a probability determined by the eigenvalue E_n of the eigenstate. More definitely, the probability that the sample be in the eigenstate $|\Psi_n\rangle$ is $p_n \equiv e^{-E_n/\mathrm{k_B T}} / \sum_s e^{-E_s/\mathrm{k_B T}}$ where $\mathrm{k_B}$ is Boltzmann's constant. Thus, if the scattering experiment is made with the sample at temperature T, Eq. (22) applies for any initial state, given by $|\Psi_n\rangle \otimes |\mathbf{p}_{\mathrm{in}}, s\rangle$, with the final state given by $|\Psi_m\rangle \otimes |\mathbf{p}_{\mathrm{out}}, s'\rangle$ with $|\mathbf{p}_{\mathrm{in}}| = |\mathbf{p}_{\mathrm{out}}|$ and $E_n = E_m$ so as to ensure the energy conservation. Observing that the right hand side of (22) is already of the first order in the perturbation, one can assume that the probability of the different eigenstates of H_{tot} are those of H_0. Hence, the differential cross-sections for unpolarized x-ray scattering and neutron scattering from a sample at temperature T respectively are

$$\left[\frac{\mathrm{e}^2}{4\pi\epsilon_0 mc^2}\right]^{-2} \left(\frac{1+\cos^2\theta}{2}\frac{d\sigma}{d\Omega}\right)^{-1} = \sum_{n,m} \frac{\mathrm{e}^{-E_n/\mathrm{k_B T}}}{\sum_s \mathrm{e}^{-E_s/\mathrm{k_B T}}} \delta_{E_n,E_m} \left| \int \langle \Psi_m | \hat{n}_{\mathrm{el}}(\mathbf{r}) | \Psi_n \rangle e^{i\mathbf{r}\cdot\mathbf{q}} dv \right|^2 \tag{39}$$

and

$$\left[\frac{ma}{M_{\mathrm{red}}}\right]^{-2} \frac{\mathrm{d}\sigma}{\mathrm{d}\Omega} = \sum_{n,m} \frac{\mathrm{e}^{-E_{\mathrm{n}}/\mathrm{k_B T}}}{\sum_{\mathrm{s}} e^{-E_{\mathrm{s}}/\mathrm{k_B T}}} \delta_{E_{\mathrm{n}},E_{\mathrm{m}}} \left| \int \langle \Psi_m | \hat{n}_{\mathrm{at}}(\mathbf{r}) | \Psi_n \rangle e^{i\mathbf{q}\cdot\mathbf{r}} dv \right|^2. \tag{40}$$

Conclusive remarks

Above we have reviewed the derivations of the scattering intensity expressions, for x-ray as well as for neutron scattering, on the basis of classical and of quantum-mechanical physics. We saw that the physical assumptions are the same in both derivations, because the particles were considered non-relativistic and we confined ourselves to the first order perturbation theory. However, the derivation based on a quantum-mechanical approach is intrinsically more rigorous and allows us to get the general definition of the quantities that determine the observed standard differential cross-sections. Hence, in the cases of x-ray and neutron scattering, the measured quantities respectively are the rhs of Eq. (39) and Eq. (40). The first is the quantum statistical average of the square modulus of the expectation values of the FT of the electron number density operator between states with the same energy, and the second is similarly defined but it involves the atom number density operator. According to the theory of quantum-many bodies at finite temperature, the aforesaid quantities are related to the imaginary parts of the temperature Green-functions of the particle number density operators [7] and, in principle, they could be evaluated by the Feynman graph technique starting from the knowledge of the "free" Green functions. In practice, it is nearly impossible to carry through such calculations for realistic choices of H_{m}. One often considers further simplifying assumptions that generally lead to the formulae usually considered in crystallography, so that instead of (39) and (40), one considers (9) and (21). This amounts to substitute the quantum expressions with the classical ones, *i.e.*:

$$\sum_{n,m} p_n \delta_{E_n,E_m} \left| \int \langle \Psi_m | \hat{n}_{\mathrm{el}}(\mathbf{r}) | \Psi_n \rangle e^{i\mathbf{r}\cdot\mathbf{q}} dv \right|^2 \leftrightarrow \langle |\tilde{n}_{\mathrm{el}}(\mathbf{q},t)|^2 \rangle_t = \langle |\tilde{n}(\mathbf{q})|^2 \rangle, \tag{41}$$

$$\sum_{n,m} p_n \delta_{E_n,E_m} \left| \int \langle \Psi_m | \hat{n}_{\mathrm{at}}(\mathbf{r}) | \Psi_n \rangle e^{i\mathbf{q}\cdot\mathbf{r}} dv \right|^2 \leftrightarrow \langle |\tilde{n}_{\mathrm{at}}(\mathbf{q},t)|^2 \rangle_t = \langle |\tilde{n}_{\mathrm{at}}(\mathbf{q})|^2. \tag{42}$$

Further approximations are considered depending on the sample under analysis. For instance, in the simplest case of mono-atomic liquids at room temperature, the electron number density can be written as $n_{\mathrm{el}}(\mathbf{r},t) = \sum_{j=1}^{N} n_0(\mathbf{r} - \mathbf{R}_j(t))$, where $\mathbf{R}_j(t)$ is the position of the jth atom of the sample at time t, $n_0(\mathbf{r})$ the electron number density of a single atom set at the origin and the sum runs over all the sample atoms. In this case, one finds that $\tilde{n}_{\mathrm{el}}(\mathbf{q},t) = \tilde{n}_0(\mathbf{q}) \sum_{j=1}^{N} e^{i\mathbf{q}\cdot\mathbf{R}_j(t)}$ and the rhs of (41) becomes

$$\langle |\tilde{n}_{\mathrm{el}}(\mathbf{q},t)|^2 \rangle_t = |\tilde{n}_0(\mathbf{q})|^2 \langle \left| e^{i\mathbf{q}\cdot\mathbf{R}_j(t)} \right|^2 \rangle_t.$$

As reported in 5.1 of Ref. [11], the above average quantity is simply related to the FT of the liquid's radial distribution function that can therefore be determined by x-rays scattering experiments. This approximation is also relevant for polyatomic liquids as well as for micellar solutions. In the case of samples where the atoms' motion

is thought to take place much more slowly, the (classical) electron number density is approximated as

$$\langle|\tilde{n}_{\mathrm{el}}(\mathbf{q},t)|^2\rangle_t \approx |\langle\tilde{n}_{\mathrm{el}}(\mathbf{q},t)\rangle_t|^2. \tag{43a}$$

By so doing, the average square modulus is approximated with the square modulus of the average. Invoking again the ergodic assumption, the previous relation can be written as

$$\langle|\tilde{n}_{\mathrm{el}}(\mathbf{q})|^2\rangle \approx |\langle\tilde{n}_{\mathrm{el}}(\mathbf{q})\rangle|^2 \tag{43b}$$

where the averages are evaluated over the Gibbs ensemble. From the previous discussion on Eq.s (37) and (38), one knows that the approximations involved in (43a) and (43b) are only accurate at very low temperature. In this case, one can really speaks of a time independent electron number or scattering length density since the previous considerations are also true for the latter.

If one introduces the further assumption, quite popular in crystallography, that atoms can be treated as point-like objects, then $n_{\mathrm{sd}}(\mathbf{r}) = \sum_j Z_j \delta(\mathbf{r} - \mathbf{R}_j)$ [where Z_j is, depending on the nature of the ingoing beam, the atomic number or the scattering-length of the jth atom located at $\mathbf{R}_j$, and the sum runs over all the atoms of the sample, while subscript "sd" is a shortening for scattering density] and its FT reads $\tilde{n}_{\mathrm{sd}}(\mathbf{q}) = \sum_j Z_j e^{i\mathbf{q}\cdot\mathbf{R}_j}$. If the sample is a crystal, one can restrict himself to a unit cell of the crystal so that the previous sums will now involve a finite number of terms. Going from the left to the rhs of (37), we can restrict ourselves to a finite dimensional subspace of the total Hilbert space and one shows that a basis of the restricted Hilbert space is formed by the position operator eigenvectors whose eigenvalues are the positions of the atoms within the considered unit cell. This observation makes it then possible to prove that the knowledge of a finite subdomain - singled out by a well defined constructive procedure - of the x-ray or neutron diffraction pattern allows one to reconstruct the full pattern [12]. In other words, the "phase problem" does not exist if atoms are really point-like.

Approximation (43) is central for characterizing amorphous systems by small-angle scattering (SAS). Since the best spatial resolution of SAS hardly exceeds 1nm, according to Debye and Bueche [13], $n_{\mathrm{sd}}(\mathbf{r})$ can fairly be approximated, for a large class of samples, by a discrete value function, denoted by $n_{\mathrm{sd,D}}(\mathbf{r})$[3]. This amounts to look at the sample as made up of different phases. Each of these occupies the region where $n_{\mathrm{sd,D}}(\mathbf{r})$ assumes one of its possible values and the interphase surfaces are the sets of the points where $n_{\mathrm{sd,D}}(\mathbf{r})$ jumps from one value to another. The behaviour of the scattering intensity in the outer portion of the q-range explored in SAS experiments is determined by the geometry of the interface. In particular the expression of the leading term [15] is $2\pi(n_1 - n_2)^2 S/q^4$ and it is known as Porod's law. However, in approximating $n_{\mathrm{sd}}(\mathbf{r})$ with $n_{\mathrm{sd,D}}(\mathbf{r})$ one neglects the variations of $n_{\mathrm{sd}}(\mathbf{r})$, occuring on a length-scale of 1nm or smaller, both within the bulk phases and at the border of the latter. These two problems were affronted in a pioner paper [16] by Ruland (1971) and the results of this analysis have found many applications over the past years. Finally, one should also recall Ruland's attempt of relaxing condition (43) by allowing for fluctuations in the positions of the interphase surfaces [17].

References

1. Guinier A (1963) X-ray Diffraction. Freeman & Co., San Francisco
2. Warren BE (1969) X-ray Diffraction. Dover, New York
3. Jackson JD (1975) Classical Electrodynamics. Wiley, New York
4. Authier A (2001) Dynamical Theory of X-ray Diffraction. Oxford Univ. Press, Oxford
5. Landau LD and Lifchitz EM (1969) Électrodynamique des Milieux Continus. Mir, Moscow
6. Feigin LA and Svergun DI (1987) Structure Analysis by Small-Angle X-ray and Neutron Scattering. Plenum Press, New York
7. Fetter AL and Walecka JD (1971) Quantum Theory of Many-particle Systems. McGraw-Hill, New York.
8. Messiah A (1959) Mécanique Quantique. Dunod, Paris
9. Schiff LI (1955) Quantum Mechanics. McGraw-Hill, New York.
10. Mandl F and Shaw G (1984) Quantum Field Theory. Wiley, New York.
11. Hansen JP and McDonald IR (1976) Theory of Simple Liquids. Academic Press, London
12. Cervellino A and Ciccariello S (2004) The algebraic approach to the phase problem for neutron scattering. arXiv:math-ph/0401044
13. Debye P and Bueche AM (1949) J. Appl. Phys. 20: 518
14. Ciccariello S (2002) Acta Cryst. A 58: 460
15. Porod G (1951) Kolloid Z. 124: 83.
16. Ruland W (1971) J. Appl. Cryst. 4: 70
17. Ruland W (1987) Macromolecules 20: 87

[3] As shown in Ref. [14], a two-phase idealization of a continuous scattering density is always possible. In fact, it is uniquely determined by the condition that $\chi \equiv [\int |\tilde{n}_{\mathrm{sd,D}}(\mathbf{q})|^2 dv_q - \int |\tilde{n}_{\mathrm{sd}}(\mathbf{q})|^2 dv_q]^2 / [\int |\tilde{n}_{\mathrm{sd}}(\mathbf{q})|^2 dv_q]^2$ be as small as possible. Clearly, the two-phase idealization will only be satisfactory for those samples characterized by a small value of χ. But, to the author's best knowledge, no estimate of this value is presently known.

Progr Colloid Polym Sci (2005) 130: 29–32
DOI 10.1007/b107348
Published online: 3 June 2005

Nicola Pinna

X-Ray diffraction from nanocrystals

N. Pinna
Max Planck Institute of Colloids and Interfaces, 14424 Potsdam, Germany

Present address:
Martin-Luther-Universität Halle-Wittembesg, Institut für Anorganische Chemie, Kurt-Mothes-Str. 2, 06120 Halle (Saale), Germany
E-mail: micola.pinna@chemie.uni-halle.de

Abstract X-ray diffraction studies on nanocrystals are discussed and the problem of structure determination is investigated. Especially a technique based on the calculation of Debye equation is presented. It permits to obtain information about the structure, the size and the shape of nanoparticles. Debye equation calculations are applied to two systems: in the first example the diffracted intensity is calculated for spherical orthorhombic Ta_2O_5 nanocrystals with sizes ranging from 1 to 6 nm to illustrate the size dependence of XRD patterns. In the second example the shape effect on XRD patterns from monoclinic HfO_2 nanocrystals is studied and, in order to determine their growth axis, the results were compared to experimental patterns.

Keywords Nanoparticles · X-ray Diffraction · Debye scattering equation

Introduction

The controlled synthesis and characterization of crystalline objects with reduced dimensionality, i.e., one, two or three dimensions being on the nanoscale, is a fascinating objective in nanochemistry. The reason for that is that practically all solid state properties, including melting point, conductivity, magnetism, or optical properties, depend on the length of the confined dimension, or in other words, the physical and chemical properties can be tuned between the bulk solid and the constituting molecules [1–3].

In order to relate the physical properties to the size, shape and crystallinity of the nanoobjects an accurate and fine characterization has to be performed. The determination of the size and shape distribution of nanometer size particles can be addressed with several techniques like for example: Analytical ultracentrifugation (AUC) [4, 5], light scattering techniques, transmission electron microscopy (TEM) [6] etc. To determine the crystal structure of these nanoobjects high resolution TEM (HRTEM) and diffraction techniques, electron diffraction and powder X-ray diffraction (XRD), are the most common employed. HRTEM permits to directly visualize the atomic columns of a single particle and to determine its structure, its defaults and so on. However, this method is not statistically applicable to a large amount of particles. Powder XRD measurements are able to overcome such a limitation and give a global information about the crystallinity of the whole sample, thus make it a perfect complementary technique to HRTEM. Moreover, it is possible to calculate the intensity scattered by a model particle, in the kinematic approach, by the so called Debye function [7–9]. A few groups applied such techniques to metallic clusters [10–12] and then extended the method to polydispered nanocrystalline systems calling it the Debye function analysis (DFA) [13, 14].

Recently this method was extended to oxidic nanoparticles [15] and applied to characterize the structure, the size and the shape of many oxidic nanoparticles synthesized by the benzyl alcohol route [16–18] that was introduced in 2002 by M. Niederberger and coworkers [19, 20]. This article gives a more detailed presentation of the Debye technique and presents how to successfully use it for difficult problems of characterization (Cf. example 2) that other techniques cannot solve.

Calculations

The intensity distribution, spherically averaged over the reciprocal space, is described by the Debye formula:[7–9]

$$I_N(b) = \sum_{n,m\neq n}^{N} f_n f_m \frac{\sin(2\pi b r_{nm})}{2\pi b r_{nm}} \quad (1)$$

Where $b = \frac{1}{d} = \frac{2\sin\theta}{\lambda}$, λ is the wavelength and 2θ the scattering angle. The sum runs over all the pair distances r_{nm} of the atoms labelled by n, m with scattering amplitudes f_n, f_m in a cluster of N atoms. The formula includes the following characteristics:

- General equation valid for any form of matter in which there is a random orientation: gases, liquids, amorphous solids, and crystalline powders.
- No limitation on the number of different kinds of atoms in the sample.
- The number of terms increases proportional to the sixth order of the linear dimension of the particle!

The latter was the major limitation of the applicability of the Debye function, restricting the applicability to particles smaller than 5-6 nm. However B. D. Hall and R. Monot introduced an efficient algorithm for calculating the Debye equation that decreases dramatically the calculation time needed [21]. In the first step the construction of model particles is performed including the atomic positions of each atom. Following the improved algorithm [21], the interatomic distances that occur several times are sorted by approximating them into discrete, evenly spaced, histogram classes[1]. This approximation reduces the number of sine terms of the Debye equation to be calculated and so the global calculation time by several orders of magnitudes. Finally the Debye equation is calculated for each discrete interatomic distance and then multiplied by the number of time each distance occurs.

Results and discussion

Patterns calculated for the Ta_2O_5 orthorombic structure

The first example presents calculations of the Debye equation for spherical nanoparticles of the orthorhombic structure of Ta_2O_5 (ICSD: 9112). The cell parameters are: $a = 6.198$, $b = 40.290$ and $c = 3.888$ Å, the elementary cell contains 168 atoms. This structure was chosen because it is rather complex and therefore it is a perfect example to illustrate that the technique may be applied to every kind of crystalline or non crystalline form of matter.

In order to present the evolution of the diffraction patterns in function of the size, spherical particles of sizes ranging from 1 to 6 nm were constructed.

Figure 1 shows their diffraction patterns calculated with the Debye equation. For sizes between 1 and 1.4 nm the diffractions are hardly discernible and appear as two large broad bands centered around $b = 0.3$ and $b = 0.6$ $Å^{-1}$ respectively. When the size increases, the reflections become better and better separated as expected. This example gives an idea how sensitive is the Debye function to the particle size.

Nonspherical HfO_2 nanocrystals

The second example presents how to use Debye scattering equation calculations to determine the shape and the preferential direction of growth of small and slightly elongated particles. In this case HfO_2 nanocrystals synthesized by the benzyl alcohol route were studied [18]. They exhibit an elongated shape as observed in HRTEM images (Fig. 2a). This nanoparticle is a monocrystal and shows several lattice planes. For this

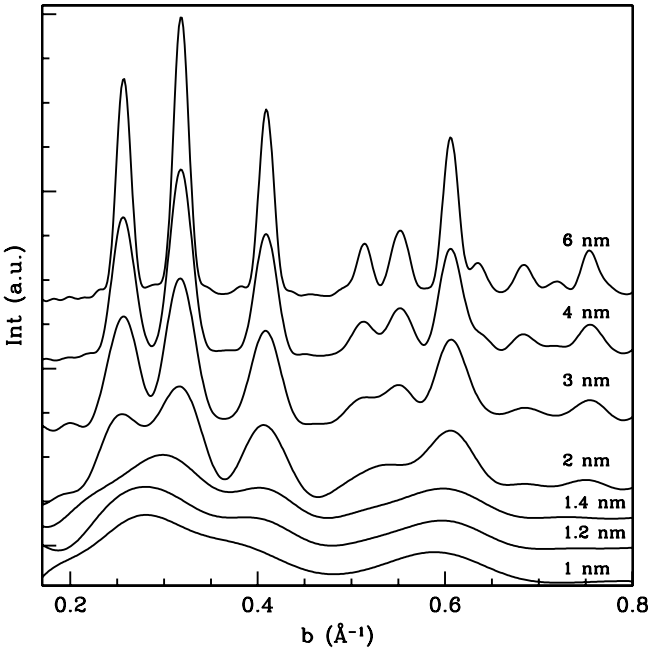

Fig. 1 Calculations of the Debye equation for spherical particles of Ta_2O_5

[1] This approximation introduces an error because the true interatomic distance and the center of the histogram class can be slightly different. If the width of the histogram class chosen is small, the discretization has an effect on the diffraction pattern that can be approximated by an exponential factor, of the same form as the Debye-Waller factor ($D = e^{-2M}$). It describes the effect of thermal movements of the atoms in the crystals on the diffraction pattern. Thus the approximation of the interatomic distances in histogram classes is equivalent to a random displacement of the atoms from their equilibrium positions, analogous to thermal movement.

reason it is a perfect example to be studied for structure determination. The power spectrum (i.e. the square of the Fourier transform of the image) is calculated (Fig. 2b). It is characterized by several sharp spots from which it is possible to extract the lattice distances and the angles between the planes. In this case it can be attributed to the monoclinic HfO_2 structure (JCPDS [43-1017] and ICSD 27313) oriented along the [0–11] direction as indexed in Figure 2b. In this case the particle is elongated along the [100] direction.

The monoclinic HfO_2 structure is characterized by similar lattice parameters: $a = 5.116$, $b = 5.172$ and $c = 5.295$ Å and $\beta = 99.2°$. Because the global precision in the determination of the distances by HRTEM is worse than 1-2%, in this particular case the particle could also be oriented along the [1-10]. In this case the long axis would be parallel to the [001] direction instead of [100]. To discriminate between the two possible growth directions experimental XRD patterns were compared to calculated ones. The X-ray powder diffraction pattern of HfO_2 nanocrystals synthesized at 250°C (Fig. 3, solid line) shows broad diffraction peaks pointing to small crystallite sizes. However, the theoretical positions of the diffractions of the monoclinic HfO_2 structure match well with the experimental ones. To prove that the Debye scattering equation is a powerful tool to characterize the preferential growth direction of these nanocrystals several calculations for model particles were performed.

Although the pattern calculated for a spherical particle of 4 nm in diameter (Fig. 3, dotted line) coincide well with the experimental data, the reflection at about $b = 0.393$ Å^{-1}, characteristic for the diffraction by the (002), (020), and (200) planes, is not well reproduced. These reflections are superimposed in the experimental patterns, because the lattice parameters of the HfO_2 monoclinic structure are similar. In fact in the experimental patterns this peak is sharper, more intense and slightly shifted towards larger diffraction angles compared to the calculated ones, suggesting that the particles exhibit an elongated shape in one of these directions. It is reasonable to assume that the intensity as well as the shift of the experimental peak around $b = 0.393$ Å^{-1} is mainly caused by the diffraction of the (200) planes, and that the particles are elongated along the [100] axis. To prove this hypothesis, the Debye scattering equation was calculated for ellipsoidal particles (long radius = 3 nm and short radius = 1.5 nm) with the long axis either parallel to the [100], [010], or [001] directions, respectively (Fig. 3 short dashed line, long dashed line and dot, short dashed line respectively). All three calculated patterns seem to be quite similar in terms of peak intensity and the only difference lies in the position of the (002) (020) (200) diffraction peaks. A comparison of the calculated patterns with the experimental pattern clearly shows that the best agreement is found, when the particles are elongated along the [100] direction. The calculated peak position is at $b = 0.393$ Å^{-1}, which fits perfectly with the experimental reflection at $b = 0.393$ Å^{-1}, whereas calculations for a particle elongated along the [010] and along the [001] give a peak position of $b = 0.388$ Å^{-1} and $b = 0.383$ Å^{-1}, respectively.

In conclusion, according to Debye calculations, the particles are about 6 nm in length and about 3 nm in width and display a preferential growth in the [100] crystal direction. So the combination of XRD data and Debye scattering equation calculations provides a powerful tool to characterize the growth orientation of crystals on the nanoscale, even when the possible axis of

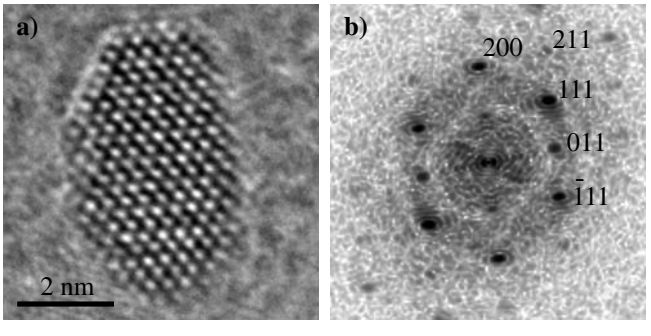

Fig. 2 HRTEM image of a single HfO_2 particle (a) and its power spectrum (b)

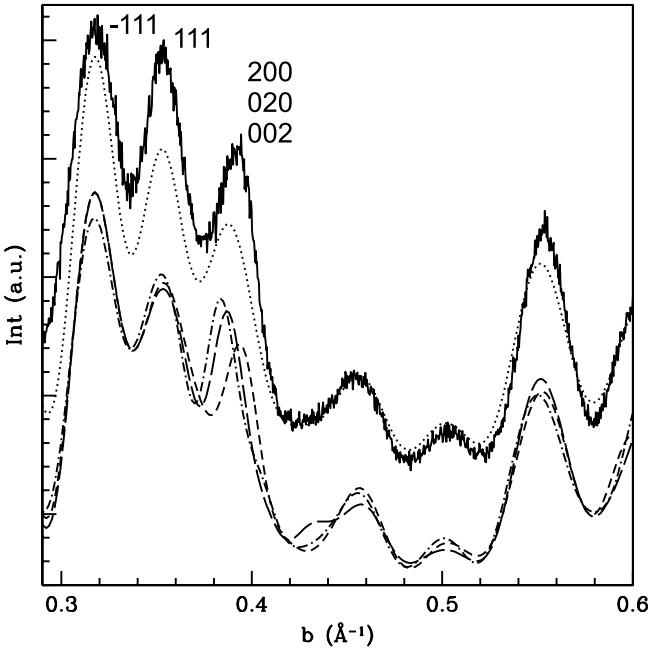

Fig. 3 Experimental pattern of HfO_2 nanoparticles synthesized at 250° C (solid line), calculated patterns for 4 nm spherical particles (dotted line), ellipsoidal particles of 6x3 nm elongated along the [100] (short dashed line), [010] (long dashed line), [001] (dot, short dashed line) respectively

growth are nearly equivalent from a crystallographic point of view.

Conclusion

This articles showed that XRD patterns of nanocrystals can give useful and valuable structural information if combined with calculation of the Debye equation. It was demonstrated that such technique could be applied to any form of matter in which there is a random orientation. In particular it was successfully applied for the determination of the preferential growing axis of elongated HfO_2 nanocrystals which was not unambiguously possible by HRTEM measurements only.

Furthermore, because XRD statistically gives structural information about the whole sample, the calculation of the Debye equation is the ideal tool to be associated with HRTEM structural studies.

Acknowledgements The author thanks Dr. Markus Niederberger, Dr. Bernd Smarsly and Prof. Dr. Markus Antonietti for helpful discussions and critical reading of the manuscript.

References

1. El-Sayed MA (2004) Acc. Chem. Res. 37: 326
2. Wang Y, Herron N (1991) J. Phys. Chem. 95: 525
3. Alivisatos AP (1996) J. Phys. Chem. 100: 13226
4. Cölfen H, Pauck T (1997) Colloid Polym. Sci. 275: 175
5. Deshpande AS, Pinna N, Beato P, Antonietti M, Niederberger M (2004) Chem. Mater. 16: 2599
6. Wang ZL (1999) Characterization of Nanophase Materials (Wiley-VCH, Weinheim)
7. Debye P (1915) Ann. Phys. 46: 804
8. Warren BE (1990) X-Ray Diffraction (Dover, New York) page 117
9. Guinier A (1994) X-Ray Diffraction in Crystals, Imperfect Crystals and Amorphous Bodies (Dover, New York) page 49
10. Vogel W (1998) Cryst. Res. Technol. 33: 1141
11. Hall BD, Ugarte D, Reinhard D, Monot R (1995) J. Chem. Phys. 103: 2384
12. Zanchet D, Hall BD, Ugarte D (2000) J. Phys. Chem. B 104: 11013
13. Gnutzmann V, Vogel W (1990) J. Phys. Chem. 94: 4991
14. Hall BD (2000) J. Appl. Phys. 87, 1666
15. Pinna N, Wild U, Urban J, Schlögl R (2003) Adv. Mater. 15: 329
16. Niederberger M, Pinna N, Polleux J, Antonietti M (2004) Angew. Chem. Int. Ed. 43: 2270
17. Pinna N, Neri G, Antonietti M, Niederberger M (2004) Angew. Chem. Int. Ed. 43: 4345
18. Pinna N, Garnweitner G, Antonietti M, Niederberger M (2004) Adv. Mater. 16: 2196
19. Niederberger M, Bartl MH, Stucky GD (2002) Chem. Mater. 14: 4364
20. Niederberger M, Bartl MH, Stucky GD (2002) J. Am. Chem. Soc. 124: 13642
21. Hall BD, Monot R (1991) Comp. in Phys. 5: 414

Progr Colloid Polym Sci (2005) 130: 33–39
DOI 10.1007/b107343
Published online: 3 June 2005

Peter Fratzl
Himadri S. Gupta
Oskar Paris
Angelika Valenta
Paul Roschger
Klaus Klaushofer

Diffracting "stacks of cards" – some thoughts about small-angle scattering from bone

Abstract Small-angle x-ray scattering (SAXS) has been used extensively in recent years to characterize the thickness and orientation of mineral particles in bone. While the determination of these parameters is straight forward, the detailed shape of the SAXS curve turned out to be much more difficult to analyze quantitatively, because it is influenced by the shape as well as by the arrangement of the particles. The spherically averaged SAXS curve $I(q)$ has been found to vary with bone type and species. For bone from mice and rats, $I(q)$ is proportional to q^{-1} at small q, which is compatible with needle-like particles, and it is proportional to q^{-2} for human bone, which is compatible with plate-like particles. On the other hand, such differences may also be due to varying spatial arrangements of plate-like particles. Results from electron microscopy and atomic force microscopy reveal parallel arrangements of platelets similar to stacks of cards in all types of mature bone tissue. In the present paper, we consider arrangements of this type and derive simple analytical expressions for small-angle scattering from short-range ordered stacks of plate-like particles. Qualitatively, these expressions can describe all types of SAXS curves published for different types of bone.

Keywords Biomineralization · Mineral platelets. Bone · Nanostructure · Small-angle X-ray scattering · SAXS

Dedicated to Prof. W. Ruland at the occasion of his 80th birthday

P. Fratzl (✉) · H. S. Gupta · O. Paris
Max Planck Institute of Colloids and Interfaces, Department of Biomaterials, 14476 Potsdam, Germany
e-mail: fratzl@mpikg.mpg.de
Fax: +49-331-567-9402

A. Valenta · P. Roschger
K. Klaushofer · P. Fratzl
Ludwig Boltzmann Institute of Osteology at the Hanusch Hospital of WGKK and AUVA Trauma Centre Meidling, 4th Medical Department, Hanusch Hospital, Vienna, Austria

A. Valenta
Erich Schmid Institute of Materials Science, Austrian Academy of Sciences & University of Leoben, Leoben, Austria

Introduction

The structure of bone at the molecular level consists of a composite of mainly type I collagen, carbonated apatite, a small fraction of non-collageneous proteins, and water. The first two components form the bulk of the dry weight of bone. During bone formation in vertebrates, the collagen matrix is deposited first and is then mineralized over a period of several months (primary and secondary mineralization). It has been known for some time that the mineral phase deposits as tiny platelets with nanometer dimensions, both in and around the collagen fibrils. Their specific loci and structural relationship to each other as well as to the organic phase remains the subject of intense research [1–5]. From transmission electron microscopy (TEM) of rat bone lamellae, Weiner et al. [1,2] proposed that the mineral platelets were ordered parallel to each other within a single collagen fibril, but that the orientation was random between different fibrils. More recently, Rubin and coworkers found similar evidence also in human bone [6]. High resolution atomic force microscopy (AFM) clearly showed a stack of cards motif, as well as demonstrating that the mineral plates follow the characteristic D-spacing (of 67 nm) of the underlying collagen fibrils, and have a thickness from 3–10 nm, and a width (or length) from 30 to 120 nm [5]. In the same study, globular noncollagenous proteins were observed laterally bridging collagen fibrils. The thin mineral plates could conceivably be accommodated inside regularly spaced pores in the collagen fibrils, as proposed by Katz

and Li [7, 8]. However, it is not entirely clear that such high regularity in fibrillar arrangement is present in bone, although it was observed to exist in mineralized turkey leg tendon [9–12]. Thus, the conclusion from microscopic investigations is that the bone mineral phase consists of very thin mineral platelets with a relatively low dispersion in thickness, but wider spread in the large lateral dimensions, which are arranged with their faces parallel to each other within a single fibril, but with less spatial correlation between fibrils. Mechanically, such a scheme where nanometer thin, stiff and brittle mineral platelets are parallel oriented and laterally staggered (as observed, for example, in [5] and [10]), with a thin intervening layer of organic matrix, has been shown to have significant mechanical advantages in stiffness and toughness [13–15].

Due to the large electron density contrast between mineral and collagen, the nanostructure of bone can be well investigated by Small-Angle X-ray Scattering (SAXS), which has the potential to provide quantitative and statistically representative information in the range of ≈ 0.5–50 nm [16–18]. Because of a wide distribution of the sizes of the mineral particles and their preferred orientation [3, 10], local order in the packing of mineral crystals [1], as well as heterogeneous fibril architecture within the sampling volume [19], the quantitative interpretation of the SAXS signal remains a challenge. Some of the pioneering theoretical work in the field of SAXS from strongly disordered, solid two-phase systems was set up already in the fifties by Debye et al. [20], and in the sixties by Ruland and co-workers for the determination of structural parameters such as average chord lengths [21] and preferred orientations [22]. These concepts have been successfully adapted to describe mineral particle size [23–25] and mineral particle orientation [26, 27] in bone. In recent years, these relations turned out to be particularly useful to obtain simple nanostructural parameters in a position resolved way by using an X-ray microbeam (''Scanning SAXS''). Examples include the spatial variation of mineral nanostructure in trabecular bone [28–30], at the bone-cartilage interface [31], in dentin [32, 33], at the mineralization front in mineralized turkey leg tendon (MTLT) [34], in archaeological bone [35], as well as local alterations in the bone material in diseases like osteogenesis imperfecta [26, 36–39].

In addition to simple parameters characterizing the thickness and the orientation distribution, it has been observed that the shape of the SAXS curve also varied in a systematic way. In particular, the scattering intensity $I(q)$ is proportional to q^{-1} at small q in some cases (e.g. murine bone [24]), and to q^{-2} in, e.g. human bone. One possible origin of this difference are needle-like crystals in the first case, versus plate-like crystals, in the second [17, 23, 25]. Moreover, a totally different shape of the SAXS curve has been found for fluorotic bone formed under the influence of sodium fluoride [36]. Analytical expressions for the SAXS intensity in simulated two-phase systems based on needles and plates resembling some representations of bone nanostructure have been derived in [40]. However, since mineral volume fractions in bone are high (around 50%), another possibility for the behaviour of $I(q)$ at low q is due to a different local arrangement of (plate-like) crystals. The aim of the present paper is to investigate whether the different shapes of the SAXS curves are compatible with a structure resembling ''stacks of cards''. We derive analytical expressions for simple arrangement of ''stacked cards'' and investigate to which extent SAXS from different types of bone can be described by such structural units.

Theoretical treatment

When considering the evaluation of the SAXS signal from bone, a starting point is to model the mineral platelets as a randomly spaced parallel stack of cards. Common SAXS pinhole instruments cover typically a range of scattering vectors $0.1\ \mathrm{nm}^{-1} < q < 5\ \mathrm{nm}^{-1}$, corresponding roughly to a spatial resolution from $\approx$ 1–50 nm (the length of the scattering vector q is defined here as usual, $q = 4\pi \sin\theta/\lambda$, with 2θ being the scattering angle and λ the X-ray wavelength). Therefore, only the thin dimension of the mineral particles (and their lateral spacing) will participate to the measurable SAXS signal, and there will be no difference between a parallel stack of cards and a staggered arrangement of mineral platelets. Attempts to construct proper correlation functions for similar situations were published in particular for lamellar polymer systems [41–43]. In most cases a ''long range order'' attempt was chosen, describing and analyzing deviations from a perfect periodic stacking of lamellae. This attempt is however inadequate for bone where the correlation between platelets is always ''short range'', as there was never a correlation maximum detected in the SAXS intensity from mineralized tissue. More recently, correlation functions were also derived for short-range ordered arrangements of lamellae in polymers [44, 45], but the obtained expressions were not analytical.

Basic definitions

Due to the difficulty of interpreting the shape of the SAXS curve $I(q)$, only simple parameters have previously been used, such as the mean degree of alignment of the particles and a linear dimension

$$T = \frac{4J}{\pi P},\ \text{where } P = \lim_{q\to\infty}[q^4 I(q)] \text{ and } J = \int_0^\infty q^2 I(q)\mathrm{d}q \qquad (1)$$

was used to characterize the typical thickness of the particles [24, 28]. Calling ϕ the volume fraction of mineral and σ its total surface per unit volume of tissue, it has been shown that

$$T = \frac{4\phi(1-\phi)}{\sigma}. \qquad (2)$$

This parameter has been introduced by Porod [46] and can be related to the mean chord lengths of the inclusions $l_I = 4\phi/\sigma$ and of the matrix $l_M = 4(1-\phi)/\sigma$ by $1/T = 1/l_I + 1/l_M$. [47]. Mean chord lengths have been used frequently to analyze small-angle scattering data [16, 17, 46] and are generally very useful for the description of random media [47]. The advantage of T is that it is independent of the shape and arrangement of the particles. All the

information about the shape and arrangement of the crystals is summarized in a rescaled function $G(x)$ of the dimensionless parameter $x = qT$, defined as [24]

$$G(x) = x^2 I(x/T)/(JT^3). \tag{3}$$

Systematic differences in $G(x)$ are found between species and possibly also with bone age or the volume fraction of mineral [24]. These differences seem to be very consistent throughout the existing literature and indicate some systematic differences between tissue structures.

In constructing our model we start from the following definition of the spherically averaged SAXS intensity [40, 48].

$$I(q) = \left\langle \left| \int \mathrm{e}^{i\mathbf{q}\cdot\mathbf{r}} (w(\mathbf{r}) - \phi) \mathrm{d}\mathbf{r} \right|^2 \right\rangle \tag{4}$$

where $w(\mathbf{r}) = 1$ if there is mineral at the position $\mathbf{r}$, and $w(\mathbf{r}) = 0$ if there is organic matrix. The volume fraction of mineral, ϕ is the average of $w(\mathbf{r})$ over the illuminated specimen volume. The brackets $\langle\rangle$ indicate the spherical average. We assume an arrangement of the mineral in arrays of parallel thin platelets (the length and breadth of the platelets are both much larger than their thickness).

Under these conditions, the scattering intensity can be written in the approximate form [40]

$$I(q) = \frac{2\pi}{q^2} \left| \int_{-\infty}^{\infty} \mathrm{e}^{\mathrm{i}qz} (w(z) - \phi) \mathrm{d}z \right|^2 = \frac{2\pi}{q^2} S_1(q). \tag{5}$$

The function w is considered here as a function of z only and not of the full position vector $\mathbf{r}$. The linear structure factor $S_1(q)$ is related to the one-dimensional correlation function $h(z)$ along z

$$S_1(q) = \tilde{h}(q) = 2 \int_0^{\infty} \cos(qz) h(z) \mathrm{d}z$$

$$\text{or (equivalently)} \quad h(z) = \frac{1}{2\pi} \tilde{S}_1(z), \tag{6}$$

where we have used a tilde to denote the (one-dimensional) Fourier transform. Using the definitions above (eqs 1 and 2), we have

$$P = 2\pi \lim_{q\to\infty} [q^2 S_1(q)] = -4\pi h'(0) = 2\pi\sigma, \quad \text{and}$$

$$J = 2\pi \int_0^{\infty} S_1(q) \mathrm{d}q = 2\pi^2 h(0) = 2\pi^2 \phi(1-\phi). \tag{7}$$

where the prime denotes the first derivative. Moreover,

$$G(x) = \frac{S_1(x/T)}{\pi T \phi(1-\phi)} = \frac{\tilde{g}(x)}{\pi}, \tag{8}$$

using the rescaled (one-dimensional) correlation function

$$g(\zeta) = \frac{h(T\zeta)}{\phi(1-\phi)}. \tag{9}$$

As a consequence, the function G(x) is directly related to the rescaled one-dimensional correlation function by a simple Fourier transform.

Simple models for stacks of cards

One-dimensional correlation functions have been calculated previously in a different context [40, 48]. Two examples are given here. Let us consider points thrown at random onto the line. Consider the points as being the limit between consecutive segments. Under these conditions the segment length distribution $p(\delta)\mathrm{d}\delta$ is just an exponential $p(\delta) = e^{-\rho\delta}$, where ρ is the density of the points on the line [48]. The first example consists of colouring a fraction ϕ of the segments (chosen at random) in black (symbolizing the mineral phase). This situation corresponds to a widely distributed range of plate thickness, with an average value of $1/\rho$ for the plate thickness (see Fig. 1a). Also, there is no correlation in the position of the plates along the line perpendicular to the plane surface. $G(x)$ has been calculated for this case in [40] to give a Lorentzian

$$G(x) = \frac{4}{\pi} \frac{1}{x^2 + 4}, \tag{10}$$

for which it follows that the correlation function is a decreasing exponential [20].

$$g(\zeta) = \mathrm{e}^{-2\zeta}. \tag{11}$$

A second example has been calculated in [48] (see Fig. 1b). It was assumed that for each interval the left portion, corresponding to a fraction ϕ of the interval, is coloured black. In this way, particles have again a wide thickness distribution (with an average thickness of ϕ/ρ) but they have now strong positional correlations, as there is an organic layer of given thickness at the right of each particle (see Fig. 1b). The scattering function is given in [48], appendix C2. Recasting these expressions into the notations of the present paper, we obtain

$$G(x) = \frac{4}{\pi} \frac{x^2}{(x^2 + 4\,\phi^2)(x^2 + 4\bar{\phi}^2)} \tag{12}$$

and

$$g(\zeta) = \frac{\phi \mathrm{e}^{-2\phi\zeta} - \bar{\phi} \mathrm{e}^{-2\bar{\phi}\zeta}}{\phi - \bar{\phi}}, \tag{13}$$

where we use $\bar{\phi} = 1 - \phi$. This clearly shows that one expects G(x) to depend on the volume of the particles as well as on their mutual arrangement. Note that for small volume fractions of mineral ($\phi \to 0$), Eq. (12) reduces to (10), which means that there is no more correlation in the position of the platelets when their density decreases.

Generally, (10) and (12) are expressions are of the type

$$G(x) = \frac{4}{\pi} \frac{x^2 + a}{x^4 + bx^2 + c} \tag{14}$$

where–due to the normalization conditions of G(x) – the constant a is given as a function of b and c. Moreover, since G(x) must not be negative, $c > b^2/4$. Another way of writing G(x) is

$$G(x) = \frac{4}{\pi} \frac{x^2 + a}{(x^2 + (\hat{\alpha} - \hat{\beta})^2)(x^2 + (\hat{\alpha} + \hat{\beta})^2)} \tag{15}$$

where $\hat{\alpha}$ and $\hat{\beta}$ are complex numbers. The fact that a, b, c are real puts constraints on these complex numbers. The analysis shows that $\hat{\alpha}$ must be real and positive (we write $\hat{\alpha} = \alpha$) and that $\hat{\beta}$ must be either real ($\hat{\beta} = \beta$) or purely imaginary ($\hat{\beta} = i\beta$). Finally, we obtain the following expressions for the model functions:

$$G(x) = \begin{cases} \frac{4}{\pi} \frac{x^2 + (\alpha-1)(\alpha^2+\beta^2)}{x^4 + 2(\alpha^2-\beta^2)x^2 + (\alpha^2+\beta^2)^2} & \text{for } \hat{\beta} = i\beta \\ \frac{4}{\pi} \frac{x^2 + (\alpha-1)(\alpha^2-\beta^2)}{x^4 + 2(\alpha^2+\beta^2)x^2 + (\alpha^2-\beta^2)^2} & \text{for } \hat{\beta} = \beta \end{cases} \tag{16}$$

and

$$g(\zeta) = \begin{cases} e^{-\alpha\zeta} [\cos(\beta\zeta) + \frac{\alpha-2}{\beta} \sin(\beta\zeta)] & \text{for } \hat{\beta} = i\beta \\ e^{-\alpha\zeta} [\cosh(\beta\zeta) + \frac{\alpha-2}{\beta} \sinh(\beta\zeta)] & \text{for } \hat{\beta} = \beta \end{cases} \tag{17}$$

These functions depend on two parameters. Note that eq. (12) and (13) are obtained for $\alpha = 1$ and $\beta = 1 - 2\phi$. It reduces to eq. (10), (11) when $\beta^2 = (\alpha - 2)^2$ (case $\hat{\beta} = \beta$) or $\alpha - 2 = \beta = 0$ (case $\hat{\beta} = i\beta$). The first parameter, β, defines an oscillatory part of the correlation function and $2\pi T/\beta$ can be interpreted as a typical

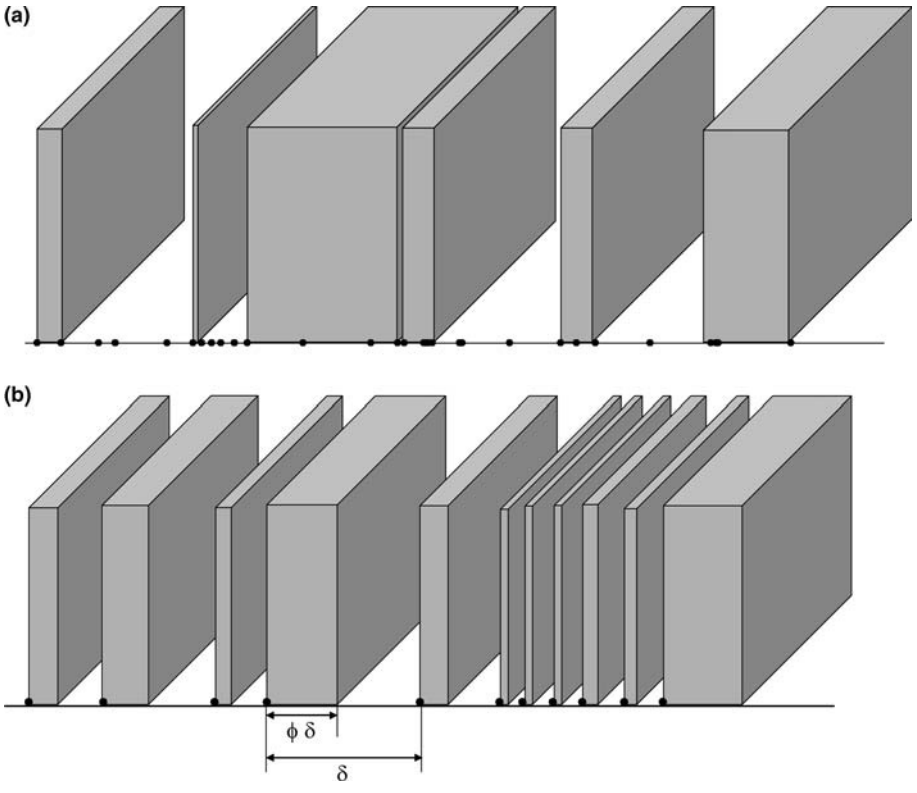

Fig. 1 Two simple distributions of parallel plates based on randomly positioned points on a line. In (a) a fraction ϕ of the segments between the points is chosen at random and the corresponding spaces filled with mineral. The corresponding SAXS signal is defined by eqs. (10) and (11). In (b) each segment of (Poisson distributed) length δ is subdivided into two parts of length $\phi\delta$ and $(1\text{-}\phi)\delta$, respectively, the first part being filled with mineral. The corresponding SAXS signal is given in eqs. (12) and (13)

distance between successive plates. The second parameter, α, describes a damping of the oscillation. The larger this (dimensionless) parameter, the stronger the damping due to disorder in the arrangement of the plates. The two parameters translate into the shape of the $G(x)$ function as shown in Fig. 2.

A wide range of maximum positions and widths of the $G(x)$ curve can be obtained by varying the parameters α and β. Hence, a model of parallel plates with varying spacing and degree of order will qualitatively described all the types of $G(x)$ curves reported for various bone tissues [24]. Fig. 3a summarizes the positions of maxima x_0 for a range of α and β values. With increasing β, the maximum x_0 of $G(x)$ shifts to larger values of x. For $\alpha = 1$, $G(0) = 0$, and the maximum in $G(x)$ is well pronounced. For $\alpha > 1$, the ratio $G(0)/G(x_0)$ increases (Fig. 3b), indicating a widening of the peak as a result of the increased disorder, until this ratio reaches one, and the maximum of $G(x)$ has shifted to $x_0 = 0$. Generally speaking, $G(x)$ has its maximum at $x_0 = 0$, when β is small or α is large. Interestingly, for $\beta > 1$, the maximum position x seems to be mostly determined by β, (i.e. the average platelet distance), while the width of $G(x)$ is essentially a function of α (i.e. the damping of the distance correlations).

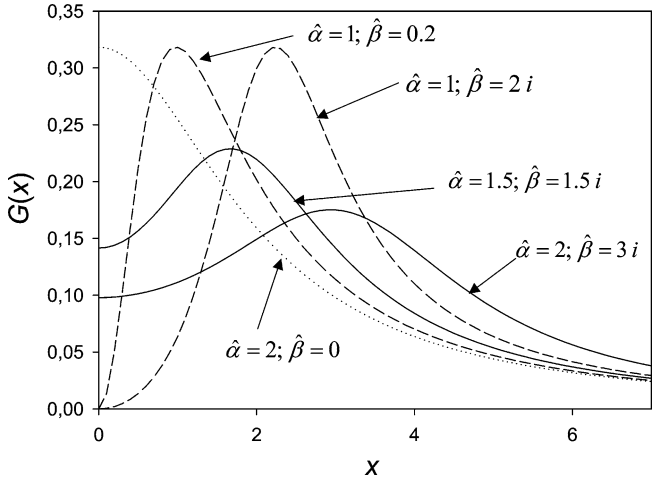

Fig. 2 Examples for $G(x)$ functions with different values of the parameters $\hat{\alpha}$ and $\hat{\beta}$. The dotted line corresponds to eq.(10). The two broken lines shows examples where $G(0) = 0$ (corresponding to $\hat{\alpha} = 1$)

Discussion

To test the agreement of the model function with SAXS data from human bone [49], we have used $G(x)$ curves determined from bone biopsies of normal patients and fitted them with the model (Eq. 16). Specimen preparation and measurement have been described in detail in earlier work [25, 30, 39]. An example for such a fit is shown in Fig. 4

When this type of fit is carried out for a large number of data sets from human bone, one obtains α and β values as shown in the graph in Fig. 5.

These data indicate that the expressions (16) and (17) can be used for a quantitative description of SAXS data from bone. It also shows that the general hypothesis of

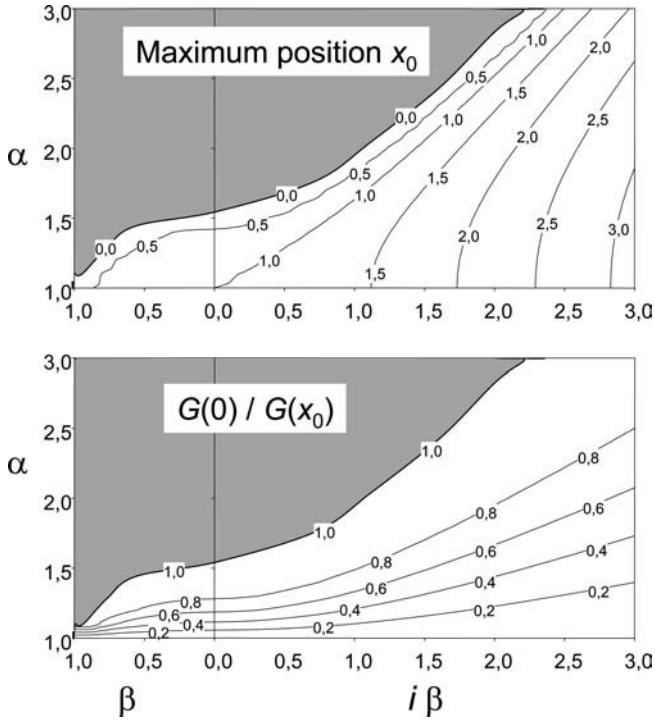

Fig. 3 Maximum position x_0 of the function $G(x)$ defined by eq. (16), as well as the ratio $G(0)/G(x_0)$, characteristic for the width of the curve. The area shaded in grey corresponds to sets of parameters where $G(x)$ is maximal at 0

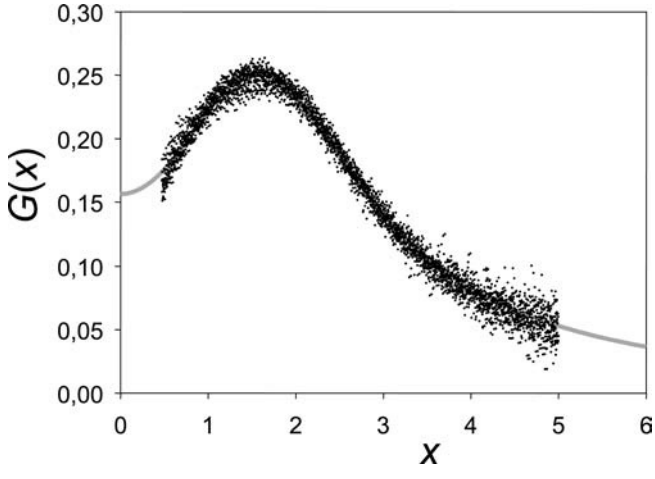

Fig. 4 Example of the fit (full line) of the G(x) curve from several measurement positions in human trabecular bone (dots) shown superimposed as a function of x

stacked mineral platelets, which is in line with TEM and AFM results [1, 4, 5, 10, 50], is a viable assumption for all types of bone, and that there is no need to interpret some previous SAXS measurements in terms of needle shaped mineral particles [23, 24]. As clearly shown in Fig. 2, it is

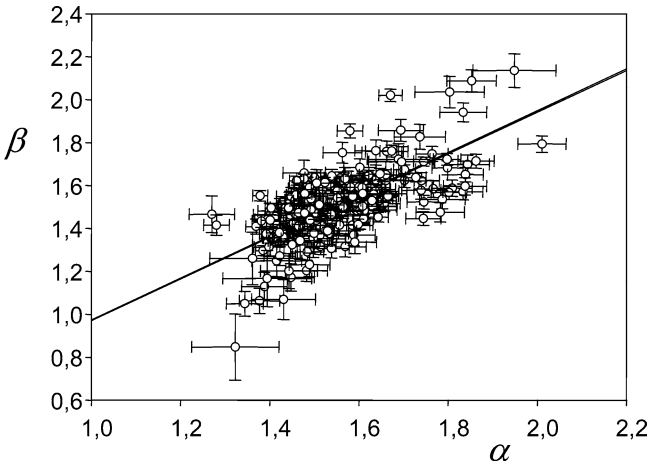

Fig. 5 Values of α and β for a large number of fits such as in Fig. 4 (where we have taken $\beta = i\beta$) fro human bone. Bone from different locations and different individuals was included. The full line indicates a slope of 1

possible to obtain $G(x)$ curves with a well-defined maximum, such as typically found for murine bone [23–25], and which may alternatively be due to needle-like crystals. But there are also examples of $G(x)$ curves without any peak away from $x = 0$, such as typically found in human bone [24, 28]. Qualitatively, it is clear that all types of typically observed G(x) shapes can be described by appropriate values of α and β, a quantitative fit of all these data is, however, beyond the scope of this paper.

Interestingly, all the data in Fig. 5 group around $\alpha \approx \beta \approx 1.5$ with a clear correlation between them. For larger β (smaller correlation distances), the damping of the correlations given by α is also stronger. This corresponds to a specific shape of the correlation function (Eq. 17) with one clear minimum but no secondary maximum. This is visualized in Fig. 6 together with the two extreme cases, $\alpha >> \beta$, and $\beta > \alpha$. The insert in Fig. 6 displays additionally the function $G(x)/x^2$ for these three correlation functions, corresponding to a (normalized) intensity distribution as it would be directly measured in a SAXS experiment. The case $\alpha = 2$ and $\beta = 0$ corresponds to the well known exponentially decreasing correlation function (Eq. 11) [20], leading to a Lorentzian form of $G(x)$. Such a behaviour was found for instance in sodium fluoride treated osteoporotic bone [36], indicating that fluoride treatment leads to full disintegration of positional correlations between the mineral platelets. The other situation displayed in Fig. 6 corresponds to the case of weak damping ($\beta > \alpha$), which leads to a secondary maximum in the correlation function. As a consequence, not only $G(x)$, but also the measured intensity (given by $G(x)/x^2$ in Fig. 6) shows now a clear interference maximum due to the inter-particle interference. Such a general behaviour is very frequently

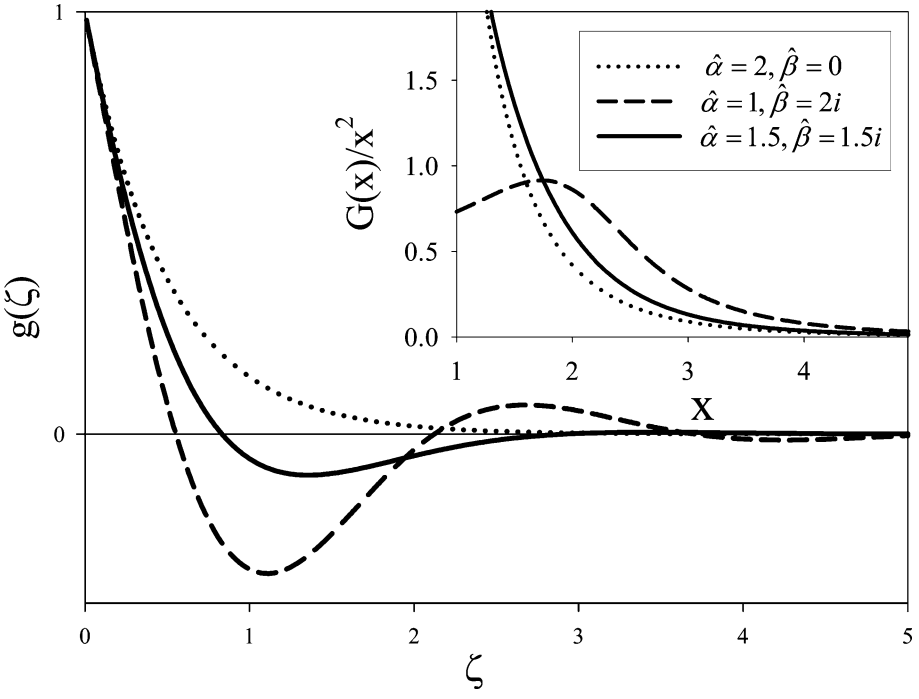

Fig. 6 Examples of correlation functions (Eq. 17) for different parameter combinations. The insert shows the function $G(x)/x^2$, which corresponds essentially to the scattering profile as measured directly by SAXS

observed for instance in decomposing 2-phase systems such as metal alloys, glasses or polymer mixtures (see, e.g. for [51] an overview), but was never found for bone.

Conclusion

A model of stacked, plate-shaped mineral particles with strongly damped short range correlations is able to quantitatively describe the small-angle X-ray scattering from bone. The scattering function $G(x)$, rescaled with respect to the "plate thickness" T, can generally be described by two parameters, an average correlation length and the damping of the correlations. This opens the possibility to add to the parameters T and ρ, already used extensively to describe particle thickness and degree of particle alignment in bone, two further parameters which describe the average spacing of stacked platelets. It also shows that it is not necessary to assume needle-like crystals to describe some of the SAXS curves from bone. Indeed, a similar effect can result from the interference due to weak positional correlations in the positions of plates arranged in the form of "stacks of cards". While quantitative fits of measured data were beyond the scope of this paper, a qualitative analysis shows that all typical SAXS curves published for different types of bone can generally be described by this approach. The differences would be due to variations in lateral spacing and degree of order in the stacking of the crystals. Unfortunately, this does not exclude the possibility that the peaked shape of $G(x)$ arises from needle-shaped particles rather than from short-range ordered stacks of cards. There is simply no way to distinguish between these possibilities by SAXS alone. Nevertheless, if a stack-of-card structure can be ascertained, e.g., by electron or atomic force microscopy, the SAXS curves can be fitted to determine particle spacing and degree of order with high statistical accuracy.

References

1. Weiner S, Arad T, Traub W (1991) FEBS Letters 285: 49
2. Weiner S, Arad T, Sabanay I, Traub W (1997) Bone 20: 509
3. Eppell SJ, Tong WD, Katz JL, Kuhn L, Glimcher MJ (2001) J Orthop Res 19: 1027
4. Rubin MA, Rubin J, Jasiuk W (2004) Bone 35: 11
5. Hassenkam T, Fantner GE, Cutroni JA, Weaver JC, Morse DE, Hansma PK (2004) Bone 35: 4
6. Rubin MA, Jasiuk L, Taylor J, Rubin J, Ganey T, Apkarian RP (2003) Bone 33: 270
7. Katz EP, Li S (1973) J Mol Biol 80: 1
8. Katz EP, Li ST (1973) J Mol Biol 73: 351
9. Landis WJ (1986) J Ultrastruct Mol Struct Res 94: 217
10. Landis WJ, Hodgens KJ, Song MJ, Arena J, Kiyonaga S, Marko M, Owen C, McEwen BF (1996) J Struct Biol 117: 24
11. Lees S, Prostak KS, Ingle VK, Kjoller K (1994) Calcif Tissue Int 55: 180

12. Arsenault AL (1992) Bone and Mineral 17: 253
13. Gao HJ, Ji BH, Jäger IL, Arzt E, Fratzl P (2003) Proc Natl Acad Sci USA 100: 5597
14. Jäger I, Fratzl P (2000) Biophys J 79: 1737
15. Fratzl P, Gupta HS, Paschalis EP, Roschger P (2004) J Mater Chem14: 2115
16. Guinier A, Fournet G (1955) Small-angle scattering of X-rays**.** Wiley, New York
17. Glatter O, Kratky O (1983) Small-angle X-ray scattering**.** Academic Press, New York
18. Fratzl P (2003) J Appl Cryst 36: 397
19. Weiner S, Wagner HD (1998) Ann Rev Mater Sci 28: 271
20. Debye P, Anderson HR, Brumberger H (1957) J Appl Phys 28: 679
21. Perret R, Ruland W (1968) J Appl Cryst 1: 308
22. Perret R, Ruland W (1969) J Appl Cryst 2: 209
23. Fratzl P, Fratzl-Zelman N, Klaushofer K, Vogl G, Koller K (1991) Calcif Tissue Int 48: 407
24. Fratzl P, Schreiber S, Klaushofer K (1996) Conn Tissue Res 35: 9
25. Fratzl P, Groschner M, Vogl G, Plenk H, Eschberger J, Fratzl-Zelman N, Koller K, Klaushofer K (1992) J Bone Miner Res 7: 329
26. Fratzl P, Paris O, Klaushofer K, Landis WJ (1996) J Clin Invest 97: 396
27. Fratzl P, Schreiber S, Boyde A (1996) Calcif Tissue Int 58: 341
28. Rinnerthaler S, Roschger P, Jakob HF, Nader A, Klaushofer K, Fratzl P (1999) Calcif Tissue Int 64: 422
29. Paris O, Zizak I, Lichtenegger H, Roschger P, Klaushofer K, Fratzl P (2000) Cell Mol Biol 46: 993
30. Roschger P, Grabner BM, Rinnerthaler S, Tesch W, Kneissel M, Berzlanovich A, Klaushofer K, Fratzl P (2001) J Struct Biol 136: 126
31. Zizak I, Roschger P, Paris O, Misof BM, Berzlanovich A, Bernstorff S, Amenitsch H, Klaushofer K, Fratzl P (2003) J Struct Biol 141: 208
32. Tesch W, Eidelman N, Roschger P, Goldenberg F, Klaushofer K, Fratzl P (2001) Calcif Tissue Int 69: 147
33. Kinney JH, Pople JA, Marshall GW, Marshall SJ (2001) Calcif Tissue Int 69: 31
34. Gupta HS, Roschger P, Zizak I, N. Fratzl-Zelman, Nader A, Klaushofer K, Fratzl P (2003) Calcif Tissue Int 72: 567
35. Wess TJ, Drakopoulos M, Snigirev A, Wouters J, Paris O, Fratzl P, Collins M, Hiller J, Nielsen K (2001) Archaeometry 43: 117
36. Fratzl P, Roschger P, Eschberger J, Abendroth B, Klaushofer K (1994) J Bone Miner Res 9: 1541
37. Roschger P, Fratzl P, Klaushofer K, Rodan G (1997) Bone 20: 393
38. Grabner B, Landis WJ, Roschger P, Rinnerthaler S, Peterlik H, Klaushofer K, Fratzl P (2001) Bone 29: 453
39. Tesch W, Vandenbos T, Roschger P, Fratzl-Zelman N, Klaushofer K, Beertsen W, Fratzl P (2003) J Bone Miner Res 18: 117
40. Fratzl P (1994) J Stat Phys 77:125
41. Ruland W (1977) Coll Polym Sci 255: 417
42. Strobl GR, Schneider MJ (1980) J Polym Sci: Polym Phys 18:1343
43. Ruland W, Smarsly B (2004) J Appl Cryst 37: 575
44. Bonnier B, Boyer D, Viot P (1994) J Phys A: Math Gen 27: 3671
45. Stribeck N (2004) Macromol Chem Phys 205: 1455
46. Porod G (1951) Kolloid Z 124:83–114; (1952) Kolloid Z 125: 51, 108
47. Mazzolo A, Roesslinger B, Gille W (2003) J Math Phys 44: 6195
48. Fratzl P, Lebowitz JL, Penrose O, Amar J (1991) Phys Rev B 44: 4794
49. Valenta A (2004) Changes in bone quality due to disease and treatment: combined study of small-angle X-ray scattering (SAXS) and Electron Backscttering (qBEI) PhD Thesis, University of Leoben, Austria
50. Landis WJ, Hodgens KJ, Arena J, Song MJ, McEwen BF (1996) Microsc Res Tech 33: 192
51. Binder K, Fratzl P (2001) Spinodal decomposition. In: G Kostorz (ed), Materials Science and Technology, Phase transformations in materials. Wiley-VCH, Weinheim

Progr Colloid Polym Sci (2005) 130: 40–50
DOI 10.1007/b107335
Published online: 3 June 2005

Bart Goderis
Philip G. Klein
Stuart P. Hill
Cor E. Koning

A comparative DSC, X-Ray and NMR study on the crystallinity of isomeric aliphatic polyamides

B. Goderis (✉)
Molecular and Nanomaterials,
Polymer Chemistry Devision,
Chemistry Department,
Catholic University of Leuven,
Celestijnenlaan 200F,
3001 Heverlee, Belgium
e-mail:
bart.goderis@chem.kuleuven.ac.be
Tel.: +32-16327806
Fax: +32-16327990

P. G. Klein · S. P. Hill
IRC in polymer Science and Technology,
University of Leeds, LS2 9JT Leeds, UK

C. E. Koning
Department of Polymer Chemistry,
Eindhoven University of Technology,
P.O. Box 513, 5600MB Eindhoven,
The Netherlands

Abstract In the polyamides 4.12, 10.6, 8.8 and 6.10 three fractions are present. The WAXD crystallinity is comparable to that of DSC and amounts to 40% in all samples. The rigid fraction obtained by solid state NMR is, however, close to 60%, pointing at 20% rigid amorphous material. A combination of the NMR, WAXD and SAXS results reveals that the latter fraction is situated inside the crystalline phase and not at the crystalline – 'mobile amorphous' interface. Accordingly, one third of the crystalline layers with a thickness between 50 and 56 Å is not truly crystalline. From the width of the WAXD 100 reflections it can be deduced that crystalline grains exist with lateral dimensions of approximately 100 Å. Hence a picture emerges of alternating solid and liquid-like layers with the former consisting of crystalline grains separated by rigid amorphous matter.

Keywords Crystallinity · Scattering · (s)NMR · DSC

Introduction

The degree of crystallinity of polymers is of extreme importance for the physical and mechanical properties of the materials based thereon. The resistance against chemicals, the moisture absorption, and mechanical properties like abrasion resistance, stiffness, tensile properties and toughness are all directly related to the crystallinity. Accordingly, an accurate knowledge of the crystallinity of polymer materials is a prerequisite for the polymer scientist and for the materials engineer.

Several experimental techniques exist to determine the degree of crystallinity of semi-crystalline polymers. A very reliable technique is Wide Angle X-Ray Diffraction (WAXD) [1], yielding a mass fraction crystallinity. Differential Scanning Calorimetry (DSC) records the heat of fusion and - provided a reference heat of fusion is known – also yields the mass fraction of crystalline material [2]. Small Angle X-ray scattering can be used as well. The result is a volume fraction crystallinity provided the data are interpreted in terms of a realistic morphological model. There exist well-established methods for semi-crystalline morphologies composed of alternating crystalline and amorphous layers [3–5]. A less frequently applied technique to determine the mass fraction degree of crystallinity is solid-state wideline proton NMR [6]. The principle is, that polymer chains present in the crystalline fraction and those present in the amorphous fraction exhibit a different mobility, and accordingly different NMR relaxation times and linewidths. All techniques should be handled with care, since crystallinity implies a crystalline-amorphous two-phase concept whereas there is abundant evidence for a third phase often thought to be situated at the interface between the crystalline and the highly mobile fully amorphous regions [7]. This third phase has hybrid characteristics in between those of crystalline and amorphous material and is often referred to as 'rigid amorphous'. The extent to which this fraction contributes to the measured crystallinity depends on the method

used. Careful analysis of all data may not only pinpoint the presence of this particular phase but may also throw a light on its topology. In this paper a morphological picture is presented that is best compatible with the obtained degrees of crystallinity by WAXD, DSC, SAXS and solid state NMR.

For this study a series of isomeric, linear aliphatic polyamides was used, *viz*. Polyamides 4.12, 6.10, 8.8 and 10.6. A study on the thermal properties, the crystallization rates and some physical and mechanical properties of these polyamide isomers was published earlier [8].

Experimental

Polymer synthesis

The polymers were synthesized using a two-step batch process [9, 10]. In a first step, at elevated pressure and in presence of significant amounts of water, a low molar mass 'prepolymer' is synthesized with $\overline{M}_n$ = 1000-2000 g/mol. The latter is partially crystalline and was postcondensated in the solid state using a static bed reactor for 24–45 h under a constant flow of nitrogen and steam at 35°C below the melting points of the resulting polymers until the desired molecular weight is reached. The starting chemical, 1,4-diaminobutane, was kindly provided by DSM, and used without further purification. 1,10-Diaminodecane was used as received from Sigma-Aldrich. All other α,ω-dicarboxylic acids and α,ω-diamines were purchased from Acros Organics and used as received.

Molecular characterization

Carboxylic acid endgroups were determined by potentiometric titration of a solution of the polyamide in *m*-cresol with a *m*-cresol solution of tetrabutylammoniumhydroxide. Amine endgroups were determined by potentiometric titration of a solution of the polyamide in phenol with a solution of hydrogen chloride in phenol/ethylene glycol. In choosing the 1,4-diaminobutane based polyamide (PA) 4.12 as one of the polyamides of study, one has to realize that during synthesis at elevated temperatures 1,4-diaminobutane, either in its monomeric form or present at the end of a polymer chain, will be partially transformed into the cyclic pyrrolidine. This group is a potential chain stopper and will be present as a third endgroup. Pyrrolidine endgroups were determined with a flow-fluorimeter. The concentration of a fluorescent compound, generated by reaction of pyrrolidine with 4-chloro-7-nitro-benzofurazane, was measured. The number of all measured endgroups was converted into a number average molar mass, $\overline{M}_n$, assuming two endgroups per polymeric chain, and accordingly the absence of branching.

Size Exclusion Chromatography (SEC/DV) was performed on polyamide 4.12 to characterize the molar mass distribution using a HP-1090M, equipped with a UV-diode array detector. The solvent/eluent was hexafluoroisopropanol. The intrinsic viscosity of the eluates was measured on line with a Viscotek differential viscosimeter detector, model 200, and the absolute molecular weights were calculated according to the universal calibration method using PS standards.

WAXD analysis

The WAXD measurements were conducted in the transmission mode at room temperature on 2 mm thick samples using a horizontal Geigerflex diffractometer on a Rigaku Rotaflex RU-200B rotating Cu anode at a power of 4 kW. The scattered Cu K_α radiation with a wavelength $\lambda = 1.542$Å was detected on a scintillation counter after filtering with Ni over the angular range $2 < 2\theta < 60°$, with 2θ the scattering angle. Data were acquired every $0.05°$ 2θ during 6 s. The powders were inserted in small aluminum frames, sealed with thin mica sheets.

The powder patterns were decomposed into a background, two amorphous halos and a series of crystalline reflections characteristic for the α phase. Reflections were labeled with Miller indices according to literature data [11]. Gaussians were used to describe the crystalline reflections and Lorentz functions for the amorphous halos using the 'Peak Fitting Module' of 'Microcal Origin', version 6.0 [12]. The mass fraction crystallinity was calculated from the ratio of the area enclosed by the crystalline reflections to that of the total intensity without the background.

Of particular importance is the position of the α-phase 001 reflection. The associated lattice distance, d_{001}, which can be calculated from it by using Bragg's Law, $\lambda = 2d\sin(\theta)$, corresponds to the distance between crystallographically identical hydrogen bonds. The associated reflecting planes lay parallel to the surface of the lamellar crystallite [11]. As a result, d_{001} corresponds to the projection of the length of the molecular repeating unit along the chain axis on an axis perpendicular to the lamellar surface. The length of the molecular repeating unit is identical for all studied isomers and equals 22.3Å. Accordingly, the tilt of the crystalline stems in the lamellae can be calculated from

$$tilt = \arccos\frac{d_{001}}{22.3}, \tag{1}$$

with d_{001} expressed in Å. Contrary to the situation for polyamide 4.12 and 10.6, the 001 reflection is weak in the case of polyamide 8.8 and 6.10 but the 002 reflection is strong. Consequently, in these cases d_{001} was calculated from the 002 reflection. The lamellar thickness can be extracted from SAXS data as discussed below or from the width of the 001 or 002 reflection by using the Scherrer equation [13]:

$$D_{hkl} = \frac{\lambda}{\beta\cos\theta} \tag{2}$$

with β the integral width of the related crystalline peak expressed in radians. The integral widths were calculated as the ratio of the peak area to its height. When the lamellar thickness is divided by d_{001}, the number of unit cells, stacked along the lamellar normal, is obtained. Eq. (2) was also applied to the 100 reflection. No corrections were made to account for instrumental peak broadening. As a result the peak widths may be slightly over estimated and accordingly the corresponding crystal sizes underestimated. However, typical polymer crystalline reflections are very broad by nature (small crystallite sizes) by which the relative influence of instrumental effects is limited.

DSC analysis

Specific heat capacity, $c_p(T)$, data were collected using a Perkin Elmer DSC7, calibrated with the melting point of Indium (156.6 °C) and benzophenone (48 °C) for the temperature and with Indium for the enthalpy (28.45 Jg^{-1}). The block surrounding the measuring unit was thermostatted at −10 °C with liquid nitrogen and the unit was flushed with dry nitrogen. Heating curves were recorded at 10 °C/min from 50 up to 260 °C on 5 mg samples in Perkin Elmer standard aluminum pans. The $c_p(T)$ based mass fraction crystallinity, $w_c(T)$, was calculated as a function of temperature according to [2, 14]:

$$w_c(T) = \frac{h_a(T) - h(T)}{h_a(T) - h_c(T)} \tag{3}$$

with $h_a(T)$ and $h_c(T)$ the temperature dependent reference enthalpies of the amorphous and crystalline phase, respectively. Reference values are available in the ATHAS data bank for polyamide 6.10 [15]. This databank contains reference heat capacity and enthalpy data for a large number of polymers, but no data are present for the polyamides 4.12, 10.6 and 8.8. However, because of the chemical similarity, the reference values for polyamide 6.10 were used also for the other polyamides in this work. The experimental enthalpy, h(T), was obtained through integration of $c_p(T)$ according to:

$$h(T) = \int_{T_{\mathrm{ref}}}^{T} c_p(T)\mathrm{d}T + h(T_{\mathrm{ref}}) \tag{4}$$

with $h(T_{ref})$ the known enthalpy of amorphous material at 250 °C, $h_a(250°C)$. Eq. (3), which only contains terms referring to the extreme states, is based on the assumption that the sample is an ideal two-phase (crystalline and amorphous) system with sharp transition zones. The glass transition of polyamide 6.10 occurs at 49.84 °C according to the ATHAS data bank.

SAXS analysis

All SAXS patterns were recorded with a Rigaku Kratky camera on a Rigaku Rotaflex RU-200B rotating Cu anode at a power of 4 kW. Cu K_α radiation was obtained by filtering with Ni and data were collected on a Braun linear position sensitive detector. The powders were measured at room temperature while being kept in a lead frame, sealed with aluminum foils. A blank scattering was subtracted taking into account the sample transmission. The obtained slit smeared intensities, $\tilde{I}(s)$, were smoothed by means of cubic splines and the tail region in the window $0.018 < s < 0.035$ Å^{-1} was fitted with the empirical relation [16]:

$$\tilde{I}(s) = B + \frac{P}{s^3}\exp\left(-38(s\sigma)^{1.81}\right) \tag{5}$$

with s the modulus of the scattering vector and equal to $2\sin(\theta)/\lambda$, B a constant background, P the Porod constant and σ a parameter that characterizes the thickness of the transition layer between crystalline and amorphous regions. This thickness equals 3σ. The constant B was subtracted and the as obtained scattering patterns were extrapolated to high scattering vector using the second term in eq. (5) in order to cut off the WAXD 001 reflection before desmearing by the Guinier-DuMond procedure [17] implemented in 'TOPAS', software developed by Dr. N. Stribeck, University of Hamburg. Fig. 1 illustrates the subsequent steps in this procedure for polyamide10.6.

Next, the desmeared intensities, I(s), were analyzed in terms of a lamellar model using the correlation function approach. Linear correlation functions, CF(x), were calculated by Fourier transformation and normalization to the integrated intensity of the corresponding ideal two-phase structure, Q_{id}:

$$CF(x) = \frac{\int_0^\infty I(s)s^2\cos(2\pi xs)\mathrm{d}s}{Q_{id}} \tag{6}$$

The corresponding ideal two-phase structure refers to the structure characterized by the reference state densities and a sharp crystalline-amorphous interface in the middle of the interphase as schematically represented in Fig. 2 [18].

Before transformation, I(s) was extrapolated nominally to infinity using the relation [19]:

$$\lim_{s\to\infty} I(s) = C\frac{P}{s^4}\exp\left(-4\pi^2\sigma^2 s^2\right) \tag{7}$$

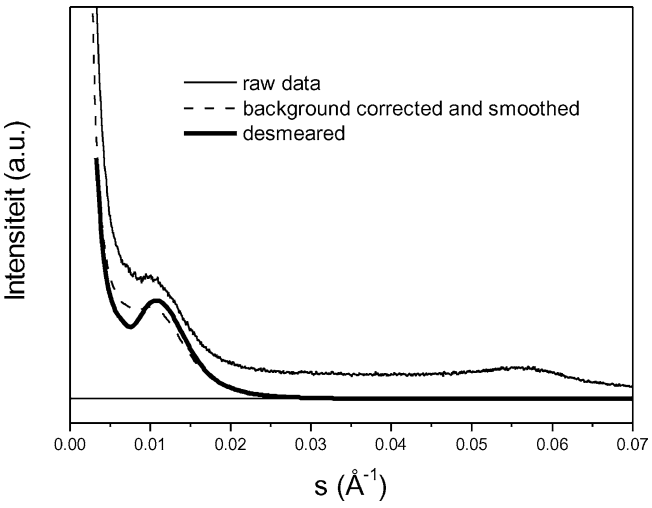

Fig. 1 Illustration of the SAXS data pre-processing for polyamide 10–6. It is representative for the other polyamides in this work with the WAXD 001 reflection around s = 0.055 Å^{-1} being very weak for the polyamides 8.8 and 6.10

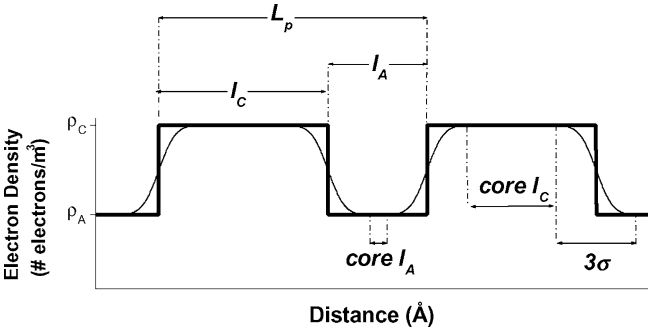

Fig. 2 Cross section through part of a lamellar stack used as a model in the analysis of the SAXS patterns. The thin full line: pseudo two-phase structure with transition layers with total thickness 3σ. Thick full line: density profile of the corresponding ideal two-phase structure with electron densities ρ_A and ρ_C for the amorphous and crystalline phase, respectively. The parameters in this figure that can be extracted when working in terms of this model are explained in the text

up to s = 0.09 Å^{-1}, with C a scaling constant. Secondly, $I(s)s^2$ was extrapolated to s = 0 Å^{-1} by the function Ds^2, with 'D' the appropriate constant to connect the zero point at s = s = 0 Å^{-1} to the first reliable measured data point. The value Q_{id} was obtained from the intercept of the linear regression to the autocorrelation triangle before normalizing the correlation function [18]. After normalization, CF(x) is obtained as illustrated for polyamide 10.6 in Fig. 3.

This Figure shows that the mentioned linear regression intersects the abscissa at x = A, which in the case of lamellar systems can be written as [20]:

$$A = \phi_L(1-\phi_L)L_p \tag{8}$$

with ϕ_L the local crystallinity in the lamellar stacks and L_p the number average distance between neighboring crystals. Solving this equation for ϕ_L with L_p read from the position of the first side maximum in CF(x), yields two solutions. One solution represents ϕ_L whereas the other one is the amorphous fraction $(1-\phi_L)$. Other

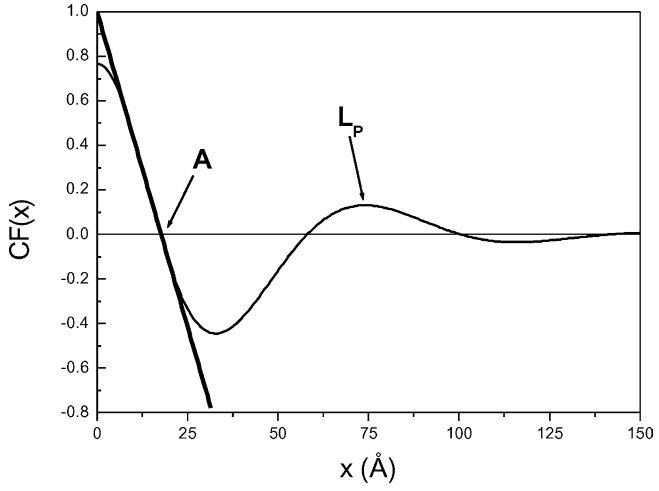

Fig. 3 Correlation function for polyamide 10.6 (thin line) with the linear regression to the autocorrelation triangle intersecting the abscissa at x = A (thick line). The position of the first side maximum corresponds to L_p

techniques, like WAXD, DSC or NMR are needed to decide which fraction corresponds to which phase. Knowing the appropriate value for ϕ_{LL} one can calculate the number average crystalline layer thickness, l_C, from (ϕ_L)Lp and the number average amorphous layer thickness, l_A, from $(1 - \phi_L)$Lp. These parameters refer to the corresponding ideal two-phase structure with the border line between the crystalline and amorphous layers at the middle of the transition layer of the pseudo two-phase structure, as depicted in Fig. 2.

Solid state NMR analysis

^{1}H NMR spectra were recorded from room temperature to 150 °C on a Varian-Chemagnetics CMX200 spectrometer operating at a frequency of 200 MHz. Samples were contained in a 5 mm diameter coil, allowing a 90° pulse width of 2 μs. Broadline spectra were recorded using the standard solid-echo pulse sequence $(90_x - \tau - 90_y - \tau_1)$ with τ and τ_1 set to 12 and 9 μs, respectively. The spectra are typically the result of 16 scans, recycle delay 5 s and a spectral width of 1000 kHz. Each spectrum was fitted to a combination of a Gaussian and Lorentzian peak, representing contributions from the rigid and mobile components of the polymer, respectively. ^{1}H $T_{1\rho}$ decays were recorded on the same sample, using for excitation a 90° pulse of 2 μs, and a spin-locking field strength of 62.5 kHz, at various spin-lock times up to 100 ms. The remnant magnetization at each spin-lock time was determined from the integrated intensity of the appropriate broadline spectrum.

Sample history

The crystallinities discussed in the present paper were measured without imposing any additional thermal program to the as synthesized powder like samples. This sample history was preferred because it yields a rather monodisperse type of crystals, judged from the relatively simple DSC melting traces. A double melting peak is observed at rather high temperatures, which is due to melting-recrystallization-remelting. During heating after cooling from the melt, both at 10°C/min, a more complex melting behavior is observed with - aside from the high temperature peaks - several additional peaks occurring below 215 °C that point at the additional presence of less perfect crystals. For the presented characterization work, well developed and nominally monodisperse semicrystalline morphologies are needed as e.g. obtained directly after synthesis and post-condensation. The complex melting behavior after cooling from the melt will be discussed separately elsewhere [25].

Results

Molecular characterization

Table 1 summarizes the endgroup concentrations of the four polyamides and the calculated $\overline{M}_n$ values. In contrast to the other polyamides polyamide 4.12 displays a majority of amine endgroups. In the synthesis of this particular polymer excessive 1,4-diaminobutane was used, as in the high temperature post-condensation step a substantial amount of this volatile product evaporates. Secondly, this excess intents to compensate for the partial transformation into (inactive) cyclic pyrrolidine.

The SEC-chromatogram of polyamide 4.12, representative for all studied polyamides, showed an almost perfectly symmetrical SEC curve, from which a linear Mark-Houwink plot could be constructed (not shown here). This linearity points to a non-branched character of the synthesized polyamides. From this experiment the following data could be deduced: $\overline{M}_n$ = 14,000 g/mol, $\overline{M}_w$ = 30,000 g/mol and $\overline{M}_w/\overline{M}_n$ = 2.1. The polydispersity index very is close to the theoretical value of 2 for linear polycondensates. Most likely the higher $\overline{M}_n$ value obtained from the endgroup measurements is due to the (inevitable) presence of some cyclic molecules, which do not contain endgroups but which are detected in a SEC/DV run. As a result, the reported endgroup based $\overline{M}_n$ values are slightly too high.

WAXD

Fig. 4 and 5 display the decomposed WAXD patterns of the polyamides 4.12 and 8.8, respectively. The scattering pattern of polyamide 10.6 is comparable to that of polyamide 4.12 and polyamide 6.10 resembles that of polyamide 8.8. The only difference in the scattering

Table 1 Endgroups and calculated $\overline{M}_n$ values of the polyamides (PRD = pyrrolidine)

	NH_2 (meq/g)	COOH (meq/g)	PRD (meq/g)	$\overline{M}_n$ (g/mole)
polyamide 4.12	0.047	0.026	0.031	19,200
Polyamide 10.6	0.009	0.068	–	26,000
polyamide 8.8	0.015	0.135	–	13,300
polyamide 6.10	0.021	0.085	–	18,900

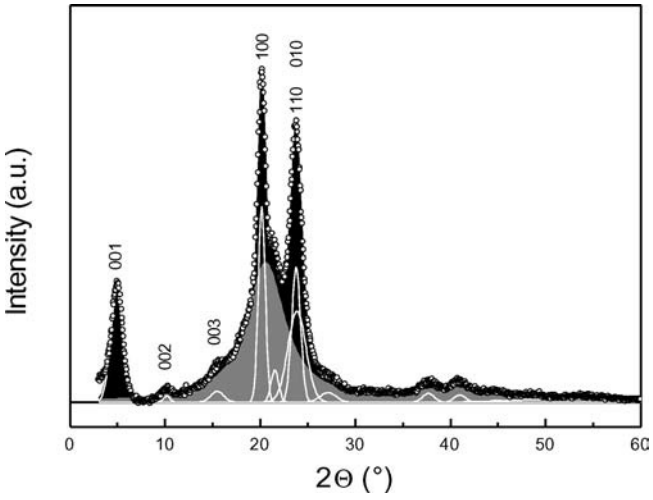

Fig. 4 WAXD patterns of polyamide 4.12 (open circles) with the amorphous and crystalline contribution highlighted in gray and black respectively. The crystalline reflections are depicted separately in white

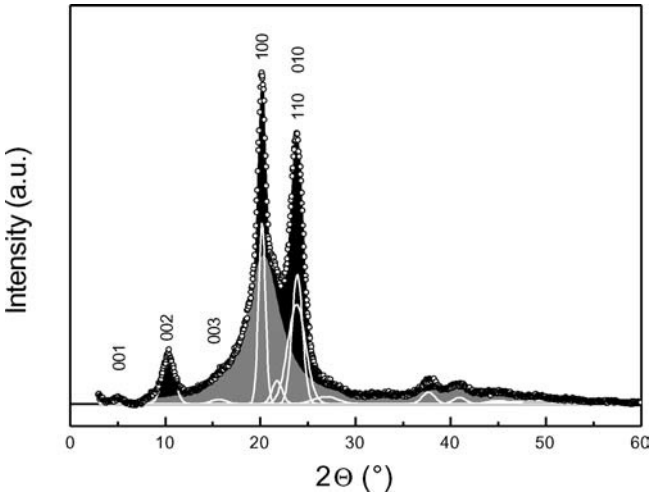

Fig. 5 WAXD patterns of polyamide 8.8 (open circles) with the amorphous and crystalline contribution highlighted in gray and black respectively. The crystalline reflections are depicted separately in white

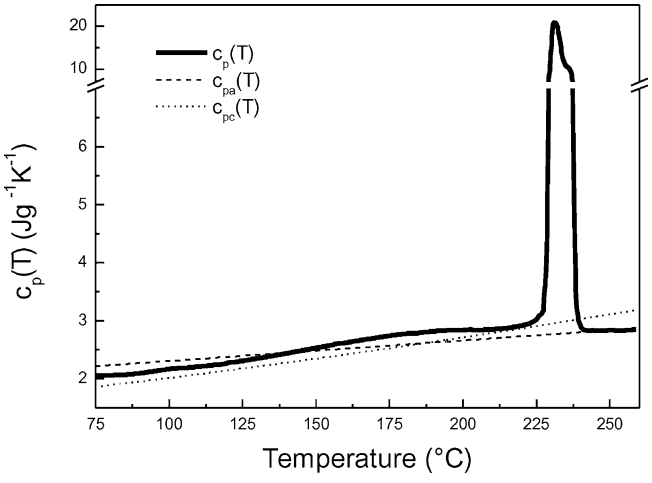

Fig. 6 Heat capacity of polyamide 4.12, $c_p(T)$, during heating at 10°C/min. The ATHAS reference heat capacities of amorphous, $c_{pa}(T)$, and crystalline, $c_{pc}(T)$, polyamide 6.10 are included for comparison

patterns between these two sets of isomers is in the relative intensity of the 001, 002 and 003 reflections. It can be shown that this depends on the relative position of the planes - parallel to the lamellar surfaces - that contain the hydrogen bonds [21]. There are two such planes per crystalline unit cell and the distances between them are identical for the polyamides 4.12 and 10.6 on the one hand and for the polyamides 6.10 and 8.8 on the other hand. The shortest distance is enclosed by the nitrogen atoms in the polyamides 4.12 and 6.10 and by the carbonyl units in the polyamides 10.6 and 8.8. Chain folded lamellae of even-even polyamides are composed of hydrogen-bonded sheets that are stacked by van der Waals interactions. Neighboring intra-sheet chains must progressively shear, for all $C = O \cdots H - N$ type hydrogen-bonds to be linear. As a result the chain axes are inclined at an angle of 13° to the normal of the chain folded sheet edge [11]. These sheets stack together either with again progressive shear, termed α-phase, or with alternating shear, termed β-phase [22]. The two phases can hardly be distinguished in WAXD powder patterns. However, in another paper, dealing with the crystal structure of these polyamides as determined form stretch aligned samples, it will be shown that only the α polymorph is present [23]. The intra-sheet and inter-sheet shearing in the α-phase results in an overall tilt of the chains with respect to the lamellar normal, which - as mentioned above - can be calculated from eq. (1).

It should be remarked that in fact more crystalline reflections exist than are actually used in the fitting of the WAXD scattering patterns [23]. They occur at angles larger than 20° and are very weak. Important clusters of these reflections are gathered in single broad reflections as e.g. the reflection around 50–60 ° in an attempt to account for those. The obtained crystallinity values are collected in Table 2 together with those obtained from DSC. The lattice characteristics, based on the positions and widths of the 001, 002 and 100 reflections, are listed in Table 3 together with the total tilt.

The values of D_{001} or D_{002} correspond to the crystal thickness and when divided by d_{001} or $(2*d_{002})$ the number of repeating units along the orthogonal to the lamellar surfaces is obtained. This number (# of units in Table 3) is in between 3 and 3.5 in the present case and corresponds to the values reported earlier for single crystals of polyamide 6.6 [24].

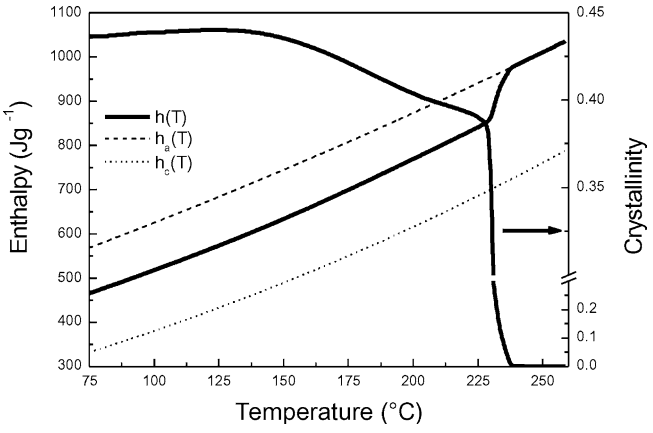

Fig. 7 Enthalpy, h(T), and crystallinity of polyamide 4.12 during heating at 10°C/min. The ATHAS reference enthalpies of amorphous, $h_a(T)$, and crystalline, $h_c(T)$, polyamide 6.10 are included for comparison. Note the axis break in the crystallinity scale

Table 2 DSC (at 120°C) and WAXD (at room temperature) mass fraction crystallinity

	DSC crystallinity at 120 °C	WAXD crystallinity at room temperature
polyamide 4–12	0.440	0.422
polyamide 10–6	0.402	0.388
polyamide 8–8	0.408	0.410
polyamide 6–10	0.387	0.390

Table 3 WAXD morphological parameters. Lattice spacings are denoted as d_{hkl} and crystal sizes based on eq. 2 as D_{hkl}.

	D_{001} or D_{002} (Å)	D_{100} (Å)	d_{001} (Å)	d_{002} (Å)	# of units	Tilt (°)
polyamide 4–12	$57.25_{(001)}$	102.68	17.96	-	3.2	36.35
polyamide 10–6	$64.25_{(001)}$	88.94	17.36	-	3.7	38.85
polyamide 8–8	$56.45_{(002)}$	104.24	-	8.55	3.3	39.91
polyamide 6–10	$49.58_{(002)}$	96.95	-	8.61	2.88	39.48

DSC

Fig. 6 displays the $c_p(T)$ curve of polyamide 4.12 and Fig. 7 the corresponding enthalpy evolution together with the crystallinity as a function of temperature. The polyamide 6.10 ATHAS reference curves are also included. The good agreement in the melt between $c_{pa}(T)$ and the experimental $c_p(T)$ curve supports the use of these references. The curves of polyamide 4.12 are representative for the other polyamides in this work, although melting and recrystallization phenomena are more apparent in the other samples (double melting behavior). These, however, do not influence the crystallinity calculation. A full discussion of the structural changes during heating will be presented in a next paper [25]. Of interest here is the crystallinity of which the values at 120°C are listed in Table 2.

The crystallinity at 120°C, which corresponds very well with the WAXD based estimates, is reported since towards lower temperatures a very small but noticeable *decrease* of the crystallinity is observed. This may be an artifact due to the presence of rigid amorphous material as demonstrated in model calculations by Mathot and van Ruiten [26]. Below 120°C some amorphous material can be present with a heat capacity below $c_{pa}(T)$, the value characteristic for truly liquid like material. As a result the used two-phase approach is no longer relevant, but - if used - may yield a decreasing rather than a constant crystallinity. The slow transformation of this fraction into liquid like material can be considered as postponed devitrification. Similar effects are noticeable in the NMR data as will be discussed below. The crystallinity decreases upon heating beyond 135 °C, which - as will be shown elsewhere [25] - correlates well with a pronounced increase of the inter-sheet distance. This process finally ends in the Brill transition [27]. Since (pre)melting only starts at 135°C a comparison of the crystallinities at 120 °C with the room temperature values obtained by other techniques is justified.

SAXS

The SAXS based morphological parameters are listed in Table 4. The *majority* fraction has been labeled 'crystalline'. At first sight this may not be the most straightforward option since the DSC and WAXD crystallinity values are more close to the SAXS minority fraction, $(1 - \phi_L)$. The fact that SAXS yields volume rather than mass fractions would not alter the case.

Instead of comparing the crystallinity, the crystal thickness was used for the assignment. Indeed, the values of l_C, as listed in Table 4, with the assumption of ϕ_L being the majority fraction, correspond most to the WAXD crystal thickness based on the widths of the 001 or 002 reflections. Often a discrepancy between the SAXS and WAXD/DSC crystallinity has been associated with the presence of large amorphous regions outside the lamellar stacks. These contribute to the DSC/WAXD estimate but are not probed by SAXS. The SAXS technicalities related to this matter have been communicated earlier [20]. Alternatively and in absence of such larger amorphous areas, part of the crystalline-amorphous interphase may contribute to the SAXS crystallinity and not to that of DSC and WAXD. Indeed, when the 'core crystallinity' in e.g. the case of polyamide 4.12 is calculated from (core l_C)/L_p a value of 0.34 is obtained, which upon transformation into mass fraction may well end close to the WAXD number. An objection, however, to this idea is that, if the transition layer would not contribute to the WAXD crystallinity, then it would

Table 4 SAXS morphological parameters. In the last 2 columns the core thickness of the crystalline and amorphous layers is added, which is the difference between l_C or l_A and 3σ

	σ (3σ) (Å)	L_p (Å)	ϕ_L (-)	$1-\phi_L$ (-)	l_C (Å)	l_A (Å)	core l_C (Å)	core l_A (Å)
Polyamide 4–12	8.2 (24.6)	84	0.63	0.37	53	31	28.4	6.4
polyamide 10–6	8.2 (24.6)	74	0.61	0.39	45	29	20.4	4.4
Polyamide 8–8	7.2 (21.6)	78	0.64	0.36	50	28	28.4	6.4
polyamide 6–10	7.6 (22.8)	84	0.65	0.35	55	29	32.2	6.2

neither contribute to the crystalline peaks and consequently neither to the width from which the WAXD crystal thickness was calculated. In that case the WAXD crystal thickness would be smaller than that obtained by SAXS, which contradicts the experimental results. Hence, at this stage – before having considered the NMR data – the presence of large amorphous areas outside the semicrystalline regions seems to be most plausible together with the thought of having transition layers that partially contribute to the WAXD crystalline reflections. Fig. 2 illustrates the concepts 'crystalline and amorphous core'.

Solid state NMR

At room temperature, the spectrum of all samples is a single, broad peak with no discrimination between crystalline and amorphous phases, consistent with the polymer being below its glass transition (Fig. 8). The small (< 5%) narrow peak is most probably due to absorbed moisture. The broad peak is fitted well to a Gaussian, which provides justification for the use of this function in fitting the broad component of the spectra at elevated temperatures. The spectra were then recorded at 10 ° intervals from 100 to 150 °C. Above 120 °C there was no change in the appearance of the spectra, and so this temperature has been used as a reference temperature for all the samples in the assessment of crystallinity.

The spectrum of polyamide 4.12 at 120 °C is shown in Fig. 9. There is a clear two-component nature to the line

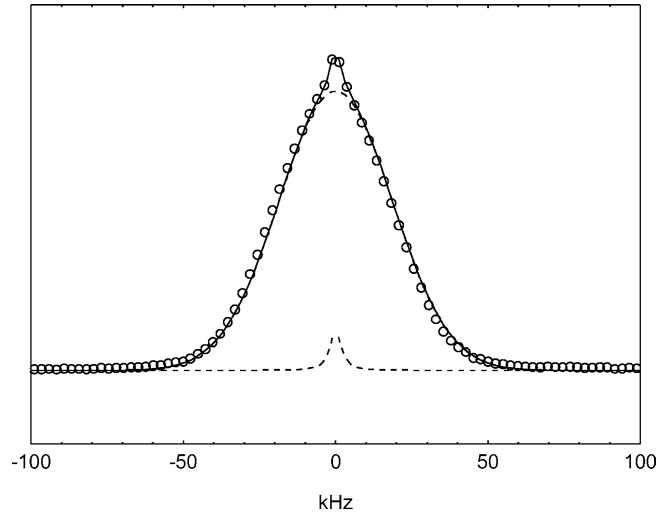

Fig. 8 Proton broadline spectrum of polyamide 4.12 at room temperature. The solid line is the fit to a sum of Gaussian and Lorentzian peaks. The individual contributions of the Gaussian and Lorentzian components are indicated as dashed lines. For clarity, only every 5th data point has been plotted

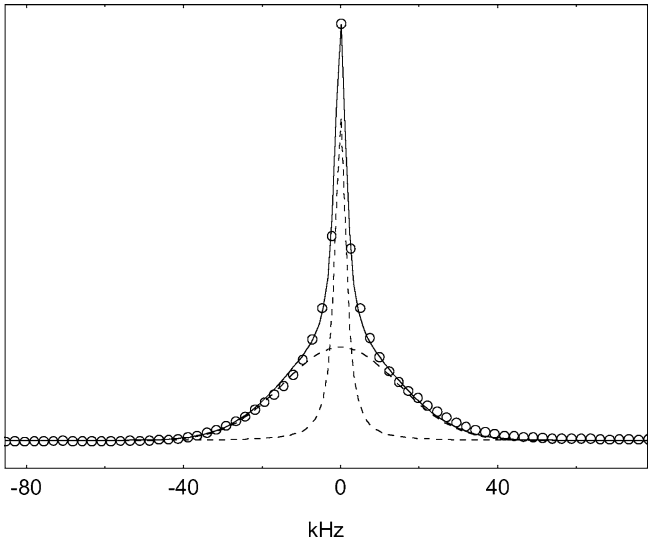

Fig. 9 Proton broadline spectrum of polyamide 4.12 at 120°C. The solid line is the fit to a sum of Gaussian and Lorentzian peaks. The individual contributions of the Gaussian and Lorentzian components are indicated as dashed lines. For clarity, only every 5th data point has been plotted

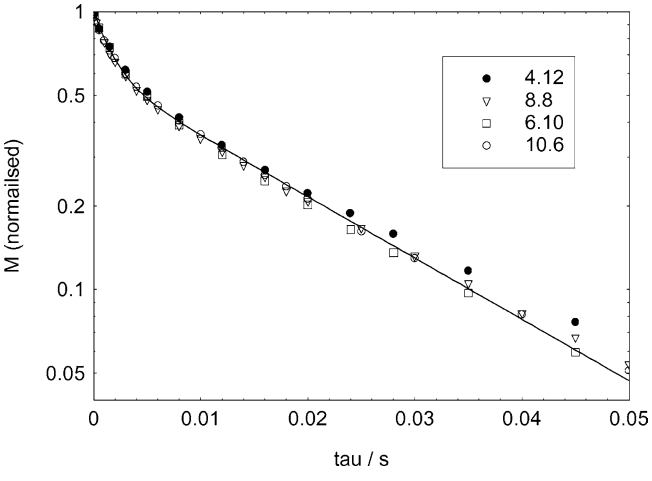

Fig. 10 Magnetisation, M versus spinlock time, tau, obtained from ^1H $T_{1\rho}$ experiments. The solid line is a bi-exponential fit through all data points. Not all points are shown, for clarity

Table 5 Results from decomposition of ^{1}H broadline spectra of each sample. The percentage of rigid component is calculated by dividing the fitted Gaussian area by the integrated area of the experimental spectrum. Areas are in arbitrary units

	Gaussian area	Lorentzian area	Spectrum area	Fitted Spectrum area	Rigid % (+/ − 1%) (Gaussian/Spectrum)
polyamide 4.12	4.84	2.42	7.42	7.27	65.2
polyamide 10.6	17.8	8.44	26.7	26.2	66.6
polyamide 8.8	17	9.03	26.4	26.1	64.6
polyamide 6.10	15.3	7.57	23.1	22.9	66.4

Table 6 Percentage of rigid component and relaxation times obtained from bi-exponential fits to $T_{1\rho}$ relaxation data in Fig. 10

	Rigid % (± 2.0)	$T_{1\rho}$ rigid ms (±1.0)	$T_{1\rho}$ mobile ms (±0.5)
polyamide 4.12	59.8	20.9	1.95
polyamide 10.6	62.8	18.5	1.56
polyamide 8.8	58.7	20.1	1.81
polyamide 6.10	57.4	19.4	2.18

shape; a broad component due to rigid material, and a narrow component due to the mobile amorphous material above its glass transition.

The spectrum is fitted well by a combination of a broad Gaussian and narrow Lorentzian peak [28]. The other samples show very similar features and quality of fits. Table 5 gives the percentage of rigid component in each material, calculated as the area of the Gaussian peak divided by the area of the experimental spectrum. All samples show very similar fractions of rigid material at 120 °C.

The ^{1}H $T_{1\rho}$ decays at 120 °C are similar for each sample, and are shown in Fig. 10. The relaxation can be fitted well by a bi-exponential, and examination of the spectra at various spin-lock times indicates that the more rapidly decaying component (shorter $T_{1\rho}$) is associated with the mobile amorphous part of the polymer, and the component of longer $T_{1\rho}$ is associated with the rigid part. Table 6 gives the $T_{1\rho}$ relaxation times obtained from the bi-exponential fits and the percentage of each component. Clearly, the smaller fraction consists of mobile material, supporting the SAXS phase assignment.

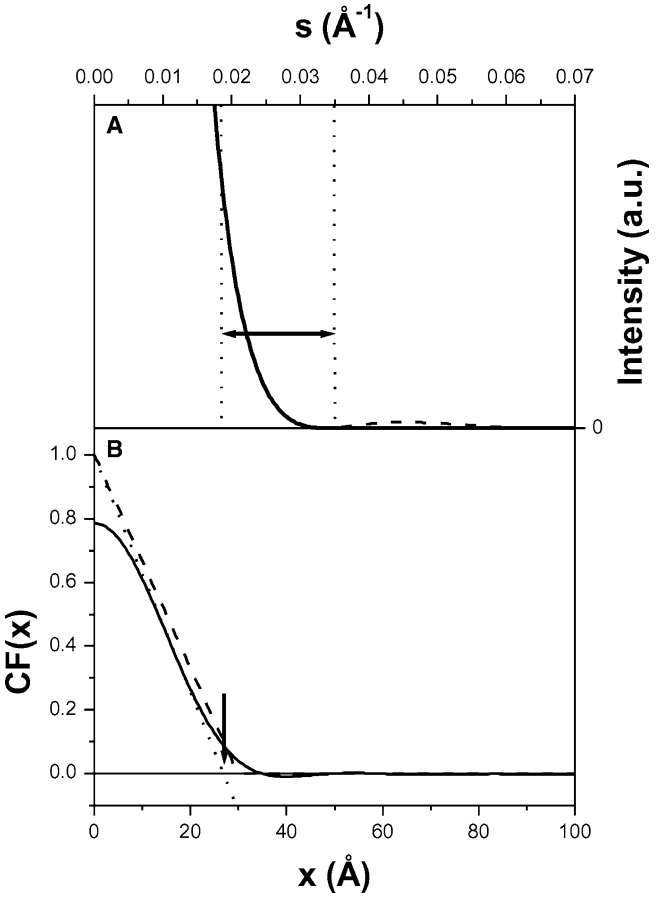

Fig. 11 **A:** Model scattering pattern of isolated, randomly oriented plate-like crystals with a thickness of 30 Å (dashed line) and corresponding truncated scattering pattern (full line). The double-headed arrow highlights the angular range of fitting with Eq. 7 **B:** Correlation functions corresponding to the complete (dashed line) and truncated (full line) scattering patterns. The intersection of the linear regression to the autocorrelation triangle of the latter curve (dotted line) with the abscissa occurs at the arrow

Discussion

Compared to the crystallinity estimates from DSC and WAXS, the amount of rigid material obtained from NMR is significantly higher, but comparable to the SAXS estimate. This is consistent with previous studies on polyethylene [29], where the rigid fraction detected by NMR was higher than the DSC crystallinity. Apparently the density based structure probed by SAXS covers the mobility distribution probed by NMR. Given this similarity the option of having larger amorphous areas outside the semicrystalline lamellar stacks can be discarded. In other words there is a non-crystalline polymer fraction present inside the semicrystalline regions with a reduced mobility compared to that of supercooled liquid like polymer. It amounts to 25% of the total mass, based on 40% crystallinity (WAXD and DSC) and roughly 65% rigid material.

The question now arises where this rigid amorphous fraction is situated: at the interface or as inclusions in the crystalline phase? The presence of such inclusions in the liquid like phase is not an option since in that case the SAXS majority phase would have to be amorphous and this is incompatible with the WAXD crystal thickness as discussed above. Secondly, the absence of small dispersed, rigid amorphous inclusions inside the liquid like regions (like e.g. hydrogen-bonded segments) can also be inferred from the ^{1}H $T_{1\rho}$ decays at 120 °C. In the interpretation of rigid/mobile fractions from $T_{1\rho}$ data one must take into account spin diffusion effects [30,31]. When the domain size of the dispersion is 1–2 nm or less, proton spin diffusion will completely average out the intrinsic relaxation characteristics of the dispersion and the matrix, resulting in a single decay. Consequently if small rigid amorphous inclusions would have been present in the mobile, liquid like phase one would detect a *majority* of 'more mobile' material (60% in total consisting of 25% dispersed rigid and 35% liquid like amorphous). This result would be opposite to that extracted from the Proton broadline spectra. As such the $T_{1\rho}$ data are compatible only with the option of rigid amorphous material inside the crystalline phase or at most at the interphase. Furthermore, the two observed phases are apparently not strongly coupled by spin diffusion at this temperature, as the data in Table 6 differ by only $\sim$ 8% from those obtained from the decomposition of the broadline spectra in Table 5, pointing at the absence of small-scale phase inter-digitization or, in other words, at the existence of sharp phase boundaries.

The latter finding somehow conflicts with the SAXS data that (apparently) reveal interfacial transition layers of considerable thickness between the crystalline and amorphous layers. Moreover, for a match of the SAXS crystal thickness with that obtained from WAXD, it has to be assumed that part of the transition layer is WAXD crystalline, which is not indisputable. Below, the idea is developed that the SAXS based transition layers are most likely artifacts.

The smallest dimension appears to be the amorphous layer with a thickness of $\pm$30Å. In Fig. 11 the desmeared scattering pattern of 30Å thick, randomly oriented, isolated lamellae is shown as calculated from:

$$I(s) \sim \frac{\sin^2(\pi l_A s)}{(\pi l_A s^2)^2} \tag{9}$$

The s-range enclosed by the double-headed arrow corresponds to the angular range in which the fit was made with eq. 5 to the experimental curves. A fit to the model curve in the same angular range with eq. 7 (the equivalent of eq. 5 for desmeared scattering patterns) works very well and a value for σ is obtained of 7.6Å, which agrees with the values reported in Table 4. However, *no transition layer is added to the model here* and hence, although the fit is good, the result is wrong.

In principle, if the fitted result describes the experimental curve well there is no objection to use the fit for e.g. a smoothing of the data, accepting that the fitting parameters have no physical meaning. However, although the fit may be reasonable in a limited angular range, it does not necessarily describe the intensities outside this window, and therefore artifacts are intro-

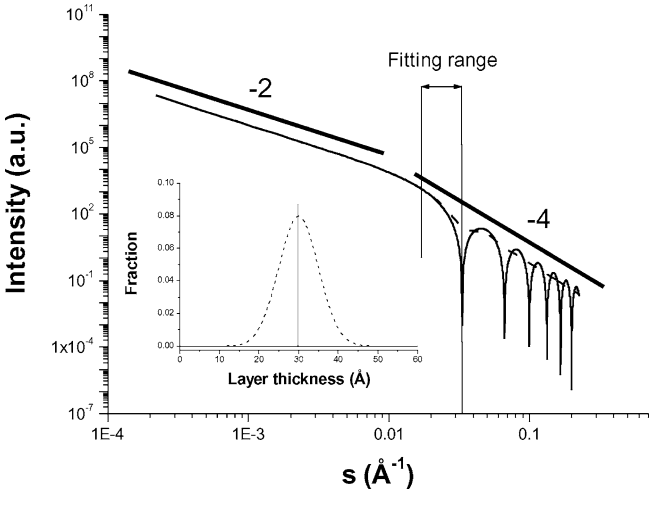

Fig. 12 Model scattering pattern of isolated, monodisperse, randomly oriented plate-like crystals with a thickness of 30 Å (full line) and scattering pattern of dispersed lamellae with a Gaussian inter-lamellar thickness distribution according to the insert (dashed line). The s-range used for fitting with Eq. 7 is marked with a double-headed arrow. The slopes in the scattering patterns correspond to the mass (-2) and surface (-4) fractal dimensions of plate-like scattering objects

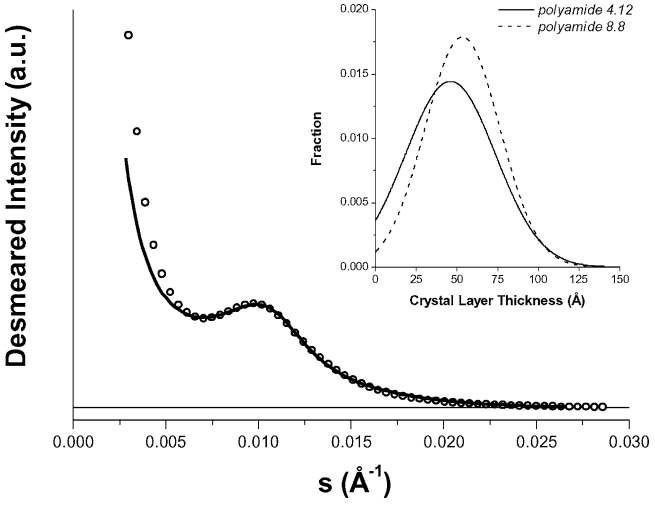

Fig. 13 Desmeared SAXS patterns of polyamide 4.12 (open circles - not all data points are shown for clarity) and fit of the pattern to Eq. 10. The insert shows the crystalline layer thickness distribution obtained for the indicated polyamides

duced in CF(x) when this function is used to extrapolate the data to higher angles prior to Fourier transformation. The model intensity curve exhibits a number of weak subsidiary maxima that are cut off when replaced by the rapidly decreasing fitting function. When this truncation is not made and intensities are included up to $s = 0.22\text{Å}^{-1}$ the expected autocorrelation triangle for isolated lamellae is obtained, intersecting the abscissa at 30Å, which is the input layer thickness. This curve, represented by the dashed line in Fig. 11B, should be compared to that represented with a full line. The latter is obtained after Fourier transformation of the truncated data and displays an *artificial transition layer*, revealed by the negative curvature at the origin, and *artificial layer thickness polydispersity*, revealed by the positive curvature at the foot of the autocorrelation triangle [3]. The remaining part of the correlation function seems to be little affected although a slightly underestimated layer thickness - highlighted with the arrow in Fig. 11B - is obtained from the intersection of the linear regression to the autocorrelation triangle with the abscissa.

The double logarithmic plot in Fig. 12 shows in more detail the tail of the model scattering pattern and how the intensity in the fitting range is influenced by true polydispersity. As the σ value, obtained from the fit of the model curve of monodisperse lamellae, equals that of the experimental curves one can deduce the presence of a rather monodisperse amorphous layer thickness for the samples in this work. Fig. 12 also shows that the s-range used for fitting is at the boarder of the lamellar mass fractal region with a slope of -2 in a double logarithmic plot and the Porod or surface fractal region with a slope of -4 [32]. The true Porod region occurs at higher s-values where in the present polyamide case WAXD reflections are present.

Given that the true Porod region is not accessible an attempt was made to interpret the SAXS data alternatively, avoiding ambiguous extrapolation procedures. The desmeared SAXS intensities were fitted directly using lamellar models that include distributions in the crystalline and amorphous layer thickness as well as finite stack heights and transition layers [33–35]. However, all fittings converge towards infinite stack systems with one of the layers being nominally monodisperse. Hence, only the results are reported of a direct fitting of the desmeared SAXS intensities with [36]:

$$I(s) = C\left[\left(\frac{1-\rho^2}{1+\rho^2-2\rho\cos(2\pi s L_P)}\right) \times \left(\frac{\sin^2(\pi l_A s)}{(\pi l_A s)^2 s^2}\right)\exp\left(-4\pi^2\sigma^2 s^2\right)\right] \quad (10)$$

where

$$\rho = \exp\left(-2g^2\pi^2 L_P^2 s^2\right) \quad (11)$$

Table 7. Left hand part: SAXS structural parameters obtained by direct fitting of the desmeared scattering patterns. Right hand part: data obtained by combining the correlation function and direct fitting approaches

	L_p (Å)	ϕ (-)	l_C (Å)	l_A (Å)	σ (Å)	g (-)	l_C (Å)	ϕ (-)	# unit cells (-)
polyamide 4–12	79	0.58	46	33	0	0.35	51	0.61	2.8
polyamide 10–6	71	0.66	47	24	0	0.34	50	0.68	2.9
polyamide 8–8	77	0.67	52	25	0	0.29	53	0.68	3.1
polyamide 6–10	85	0.67	57	28	0	0.28	56	0.67	3.3

In this equation C is a constant that accounts for not having recorded the patterns in absolute units. In this equation a model is assumed of infinite lamellar stacks built of monodisperse amorphous layers with the separating crystalline layers distributed in a paracrystalline manner. The first term between the square brackets indirectly characterizes the crystal layer thickness distribution, with g the ratio σ_{Lp}/L_P and σ_{Lp} the standard deviation of the Gaussian distance distribution of L_P. The l_C distribution is obtained by subtracting l_A from the L_p distance distribution and of course the average l_C value results from $L_p - l_A$. In the second term one recognizes the amorphous layer form factor and in the third term the potential presence of a transition layer is included. Fig. 13 illustrates the good quality of the fit in the representative case of polyamide 4.12 and the as obtained l_C thickness distributions for polyamide 4.12 and 8.8. The obtained parameters for all samples are listed in Table 7.

For all samples the largest deviation in fitting occurs at the smallest angles and probably results from stack heterogeneity. The obtained L_p values may as a result also be less reliable compared to those extracted from the first side maxima in CF(x). The latter are not affected by high angle truncation in contrast to the intensities in the autocorrelation triangle. The two methods are complementary, and most reliable values for l_C are obtained from the difference between L_p obtained from the correlation function and l_A from the direct fitting approach, since the agreement between experiment and fit is particularly good in the tail region where the l_A value has its largest influence. When this hybrid l_C value is divided by L_p from CF(x), hybrid ϕ_L values are obtained. All hybrid data are listed in the right hand part of Table 7. When the latter l_C values are divided by the corresponding D_{001} values, numbers of unit cells along the lamellar thickness are obtained close to 3, as can be read in Table 7.

Conclusions

In the polyamides 4.12, 10.6, 8.8 and 6.10 three fractions are present. The WAXD crystallinity is comparable to

that of DSC and amounts to 40% in all samples. The rigid fraction obtained by solid state NMR is, however, close to 60%, pointing at 20% rigid amorphous material. A detailed analysis of the SAXS patterns reveals that the latter fraction is situated inside the crystalline phase and not at the crystalline - 'mobile amorphous' interface. Accordingly, 1/3 of the crystalline layers with a thickness between 50 and 56 Å is not truly crystalline. From the width of the WAXD 100 reflections it can be deduced that crystalline grains exist with lateral dimensions of approximately 100 Å (see Table 3). Hence a picture emerges of alternating solid and liquid-like layers with the former consisting of crystalline grains separated by rigid amorphous matter.

It is important to note that this result would not have been obtained without the NMR input and secondly that the materials are rather unique from a WAXD point of view, as they produce reflections from which the crystalline layer thickness can be obtained independently from the SAXS data. Both the NMR and WAXD experiments allowed for a correct phase assignment in SAXS, which for sure would have been made wrongly when relying on the WAXD and DSC crystallinities only.

Polyamides deform by shear yielding, involving the rupture of crystals [37]. The present study calls for systematic work on how the extent and distribution of the rigid amorphous fraction can be manipulated by e.g. changing the thermal history or the chain microstructure and how in turn this affects mechanical behavior. Most likely, the rigid amorphous parts are weak points in the 'crystals' where shear yielding may well be initiated.

Acknowledgements BG is a postdoctoral fellow of the FWO-Flanders (Belgium). The authors thank FWO-Flanders and Prof. H. Reynaers for their support of the X-ray facilities at the laboratory of Macromolecular and Structural Chemistry.

References

1. Balta-Calleja FJ, Vonk C (1989) X-ray Scattering of Polymers, Elsevier, Amsterdam
2. Mathot VBF (1994) In Calorimetry and Thermal Analysis of Polymers, Mathot V.B.F. (Ed.), Hanser Publishers, New York, Chap. 5, 105
3. Strobl GR, Schneider M (1980) J. Polym. Sci.: Polym. Phys. Ed. 18, 1343
4. Vonk CG, Pijpers AP (1985) J. Polym. Sci.: Polym. Phys. Ed. 23, 2517
5. Goderis B, Reynaers H, Koch MHJ, Mathot VBF (1999) J. Polym. Sci.: Part B: Polym. Phys. 37, 1715
6. Unterforstunghuber K, Bergman K (1979) J. Mag. Res. 33, 483
7. Mandelkern L (1992) Chemtracts Macr. Mol. Chem. 3, 347
8. Koning C, Teuwen L, De Jong, R, Janssen G, Coussens B (1999) High Perform. Polym. 11, 387
9. Roerdink E, De Jong, PJ, Warnier JMM (1984) Polym Commun 25, 194
10. Roerdink E, Warnier JMM (1985) Polymer 26, 1582
11. Jones NA, Atkins EDT, Hill MJ, Cooper SJ, Franco L (1997) Polymer 38, 2689
12. Microcal Software, Inc., One Roundhouse plaza, Northampton, MA 01060 USA
13. Alexander LE (1979) X-ray Diffraction Methods in Polymer Science, Robert E. Krieger Publishing company, Huntington, New York , 423
14. Mathot VBF, Pijpers MFJ (1983) J. Therm. Anal. 28, 349
15. http://web.utk.edu/~athas/
16. Koberstein JT, Morra B (1980) J. Appl. Cryst. 13, 34
17. DuMond JWM (1947) Phys. Rev. 72, 83
18. Strobl GR, Schneider M (1980) J. Polym.Sci.: Polym.Phys.Ed 18, 1343
19. Ruland W (1971) J.Appl.Cryst., 4, 70
20. Goderis B, Reynaers H, Koch MHJ, Mathot VBF (1999) J.Polym.Sci.PartB. Polym.Phys. 37, 1715
21. Atkins EDT, Keller A, Sadler DM (1972) J. Polym. Sci.: Part A-2 10, 863
22. Bunn, CW, Garner EV (1947) Proceedings of the Royal Society (London) 189, 39
23. Kroon L, Goderis B, Koning CE in preparation
24. Atkins EDT, Keller A, Sadler DM (1972) J. Polym. Sci.: Part A-2 1972, 10, 863
25. Goderis B et al. in preparation
26. Mathot VBF (1994) In Calorimetry and Thermal Analysis of Polymers, Mathot V.B.F. (Ed.), Hanser Publishers, New York, Chap. 5, 105
27. Brill R (1943) Z. Physik. Chem. 61, 1353
28. Cook JTE, Klein PG, Ward IM, Brain AA, Farrar DF, Rose J Polymer 2000, 41, 8615
29. Robertson MB (1996) PhD thesis, University of Leeds, UK
30. Packer KJ, Poplett IJF, Taylor MJJ (1988) Chem. Soc: Faraday Trans. 84, 3851
31. McBrierty VJ, Douglass DC (1981) J. Pol. Sci., Macromolecular Revs. 16, 295
32. Schmidt PW (1991) J. Appl. Cryst. 24, 414
33. Blundell DJ (1978) Polymer, 19, 1258
34. Blundell DJ (1970) Acta Cryst., A26, 472
35. Blundell DJ (1970) Acta Cryst.,A26, 476
36. Vignaud R, Schultz JM (1986) Polymer 27, 651
37. Groeninckx G, Dompas D (1998) In Structure and Properties of Multiphase Polymeric Materials, Chapter 12: Plastic Deformation Mechanisms of Polymers and Rubber-Modified Thermoplastic Polymers: Molecular and Morphological Aspects, Araki T, Tran-Cong Q, Shibayama M, Eds. Marcel Dekker, Inc, New York

Progr Colloid Polym Sci (2005) 130: 51–63
DOI 10.1007/b107345
Published online: 3 June 2005

Bart Goderis
Young He
Monikce Basiura
Gaetan de Schaetzen
Vincent B. F. Mathot
Michel H. J. Koch
Harry Reynaers

(Re)Crystallization induced component segregation in a miscible binary polyethylene blend

B. Goderis (✉) · Y. He · M. Basiura · G. de. Schaetzen · V. B. F. Mathot · H. Reynaers
Molekular and Nanomaterials,
Polymer Chemistry Division,
Catholic University of Leuven,
Chemistry Department,
Celestijnenlaan 200F,
3001 Heverlee, Belgium
e-mail:
bart.goderis@chem.kuleuven.ac.be
Tel.: +32-16327806
Fax: +32-16327990

V. B. F. Mathot
DSM Research, P.O. Box 18,
6160 MD Geleen, The Netherlands

M. H. J. Koch
European Molecular Biology Laboratory,
EMBL c/o DESY, Notkestraße 85,
22603 Hamburg, Germany

Abstract The crystallization and melting behavior of a polyethylene blend during cooling and subsequent heating at 10 °C/min is compared to melting after cooling by fast quenching. The blend contains 15% linear polyethylene and 85% of a homogeneous (5.2 mole% 1-octene) ethylene copolymer. The components separate on a micrometer length scale during cooling at 10 °C/min and crystallize separately. Quenching results in cocrystallization without pronounced component segregation. Very local segregation, however, occurs during heating as these (co)crystals repeatedly melt, recrystallize and remelt. This recrystallization occurs at high supercooling and is accordingly so fast that it cannot be suppressed by increasing the heating rate in a standard Differential Scanning Calorimeter (DSC). Consequently, the DSC melting traces after quenching cannot be used to identify crystal populations that are related to the preceding cooling history. The structural changes are studied using Small Angle Light Scattering, synchrotron Small Angle X-ray Scattering and Wide Angle X-ray Diffraction and Atomic Force Microscopy.

Keywords Crystallization · Scattering · Polyethylene · Blend

Introduction

In the nineties a series of papers appeared, discussing blends of linear polyethylene (LPE) with moderately branched low-density polyethylene (LDPE) or with homogeneous copolymers of ethylene and a relatively low amount of α-olefin comonomer [1–16]. These systems represent a special class of polyolefin mixtures, exhibiting thermal and morphological features that cannot be explained by existing theories but that were interpreted as the result of liquid-liquid phase separation [1]. This demixing hypothesis is incompatible with small angle neutron scattering (SANS) data that are in favor of homogeneous melts [17–19]. Nowadays a consensus is reached in favor of melt miscibility [20] and most researchers agree on the minimum comonomer contents needed to induce liquid-liquid phase separation in blends of LPE with a homogeneous ethylene-1-octene copolymer, i.e. 8 mol% [19–21]. The peculiarities described in the nineties for blends involving copolymers with a lower comonomer contents remain, however, unexplained.

Part of the previous confusion is related to the methodology used at that time. To map out phase diagrams, one relied on transmission electron microscopy (TEM) and Differential Scanning Calorimetry (DSC) based 'indirect methods' because the nearly identical physical properties of the components in the melt were thought to hamper their discrimination.

The crystalline texture was studied by TEM after rapidly quenching a sample from a temperature in the melt into acetone at its freezing point. It was argued that the state of the solid, after fast quenching, reflects the state of the melt prior to quenching [2, 6]. Blends with a single crystal population were designated as 'mixed' and

those with two well-separated populations as 'demixed' at the melt temperature.

In the present paper, the second key method will be discussed. DSC melting traces recorded at 10 °C/min were examined after rapidly quenching 2–3 mg samples from a given temperature in the melt [2, 3, 6, 10]. If a single endothermic peak appeared, the components were said to have cocrystallized into a single crystal population from a homogeneous melt. Two melting peaks were taken as an indication for a double crystal population originating from two separate phases with different compositions in the melt. The position of a given peak was said to be related to the composition of the phase: i.e. the lower the melting peak temperature, the lower the amount of LPE in the corresponding phase [10]. The window associated with the assumed phase separation is positioned at a low LPE contents and displays upper and lower critical solute temperatures (UCST and LCST behavior) with the LCST often being masked by crystallization.

It was recognized that this DSC method should be applied cautiously [10]. An efficient quenching procedure is crucial. A double DSC melting peak at a blend composition outside the window associated with (previously assumed) demixing, occurs readily when the applied cooling rate is not sufficiently high due to crystallization induced component segregation [22]. For the same reason a blend, quenched from the homogeneous melt above the demixing gap, may give rise to a double melting peak [10]. Besides crystallization induced segregation it was argued that in the latter case the interior of the sample may cool down so slowly that it phase separates while passing through the demixing gap prior to crystallization [10].

In the present paper it will be demonstrated that the double melting behavior obtained after quenching a homogeneous sample through the (formally assumed) demixing gap is not due to crystallization induced segregation, nor to fast liquid-liquid phase separation but to melting and recrystallization of the originally cocrystallized blend components. By using time resolved morphological techniques under DSC typical thermal conditions it will be shown that the high temperature melting peak observed after quench cooling reflects a heating induced reorganization process. The most fundamental assumption in the earlier DSC procedure that a melting peak can directly be linked to a given quenching induced crystal population, is thus unjustified.

The present paper reports on the cooling-heating induced structural changes in a (15/85 w/w) blend of an LPE and a homogeneous ethylene copolymer with 5.2 mole% 1-octene. Figure 1 represents the phase diagram mapped out earlier for binary blends of the components used in this paper [7]. In fact, according to current insights 'phase diagram' is no longer the appropriate term since these components are miscible at all concentrations. Lately, 'morphology map' was coined as an alternative [20] since the morphologies obtained by TEM are beyond any dispute. Nevertheless, in the context of the present paper, reference will be made to 'phase diagram' to emphasize the link with earlier work. Our 15/85 blend is situated in the center of the closed loop region (region B in Figure 1). Components and blending/quenching methods identical to those of the original phase diagram [7] are used. According to Figure 1 the blend is homogeneously mixed at 200 °C but during cooling the demixing loop is entered before crystallization.

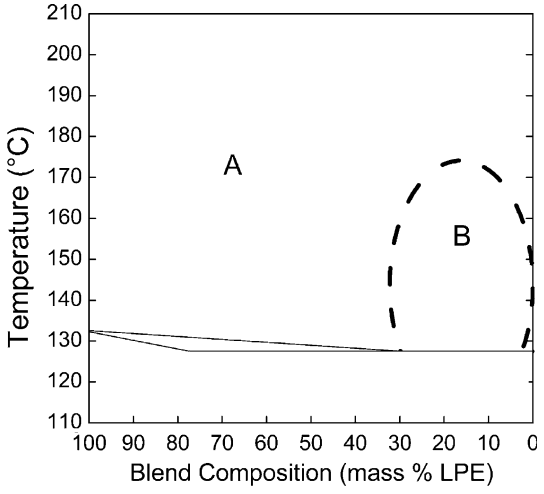

Fig. 1 'Phase diagram' for blends of JW1114 (LPE) and JW1120 (homogeneous ethylene-1-octene copolymer). The thick dashed line represents the border between regions where the melt is mixed (region marked A) or demixed (region marked B). The thin lines represent liquid-solid borders[7]

The melting during heating at 10 °C/min after cooling at the same rate is compared to that after rapid quenching from 200 °C. The techniques used for morphological characterization are synchrotron small angle X-ray scattering (SAXS), wide angle X-ray diffraction (WAXD), small angle light scattering (SALS) and atomic Force Microscopy (AFM). Evidence for melting and recrystallization phenomena in other blend compositions will be given in another paper together with a possible explanation for the heterogeneous morphologies that occur occasionally but systematically after rapid quenching [23].

Experimental

Materials, blend preparation and quenching

The LPE and the homogeneous copolymer used for blending were prepared with a promoted Vanadium-based catalyst [24]. The LPE (DSM code [25]: JW1114 and referred to as LPE in reference 7) has a weight average molar mass, Mw, of 52300 g/mole and a polydispersity, Mw/Mn, of 3. The homogeneous ethylene-1-octene

copolymer (DSM code [25]: JW1120 and referred to as O(5) in reference 7) contains 5.2 mole% 1-octene, has an Mw of 30,800 g/mole and an Mw/Mn of 2. The 15/85 (m/m) blend (LPE/copolymer) was prepared by dissolving the two polymers in p-xylene at boiling point (15 min reflux) at 1% (v/v) followed by coprecipitation into cold acetone at −78 °C. The blend was filtered, collected and dried in a vacuum oven at room temperature for 24 hours. Blend samples were quenched after 10 minutes at 200 °C into acetone at its freezing point (−94 °C) in a sample holder suited for the corresponding experiment.

AFM

AFM images were obtained with a Nanoscope III scanning probe microscope equipped with a J-scanner under ambient conditions while operating the instrument in the tapping mode as described earlier [26]. Height and phase images were recorded simultaneously.

DSC

Specific heat capacity, $c_p(T)$, data were collected on 2 mg flat samples using a Perkin Elmer Pyris DSC, calibrated at the same rate as the actual experiments with the melting point of Indium (156.6 °C) and benzophenone (48 °C) for the temperature, and with Indium for the enthalpy (28.45 Jg^{-1}). The block surrounding the measuring unit was thermostatted at −10 °C with liquid nitrogen and the unit was flushed with dry nitrogen. The $c_p(T)$-based mass fraction crystallinity as a function of temperature was calculated according to standard procedures [27, 28].

SALS

SALS was measured on a home-made apparatus as described in detail earlier [29]. The blend, compression molded to a 50 μm thick film between two glass cover slips, was quenched into acetone at freezing point prior to heating at 10 °C/min from 40 °C up to 200 °C. Afterwards the same sample was cooled and heated again between the same temperatures. Temperature was controlled by a Mettler FP-82HT hot stage. Two-dimensional scattering patterns were recorded for 200 ms every 3 s with the analyzer alternating between the *Hv* (crossed polarizers) and *Vv* (parallel polarizers) settings to obtain an effective time resolution of 6 s for a given configuration. The total relative light scattering intensity Q_{Hv} and Q_{Vv} for *Hv* and *Vv* configurations were obtained by integration after subtracting the intensity of the melt as a background and finally the ratio Q_{Vv}/Q_{Hv} was calculated. Since *Vv* and *Hv* data were recorded with a 0.5 °C (3 sec.) offset, a linear extrapolation of the data was used to obtain the Q_{Vv}/Q_{Hv} ratio for the times when either *Vv* or *Hv* data were not recorded.

In the case of spherulites that are imbedded in a matrix with a different polarizability this ratio equals:

$$\frac{Q_{Vv}}{Q_{Hv}} = \frac{15(1-\phi_{sp})(\overline{\alpha_{sp}}-\alpha_0)(\alpha_t-\alpha_0)}{\left(\phi_{csp}\delta^0_{cr}P_2\right)^2} + 15\left(\frac{1}{5}-\frac{\phi_{sp}}{9}\right) \quad (1)$$

based on the expression for Q_{Vv} and Q_{Hv} [30]. The increase of the spherulite fraction, ϕ_{sp}, during crystallization induces a decrease in Q_{Vv}/Q_{Hv} towards the limiting value of 4/3 for $\phi_{sp} = 1$. The influence of the spherulite internal crystallinity, ϕ_{csp}, and the orientation of the crystals with respect to the spherulite radius, P_2, on this ratio is less obvious since also the spherulite polarizabilities depend on these parameters according to:

$$\alpha_r = \alpha^0_b \phi_{csp} P_2 \quad (2)$$

$$\alpha_t = \frac{\alpha^0_a + \alpha^0_c}{2}\phi_{csp}P_2 \quad (3)$$

$$\overline{\alpha}_{sp} = \frac{\alpha_r + 2\alpha_t}{3} \quad (4)$$

with α_r the radial, α_t the tangential and $\overline{\alpha}_{sp}$ the average spherulite polarizability. Here a typical polyethylene spherulite is assumed in which the crystalline unit cells lay with the *b*-axis (intrinsic polarizability $\alpha_b{}^0$) parallel to the spherulite radius and both the *a* and *c*-axis (intrinsic polarizabilities $\alpha_a{}^0$ and $\alpha_c{}^0$) perpendicular to the spherulite radius. In this case:

$$\delta^0_{cr} = \alpha^0_b - \frac{\alpha^0_a + \alpha^0_c}{2} \quad (5)$$

Combination of Eqs. 2–5 reveals that Q_{Vv}/Q_{Hv} increases with ϕ_{csp} or P_2 when:

$$\frac{\overline{\alpha}_{sp} + \alpha_t}{2} > \alpha_0 \quad (6)$$

Q_{Vv}/Q_{Hv} thus increases with ϕ_{csp} or P_2 if the characteristic average polarizability of the spherulite exceeds that of the matrix. In other words, Q_{Vv}/Q_{Hv} is contrast sensitive and increases whenever the polarizability difference between the spherulite and matrix increases. The spherulite or matrix polarizability is proportional to the internal crystallinity.

Obviously, when ϕ_{sp} equals one, contrast issues are irrelevant and the ratio reduces to 4/3, except when there are inclusions inside the spherulites with a sufficiently large size and a polarizability differing from that of the spherulite main part. Such inclusions give rise to (circularly symmetric) excess *Vv* scattering with a scattering power proportional to:

$$\langle \eta^2 \rangle = \phi_a \phi_b (\alpha_a - \alpha_b)^2 \quad (7)$$

where ϕ_a and α_a are the volume fraction and polarizability of the spherulitic matrix and ϕ_b and α_b the values associated with the inclusions, with $\phi_a = 1-\phi_b$. The respective polarizabilities are determined by the internal crystallinity. Under these conditions, the Q_{Vv}/Q_{Hv} ratio will be larger than 4/3 by an amount proportional to the relative abundance and polarizability of the different semicrystalline fractions.

The spherulite diameter could not accurately be determined from the *Hv* data [31] since the maxima in the patterns are not well-defined, which is typical for (c)-type spherulites according to the classification proposed by Maxfield and Mandelkern [32]. The spherulite diameter after cooling at 10 °C/min could only roughly be estimated to be around 50 μm.

SAXS and WAXD data collection

SAXS and WAXD time resolved X-ray scattering data, were collected simultaneously every 6 s (i.e. one pattern per °C) during heating (after quenching), cooling and reheating at 10 °C/min between 40 and 200 °C. The X33 double focusing camera of the EMBL in HASYLAB, on the storage ring DORIS of the Deutsches Elektronen Synchrotron (DESY), Hamburg, Germany was used with a wavelength of 1.5 Å [33]. The 0.5 mm thick samples were sealed between thin (15 μm) aluminum foils and the temperature was controlled by a Mettler FP-82HT hot stage, flushed with cooled air to achieve the required cooling rate. A standard data acquisition system [31] was used with two linear delay line detectors connected in series [35]. The WAXD and SAXS intensities were normalized to the intensity of the primary X-ray beam and the SAXS patterns were additionally corrected for the detector response. The scattering

vector axis of the SAXS region was calibrated using the first nine orders of dry calcified collagen. The 110 and 200 reflections of LPE were used to calibrate the WAXD data.

SAXS data processing

From the SAXS patterns, collected over the scattering vector range $0.0015 \leq s \leq 0.032$ (Å^{-1}) (with $s = 2\sin\theta/\lambda$, 2θ the scattering angle and λ the wavelength), an averaged melt pattern was subtracted as a background and linear correlation functions, $K(x)$, were calculated by simple cosine transformation as described earlier [36]. The relative invariant of the corresponding ideal two–phase structure, Q_{id}, was obtained from the intercept of the linear regression to the autocorrelation triangle [37]. The correlation functions were further analyzed according to the A–CA and CA–CA models as described in detail elsewhere [26, 36]. In the A–CA model the structure consist of separate amorphous (A) and semi–crystalline volumes (crystalline–amorphous: CA). The fraction occupied by semi-crystalline material is called α_S and the local crystallinity in these regions ϕ_L. The product $\alpha_S\phi_L$ represents the overall volume fraction crystallinity. Such a model is well suited to describe the spherulitic crystallization of polymers where semicrystalline spherulites are growing in an amorphous matrix [36]. An analysis according to the CA–CA model is superior for systems with an inhomogeneous crystallinity distribution and in absence of fully amorphous volumes [26]. Such analysis splits the sample volume in two fractions with a different crystallinity that best describe the actual (potentially multi-fraction) structure. Analyses according to the two models yield identical results if the crystallinity in one of the fractions equals zero. The results are also identical if the crystallinity is uniformly distributed over the volume. In the latter case Q_{id} can be written as:

$$Q_{id} = C\phi_L(1-\phi_L)(d_c - d_a)^2 \tag{8}$$

with C a temperature independent constant and d_c and d_a the temperature dependent mass densities of the crystalline and amorphous phases respectively. In principle electron densities should be written but as only PE is present, mass densities can be used instead, provided that a scaling factor is included in the constant C. In equation (8) ϕ_L equals the overall volume fraction crystallinity since α_S equals 1. For the present sample, in the temperature range between 40 and 50 °C the crystallinity is uniformly distributed according to the SALS Q_{Vv}/Q_{Hv} ratio (see above). Hence, in that particular temperature range C was determined from equation (8) for each cooling or heating sequence using the factor $(d_c\text{-}d_a)^2$ from the literature [38] (for the amorphous density the extrapolation of the melt was used [38]) and the product $\phi_L(1\text{-}\phi_L)$ obtained from [36]:

$$\phi_L(1-\phi_L) = \frac{A}{L_P} \tag{9}$$

where A represents the intersection of the linear regression to the autocorrelation triangle with the abscissa and L_P, the long period, obtained from the position of the first side-maximum in $K(x)$. The quantity Q_C is defined over the *full* temperature range of the experiments as:

$$Q_C = \frac{Q_{id}}{C(d_c - d_a)^2} \tag{10}$$

In the framework of the A-CA model ϕ_L can be calculated from equation (9) even when $\alpha_S < 1$. Independent information is needed to decide whether the local crystallinity actually corresponds to the minority or the majority phase, ϕ_L or $(1\text{-}\phi_L)$. Here the DSC crystallinity values were used as a guideline and accordingly ϕ_L was always related to the minority phase. In this context it furthermore holds that:

$$Q_C = \alpha_S\phi_L(1-\phi_L) \tag{11}$$

Using equation (11) and ϕ_L from equation (9), α_S was calculated over the full temperature range. The average crystalline lamellar thickness, l_C, was calculated from the product of L_P with ϕ_L.

At temperatures where α_S deviates from unity an analysis was also performed according to the CA-CA model. If the sample contains two well ordered fractions of different crystallinities, two long periods should be observed which could be used as input for the analysis [26]. If only one side-maximum in $K(x)$ is observed (as is the case for the present blend sample), the analysis has to make use of $K(x)_{\min.}$, the minimum of $K(x)$, and the crystallinity in all fractions should be sufficiently low as to yield a plateau minimum in $K(x)$ [26]. The blend sample under investigation has a low degree of crystallinity at high temperatures where the analysis is performed. The single observed L_P is assumed characteristic for fraction 1 ($L_P = L_{P1}$) whereas the second fraction is less ordered and only has a characteristic specific inner surface [26], O_{S2}. Under the CA-CA model [26]

$$Q_C = \alpha_1\phi_1(1-\phi_1) + \alpha_2\phi_2(1-\phi_2) \tag{12}$$

with α_1 the volume fraction with an internal crystallinity, ϕ_1, and α_2 the volume fraction with an internal crystallinity, ϕ_2, and of course $\alpha_1 + \alpha_2 = 1$. The (average) l_C was obtained from the intersection of the linear regression to the autocorrelation triangle of $K(x)$ with a horizontal line drawn through $K(x)_{\min}$ [26]. Assuming an overall l_C thickness distribution with a center around a common average value in both fractions, ϕ_1 is calculated from l_C/L_{P1}, with L_{P1} the observed L_P and ϕ_2 is calculated from [26]

$$\phi_2 = \frac{-Y + \sqrt{Y^2 - 4XZ}}{2X} \tag{13}$$

with

$$X = \frac{Q_C}{A} - \frac{1}{L_{P1}}$$

$$Y = \frac{Q_C - \phi_1(1-\phi_1)}{l_C} + \frac{1}{L_{P1}} - \frac{Q_C}{A}$$

$$Z = -\frac{Q_C}{L_{P1}} + \frac{Q_C\phi_1(1-\phi_1)}{A}$$

α_1 was calculated according to [26],

$$\alpha_1 = \left(\frac{Q_c}{A} - \frac{\phi_2}{l_C}\right) \cdot \left(\frac{1}{L_{P1}} - \frac{\phi_2}{l_C}\right)^{-1} \tag{14}$$

and $\alpha_1\phi_1 + \alpha_2\phi_2$ represents the overall crystallinity under the CA-CA model.

WAXD data processing

To improve the signal to noise ratio every two subsequent scattering patterns were added, thus lowering the WAXD time-resolution to one scattering pattern per 2 °C. Data were collected over the angular range $11.7 \leq 2\theta \leq 46°$ (with 2θ the scattering angle). The 110 and 200 reflections were stripped from the amorphous halo using second order sectors and subsequently fitted by Gaussians. The area under the 110 Gaussian was taken as a WAXD crystallinity index. The latter was scaled to the DSC (mass fraction) crystallinity at 40 °C. The crystalline density was calculated from the angular positions of the Gaussian's maxima through the 110 and 200 reflections and assuming a constant length of the orthorhombic unit cell in the c-direction (the molecular chain direction) equal to 2.547 Å. Since the crystalline reflections below a crystallinity of 10% are weak and their positions thus not very accurate, corresponding density data are not available.

Results

AFM

In Fig. 2 the phase images are displayed in A and B after quenching and in C and D after cooling at 10 °C/min. In image A spherulitic entities with a diameter of approximately 2.5 μm are clearly visible. The crystals that can be observed at a higher magnification are uniform but laterally limited in size and seem to be oriented quite randomly. Some lamellar crystals are scanned flat on whereas others are taken edge on. This random orientation points at a high degree of crystal branching, even though the crystals are organized in a spherulitic manner. The surface after cooling at 10 °C/min is quite rough and did not allow large area scans in which entire spherulites (Ø > 30 μm) could be imaged. The spherulite internal structure reveals well-ordered stacks of laterally extended lamellae. A distinction between dominant (spherulite building) and subsidiary (secondary) lamellae could not be made. Some crystals are, however, clearly larger than others both in terms of thickness and lateral dimensions.

DSC

According to the 'phase diagram' in Figure 1, the (15/85) blend under investigation should be homogeneously mixed at 200 °C. According to earlier beliefs this homogeneity should be preserved in the solid state by quenching rapidly and this should manifest itself in a single DSC melting endotherm [2–14]. Curve (c) in Figure 3 represents such a heating curve, which in contrast clearly displays a *double* melting behavior. This effect cannot be due to excessive sample thickness and poor thermal conductivity of PE since our DSC sample is less than one tenth of a millimeter thick.

Alternatively, a high cooling rate resulting in the formation of relatively thin and imperfect crystals could lead to a double melting peak because of melting, recrystallization and remelting during heating. In principle, such reorganization processes can be avoided by increasing the heating rate. However, increasing the heating rate up to 40 °C/min did not significantly reduce the contribution of the high-temperature melting peak. In the past this was taken as an argument against the

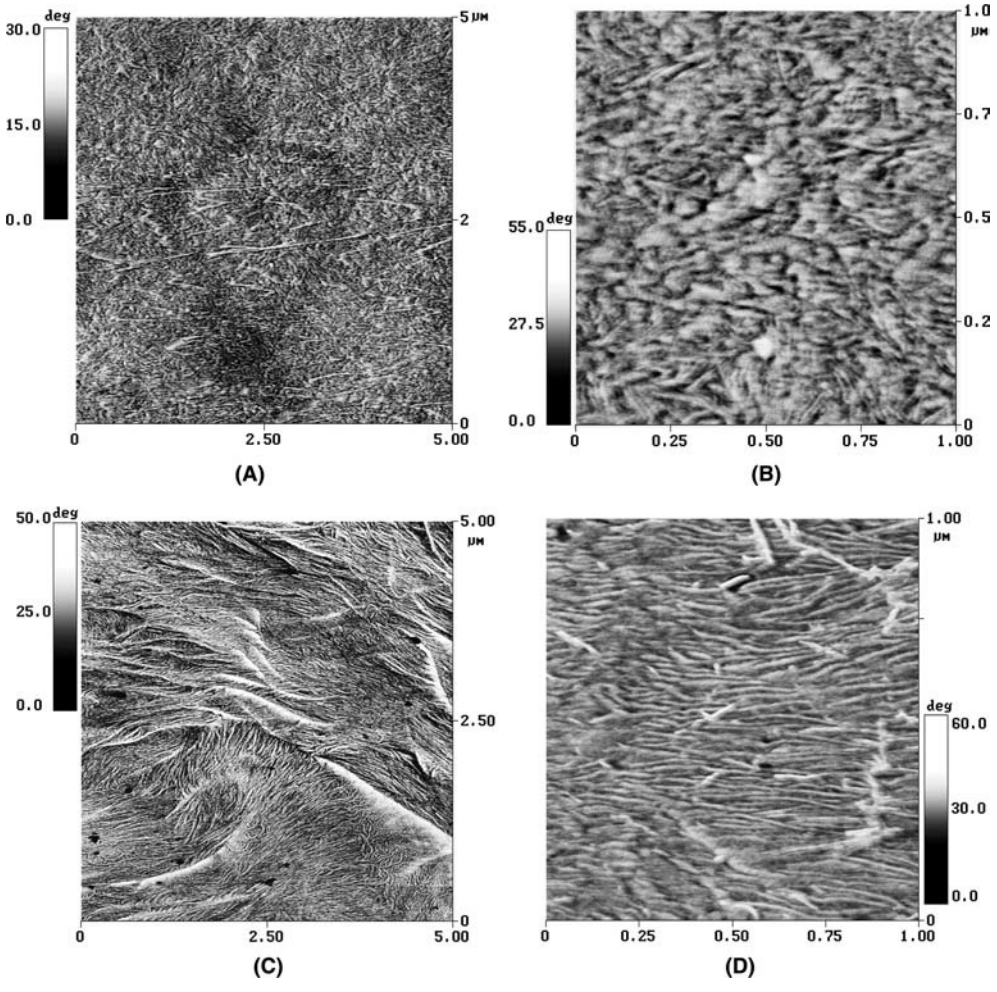

Fig. 2 AFM phase images: (A) and (B) at room temperature after quenching and (C) and (D) after cooling at 10 °C/min

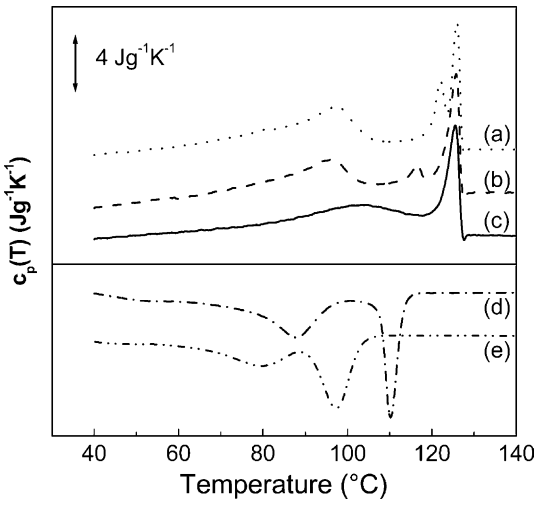

Fig. 3 DSC cooling and heating curves recorded between 200 and 40 °C. (a), (b) and (c): heating curves at 10 °C/min after (a) cooling at 10 °C/min, (b) cooling at 100 °C/min and (c) quenching into acetone at its freezing point. (d) represents the curve recorded during cooling at 10 °C/min and (e) during cooling at 100 °C/min

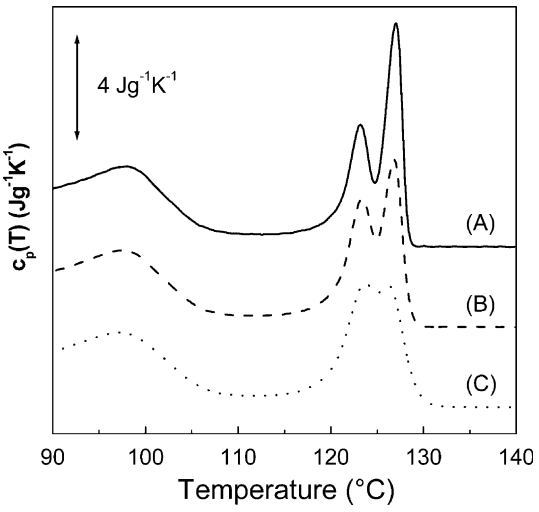

Fig. 4 DSC heating curves at (A) 10 °C/min, (B) 20 °C/min and (C) 40 °C/min after cooling from 200 °C at 10 °C/min

occurrence of melting-recrystallization-remelting [10]. This persistence of the melting allure is, however, deceptive since recrystallization during heating *does* occur even after cooling at much *lower* rates!

Curves (d) and (a) in Figure 3 are cooling and subsequent heating runs at 10 °C/min. respectively. The high temperature crystallization peak are mainly due to LPE solidification since at this cooling rate pure copolymer does not crystallize at these temperatures [27]. The low temperature crystallization peak is associated with copolymer crystallization. There are two exothermic maxima in curve (d) but *three* melting peaks in curve (a). Clearly, one of the endothermic peaks has no counterpart in the previous cooling curve, suggesting that one of the peaks is caused by a reorganization process. Figure 4 displays different DSC heating curves, recorded at increasing heating rates. The intensity of the highest temperature peak decreases with increasing heating rate, indicating that it originates from melting after recrystallization during heating.

Heating at 10 °C/min was also recorded after cooling at 100 °C/min. Again there are only two exothermic peaks in the cooling curve (curve (e) in Figure 3) whereas during heating an additional peak appears (curve (b) in Figure 3). The second melting peak after cooling at 10 and 100 °C/min corresponds to the melting of the original LPE crystallites, since it has shifted to a lower temperature just like the corresponding crystallization peak. The highest temperature melting peaks in the curves (a) and (b) are not affected by the cooling rate indicating again that it is due to the melting of material that recrystallized during heating. After quenching, the high temperature melting peak coincides with the melting peak that is due to melting of recrystallized material when slower cooling rates are used, indicating that it also may be due to the melting of material that recrystallized during heating. However, only two melting peaks are observed in this case rather than three. Moreover, the low-temperature melting peak is situated in between the LPE and copolymer melting peaks obtained during heating after slower cooling. This intermediate melting behavior points at a cocrystallization of the two components. Apparently, after the cocrystals have melted the LPE fraction is able to recrystallize and remelt in the high-temperature peak.

In Figure 5 the mass fraction crystallinity is displayed as a function of temperature based on the c_p(T) curves of Figure 3 that were recorded at 10 °C/min. It is of interest to compare the heating runs after the two different cooling histories. In the temperature window labeled (1), the crystallinity after cooling at 10 °C/min is higher than that of the quenched sample. In window (2) the crystallinity of the quenched samples is higher, in window (3) the situation reverses again and finally in window (4) both crystallinities are identical. A similar effect was observed earlier [39] for the pure copolymer when a comparison was made in heating after quenching or slowly cooling.

SALS

The SALS ratio for cooling and subsequent heating at 10 °C/min is displayed in Figure 6. No SALS intensity was observed after quenching at room temperature nor during heating although AFM clearly reveals the presence of spherulitically organized crystal aggregates that are sufficiently large to produce scattering in the angular range covered by the experiment. This implies firstly that

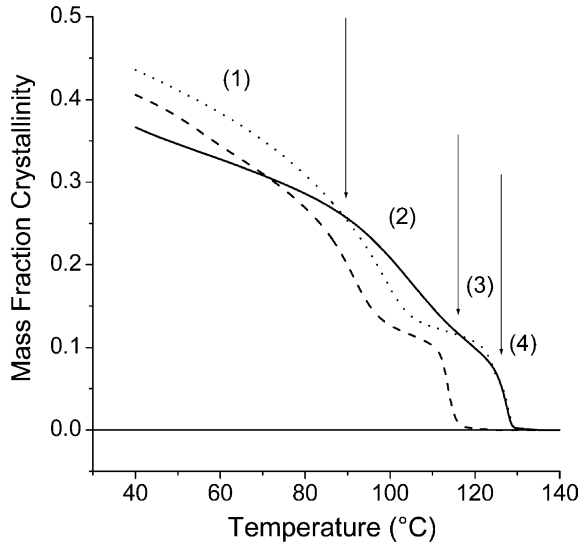

Fig. 5 DSC based mass fraction crystallinity as a function of temperature: heating at 10 °C/min after quenching (full line), cooling at 10°C/min (dashed line) and subsequent heating at 10 °C/min (dotted line). The temperature regions indicated by arrows and labeled with numbers are explained in the text

the crystallinity after quenching is homogeneously (down to a scale of approximately 0.25 μm) distributed over the sample volume (absence of excess *Vv* scattering) at all temperatures. Secondly, there is a total absence of orientation correlation between the constituting crystals (absence of *Hv* and *Vv* scattering), which is compatible with the random orientation of the crystals within the spherulites deduced from AFM.

A Q_{Vv}/Q_{Hv} ratio of 4/3 is reached during cooling at 10 °C/min below 70–80 °C and it stays at this value during heating up to 80–90 °C. At higher temperatures there is a clear positive deviation, pointing at the presence of volumes with a different crystallinity. Between 118 and 109 °C during cooling the ratio is quite high but drops quite rapidly. This temperature window coincides with the rapid earliest DSC crystallinity increase and is related to the growth of spherulites involving essentially LPE material. Optical microscopy studies reveal that at 109 °C spherulites are filling space completely (not shown). Between 109 and 95 °C a plateau is reached, just like in the DSC crystallinity. Here the Q_{Vv}/Q_{Hv} ratio equals 2, pointing at a (spherulite internal) spatial segregation of the blend components. Below 95 °C the Q_{Vv}/Q_{Hv} ratio drops when the copolymer fraction crystallizes and finally reaches the limit of 4/3. At this stage the samples are homogeneous in terms of crystallinity, at least from a SALS point of view. This sequence of events is reproduced during heating with a slight hysteresis in temperature. However, the top value at the highest temperature is almost two orders of magnitude lower than the value reached during cooling, indicating that spherulites do not melt back to their center and that the crystallinity disappears by the complete collapse of spherulites.

Finally, Figure 7 displays the typical (c)-type *Hv*-pattern at 40 °C. The excess scattering in the center is due to pronounced spherulite internal disorder [32].

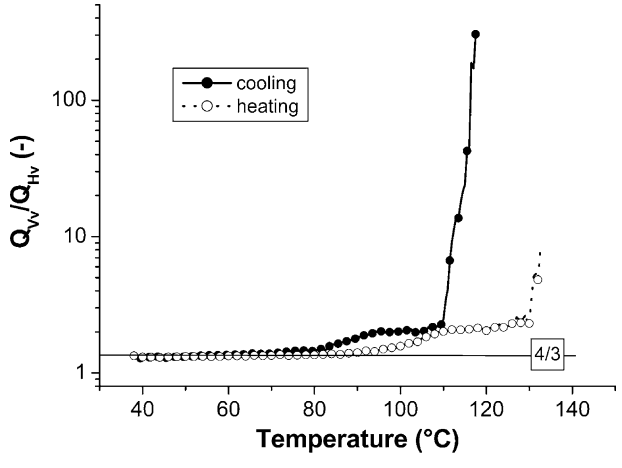

Fig. 6 SALS Q_{Vv}/Q_{Hv} ratio during cooling and subsequent heating at 10 °C/min

SAXS

Figures 8, 9 and 10 give the different SAXS volume fractions during respectively cooling at 10 °C/min,

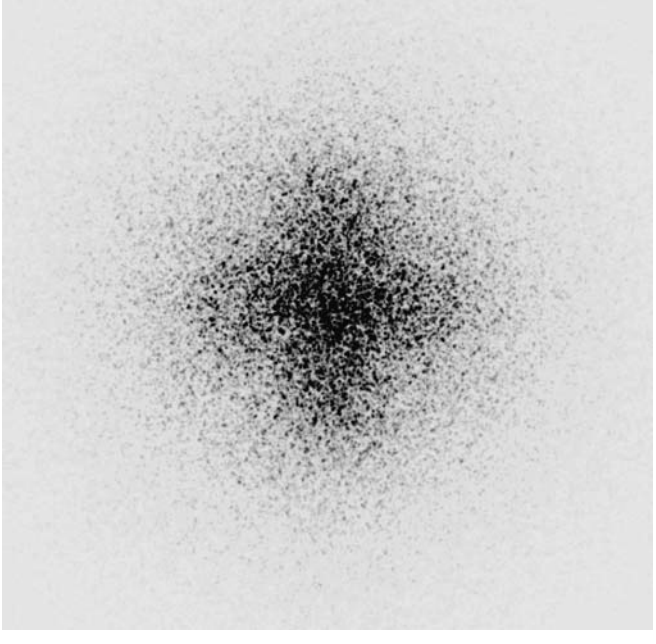

Fig. 7 *Hv* SALS pattern at 40 °C after cooling at 10 °C/min

subsequent heating at the same rate and heating after quenching. The overall crystallinities related to the A-CA or the CA-CA model are very similar and in excellent agreement with the DSC values if the latter were converted to a volume fraction crystallinity (not shown).

For the cooling experiment at 10 °C/min ϕ_2 equals zero within experimental error, indicating that an analysis according to the A-CA model is justified (Figure 8). α_S is the product of ϕ_{sp} with the fraction of semi-crystalline regions inside the spherulites and where ϕ_{sp} equals 1, α_S is a direct measure for the spherulite internal volume fraction of semi-crystalline regions. The first steep increase of this parameter at about 115 °C is due to the increase of ϕ_{sp}. At 95 °C, just prior to the copolymer crystallization, SAXS reveals that only 50% of the spherulite internal volume is occupied with semi-crystalline regions. Here α_S equals 0.5. During cooling below 95 °C the amorphous regions inside the spherulite gradually transform into semi-crystalline ones by the copolymer crystallization. Below 70–80 °C the crystals are homogeneously spread over the volume and the crystallinity inside the semicrystalline regions only very slightly increases further.

Since at high temperatures, ϕ_2 really equals zero there is a very pronounced segregation of the copolymer molecules from the primary semi-crystalline regions that mainly consist of LPE crystals. Moreover, the length scale involved is rather large as it is detected by SALS. The LPE and copolymer molecules thus crystallize in separate regions. During melting the process is reversed (Figure 9). First, there is a slight decrease of the crystallinity inside the semi-crystalline regions and above 80–90 °C the amorphous regions between the semi-crystalline regions of the primary (LPE) crystals are

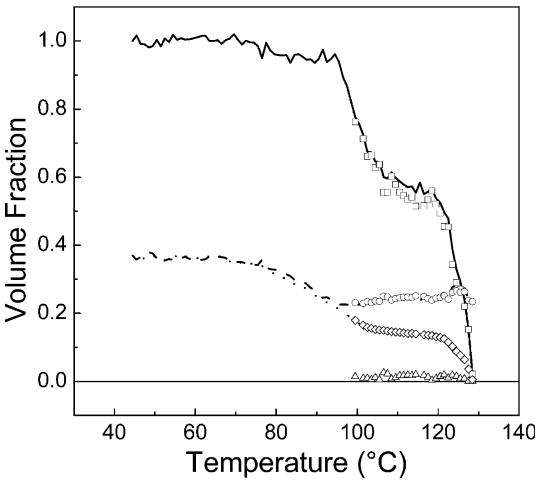

Fig. 9 Comparison of characteristic volume fractions during heating at 10 °C/min after cooling at 10 °C/min. For the A-CA model: α_S (full line), ϕ_L (dashed line) and $\alpha_S\phi_L$ (dotted line); and for the CA-CA model: α_1 (open squares), ϕ_1 (open circles), ϕ_2 (open triangles) and $\alpha_1\phi_1 + \alpha_2\phi_2$ (open diamonds)

formed abruptly again by pronounced copolymer melting. Finally, the LPE crystals melt in a very narrow temperature range, resulting in the steep drop of the crystallinity to zero. In this final process, entire stacks melt since it is mainly the decrease of α_S that causes the decrease of the overall crystallinity, $\alpha_S\phi_L$.

During heating after quenching (Figure 10), ϕ_2 only *gradually* decreases to zero in contrast to the sample that was cooled at 10 °C/min where ϕ_2 is zero as soon as the copolymer starts to melt. The A-CA model thus only holds above 110 °C during heating after quenching

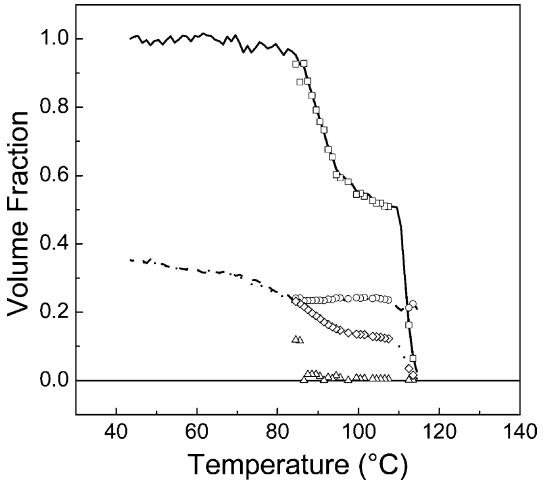

Fig. 8 Comparison of characteristic volume fractions during cooling at 10 °C/min. For the A-CA model: α_S (full line), ϕ_L (dashed line) and $\alpha_S\phi_L$ (dotted line); and for the CA-CA model: α_1 (open squares), ϕ_1 (open circles), ϕ_2 (open triangles) and $\alpha_1\phi_1 + \alpha_2\phi_2$ (open diamonds)

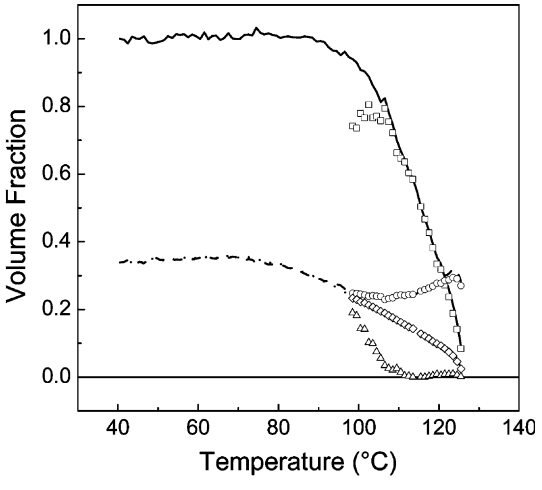

Fig. 10 Comparison of characteristic volume fractions during heating at 10 °C/min after quenching from 200 °C into acetone at its freezing point. For the A-CA model: α_S (full line), ϕ_L (dashed line) and $\alpha_S\phi_L$ (dotted line); and for the CA-CA model: α_1 (open squares), ϕ_1 (open circles), ϕ_2 (open triangles) and $\alpha_1\phi_1 + \alpha_2\phi_2$ (open diamonds)

where real amorphous regions are present. The gradual decrease of ϕ_2 reflects a gradual separation of crystalline and amorphous material during heating. However, it is a very local process since at any moment in time the segregation length scale stays below the limit required for light scattering.

Note that ϕ_1 at the highest temperatures is too high for a reliable use of $K(x)_{min}$ [26]. At these temperatures the A-CA model holds ($\phi_2 = 0$) and equation (9) can be used to calculate ϕ_1 correctly, which is then equal to ϕ_L.

l_C is given as a function of temperature in Figure 11. The values according to the two models are almost identical. When cooled at 10 °C/min, 80 Å thick LPE crystals are formed during primary crystallization. During copolymer crystallization thinner crystals are formed giving rise to the observed decrease of the *average* l_C. The best estimate for the thickness of the copolymer crystals probably is that of the pure component cooled at the same rate. In that case l_C hardly depends ontemperature and is around 50 Å [26]. The observed decrease reflects the increasing amount of 50 Å thick crystals. The temperature evolution of l_C during melting is comparable, aside from some hysteresis. The *bimodal* crystal thickness population gradually melts, starting with the thinnest crystals, thus yielding an increasing l_C and a plateau value at temperatures where the thinner (copolymer) mode has melted and the thicker (LPE) mode is still intact. Only at the highest temperatures there is a sudden increase, where, according to DSC (Figure 4), part of the LPE crystal fraction recrystallizes.

The average crystal thickness after quenching is lower than after cooling at 10 °C/min throughout but increases gradually during heating to reach at the highest temperatures a value comparable to that after cooling at 10 °C/min. This *gradual* increase of l_C can either be taken as evidence for the gradual melting of an unimodal crystal thickness distribution or for a *continuous* recrystallization into thicker crystals over a fairly broad temperature range. DSC reveals a *double* melting peak, which is incompatible with the first suggestion, leaving continuous recrystallization as the best option.

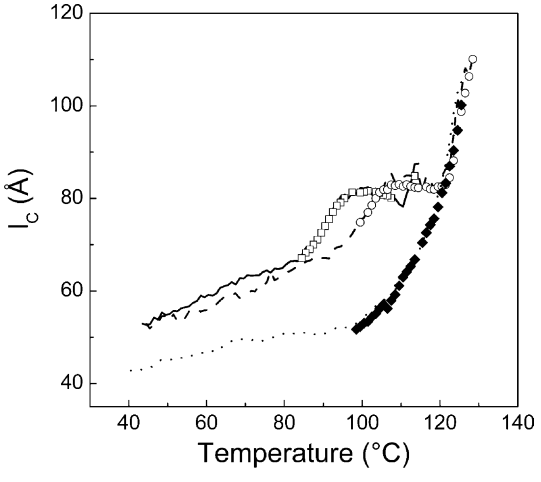

Fig. 11 l_C based on the CA-CA model, during cooling (open squares) and subsequent heating (open circles) at 10 °C/min. l_C based on the CA-CA model, during heating at 10 °C/min after quenching (solid diamonds). The results according to the A-CA model are represented with a full line for the cooling and a dashed line for the subsequent heating experiment at 10 °C/min whereas the data during heating after quenching are represented by a dotted line

WAXD

The temperature dependence of the WAXD crystallinity in Figure 12 is in agreement with the DSC and SAXS values. In Figure 13, the WAXD based crystalline density is displayed as a function of temperature. During cooling at 10 °C/min, crystals with a density typical for LPE are first formed. The full line in Figure 13 represents the expected temperature dependent density evolution for LPE [38]. During further cooling below 95 °C, where the majority of the copolymer fraction crystallizes, the density deviates from the LPE reference line. At 40 °C the measured crystalline density agrees well with that after cooling the pure copolymer at the same rate [26]. The experimentally observed density resembles a mass fraction weighted average of the high-density LPE and lower density copolymer crystals. An identical temperature-density evolution with some hysteresis can be observed during heating. In the crystallinity plateau regions between the copolymer and LPE melting, only LPE crystals are present and the change in density is due to the thermal contraction and expansion conform the LPE reference line.

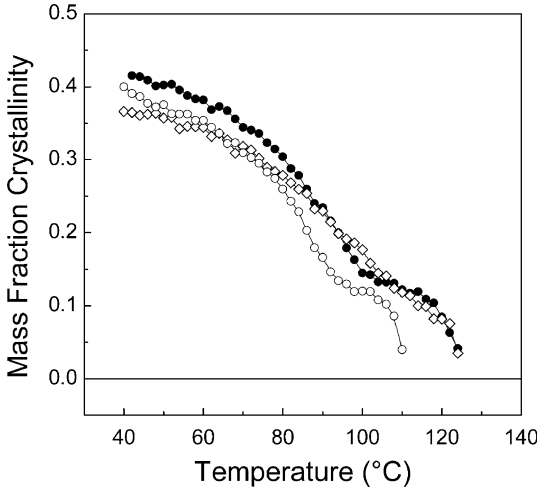

Fig. 12 WAXD crystallinity estimates during cooling at 10 °C/min from 200 °C (open circles), during subsequent heating at 10 °C/min (solid circles) and during heating at 10 °C/min. after quenching from 200 °C into acetone at its freezing point (open diamonds)

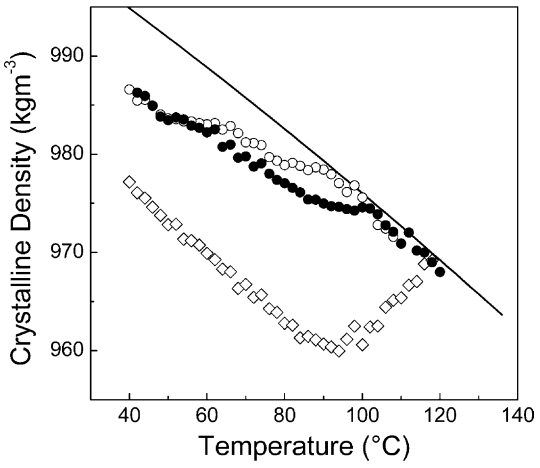

Fig. 13 WAXD based crystalline density as a function of temperature during cooling at 10 °C/min from 200 °C (open circles), during subsequent heating at 10 °C/min (solid circles) and during heating at 10 °C/min after quenching (open diamonds). The full line represents the reference crystalline density for LPE after Swan[38]

The crystalline density at 40 °C after quenching is below that after cooling at 10 °C/min and agrees well with that after quenching the pure copolymer [25]. In the present case, however, there is no gradual but an abrupt increase in density starting at 90 °C and ending at 118 °C close to the LPE reference density. The density of the quenching induced crystals stays intact up to 90 °C and only decreases due to thermal expansion (the slope of this density is identical to that of the LPE reference line). The increase of the crystalline density beyond 90 °C coincides with the crystallinity segregation derived from SAXS, a pronounced l_C increase and the development of the first DSC melting maximum.

Note that in the SAXS data processing it was assumed that the experimental deviation from the LPE crystalline density values is caused by a unit cell expansion at the interphase between crystalline and amorphous material. With the core of the crystals resembling high-density reference PE it is appropriate to use reference mass densities of fully crystalline and amorphous PE in the SAXS data processing [26].

Discussion

The data presented above are compatible with the following line of thought. The high temperature DSC exothermic peak during cooling at 10 or 100 °C essentially corresponds to the crystallization of LPE. This peak shifts to lower temperatures with increasing cooling rate as expected for nucleation controlled crystallization and crystallization that involves (time consuming) segregation of a not crystallizable component. At high temperature the copolymer cannot crystallize as (most of) the ethylene sequences are too short compared to the length needed for crystallization in thick crystals. Hexyl branches cannot be incorporated into the PE crystalline lattice [40]. The low-temperature crystallization peak during cooling at 10 or 100°C thus corresponds to copolymer crystallization and also shifts to lower temperatures with increasing cooling rate for the same reason. These peak shifts are reflected in the melting peak temperatures. The third (highest-temperature) melting peak is due to the melting of recrystallized LPE material.

Besides lowering the actual crystallization temperature, an increase of the cooling rate also promotes LPE-copolymer cocrystallization. In fact the DSC experiments show that, during cooling at 10 °C/min, the longest ethylene sequences of the copolymer cocrystallize with the LPE fraction since the melting peak temperature of the copolymer fraction in the blend is *below* that of the pure copolymer, cooled at the same rate [26]. In other words, cocrystallization extracts the longest copolymer ethylene sequences which results in an increase of the average comonomer content in the remaining copolymer fraction and hence a decrease of the corresponding crystallization and melting temperatures. By increasing the cooling rate, the extent of cocrystallization increases since crystallization occurs at lower temperatures and slightly shorter ethylene sequences are also involved. These two effects cause the copolymer melting peak after cooling at 100 °C/min to be below that after cooling (more slowly) at 10 °C/min.

Beyond a given cooling rate this negative shift of the low-temperature melting peak seems to reverse. The low-temperature melting peak after rapid quenching is situated at a *higher* temperature (curve (c) in Figure 3). Clearly, this peak cannot be due to the melting of copolymer alone, since it is not expected to shift to higher temperatures with increasing cooling rate. On the other hand, the LPE melting peak should have shifted further to lower temperatures because crystallization occurred at higher supercooling during quenching. In addition, at high supercooling, cocrystallization is maximized. Accordingly, the low-temperature endothermic peak after quenching corresponds to the melting of LPE-copolymer cocrystals. Some excess copolymer may have crystallized separately, but the corresponding endothermic signal links up or coincides with the melting peak of the LPE-copolymer cocrystals. The high temperature melting peak after quench-cooling corresponds to the melting of recrystallized LPE material, just like the highest temperature peaks after cooling more slowly do. There is no reason to assume that a rapidly cooled PE sample would not recrystallize if a more slowly cooled sample already does so.

This scenario is fully supported by the scattering experiments. Cocrystallization produces crystals with a lower density compared to LPE. Upon melting the LPE fraction and the longest copolymer ethylene sequences

are able to recrystallize and produce crystals with a higher density. The selection of ethylene sequences involves a spatial segregation of material but on a length scale smaller than what is reached during cooling at 10 °C/min. Segregation during cooling at 10 °C/min can be observed by SAXS and SALS whereas only SAXS sees the segregation taking place during heating after quenching. This segregation length scale decreases with increasing crystallization rate and decreasing component diffusion rate. Both parameters cooperate and promote lower segregation lengths with decreasing temperature. Recrystallization after cocrystal melting occurs at about 95 °C whereas the LPE crystallization (and component segregation) during cooling at 10 °C/min takes place at 115 °C.

This difference in (re)crystallization temperature should also be reflected in the corresponding melting temperature, but this is experimentally not observed. The fact that the high temperature melting peak after quenching is identical to that after cooling at 10 °C/min, together with the continuous increase of the lamellar thickness, suggests that the crystals, formed by recrystallization after cocrystal melting, continuously remelt and recrystallize until they finally are no longer able to do so at the highest temperatures. This limiting temperature is identical for recrystallization after cooling at 10 °C/min since the heating rate is identical. Accordingly the recrystallization-induced melting peaks coincide.

During this melting-recrystallization process endothermic heat is (partially) compensated by exothermic heat until only endothermic heat is left at the highest temperatures, giving rise to a second peak. The LPE melting peak associated with the melting of crystals that were formed during cooling (second melting peak) seems - after cooling at 100 °C/min - to be smaller than that after cooling at 10 °C/min. In the latter case, there is less recrystallization (and hence less exothermic overlap) because not all original LPE crystallites recrystallize. Some original LPE crystals are sufficiently stable to melt at sufficiently high temperatures where recrystallization cannot occur during the time allowed in the heating run. Obviously, if even slower cooling rates had been used, crystallization would have occurred at such high temperatures that there would be no time at all for recrystallization at the high melting temperatures of these crystals during heating at 10 °C/min.

The recrystallization after quenching happens very fast since it occurs a high degree of supercooling. This explains why recrystallization can hardly be suppressed by increasing the DSC heating rate.

It is of interest to reflect on the evolution of the crystallinity during heating, in particular on the effect causing the crystallinity after quenching in temperature window (2) of Fig. 5 to exceed that after cooling at 10 °C/min. The arguments given previously to account for this effect in the case of the pure homogeneous copolymer [39], where the ethylene sequence length distribution (ESLD) is mainly *intra*molecular, can be translated to the present blend case with an *inter*molecular ESLD. In the present case the shorter ethylene sequences are all part of the copolymer whereas the majority of the longer, nominally infinite, sequences belong to the LPE fraction.

According to nucleation theory, the thickness of a crystalline lamella is inversely proportional to the crystallization temperature (i.e. the supercooling). During slow cooling, at high temperatures, only relatively thick LPE crystals can be formed. The copolymer ethylene sequences that have the critical length for nucleation at that temperature are also involved, but the majority of the copolymer fraction is segregated from the crystallization front and crystallizes separately at lower temperatures into thinner crystals according to the ESLD. The required minimum ESL for cocrystallization with the LPE fraction decreases with decreasing LPE crystallization temperature. In a given miscible LPE-copolymer blend the copolymer fraction that cocrystallizes increases with the cooling rate. During quench cooling, cocrystallization is maximized. Besides a minimum ethylene sequence length for crystallization at a given temperature a minimum amount of refolding chains is also needed to avoid a density conflict [41–43]. According to Vonk [42] at least 60% of the stems reaching the surface of a PE crystal have to bend back into the crystal of origin. On this account, while slowly cooling an LPE-copolymer blend some copolymer ethylene sequences, with the critical length for nucleation at a given temperature, nevertheless do *not* (co)crystallize. These sequences only crystallize at lower temperatures where thinner crystals are formed and their length is sufficient for a re-entry loop without overcrowding problems. At higher temperatures they can only crystallize provided they cocrystallize with a sufficient number of longer sequences, that are able to crystallize with a re-entry loop. Most of the LPE (infinite) sequences and the longest copolymer ethylene sequences are, however, consumed in very thick crystals formed at higher temperatures in a slow cooling process. Quenching as well as recrystallization at high supercooling results in extensive cocrystallization. Such cocrystals can contain a high fraction of relatively short ethylene sequences without overcrowding problems because the (folded) LPE sequences are present in the same crystal. The relatively higher mass fraction of crystallized ethylene sequences causes the higher crystallinity in the temperature window (2) of Figure 5.

After cooling at 10 °C/min and in the low temperature region (1) all sequences that can potentially crystallize are to some extent in the crystalline state. In contrast, an amount of ethylene sequences with a potential for crystallization may be immobilized in the amorphous

state after quenching, due to the attachment of other chain parts to crystals. This obviously also holds after cooling at 10 °C/min., but this effect is thought to be more important after quenching since little time is allowed for the selection and segregation of ethylene sequences. Consequently, the overall amount of ethylene sequences incorporated in crystals by cooling at 10 °C/min in region (1) is larger than that reached by quenching. The crystals that consist of relatively short ethylene sequences after cooling at 10 °C/min and that melt in region (1) cannot recrystallize because the longer sequences needed to cocrystallize with - in order to avoid overcrowding - are incorporated in crystals that only melt at higher temperatures. As explained above, such short sequences *are* included after quenching by which the crystallinity after quenching is higher in window (2).

In the temperature region (3) the crystallinity of the sample cooled at 10 °C/min is again higher than after quenching. At these high temperatures only relatively thick crystals are stable, which can be formed after sufficient time at high temperatures (i.e. during a relatively slow cooling or slow heating by annealing and/or recrystallization). The small excess of thicker crystals in region (3) for the sample cooled at 10 °C/min is due to the crystals formed during cooling. Probably all the crystals in that region after quenching are generated by recrystallization. The amount of thickest lamellae in region (4) for the quenched sample is identical to that of the sample cooled at 10 °C/min. These crystals are nearly all formed by recrystallization independent of the previous cooling rate.

Conclusions

The *double* melting behavior of a quenched (15/85) blend of LPE with a lightly branched ethylene copolymer is not linked to the presence of two crystal populations. The observed thermal behavior is the result of a superposition of endo- and exothermic signals. By quenching a *unimodal* crystal thickness population is created. The LPE fraction cocrystallizes with at least part of the copolymer fraction without segregation of the components. During heating the cocrystals repeatedly melt and recrystallize into thicker crystals over a large temperature range, thereby progressively excluding more copolymer material. The concomitant spatial segregation of species is observable by SAXS but is too small to be detected by SALS. The LPE crystals formed at the end of this reorganization process, melt at high temperatures where accordingly a (second) endothermic peak appears in DSC. Recrystallization during heating after quenching cannot be suppressed by increasing the heating rate in a standard DSC because it requires extremely high heating rates when recrystallization occurs at a high supercooling.

During cooling at 10°C/min the LPE fraction crystallizes first to form space-filling spherulites of low crystallinity with the amorphous copolymer segregated into relatively large intraspherulitic regions. This copolymer fraction crystallizes later upon further cooling. During heating the sequence of events is reversed but part of the LPE fraction recrystallizes at high temperatures. From SALS it can be deduced that no μm scaled domains of different crystallinity are present after quenching.

Acknowledgment Y.H. and B.G. thank the Research council of the Catholic University of Leuven for a postdoctoral grant. Currently, B.G. is a postdoctoral fellow of the Fund for Scientific Research Flanders (FWO-Vlaanderen). H.R. is grateful to FWO-Vlaanderen for continuous support and equipment. B.G. and H.R. thank DSM for financial support. The E.U. is acknowledged for support under the TMR/LSF program to the EMBL Hamburg Outstation, reference number: ERBFMGECT980134.

References

[1] B. Crist, M.J. Hill, J. Polym. Sci.: Part B: Polym. Phys., 35, 2329 (1997)
[2] P.J. Barham, M.J. Hill, A. Keller, C.C.A. Rosney, J. Mat. Sci. Letters, 7, 1271 (1988)
[3] M.J. Hill, P.J. Barham, A. Keller, C.C.A. Rosney, Polymer, 32, 1384 (1991)
[4] M.J. Hill, P.J. Barham, A. Keller, Polymer, 33, 2530 (1992)
[5] M.J. Hill, P.J. Barham, Polymer, 33, 4099 (1992)
[6] M.J. Hill, P.J. Barham, Polymer, 33, 4891 (1992)
[7] M.J. Hill, P.J. Barham, J. van Ruiten, Polymer, 34, 2975 (1993)
[8] P.J. Barham, M.J. Hill, G. Goldbeck-Wood, J. van Ruiten, Polymer, 34, 2981 (1993)
[9] D. Thomas, J. Williamson, M.J. Hill, P.J. Barham, Polymer, 34, 4919 (1993)
[10] M.J. Hill, S.J. Organ, P.J. Barham, Thermochimica Acta, 238, 17 (1994)
[11] M.J. Hill, P.J. Barham, Polymer, 35,1802 (1994)
[12] M.J. Hill, Polymer, 35, 1991(1994)
[13] M.J. Hill, P.J. Barham, Polymer, 36,1523 (1995)
[14] M.J. Hill, P.J. Barham, Polymer, 36, 3369 (1995)
[15] C. Schipp, M.J. Hill, P.J. Barham, V.M. Cloke, J.S. Higgins, L. Oiarzabal, Polymer, 37, 2291 (1996)
[16] R.L. Morgan, M.J. Hill, P.J. Barham, C.J. Frye, Polymer, 38, 1903 (1997)
[17] R.G. Alamo, J.D. Londono, L. Mandelkern, F.C. Stehling, G.D. Wignall, Macromolecules, 27, 411 (1994)
[18] B. Crist, Polymer, 38, 3145 (1997)
[19] R.G. Alamo, W.W. Graessley, R. Krisnamoorti, D.J. Lohse, J.D. Londono, L. Mandelkern, F.C. Stehling, G.D. Wignall, Macromolecules, 30, 561 (1997)

[20] R.L. Morgan, M.J. Hill, P.J. Barham, A. van der Pol, B.J. Kip, R. Ottjes, J. van Ruiten, Polymer, 42, 2121 (2001)
[21] C.H. Stephens, A. Hiltner, E. Baer, Macromolecules, 36, 2733 (2003)
[22] R.L. Morgan, M.J. Hill, P.J. Barham, Polymer, 40, 337 (1999)
[23] B. Goderis, L. Theunissen, V.B.F. Mathot, H. Reynaers, in preparation
[24] Hunter, B.K.; Russell, K.E.; Scammel, M.V.; Thompson, S.L., J. Polym. Sci. Polym. Chem. Ed., 22, 1383 (1984)
[25] M. Peeters, B. Goderis, C. Vonk, H. Reynaers, V. Mathot, J. Polym. Sci.: Part B: Polym. Phys.: 35, 2689 (1997)
[26] B. Goderis, M.H.J. Koch, H. Reynaers, Macromolecules, 35, 5840-5853 (2002)
[27] V.B.F. Mathot, M.F.J. Pijpers, J. Therm. Anal., 28, 349 (1983)
[28] V.B.F. Mathot, in 'Calorimetry and Thermal Analysis of Polymers', V.B.F. Mathot (Ed.), Hanser Publishers, New York, Chap. 5, 105 (1994)
[29] S. Rabiej, B.Goderis, J. Janicki, V.B.F. Mathot, M.H.J. Koch, G. Groeninckx,H. Reynaers, J. Gelan, A.Wochowicz, Polymer, in press
[30] Akpalu, Y.; Kielhorn, L.; Hsiao, B.S.; Stein, R.S.; Russell, T.P.; van Egmond, J.; Muthukumar, M. Macromolecules 1999, 32, 765
[31] R.S. Stein, M.B. Rhodes, J. Appl. Phys., 31, 1873 (1960)
[32] J. Maxfield, L. Mandelkern, Macromolecules, 10, 1141 (1977)
[33] M.H.J. Koch, J. Bordas, Nucl. Instrum. and Methods, 208, 435 (1983)
[34] C.J. Boulin, R. Kempf, A. Gabriel, M.H.J. Koch, Nucl. Instrum. and Methods, A269, 312 (1988)
[35] G. Rapp, A. Gabriel, M. Dosière, M.H.J. Koch, Nucl. Instrum. and Methods, A357, 178 (1995)
[36] B. Goderis, H. Reynaers, M.J.H. Koch, V.B.F. Mathot, J. Polym. Sci.: Part B: Polym. Phys. Ed., 37, 1715 (1999),
[37] G.R. Strobl, M. Schneider, J. Polym. Sci.: Polym. Phys. Ed., 18, 1343 (1980)
[38] P.R. Swan, J. Polym. Sci., 42, 525 (1960)
[39] B. Goderis, M. Peeters, H. Reynaers, M.H.J. Koch, W. Bras, V.B.F. Mathot, A.J. Ryan, J. Polym. Sci.: Part B: Polym. Phys., 38, 1975 (2000)
[40] C.G. Vonk, H. Reynaers, Polym. Comm., 31, 190 (1990)
[41] P.J. Flory, J. Am. Chem. Soc., 84, 2857 (1962)
[42] C.G. Vonk, J. Polym. Sci.: Part C: Polym. Lett., 24, 30 (1986)
[43] L. Mandelkern, Chemtracts Macromol. Chem., 3, 347 (1992)

Progr Colloid Polym Sci (2005) 130: 64–69
DOI 10.1007/b107346
Published online: 3 June 2005

Yael Dror
Wael Salalha
Wim Pyckhout-Hintzen
Alexander L. Yarin
Eyal Zussman
Yachin Cohen

From carbon nanotube dispersion to composite nanofibers

Abstract Composite polymer nanofibers containing single-walled carbon nanotubes (SWCNT) are fabricated by electrospinning. We describe the path from dispersing individual SWCNTs or thin bundles in water using amphiphilic polymers, through a structural characterization of the polymer conformation in the SWCNT/polymer hybrid to the characteristics of the electrospun composite nanofibers. An alternating copolymer of styrene and sodium maleate (PSSty) and gum arabic (GA)-a highly branched natural polysaccharide were successfully used to produce stable aqueous dispersions. Measurements of small angle neutron scattering (SANS) show that both polymers form a thick corona of adsorbed coils on the nanotubes, resulting in a thick cylindrical hybrid. The large coils introduce a significant steric barrier stabilizing the dispersions, in addition to electrostatic repulsion by charged groups. The composite nanofibers showed good distribution and alignment of the SWCNTs in the poly(ethylene oxide) (PEO) matrix. Enhanced tensile properties were achieved due to a high degree of alignment of both nanotubes and PEO crystals, and a strong interface, especially with PSSty.

Keywords Carbon nanotube · Neutron scattering · Electrospinning

Abbreviations

CCD	Charge coupled device
CEVS	Controlled environment vitrification system
CNT	Carbon nanotube
GA	Gum Arabic
PEO	Poly(ethylene oxide)
PSSty	''Polysoap styrene''-alternating styrene/sodium-maleate copolymer
SANS	Small-angle neutron scattering
SDS	Sodium dodecyl sulfate
SWCNT	Single-walled carbon nanotube
TEM	Transmission electron microscopy

Dedicated to Professor Wilhelm Ruland, who has taught us scattering methods and the wonders of carbon materials, on the occasion of his 80th birthday

Y. Dror · Y. Cohen (✉)
Department of Chemical Engineering, Technion, Haifa, Israel 32000
e-mail: yachinc@tx.technion.ac.il
Tel.: +972-4-8292010
Fax: +972-4-8295672

W. Salalha · A. L. Yarin · E. Zussman
Department of Mechanical Engineering, Technion, Haifa, Israel 32000

W. Pyckhout-Hintzen
Institut für Festkörperforschung, Forschungszentrum Jülich GmbH, 52425 yülich, Germany

Introduction

Since the discovery of Iijima [1] a decade ago, carbon nanotubes (CNTs) have attracted a lot of interest and scientific efforts due to their unique and fascinating structure and properties. These properties [2,3] opened a wide range of potential applications such as nano-electronic devices, field electron emitter, nano-sensors, ultra strong wires, nanocomposites materials and more [4,5]. Nevertheless, the realization of the superior molec-

ular properties (often anisotropic) of the nanotubes in the final products is still an unsolved challenge hampered by processing difficulties. These difficulties arise from the fact that carbon nanotubes, single-walled carbon nanotubes (SWCNTs) in particular, tend to form tight, long bundles due to strong short-ranged van der Waals interaction [6] resulting in a complex entangled network. In this network the molecular properties cannot be expressed. Hence, separation of the bundles, dispersion and alignment of the nanotubes become vital for the achievement of controllable product with desirable performance. Indeed, much work is being done worldwide to achieve stable dispersions. Two main routes for dispersing nanotubes are reported: Chemical and physical approaches. The first involves chemical modification of the carbon nanotubes lattice and thus affect the molecular properties. The latter is based on adsorption of potential dispersants onto the surface of the nanotubes. For example, aqueous dispersions were attained using small surfactant molecules [7–9] large amphiphilic polymers [10] and natural macromolecules [11]. Also, conjugated polymers were successfully used as effective dispersants in organic medium [12–14]. It was recently shown that a generic mechanism to disperse isolated nanotubes in any solvent is based on the adsorption of block copolymer providing selective interaction of the different blocks with the solvent [15].

Concerning the alignment of nanotubes, several techniques have been applied to this end. For example, deposition of carbon nanotubes suspension under magnetic field [16], mechanical stretching of a polymer/nanotube composite film [17,18] and more. Other approaches are based on the processing of the carbon nanotubes dispersions. Among these, a direct technique to spin carbon nanotubes from an aqueous dispersion in SDS to form a fiber or ribbon has been reported by Vigolo and co workers [7,19,20]. The electrospinning technique has also been used recently in order to incorporate carbon nanotubes in a polymeric matrix resulting in a composite nanofiber [21–26]. In these techniques the quality of the original dispersions has a key role in the aptitude to align and distribute the nanotubes in the final product and hence to control its properties. Consequently, the characterization of the dispersions and evaluation of their quality in terms of their ''debundling'' power and stabilization are of central importance.

In this paper we aim to report a full path starting with the formation of a stable dispersion and ending with the processing of the dispersion into a final product. Specifically, this path went through three stages: (1) Formation of a stable dispersion of carbon nanotubes in aqueous polymeric solution. (2) Characterization of the resulting dispersion in terms of its structure and interaction between its components. (3) Processing the dispersion to form composite nanofibers by electrospinning. In order to achieve stable dispersions, two different polymers were used: gum arabic (GA) [11] and an alternating copolymer of styrene and sodium maleate (PSSty). These polymers were chosen for being large, amphiphilic and charged molecules, which thus provide steric stabilization reinforced by electrostatic repulsion. However, the polymers differ in their conformation. The PSSty is a linear copolymer of alternating hydrophobic and hydrophilic units, while GA is a highly branched polysaccharide. Characterization of the dispersions was done by small angle neutron scattering (SANS) and cryo- transmission electron microscopy (cryo- TEM), and finally electrospinning was used to fabricate composite nanofibers.

Experimental

Materials

Alternating styrene/maleic anhydride copolymer (MW 50,000) was boiled with a stoichiometric amount of NaOH for two hours for hydrolysis of the anhydride ring. The resulting polyelectrolyte (''polysoap'') is termed PSSty. Gum arabic (GA) – a natural branched polysaccharide derived from exudates of *Acacia senegal* and *Acacia seyal* trees was used without further purification. SWCNTs synthesized by the electric-arc evaporation method were purchased from Carbolex and used as received. The dispersions were prepared by mixing the nanotubes in aqueous solutions of the polymers at the concentrations given in table 1. The dispersions were sonicated for 1 hour in a 43 KHz Delta D2000 sonicator and centrifuged for 30 minutes at 15,000 rpm (3g) in a Hettich Mikro 12–24 centrifuge. For small angle neutron scattering measurements, the dispersions were prepared in D_2O. Solutions for electrospinning were prepared by mixing 50% (w/w) of the dispersions with 50%(w/w) of a 6%(w/w) poly(ethylene oxide)-(PEO) solution in ethanol/water mixture. Procedure of the electrospinning is reported previously [25, 26].

Cryo-transmission electron microscopy (cryo-TEM)

Vitrified samples of the dispersions were prepared in a controlled environment vitrification system (CEVS) [27] at a controlled temperature of 25 °C and 100% relative humidity. The transfer of the sample to the microscope was done using an Oxford Instruments CT-3500 cryo-specimen holder and transfer system. The samples were investigated using low electron dose imaging and acceleration voltage of 120 kV in a Philips CM120 TEM. Images were recorded with a Gatan MultiScan 791 CCD camera, using the Gatan DigitalMicrograph 3.1 software package.

Small angle neutron scattering (SANS)

Measurements of the dispersions were carried out at the KWS1 diffractometer at the FRJ-2 research reactor in Fz-Jülich, Germany. The raw data were corrected for empty cell, detector efficiency and background scattering. The absolute intensity was

Table 1 compositions of the SWCNT dispersions

SWCNT/PSSty	SWCNT/GA
0.2% (w/w) SWCNTs 1% (w/w) PSSty	0.2% (w/w) SWCNTs 5% (w/w) GA

obtained using secondary scattering standards. The data are presented as intensity (scattering cross-section, cm^{-1}) as a function of the scattering vector ($q = 4\pi \sin \theta/\lambda$ were 2θ is the scattering angle and λ is the wavelength).

Results and discussion

Dispersions of SWCNTs were prepared in GA and PSSty solutions according to the compositions in table 1. The resulting dispersions were homogeneous having a dark smooth ink-like appearance and were stable for months. Cryo-TEM imaging of the vitrified SWCNTs/PSSty dispersion is presented in figure 1. Long and thin threads of either isolated or very thin bundles of carbon nanotubes are observed. The diameter of the thread ranges from 10 to 40A and the length, which is not entirely seen in the micrographs, is not less than 4000A. Also, the nanotubes seem as expected to have a large persistence length.

Scattering patterns of SWCNTs/PSSty and SWCNTs/GA are shown in figure 2. These data represent the scattering of the SWCNT/polymer hybrid particles after the subtraction of the unbounded (free) polymer. The scattering patterns do not exhibit a q^{-1} power law, as would have been expected for rod-like particle [28]. This is even more surprising considering the cryo-TEM micrographs presented above. Indeed, no simple model of cylindrical particle or even core-shell cylindrical model could fit the data. However, the carbon nanotubes/polymer interaction in the dispersion can be depicted as a cylindrical core decorated by adsorbed chains. Hence, we followed the model of a ''block copolymer micelle'', which was derived by Pedersen for spherical amphiphilic block-copolymers [29–31] and adapted for cylindrical geometry [32], modified for present system.

$$F_{\mathrm{HYB}} = (\Delta\beta)^2_{\mathrm{core}} F_{\mathrm{core}}(q) + N_{\mathrm{agg}}(\Delta\beta)^2_{\mathrm{chain}} F_{\mathrm{chain}}(q) + 2N_{\mathrm{agg}}(\Delta\beta)_{\mathrm{core}}(\Delta\beta)_{\mathrm{chain}} S_{\mathrm{core-chain}}(q) + N_{\mathrm{agg}}(N_{\mathrm{agg}} - 1)(\Delta\beta)^2_{\mathrm{chain}} S_{\mathrm{chain-chain}}(q) \quad (1)$$

This expression describing the hybrid particle (F_{HYB}) consists of four terms.The cylindrical core form factor, F_{core} is a function of R - the radius of the cylindrical core made of one or a few bundled nanotubes. F_{chain}, the adsorbed chain form factor, is taken as that of a Gaussian chain and is thus a function of the chain's radius of gyration R_{g}. The cross term between the core and the chain, $S_{\mathrm{core\text{-}chain}}$, and the cross term between the chains in the corona, $S_{\mathrm{chain\text{-}chain}}$ do not not bring essentially new structural parameters. Nevertheless they depend strongly on the spatial arrangement of the polymer coils adsorbed on the cylindrical core. N_{agg} is the number of chains attached to one cylinder per unit length. $\Delta\beta_{\mathrm{core}}$ and $\Delta\beta_{\mathrm{chain}}$ are the excess scattering lengths of the core and the chain, respectively. In this model there are three fit parameters: R, R_{g} and N_{agg}. The full description of the model and its analysis will be presented separately. Nevertheless, we bring herein the main results and conclusions. This model fits the data as shown by the solid lines in figure 2. The values of the fit parameters reveal a picture of a thick rod-like particle made of a thin and long cylindrical core having a radius of about 20Å. The core is surrounded by a thick and swollen polymeric corona with a large radius of gyration of about 150–170Å. The coverage of the core by the polymer is described by N_{agg} where the number of polymer chains per length of the core (N_{agg}/length) is 3–6 chains per 100Å. The core may thus be a thin bundle of nanotubes, with an average of about 4. The nanotube core imposes an elongated structure to the adsorbed polymer which

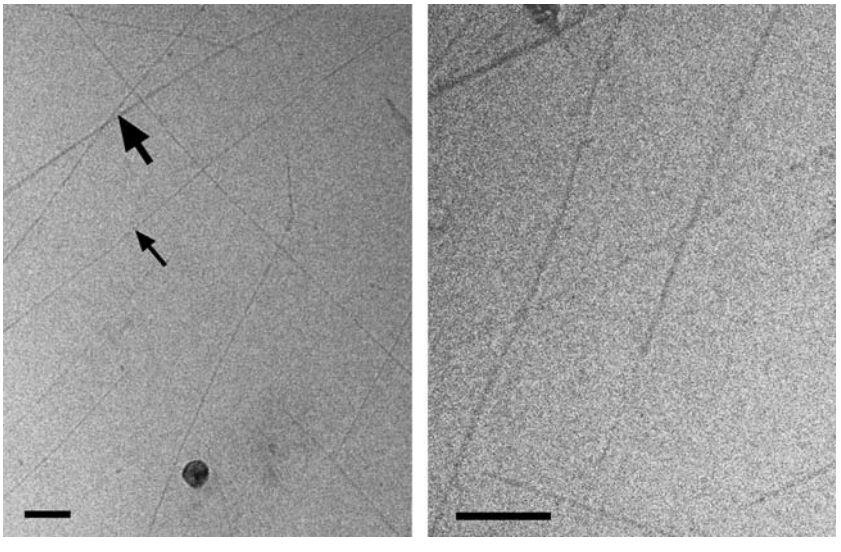

Fig. 1 Cryo-TEM micrographs of SWCNTs/PSSty dispersion in D_2O. The thick arrow indicates a thin bundle and the thin arrow indicates an isolated nanotube. The dark sphere in the left image is an ice spot. Bar = 500Å

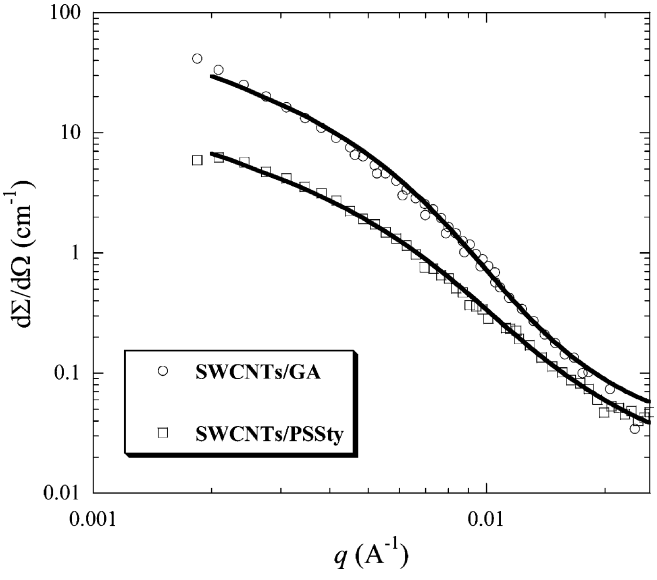

Fig. 2 SANS patterns of SWCNTs/PSSty and SWCNTs/GA dispersions, after subtraction of the polymer solution scattering. The solid lines are fits of the measured data according to equation (1)

results in a large cross section radius of the composite hybrid. The model is most sensitive to the structural parameters related to polymer, i.e. Rg and N_{agg}, which control the curvature of the scattering pattern in the measured q-range. On the other hand, the fit is less sensitive to the radius of the nanotube core, since the thin core is only 11% of the entire cross section. With this description it is comprehendible that the q^{-1} power law cannot be observed in these scattering patterns. Whereas a thinner hybrid would have exhibited this q^{-1} power law, the large cross section due to the polymer coils adsorbed on the nanotube core, significantly affect the pattern in the measured small q-range, altering the apparent power law. The interpretation of the cryo-TEM image is to be done accordingly. Only the cylindrical core is observed while the attached polymers cannot be imaged due to its low contrast.

These results demonstrate that steric interaction of the large polymer coils, adsorbed onto the nanotube surface, controls the stabilization of the dispersions and prevents re-bundling of the nanotubes. Charged groups distributed along the polymer further add electrostatic stabilization. It is interesting to note that although the polymers have totally different molecular structures their association with the nanotubes is basically the same, exhibiting a common scattering pattern and stabilization mechanism.

The dispersions, characterized above, were used subsequently to produce composite nanofibers by electrospinning. The dispersions were mixed together with spinable solutions of poly(ethylene oxide) – (PEO) and electrospun according to the procedure reported previously [26]. The resulting nanofibers contained a small amount of embedded SWCNTs accompanied by the polymeric dispersant (GA or PSSty) and a PEO matrix. The nanofibers' diameter was about 70 nm. Etching of PEO with oxygen plasma was used to expose the nanotubes within the nanofibers, as shown in figure 3, revealing isolated or thin bundled nanotubes.

This supports the assertion by the SANS measurements that the nanotubes were well dispersed. The nanotubes are straight and well aligned along the nanofiber axis. It is important to emphasis that poor dispersions containing large entangled bundles can be incorporated into nanofibers as well. However, although the flow during the electrospinning process induces alignment of rod-like particles, the bulbs of bundled nanotubes cannot be unraveled by electrospinning and remain as such in the nanofiber, as was shown previously [26]. This illustrates the importance of the quality of the dispersion in order to achieve distribution and alignment of the nanotubes within the nanofibers. X-ray

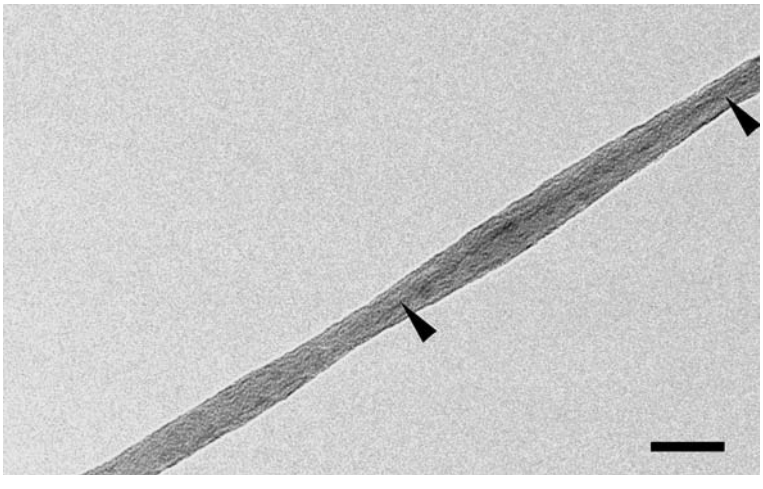

Fig. 3 TEM micrograph of etched SWCNTs/PSSty/PEO nanofiber. The arrows indicate the edges of the embedded SWCNT. Bar = 500Å

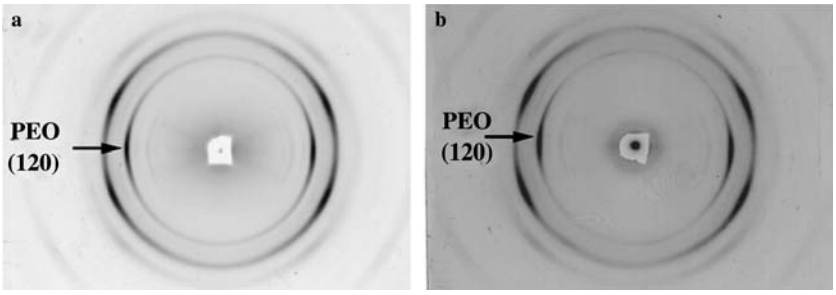

Fig. 4 X-ray diffraction pattern of: (a) PEO nanofibers and (b) SWCNTs/PSSty/PEO nanofibers

diffraction from ropes of nanofibers with and without nanotube dispersion with PSSty is shown in figure 4. Ropes of PEO exhibit a characteristic fiber diffraction pattern of the common monoclinic unit cell. The sharp equatorial reflections indicate that the PEO chains are aligned along the nanofiber axis. Similar good alignment of PEO chains is achieved also in the composite nanofibers with SWCNT and PSSty. Thus, well-aligned and separated nanotubes can be integrated in the polymeric matrix without disturbing the oriented crystallization of the PEO.

The high degree of alignment of carbon nanotubes and PEO crystals along the nanofiber axis results in unique tensile properties. Preliminary measurements indicate that the modulus of PEO nanofibers containing about 3% (w/w) SWCNTs from PSSty dispersion is about 1700 MPa which is 7 fold the modulus of PEO nanofibers. On the other hand, the modulus of nanofibers containing the same amount of nanotubes from GA dispersion is only 700 MPa. The significant difference between the results reflects the role the polymer dispersant plays at the interface between the nanotube and the nanofiber matrix. As concluded from the scattering measurements the dispersing polymer has a swollen coil conformation around the nanotubes which may readily interact with dissolved PEO chains. In the electrospun nanofibers, the dispersant polymer may thus serve as a bonding interphase between the nanotubes and the PEO matrix. The results indicate that the interaction between the nanotubes and PSSty and between PSSty and PEO is stronger than those achieved with GA thus providing a more effective load transfer. The details of the procedure for collection of aligned nanofibers and their tensile testing will be reported separately.

Conclusions

PSSty and GA were successfully used to produce stable aqueous dispersions of SWCNTs containing isolated nanotubes or thin bundles. Both polymers were attached to the nanotubes forming a thick corona of polymer coils providing an effective steric barrier combined with electrostatic repulsion. These large hybrid cylinders exhibited a characteristic scattering pattern which fits well a modification of the cylindrical ''block copolymer micelle'' model. Thus, long-term stable dispersions of SWCNTs can be accomplished by adsorption of diverse types of polymers such as linear alternating copolymer and branched polymer as long as the polymer introduces a significant steric barrier by thick envelopment of the nanotubes.

The well-dispersed SWCNTs could be incorporated in a distributed and aligned manner into PEO nanofibers by the electrospinning process, maintaining a high orientation of the polymeric matrix. The significant reinforcement of the tensile modulus of the composite nanofibers is optimal when the dispersing polymer also forms a strong interface between the nanotubes and the matrix, as in the case of PSSty. The entire route starting with dispersion of SWCNTs through structural characterization and ending with a composite nanofiber illustrates the direct link between the ''quality'' of the dispersion and the outcome accomplished by its processing.

Acknowledgements The work was partially supported by the Israel Science Foundation, the Israel Academy of Science, grants 287/00 and 26/03. Neutron scattering at Fz. Jülich was supported by the Jülich Neutrons for Europe program.

References

1. Iijima S (1991) nature 354: 56
2. Saito R, Dresselhaus G, Dresselhaus MS (1998) Physical Properties of Carbon Nnotubesa. Imperial College Press, London
3. Terrones M (2003) Ann Rev Mater Res 33: 419
4. Ajayan PM, Zhou OZ (2001) Top Appl Phys 80: 391
5. Dai L, Patil A, Gong X, Guo Z, Liu L, Liu Y, Zhu D (2003) ChemPhysChem 4: 1150
6. Girifalco LA, Hodak M, Lee RS (2000) Phys Rev B 62: 13104

7. Vigolo B, Penicaud A, Coulon C, Sauder C, Pailler R, Journet C, Bernier P, Poulin P (2000) Science 290: 1331
8. Moore VC, Strano MS, Haroz E, Hauge RH, Smalley RE, Schmidt J, Talmon Y (2003) Nano Letters 3: 1379
9. Islam MF, Rojas E, Bergey DM, Johnson AT, Yodh AG (2003) Nano Letters 3: 269
10. O'Connell MJ, Boul PJ, Ericson LM, Huffman CB, Wang Y, Haroz E, Kuper C, Tour J, Ausman KD, Smalley RE (2001) Chem Phys Lett 342: 265
11. Bandyopadhyaya R, Nativ-Roth E, Regev O, Yerushalmi-Rozen R (2001) Nano Letters 0: 1
12. Dalton AB, Stephan C, Coleman JN, McCarthy B, Ajayan PM, Lefrant S, Bernier P, Blau WJ, Byrne HJ (2000) J Phys Chem B 104: 10012
13. McCarthy B, Curran SA, Dalton AB, Davey AP, Konya Z, Fonseca A, Nagy JB, Blau WJ (2000) J Mater Sci Lett 19: 2239
14. Dalton AB, Blau WJ, Chambers G, Coleman JN, Henderson K, Lefrant S, McCarthy B, Stephan C, Byrne HJ (2001) Synthetic Met 121: 1217
15. Shvartzman-Cohen R, Levi-Kalisman Y, Native-Roth E, Yerushalmi-Rozen R (2004) Langmuir 20: 6085
16. Smith BW, Benes Z, Luzzi DE, Fischer JE, Walters DA, Casavant MJ, Schmidt J, Smalley RE (2000) Appl Phys Lett 77: 663
17. Bower C, Rosen R, Jin L, Han J, Zhou O (1999) Appl Phys Lett 74: 3317
18. Jin L, Bower C, Zhou O (1998) Appl Phys Lett 73: 1197
19. Launois P, Marucci A, Vigolo B, Bernier P, Derre A, Poulin P (2001) J Nanosci Nanothechno 1: 125
20. Poulin P, Vigolo B, Laonois P (2002) Carbon 40: 1741
21. Ko F, Han WB, Khan S, Rahaman A, Zhou O (2002) ASC 16th Annual Technical Conference
22. Ko F, Gogotsi Y, Ali A, Naguib N, Ye H, Yang G, Li C, Willis P (2003) Adv Mater 15: 1161
23. Schreuder-Gibson H, Senecal K, Sennett M, Huang Z, Wen JG, Li W, Wang D, Yang S, Tu Y, Ren Z, Sung C (2000) Proc Electrochem Soc 2000
24. Seoul C, Kim YT, Baek CK (2003) J Polym Sci Pol Phys 41: 1572
25. Dror Y, Salalha W, Khalfin R, Cohen Y, Yarin AL, Zussman E (2003) Langmuir 19: 7012
26. Salalha W, Dror Y, Khalfin R, Cohen Y, Yarin AL, Zussman E (2004) Langmuir 20: 9852
27. Bellare JR, Davis HT, Scriven LE, Talmon Y (1988) J Electron Micr Tech 10: 87
28. Glatter O and Kratky O (1982) Small Angle X-Ray Scattering. Academic Press, London
29. Pedersen JS, Gerstenberg MC (1996) Macromolecules 29: 1363
30. Pedersen JS (1997) Adv Colloid Interfac Sci 70: 171
31. Pedersen JS, Svaneborg C, Almdal K, Hamley IW, Young RN (2003) Macromolecules 36: 416
32. Pedersen JS (2000) J Appl, Crystallogr 33: 637

Progr Colloid Polym Sci (2005) 130: 70–78
DOI 10.1007/b107350
Published online: 3 June 2005

Jan Skov Pedersen
Cornelia Sommer

Temperature dependence of the virial coefficients and the chi parameter in semi-dilute solutions of PEG

Abstract Poly(ethylene glycol) (PEG) with a molecular weight of about 4600 in semidilute solutions with D2O as solvent has been studied by small-angle x-ray scattering in a broad temperature range from 10 to 100° C at concentrations from 1wt% to 20wt%. The scattering from the PEG solutions can be very well described by a random phase approximation (RPA) type expression. The forward scattering of the chains is analysed by two different approaches: In terms of temperature dependent virial coefficients and in terms of the recently derived Flory-Huggins theory for polymers solutions with a temperature dependent chi parameter. The virial approach gives a theta temperature of 100° C. A satisfactory fit by the virial approach requires only a second and a forth order virial coefficient. In the Flory-Huggins theory a correction for the finite polymer volume fractions results in a lower value of the theta temperature of 86° C. The chi parameter varies from 0.32 at 10° C from 0.52 at 100° C. The analysis of the temperature dependence of chi shows that it is predominately due to entropic effects.

This paper is dedicated to Prof. W. Ruland on the occation of his 80th birthday

J. Skov Pedersen (✉) · C. Sommer
Department of Chemistry and iNANO Interdisciplinary Nano Science Centre, University of Aarhus, Langelandsgade 140, 8000 Aarhus C, Denmark
e-mail: jsp@chem.au.dk
Tel.: +45-8942-3858

Present address: C. Sommer
Nestlé Research Center, P.O.Box 44, Lausanne 26, 1000 Vers-chez-les-Blanc, Switzerland

Introduction

Poly(ethylene glycol) (PEG) is probably the simplest water soluble synthetic polymer. Due to its biocompatibility it is used in a very broad range of pharmaceutical [1] and cosmetic products [2]. For example, amphiphilic block copolymers with one of the blocks being PEG are frequent components in pharmaceutical formulations and in drug delivery systems. It is the biocompatibility of the PEG corona of nano-sized drug delivery particles, which provides the 'stealth' properties, so that the particles are not immediately degraded by the immune system [3]

The PEG-water system is also an interesting system from a fundamental point of view due to the large change in solvent quality of water for PEG with variation of temperature. Water becomes a poorer solvent as the temperature is raised and it has a theta temperature of about 100°C.[4,5] The pronounced temperature dependence of PEG in aqueous solutions is crucial for the thermal stability of products containing the polymer. As an example of the influence of the temperature dependence of the solvent quality of water for PEG, one can mention the change in micelle structure and rheological properties of block copolymer micelles of PEG and poly(propylene oxide) at high temperature [6]

The change in solvent quality is associated with water molecules, which forms strong hydrogen bonds with the oxygen in the backbone of the PEG at low temperature.[7, 8, 9] As the temperature is increased, the hydrating water gradually disorders and the solvent quality gradually decreases. The change in the hydrating water is reflected in a large change in the apparent partial specific volume of the PEG chains.[10] The solvent quality is also directly reflected in the chain-chain interactions in dilute and semi-dilute polymer solutions. The present work is a study by small-angle scattering of such solutions of PEG in water in a broad temperature and concentration range.

Scattering techniques are well suited for investigating the structure and interactions in polymer solutions.

However, the interpretation of the scattering data depends crucially on whether suitable expressions are available for fitting the data. It has been demonstrated that the scattering intensity of semi-dilute solutions can be well described by a random phase approximation (RPA) expression, [11, 12] which in fact is also in agreement with suggestions by Zimm [13] and Benoit and Benmouna [14]. In the present work we have performed a small-angle x-ray scattering study (SAXS) of PEG in water. We apply the RPA expression to obtain information on the concentration effects and thus on the chain-chain interactions in the solutions as a function of temperature. The results are described by two different approaches: (i) In terms of temperature-dependent virial coefficients and (ii) in terms of a temperature-dependent Flory-Huggins chi parameter via recently derived expressions.

Experimental

The PEG homopolymer used in the study is PEG 4600 from Sigma-Aldrich. The polymer weight average molar mass was determined to be 4600 by MALDI-TOF mass spectroscopy and HPLC at the Danish Polymer Centre at Risø National Laboratory. A polydispersity index of 1.2 was calculated from the mass distribution. The polymer was used as received.

The samples were prepared by weight by dissolving PEG 4600 in D_2O (D purity higher than 99.9%) from Sigma-Aldrich. Samples with concentrations of 1, 2, 5, 10 and 20 wt% were mixed. The samples were left overnight and clear homogeneous solutions formed. D_2O was used in case future small-angle neutron scattering (SANS) would be performed, as the D_2O gives good contrast and low background in SANS.

SAXS measurements were performed on the pin-hole SAXS instrument at the University of Aarhus.[15] The instrument is a modified version of the original small-angle x-ray equipment known as the 'NanoSTAR', which was produced by Anton Paar, Graz, and distributed by Bruker AXS. The camera employs a rotating anode (MacScience with Cu anode, $0.3\times\ 0.3$ mm^2 projected source point, operated at 4.05 kW) and it has a three-pin-hole collimation. The instrument is optimised for solution scattering to have a high flux and a low background. The divergent Cu Kα radiation from the anode is monochromatized and made parallel by two cross-coupled Göbel mirrors. The samples are kept in a reusable home-built capillary holder with a quartz capillary with a pathlength of about 1.75 mm. The capillary is placed in the integrated vacuum chamber of the camera, and extra windows are avoided. The capillary holder is thermostated with a Peltier element which is computer controlled (Bruker AXS and Anton Paar). The temperature inside the capillary was checked by a thermoelement placed in the water-filled holder in vacuum. The temperature was varied from 10 to 100°C in steps of 10° C.

The sample detector distance is 66 cm and the beamstop is 3.0 mm in diameter. The instrument configuration gives access to a range of scattering vectors q from about 0.01 to 0.34 Å^{-1}, where the scattering vector modulus is given by $q=(4\pi/\lambda)\sin\theta$, where 2θ is the scattering angle and λ is the wavelength. The two-dimensional data sets are recorded using a two-dimensional position-sensitive gas detector (HiSTAR). The data were normalized to the integrated incident flux and sample transmission. The latter was measured indirectly by recording the integrated scattering from a strongly scattering sample (glassy carbon) with and without the sample inserted in the beam path before the glassy carbon. The spectra of all samples, corrected for variations in detector efficiency, were isotropic and the data were azimuthally averaged and corrected for spatial distortions. A pure D_2O samples was measured at the same temperatures as the samples and used for background subtractions. Finally the resulting data were converted to absolute scale using the scattering from pure water as a primary standard [16].

The apparent partial specific volume of PEG 4600 was determined from density measurements performed at 5–90°C with a DMA5000 densitymeter (Anton Paar) on solutions of PEG 4600 with concentrations 1, 2, and 5 wt%. The excess scattering length density of PEG in D2O was calculated from the partial specific densities.

Theory

For dilute solutions the scattering intensity can be described by the RPA/Zimm scattering cross-section expression [11,12,13,14]:

$$\frac{d\sigma(q)}{d\Omega} = cM_w\Delta\rho_m^2\frac{P(q)}{1+vP(q)} \tag{1}$$

where c is the concentration in g/mL, M_w is the weight-average molecular mass, and $\Delta\rho_m$ is the excess scattering length per unit mass of polymer. $P(q)$ is the single chain form factor and v is a parameter depending on the reduced concentration c/c^* and the binary cluster integral β, which describes the effective monomer-monomer interaction:

$$\beta = 4\pi\int r^2 dr[1-\exp(-V(r)/kT)] \tag{2}$$

where k is Boltzmann's constant, T is the absolute temperature and $V(r)$ is the effective monomer-monomer interaction potential. For low concentrations (i.e. below the overlap concentration of the chains) v is proportional to the second virial coefficient A_2. At the theta temperature T_θ, the second virial coefficient A_2 vanishes and there are no concentration effects at low concentrations.

In the recently developed Flory-Huggins theory[12] for semi-dilute solution, (1) is still valid. A simple calculation shows that

$$v = \eta\frac{V_{PEG}}{V_{H2O}}\left[\frac{1}{1-\eta}-2\chi\right] \tag{3}$$

where η is the polymer volume fraction, V_{PEG} is the PEG molecular volume, V_{H2O} is the volume of a water molecule, and χ is the temperature dependent Flory-Huggins interaction parameter. For $T\rightarrow T_\theta$ and small concentrations ($\eta << 1$), $\chi\rightarrow$ ½ and $v\rightarrow 0$, so that the concentration effects also vanish for this expression, in agreement with behaviour of the Zimm expression at the theta temperature.

Considering higher order-terms in a virial expansion at $q = 0$ in terms of η, one has

$$v = \eta 2A_2M + \eta^2 3A_3M + \eta^3 4A_4M + \cdots \tag{4}$$

Equation (3) from the Flory-Huggins theory also contains higher-order terms. A series expansion gives:

$$v = \eta\frac{V_{PEG}}{V_{H2O}}\left[1-\eta-\eta^2-\eta^3-\eta^4\cdots-2\chi\right] \tag{5}$$

so that:

$$2A_2M = \frac{V_{PEG}}{V_{H_2O}}[1-2\chi], \quad 3A_3M = -\frac{V_{PEG}}{V_{H_2O}},$$
$$4A_4M = -\frac{V_{PEG}}{V_{H_2O}}\cdots \tag{6}$$

which provides a direct link between χ and A_2, and which in addition shows that all higher virial coefficient are constant in the Flory-Huggins theory. Therefore the concentration effects do not vanish at the theta temperature at finite concentrations.

In the model we used the form factor of semi-flexible chains [17]. The data at low concentration and at high temperature, where the concentrations effects are very small, were fitted with the form factor without inclusion of concentration effects. This gave a radius of gyration of R_g = 26 Å, which was kept fixed while fitting the RPA expression (1) to all the data.

At good solvent condition where the chains have self-avoiding configurations, an increase in concentration leads to a screening of excluded volume effects as predicted by Flory. However, this effect is not directly observable in the recorded data since it occurs at low q where nominator and denominator in the RPA expression display similar q dependence so that the intensity is constant in this region. In addition the excluded volume effects are expected to be small since the chains are relatively short, i.e. L/b = 45 [18,19]. Therefore the effects of screening of excluded volume interactions were not included in the form factor.

The expression (1) was fitted to the data and the effective forward scattering of the chains

$$P'(0) = \frac{1}{1+v} \tag{7}$$

was used as a fit parameter.

Results

The SAXS data are shown in Fig. 1 at three different temperatures. The data have been normalized by the concentration and by the contrast factor $\Delta\rho^2$ as calculated from the partial specific volumes. The latter was done in order to eliminate the effects of temperature dependence of this prefactor. An example of the influence of this normalization is shown in reference [10]. At low q, the data from some of the samples show an upturn at low q. This is due to the formation of a small fraction of larger clusters and it has recently been shown that it has its origin in chain end effects.[20] Note that this contribution is absent at the highest temperature. The data clearly shows that the concentration effects become weaker at elevated temperatures. At 100 °C only the 10 wt% and 20 wt% data clearly deviates from the other samples.

Figure 2 displays the data for selected temperatures for the 1, 2, 5, and 10 wt% samples. The temperature dependence is weak for the 1 wt% sample. The effects become increasingly more important as the concentration is increased.

Figures 1 and 2 also contain the fits by the RPA expression. The fits are satisfactory except at low q for the samples with a significant cluster contribution. In addition the fit to the 20 wt% data deviate significantly from the data at low q.

Virial analysis

The results for $P'(0)$ from the fits are shown in Fig. 3. There is a clear increase in $P'(0)$ with temperature at all concentrations, which is in agreement with the weakening of the polymer interactions with increasing temperature. In a first step of an analysis of $P'(0)$, we will use only the second virial coefficient and assume the simplest functionality. We set $v = 2McA_2$, where M = 4600 and take c as the weight fraction of the solution. Furthermore, we use the proportionality $A_2 = A_2^{fit}(T - T_\theta)$ and fit the $P'(0)$ data as a function of T. This provides a first crude estimate of the value of T_θ (and A_2^{fit}). The fits are shown in Fig. 3 and the corresponding values for T_θ are, respectively, 94 +/−6, 97 +/−2, 100 +/−1, 105 +/−2, and 109 +/−3°C, for 1, 2, 5, 10 and 20 wt%. For the three lowest concentrations, the values are in excellent agreement with the expected value of about 100° C[5]′. At higher concentrations, the higher virial coefficients are important and these do not vanish at the theta temperature. We have furthermore, for, respectively, 1, 2, 5, 10 and 20 wt%, A_2^{fit} = 0.000056 +/−0.000008, 0.000058 +/−0.000003, 0.000065 +/−0.000003, 0.000074 +/−0.000004, and 0.000135 +/−0.000014 (g/mol °C)$^{-1}$. The increase of the value at the highest concentration also shows the influence of higher order virial terms at high concentration.

As the data for $c \leq 5\%$ are not influenced by higher order virial terms, one can perform a simultaneous fit of these data with the same value for T_θ (fit not shown). One obtains by this for A_2^{fit} = 0.000057 +/−0.000002 (°C)$^{-1}$ and T_θ = 100.1 +/−1°C, where the theta temperature is again in excellent agreement with the expected value.

At high concentrations (10 and 20 wt%), the contributions from the higher order virial coefficients leads to systematic errors and higher order terms have to be included in order to obtain good fits to the data. Fitting each temperature individually shows that the A_3 term is so small that it can be neglected, whereas the A_4 term is significant. The temperature dependence of it can be reproduced by an expression with a term which vanish at T_θ and a residual term: $A_4 = A_4^{fit}(T - T_\theta)^3 + A_4^0$. In this expression A_4^{fit} and A_4^0 are additional fitting parameters. The equation (5) with this expression and the corresponding one for the second order virial coefficient gives an excellent simultaneous fit to all the data (Fig. 3(b)). The results from this fit are A_4^0 = 99.5 +/−0.5°C, A_2^{fit} = 0.000057 +/−0.00001 1/°C, A_4^{fit} = (1.97 +/−0.09)×10^{-7} (g/mol)$^{-1}$(°C)$^{-3}$, and A_4^0 = 0.0215 +/−0.0009 (g/mol)$^{-1}$.

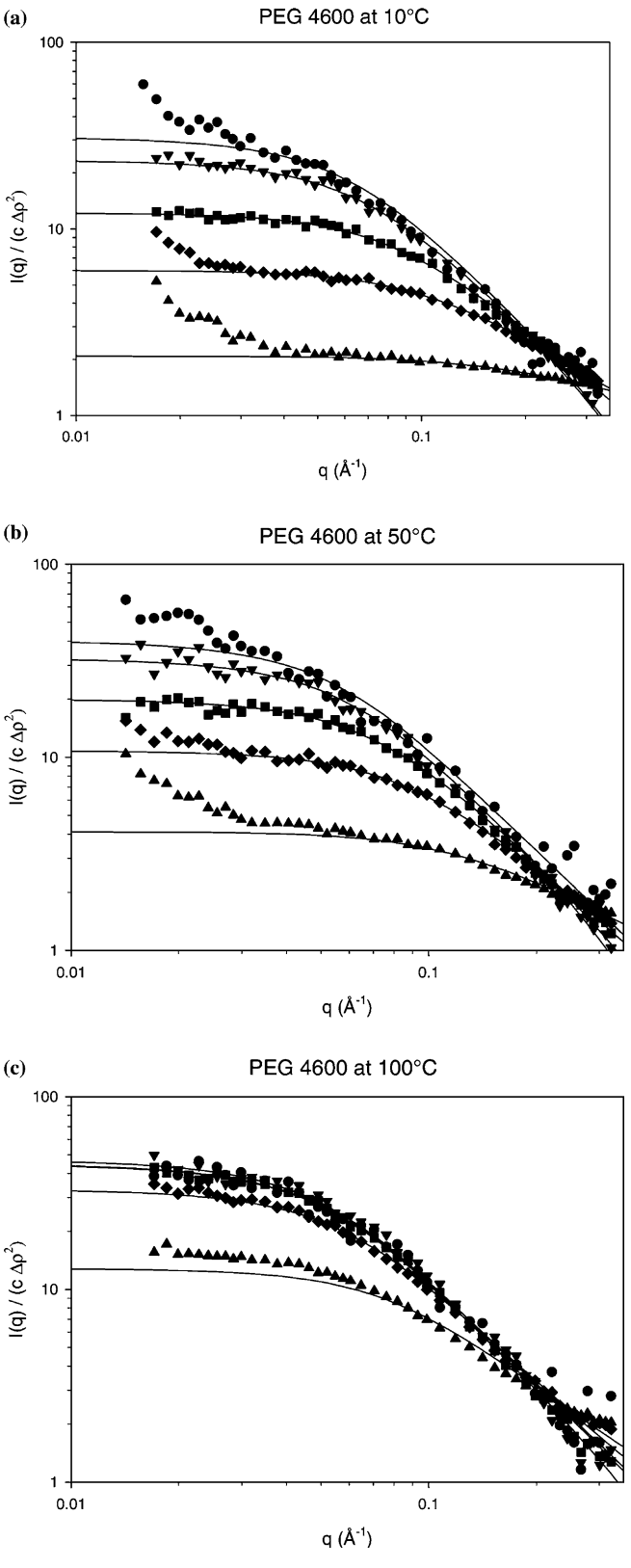

Fig. 1 SAXS data with fits (curves) for PEG 4600 solutions at fixed temperature as a function of concentration. (a) 10°C (b) 50° C (c) 100° C. Signatures: 1 wt% circles, 2 wt% triangle down, 5 wt% square, 10 wt% diamond, 20 wt% triangle up. The data have been divided by the square of the excess electron density ($\Delta\rho$ was in units of e/Å^3) of the PEG chains in order to eliminate the influence in the plot of the change in contrast with temperature

Flory-Huggins Theory

As already mentioned, the higher order terms are already included in the Flory-Huggins theory and all temperature dependence is assigned to the chi parameter (3). In a first approach we used a chi parameter at each temperature to fit the data. The polymer volume fraction η, the PEG volume V_{PEG}, and the volume of a water molecule V_{H2O} were calculated at each temperature from the density results. Since the osmotic pressure is related to the number-averaged molecular mass, V_{PEG} was taken as number average volume. The expression did not fit the high volume fraction data at high temperature, and therefore only the data for $c \leq 5$ wt% were fitted and the curves for c > 5 wt% calculated from the resulting fit. The curves are shown in Fig. 4(a), where linear interpolations between the values at the data points have been introduced. One sees that the model reproduces the concentrations effects very well at low temperature even at the highest concentration, however, at high temperatures, where the system approaches the theta condition, the model overestimates the concentration effects. The chi parameter corresponding to the fit is shown in Fig. 5. It is around 0.32 at 10°C and goes smoothly to the theta value of 0.5 between 80 and 90°C. For comparison, for polystyrene in toluene, for which the solvent is considered to be a good solvent, the chi parameter is about 0.44,[21, 22] so the solvent conditions are indeed very good for PEG in water at low temperature. The volume fraction correction in (3) to the theta condition $\chi = ½$ leads to a lowering of the theta temperature compared to the value found in the virial analysis.

In the final step of the analysis, we assumed a temperature dependence of χ:

$$\chi = 0.5 + \chi_1(T - T_0) + \chi_2(T - T_0)^2 \qquad (8)$$

where the second term is included due to the curvature of temperature dependence of χ as observed in the previous fit (Fig. 5(a)). The number of fit parameters is in this way greatly reduced since we do not need a chi parameter at each temperature. Again only the data for $c \leq 5$ wt% were fitted and the curves for c > 5 wt% calculated from the resulting fit (Fig. 4(b)). Also for this fit, the model overestimates the concentration effects at high temperatures, where the system approaches the theta condition. The chi parameter is shown in Fig. 5(a) and agrees very well with the values determined by having individual fit parameters for each temperature. The

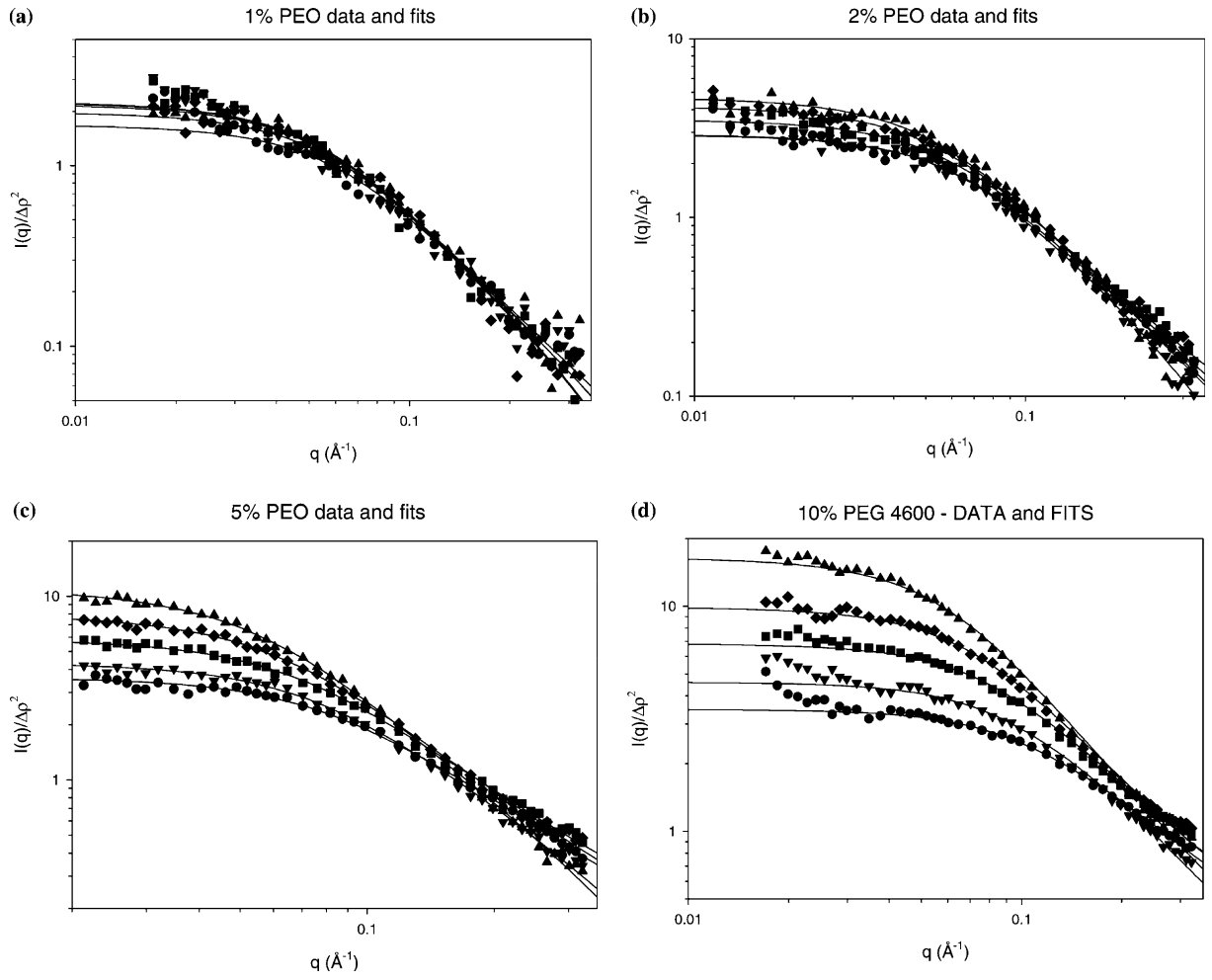

Fig. 2 SAXS data with fits (curves) for PEG 4600 solutions at fixed concentration as a function of temperature. (a) 1 wt% (b) 2 wt% (c) 5 wt% (d) 10 wt%. Signatures: 20°C circles, 40°C triangles down, 60°C squares, 80°C diamonds and 100°C triangles. The data have been divided by the square of the excess electron density of the PEG chains in order to eliminate the influence in the plot of the change in contrast with temperature

values for the two coefficients in the expression for chi are $\chi_1 = 0.00142 +/-0.00009$ and $\chi_2 = -0.000011 +/- -0.000002$, and the theta temperature is $85.7 +/-1.1$°C

In a previous light scattering study, Venohr et al. [23] used the expression

$$\chi = \alpha + \frac{\beta}{T} \tag{9}$$

to describe the temperature dependence of χ. In order to investigate whether the χ follows this relation, we have in Fig. 5(b) plotted the χ versus $1/T$ using the values obtained by fitting the individual temperatures. The data shows a remarkable linear behaviour and we have therefore used the expression (9) for chi and fitted the forward scattering $P'(0)$. We have also in this case only fitted the data for $c \leq 5$ wt% and calculated the curves for $c > 5$ wt% due to the overestimation of the concentration effects close to the theta temperature. The agreement for this two-parameter fit is as good as for the three-parameter fit using (8). The results are $\alpha = 1.156 +/-0.002$ and $\beta = -235.3 +/-0.9$ K.

In the Flory-Huggins theory [24]

$$\chi = \frac{z\Delta\varepsilon}{kT} = \frac{z\left(\varepsilon_{pw} - \frac{1}{2}[\varepsilon_{ww} + \varepsilon_{pp}]\right)}{kT} \tag{10}$$

where z is the coordination number on the lattice, k is Boltzmann's constant and $\Delta\varepsilon$ is the free energy of forming a polymer-water contact. In the last expression ε_{pw} is the free energy of a polymer-water contact, ε_{ww} is the free energy of a water-water contact, and ε_{pp} is the free energy of a polymer-polymer contact. $\Delta\varepsilon$ can also be expressed in terms of an enthalpic and an entropic contribution $\Delta\varepsilon = \Delta H - T\Delta S$. So in agreement with reference (4), the two terms in (9) can be identified with, respectively, an entrophy and an enthalpic energy term:

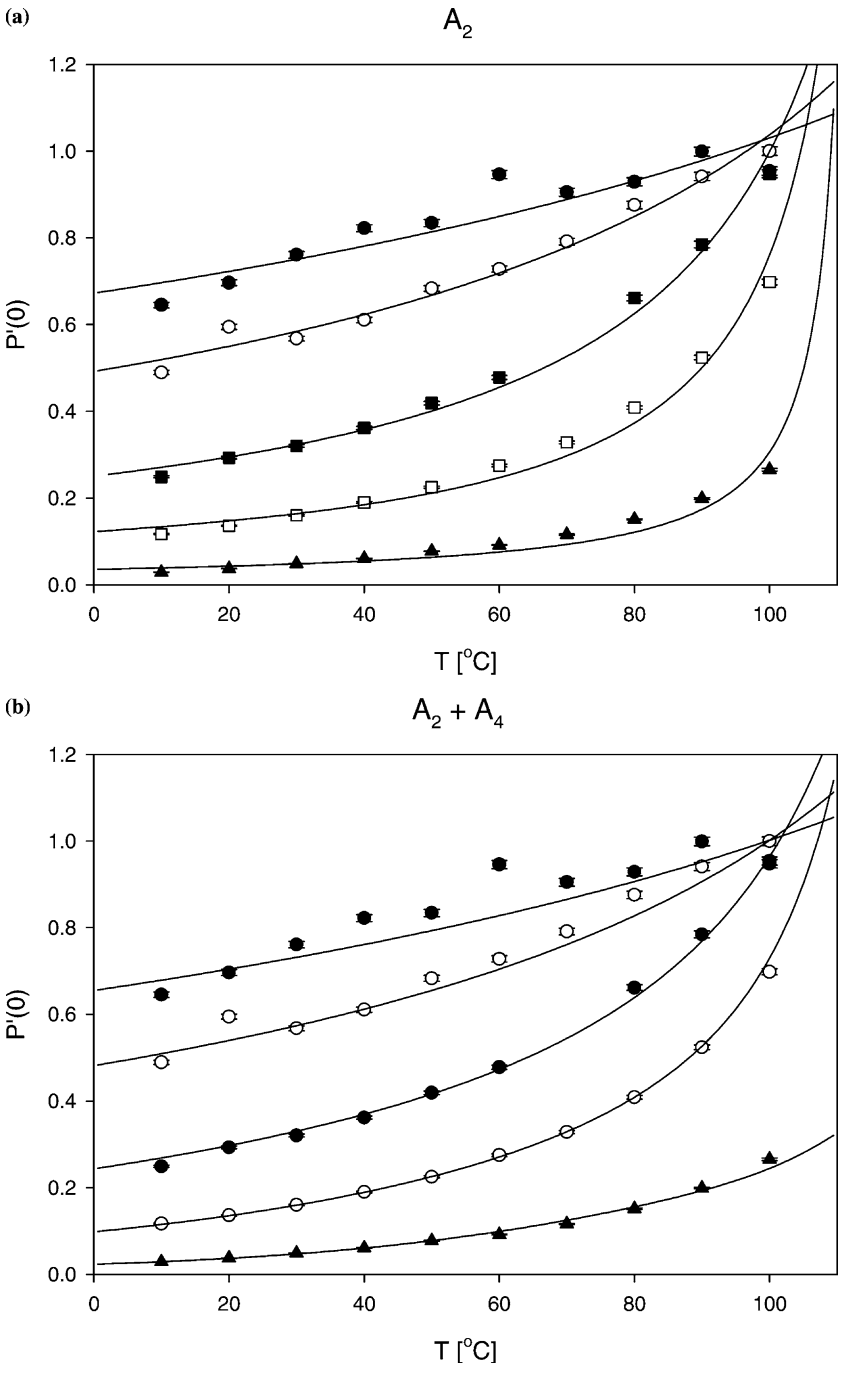

Fig. 3 The forward value of the effective single chain form factor of the PEG chains at 1%wt (filled circles), 2 wt% (open circles), 5 wt% (filled squares), 10 wt% (open squares) and 20 wt% (filled triangles). The curves are fits with virial expressions. (a) Including only a second virial coefficient, which goes linearly to zero at the theta temperature. (b) Including both a second and a fourth virial coefficient with temperature dependence (see text for details)

$$\chi = \chi_{\Delta S} + \frac{\chi_{\Delta H}}{T} \tag{11}$$

If it is assumed that ΔH and ΔS are independent of temperature, a temperature change from 10 to 100°C as in the present work, corresponds to ratios of $\Delta H / \Delta\varepsilon$ and $\Delta S/\Delta\varepsilon$ of

$$\Delta H/\Delta\varepsilon = 0.31 \text{ and } \Delta S/\Delta\varepsilon = 0.69 \tag{12}$$

and one sees that the free energy change is dominated by entropy.

Discussion

Scattering studies of polymer solutions can be performed using light [22], neutrons [25] or x-rays. The former is the

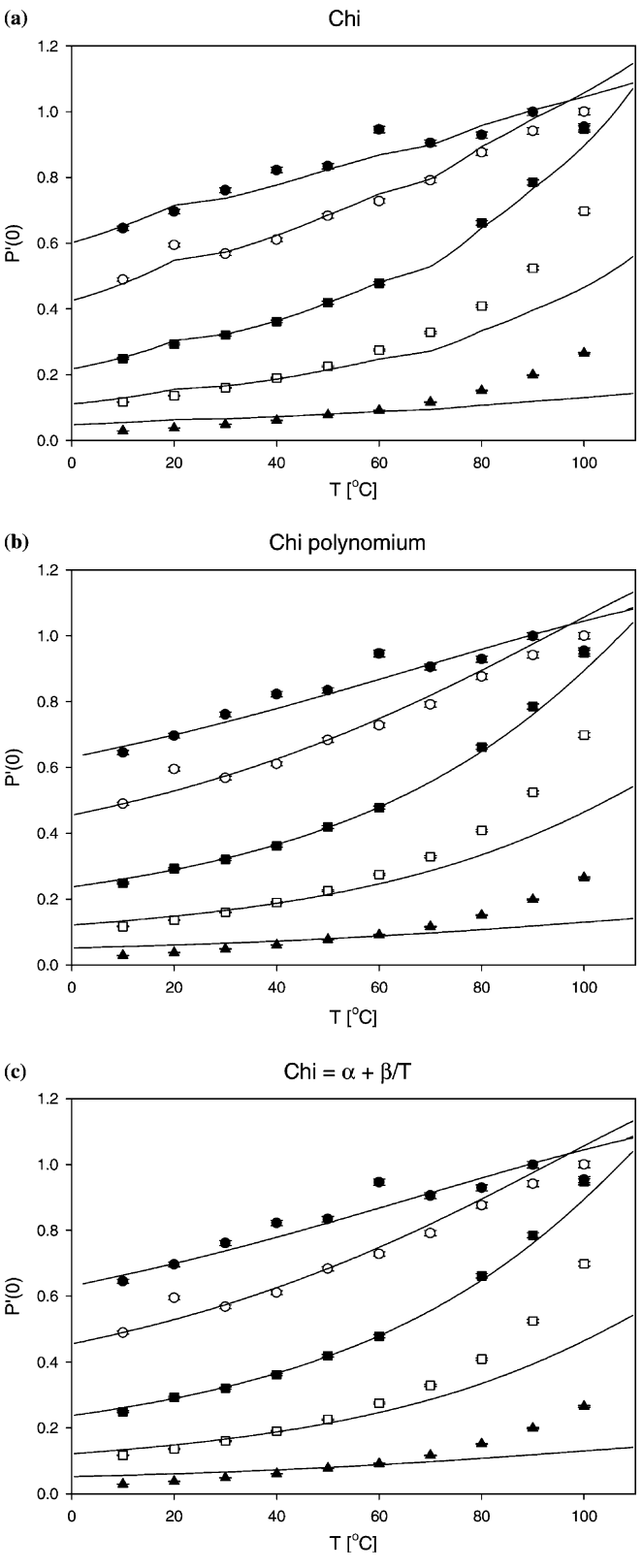

Fig. 4 The forward value of the effective single chain form factor of the PEG chains with signatures as in Fig. 3. The curves are fits using the Flory-Huggins theory. (a) With individual chi parameters at each temperatures and interpolations. (b) A second order polynomium for chi. (c) Using $\chi = \alpha + \beta/T$

choice for high molecular weight polymers, whereas the two latter are the choice for lower molecular weights. For the PEG-water system the scattering contrast is favourable for light and for neutrons (when using D_2O as solvent), whereas it is weak for x-rays. In spite of this, the present study employs small-angle x-ray scattering on a laboratory-based instrument. Such a study of a weakly scattering system has become feasible due to the developments in optimised instrumentation for solution scattering[15].

In the present study experiments have been performed as a function of concentration in a particularly broad temperature range. Very pronounced concentration and temperature dependence have been observed. The forward scattering was derived from applying the RPA expression to the SAXS data. The data could be fitted with a temperature- and concentration independent radius of gyration for the chains.

Analysis of the forward scattering for low concentrations in terms of a virial expansion gave $A_2 \approx 0.005$ (g mol)$^{-1}$ at 10°C in agreement with results by Venohr et al. for PEG with a molecular weight of 10000. The linear temperature dependence and the theta temperature of 100°C are also very similar to that found Venohr et al. Analysis of our data for higher concentrations showed that the data could be fitted perfectly with only a second and a fourth virial coefficient, which both depend on the temperature separation from the theta point. The second virial coefficient depends linearly on this temperature separation whereas the fourth virial coefficient depends on the separation to the power three and in addition has a residual value at the theta point. Due to the similarities of the temperature dependence of the two virial effects we suggest that the temperature dependent part of both coefficients is related to the effective pair potential and that the residual of the fourth coefficient at the theta point originates from steric contributions which are not vanishing at the theta point.

The application of the Flory-Huggins theory to the data showed that this theory gives a good description of the data except close to the theta temperature where it exaggerates the concentration dependence of the forward scattering. The magnitude and the temperature dependence of the chi parameter is in good agreement with previous findings [4,23] The temperature dependence of chi follows $\chi = \alpha + \beta/T$ and when making the connection to the interaction energies in the Flory-Huggins theory one can identify α with an entropic free energy contribution and β with an enthalpic. Using the

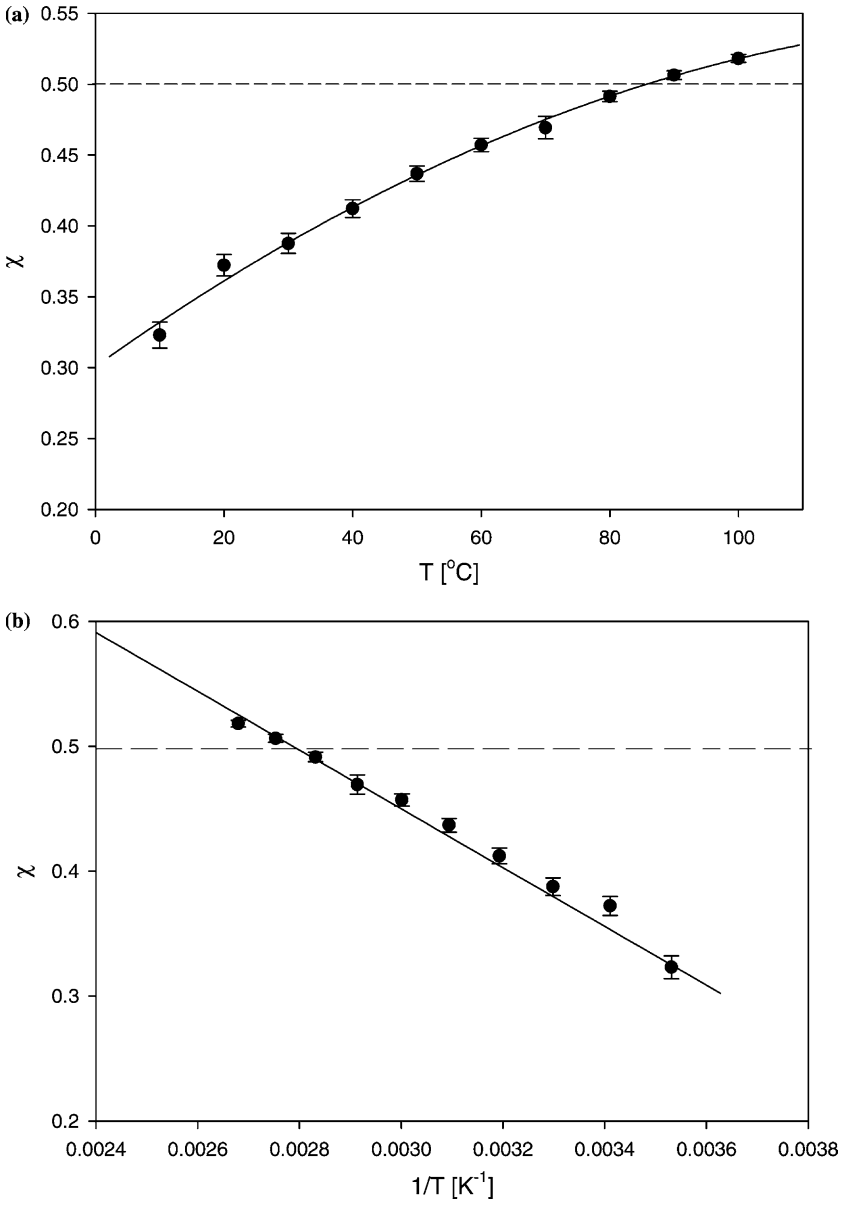

Fig. 5 The temperature dependence of the chi parameter. The points are the individual chi parameters at each temperatures. (a) The curve is from a second order polynomium for chi. (b) The curve is $\chi = \alpha + \beta/T$ from the fit in 4(c)

observed temperature dependence of chi, one finds that about 70% of the change in the free energy is entropy related and 30% are enthalpy related. This is en good accordance with the suggestion [8,9] that the change in solvent quality is due to a gradual disordering of water molecules which are tightly bound to the PEG chain and relatively well-ordered. This conclusion is further cooperated by the large change in apparent partial specific volume of PEG in water [10]. As the temperature is increased the PEG chains have a gradual increase in the apparent volume due to the disordering of the tightly bound water.

Acknowledgements We thank Lotte Nielsen and Dr. Kristoffer Almdal at Risø National Laboratory for characterizing the PEG 4600 sample. The support from the Danish Natural Science Council is gratefully acknowledged.

References

1. Yokoyama M , Fukushima S, Uehara R, Okamoto K, Kataoka K, Sakurai Y, Okano T (1998) Journal of Controlled Release 50: 79
2. Johnson W, Int J (2001) Toxicology 20: 13
3. Gabizon A, Shmeeda H, Horowitz AT, Zalipsky S (2004) Adv Drug Delivery Rev 56: 1177
4. Fischer V, Borchard W (2000) J Phys Chem B, 104: 4463
5. Karlström G, Engquist O (1997) ACS Sym Ser 680: 16
6. Mortensen K, Pedersen JS (1993) Macromolecules 26: 805
7. Lusse S, Arnold K (1996) Macromolecules 29: 4251
8. Smith GD, Bedrov D (2003) J Phys Chem B 107: 3095
9. Bedrov D, Smith GD (1999) J Phys Chem B 103: 10001
10. Sommer C, Pedersen JS, Stein PC (2004) J. Phys. Chem. B 108: 6242
11. Pedersen JS, Schurtenberger P (1999) Europhys Lett 45: 666
12. Graessley WW (2002) Macromolecules 35: 3184
13. Zimm BH (1948) J Chem Phys 16: 1093
14. Benoit H, Benmouna M (1984) Polymers 25: 1059.
15. Pedersen JS (2004) J Appl Crystall 37: 369
16. Orthaber D, Bergmann A, Glatter O (2000) J App Crystall 33: 218
17. Pedersen JS, Schurtenberger P (1996) Macromolecules 29: 7602
18. Fujita H (1988) Macromolecules 21:179
19. Pedersen JS, Laso M, Schurtenberger P (1996) Phys Rev E 54: R5917
20. Hammounda B, Ho DL, Kline S (2004) Macromolecules 37: 6932
21. Kinugasa A, Hayashi H, Hamada F, Nakajima A (1985) Macromolecules 18: 582
22. Falcao AN, Pedersen JS, Mortensen K (1993) Macromolecules 26: 5350
23. Venohr H, Fraaije V, Strunk H, Borchard W (1998) Eur Polym J 34: 723
24. See for example: Holmberg K, Jönsson B, Kronberg B, Lindman B (2003) Surfactants and Polymers in Aqueous Solutions. Wiley, Chichester
25. Hammouda B, Ho D, Kline S (2002) Macromolecules 35: 8578

Progr Colloid Polym Sci (2005) 130: 79–84
DOI 10.1007/b107333
Published online: 3 June 2005

Roberto Triolo
Fabrizio Lo Celso
Valerio Benfante
Alessandro Triolo
Albrecht Wiedenmann
Sigrid Bernstorff

Small angle scattering study of poly(methylmethacrylate)-block-poly(ethylene oxide) block co-polymer in aqueous solution

R. Triolo (✉) · F. Lo Celso · V. Benfante
Dipartimento di Chimica Fisica
"F. Accascina", Universitá di Palermo,
Palermo, Italy
e-mail: triolo@unipa.it
Tel.: +39-091-6459841
Fax: +39-091-590015

A. Triolo
Istituto Processi Chimico-Fisici,
Sezione di Messina - CNR, Messina, Italy

A. Wiedenmann
BENSC-HMI, Berlin, Germany

S. Bernstorff
Elettra Synchrotron, Basovizza, Italy

R. Triolo
Dipartimento di Chimica Fisica,
V.le delle Scienze, Padiglione 17,
90128 Palermo, Italy

Abstract A combined Small Angle X ray (SAXS) and Neutron (SANS) Scattering study of aqueous solutions of a symmetric block copolymer consisting of poly(methyl methacrylate) (PMMA) and poly(ethylene oxide) (PEO) moieties is presented. The polymer forms slightly polydisperse spherical micelles in a wide range of concentration (0.03–6.7 w/V) and temperature (20 °C ≤T ≤ 65 °C). A good description of the SANS data is obtained using a polydisperse core-shell model with a structure factor for a modified hard sphere potential. By increasing the concentration at constant T we observed a decrease of the aggregation number and an increase of solvation of PEO groups in the shell, opposite to what happens by increasing the temperature at constant concentration.

Keywords Small Angle Scattering Di-Block Copolymer · Micelles · Structure

Introduction

Di-block copolymers are formed by two different polymeric moieties A and B, chemically bonded [1]. The structural and dynamical behaviour of the resulting polymer is strongly related to the interactions between the blocks. Even simple co-blocks may show interesting morphologies [2] depending on their thermodynamic state. When a further component is added, the additional interactions of each block with the new component will greatly affect the behaviour of the complex system thus formed. This is the case of solutions of co-blocks, whose behaviour will greatly depend on the affinity of each block toward the solvent. Self-organization processes are observed in solution when each block presents different affinity for the solvent. In the dilute regime, and above a reasonably well defined concentration (conceptually similar to the critical micellar concentration, cmc, of regular surfactants), the aggregates formed are spherical micelles. Strictly one should not speak of cmc, as in the case of co-blocks the aggregation process goes through a series of steps leading, eventually, to well-defined aggregates with dimensions in the range of 1 – 100 nm. This size falls in the domain of scattering techniques, and thus Small Angle Neutron Scattering (SANS) and Small Angle X-ray Scattering (SAXS) have been extensively used to investigate the structure and the kinetics of formation of block co-polymer aggregates [3]. The large number of studies on these macromolecules is justified by their importance in many industrial fields like detergency, cosmetics, pharmacology, etc., the main goal of these studies being to relate geometrical and chemical characteristics of the copolymer molecules with the structural properties in solution.

In this paper we present data on a co-block PMMA-b-PEO [4] in which PMMA has the same molecular weight ($W_n = 1$ kDa) of the PEO block, dissolved in water. To the best of our knowledge there is only one structural study performed on this polymer: solutions in toluene and in methyl ethyl ketone have been investigated by

means of Quasi Elastic Light Scattering (QELS) [5], providing evidence of formation of inverse micelles. We have performed a detailed SAXS study as a function of the concentration and of the temperature in order to have preliminary information on the phase diagram of the system PMMA-b-PEO/water. Then SANS measurements have been performed by using also external isotopic substitution (i.e. by substitution of H_2O with D_2O), as a mean to change contrast and get information on the internal structure of the aggregates.

Experimental section

The poly(methyl methacrylate)-b-poly(ethylene oxide) block copolymer, which in what follows we shall indicate as ME1010, was supplied by Goldschmidt AG and was used as received. A stock solution (~20 wt.%) was prepared by dissolving the block copolymer in D_2O at 60 °C. After stirring for 1 hour at this temperature, the solution was cooled at room temperature and no turbidity was observed. Concentrations in the range between 0.01% w/V and 7% w/V were obtained by dilution of the stock solution with pure D_2O. Solutions for SANS using external isotopic contrast variation measurement were prepared by mixing two stock solutions in heavy and light water, at the same known block copolymer concentration (~5 wt%).

SANS data have been collected at the V4 SANS instrument (BENSC, Berlin) [6] in which the Q range covered was (0.01 – 0.097) $Å^{-1}$ and at the 12m-SANS instrument (HIFR, Oak Ridge) [7] in which the Q range covered was (0.006–0.17) $Å^{-1}$. Here $Q = (4\pi/\lambda)\sin(\theta)$, 2θ being the scattering angle and λ the wavelength of the neutron used. Absolute scattering cross-sections were obtained after correction of raw data for thickness, transmission, background and normalization using secondary standards. The temperature of the multi-sample rack was controlled to better than +/−0.5 °C by circulating thermostated fluid. SAXS measurements were performed at the SAXS beam line of the Elettra Synchrotron facility (Trieste, Italy) using a fixed wavelength ($\lambda = 1.54$ Å) and variable sample-to-detector distance which provided an effective Q-range 0.017 → 0.31 $Å^{-1}$. Samples were held in place in glass capillaries mounted in a stainless steel block sandwiched between two copper blocks. The temperature of the sample was controlled to +/− 0.5 °C by a Huber bath circulating the thermostated fluid through the copper blocks. The intensity of photons was recorded on a linear position-sensitive detector. Further details of technical and experimental aspects are given elsewhere [8,9].

Theoretical basis

At low enough concentration the copolymer chains behave as non interacting random coils (RC). Therefore, the SANS elastic coherent scattering cross section [10] can be computed by means of the Debye equation [11]

$$(d\Sigma(Q)/d\Omega)_R C = 2N_{RC}[(QR_g)^2 + \exp[(-QR_g)^2] - 1]/(QR_g)^4 \quad (1)$$

where N_{RC} is the number of random coil chains of radius of gyration R_g. By increasing the concentration, aggregates are formed and the elastic coherent scattering cross section for monodisperse particles, in the decoupling approximation, [10] reads:

$$(d\Sigma(Q)/d\Omega)_{agg} = N_{agg}P(Q)S(Q) \quad (2)$$

where N_{agg} is the number of aggregates of form factor P(Q) and S(Q) is the structure factor of the aggregate. In the case of spherical core-shell particles with core of radius R_1, scattering length density B_1, and shell of thickness $R = R_2 - R_1$ (where R_2 is the total radius of the aggregate) and scattering length density B_2, P(Q) is given by:

$$P(Q) = [4\pi\Sigma_{i+1}(B_{i+1} - B_i)(\sin QR_i - QR_1\cos QR_1)/Q^3]^2 \quad (3)$$

where B_3 is the scattering length density of the solvent. The scattering length density of the solvent, of the core and shell (B_0, B_1 and B_2 respectively) are obtained from the composition of the three regions.

The structure factor S(Q) is related to inter-particles correlations and depends on the interaction potential considered: the simplest and most used form is based on the hard spheres (HS) potential. The corresponding analytical expression, for particles of radius R, has been derived in the Percus-Yevick (PY) approximation [12,13]:

$$S_{HS}(Q) = 1/[1 - C_{HS}(Q)] \quad (4)$$

$$\begin{aligned} C_{HS}(Q) = {} & -24\eta/(QR)^6\{\alpha(QR)^3(\sin QR - QR\cos QR) \\ & + \beta(QR)^2[2QR\sin QR - (Q^2R^2 - 2)\cos QR - 2] \\ & + \gamma[(4Q^3R^3 - 24QR)\sin QR \\ & - (Q^4R^4 - 12Q^2R^2 + 24)\cos QR + 24]\} \end{aligned}$$

where α, β, and γ are simple functions of the volume fraction η [14]. A simple, variational modification of the PY equation has been obtained [14] for a HS plus square well potential. This equation can be obviously modified for a HS plus repulsive step, and as such has been used to model SAXS data from phase separated Li-Al alloys [15] and for block copolymer solutions [16]. By indicating with ε the attractive (<0) or repulsive (>0) step (in units k_BT, with k_B Boltzman constant and T the absolute temperature) one obtains:

$$S_{SS}(Q) = 1/[1 - C_{SS}(Q)] \quad (5)$$

with

$$\begin{aligned} C(Q)_{SS} = {} & C(Q)_{HS} + \varepsilon/(k_BT)24\eta/(Q^3R^3)[\sin\lambda' QR \\ & - \lambda' QR\cos\lambda' QR + QR\cos\lambda' QR - \sin QR] \end{aligned}$$

λ' being the width (in relation to the number of spheres diameters) of the step.

Scattering cross section for polydisperse systems may be obtained by integrating equation 2 over a given size distribution function. Analytical equations for polydisperse spherical samples have been derived in the mean Spherical Approximation and using a Schultz distribution function for the radii [17, 18].

Results and Discussion

SAXS results

Figure 1 shows the SAXS curves for a 5% (wt.) solution of ME1010 in D_2O as a function of the temperature between 30 and 75 °C. It can be noticed that the temperature does not seem to alter the structure of the system in a significant way. In the inset of Figure 1 the SAXS patterns from solutions at 30 °C and at the concentrations indicated (expressed in wt. %) are shown.

By increasing the concentration the intensity increases and the most concentrated solution shows signs of interparticle interaction.

Guinier radii in the range of 9 nm were obtained for all the scattering curves. Therefore, it is apparent that in the range of concentration and of temperature explored by SAXS, ME1010 forms aggregates. Figure 2 shows Guinier plots of the concentration data of Figure 1; the same data, scaled for the concentration, are presented in the inset of Figure 2.

It can be noticed that the data at concentration below 10% wt. scale almost linearly with the concentration, indicating that in this range of concentration the aggregates can be described by a single model.

SANS results

Details of the internal structure of the aggregates can be obtained by means of SANS, which is known to be a powerful technique to investigate the structure of aggregates formed by hydrogenated materials because the contrast between the different regions of the aggregates and between these regions and the solvent can be widely changed by isotopic substitution: quite simply different regions can be highlighted by using D_2O/H_2O mixtures as solvent (external isotopic substitution method). For this reason, in order to get detailed information on the internal structure of the aggregates, we have performed SANS measurements on a series of solutions in five D_2O-H_2O mixtures (0, 25, 50, 75 and 100% H_2O, respectively). Contrast measurements have been performed at 25, 45 and 65 °C. Because the density of the solvent mixtures varies, the co-block concentration was not exactly the same for all the samples, but varied between 5.4% and 5.13% (w/V). Of course, the correct concentrations were used in the fit procedure. Experimental scattering cross section have been fit to equation 2, using equation 3 for P(Q) and equation 4 for S(Q) and correcting for the fraction of polymer not aggregated according with the procedure described in what follows. A Schultz size distribution function has been used to account for polydispersity [19]. Details on the fitting procedure can be found in the literature [3, 10]. The fits were all reasonable, although the calculated intensities would show consistently positive deviations from experimental points in the low Q portion of the scattering curve; this meant that the thermodynamic limit ($Q \rightarrow 0$) of S(Q), and hence the compressibility of the solutions, was actually lower than the one computed for a model of hard spheres, indicating that a repulsive step had to be added to the HS interaction potential [15]. The origin of this extra repulsive potential is due to two main components, one arising from the tendency to swell the shell layer by excluded volume effects and the other one due to elastic free energy opposing to the stretching of the PEO blocks [20–22]. Therefore, fits have been repeated with the structure function obtained through equation 5. For each temperature a single set of parameters has been used to fit all the different contrast solutions.

Figure 3 shows the quality of the best fits obtained using equations 4 and 5 for S(Q). Experimental points refer to solution 8a of Table 1. Figure 4 shows the agreement between experimental and calculated intensities at 25 °C. Similar agreement has been obtained at 45 and 65 °C.

It can be noticed that the agreement between experimental (symbols) and calculated (lines) scattering cross sections is excellent for all the contrast conditions, even

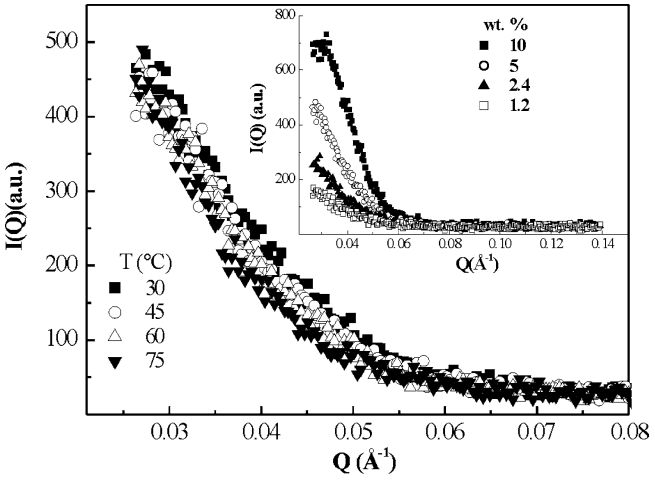

Fig. 1 SAXS data for ME1010 5% (w/V) as a function of temperature. In the inset data at 30 °C for concentrations between 1.2 and 10% (w/V)

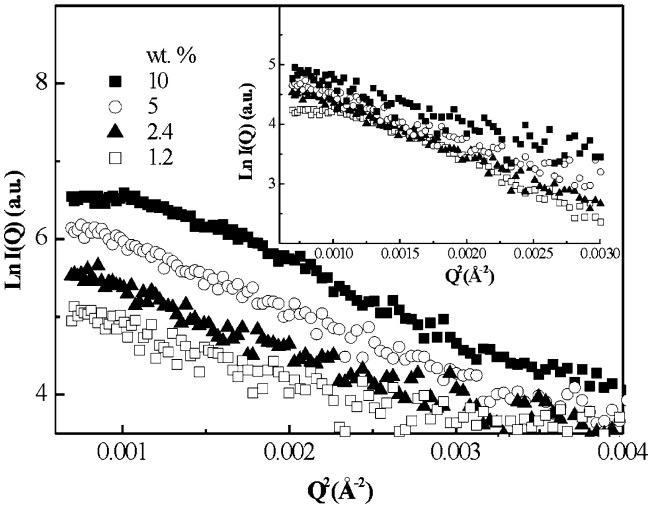

Fig. 2 Guinier plots of the SAXS data at 30 °C for concentrations between 1.2 and 10% (w/V). In the inset the same data are normalized to unit concentration

for the solution 75% in H_2O, whose low intensity indicates that we are close to the contrast match conditions, supporting the validity of the model at least up to co-block concentrations close to 5% w/V. Parameters of the fits are reported in Table 1. From the different contrast experiments the picture of micelles characterized by temperature dependent parameters emerges, i.e., a dry core formed by PMMA blocks with radius varying from 3.3 to 3.9 nm and a shell formed by the PEO chains heavily solvated with thickness varying from 1.9 to 2.5 nm. A repulsive step 0.36 k_BT high and 1.5 σ wide, σ being the particle diameter, has been used to fit the data. The core-shell model just described has been applied to the analysis of scattering data of solutions in D_2O at T = 20 °C listed in Table 1. Figure 5 shows a plot of the forward scattering cross sections normalized by the concentration. The two most dilute solutions do not show any evidence of aggregation and this fact allows us to determine the fraction of co-block remaining in solution as random coil (in a sense a concept similar to the cmc). In all the fits, the scattering cross section has been computed as a weighted average of the contribution due to the micellized and unmicellized block co-polymer. In other words we have used a linear combination of equations 1 and 2 in which P(Q) was given by equation 3 and S(Q) by equation 5. Again a Shultz polydispersity function has been used to take into account the polydispersity of the aggregates.

In principle the parameters of the repulsive step could be temperature and concentration dependent. Preliminary fits have shown that, within the errors in the fitting procedure, the values found were in good agreement with those obtained in the contrast series. Therefore we have fixed them in the remaining fits. Figure 6 shows the

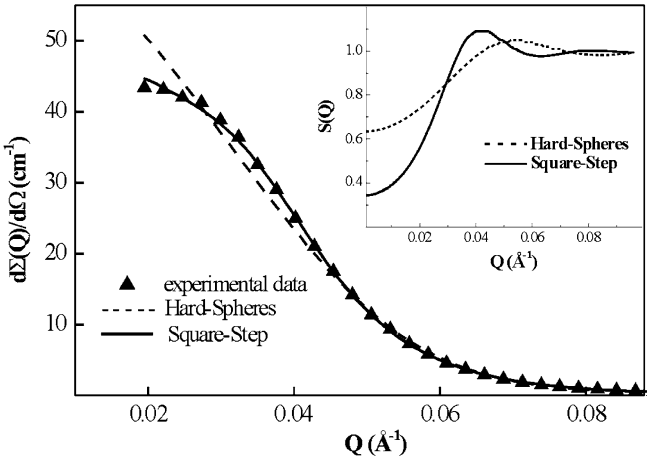

Fig. 3 Effect of the potential used to compute S(Q)

comparison between the experimental data and the scattering cross-sections computed with the parameters of Table 1. In the inset of the same figure, the two most dilute solutions are shown together with the fits to equation 1 (Random Coil). The agreement between experimental and calculated scattering cross-sections is very good for all the solutions. In the most concentrated solution the calculated curve shows small systematic deviations. This is an indication that our model holds for concentrations up to about 6% w/V, while for volume fractions higher than the ones presented in this paper the model should be revisited and new contrast measurements in the proper concentration range should be planned.

Concerning the concentration and temperature dependence of the fit parameters it can be noticed that, by

Table 1 Fit parameters for all the solutions investigated by SANS. ε and λ' parameters (see text) are equal to 0.36 k_BT and 1.5, respectively

Solution	Concentration w/V %	Temperature(°C) / Solvent	Agg[a]	SEO[b]	D(nm)[c]
1	6.70	20/D_2O	104(2)	7.5(1)	11.8
2a	3.53	20/D_2O	107(1)	7.3(1)	11.8
2b	3.53	25/D_2O	121(1)	4.02(9)	10.9
2c	3.53	45/D_2O	148(1)	2.8(1)	11.1
2d	3.53	65/D_2O	186(1)	2.09(4)	11.5
3	2.62	20/D_2O	108(1)	6.8(1)	11.6
4	0.65	20/D_2O	114(1)	6.5(3)	11.7
5	0.19	20/D_2O	115[§]	6.3[§]	11.6
6	0.066	20/D_2O	1		R_g = 6.23
7	0.033	20/D_2O	1		R_g = 8.32
8a	nominal 5[§§]	25/D_2O-H_2O	119(1)	5.7(2)	11.5
8b	nominal 5[§§]	45/D_2O-H_2O	145(1)	4.0(1)	11.5
8c	nominal 5[§§]	65/D_2O-H_2O	199(1)	2.0(2)	12.2

[a]Aggregation number;
[b]D_2O molecules per EO unit;
[c]Diameter of the aggregate;
[§]Parameters extrapolated from the concentration dependence of the parameters of solutions 1,2a,3, and 4;
[§§]Because of variable density actual concentrations vary in a known manner between 5.1 and 5.4 w/V%

increasing the concentration at constant temperature (20 °C, solutions 1, 2a, 3, 4 and 5 of Table 1), aggregation numbers decrease slightly, while the number of water molecules per EO segment increases slightly. Despite a tenfold increase in concentration, the aggregation numbers and the solvation numbers of the PEO chains show a maximum variation of about 10%. However, these changes are such that the total average size of the aggregate remains approximately constant. All the solutions are slightly polydisperse (the Schultz z parameter is approximately equal to 21 for all solutions investigated). Opposite trend, but equal net result (approximately constant size and polydispersity index) has been found for the 3.5% w/V solution in D_2O at 20, 25, 45 and 65 °C (solutions 2a, 2b, 2c and 2d of Table 1). Upon increasing the temperature, the solvation number of EO segments will decrease thus causing a strong increase of aggregation number and yet maintaining the average dimension essentially constant at about 11.7 nm.

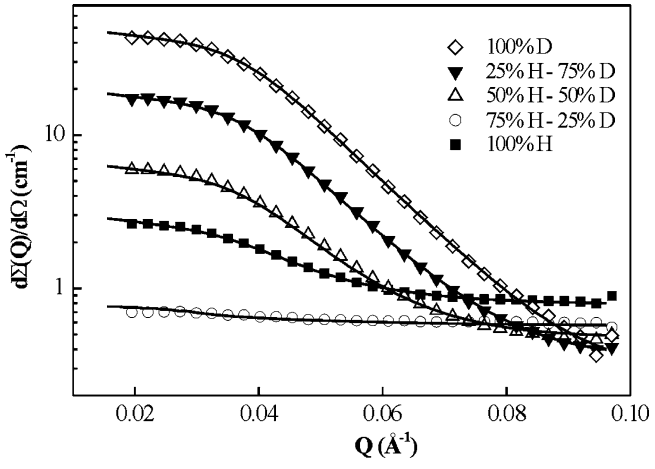

Fig. 4 External contrast SANS data for 5% (w/V) solution of ME1010 at 25 °C. Symbols are experimental data, lines are scattering cross section computed with the fit parameters of table 1

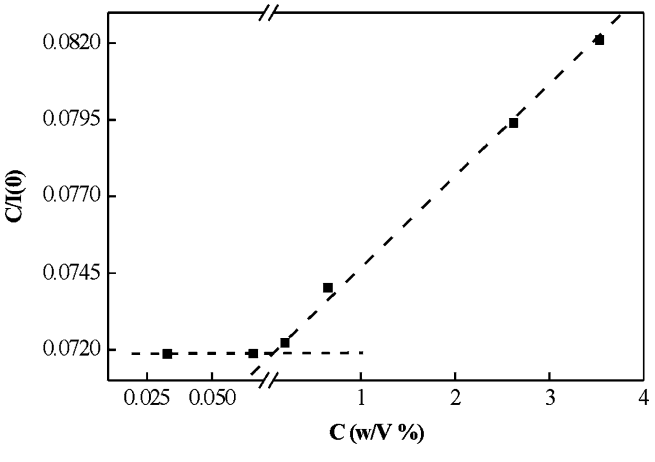

Fig. 5 SANS estimation of the fraction of polymer aggregated

Comparison SAXS–SANS

Figure 7 shows the comparison between experimental SAXS measurements (circles) and the scattering cross section computed (line) with the fit parameters obtained for the same solution by using SANS (solution 3 of Table 1). Only a scaling parameter was used in this comparison, as the SAXS data were not in absolute units.

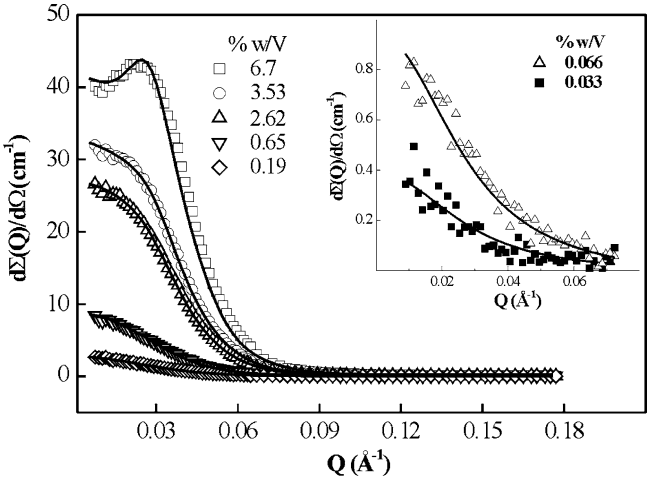

Fig. 6 SANS data at 20C for solutions of ME1010 in D_2O. The inset shows the data at the two lowest concentrations where no aggregates exist. Symbols are experimental data, lines are scattering cross section computed with the fit parameters of table 1

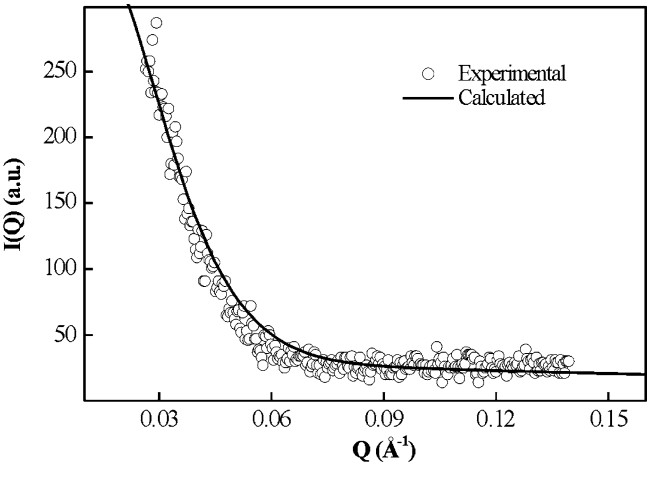

Fig. 7 Experimental SAXS scattering curve (symbols) and calculated scattering cross sections (line) using the parameters obtained in the fit of SANS data

The excellent agreement is an indication of the goodness of the model used.

Conclusions

The structure of water solutions of a PMMA-b-PEO block copolymer with Mn = 2000 Da and the same weight of the two blocks, has been investigated in the concentration range from 3×10^{-4} g/ml to 6.7×10^{-2} g/ml. Solutions of concentration below 7×10^{-4} g/ml show no indications of aggregate formation and scattering data have been analysed in terms of non interacting random coils (equation 1). For concentrations higher than 7×10^{-4} g/ml SAXS measurements show the presence of aggregates whose size is roughly independent from the concentration and the temperature as well. SANS measurements as a function of the concentration and temperature, as well as SANS investigation of a 5% solution by making use of the method of external contrast variation, allow the derivation of accurate information on the internal structure of these aggregates. Aggregates consist of a dry PMMA core surrounded by a shell of solvated PEO. Particle-particle interactions are well described by Hard Sphere plus a repulsive step potential. A small decrease of the aggregation number with a simultaneous increase of hydration of the PEO chain is observed upon isothermally increasing the concentration, while a strong increase of the aggregation number and an equally strong decrease of hydration of the PEO chain is observed upon increasing temperature at constant concentration. However, in both cases the total average diameter of the aggregates hardly changes. The strong effect of the temperature can be rationalized in terms of reduction of the PEO solvation. This, in turn, reduces the excluded volume interactions in the shell and allows for more monomers to enter the aggregate, in order to optimize the core-shell interface curvature. The effect of the increase in concentration at constant temperature is quite small and often not much greater than the error bars of the fitting procedure. Therefore, we make no attempt to rationalize this small effect, other than pointing once more that the total size of the aggregates is remarkably constant in all the range of concentration and temperatures. The goodness of the model of the aggregates has been assessed by means of SANS measurements using the external contrast variation method. Scattering cross sections for X rays have been computed with the parameters obtained in the analysis of SANS data. The computed curve and the experimental data are in excellent agreement and this strongly supports the uniqueness of the model used.

Acknowledgments The authors thank Elettra (I) and HMI-BENSC (D) for provision of beam time, the Italian National Research Council (CNR), the Istituto Nazionale Fisica della Materia (INFM), the Italian Department of Education and Research (MIUR) and Elettra Users' & European Relations Service for financial support. This work was also supported by the European Union through the TMR-LSF contract ERBFMGE-CT950060 and the Human Potential Programme under IHP-ARI contract HPRI-CT-1999 – 00020.

References

1. Hamley IW (1998) The Physics of Block Copolymers , Oxford University Press, Hamley IW (2001) Philosophical transactions of the royal society of London series A - mathematical physical and engineering sciences 359(1782): 1017
2. Mortensen K Almdal K Schwahn D Bates FS (1997) J Appl Cryst 30: 702
3. Triolo A et al. J Non-Cryst Sol In press; Triolo, F. et al.; J. Appl. Cryst. 2000, 33: 641; Triolo A. et al Phys. Rev. E (2000), 62: 5839; Triolo R, et al Phys. Rev. E 2000, 61: 4640; Liu LZ, Inomata K Zhou SQ, Chu B, (2001) Macromolecules (1999)32(18): 5836; Mortensen, K (2001) Polymers for advanced technologies 12: 2
4. Wu WL, Piirma I (1993) Polymer Bulletin 31: 531
5. Bogumil Th, Horing S, Budde H, Arndt K.–F (1999) Polymer 40: 1833
6. Keiderling U, Wiedenmann A (1995) Physica B 213: 895
7. Wignall GD, Bates FS (1986) J Appl Cryst 20:28
8. Pressl K, Kriechbaum M, Steinhart M, Laggner P (1997) Rev Sci Instrum 68: 4588
9. Steinhart M, Kriechbaum M, Pressl K, Amenitsch H, Laggner P, Bernstorff S (1999) Rev Sci Instrum 70: 1540
10. Triolo R, Caponetti E (1990) Adv Coll Inter Sci 32: 235
11. Debye P (1944) J Appl Phys 15: 338
12. Percus JK, Yevick G (1958) Phys Rev 110: 1
13. Ashcroft NW, Leckner J (1966) Phys Rev 145: 83
14. Sharma RV, Sharma KC (1977) Physica A 89: 213
15. Floriano MA, Caponetti E, Triolo R, (1992) Phys Rev B 45: 1016
16. Hickl P, Ballauff M, Lindner P, Jada A (1997) Colloid Polymer Sci 275: 1027
17. Griffith WL, Triolo R, Compere A(1987) Phys Rev A 35: 2200
18. Griffith WL, Triolo R, Compere A (1986) Phys Rev A 33: 2197
19. Kotlarchyk M, Chen SH (1983) J Chem Phys 79: 2461
20. Brown GJ, Richards RW, Heenan RK (2001) Polymer 42: 7663
21. Patel S, Tirrel M, Hadzioannou G (1988) Colloids Surf 31: 157
22. Watanabe H, Tirrel M (1993) Macromolecules 26: 6455

Progr Colloid Polym Sci (2005) 130: 85–96
DOI 10.1007/b139119
Published online: 3 June 2005

Ryuhei Motokawa
Satoshi Koizumi
Masahiko Annaka
Takayuki Nakahira
Takeji Hashimoto

Ultra-small- and small-angle neutron scattering studies of self-assembly in poly(*N*-isopropylacrylamide)-block-poly (ethylene glycol) aqueous solution

Abstract Poly(*N*-isopropylacrylamide)-*block*-poly(ethylene glycol) copolymers (NE) having nearly symmetric (s-NE) and highly asymmetric (a-NE) compositions in terms of constituent block chains were synthesized and purified: the s-NE and a-NE had a volume fraction f_{PNIPA} of poly(*N*-isopropylacrylamide) (PNIPA) block chains equal to 0.46 and 0.83, respectively. Their phase behaviors in water and self-assembled structures have been studied in the parameter space of temperature (T) and weight percent of block copolymers (w_P, weight/volume), by means of macroscopic observations on turbidity, fluidity and volume change, and of microscopic observations with ultra-small and small-angle neutron scattering. The results revealed that various states of the solutions exist as a consequence of interplay of short-range interactions among PNIPA, poly(ethylene glycol) (PEG) block chains, and solvent (especially temperature-dependent solvent selectivity) and with long-range interactions arising from elastic energy of PNIPA and PEG in the domain structures. At low polymer concentrations ($w_P < w_{P,C}$, $w_{P,C} \cong 3.5\%$, slightly depending on f_{PNIPA}), with increasing T and therefore selectivity of solvent, states of both a-NE and s-NE systems changed from (I) homogeneous solution of NE, (II) transparent solution, which contains disordered micelles, composed of PNIPA cores and PEG brush emanating from the core and dispersed in water with only short-range liquid-like order) and to (III) opaque sol comprised of macrophase-separated domains rich in NE in the water rich matrix. At higher polymer concentrations ($w_P > w_{P,C}$), and with increasing T, the a-NE system changed from state (I), state (II), as described above, (IV) an opaque gel comprised of fractal network-like domains rich in NE in the water rich matrix, and to state (V) where syneresis of the opaque gel occurs, giving rise to coexistence of macroscopic opaque gel phase and squeezed-water phase. On the other hand, in between state (II) and state (IV), the s-NE system exhibits an extra state (VI) of transparent gel, as a consequence of ordered micelles due to microphase separation of NE in water. The ordered micelle are stabilized by long coronal PEG chains in s-NE, reflecting elastic energy contribution of coronal chains to the system state. The observed syneresis is unique in that it is involved in the system comprised of the fractal network-like domain rich in PNIPA and the medium rich in water.

R. Motokawa
Graduate School of Science
and Technology, Chiba University,
Chiba-shi, Chiba 263-8522, Japan

S. Koizumi (✉) · T. Hashimoto
R. Motokawa
Research Group of Neutron Scattening
and Soft Matter,
Advanced Science Research Center,
Japan Atomic Energy Research Institute,
Tokai-mura, Ibaraki-ken 319-1195,
Japan
e-mail:
koizumi@neutrons.tokai.jaeri.go.jp
Tel.: .+81-29-287-3511
Fax: +81-29-282-5939

M. Annaka
Department of Chemistry,
Kyushu University,
Fukuoka 812-8581, Japan

T. Nakahira
Department of Applied Chemistry and
Biotechnology, Chiba University,
Chiba-shi, Chiba 263-8522, Japan

T. Hashimoto
Department of Polymer Chemistry,
Graduate School of Engineering,
Kyoto University,
Katsura, Kyoto 615-8510, Japan

Introduction

The self-assembly of block copolymers into nano-scale microdmain structures continues to be an attractive research theme in contemporary polymer physics and chemistry [1]. Industrial applications of block copolymers, which have also been extensively advanced, are performed by mixing of block copolymer with low-molecular-weight constituents (or solvents). Those industrial materials are, for example, (i) multicomponent systems where the block copolymers are mixed with one of the parent homopolymers comprising of the block copolymers [2], with a low-molecular-weight tackifying resin, or with plasticizer [3], or (ii) detergents and drug-delivery microcapsules where the block copolymers form micelles in a large amount of solvents [4]. For the multicomponent systems comprised of block copolymers and a low-molecular-weight solvent, "***solvent selectivity***" (selectivity of the solvent to constituent block chains) is a key parameter to control structures and properties of block copolymer in the solution.

Motivated by such academic and industrial interests, we synthesized a new type of amphiphilic block copolymer, poly(*N*-isopropylacrylamide)-*block*-poly(ethylene glycol) (NE) by employing soap-free emulsion polymerization [5, 6]. Aqueous solutions of NE block copolymers have ***strong temperature-dependent solvent selectivity***, which is crucial to obtain rich varieties in self-assembled structures in the solution. In this paper, we aim to present some results concerning phase behaviors and self-assembled structures for aqueous solution of NE in the parameter space of temperature (T) and weight percent of NE in the solution (w_P, weight/volume). The phase behaviors were investigated by macroscopic observations of turbidity, fluidity, and syneresis, while the self-assembled structures were investigated by microscopic observations with a combined ultra-small-angle neutron scattering (USANS) and small-angle neutron scattering (SANS) method. To our best knowledge, the phase behaviors and the self-assembled structures of this system have never been reported so far.

The strong temperature-dependent solvent selectivity is attributed to strong temperature-dependent thermodynamic interactions of poly(*N*-isopropylacrylamide) (PNIPA) with water. PNIPA is a well-known thermosensitive polymer in water and exhibits a lower critical solution temperature (LCST) in aqueous solution (≅34 °C); a very dilute solution exhibits a coil-globule transition, while swollen PNIPA gel in water exhibit a volume-phase transition [7,8]. Poly(ethylene glycol) (PEG), on the other hand, is hydrophilic over a wide temperature range from far below room temperature to near the boiling point of water. With the unique combination of PNIPA and PEG, we expect a strong temperature-induced solvent selectivity and therefore a rich variety in microdomain structures in the aqueous solutions.

Due to a chemical junction connecting immiscible A and B block chains, neat AB block copolymers undergo an ***order-disorder transition*** (ODT) or ***microphase separation*** into A-rich and B-rich microdomains [9]. The thermodynamic interactions between A and B segments, given by the Flory interaction paprameter χ_{AB} ($\sim 1/T$) where T is absolute temperature), the low translational entropy of mixing due to chain connectivity ($\sim 1/N$ where N is a degree of polymerization) and conformational entropy of polymer chains are coupled to determine the ODT temperature T_{ODT} ($\sim N\chi_{AB}$). The interface curvature or packing symmetry of microdomains is strongly controlled by a volume ratio between two block chains f_i (i = A or B). By changing f_i, we observe the classical morphologies of lamellae, hexagonally-packed cylinder, and body-centered-cubic spheres or more complicated double gyroids and perforated (or mesh) lamellae, which appear in narrow ranges of f_i in between lamellae and cylinders. With a temperature change in the ordered phase, the ***order-order transition*** (OOT) is also attainable. The phase behaviors involving ODT and OOT have been extensively studied also for mixtures of AB block copolymer mixtures with A and/or B homopolymers (AB/A, AB/A/B, etc.) or with other block copolymers (AB/AC, etc.) [10, 11].

For the mixtures of AB and a solvent (i.e., for block copolymer solutions), ***solvent selectivity*** controls phase behaviors of the AB block copolymer solutions in addition to the molecular parameters (χ_{AB}, N, and f_i). The solvent selectivity is defined as relative values of interaction parameters between A or B block and solvent χ_{AS} and χ_{BS}. When $\chi_{AS} > 0.5$ and $\chi_{BS} < 0.5$, for example, we call the solvent is selectively good for B but poor for A. The case of selective solvents [12] involves more complicated problems because of following reasons. When the selectivity changes with T, swelling of A and B block chains becomes asymmetrical so that morphological transitions of microdomains in the solution occur, which should be clearly distinguished from OOT induced by changing χ_{AB}. If the solvent selectivity further increases, macrophase separation between AB block copolymers and solvents may occur in addition to ODT and OOT inherent in block copolymers. Thus we expect a variety of microdomain structures and phases, depending on the solvent selectivity.

In the case of neutral solvents ($\chi_{AS} \cong \chi_{BS}$) [12–20], the neutral solvent equally swells each block chain and reduced A/B monomer contacts. Therefore, the neutral solvent simply decreases $N\chi_{AB}$ and hence lowers T_{ODT} and T_{OOT} (***dilution approximation***) [12, 14, 17, 19, 20]. Within the mean field description, dilution approximation is given by replacing $N\chi_{AB}$ with $\phi N\chi_{AB}$where ϕ is a volume fraction of the AB block copolymer in the solution. The equal swelling of A and B block chains by

the neutral solvent and changes in degree of swelling with T and ϕ do not induce a morphological transition, which have been confirmed for the concentrated polystyrene-*block*-polyisoprene (SI) copolymers in neutral solvents of toluene and dioctylphtalate [14, 15, 17, 19–22].

To investigate the microdomain structure in the aqueous solution of NE, we employed ultra-small- and small-angle neutron scattering (USANS and SANS, respectively). Thus a wide q-range from 10^{-4} to 1 nm^{-1}, is covered by the combined data, which is crucial to elucidate hierarchical structures in the NE solution. We investigated two different NE's having nearly "symmetric" and highly "asymmetric" block compositions, respectively. They are coded as s-NE and a-NE whose volume fractions of PNIPA f_{PNIPA} are equal to 0.46 and 0.83, respectively.

Prior to USANS and SANS measurements, we have determined a phase diagram by macroscopic observations with respect to turbidity, fluidity, and syneresis in the parameter space of T and w_P. We shall elucidate the following pieces of evidence: as T increases, the s-NE or a-NE solution of $w_P < w_{P,C}$ ($\cong$ 3.5%) changes from transparent sol to turbid sol without gelation. On the other hand the s-NE and a-NE solutions of $w_P > w_{P,C}$ shows the following behaviors: The a-NE solution changes with T from transparent sol, opaque gel, and subsequently gel with syneresis, whereas in the case of s-NE, transparent gel phase exists in between transparent sol and opaque gel. Thus in the solutions with $w_P > w_{P,C}$, we found two non-fluid states; (i) transparent gel for the s-NE solution and (ii) opaque gel for the s-NE and a-NE. According to microscopic observations with SANS and USANS, non-fluidity of transparent gel is attributed to ordered micelles due to microphase separation, whereas that of opaque gel is attributed to a fractal network-like domain due to macrophase separation between polymer-rich and solvent-rich phases. We shall discuss these microphase and macrophase separations observed by SANS and USANS in relation to the strong solvent selectivity.

These various solution states discussed in this paper cannot be achieved by conventional water-soluble block copolymers with a weak solvent selectivity, such as poly(ethylene oxide)-*block*-poly(propylene oxide)-*block*-poly(ethylene oxide) (Pluronic®) where water is selectively good for the ethylene oxide and the solubility of poly(propylene oxide) against water gradually decreases with increasing temperature [23–27].

Experimental

Sample specimens

The soap-free emulsion polymerization, performed at 34 °C, successfully provided NE with a narrowly-dispersed molecular weight; the micelle formation by polymerized NE in the polymerization process brings about quasi-living radical polymerization [5]. The details of this polymerization method should be referred to ref [6]. In this paper, we investigate two block copolymers with different block ratios as coded of a-NE and s-NE. The characteristic parameters for a-NE and s-NE are summarized in Table 1.

The molecular weight and its distribution of NE were determined by gel permeation chromatography (GPC), using a TOSOH HLC-8220 apparatus. We carefully selected the solution temperature and the GPC column in order to observe homogeneously dissolved NE chains, because the GPC measurement on PNIPA is rather difficult, due to PNIPA aggregation or its adsorption on the GPC column as reported in ref [28]. Therefore, GPC measurements were carried out at 10 °C, which is crucial to avoid the micelle formation, and we used TSKgel@ columns with different pore sizes, $GMPW_{XL} \times 2$ and $G2500PW_{XL}$ (TOSOH Co., Tokyo, JAPAN). An aqueous solution of 10 mM $NaNO_3$ was used as a mobile phase at a flow rate of 1 ml/min. The molecular weights of NE were calibrated with PEG. Only a narrow peak originated from a-NE and s-NE were observed from each GPC chart, indicating that un-reacted PEG, NIPA monomer, and cerium ion are effectively removed by precipitation in hot acetone, which has been reported in ref. [6].

The block ratio between PNIPA and PEG block chains $r_{PNIPA/PEG}$ (ratio of degree of polymerization) was determined by ^1H NMR in D_2O using a JEOL JNM-LA400 spectrometer, evaluating the methyl protons of PNIPA and the methylene protons of PEG.

Macroscopic observations

From fluidity, turbidity, and volume change, we visually determined temperatures of the sol-gel transition point, phase boundary for macrophase separation, and syneresis. The solution temperature was increased from 5 °C to 45 °C with a step of 1 °C. A sol-gel transition temperature was determined by a falling ball method; we defined the gel state when a teflon ball with density of 2 g/cm^3 and 3 mm diameter does not fall in a vial tube filled with the solution

Table 1 Molecular characterizations of poly(*N*-isopropylacrylamie)-*block*-poly(ethylene glycol)

Sample Code	$M_n \times 10^{-4}$	M_w/M_n	$r_{PNIPA/PEG}$[a]	f_{PNIPA}[b]
a-NE	11	1.51	2/1	0.83
s-NE	5.2	1.49	1/3	0.46

[a,b] estimated by ^1H NMR in D_2O. The ratio of the methyne protons in isopropyl groups to methylene protons of PEG was used to determine by the molar ratio of PNIPA and ethylene glycol repeat units ($r_{PNIPA/PEG}$) and the volume fraction of PNIPA (f_{PNIPA})

for period of at least 15 min. The macrophase separation between NE and water was determined by a turbidity measurement using a HITACHI U-3210 spectrophotometer with an incident beam of $\lambda = 500$ nm. The NE solutions in a quartz cell of 1 mm thickness were heated with a step of 1 °C. We determined the macrophase boundary as the temperature at which transmission of the system abruptly decreases. By observing a volume change of opaque gel phase and that of transparent water phases, we determined the temperature of syneresis.

Microscopic observation by small-angle neutron scattering

We performed USANS and SANS measurements with research reactor JRR-3 of Japan Atomic Energy Research Institute (JAERI), at Tokai, Japan. The SANS apparatus (SANS-J) utilizes pinhole collimations, while the USANS apparatus (PNO) utilizes grooved (channel-cut) crystals both for incident and scattered beam paths.

SANS-J covers a q-range of $0.03 < q < 0.25$ nm^{-1} and $0.1 < q < 2$ nm^{-1} at two detector positions 10 m and 1.5 m, respectively, with the incident neutron of $\lambda = 0.65$ nm ($\Delta\lambda/\lambda = 13\%$). The scattered neutrons were detected by a two-dimensional position-sensitive ^{3}He detector of 0.58 m diameter. The data were corrected for counting efficiency, instrumental background, and air scattering. After circular-averaging, we converted the scattering intensity to absolute intensity unit of cm^{-1} using a secondary standard of irradiated Al. Incoherent scattering from hydrogen was subtracted as the background by using scattering intensity at a high q-region where the scattering intensity profile becomes q independent. Sample specimens were filled in a quartz cell of 2 mm thickness, which typically gives transmission of ca.70%. SANS measurements were conducted with D_2O solutions having polymer concentrations of $w_p = 7.0\%$, 3.0%, and 0.5% for a-NE, and $w_p = 5.0\%$ and 1.0% for s-NE. The sample temperature was controlled in between 5 °C and 45 °C with accuracy of ±0.1 °C.

The PNO spectrometer is capable of covering a q-region of ultra-small scattering ($10^{-4} < q < 10^{-2}$ nm^{-1}) using monochromatized neutrons beam ($\lambda = 0.2$ nm), channel-cut crystals of Si (111) and a triple bounce reflection condition [29,30]. Due to the lack of high brilliance of the monochromatized and collimated incident neutron beam, a measurement time as long as 24 h is typically required for one scanning from $q = 10^{-4}$ to 10^{-2} nm^{-1}. Sample area and thickness are, respectively, 40 × 18 mm^2 and 2 mm. The scattering profiles obtained by PNO were corrected for background scattering and then for slit height smearing according to the infinite beam height assumption [31]. Finally the USANS q-profiles were calibrated for absolute intensity as follows. We measured USANS and SANS from the same polymer blend film whose thickness and transmission are known. Due to phase-separated macrodomains in the film, both SANS and USANS exhibited a strong scattering having the same power law of q^{-2} over the respective q-regions, which were sufficiently wide, as will be described later in conjunction with (Fig. 3). We determined a calibration factor to obtain the absolute intensity of the USANS by shifting the USANS profile in the power law region to that of the calibrated SANS profile in absolute unit.

Results and discussion

Macroscopic Observations

Figures 1 (a) and (b) show phase diagrams of the aqueous solutions of a-NE and s-NE, respectively. We first discuss the solution of a-NE in Figure 1(a). As the temperature increases, the a-NE solution exhibits transparent sol [regions (I) and (II)], opaque sol [region (III)], opaque gel [region (IV)] and gel exhibiting syneresis [region (V)]. These changes occur reversibly with temperature without hysteresis when time scale of observation is sufficiently long. In the regions of (I) and (II) below 32 °C, the a-NE solution of a sol state is transparent and flows. A distinction between (I) and (II) is possible in terms of an excess small-angle scattering as discussed later. Above 32 °C, there is a crossover in its flow behavior with respect to the polymer concentration; the a-NE solution of $w_P < w_{P,C}$ flows without gelation [opaque sol in region (III)], whereas the NE solution of $w_P > w_{P,C}$ does not flow with gelation [opaque gel state of region (IV)]. Upon further increase in the temperature, the NE solution of $w_P > w_{P,C}$ undergoes macrophase separation at the boundary between the regions (II) and (IV). The NE solution of $w_P > w_{P,C}$ exhibits syneresis of the opaque gel in the region (V). Macroscopic appearances of the a-NE solution at $w_p = 7.0\% > w_{P,C}$ are shown in Figure 2; (a) transparent sol at 20 °C, (b) opaque gel at 30 °C, and (c) syneresis of the opaque gel at 35 °C.

The aqueous solution of s-NE, whose behaviors are similar to that of a-NE, exhibits an extra phase (VI) of transparent gel between ca. 20 °C and ca. 26 °C for $w_P > w_{P,C}$ (see Figure 1(b)). Figure 2(d) shows a photograph of the transparent gel at 24 °C for the s-NE solution of $w_P = 5.0\%$.

Microscopic observation by USANS and SANS

Overall features in temperature dependence of USANS and SANS

Figures 3(a) and (b) show USANS and SANS profiles I(q) for the a-NE solution with $w_P = 7.0\%$ and those of

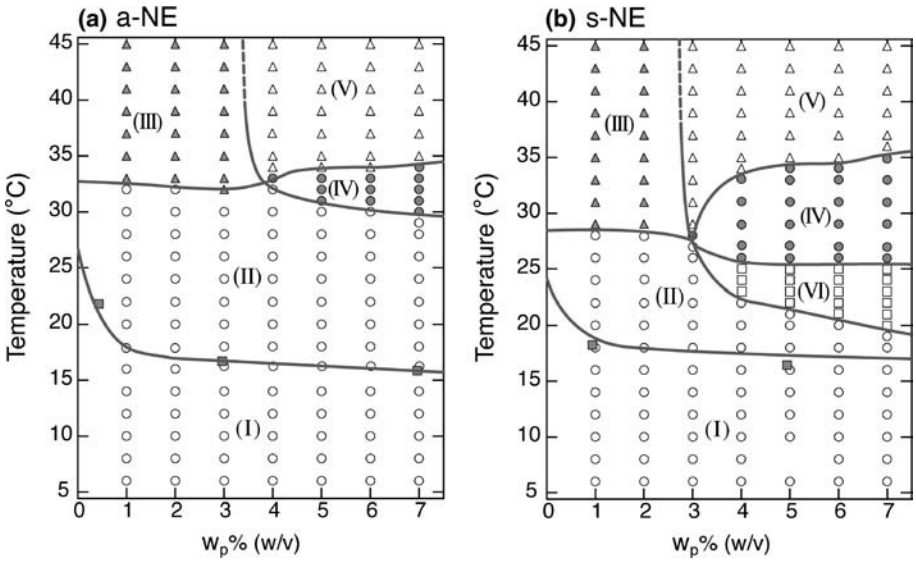

Fig. 1. Phase diagrams of (a) a-NE and (b) s-NE aqueous solutions, showing transparent sol states (I) and (II) (open circles), an opaque sol state (III) (filled triangles), an opaque gel state (IV) (filled circles), a gel exhibiting syneresis (V) (open triangles), and a transparent gel state (VI) (open squares). The boundary between two regions (I) and (II) was determined by SANS studies and indicated formation of micelles with short-range liquid-like order (disordered micelles) due to an increased selectivity of solvent

s-NE solution with $w_P = 5.0\%$, respectively. It is impressive to note that the scattering profiles depends very much on T: At a low q limit, the intensity changes with T by more than $6 \sim 7$ orders of magnitude, while at a high q limit, it hardly changes with T. As indicated in inset of Fig. 3 (a), the intensity slightly decreases as T increases. USANS measurements are limited to temperatures above 30 °C for both a-NE and s-NE, where the NE solutions exibit large scattering cross section due to domain structures formed in the NE solutions compared with the background noise level of the USANS apparatus used in this work.

Region I: Homogeneous solutions:

In transparent sol state (I) of the a-NE and s-NE solutions at 10 °C and 15 °C, we obtained small-angle scattering due to the thermal concentration fluctuations of NE in D_2O. The SANS q-profile I(q) is well reproduced by the Ornstein-Zernike (OZ) type scattering function [32],

$$I_{OZ}(q) \sim I(0)/[1 + (q\xi_{OZ})^2] \quad (1)$$

where ξ_{OZ} is the thermal correlation length for the fluctuations, and I(0) is the forward scattering intensity in the limit of q-c, which is determined by the osmotic

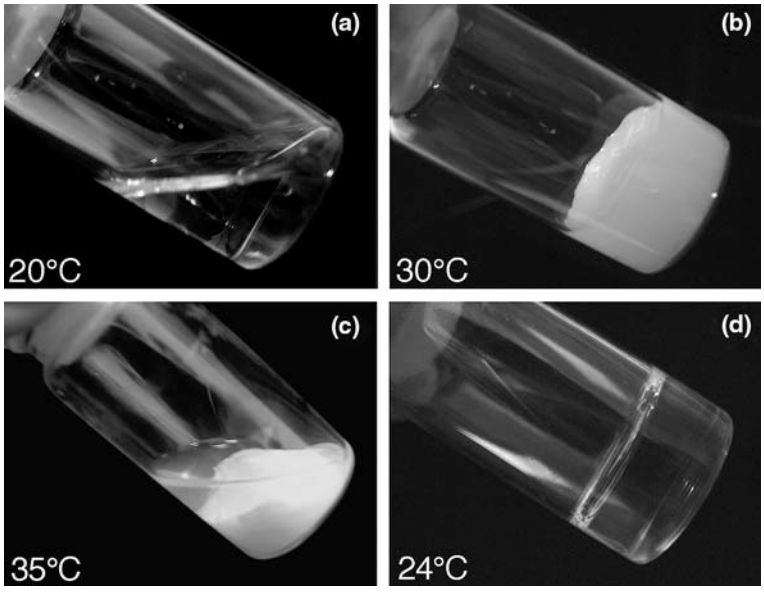

Fig. 2 Photographs for a-NE aqueous solutions of $w_P = 7\%$ (w/v), demonstrating (a) a transparent sol at 20 °C, (b) an opaque gel at 30 °C, and (c) a gel exhibiting syneresis. Photograph (d) represents transparent gel with s-NE of $w_P = 5\%$ (w/v) at 24 °C

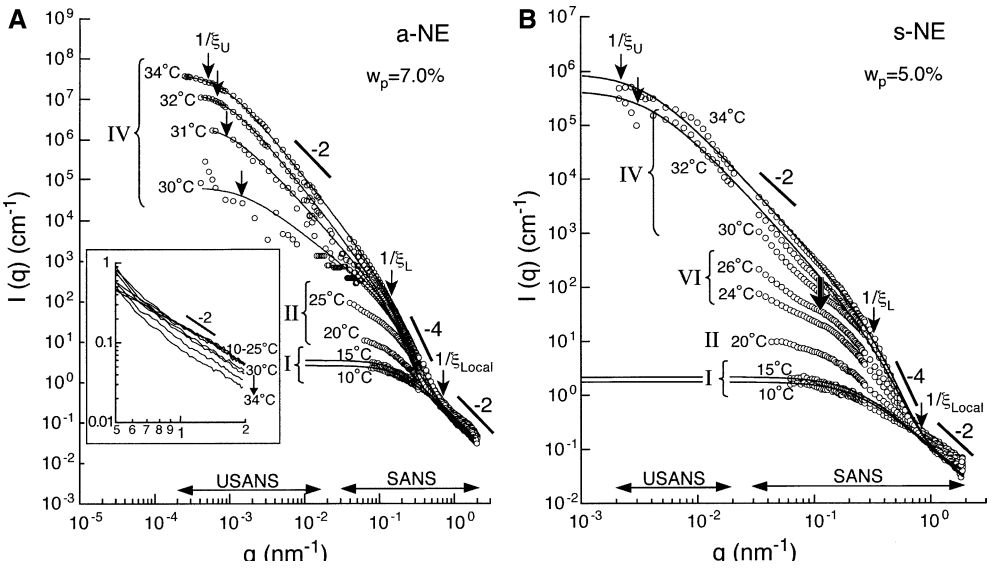

Fig. 3 SANS and USANS profiles (open circles) obtained for (a) a-NE solution of $w_P = 7\%$ (w/v) in D_2O and (b) s-NE solution of $w_P = 5\%$ (w/v) in D_2O. The solid lines are the predicted profiles based on the fractal model given by eq. (5); ξ_U and ξ_L indicate upper and lower cut-off lengths for mass fractal structures. ξ_{Local} indicates thermal correlation length for concentration fluctuations. The inset to part (a) shows a close-up higher q-region from 0.5 to 2 nm^{-1}

compressibility of the solution. The solid lines in Fig. 3 show the theoretical scattering curves best-fitted by using Eq. (1) to the experimental scattering curves obtained at 10 and 15 °C. At the length scale satisfying scattering $q\xi_{OZ} > 1$, I(q) obeys the power law,

$$I(q) \sim q^{-\alpha}. \quad (2)$$

In the low temperature region below 15 °C, we obtained the Flory exponent of $\alpha \cong 5/3$[33], indicating that both block chains of PNIPA and PEG are swollen by D_2O. The mass fractal dimension of 5/3 is due to the excluded volume effect [34].

In region (II) ($17\,°C \leq T \leq 25\,°C$), I(q) for both a-NE and s-NE solutions deviates from the OZ formalism, showing the steeper q-dependence or excess scattering at $q \leq 0.5$ nm^{-1}. At the higher q-region of $q \geq 0.5$ nm^{-1}, on the other hand, we observed the asymptotic q-behavior close to $\alpha = 2$, indicative of the PNIPA chains being still in Θ-state. The mass fractal dimension of 2 is due to the unperturbed chain. At $T \geq 25$ °C, the scattering intensity level in the power law of q^{-2} begins to decrease as shown in the inset of Fig. 3(a). This behavior at $T \geq 25$ °C will be clarified later.

Crossover between region (I) and region (II)

In order to investigate the temperature change in the SANS q-profiles, we estimated the forward scattering intensity I(0) in a plot of $1/I_{OZ}(q)$ vs. q^2 according to the OZ formalism. Figures 4(a,b) show 1/I(0) as a function of the reciprocal of absolute temperature 1/T. For each polymer concentration, in region (I) of $T < T_E$, 1/I(0) changes linearly with 1/T, whereas above T_E, 1/I(0) deviates from the linear relation of 1/I(0) vs 1/T. T_E, thus determined, gives the boundaries between regions (I) and (II) shown in Fig. 1. (In Figure 1, the filled squares show T_E determined by this kind of SANS analysis.) Above T_E, the system enters into region (II).

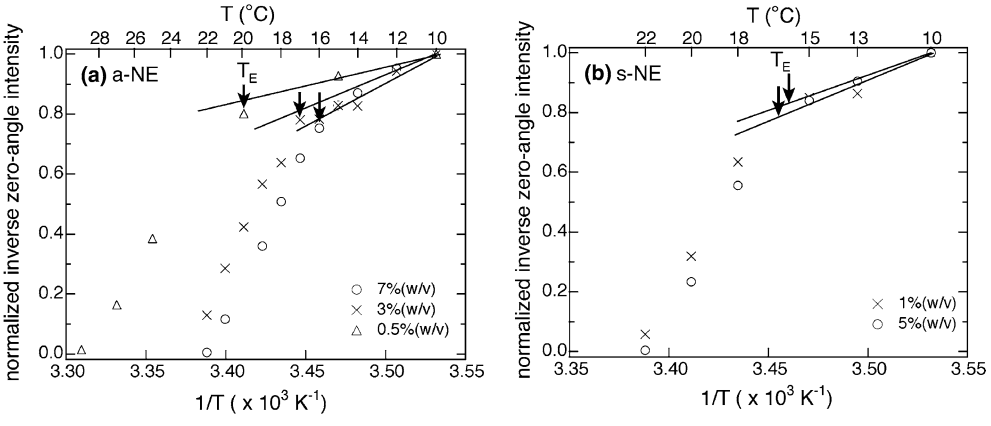

Fig. 4 Inverse forward scattering intensity, 1/I(0), plotted as a function 1/T for (a) a-NE aqueous solutions of $w_P = 7\%$ (w/v) (open circles), 3% (w/v) (crosses), and 0.5% (w/v) (open triangles) and (b) s-NE aqueous solutions of $w_P = 5\%$ (w/v) (open circles) and 1% (w/v) (crosses)

Region (II): Solution having disordered micelles

The excess small-angle scattering observed in region (II) (downward deviation of 1/I(0) with decreasing 1/T in Fig. 4) is attributed to formation of ***disordered micelles***, which includes a range of states from (i) asymmetric swelling to (ii) micelle formation with only short-range liquid-like order.

In region (II), water gradually becomes a poor solvent for PNIPA but is kept being a good solvent and for the PEG chain; so that $\chi_{NW} > \chi_{EW}$, where χ_{NW} and χ_{EW} are the Flory segmental interaction parameter between water and NIPA and between water and ethylene glychol (EG), respectively. The micelles having scattering contrast between the poorly swollen PNIPA and the well swollen PEG chains should give the excess small-angle scattering over the OZ scattering from the thermal concentration fluctuations. The micelles thus formed should have a short-range liquid-like order because the NE solution is still in a sol state according to the macroscopic observations (see Fig. 2(a)). However, as the temperature further increases in region (II), the excess small-angle scattering becomes more pronounced and starts to show an asymptotic decay of I(q) steeper than q^{-2}, implying that micelles become more and more a distinct structural entity having well defined interface; both association number of block chains in a micelle and number of micelles are expected to increase.

In region (II) for both a-NE and s-NE, we decomposed the SANS q-profiles into two components of $I_{OZ}(q)$ and the excess scattering $I_E(q)$ from micelles with a short range order. The decomposed profiles for the a-NE and s-NE solutions are shown in Fig. 5. For the decomposition, we first estimated $I_{OZ}(q)$ at given T's in region II (broken lines) by extrapolating the linear changes in $I(q)^{-1}$ vs T^{-1} at various q's. Then we obtained $I_E(q)$ (solid lines) by subtracting the estimated $I_{OZ}(q)$ from total scattering I(q) (shown by open circles): $I_E(q) = I(q) - I_{OZ}(q)$. The asymptotic behavior of $I_E(q) \sim q^{-4}$ supports the scenario of microphase separation into micelles of PNIPA block chains in the matrix of PEG block chains, where the PNIPA micelles are less swollen with water than the PEG block chains. However, there exist no characteristic scattering maxima due to inter- or intra microdomains scattering, which are often observed for block copolymer melts [1]. The micelles are therefore expected to have the short-range liquid-like order in real space.

In order to quantitatively discuss $I_E(q)$, we employed a squared Lorentzian scattering function as follows,

$$I_E(q) \sim \xi_E^3 \left(\frac{1}{1 + q^2 \xi_E^2} \right)^2 \tag{3}$$

which is a so-called Debye-Bueche function originally derived for a random two-phase model [35]. Here, ξ_E is a correlation length related to size and volume fraction of micelles. The correlation lengths ξ_{OZ} and ξ_E thus estimated were summarized in Table 2.

Region (VI): Solutions having ordered micelles

The aqueous solution of s-NE shows an extra phase (VI) of transparent gel at $w_P > w_{P,C}$, which was not observed for the a-NE solution. This change from (II) to (IV) for s-NE is attributed to ODT, resulting in micelles with a long-range order. Indeed, at 26 °C we recognize a broad scattering maximum or shoulder due to interdomain scattering as indicated by the thick arrow in Fig. 3(b). However, the higher-order maxima from inter- and intradomain interference are not observed.

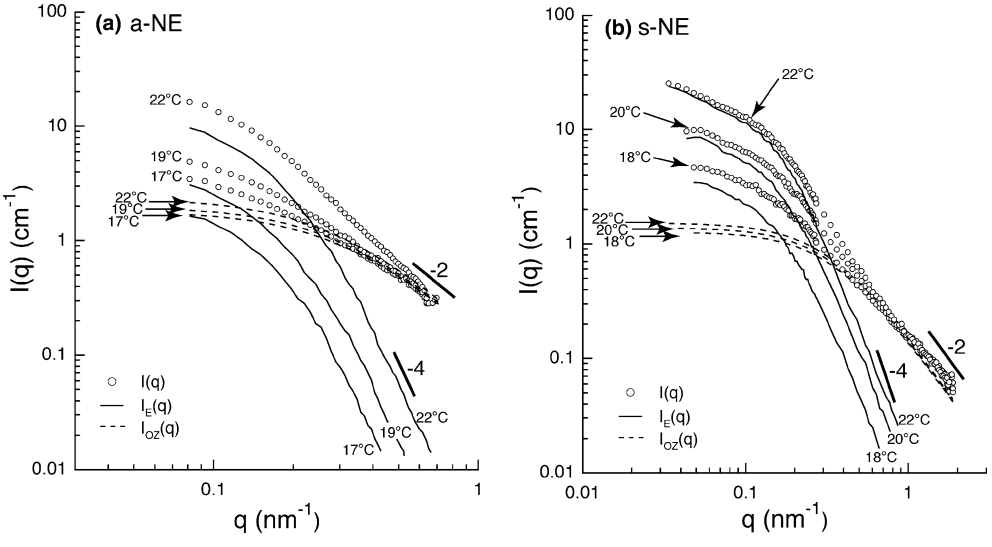

Fig. 5 Decomposition of the scattering profile into that from thermal concentration fluctuations $I_{OZ}(q)$ (broken) and excess scattering $I_E(q)$ (solid lines) arising from micelles for (a) a-NE aqueous solution of $w_P = 7\%$ (w/v) and (b) s-NE aqueous solution of $w_P = 5\%$ (w/v)

Table 2 Summary of characteristic length scales determined by SANS

Temperature (°C)	a-NE		s-NE	
	ξ_{OZ}(nm)	ξ_E(nm)	ξ_{OZ}(nm)	ξ_E(nm)
17	3.3	7.0	–	–
18	3.4	6.4	2.9	5.7
19	3.4	6.4	–	–
20	3.6	6.3	3.0	5.7
22	3.6	6.3	3.1	6.4

Region (IV): Growth of micelles into gel-networks having mass-fractal-structures

In the temperature range above around 30 °C, where the a-NE and s-NE solutions of $w_P > w_{P,C}$ exhibit the opaque gel (IV) and subsequently gel with syneresis (V), we observed a strong increase of scattering intensity in the USANS region at $q < 0.01$ nm^{-1} (see Fig. 3). The q-behavior in the USANS region obeys the power law given by Eq.(2) with α close to 2. In the SANS q-range, the asymptotic behavior of I(q) at $1/\xi_L < q < 1/\xi_{Local}$ shows the q-dependence slightly steeper than q^{-4} as shown in Figure 3, indicative of the scattering from the micelle interfaces with a slightly diffuse concentration gradient across the micelle interface. ξ_L and ξ_{Local} will be discussed below. Therefore the strong intensity in the USANS region is attributed to the structures occurring in the larger length scale, i.e., percolated macrodomains rich in NE in the water rich matrix. They are spatially arranged with a mass fractal dimension less than or equal to 2.

In the USANS and SANS profiles at $T > 30$ °C in region (IV), the crossovers of asymptotic q-behavior are clearly seen at $q = 1/\xi_U, 1/\xi_L$, and $1/\xi_{Local}$ as indicated by arrows in Fig. 3(a) and (b). These characteristic lengths represent an intriguing hierarchical structure formed by NE. The values ξ_U and ξ_L are considered to be upper and lower cut-off lengths of the mass fractal of the macrodomains. In the q-range larger than $1/\xi_L$, we observe interfacial structure of macrodomains (at $1/\xi_L < q < 1/\xi_{Local}$) and segmental distribution of swollen chains in the macrodomain and the matrix at ($q > 1/\xi_{Local}$).

Region (IV): Quantitative analyses of hierarchical structure

In order to quantitatively analyze the crossovers in the asymptotic q-behavior in I(q) above 30 °C, we assumed a scattering function which is composed of domain scattering $I_d(q)$ and $I_{oz}(q)$ ($I(q) = I_d(q) + I_{oz}(q)$) as here. $I_d(q)$ is composed of a form factor P(q) and a structure factor S(q) ($I_d(q) \sim P(q)S(q)$). For P(q), we employed a squared Lorentzian function as follows.

$$P(q) = \left(\frac{1}{1+q^2\xi_L^2}\right)^2 \exp(-\sigma^2 q^2 \tag{4}$$

where the second term of Gaussian function in right hand side of Eq. 4 describes an interfacial structure [36], which will be discussed later. According to ref. [37,38], for S(q), we employed a scenario for mass fractal structures, as follows,

$$S(q) = 1 + \frac{C(d_m-1)\Gamma(d_m-1)\xi_U^d}{(1+q^2\xi_U^2)^{d/2}} \frac{(1+q^2\xi_U^2)^{1/2}}{q\xi_U} \frac{\sin[(d_m-1)\arctan(q\xi_U)]}{(d_m-1)} \tag{5}$$

where d_m, Γ, and C are the mass fractal dimension ($1 < d_m < 3$), gamma function, and a proportionality constant. Eqs.(4) and (5) take into account the lower and upper cut-off lengths for mass fractal structures by employing ξ_L and ξ_U, respectively.

Figure 3 shows the predicted scattering profiles (solid lines), which are best-fitted to the experimental ones (open circles) using Eqs.(4) and (5). They well reproduce our experimental results. Tables 3 and 4 summarize characteristic parameters, d_m, ξ_L, and ξ_U for the hierarchical structures in the a-NE abd s-NE solutions in region (IV). As the temperature increases, ξ_U increases, while ξ_L, reflecting that the lateral size, i.e., the size normal to the interface of the NE-rich domain, does not very much depend on the temperature. d_m for the a-NE/solution increases with temperature from 1.51 to 2.39, while that for the s-NE/solution increases from 2.08 to 2.43. The increase of d_m implies that the macrodomains are more densely packed in space.

The parameter σ in the second term in the right hands side of Eq. (4) is related to the characteristic interfacial thickness t_I [36,39], as follows,

$$t_I = (2\pi)^{1/2}\sigma. \tag{6}$$

The interface structure of the NE solution is schematically shown in Figure 6, where the interface of macrodomains includes PEG chain brushes swollen with water. It should be noted that the scattering lengths *b* of both PNIPA and PEG chains are similar and smaller, compared to that of deuterated water D_2O: b_{PNIPA},

Table 3 Summary of characteristic parameters determined by SANS and USANS for a-NE aqueous solution.

Temperature (°C)	ξ_L (nm)	ξ_U (nm)	d_m	σ (nm)	t_I (nm)
30	4.90	802	1.51	1.03	2.6
31	4.93	1139	2.08	1.08	2.7
32	4.97	1221	2.39	1.99	5.0
34	5.03	1384	2.39	2.21	5.5
40	–	–	–	2.47	6.2

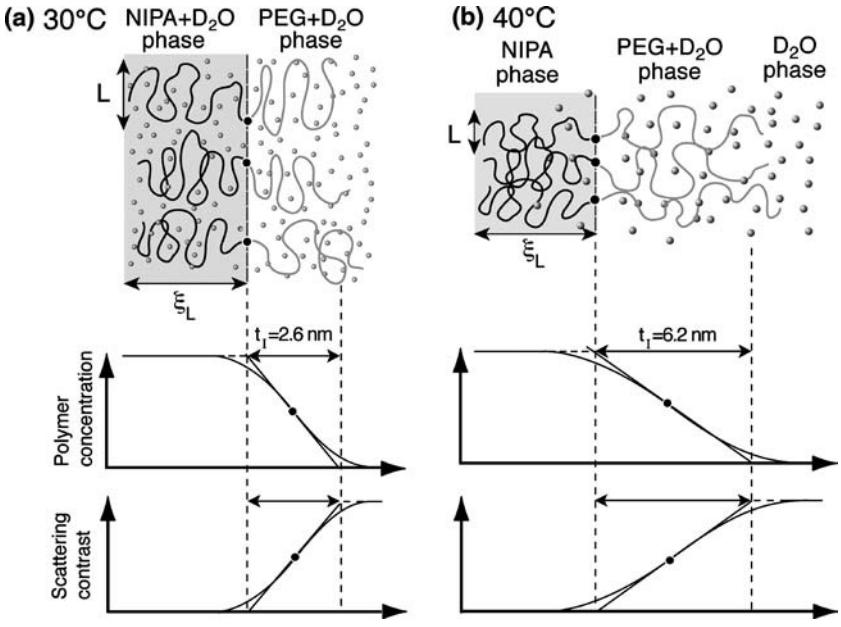

Fig. 6. Schematic diagrams of interfacial structures for a-NE with $w_p = 7\%$ (w/v); (a) opaque gel at 30 °C and (b) the gel showing syneresis at 40 °C. The characteristic interfacial thickness t_I corresponds to the segmental distribution of PEG chains across the interface

b_{PEG}, and bD_2O are 1.23, 0.94, and 9.49 ($10^{-14} \times cm^{-2}mol$). Therefore, t_I observed by SANS corresponds to a spatial distribution of D_2O across the interface between the PNIPA-rich macrodomain to the swollen PEG chains.

In order to determine t_I, we examined the scattering profiles in the q-range of $1/\xi_L < q < 1/\xi_{Local}$ (see Fig. 3), using the Porod plot of $\ln[I_d(q)q^4]$ vs q^2 [36, 39, 40]. Figures 7(a) and (b) show the Porod plots for the a-NE/water and s-NE/water systems, respectively. As the temperature increases, the slope becomes steeper and hence t_I becomes larger. From the slope of the plot, we determined t_I at each temperature, the results of which are summarized in Tables 3 and 4. The increase of t_I with temperature is interpreted as follows; as the temperature increases, PNIPA chains become hydrophobic, less swollen with water. Therefore, the PNIPA chains are more densely packed in the PNIPA rich domain. The dense packing of PNIPA chains decreases the interfacial area per block chain or the average length L between the junctions of block chains, as defined in Fig. 6. As a result of the dense packing of the PNIPA chains, the PEG block chains are forced to stretch because PNIPA and PEG chains are covalently bonded with each other (see Fig. 6).

Morphologies and interpretations of various regions

On the basis of the microscopic observations by SANS, we schematically present the elucidated morphologies of the systems for various regions in Fig. 8. The transparent sol state in region (II) (Fig. 1) is attributed to disordered micelles in short-range liquid-like order as shown in part (b) where the micelles are comprised of the PNIPA cores and PEG brushes emanating from cores. States of

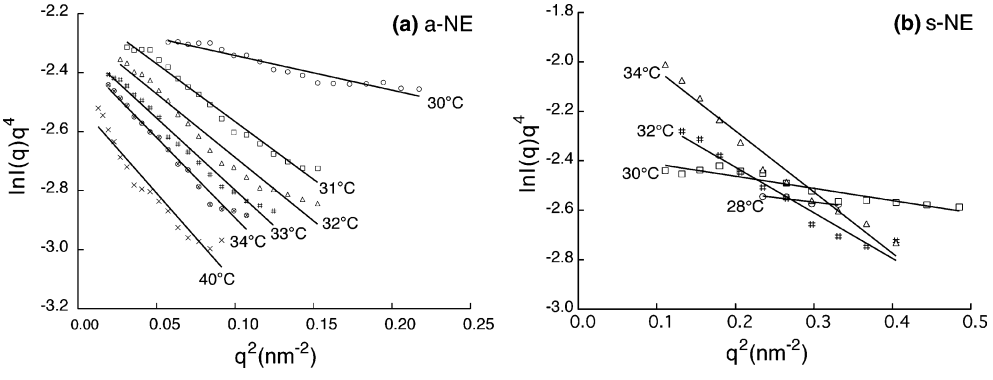

Fig. 7 Porod plots of $\ln[I(q)q^4]$ vs. q^2 for (a) a-NE aqueous solutions of $w_P = 7\%$ (w/v) at range of temperature from 30 to 40 °C and (b) s-NE aqueous solutions of $w_P = 5\%$ (w/v) at range of temperatue from 28 to 34 °C

Table 4 Summary of characteristic parameters determined by SANS and USANS for s-NE aqueous solution

Temperature (°C)	ξ_L (nm)	ξ_U (nm)	d_m	σ (nm)	t_I (nm)
28	2.78	–	2.08	0.83	1.5
30	2.87	–	2.36	0.95	1.8
32	3.36	290	2.40	1.36	3.4
34	3.40	315	2.43	1.56	3.9

micelles such as number of micelles, association number of block chains and degree of swelling may change in region (II) as a function of T and w_p. Near the boundary between region (I) and (II), unimolecular micelles (part (a)) might occur as a consequence of the asymmetric swelling of PNIPA and PEG block chains.

The transparent gel state observed in region (VI) is attributed to ***ordered micelles*** with a long-range order (part (c)). The opaque gel observed in region (IV) is due to the percolated domain rich in NE coexisting with that rich in PEG where the NE domain is less swollen with water than the PEG domain (part (d)). In region (III) of $w_P < w_{P,C}$, on the other hand, we could not observe the gel state, which implies that the PNIPA-rich domains are not percolated (part (e)). The characteristic length ξ_L in Figure 3 and Tables 3 and 4 corresponds to that of the PNIPA-rich domain shown in Figs. 8(d, e). The percolated network in region (IV) (Fig. 8(d)) has the mass-fractal structure with d_m ($\cong 1.5 \sim 2.4$) in the length scales limited by ξ_L and ξ_U (ξ_U was not shown in part(d)). The increase of d_m with T is also attributed to the dense packing of the PNIPA domains in region (IV).

ξ_L, related to the size of the PNIPA-rich network, does not change much in region (IV), This may be interpreted as a balance of two opposing effects: a shrinking of ξ_L due to dehydration of PNIPA domains and an expansion of ξ_L due to chain stretching of PEG in the PEG domains as demonstrated in Fig. 6. As the temperature further increases into region (V), the excess water in the gel is squeezed out from the gel phase, where the 3 dimensional network shows up syneresis.

The ordering mechanism in the NE solution proceeds by an interplay between (i) microphase separation between PNIPA and PEG block chains and (ii) macrophase separation between NE and water. The NE solution is a ternary system of PNIPA block, PEG block, and water so that there are three interaction parameters χ_{NE},

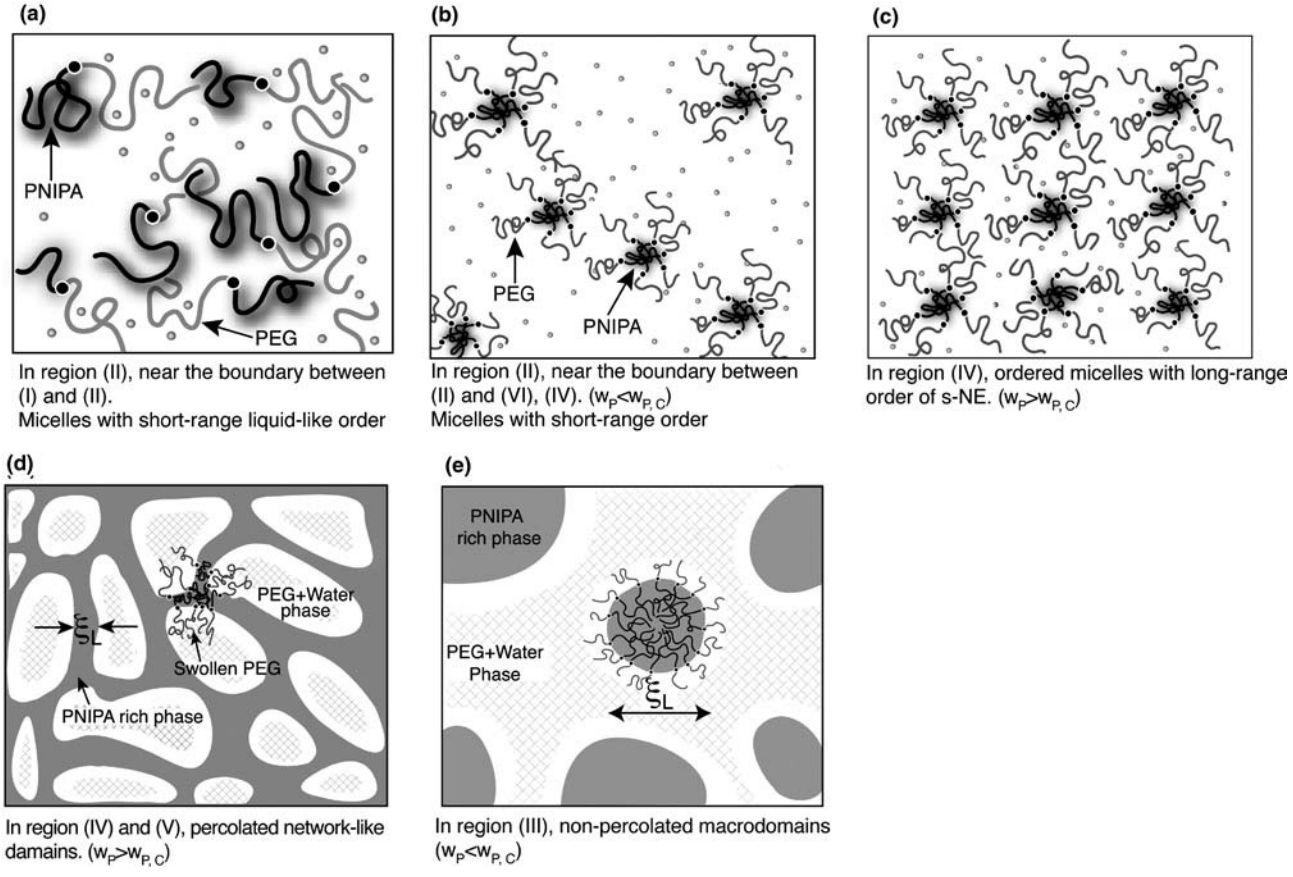

Fig. 8 Schematic diagrams showing various stated and structures elucidated by SANS and USANS

χ_{NW}, and χ_{EW} determining the thermodynamic instabilities of macro- and microphase separations.

In region (I), we denote that both block chains of PNIPA and PEG are swollen by water. According to the dilution approximation [12], the interaction between PNIPA and PEG block chains is weakened into $\phi\chi_{NE}$, and a disordered state is stabilized by swelling. However, when temperature increases into region (II), solvent selectivity (relative difference in χ, $\Delta\chi(=\chi_{NW}-\chi_{EW})$) should become larger. $\Delta\chi$ also contributes to increase the interaction between PNIPA and PEG block chains. As a result, both a-NE and s-NE start to form micelles in region (II).

In region (II), SANS exhibited excess scattering $I_d(q)$ due to the disordered micelles, deviating from OZ scattering found in region (I). The micelle formation in region (II) is common for both a-NE and s-NE. For a-NE, short coronal PEG chains emanating from the cores composed of the long PNIPA chains cannot stabilize a long-range order of the micelles. This is because the short coronal chains do not sufficiently overlap one another. However, for s-NE, the coronal PEG chains are sufficiently long as compared to the core size so that they can overlap one another in the matrix and stabilize long range order of the micelles. This a reason why we observed a broad scattering maximum for the s-NE sysytem, which should originate from regular interdomain distance in the ordered structure. Since the micelle size is much smaller than the wavelength of visible light, the a-NE and s-NE solutions in region (II) appear transparent.

In the context of mean-field approximation, macrophase separation between NE and water is determined by χ_{macro}, which is averaged for two block chains as $\chi_{macro} \cong 0.83\chi_{NW}$. In a temperature range we employed, water behaves as a good solvent for the PEG chain. Thus we assume that χ_{EW} is much smaller than χ_{NW} and therefore $\chi_{macro} \cong f_{PNIPA}\chi_{NW}$. According to this assumption, we obtain $\chi_{macro} \cong 0.83\chi_{NW}$ for a-NE, while $\chi_{macro} \cong 0.46\chi_{NW}$ for s-NE. We qualitatively understand that macrophase separation of s-NE is much more suppressed, compared to that of a-NE. This is a reason why s-NE exhibits the extra phase of transparent gel [region (VI)].

Upon further increase of temperature, χ_{NW} should further increase. Then χ_{macro} finally satisfies the condition of macrophase separation, which happens above around 30 °C both for a-NE and s-NE. This condition determines the boundaries between regions (II) and (III) or (VI) and (IV) in Figure 1. The turbid solutions observed in temperature regions (III), (IV), and (V) (a part of the solutions having the opaque gel) are attributed to macrophase separation, where the domains rich in PNIPA are dispersed in the matrix composed of the swollen PEG chains and water.

In region (IV), we observed the network-like domain, having mass fractal structure with power law scattering ($\sim q^{-2}$) in the USANS q-region of $1/\xi_U < q < 1/\xi_L$. This network-like domain, which is common for both a-NE and s-NE, may have a morphology characteristic for "***viscoelastic phase separation***"[41–44]. Ordering mechanism of such network may be envisaged to be ***diffusion limited association*** (DLA) of micelles; as the temperature and therefore χ_{NW} increases, the micelles diffuse and aggregate to minimize an interfacial area. Here in the DLA process,"***dynamical asymmetry***" between micelles and water also becomes important, where the term"asymmetry" denotes difference in mobility. It is well established both by the experimental [42–47] and theoretical works [41, 48] that the dynamical asymmetry induces local stress imbalance between the fast and slow components and affects the phase separation or relaxation of concentration fluctuations in order to transiently release imbalanced stress (***dynamical coupling between stress and diffusion***) during ordering process [41–48].

In our study, the micelles formed by NE correspond to the slower component, whereas water corresponds to the faster component. The dynamical coupling in the DLA process involves association of the micelles into the network-like domain in the matrix rich-in water. If reorganization of the domain structures is allowed, the network-like domains should be eventually transformed into clusters of droplets, in hydrodynamic limits, in order to reduce the interfacial free energy. However, we recognized that the breakage of network does not occur in the NE system.

The pinning of the domain growth at the stage of the percolated network domains should be due to vitrification of PNIPA chains in the domain. In region (V), the almost vitrified network-like domain squeezes water to result in the observed syneresis.

Conclusion

By using USANS and SANS, we investigated domain structures formed in the aqueous solution of poly(*N*-isopropylacrylamide)-*block*-poly(ethylene glycol) (NE), in relation to macroscopic behaviors such as fluidity, turbidity, and syneresis. We found various states of the NE solution in a narrow temperature range between 15 °C and 35 °C, which is attributed to a strong solvent selectivity due to the LCST behavior of PNIPA block chains in water. We elucidated six different states as summarized in Figs. 1 and 8 and their hierarchical structures appearing in a wide q-range from $10^{-4} < q < 2\ nm^{-1}$ covered by SANS and USANS.

References

1. Hamley IW (1998) The Physics of Block Copolymers: Oxford University Press: New York
2. Hashimoto T (1996) Thermoplastic Elastomers, A Comprehensive Review; Legge NR, Holden G, Schroeder HE, Eds.; Hanser: Munich, Germany; p 429. Hasegawa H, Hashimoto T (1996) In Comprehensive Polymer Science, Second Supplement; Agaarwal SL, Russo S, Volume Eds.; Pergamon: New York, 1996; p 497
3. Kraus G, Hashimoto T (1982) J Appl polym Sci 27: 1745
4. Schmolka IR, in Tarcha PJ, Ed. Polymers for Controlled Drug Delivery; CRC Press: Boston, 1991
5. Topp MDC, Leunen IH, Dijkstra PJ, Tauer K, Schellenberg C, Feijen J (2000) Macromolecules 33: 4986
6. Motokawa R, Nanahira T, Annaka M, Hashimoto T, Koizumi S (2004) Polymer 145: 9019
7. Hirokawa Y, Tanaka T (1984) J Chem Phys 81: 6379
8. Wang X, Qiu X, Wu C (1998) Macromolecules 31: 2972
9. Bates FS, Fredrickson GH (1999) Phys Today 52: 32
10. Hashimoto T, Tanaka H, Hasegawa H (1990) Macromolecules 23: 4378
11. Hashimoto T, Kimishima K, Hasegawa H (1991) Macromolecules 24: 5704
12. Helfand E, Tagami Y (1972) J Chem Phys 56: 3592
13. Hong KM, Noolandi J (1983) Macromolecules 16: 1083
14. Hashimoto T, Shibayama M, Kawai H (1983) Macromolecules 16: 1093
15. Shibayama M, Hashimoto T, Hasegawa H, Kawai H (1983) Macromolecules 16: 1427
16. Nagarajan R, Ganesh K (1989) J Chem Phys 90: 5843
17. Hashimoto T, Mori K (1990) Macromolecules 23: 5347
18. Fredrickson GH, Bates FS (1996) Annu Rev Mater Sci 26: 503
19. Mori K, Okawara A, Hashimoto T (1996) J Chem Phys 104: 7765
20. Mori K, Hasegawa H, Hashimoto T (2001) Polymer 42: 3009
21. Lodge TP, Pan C, Jin X, Liu Z, Zhao J, Maurer WW, Bates FS (1995) J Polym Sci: Polym Phys Ed 33: 2289
22. Sakurai S, Hashimoto T, Fetters LJ (1996) Macromolecules 29: 740
23. Mortensen K, Pedersen JS (1993) Macromolecules 26: 807
24. Mortensen K, Brown W, Jorgensen E (1994) Macromolecules 27: 5654
25. Alexandridis P, Zhou D, Khan A (1996) Langmuir 12: 2690
26. Alexandridis P, Olsson U, Lindman B (1998) Langmuir 14: 2627
27. Hajduk DA, Kossuth MB, Hillmyer MA, Bates FS (1998) J Phys Chem B 102: 4269
28. Ganachaud F, Monterio MJ, Gilbert RG, Dourges MA, Thang SH, Rizzardo E. (2000) Macromolecules 33: 6738
29. Bonse U, Heart M (1968) Appl Phys Lett 7: 238
30. Aizawa K, Tomimitsu H (1995) Phisica B 213–214: 884
31. Glatter O, Kratky O (1982) Small Angle X-ray Scattering: Academic Press: London
32. Ornstein LS, Zernike F (1914) Proc Akad Sci Amsterdam 14: 793
33. Daoud M, Cotton JP, Farnoux B, Jannink G, Sarma G, Benoit H, Duplessix R, Picot C, de Gennes PG (804) Macromolecules 8: 1975
34. Flory PJ (1953) Principle of Polymer Chemistry. Cornel University, New York
35. Debye P, Bueche AM (1949) J Appl Phys 20: 518
36. Ruland WJ (1971) Appl Cryst 4: 70
37. Freltoft T, Kjems JK, Sinha SK (1986) Phys Rev B 33: 269
38. Schaefer DW, Keefer KD (1986) Phys Rev Lett 56: 2199
39. Hashimoto T, Shibayama M, Kawai H (1980) Macromolecules 13: 1237
40. Koberstein JT, Morra B, Stein RS (1980) J Appl Cryst 13: 34
41. Doi M, Onuki A (1992) J Phys II France 2: 1631
42. Tanaka H (2000) J Phys: Condens Matter 12: 207
43. Toyoda N, Takenaka M, Saito S, Hashimoto T (2001) Polymer 42: 9193
44. Takenaka M, Takeno H, Hasegawa H, Saito S, Hashimoto T, Nagao M (2002) Phys Rev E 65: 021806–1
45. Koizumi S (2004) J Polym Sci Part B: Polym Phys 42: 3148

Progr Colloid Polym Sci (2005) 130: 97–104
DOI 10.1007/b107344
Published online: 3 June 2005

Mikihito Takenaka
Masaaki Miyazawa
Shotaro Nishitsuji
Takeji Hashimoto

Viscoelastic effects on dynamics of concentration fluctuations for non-entangled polymer mixture: Time-resolved synchrotron–SAXS studies after pressure-jump

M. Takenaka · M. Miyazawa
S. Nishitsuji · T. Hashimoto (✉)
Department of Polymer Chemistry,
Graduate School of Engineering,
Kyoto University, Nishikyo-ku,
Kyoto 615-8510, Japan
e-mail:
hashimoto@alloy.polym.kyoto-u.ac.jp
Tel.: +81-75-383 2619
Fax: +81-75-383 2623

Abstract Relaxation processes of the concentration fluctuations induced by a rapid pressure drop inside the single phase were investigated for a non-entangled polymer blend (polystyrene (PS) / polybutadiene (PB)) with a composition of 50/50 wt/wt by using time-resolved small angle X-ray scattering. The pressure drop was carried out with the cell designed for polymeric systems under high pressure and high temperature. Time change in the scattered intensity with wave number (q) during the relaxation processes was found to be approximated by Cahn-Hilliard-Cook linearized theory. The theoretical analysis yielded the q-dependence of Onsager kinetic coefficient $\Lambda(q)$. The obtained $\Lambda(q)$ has the q^{-2}-dependence even at $q\,R_g < 1$, which does not agree with theoretical prediction by Binder. We clarified that the q^{-2}-dependence was caused by the viscoelastic effects arising from the dynamical asymmetry between the component polymers due to the difference in the glass transition temperature.

Keywords Viscoelastic effects · Pressure jump · Polymer mixture · Small-Angle · X-ray Scattering

Introduction

The dynamics of concentration fluctuations in binary polymer blends has been well investigated for many years, since the dynamics is one of the interesting research problems in soft-matter physics. Time-resolved scattering technique has been the most powerful tool to investigate the dynamics and contributed to unveil many important features of the dynamics.

Time-resolved light scattering studies of the phase separation processes of polymer blends [1–4] have found the following common features between polymer blends and simple liquid mixtures: the phase-separated structures of polymer blends and simple liquid mixtures grow with dynamical self-similarity in the late stage spinodal decomposition (dynamical scaling concept [5–7]), and the coarsening behaviors of them, as observed by time-evolution of the characteristic wave number and scattered intensity at different quenches, become universal, independent of the quench depths and the systems, when the relevant physical quantities are reduced with the quench-depth-dependent characteristic parameters (Langer-Baron-Miller's scaling postulate [8, 9]).

By using time-resolved small angle neutron scattering (SANS) or small angle X-ray scattering (SAXS), we can observe the dynamics in polymer blends at the length scale much smaller than light scattering, e.g., at the length scale close to radius of gyration of polymer coils R_g where some unique features have been found in the dynamics of phase separation processes. This is because linear flexible polymers have many internal degrees of freedom and hence internal modes of vibrations [10–12]. The effects of the normal modes make the Onsager kinetic coefficient Λ q-dependent ($\Lambda = \Lambda(q)$), where q is magnitude of scattering vector defined later in Eq. (2) or wave number of particular Fourier modes of the concentration fluctuations. This feature is not observed in other systems such as simple-liquid mixtures. It is

expected that upon decreasing q toward $1/R_g$ the Onsager kinetic coefficient asymptotically increases according to q^{-2} and upon further decreasing q it increases and reaches a constant limiting value $\Lambda(0)$ with $qR_g \to 0$. de Gennes [13] and Pincus [14] theoretically elucidated this effect for the case where the constituent polymers in the polymer blends are entangled and their diffusion occurs via reptation. Pincus[14] predicted that the following q-dependent Onsager kinetic coefficients for entangled symmetric polymer blends:

$$\Lambda(q) = \Lambda(0)\frac{1-\exp\left(-q^2R_\Lambda^2\right)}{q^2R_\Lambda^2} \quad (1)$$

where R_Λ is R_g for the symmetric polymer blends. Here the symmetric blends denote that each component in polymer blends has an identical polymerization index N, and self-diffusion coefficient D_s. Pincus's theory predicts $\Lambda(q)$ becomes q^{-2} at $qR_\Lambda > 1$, while $\Lambda(q)$ is effectively constant at $qR_\Lambda \leq 0.33$ for the symmetric blends. Jinnai et al.[15] investigated the dynamics of the early stage spinodal decomposition for the nearly symmetric deuterated polybutadiene (DPB)/ polybutadiene (PB) blend by using time-resolved SANS and determined the q-dependence of the Onsager kinetic coefficients. According to their study, the q-dependence is well expressed by Pincus theory but the estimated R_Λ is about twice as large as R_g's of DPB or PB. Müller et al. [16] also found the $R_\Lambda/R_g = 2$ for the nearly symmetric deuterated polystyrene (dPS) / polystyrene (PS) blend. In both cases if the theories are correct, R_Λ should be equal to R_g.

As for entangled asymmetric blends in which each component in blends has different self-diffusion coefficient and/or viscosity, Schwahn et al. [17] found that the R_Λ/R_g is about 5 to 7 in the dynamics of the early stage spinodal decomposition of the dPS / poly(vinyl methyl ether) (PVME) blend by using time-resolved SANS. We also found that R_Λ/R_g is about 4 in the dynamics of the relaxation processes of concentration fluctuations in one phase region for dPB/polyisoprene (PI) blend [18, 19]. Kawasaki and Koga [20] suggested that this large R_Λ originates from the dynamical coupling between diffusion and stress which is predicted as "viscoelastic effects" by Doi and Onuki [21, 22] (DO). According to the DO theory, the stress relaxation governs the dynamics of the concentration fluctuations at the length scale of observation ℓ shorter than a certain characteristic length ξ_{ve}, defined as "viscoelastic length", and the Onsager kinetic coefficient has q^{-2}-dependence at $q\xi_{ve} > 1$. ξ_{ve} increases with asymmetry in polymerization indices and self-diffusion coefficients of the component polymers and can be much larger than R_g and R_Λ. We compared ξ_{ve} obtained from the investigation of the dynamics of dPB/PI with that predicted by DO theory together with the fundamental parameters as obtained from viscoelastic data independently. Both values agree well each other, and the DO theory can well describe the q-dependence of the Onsager kinetic coefficient of the asymmetric polymer blends observed at $q < 1/R_g$.

Although the dynamics of concentration fluctuations in binary asymmetric polymer blends have been well investigated experimentally as described above and also by real space studies[23], the polymers used in these studies have high molecular weight and are well entangled. There have been no experimental works reported so far on the dynamics of the concentration fluctuations of "non-entangled", asymmetirc polymer blends. The aim of this paper is thus to explore the dynamics of the concentration fluctuations of non-entangled dynamically asymmetric polymer blends and study their q-dependence of Onsager kinetic coefficients.

However, to pursue the focused experimental works as described above, we face experimental difficulties arising from the fact that the dynamics of the concentration fluctuations of non-entangled polymer blends become much faster than those of entangled polymer blends. In order to overcome the difficulties, we employed the pressure-jump technique for the quench and the time-resolved SAXS with synchrotron X-ray radiation (designated Synchrotron-SAXS). The pressure jump enables us to attain the quick quench to trace the fast isothermal relaxation process of the concentration fluctuations. The time-resolved SAXS with synchrotron radiation enables us to measure very quickly the quantitative time change in the scattering structure factor.

This paper has the following contents. Introduction describes backgrounds and motivation of this study. The blend samples and the experimental techniques used in this study are described in Experimental Section. In Results and Discussion Section, we shall first show equilibrium structure factors for the blend in a single phase state at a given temperature as a function of pressure so that we can design the pressure-jump experiments to explore the relaxation of the concentration fluctuations inside the single phase. Then, we will present the experimental results on the time changes in the scattering structure factors during the relaxation processes of the concentration fluctuations induced by the pressure change and analyze the data by using the Cahn-Hilliard-Cook (CHC) theory. We shall discuss the q-dependence of the Onsager kinetic coefficient estimated by the CHC theory in the latter of this Section. Finally, in Conclusion Section, we shall summarize our results.

Experimental section

The polystyrene (PS) and polybutadiene (PB) used in this study were synthesized by living anionic polymerization. The characterization of PS and PB are listed in Table 1, where M_n, M_w, v, and R_g designate number-averaged molecular weight, weight-averaged molecular weight, molar volume of monomer unit, and radius of gyration, respectively. M_n and M_w are much less than the molecular

Table 1 Characterization of polymers used in this study

Sample Code	$M_w \times 10^{-3}$	M_w/M_n	Volume of monomer unit $v \times 10^{28}$ (m^3)	Unperturbed radius of gyration R_g (nm)	T_g (°C)
PS	1.67	1.10	1.68	1.12	63
PB	0.78	1.18	1.03	1.00	−100

weight between entanglements (3.0×10^3 for PB and 1.0×10^4 for PS) of each sample[24]. The glass transition temperature (T_g) of the neat PS, and the neat PB, are, respectively, 63, and −100 °C, which we obtained by using differential scanning calorimeter, DSC. The composition of a PS/PB mixture studied was 50/50 by weight. The T_g of the mixture is estimated to be −45°C by using Fox equation with T_g of the neat PS and the neat PB.

The PS and PB were dissolved into a homogeneous solution with benzene in which total weight fraction of the polymers are 0.1. The homogeneous blend was obtained by evaporating the solvent with a freeze-dry method. We installed the sample into the cell which is specially designed for the SAXS measurement under high pressures (up to 600 MPa) and at high temperatures (up to 523 K). The details of the cell for high pressure and temperature are described elsewhere [25]. The SAXS experiments were performed with BL45XU at SPring-8 and the CCD camera with an Image-Intensifier [26]. The X-ray wavelength λ used here was 0.11 nm. All measured intensities were circularly averaged after corrections for the electrical background scattering, the sample transmittance, and the scattering from the empty cell used in this experiment.

We measured the pressure dependence of the SAXS intensity at $T = 311.6$ K and 314.1 K in order to investigate the pressure dependence of the Flory-Huggins segmental interaction parameter χ between PS and PB at those temperatures. The pressure P used here is 0.1, 10.0, 20.0, 30.0, 35.0, and 40.0 MPa at 311.6 K, and 0.1, 10.0, 20.0, 30.0, 40.0, 45.0, and 50.0 MPa at 314.1 K.

We took the following procedure to measure the time changes in the scattered intensity distribution induced by pressure changes (hereafter defined as "quench") from 40.0 to 0.1 MPa at 311.6 K and from 50.0 to 0.1 MPa at 314.1 K: In the case of the former quench, the sample was first equilibrated at 311.6 K and 40.0 MPa for 15 min. before the SAXS measurement. We note that the blends are above T_g at those pressures and temperatures but that their components of PS and PB have a large dynamical asymmetry as will be discussed later in the text, due to a difference in proximity of their T_g's with the temperatures set in this experiment. The sample was then quenched from 40.0 to 0.1 MPa at 311.6 K, followed by a time-resolved SAXS measurement as a function of time t after the completion of the quench. The data acquisition time is 36 m sec/scan. The similar procedure was used for the quench from 50.0 to 0.1 MPa at 314.1 K.

Results and discussion

Quench depth induced by pressure jump

Figure 1 shows the pressure (P) dependence of the equilibrium scattering function $I_{eq}(q)$ at 311.6 K (a) and 314.1 K (b). In the figures, $I_{eq}(q)$ is plotted as a function of wave number q defined by

$$q = (4\pi/\lambda)\sin(\theta/2), \tag{2}$$

where θ is the scattering angle. $I_{eq}(q)$ increases with pressure, indicating that the PS/PB mixture has a lower critical solution pressure type phase diagram so that the system approaches a critical pressure for phase separation as pressure increases.

According to the scattering theory based on the random phase approximation (RPA)[27–29], $I_{eq}(q)$ and the structure factor $S_{eq}(q)$ is expressed by

$$I_{eq}(q) = k_N S_{eq}(q) = k_N \left[\frac{1}{\phi_{PS} v_{PS} S_{PS}(q)} + \frac{1}{\phi_{PB} v_{PB} S_{PB}(q)} - \frac{2\chi}{v_0} \right]^{-1} \tag{3}$$

with

$$k_N = C N_A \left(\frac{a_{PS}}{v_{PS}} - \frac{a_{PB}}{v_{PB}} \right)^2, \tag{4}$$

and $S_i(q)$ is the structure factor for i-th component polymer (i = PS or PB) given by

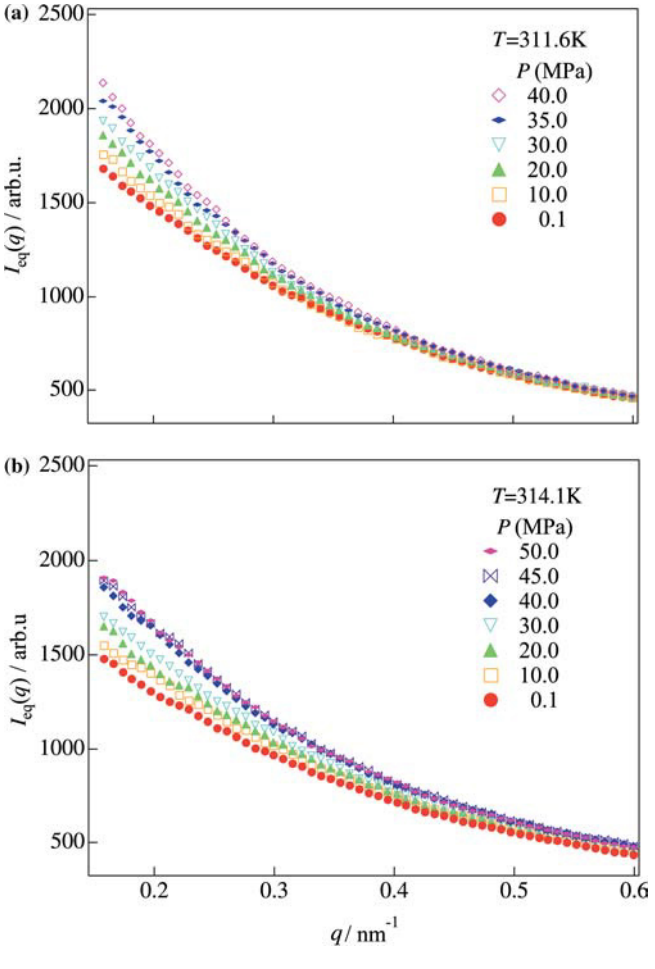

Fig. 1 Pressure dependence of the equilibrium scattering function $I_{eq}(q)$ at 311.6 K (a) and 314.1 K (b) plotted as a function of q

$$S_{\mathrm{i}}(q) = \frac{2}{x_{\mathrm{i}}^2}\left[\left(\frac{h_{\mathrm{i}}}{h_{\mathrm{i}} + x_{\mathrm{i}}}\right)^{h_i} - 1 + x_{\mathrm{i}}\right] \tag{5}$$

where

$$x_{\mathrm{i}} = q^2 N_{\mathrm{n,i}} b_{\mathrm{i}}^2/6, \tag{6}$$

and

$$h_{\mathrm{i}} = \left[\left(N_{\mathrm{w,i}}/N_{\mathrm{n,i}}\right) - 1\right]^{-1}. \tag{7}$$

$N_{\mathrm{n,i}}$ and $N_{\mathrm{w,i}}$ denote the number- and weight-averaged degrees of polymerization for the i-th component (i=PS or PB), respectively. C, b_{i}, a_{i}, and v_{i} are, respectively, the instrumental constant for SAXS measurement, the statistical segment length, the electron density and the molar volume of monomer unit, and ϕ_{i} the volume fraction of the i-th component. N_{A} is Avogadro's number, χ is the Flory-Huggins interaction parameter between PS and PB per monomer unit, and v_0 is the reference cell volume defined as

$$v_0 = \left(\phi_{\mathrm{PS}}/v_{\mathrm{PS}} + \phi_{\mathrm{PB}}/v_{\mathrm{PB}}\right)^{-1}. \tag{8}$$

We fitted SAXS profiles with Eq.(3) with χ, b_{i} , and k_{N} as adjustable parameters. b_{PS} and b_{PB} vary from 0.65 to 0.67 nm, and from 0.86 to 0.89 nm, respectively. The variations of b_{PS} and b_{PB} are in a reasonable range since b_{PS} and b_{PB} calculated from the radius of gyration at 0.1 MPa are 0.67, and 0.88 nm, respectively. Unfortunately, we can not compare k_{N} with those calculated with electron density and molar volume since k_{N} includes the unknown instrumental constant, However, we found that k_{N} slightly decreases with pressure.

Figure 2 shows the pressure dependencies of χ-parameter thus measured at 311.6 and 314.1 K: The pressure dependence of χ are given by

$$\chi = 9.69 \times 10^{-2} + 9.64 \times 10^{-5} P \text{ (MPa)} \quad \text{at 311.6K}, \tag{9}$$

and

$$\chi = 9.57 \times 10^{-2} + 8.96 \times 10^{-5} P \text{ (MPa)} \quad \text{at 314.1K}. \tag{10}$$

The χ increases with pressure as expected from the results in Figures 1 and 2, indicating that the PS/PB mixture has the lower critical solution pressure type phase diagram. Figure 3 shows the spinodal line (solid line) plotted as a function of ϕ_{PS} for the PS/PB mixture at 0.1 MPa. The spinodal line was calculated with

$$\chi_{\mathrm{s}} = \frac{v_0}{2}\left[\frac{1}{\phi_{\mathrm{PS}} v_{\mathrm{PS}} N_{\mathrm{w,PS}}} + \frac{1}{\phi_{\mathrm{PB}} v_{\mathrm{PB}} N_{\mathrm{w,PB}}}\right]. \tag{11}$$

The following temperature dependence of χ at 0.1 MPa which in turn was measured from SAXS experiments on the same blend in the single-phase state at 0.1 MPa as a function of temperature:

$$\chi = -0.0875 + 65.5/T \quad \text{at 0.1 MPa}. \tag{12}$$

The spinodal temperature of this mixture at P = 0.1 MPa is 299.3 K. The figure also includes changes in a thermodynamic state of the blend induced by the pressure-jump from 40.0 to 0.1 MPa (squares and solid line) at 311.6 K, and 50.0 to 0.1 MPa at 314.1 K (circles and broken line)

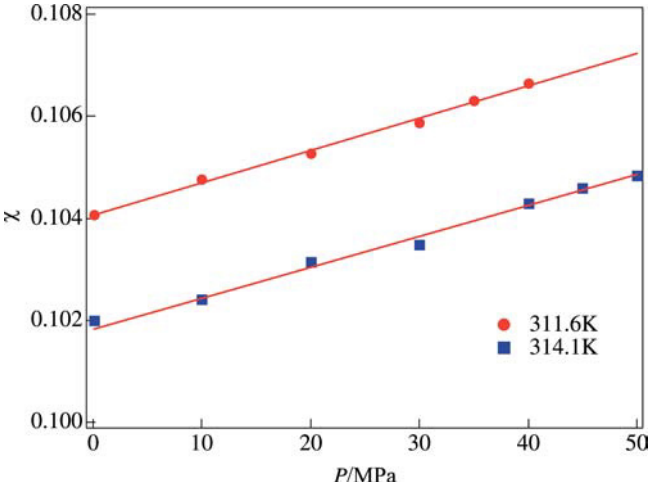

Fig. 2 Estimated χ parameters plotted as a function of pressure P at 311.6 K (circles) and 314.1 K (squares)

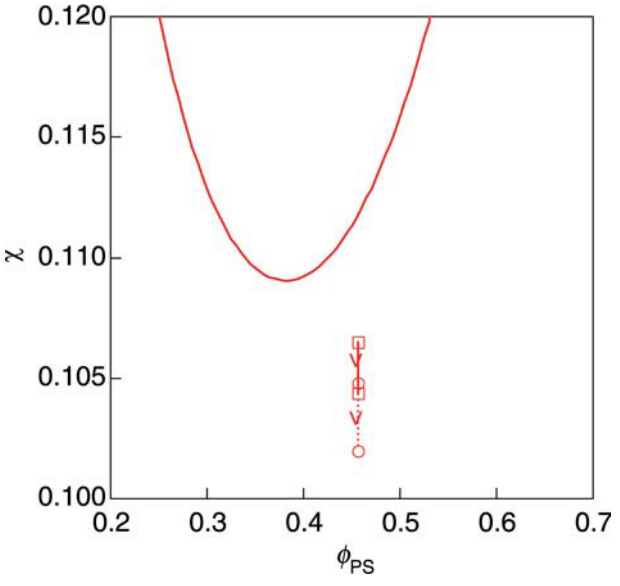

Fig. 3 Phase diagram of the PS/PB blend in the parameter space of χ and volume fraction of PS ϕ_{PS} in the blend. The solid line corresponds to the spinodal line which is estimated from the small-angle X-ray scattering experiment in one phase region. Solid line with squares and solid line with circles represent the quench depth corresponding to the pressure-jumps at 311.6 K and 314.1 K, respectively

which are estimated from Eqs.(9) and (12), and Eqs.(10) and (12), respectively. The arrows indicate directions along which the system change with pressure drops. The pressure jumps at 311.6 K and 314.1 K, respectively, correspond to the drop in the χ value $\Delta\chi = 2.1 \times 10^{-3}$ and 2.8×10^{-3} or the temperature jump $\Delta T = 3.7$ K and 3.1 K from Eqs. (9) to (12).

Changes in scattered intensity with time after the onset of pressure jump

Figure 4 shows the changes in the scattered intensity profiles for the PS/PB mixtures with time after the onset of the quench from 40.0 to 0.1 MPa at 311.6 K (a) and from 50.0 to 0.1 MPa at 314.1 K (b). In both figures, after the quench, the scattering function $I(q,t)$ decreases with time t at an observed q-region toward the equilibrium scattering function $I(q, \infty)$ at 0.1 MPa. The slower decay rate of the intensity is found to be at lower q-region as will be more clearly demonstrated later.

The dynamics of concentration fluctuations in A/B binary mixtures is described by CHC theory. The time-evolution of q-Fourier modes $\delta\phi_A$ (q,t) for the local concentration fluctuations of component A is given by[30–34]:

$$\frac{\partial}{\partial t}\delta\phi_A(q,t) = -\Lambda(q)q^2\mu(q,t) + \zeta(q,t), \tag{13}$$

where $\Lambda(q)$ is the Onsager kinetic coefficient, $\mu(q,t)$ is the local chemical potential, $\zeta(q,t)$ is the random thermal force term as expressed by the following fluctuation-dissipation relation[35, 36]:

$$\langle\zeta(q,t)\zeta(q^*,t')\rangle = -2k_BT\Lambda(q)q^2\delta(t-t'), \tag{14}$$

where q^*, k_B, and T are, respectively, the hermitian conjugate of q, the Boltzman constant and absolute temperature, and $\langle\rangle$ denotes thermal average. If $\delta\phi_A$ (q,t) is small, Eq.(13) can be linearized in terms of $\delta\phi_A$ (q,t):

$$\frac{\partial}{\partial t}\delta\phi_A(q,t) = -\frac{\Lambda(q)q^2}{[S(q,\infty)/k_BT]}\delta\phi_A(q,t) + \zeta(q,t), \tag{15}$$

where $S(q, \infty)$ is the structure factor corresponding to $S_{eq}(q)$ in Eq.(3).

We can solve Eq. (15) in terms of the scattering function $I(q,t) = k_N S(q,t) \propto \langle|\delta\phi_A(q,t)|^2\rangle$ and hence obtain the following time-evolution equation:

$$I(q,t) = I(q,\infty) + [I(q,0) - I(q,\infty)]\exp[-2R(q)t], \tag{16}$$

where $I(q, 0)$ and $R(q)$ are, respectively, $I(q, t)$ at $t = 0$ and the relaxation rate of the q-Fourier modes of the concentration fluctuations. $R(q)$ is expressed by

$$R(q) = q^2\frac{\Lambda(q)}{[S(q,\infty)/k_BT]}. \tag{17}$$

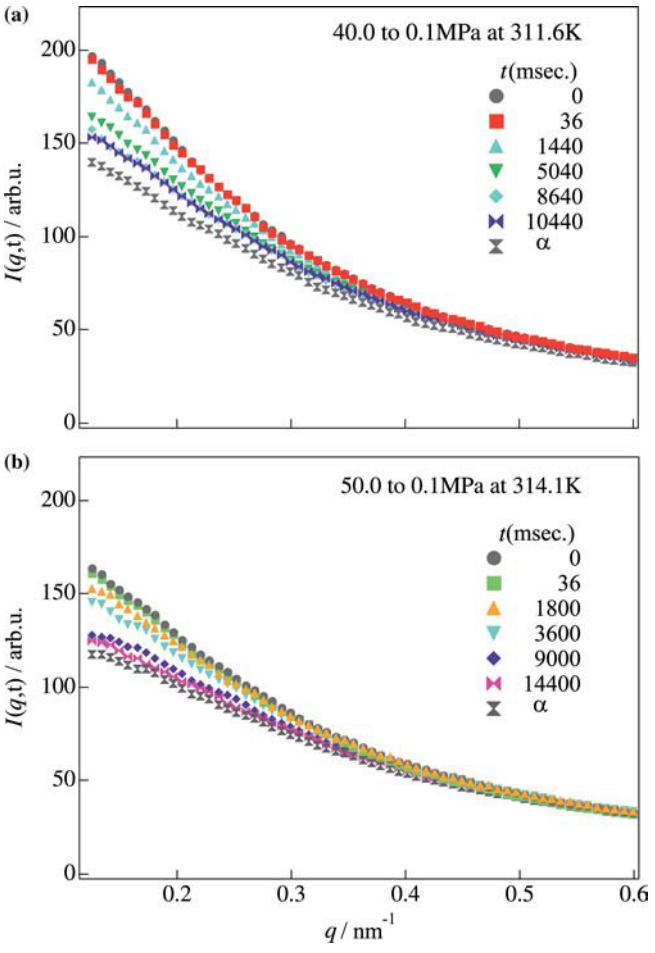

Fig. 4 Change in SAXS scattering function $I(q, t)$ with time after the pressure jump from 40.0 MPa to 0.1 MPa at 311.1 K (a) and from 50.0 MPa to 0.1 MPa at 314.6 K (b)

Rearranging Eq. (16), we obtain

$$\mathrm{Log}[I(q,t) - I(q,\infty)] = \mathrm{Log}[I(q,0) - I(q,\infty)] - 2R(q)t. \tag{18}$$

Thus we can estimate $R(q)$ from the slope of $Log[I(q, t) - I(q, \infty)]$ vs t plot where Log denotes natural logarithms. In Figure 5, $Log[I(q, t) - I(q, \infty)]$ is plotted as a function of t after the onset of quench at 311.6 K (a) and 314.1 K (b). The linearity between $Log[I(q, t) - I(q, \infty)]$ and t can be found in each plot.

Figure 6 shows the q-dependence of $R(q)$ estimated from the plots of $Log[I(q, t) - I(q, \infty)]$ vs t. In both experiments, the $R(q)$ increases with q. The values of $R(q)$ at 314.1 K (part b) are comparable with those at 311.6 K (part a) in the observed q-region, which seems to indicate that the critical slowing down is not clearly observed. This is primarily because 311.6 K and 314.1 K for the pressures covered in this work are far above spinodal temperature as shown in Figure 3.

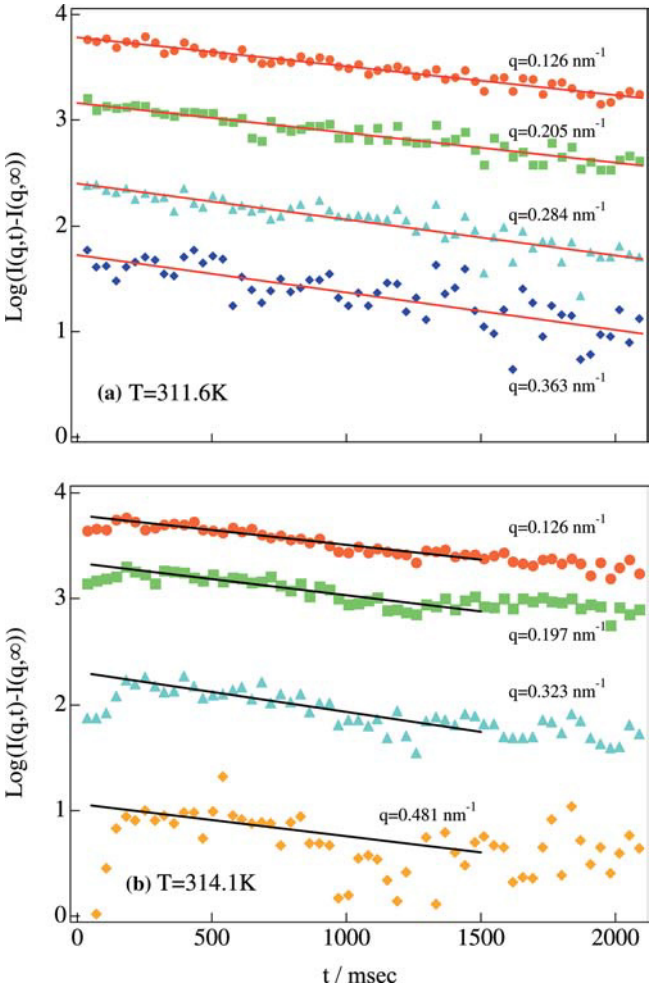

Fig. 5 $Log[I(q, t) - I(q, \infty)]$ plotted as function of time t at 311.6 K (a) and at 314.1 K (b) at fixed q-values. Solid lines were obtained by linear regression of data

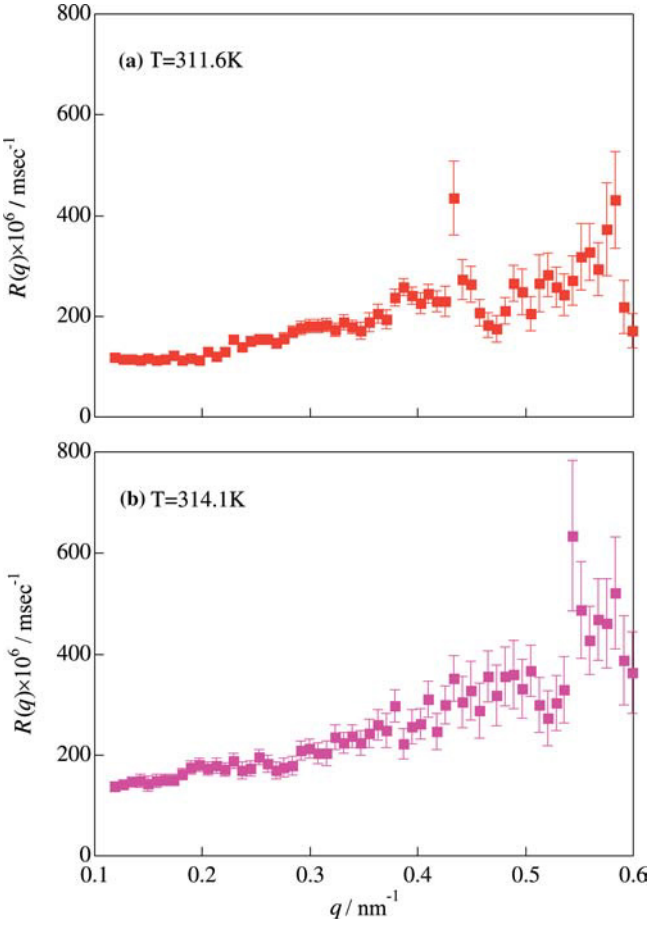

Fig. 6. Relaxation rate $R(q)$ for the q-Fourier modes of the concentration fluctuations plotted as a function of q at 311.6 K (a) and at 314.1 K (b)

Q-dependence of Onsager kinetic coefficient

Figure 7 shows the q-dependence of the Onsager kinetic coefficient at 311.6 K (a) and at 314.1 K (b), as estimated from Eq. (17), i.e.,

$$\Lambda(q) = \frac{R(q)[S(q,\infty)/k_B T]}{q^2}, \tag{19}$$

where $R(q)$ was directly measured as described in the previous section and shown in Fig. 6, and $S(q, \infty)$ is the structure factor $S_{eq}(q)$ at each temperature given by Eq. (3). We found that the q^{-2} behavior at all-observed q-region even in the region of $qR_g < 1$, in both quench experiments. The q^{-2} behaviors in the Onsager kinetic coefficient are shown more clearly in Figure 8. Note that $R_g^{-1} \cong 1$ nm^{-1} for this experiment as shown from Table 1.

Comparison between experimental and theoretical results for Onsager kinetic coefficient

Binder [35] derived the q-dependence of the Onsager kinetic coefficient for non-entangled asymmetric blends:

$$\Lambda(q) = \frac{\Lambda_A(q)\Lambda_B(q)}{\Lambda_A(q) + \Lambda_B(q)}, \tag{20}$$

with

$$\Lambda_i(q) = D_i N_i \phi_i \frac{x_i - 1 + \exp(-x_i)}{x_i^2} \tag{21}$$

and

$$x_i = q^2 R_{g,i}^2 \tag{22}$$

where D_i, N_i, and $R_{g,i}^2$ are, respectively, the self-diffusion coefficient, the polymerization index, and radius of gyration of i-th component (i = A or B in this case). Eq. (20) predicts q^{-2}-dependence at $x_A > 1$ and $x_B > 1$. However, q^{-2}-dependence is observed even at $x < 1$ in

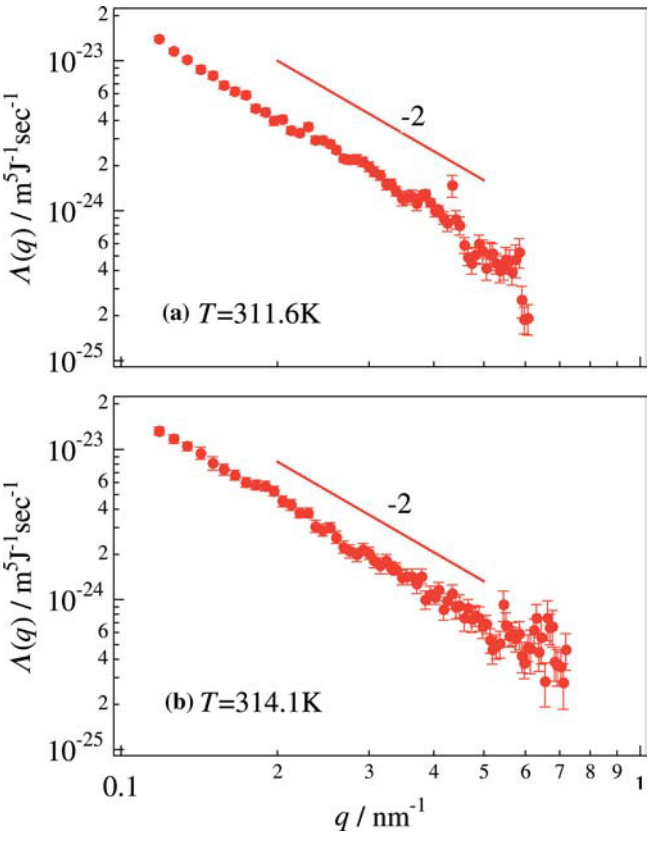

Fig. 7 Q-dependence of Onsager kinetic coefficient at 311.6 K (a) and at 314.1 K (b)

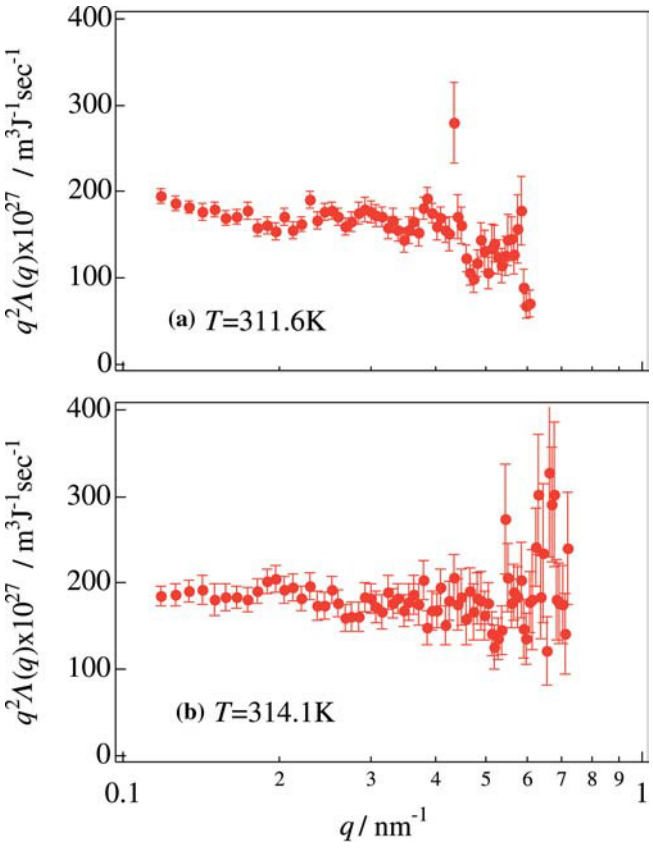

Fig. 8. $q^2\Lambda(q)$ is plotted as a function of q at 311.6 K (a) and at 314.1 K (b)

experimental results, however, which does not agree with the Binder theory. Such a q^{-2}-dependence at $x_i < 1$ has been observed by Schwahn et al. [17] for dPS/PVME and by us [18, 19] for DPB/PI, though the systems used in these works were entangled polymer blends. As described in Sec. I, we suggested that the q^{-2}-dependence at $x < 1$ results in the viscoelastic effects originating from the dynamical asymmetry between each component polymer in blends. Doi and Onuki [21] took into account the viscoelastic effects for dynamically asymmetric blends and derived the q-dependence of the Onsager kinetic coefficient which we shall define hereafter as $\Lambda_{ve}(q)$. The $\Lambda_{ve}(q)$ was derived at the limit of $qR_g \ll 1$ and is given by

$$\Lambda_{ve}(q) = \frac{\Lambda(0)}{1 + q^2\xi_{ve}^2} \tag{23}$$

with the viscoelastic length ξ_{ve} defined by

$$\xi_{ve} = \left(\frac{4}{3}\alpha\eta\Lambda(0)\right)^{1/2}, \tag{24}$$

where η is the zero shear viscosity of the mixture, and $\Lambda(0)$ is $\Lambda(q)$ in Eq.(20) in the limit of $q \to 0$ and expressed by

$$\Lambda(0) = \phi_A\phi_B(D_AN_A\phi_A + D_BN_B\phi_B)v_0/k_BT, \tag{25}$$

and α is dynamical asymmetry parameter defined by

$$\alpha = \frac{D_AN_A - D_BN_B}{D_AN_A\phi_A + D_BN_B\phi_B}. \tag{26}$$

Eq. (23) predicts q^{-2}-dependence for $\Lambda(q)$ at $q\xi_{ve} > 1$ even in the small q-limit of $qR_g \to 0$ where the dynamically symmetric blends with $\alpha = 0$ and hence $\xi_{ve} = 0$ shows a constant limiting value $\Lambda(0)$. As expressed in Eq. (24), ξ_{ve} depends on the dynamical asymmetry of each component in the blends, i.e., the parameter α as well as viscosity and Onsgaer kinetic coefficient $\Lambda(0)$. Symmetric blends satisfy $D_A = D_B$ and $N_A = N_B$, and hence $\alpha = 0$, giving rise to $\xi_{ve} = 0$ and $\Lambda_{ve}(q)$ becomes identical to $\Lambda(q)$ in Eq. (20). However for asymmetric blends with $\alpha \neq 0$, ξ_{ve} may become much larger than the radius of gyration of polymers. For example, in the case of semidilute polymer solution of PS/dioctylphthalate, where M_w of PS is 5.46×10^6 and the concentration of polymer is 6.0 wt% so that PS chains are extensively entangled, ξ_{ve} was found to reach about 1 μm whereas $R_g \cong 0.06$ μm = 60 nm. In the PS/PB blend studied in this work, although both PB and PS have no entanglements to cause the dynamical asymmetry, T_g of the neat PS (68.0 °C) is higher than the experimental temperatures, while T_g of the neat PB (−100 °C) is much lower than the experimental temper-

atures. This difference makes the asymmetry in self-diffusion coefficient and viscosity between PS and PB very large so that ξ_{ve} is also expected to be very large, much larger that R_g of PS and PB ($\sim$1 nm), strikingly affecting and suppressing $R(q)$ even in the q-region of $qR_g < 1$ (o $q < 1\ nm^{-1}$). Thus even in the observed q-region, $q\xi_{ve} \geq 1$ is satisfied, and as a consequence q^{-2}-dependence appears. This exciting effect is considered to be due to the viscoelastic effects arising from the asymmetry between PS and PB. We need to estimate the value of ξ_{ve} quantitatively from independent experiments with viscoelastic measurement and dynamic light scattering measurement with Eq. (24) to confirm further the proposed scenario of the q^{-2}-dependence in the future.

Conclusion

We measured relaxation processes of the concentration fluctuations in a single-phase state that was induced by a rapid pressure change for a non-entangeld polymer blend (polystyrene (PS)/polybutadiene (PB)) by using time-resolved small-angle X-ray scattering with synchrotron X-ray radiation. The changes in the scattered intensity with time during the relaxation processes were found to be approximated by the Cahn-Hilliard-Cook linearized theory (CHC). The CHC analysis yielded q^{-2}-dependence in the q-dependence of the Onsager kinetic coefficient $\Lambda(q)$ even at $qR_g \ll 1$, which cannot be predicted by the Binder theory. This anomalous q^{-2}-dependence is elucidated to originate from the viscoelastic effects arising from dynamical asymmetry associated with a difference in glass transition temperature of constituent components PS and PB.

Acknowledgment This work was financially supported in part by a Grant-in-Aid for Scientific Research (under Grant No. 13031053, 14045245, and 1540392) from the Ministry of Education, Science, and Culture, Japan.

References

1. Hashimoto T (1988) Phase Transitions 12: 47
2. Hashimoto T, Koga T, Jinnai H, Nishikawa Y (1998) IL NUOVO CIMENTO 20D: 1947
3. Hashimoto T (2004) Journal of Polymer Science Part B-Polymer Physics 42: 3027
4. Takenaka M, Hashimoto T (1992) J Chem Phys 96: 6177
5. Binder K, Stauffer D (1974) Phys Rev Lett 33: 1006
6. Binder K (1977) Phys Rev B15: 4425
7. Furukawa H (1985) Adv Phys 34: 703
8. Langer JS, Bar-on M, Miller HD (1975) Phys Rev A 11: 1417
9. Chou Y, Goldburg WI (1979) Phys Rev A 20: 2105
10. Rouse PE (1953) J Chem Phys 21: 1272
11. Zimm BH (1956) J Chem Phys 24: 269
12. Doi M, Edwards SF (1986) The theory of Polymer Dynamics. Clarendon Press, London
13. de Gennes PG (1980) J Chem Phys 72: 4756
14. Pincus P (1981) J Chem Phys 75: 1996
15. Jinnai H, Hasegawa H, Hashimoto T, Han CC (1993) J Chem Phys 99: 4845
16. Müller G, Schwahn D, Eckerlebe H, Rieger J, Springer T (1996) J Chem Phys 104: 5326
17. Schwahn D, Janssen S, Springer T (1992) J Chem Phys 97: 8775
18. Takenaka M, Takeno H, Hasegawa H, Saito S, Hashimoto T, Nagao M (2002) Physical Review E 65: 021806
19. Takenaka M, Takeno H, Hashimoto T, Nagao M (2003) Journal of Applied Crystallography 36: 642
20. Kawasaki K, Koga T (1993) Physica A 201: 115
21. Doi M, Onuki A (1992) J Phys II (France) 2: 1631
22. Onuki A, Taniguchi T (1997) J Chem Phys 106: 5761
23. Tanaka H (2000) J Phys Condes Matter 12: R207
24. Ferry JD (1980) Viscoelastic Properties of Polymers. Willey, New York
25. Kato M, Taniguchii Y (1995) Review of Scientific Instruments 66: 4333
26. Fujisawa T, Inoue K, Oka T, Iwamoto H, Uruga T, Kumasaka T, Inoko Y, Yagi N, Yamamoto M, Ueki T (2000) Journal of Applied Crystallography 33: 797
27. de Gennes PG (1979) Scaing Concepts in Polymer Physics. Ithaca, Cornell University
28. Sakurai S, Mori K, Okawara A, Kimishima K, Hashimoto T (1992) Macromolecules 25: 2679
29. Sakurai S, Izumitani T, Hasegawa H, Hashimoto T, Han CC (1991) Macromolecules 24: 4844
30. Cahn JW (1965) J Chem Phys 42: 93
31. Cook HE (1970) Acta Met 18: 297
32. Kawasaki K (1977) Progr Theor Phys 57: 826
33. Kawasaki K, Ohta T (1978) Progr Theor Phys 59: 362
34. Koga T, Kawasaki K (1991) Phys Rev A 44: R817
35. Binder K (1983) J Chem Phys 79: 6387
36. Gunton JD, Miguel MS, Sahni PS (1983) Phase Transitions 8: 269

Progr Colloid Polym Sci (2005) 130: 105–113
DOI 10.1007/b107347
Published online: 3 June 2005

Bernd Smarsly
Matthijs Groenewolt
Markus Antonietti

SAXS analysis of mesoporous model materials: a validation of data evaluation techniques to characterize pore size, shape, surface area, and curvature of the interface

B. Smarsly (✉) · M. Groenewolt
M. Antonietti
Max Planck Institute of Colloids and Interfaces, Am Muehlenberg 1, 14476 Potsdam-Golm, Germany
e-mail: smarsly@mpikg.mpg.de
Tel.: +49-331-5679508
Fax: +49-331-5679502

Abstract Two model mesoporous silicas with cylindrical and spherical mesopore architectures were analyzed with SAXS, using evaluation principles introduced by Ruland. The comparison with sorption measurements and transmission electron microscopy revealed that suitable SAXS analysis methods are a very precise technique to determine a whole range of structural properties of two-phase systems with mesostructure, namely the characteristic size of both phases, the surface area, the curvature of the phase boundary, and – applying the so-called κ-ι formalism – even the type of mesophases under consideration.

Keywords SAXS · Porod-law · Curvature · Kappa-iota · Silica · Mesopores

Introduction

In the recent decade, mesostructured materials with structural units on the nanometer scale have attracted a great deal of attention, both because of potential applications and the fundamental interest in the special properties of matter (confinement effects, etc.) [1]. Among the most prominent representatives of this new class of materials are the mesophases of block copolymers, nanoparticulate composites, and mesoporous materials. Another way which leads to an illustrative understanding of the partial exceptional physical properties of such materials is to point to the large internal interfacial area, amounting easily up to 1000 m^2/g, i.e. such material can be regarded as interface-dominated. Most of the macroscopic properties are therefore in delicate dependence on the size and shape of the constituting objects (pores, particles or aggregates) and their interfacial properties (especially energy and curvature), and suitable characterization techniques are inevitably needed.

The most important analytical techniques for the structural characterization of mesostructured materials are transmission electron microscopy (TEM), small-angle scattering (SAXS, SANS for X-rays and neutron, respectively) and – for porous materials-physisorption, and many of papers in the last decade have shown that analysis of such materials is incomplete without one of them. However, it is also regularly observed that a thorough TEM analysis suffers from the instability of soft matter in the electron beam, which restricts spatial resolution to some nanometers, and that sorption measurements are plagued by unspecific adsorption (e.g. on grains' external surface) and the inaccessibility of significant parts of the pore system.

In conclusion, SAXS often represents the only feasible technique for structural analysis. Up to now, SAXS is mostly used in the simplest mode: if several well-defined interference maxima (''Bragg peaks'') are observed, the data are evaluated in terms of basic concepts of classical crystallography, that is the assignment of the corresponding space group. If SAXS data lack pronounced features, the data are often not further used. This is a waste of accessible information, because it was already demonstrated decades ago by Tchoubar [2–4] and by Ruland in

various publications that for various materials of different chemical nature the concept of the chord-length distribution $g(r)$ provides a suitable tool to get a reasonable characterization of nanostructured materials lacking a high degree of mesoscopic order. The approaches developed by Ruland were shown to be suitable to characterize semicrystalline polymers with lamellar superstructures [5], microporous carbon [6–8], block copolymers [9] and polymer fibers [10,11] by SAXS data. The calculation of $g(r)$ from the raw scattering data is however not too simple, but Burger and Ruland [12] and later Smarsly [13] developed a novel and stable evaluation approach, which is based on the regularization of SAXS data by suitable analytical functions.

Beside characteristic length information, such as the thickness of both subphases, $g(r)$ also contains important topological information. In fact, Kirste and Porod demonstrated already 40 years ago that the second and fourth term in the series expansion of the correlation function $g(r)$ (whose second derivative is proportional to $g(r)$ at $r = 0$ respectively yield the absolute surface area [14] and a measure of the mean curvature of the interface plus, potentially, the genus of the mesostructure [15].

By normalizing those quantities to the characteristic length scales (also accessible from $g(r)$), Burger et al. introduced a generalization (''κ-ι'' formalism) where even on the base of one single broad scattering peak the scale invariant relative interface area ι and the scale invariant relative curvature κ could be determined [16]. As any κ-ι couple usually corresponds to one specific mesophase structure (except at phase boundaries), this principle inevitably allowed the determination of phase structure on the base of scattering curves without a sequence of distinct interferences. Grafically spoken, the κ-ι concept makes use of the fact that curvature and interface are local properties which quickly relax in their local energetic minima, whereas classical crystallography relies on larger ordered domains the formation of which might even be kinetically hindered.

The κ-ι concept was applied in several recent studies, e.g. on polypeptide-containing block copolymers [17, 18], and showed its usefulness, but a strict validation of this method with ideal model materials has not been performed. The accuracy of κ and ι especially depends on a correct evaluation of the asymptotic behavior of SAXS data at large scattering vectors. However, in this region of SAXS curves the scattering intensity is low and affected by several complex scattering effects. The importance of these scattering effects was demonstrated by Ruland in several detailed studies, especially on carbon [19,20] and block copolymers [21–24]. One important factor is the finite transition region between the two phases, leading to a multiplication of the theoretical curve by $H_z^2(s) = \exp(-2\pi^2 \mathrm{d}_z^2 s^2)$ with d_z equal to the width of the transition region, where an error function is used to describe the transition [21]. Interdigitation of the two interfaces leads to complex additive scattering contributions I_{inter} [9, 23]. Another important contribution are density fluctuations within the nanodomains (1D, 2D or 3D) leading to an additive scattering contribution [20, 21]. As demonstrated by Ruland for the case of block copolymers, all these contributions are important and have to be appropriately considered. Hence, the general asymptotic behavior of SAXS curves of two-phase systems (''Porod-law'', ignoring higher exponents of 1/s for simplicity) for an ideal pin-hole collimation is given by

$$I_{\mathrm{asym}}(s) = H_z^2(s)\mathrm{a}/\mathrm{s}^4 + I_{\mathrm{fluct}} + I_{\mathrm{inter}}. \quad (1)$$

It is evident that these factors can massively modify SAXS curves in the asymptotic regions and that any numerical analysis which is based on the asymptotic behavior has to carefully take into account these effects in determining κ and ι.

A suitable approach to test the general applicability and practicability of the κ-ι-concept is the SAXS investigation of materials for which the SAXS asymptote in eq. (1) is only weakly influenced by the effects described above. These requirements are quite ideally fulfilled by well-defined mesoporous materials with distinct pore morphologies (e.g. spherical or cylindrical pores), in particular mesoporous silicas. Since these systems consist of pores distributed in compact silica, they can be regarded as almost perfect ''two-phase systems''. The scattering contribution I_{inter}, which is significant for block copolymers, can be neglected, and the maximum width d_z of the interface between mesopores and silica is on the order of the size of a silica tetrahedron at maximum, i.e. < 0.3–0.4 nm. Furthermore, I_{fluct} is just a constant in case of SiO_2, because silica can be treated as an isotropic glass [20, 21]. It has to be pointed out that the aforementioned aspects do not apply for fractal-like silica aerogels with porosities of up to 99.9% because of the absence of real interfaces.

Meanwhile mesoporous silica is accessible in a practically complete range of pore sizes and pore geometries. The process which allows the best adjustment is called ''nanocasting'' and works via solification of the silica around an organic template with predescribed size and symmetry [25]. It was also shown that this technique allows adjustment and replication with Angstrom precision, i.e. this is presumably the most appropriate biphasic model system for the validation of high precision SAXS techniques [26].

In the present study, two types of high-quality mesoporous silicas were prepared using nanocasting. A mesoporous silica with cylindrical mesopores of diameter ca. 2.5–3 nm on a 2D hexagonal lattice was obtained from an ionic-liquid template (called ''CYL'' in the following) [27]. Using a novel block copolymer, porous silica with spherical mesopores of ca. 13–14 nm in

diameter was obtained (sample "SPHERE"), placed on a distorted cubic lattice [28–30]. These materials were studied in detail by nitrogen sorption, TEM and SAXS. The SAXS curves were then analyzed, using the algorithm described in ref. 13, to determine κ and ι. Because of the well-known mesostructures, their theoretical scattering curves and, thus, κ and ι can be predicted based on the lattice parameter, the pore size distribution and the porosity (i.e. volume fraction of pores). These theoretical values were then compared with those obtained from the SAXS analysis to check the validity of the evaluation. Furthermore, the SAXS curves were analyzed by fitting with scattering functions based on a Ruland-approach [31]. It will be validated with our model systems that this approach also allows for a precise determination of pore sizes and a meaningful comparison with the pore sizes obtained from nitrogen sorption and TEM. With such high precision SAXS data, it will then become possible to improve the adaption of sorption theories to such materials.

SAXS of two-phase systems – Theory

In general, the SAXS of a two-phase system is given by the Fourier-Transform of the characteristic function $\gamma(\vec{r})$

$$I(\vec{s}) = kF(\gamma(\vec{r})),$$

where $\vec{s}$ represents the scattering vector with $|s| = \frac{2}{\lambda}\sin(\theta)$ (λ wavelength, 2θ scattering angle). For a two-phase system, the radially averaged characteristic function is given by

$$\gamma(\vec{r}) = \gamma(r) = 1 - \frac{|\vec{r}|S}{4\phi(1-\phi)V} + \cdots = 1 - \frac{r}{l_p} + \cdots,$$

where l_p is the "Porod-length" (average chord-length). l_p is related to the porosity ϕ and the interfacial area S/V via

$$l_p = \frac{4\phi(1-\phi)V}{S}. \tag{2}$$

l_p is determined by the average segment lengths l_i of the two phases by

$$\frac{1}{l_p} = \frac{1}{l_1} + \frac{1}{l_2} = \frac{1}{\phi_1 l_2} = \frac{1}{\phi_2 l_1}.$$

The latter relationship allows the calculation of pore sizes (independently of a specific geometric model) and wall thicknesses on the basis of l_p.

The Porod-length itself is related to SAXS data via $\lim_{s\to\infty} s^4 I(s) = \frac{k}{2\pi^3 l_p}$, where k is the Porod invariant.

It was demonstrated by Méring, Tchoubar and Ruland that a suitable approach to describe the pore structure of materials with substantial disorder is the concept of the "chord-length distribution" $g(r)$, which is proportional to the second derivative of $\gamma(r)$: $g(r) = l_p\gamma''(r)$

$$g(r) = -8\int_0^\infty \left[1 - 2\pi^3 s^4 l_p k^{-1} I(s)\right] \frac{d^2\sin(z)}{dz^2 z} ds, \quad z = 2\pi rs. \tag{3}$$

If the higher orders of r in $\gamma(r)$ are taken into account, one obtains

$$\gamma(r) = 1 - \frac{r}{l_p} + \frac{r^3}{8l_p}\left(\langle H^2\rangle_S - \frac{1}{3}\langle K\rangle_S\right) + O(r^5) \tag{4}$$

where $\langle H^2\rangle_S$ and $\langle K\rangle$ are the mean and Gaussian curvature, respectively.

with

$$H^2 = (c_1 + c_2)^2/4 \quad K = c_1 c_2 \tag{5}$$

where c_i are the principal curvatures.

It is the idea of the κ and ι- phase diagram to classify the various morphologies (lamellar, 2D hexagonal, bcc, etc.) in terms of two normalized parameters, namely the parameter ι (interface area) and κ (curvature) [16]. The only precondition of the applicability, aside from the determination of the Porod asymptote, is the presence of at least one interference with long period L.

The parameters are defined by

$$\iota = \frac{S}{V}L$$
$$\kappa = L\sqrt{\langle H^2\rangle_S} = L\sqrt{8b}, \tag{6}$$

where b is the so-called "Kirste-Porod parameter".

It is evident that the parameter κ defined by the latter relationship is only related to the mean curvature, but does not take into account the Gaussian curvature. While for lamellar and cylindrical morphologies (even with undulations parallel among themselves and to the cylinder's axis) $K = 0$ (Gauss-Bonnet theorem), K does not vanish for cubic morphologies. In general, b then has to be renormalized by

$b = b^* + \frac{1}{3*8}\frac{4\pi(1-\Gamma)L}{\iota V}$, where Γ is defined as the Genus per unit cell. For the renormalization a specific type of unit cell has to be defined. For instance, if two spheres are within the unit cell, $\Gamma = -1$, while a single sphere has $\Gamma = 0$. The procedure for the renormalization is described in detail in ref. 16 and 32.

In conclusion, the parameters κ and ι can be extracted from $I(s)$ (providing L) and $g(r)$ (providing l_p as the first moment of $g(r)$) and $g'(0)$).

The κ–ι-diagram is shown in Scheme 1, illustrating the values for various morphologies.

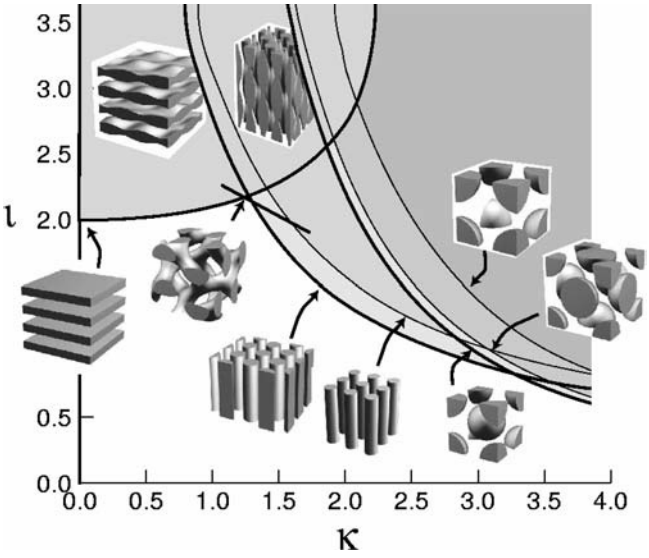

Scheme 1 κ–ι-diagram according to ref. 16

Experimental

The SAXS measurements were performed using a CuK_α rotating anode device (Nonius) with 3-pinhole collimation, equipped with a 2D image plate detector.

Nitrogen sorption isotherms were obtained from a Micromeritics ASAP instrument.

Transmission electron microscopy (TEM) images were taken with a Zeiss EM 912Ω at an acceleration voltage of 120 kV. Samples were ground in a ball mill and taken up in acetone. One droplet of the suspension was applied to a 400 mesh carbon-coated copper grid and left to dry in air.

Preparation of sample SPHERE: A solution of the block copolymer (see ref. 25) was prepared by dissolving 100 mg of the block copolymer in 1g of ethanol. 500 mg of the organic silica precursor tetramethoxysilane (TMOS) was added. After the dropwise addition of 250 mg aqueous hydrochloric acid (pH = 2), the sample was treated with ultrasound for 5 minutes, and then the alcohol was evaporated under gentle vacuum. The resulting gel was aged at 60 °C in a drying oven for 10 hours. Finally the dried silica gel was calcined in air at 550 °C for 5 hours.

Sample CYL: In a typical synthesis with C_{16}mimCl as template (see ref. 24), tetramethylorthosilicate (TMOS) was used as the sol-gel precursor. 0.36 g (1.05 mmol) of C_{16}mimCl was dissolved into 2 ml of EtOH, then mixed with 2.0 ml of TMOS under mild magnetic stirring. After homogenization of the mixture, 1.0 ml of aqueous solution of 0.01 M HCl as an acid catalyst was added dropwise. The resulting mixture was stirred for 30 min. Complete gelation was accomplished by leaving the sample in an open flask at room temperature C_{16}mimCl was removed from the silica by calcination of the sample at 550 °C for 5 h with a temperature ramp of 100 °C h^{-1} from room temperature to 550 °C. The final product was ground into powders for further characterization.

Results and discussion

TEM analysis

TEM images of the samples SPHERE and CYL are shown in Fig. 1. For SPHERE, a highly ordered array of almost close-packed spherical mesopores of ca. 13 nm in diameter is found, and the mesophases domains extend over several hundred nanometers each. Accordingly, the TEM images of CYL indicate regular arrays of long cylindrical mesopores with a pore diameter of ca. 2–3 nm and a length above 100 nm. Thereby, the microscopic study shows that the pore morphologies are well-defined in each case, being spheres for sample SPHERE and cylinders for sample CYL.

Nitrogen sorption

The porosities of CYL and SPHERE were analyzed by nitrogen sorption at T = 77 K (see Fig. 2), the data are summarized in Table 1. For physisorption data of sample CYL, see also ref. 24.

Based on the TEM and SAXS results, the sorption data were evaluated by the BJH approach in case of sample CYL and in terms of a recently developed NLDFT approach in case of sample SPHERE [33]. The sorption data of both materials support the interpretation that they are well-defined mesoporous materials with distinct pore sizes. From the overall porosities, the volume fraction of mesopores was calculated assuming a density of amorphous silica of 2.2 g/ml.

SAXS analysis

SAXS fitting based on model scattering functions

Fig. 3 shows the SAXS curves of the samples CYL and SPHERE. The SAXS pattern of CYL is characteristic of a 2D hexagonal lattice with the interference maxima obeying the theoretical ratio 1: sqrt(3): 2. While weak higher order peaks are visible at higher magnification, the bare SAXS data already indicate a certain degree of lattice distortion. However, the SAXS pattern is ideal for a detailed κ-ι analysis, because the curve shows an extended Porod asymptote at larger s. Similarly, the SAXS curve of SPHERE reveals a sequence of several interference maxima, attributable to a cubic pore arrangement, while it is not possible to distinguish between an fcc or hcp packing. Also in this case, the asymptote of the SAXS curve is in almost perfect agreement with the Porod law, thus representing an ideal candidate for a mesoporous model system with

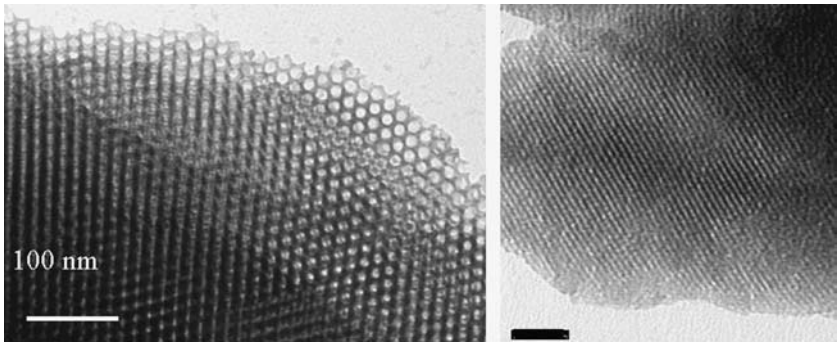

Fig. 1 TEM images of SPHERE (left image) and CYL (right image). The scale bar for sample CYL is 25 nm

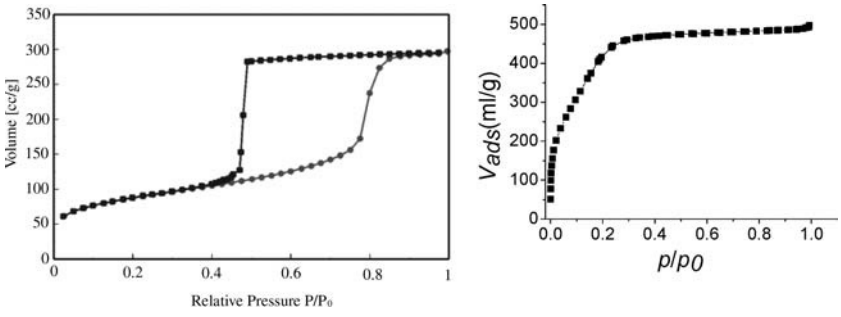

Fig. 2 Nitrogen sorption isotherm at 77 K for sample SPHERE (left) and CYL (right)

Table 1 Porosity parameters for the two samples under study. The SAXS surface areas were obtained from eq. 2

Sample	Pore size (adsorption) [nm]	Pore size SAXS fitting, and variance σ_R [nm]	BET surface area [m^2/g] / SAXS	Pore volume [cm^3/g]	Pore volume fraction ϕ
CYL	2.6	2.8 ± 0.2	1600/1450	0.76	0.62
SPHERE	13.8	13.9 ± 0.2	320/250	0.59	0.56

spherical pores. The presence of the Porod-law behavior at moderate values of s in both cases proves the high quality of these mesosporous silicas in terms of the pore uniformity and, additionally, excludes the presence of significant amounts of undesirable micropores, which are frequently observed in mesoporous materials and which would aggravate the SAXS analysis [34, 35].

The SAXS data were then fitted using an approach used previously by Ruland [31, 34] for the evaluation of SAXS data of mesostructured materials, constituted of objects with a finite size distribution (''polydispersity''), placed on a certain lattice (cubic, 2D hexagonal etc.)

$$I(s) \propto \left(\left\langle |F(s)|^2 \right\rangle + |\langle F(s) \rangle|^2 \left(\frac{|Z|^2}{N}(s) - 1 \right) \right) \qquad (6)$$

F are the form factors of the corresponding objects (spheres, cylinders) and $\frac{|Z|^2}{N}$ is the lattice factor. For $\frac{|Z|^2}{N}$, Ruland developed suitable approaches to include the effects of both lattice distortions and finite domain sizes. $\langle\ \rangle$ stands for the number average of the object sizes. While this expression corresponds to the so-called ''Laue-scattering'' in general, it was Ruland who developed suitable evaluation procedures for the SAXS of mesoscopic materials and applied them to mesoscopic materials such as block copolymers [31] and mesoporous materials [34]. The principal idea is to fit experimental SAXS data by eq. 6, using physically meaningful parameters such as the average diameter $\bar{R}$ of the objects, its variance σ_R, the average lattice parameter $\bar{a}$ and its variance σ_a. Also, it should be emphasized that Ruland developed suitable approximations, facilitating the computational implementation of the polydisperse form factors F [22]. Fig. 4 shows the evaluation of the SAXS of SPHERE using eq. 6, similar to ref. 31 and ref. 34, using an fcc lattice for $\frac{|Z|^2}{N}$ and Lorentz profiles for the shape of the interferences. Since the TEM study indicated a large size of the mesostructured domains, it was assumed that the integral width of the interferences is only determined by lattice imperfections, thus increasing with s (see the procedure described below for CYL). It has to be pointed out that the fitting is similarly good using an hcp lattice model. It is clearly

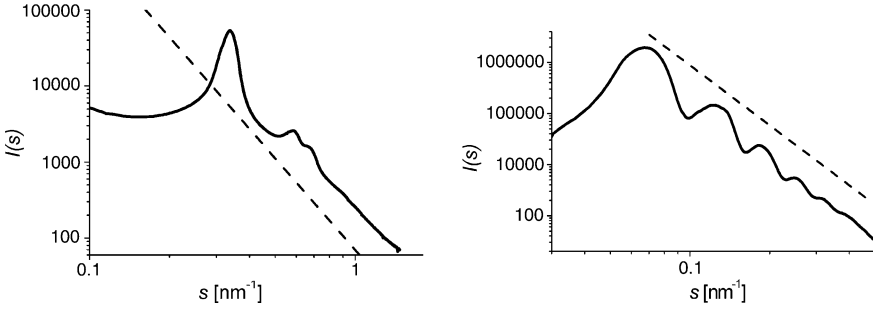

Fig. 3 SAXS curves of samples CYL (left) and SPHERE (right). The porod asymptote is indicated by dashed lines in both cases

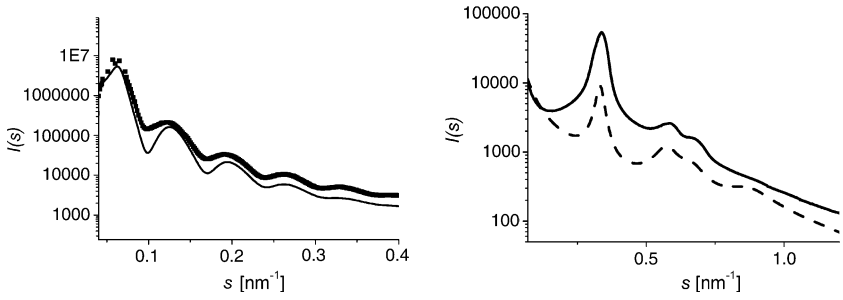

Fig. 4 SAXS analysis of sample SPHERE (left) and CYL (right) using eq. 6

seen that the approach in eq. 6 is able to describe the experimental data reasonably over the full range of scattering vectors in terms of a system of spherical pores with finite size distribution, providing a pore diameter of 13.9 nm and $\sigma_R = 0.2$ nm. For the interferences of the lattice factor Lorentz profiles were used with $\bar{d}_{111} = 17$ nm and a variance $\sigma_{111} = 0.3$ nm. Evidently, this analysis is in excellent agreement with the sorption analysis, thereby proving the applicability of the approach.

A comparable approach was used to evaluate the SAXS data of sample CYL. In this case, it has to be taken into account that 2D hexagonal array of cylinders is anisotropic, thus requiring the calculation of the radial average for the SAXS of such mesopores. If I_2 denotes the SAXS in the plane s_{12} (perpendicular to the cylinder axis), for sufficiently long cylinders the radially averaged SAXS is given by

$$I(s) \propto \frac{1}{S} I_2(s).$$

Hence, *I(s)* can be calculated similarly to eq. 6, using expressions for the form factors according to ref. 22. Compared to sample SPHERE, the interferences are separated more distinctly. For the lattice factor, a suitable approach was used to take into account that the integral width of the reflections is determined both by the finite domain size and also lattice distortions: for the shape of the interferences I_{hk} we have chosen

$$I_{\mathrm{hk}}(s) = \frac{B_{\mathrm{hk}}(s_j)}{B_{\mathrm{hk}}(s_j)^2 + \pi^2 s^2},$$

and the integral width B_{hk} of the interferences at $s = s_{\mathrm{j}}$ was calculated by

$$B_{hk}(s_j) = \frac{1}{d_{10}N} + s_j^2 \pi^2 \sigma_{10}^2 / \mathrm{d}_{10}^3,$$

where σ_{10} is the variance of $d_{10} = \bar{a}\ 2/\mathrm{sqrt}(3)$ with $\bar{a}$ equal to the lattice constant of a 2D hexagonal lattice.

It is seen (Fig. 4) that also in this case in eq. 6 provides a reasonable evaluation of the experimental SAXS data ($\bar{a} =$ 3.5 nm, $\sigma_{10} = 0.35$ nm). The values for the pore sizes of both CYL and SPHERE are shown in Table 1.

κ-ι analysis of the SAXS data

In the following, the SAXS data of samples CYL and SPHERE are further analyzed using the concept of the chord-length distribution, aiming at both the verification of pore sizes and the determination of *κ-ι* curvature parameters. As pointed out, the *κ-ι* formalism requires the presence of the Porod law a reasonable statistics in the high *s* region. The validity of the experiment and the analysis is demonstrated in Fig. 5. The s^4–*I*-plot levels off to a plateau at large *s*, after substraction of a small additive background scattering I_{fluct}. Obviously, the rotating anode device used was able to produce scattering data of reasonable intensity also at high *s*. It is important to note that the strong SAXS intensity at large *s* is also attributable to the significant electron density contrast between the matrix and the pores, thus further indicating that the present materials are highly suitable for this kind of analysis. This asymptotic behavior is in good agreement with the ideal Porod asymptote s^{-4}, thus allowing for a meaningful *κ-ι*

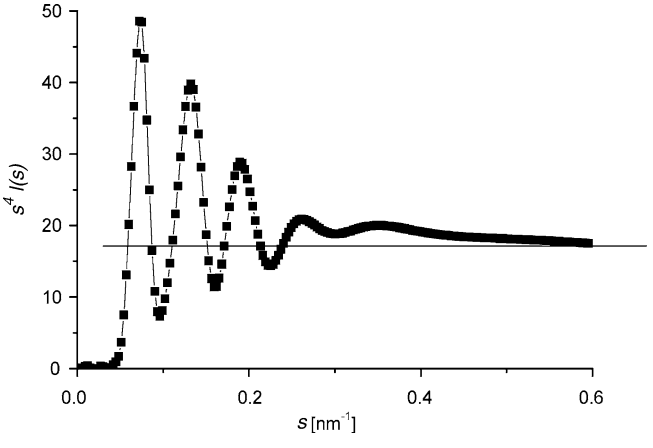

Fig. 5 s^4-I plot for sample SPHERE. Squares: experimental data. Solid line: Fitted curve according to the regularization algorithm in ref. 13

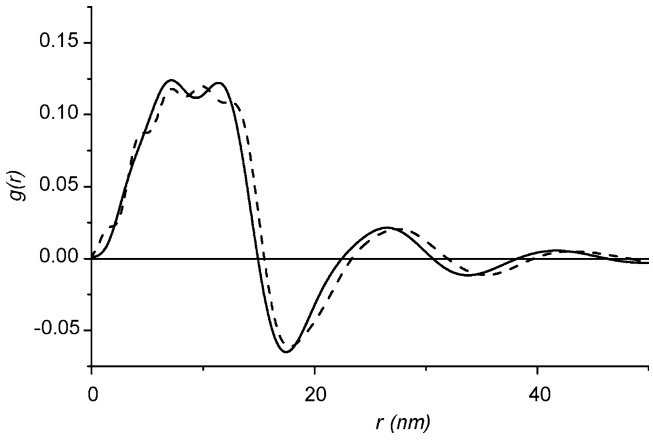

Fig. 6 Chord-length distribution $g(r)$ of sample SPHERE, obtained from the algorithm in ref. 13 (solid line). Dashed line: $g(r)$obtained as the transform according to eq. 3 of the fitting in Fig. 4

analysis. Recently, also Ciccariello reported a detailed study for the analysis of SAXS data of cylindrical and spherical domains in the asymptotic region of scattering data [36].

In principle, the κ-ι formalism is only applicable if $g(0) = 0$, because otherwise $\gamma(r)$ would contain an r^2 term. Without the constraint $g(0) = 0$, for the two samples under study $g(0)$ was slightly positive ($g(0) < 0.01$). Within the margin of errors, it was therefore justified to assume $g(0) = 0$ to allow for the calculation of κ. Fig. 6 shows the chord-length distribution $g(r)$ of sample SPHERE, obtained from the algorithm in ref. 13. It is seen that the first maximum at $r = 6.4$ nm is attributable to the pore wall thicknesss, which is in reasonable agreement with the value obtained from the lattice parameter and pore size from the SAXS fitting in section 3.1. If the second maximum is interpreted as originating from the mesopores themselves, one obtains a mesopore size of ca. 12.5 nm, which is in relatively good agreement with the analysis shown above. Hence, it is even possible to extract meaningful pore sizes from $g(r)$ itself, if the two contributions are separable. In this context, it has to be emphasized that the determination of mesopore sizes above 10 nm by physisorption can still have an error of 20%.

In the following, we are mainly interested in the κ-ι analysis. As described recently, the Porod length l_p (which is required for the determination of κ and ι) can be obtained with good precision as the first moment of $g(r)$ based on ref. 13. On the contrary, κ (determined from $g'(0)$) might be more heavily affected by numerical uncertainties. In the present case, $g'(0)$ was obtained directly from $g(r)$ by determining its slope at $r = 0$. Based on this procedure, for sample SPHERE we obtain $\kappa = 3.3 \pm 0.5$ after renormalization for an fcc lattice and $\iota = 2.6 \pm 0.2$. If the renormalization is not carried out, κ has an unrealistically small value. It was pointed out by Burger that this procedure provides a suitable criterion to exclude other morphologies (cylindrical) [16]. Taking into account the consideration concerning the mean and average curvature, as pointed out in ref. 16, these values correspond to a cubic phase in the κ-ι diagram and strongly deviate from any other pore structure, which is in agreement with TEM and the aforementioned SAXS analysis. However, based on the renormalization of the Kirste-Porod parameter according to ref. 16, it is not possible to unambiguously determine the nature of the phase (bcc, fcc, hcp), because a major uncertainty originates from the numerical determination of $g'(0)$.

In order to obtain theoretical values for κ and ι for sample SPHERE, first these two values were theoretically calculated assuming monodisperse spheres and an fcc/hcp lattice without distortion, based on the average size of the spheres and the lattice parameter. From this simple calculation, we obtain $\iota = 0.8$ and $\kappa = 3.1$. Evidently, especially the ι deviates significantly from the values obtained from $g(r)$. In order to take into account the polydispersity and the lattice distortions, the fitting curve in Fig. 4 was numerically transformed to the corresponding $g(r)$, which was then evaluated as described above to obtain κ and ι. By this procedure, the effects of polydisperse pores and lattice disorder on κ and ι were automatically taken into account. Interestingly, the theoretical $g(r)$ obtained in this way differs slightly at $r < 20$ nm in the general shape of the curves. These differences might be due to fine deviations of the real mesopores from a perfectly spherical shape. The corresponding values for κ and ι are listed in Table 2. Obviously, a reasonable agreement is observed with the experimentally determined values, showing a deviation of only ca. 10–15%. Therefore we speculate that the aforementioned deviation in κ assuming monodisperse pores could be attributable to the finite polydispersity of the mesopores.

A similar procedure was carried out for sample CYL (see Table 2). Although $g(r)$, calculated from the transformation of the fitted $I(s)$ curve in Fig. 3 [13], is slightly different a small r, the agreement between both curves is reasonable. The deviation between the curves in the region of the first maximum in $g(r)$ can be attributed to uncertainties of the algorithm a large s or deviations from a perfect cylindrical shape. Similar to sample SPHERE,

Table 2 κ and ι values for the two samples. The κ value for sample SPHERE is normalized for an fcc lattice. The "theoretical" values of the parameters were obtained from transforming the fitted curves in Fig. 4 to $g(r)$

Sample	$l_{p,exp}$[nm]/$l_{p,theo}$	$\kappa_{exp}/\kappa_{theo}$	ι_{exp}/ι_{theo}	Phase
CYL	0.97/1.1	2.7/2.8	2.6/2.1	2D hex
SPHERE	5.23/5.5	3.3/3.0	2.4/2.2	fcc - hcp

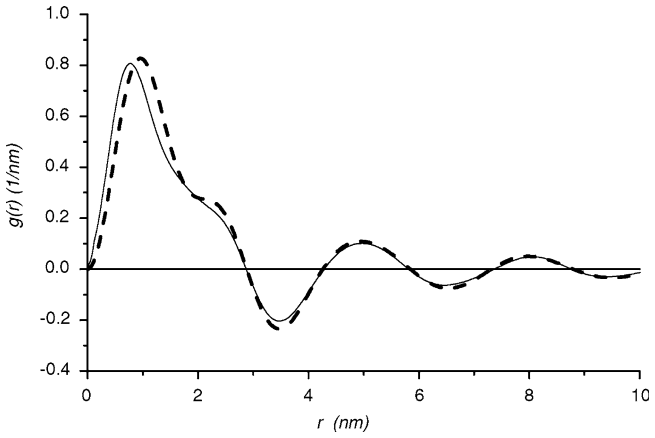

Fig. 7 Chord-length distribution $g(r)$ of sample CYL (solid line), obtained from the algorithm in ref. 13. Dashed line: $g(r)$ obtained as the transform according to eq. 3 of the fitting in Fig. 4

already the bare shape of the chord-length distribution allows for a semi-quantitative determination of pore sizes and wall thicknesses. From $g(r)$ of sample CYL we obtain a pore size of ca. 2.6 nm (second maximum) and a wall thickness of ca. 1.2 nm, both being in good agreement with the aforementioned SAXS analysis and sorption data.

Summarizing the results of the application of the κ-ι formalism, interesting trends can be observed for the two samples. In both cases, the ι -values are relatively high, indicating higher surface area than theoretically expected. Possible reasons are undulations of the cylinders or additional micropores in the matrix. Since the sorption data did not reveal any hint for micropores, we speculate that the cylinders may not be perfectly smooth, but might show certain variations of the cylinder radius along its axis. Similarly, local deformations of the spherical mesopores would contribute to a higher surface area in case of sample SPHERE.

Conclusions

Analyzing the data of two model mesoporous silica with cylindrical and cubic symmetry, it was shown that SAXS using evaluation principles introduced by Ruland is a very precise technique to determine a whole range of structural properties of two-phase systems with mesostructure, namely the characteristic size of both phases, the surface area, the curvature of the phase boundary, and – applying the κ-ι formalism- even the type of mesophases under consideration. Comparison of the data determined with SAXS with data of sorption isotherms and electron microscopy gave an almost perfect agreement, thus validating the applied technique also for systems with lower structural definition. It is interesting to note that even the surface areas can be reasonably extracted from the analysis in terms of the concept of chord-length distributions.

We regard this tool to be of extraordinary importance for all nanocomposite materials where application of electron microscopy is restricted, e.g. for beam sensitive materials or systems with structural elements below TEM resolution.

As the evaluation of sorption data of mesoporous materials in certain ranges of pore size is also heavily under discussion, well defined silica materials fully characterized by SAXS are expected to be of great use as reference standards to improve numerical evaluation procedures.

References

1. Antonietti M, Ozin GA (2004) Chem Eur J 10: 29
2. Méring J, Tchoubar C (1968) J Appl Crystallogr 1: 153
3. Tchoubar-Vallat D, Méring J (1965) C. R. Hebd. Seances Acad Sci 26: 3096
4. Méring J, Tchoubar-Vallat D (1966) C. R. Acad. Sci. Paris 262: 1703
5. Stribeck N, Ruland W (1978) J Appl Cryst 11: 535
6. Perret R, Ruland W (1968) J Appl Cryst 1: 308
7. Perret R, Ruland W (1969) J Appl Cryst 2: 209
8. Perret R, Ruland W (1971) J. Appl. Cryst. (1972) 5: 183
9. Wolff T, Burger C, Ruland W (1994) Macromolecules 27:3301
10. Perret R, Ruland W (1970) 3: 525
11. Thüneman AF, Ruland W (2000) Macromolecules 33: 2626
12. Burger C, Ruland W (2001) Acta Crystallographica Section A 57: 482
13. Smarsly B, Wolff T, Antonietti M (2002) J. Chem. Phys. 116: 2627
14. Porod G (1951) Kolloid Z. Z. Polym. 124: 83; Porod G (1952) Kolloid Z. Z. Polym. 125: 108.
15. Porod G, Kirste R (1962) Kolloid Z. Z. Polym. 184: 1
16. Micha MA, Burger C, Antonietti M (1998) Macromolecules 31: 5930
17. Schlaad H, Kukula H, Smarsly B, Antonietti M, Pakula T (2002) Polymer 43: 5321
18. Schlaad H, Smarsly B, Losik M (2004) Macromolecules 37: 2210
19. Ruland W (2001) Carbon 39: 32
20. Ruland W (1974) J. Appl. Cryst. 7: 383
21. Ruland W (1971) J. Appl. Cryst. 4: 70
22. Siemann U, Ruland, W (1982) Coll. Polym. Sci. 260: 999
23. Ruland W (1987) Macromolecules 20: 87
24. Ruland W (1977) Colloid and Polymer Science 255: 417
25. Polarz S, Antonietti M (2002) Chemical Communications 22: 2593
26. Smarsly B, Polarz S, Antonietti M (2001) J. Phys. Chem. B 105: 10473
27. Smarsly B, Kuang D, Antonietti M (2004) Coll. Polym. Sci. 282: 892
28. Thomas A, Schlaad H, Smarsly B, Antonietti M (2003) Langmuir 19: 4455
29. Groenewolt, M, Thomas A, Antonietti M (2004) Macromolecules 27: 4360

30. Groenewolt M, Antonietti M, Polarz S (2004) Langmuir 20: 7811
31. Brandt M, Ruland W (1996) Acta Polymer. 47: 1996
32. Micha MA, PhD Thesis, 1997.
33. Ravikovitch PI, Neimark AV (2001) Microporous Mesoporous Mat, 44–45: 697
34. Smarsly B, Göltner C, Antonietti M, Ruland W, Hoinkis E (2001) J. Phys. Chem. 105: 831
35. Goltner CG, Smarsly B, Berton B, Antonietti M (2001) Chem. Mater. 13: 1617
36. Ciccariello S, Sobry R (1999) J. Appl. Cryst. 32: 892

Progr Colloid Polym Sci (2005) 130: 114–126
DOI 10.1007/b107329
Published online: 3 June 2005

Jong Kahk Keum
Christian Burger
Benjamin S. Hsiao
Rajesh Somani
Ling Yang
Benjamin Chu
Rainer Kolb
Hongyu Chen
Ching-Tai Lue

Synchrotron X-ray scattering studies of the nature of shear-induced shish-kebab structure in polyethylene melt

Abstract Synchrotron small-angle X-ray scattering (SAXS) and wide-angle X-ray diffraction (WAXD) have been utilized to elucidate the nature of shear-induced shish-kebab structures at the early stages of crystallization in a binary blend, containing 5 wt% of high-density polyethylene (HDPE) and 95 wt% of linear low-density polyethylene (LLDPE, $\bar{M}_w = 120$ kg/mol). The HDPE component possessed a bimodal molecular weight distribution with weight-average molecular weights M_w of 99 kg/mol and 1,100 kg/mole, respectively. X-ray results indicated that the crystallization kinetics and molecular orientation of the blend were significantly enhanced under shear as compared to LLDPE, even though the blend contained only a low concentration of high molecular weight HDPE chains (ca. 1 wt% of $\bar{M}_w = 1{,}100$ kg/mol above the overlap concentration, $c^* = 0.5$ wt%). The Avrami exponent of the blend, $n = 1.9$, derived from the WAXD crystallinity evolution under shear, suggested that the two-dimensional (2D) kebabs are developed under diffusion-controlled and spontaneous nucleation conditions. The Avrami exponents were found to decrease with the increase in shear duration time (strain). The corresponding SAXS patterns showed a meridional streak, which can be modeled by a shish-kebab structure containing cylindrical symmetry along the shish axis and polydispersities in diameter, thickness and long period of kebabs. The shish-kebab model was formulated in a closed analytical form under the assumption of independent statistics. Furthermore, Ruland's method to separate the effects of size and orientation, usually used for the equatorial streaks, was applied to the meridional streak for the first time, under the assumption that the widths of the distributions add as in Lorentzian-type distributions. The fitted mean diameter of kebabs using our shish-kebab model was found to be consistent with the value obtained by using the Ruland's streak method. The radial growth rate, G, calculated from the kebab evolution initially followed the relationship $G \propto t^{-1/2}$, which confirmed the diffusion-controlled growth with spontaneous nucleation in the polymer blend.

Keywords SAXS · WAXD · shear · crystallization · shish-kebab · polyethylene

Dedicated to Professor W. Ruland on his 80th birthday

J. K. Keum · C. Burger (✉)
B. S. Hsiao · R. Somani · L. Yang
B. Chu
Department of Chemistry,
State University of New York at Stony Brook, Stony Brook, NY 11794-3400, USA
E-mail: cburger@sunysb.edu
Tel.: +1-631-6321315; +1-631-6327793
Fax: +1-631-6326518

Present address: R. Kolb · H. Chen
C.-T. Lue
Univation Technology Inc.,
Baytown, TX 77522, USA

R. Kolb · C.-T. Lue
ExxonMobil Chemical Company,
Baytown, TX 77520, USA

H. Chen
The Dow Chemical Company,
Freeport, TX 77541, USA

Introduction

Although the subject of flow-induced crystallization has been extensively investigated, the exact nature of the shish-kebab formation and the early stages of crystallization are still unclear [1–6]. For example, it has been well documented that the shish-kebab structure contains oriented lamellae (kebabs) arranged perpendicularly to

the central shish backbone. However, the mechanisms proposed for the formation of such a structure vary quite extensively. Some groups argued that the folded chain lamellae are originated from free chain ends (cilia) near the central shish backbone surface or from protrudes of the central backbones [1, 2]. Some recent simulation works suggested that the flow-induced shish-kebab structure is closely related to the *coil-stretch* transition of isolated polymer chains under flow, where the stretched chains form extended chain crystals (shish) while the coiled chains collapse and can be adsorbed onto the shish and form kebabs [3]. These different mechanisms cannot be easily verified by microscopic techniques (e.g. atomic force microscopy, AFM [5, 6], or transmission electron microscopy, TEM [7, 8]), as their *in-situ* examinations under flow are very difficult to carry out.

Recently, synchrotron small-angle X-ray scattering (SAXS) and wide-angle X-ray diffraction (WAXD) [9, 12] have been proven to be very useful to extract real time information of the shish-kebab formation under flow [10–15]. However, the lack of proper schemes for the analysis of scattering data continues to hinder the progress that can be made on this subject, which forms the basis for this work.

In this study, we have devised a simple shish-kebab model, based on the observed microscopic images in real space [5–8] and X-ray data in reciprocal space [11–13, 15], to fit the real-time SAXS data, whereby the main scattering feature and the scattered intensity are arisen from the spatial arrangement of kebabs (lamellae) with a disk-like geometry. The model consists of polydispersities in diameter of disk-like kebabs (lamellae), lamellar thickness, and lamellar long period. Our goal is to extract the structural information of the shish-kebab entity formed under flow at the initial crystallization stages and, thus, to understand the shish-kebab formation mechanism. The chosen sample is a miscible high-density polyethylene (HDPE, 5 wt%) and linear low-density polyethylene (LLDPE, 95 wt%) binary blend. HDPE is a long-chain branched homopolymer with fast crystallization rate and high crystallinity, while LLDPE is a short-chain branched copolymer (hexene) with slow crystallization rate and low crystallinity. Thus, the initial formation of the shish-kebab structure is primarily dominated by the HDPE component in the blend, especially the small fraction of high molecular weight HDPE chains (their relaxation times are exceedingly long) under the flow conditions.

Experimental section

Materials and preparations

A small amount of HDPE (5 wt%) was melt blended with LLDPE (95 wt%) to prepare the HDPE/LLDPE binary blend. The GPC profiles of HDPE and LLDPE before blending are illustrated in Figure 1. The corresponding molecular weight information is summarized in Table 1. The HDPE sample was made by the Ziegler-Natta method and possessed a bimodal molecular weight distribution. The weight-averaged molecular weight, $\bar{M}_w$, of each distribution in HDPE was 99 kg/mol (ca. 80 wt%) and 1,100 kg/mol (ca. 20 wt%), respectively (the two HDPE chain distributions were estimated by separating the GPC profile into two Gaussian functions). The LLDPE sample was synthesized by the metallocene method and contained 2.4 mol % of hexene comonomer ($\bar{M}_w$ of LLDPE was 120 kg/mol). Thus, in the HDPE/LLDPE blend (5 wt% of HDPE and 95 wt% of LLDPE), the percentage of the high molecular weight HDPE chain distribution ($\bar{M}_w$ = 1,100 g/mol) was about 1.0 wt%. The corresponding overlap concentration, c^*, of this molecular weight component could be estimated by the expression [16, 17]:

$$c^* \approx \frac{\bar{M}_w}{\left[\left\langle R_g^2 \right\rangle^{1/2}\right]^3 N_a} \tag{1}$$

with $\langle R_g^2 \rangle^{1/2}$ being the root-mean-square radius of gyration and N_a being the Avogadro's number. The characteristic ratio, $\langle R_g^2 \rangle^{1/2} / \bar{M}_w^{1/2}$ was 0.46 for the high molecular weight HDPE population ($\bar{M}_w$ = 1,100 g/mol) calculated based on SANS measurements [18]. The concentration (1 wt%) of the high molecular weight HDPE chains in the blend will be near the range of the overlap concentration, c^* (i.e., 0.5–2 wt% in the melt, depending if one considers the use of $4\pi/3$ factor) estimated by Equation (1). We are particularly interested in the role of the high molecular species ($\bar{M}_w$ = 1,100,000 g/mol) in the blend because of their long relaxation times, which would lead to the formation of nucleating scaffolds under flow conditions [13].

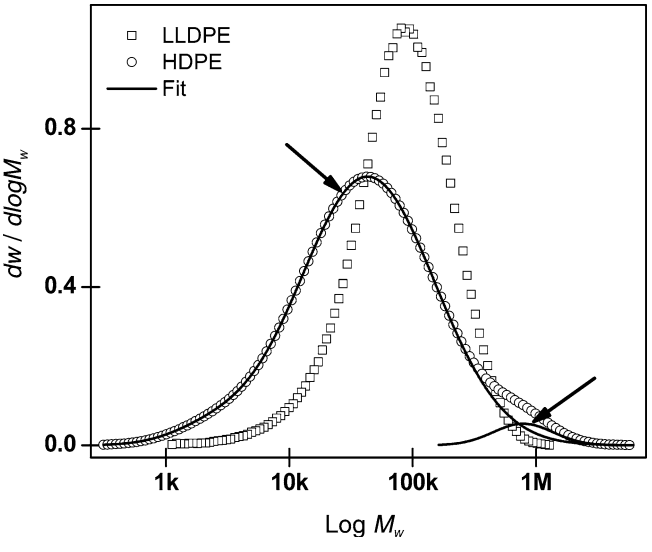

Fig. 1 GPC profiles of pure LLDPE and HDPE before blending. The GPC profile of pure HDPE indicates a bimodal molecular weight distribution (labeled by arrows), which was deconvoluted to estimate the fraction of each component (Table 1). 5 wt% of HDPE was melt-blended with LLDPE to prepare the HDPE/LLDPE binary blend, which GPC profile was very similar to that of LLDPE

Table 1 Molecular weight information of HDPE and LLDPE, where $\bar{M}_w$, $\bar{M}_n$ and MWD represent the weight average molecular weight, the number average molecular weight and the molecular weight distribution

Samples	Density, ρ (g/cc)	$\bar{M}_w$ (kg/mol)	$\bar{M}_n$ (kg/mol)	MWD ($\bar{M}_w/\bar{M}_n$)
LLDPE[a]	0.920	120	46	2.2
HDPE[b]	0.964	130	15	9.1

[a]Polymerized with 2.4 mol % of hexene comonomer using metallocene catalyst
[b]Polymerized with Ziegler-Natta catalyst, which contained a bimodal molecular weight distribution ($\bar{M}_w$ = 99 kg/mol at about 80 wt% and 1,100 kg/mol at about 20 wt%)

Rheo-SAXS, Rheo-WAXD and DSC measurements

A modified Linkam CSS-450 shear stage was utilized to perform *in-situ* rheo-SAXS and rheo-WAXD measurements. Polymer films with 0.5–0.8 mm thickness were prepared by compression molding at 160 °C. Samples in the form of a ring (inner and outer diameters were 10 and 20 mm, respectively) were cut from the molded films for rheo-SAXS or rheo-WAXD measurements. A diamond disc and a Kapton film were used as X-ray windows and were placed along the X-ray path. The sample was placed in the gap between the two X-ray windows. Shear flow was applied to the sample by rotating the bottom window while the top window was maintained stationary. The shear experiments were carried out at 116 °C with two duration times: 5 and 10 s at the shear rate of 60 s^{-1}. The detailed experimental information has been described elsewhere [11].

SAXS and WAXD measurements were carried out at the X27C beamline in the National Synchrotron Light Source (NSLS), Brookhaven National Laboratory (BNL). The wavelength of the X-ray was 1.366 Å. 2D SAXS and WAXD patterns were collected with a MAR CCD X-ray detector (MARUSA) with the resolution of 1024×1024 pixels (pixel size = 158.44 μm). The data collection time and the data storage time were 15 and 5 s, respectively. The total data collection times were 30 minutes (i.e., 90 frames). The sample to detector distances were calibrated with silver behenate for SAXS (1863 mm) and with Al_2O_3 (aluminum oxide) for WAXD (123 mm), respectively. All X-ray images were corrected for sample absorption and synchrotron beam fluctuations using an ionization chamber and a pinhole photodiode placed before and after the sample, respectively. In addition, X-ray images of completely molten samples were also collected as references.

DSC measurements were carried out using a Perkin-Elmer DSC 7 instrument. The cooling rate was 10 °C/min. All DSC runs were carried out under a nitrogen gas flow to minimize the sample oxidation. An indium standard was used to calibrate the temperature.

The WAXD crystallinity index, which is proportional to crystallinity and termed 'crystallinity' hereafter, was estimated from Equation 2 by separating the integrated diffraction intensity profiles from 2D WAXD images corrected for effects of the curvature of the Ewald sphere (Fraser correction) into amorphous and crystal phases [19] using the PeakFit™ program (AISN Software Inc.). (Note that we assumed the shear-induced shish-kebab structure had a fiber symmetry, with the shish axis along the flow direction). The Voigt function was used for this purpose, as it gave the best fitting results for the WAXD data.

$$X_C = \frac{I_c}{I_t},\ I_t = I_c + I_a \tag{2}$$

where I_c and I_a represent the diffracted intensities of the crystal phase (sum of (110) and (200) reflections) and of the amorphous phase, I_t is the total diffraction intensity due to the sum of amorphous and crystal phases.

Results and discussions

DSC results (quiescent crystallization)

DSC cooling scans, exhibiting the crystallization exotherms, for LLDPE and HDPE/LLDPE (5/95) samples are shown in Figure 2. The HDPE/LLDPE blend exhibited a single narrow exotherm with a peak temperature around 104 °C, which was higher than that of LLDPE (ca. 101 °C). As no sign of two discrete exotherms or even peak broadening was seen, DSC results indicated that the two components in the blend (HDPE and LLDPE) were completely miscible at the molecular level and could co-crystallize. The increase of the crystallization temperature in the blend suggests that the added HDPE component facilitates the crystallization of the LLDPE matrix [20]. This can be understood since the HDPE is a homopolymer with faster crystallization rate and higher crystallization temperature, which would nucleate the LLDPE matrix. Under quiescent crystallization conditions, the crystallization behavior of the blend is probably dominated by HDPE chains in the lower molecular weight distribution (i.e., 4 wt% of $\bar{M}_w$ = 99 kg/mol). This behavior has been reported before, where the crystallization temperature was found to decrease with the increase in the LLDPE content in HDPE/LLDPE blends [21].

Rheo-WAXD results

Selected 2D WAXD patterns and azimuthal intensity profiles taken at the (110) reflection of LLDPE and HDPE/LLDPE blend, respectively, at different times after shear are illustrated in Figures 3(a)–3(d). The chosen WAXD patterns represent the first images exhibiting the crystalline (110) reflections of the orthorhombic unit cell of PE in these two samples after the cessation of shear. The initial patterns prior to shear showed only an amorphous halo, indicating that both samples were completely amorphous in the molten state without crystalline ordering and preferred orientation. In Figure 3, the blend exhibited well oriented (110) reflections around the equator, while LLDPE showed only a ring-like (110) reflection with poor orientation. This observation can be explained as follows. In HDPE/LLDPE blend, the HDPE chains in the high molecular weight distribution ($\bar{M}_w$ = 1,100 kg/mole) possess very long relaxation times (the relaxation time is proportional to $M^{3.4}$), thus they will remain oriented even after shear

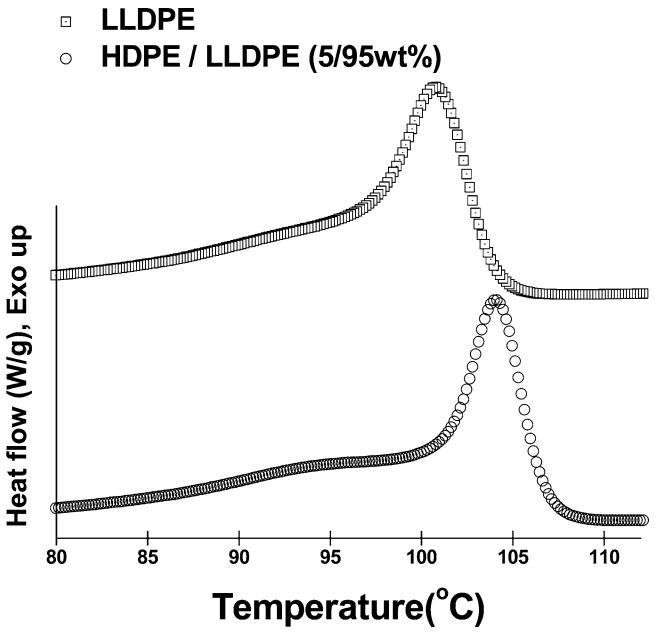

Fig. 2 DSC cooling scans of LLDPE and HDPE/LLDPE blend samples after being cooled (at 10 °C/min) from isotropic melt. The molten samples were first held at 160 °C for 5 minutes to remove the thermal history

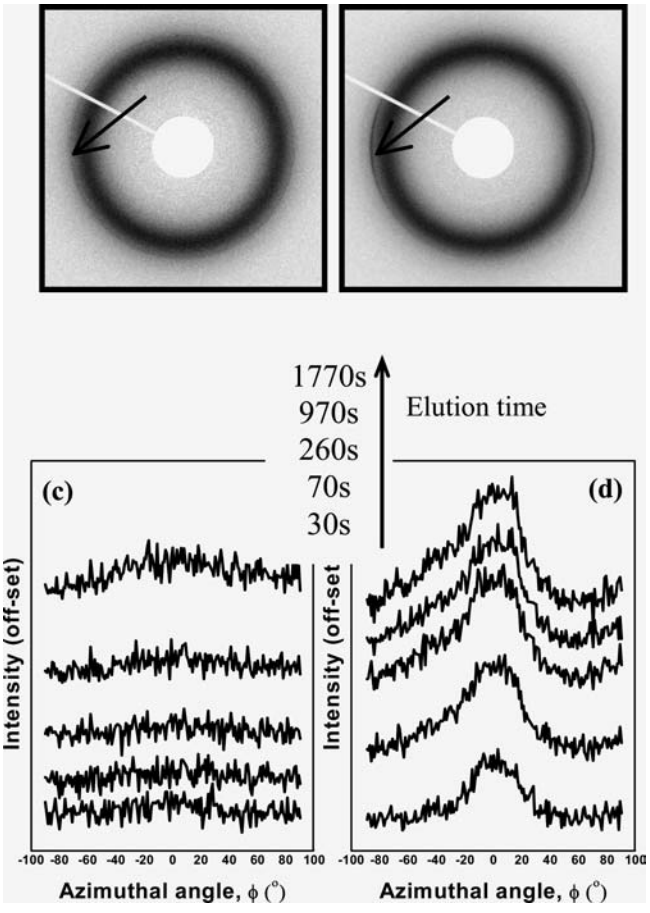

Fig. 3 Selected 2D WAXD patterns for (a) LLDPE and (b) HDPE/LLDPE during flow-induced crystallization at 116 °C after cessation of shear (rate was 60 s^{-1} and shear duration time was 10 s). The patterns were the first images that showed crystalline reflection (marked by arrow), where t = 210 s for LLDPE and t = 30 s for HDPE/LLDPE. Azimuthal intensity profiles of the (110) reflection for (c) LLDPE and (d) HDPE/LLDPE at different times are also shown

and may form oriented primary nuclei (or shish). As the concentration of the high molecular weight distribution in HDPE (1.0 wt%) is above its c^* value (0.5 wt%), a network of oriented chains (or needle-like homogenous nuclei) can be formed. Such a nucleating scaffold will induce the lateral lamellar (kebab) growth from the surrounding HDPE chains (in the lower molecular weight distribution, $\bar{M}_w$ = 99 kg/mol) and/or LLDPE chains. This hypothesis is consistent with the SAXS data, which will be described later. Based on the orientation of the (110) reflection in the HDPE/LLDPE blend (Figures 3(b) and 3(d)), the lamellae formed under shear at the experimental temperature (116 °C) are non-twisted [22].

The crystallinity changes in both LLDPE and HDPE/LLDPE samples after cessation of shear at 116 °C are shown in Figure 4. It was found that the crystallization process in the HDPE/LLDPE blend proceeded immediately after shear, while LLDPE began to crystallize at 210 s after shear. The corresponding crystallization half-time in the HDPE/LLDPE blend was more than five times shorter than that of LLDPE, confirming the role of the long chains in HDPE as nucleating agents in the blend under flow. Although LLDPE showed a slow crystallization rate, its slight orientation in the (110) reflection (Figure 3(c)) indicated that it was still affected by shear, which could be attributed to the very small amount of high molecular weight species in its chain distribution. It was interesting to note that, at 116 °C, the maximum crystallinity induced by shear in LLDPE was about 5% and that in HDPE/LLDPE was about 9% (Figure 4). The difference was about 4%, which must be due to the presence of HDPE (5 wt%) in the blend, suggesting that the majority of HDPE in the blend was crystallized under the chosen shear conditions.

The crystallinity change was fitted by the Avrami analysis using Equation 3 [23],

$$\ln[-\ln(1 - X_C(t))] = \ln k + n \ln t \quad (3)$$

where $X_C(t)$ represents the crystallinity at time t, k represents the overall crystallization rate constant and n represents the Avrami exponent (which varies with the nucleation type, growth geometry and growth velocity). In the nucleation process of quiescent polymer melts, the number of nuclei per volume can be either constant or variant with time during isothermal crystallization. The former is termed 'athermal' nucleation (or instantaneous nucleation), while the latter is termed 'thermal' nucleation (or sporadic nucleation). The growth of the nuclei

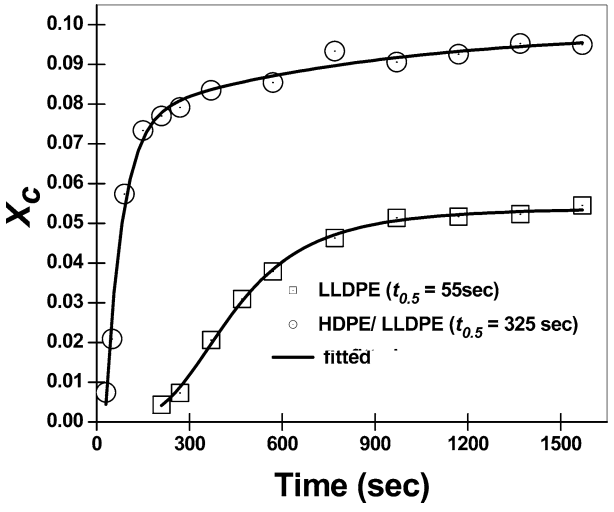

Fig. 4 Crystallinity development for LLDPE and HDPE/LLDPE at 116 °C under shear as a function of crystallization time. The half-time of crystallization, $t_{0.5}$, defined as the half of crystallization time when the primary crystallization is completed, for each PE was derived from the crystallinity evolution. The primary and secondary stages of crystallization were determined as the intercepts of extrapolations of initial and final slopes in the crystallinity evolution curve

can be 1D, 2D or 3D. For example, under instantaneous nucleation (predetermined or athermal nucleation, i.e., constant number of nuclei per volume) and constant growth velocity conditions, $n = 1$ represents the rod-like crystal growth geometry; $n = 3/2$ represents the disk-like crystal growth geometry; and $n = 3$ represents the spherulitic crystal growth geometry. However, under spontaneous nucleation (sporadic or thermal nucleation, i.e., nucleation is random in time and space) and diffusion-controlled (the radial growth rate (G) is proportional to $(\kappa/t)^{-1/2}$ with κ being the diffusion coefficient) conditions, $n = 3/2$ represents the rod-like crystal growth geometry; $n = 2$ represents the disk-like crystal growth geometry; and $n = 5/2$ represents the spherulitic crystal growth geometry [24].

The Avrami plots ($\ln[-\ln(1 - X_C(t))]$ *versus* $\ln t$) for LLDPE and HDPE/LLDPE under shear at a constant shear duration time of 10 s are illustrated in Figure 5(a). The Avrami exponents (taken from the initial slope of the Avrami plot) at different shear duration times but under a constant shear rate (60 s^{-1}) are illustrated in Figure 5(b). It was seen that the Avrami exponent decreased with the increase in shear duration time (or strain), and the Avrami exponent was significantly higher in pure LLDPE than that in HDPE/LLDPE. For the sheared HDPE/LLDPE blend taken at a duration time of 10 s, the Avrami exponent was approximately 2. The value of $n = 2$ suggests that there are two possible growth geometries at the initial stage of shear-induced crystallization in HDPE/LLDPE: the 1D rod-like growth with a constant velocity, or the 2D disk-like growth with a diffusion-controlled velocity ($G(t) \propto t^{-1/2}$), both under spontaneous nucleation conditions. The latter condition has been verified as the correct mechanism, which will be discussed later (G was calculated from the time-evolution of the kebab formation based on the SAXS data). The underlying physics of the diffusion-controlled growth in the HDPE/LLDPE blend is more reasonable, as one can envision that the growth rate of the HDPE crystallite front should be dependent upon the diffusion process of the non-crystallizing LLDPE segments.

Rheo-SAXS results

2D SAXS patterns in LLDPE and HDPE/LLDPE collected after shear at two selected times at 116 °C, and at room temperature after cooling down, are illustrated in Figures 6(a) and 6(b), respectively. Both SAXS patterns exhibited a streak-like scattering feature along the shear direction (meridian). The orientation and scattered intensity of the streak in HDPE/LLDPE were significantly stronger than those in LLDPE. The room temperature patterns were more disoriented than the high temperature patterns, however, the major feature of the streak was still preserved upon cooling. The appearance of the meridional streak under shear is quite different from the typical discrete meridional scattering pattern (with distinct scattering maxima) observed in oriented semi-crystalline polymers having a well-developed lamellar structure. This meridional streak is also different from the equatorial streak resulted from the flow-induced shish structure, which has been reported in some rheo-SAXS studies of the sheared melts [15]. The unique feature of the meridional streak suggests the presence of a kind of disorder that creates a large density fluctuation at short angles, e.g. due to lamellae varying significantly in their sizes (diameters and/or thicknesses), as will be discussed later.

Although the observed SAXS patterns did not show any sign of equatorial streak, this does not mean that the flow-induced shish structure did not occur. This is because only a small fraction of high molecular weight HDPE chains in the blend can retain their extensions and form the shish entity (oriented nuclei) after the cessation of shear. Thus, the dimensions of the shish may be too small and/or the concentration too dilute (less than 1 %) to be detected by SAXS. Recently, Hu et al. reported that even a single oriented chain stem can nucleate the lamellar growth perpendicular to the chain axis [4]. Simulation works by Muthukumar et al. further suggested that the formation of the shish-kebab structure under flow is closely related to the coil-stretch transition of isolated polymer chains, where the stretched chains can crystallize into shish and the coiled chains can

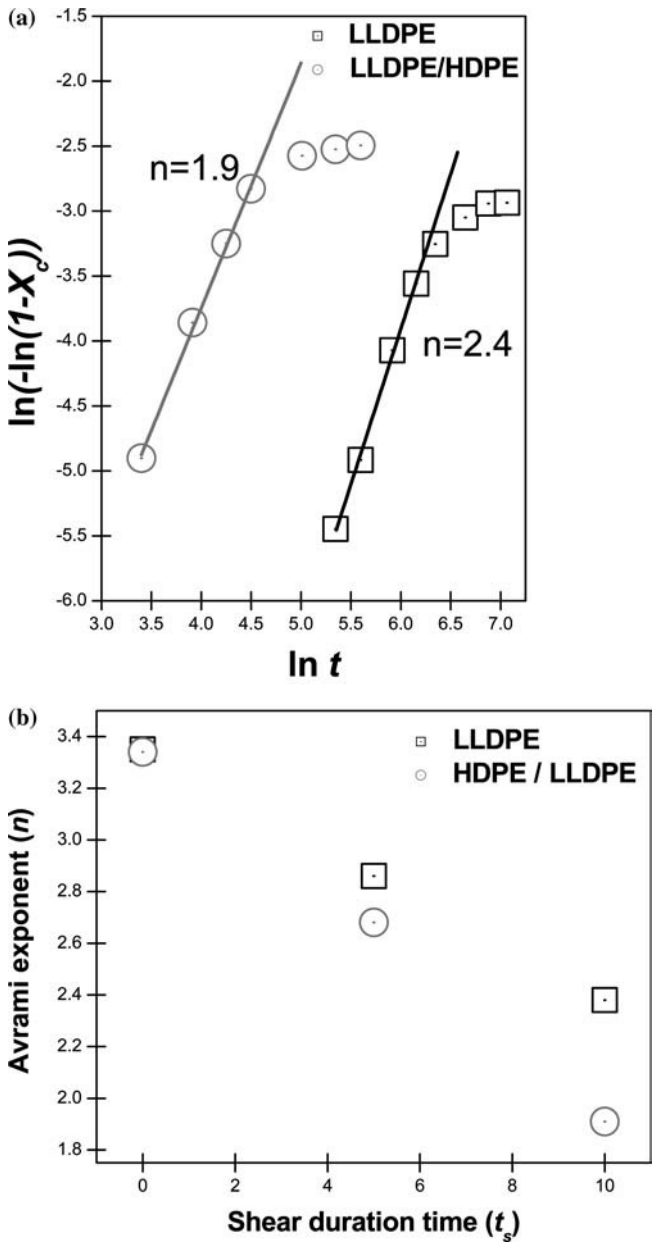

Fig. 5 **a** Avrami plots of LLDPE and HDPE/LLDPE at 116 °C under shear (shear duration time, t_s, was 10 s and the rate was 60 s^{-1}). **b** The change of the Avrami exponent as a function of shear duration time, (t_s = 0, 5 and 10 s) under the same shear rate (60 s^{-1}); 0 s of shear duration time implies the quiescent crystallization

collapse and form kebabs through diffusion and adsorption processes [3]. In these scenarios, the SAXS technique may not be sufficiently sensitive to detect the presence of shish.

The changes of the integrated SAXS intensity for LLDPE and HDPE/LLDPE as a function of crystallization time are illustrated in Figure 6(c). The blend exhibits a sharp increase in the SAXS intensity immediately after shear, while LLDPE does not show any increase in intensity until the time reaches 110 s. The trend of the intensity increase in SAXS is similar to that in WAXD (Figure 4), except the onset time of the increase in SAXS occurs at a lower value than that in the corresponding WAXD. This behavior has been reported before, which can be attributed to the better detection limit and the higher detection sensitivity in SAXS than those in WAXD [25].

Development of the Shish-Kebab model for SAXS analysis

We believe that the inter-lamellar impingement (so called interdigitation) did not occur at the earlier stages of crystallization under the chosen shear conditions. This is because while the linear crystallinity in the shish-kebab structure determined from SAXS was high ($\phi = T/L \approx$ 30%), the total crystallinity (determined from WAXD) in the HDPE/LLDPE blend under shear was low (less than 10% as shown in Figure 4). This suggests that the shish-kebab entities were sparsely distributed in the matrix of amorphous chains, forming a dilute system.

Based on SAXS and WAXD results, a shish-kebab model, consisting of a central shish (or oriented nucleus, which cannot be detected by SAXS) and a periodic arrangement of disk-like kebabs (lamellae, which can be detected by SAXS), can be constructed. The spatial arrangement of the oriented shish-kebabs is assumed to be uncorrelated so that the model can be reduced to a single shish-kebab as shown in Figure 7. The shish-kebab model is assumed to have a cylindrical symmetry around the shish axis. The kebab is given as disks with a diameter distribution $h_D(D)$ and a thickness distribution $h_T(T)$, which are assumed to be statistically independent. The distance distribution between the centers of the nearest neighboring disks (lamellae) is given by a long period distribution $h_L(L)$, again assumed to be statistically independent of next neighbor distances and also of the disk size parameters. The moderately ordered stack of disks is further assumed to have an infinite height. Although a finite stack height can be easily added here, for the parameters and scattering vector range of interest, its effect will be indistinguishable from stacking disorder. This is because the separation of disorder and stack height effects requires higher order peaks or at least some modulations in the corresponding region of the scattering curve. In this study, these two effects cannot be separated, thus the assumption of an infinite stack height is an approximation. However, the effects of the variances of D and T can be separated since they manifest themselves at relatively small angles, where the scattering curve has enough distinguishing features. Finally, in this model, the scattering contribution of the shish is neglected.

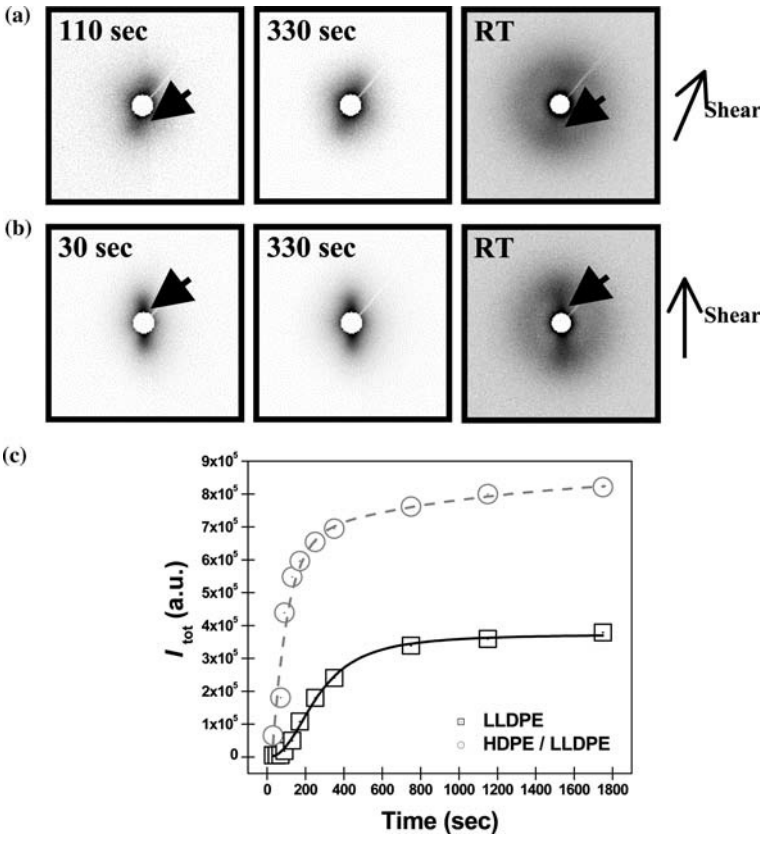

Fig. 6 Selected 2D SAXS images for (a) LLDPE and (b) HDPE/LLDPE during flow-induced crystallization after cessation of shear at 116°C (rate was 60 s^{-1} and shear duration time was 10 s). Thick arrows inside the SAXS images mark the oriented streak-like scattering patterns along the meridional direction. (c) The change of the integrated scattered intensity for LLDPE and HDPE/LLDPE

Using a standard substitution disorder approach, with the absolute value of the scattering vector $s = |\vec{s}| = 2\lambda^{-1}\sin\theta$ (where λ is wavelength of the X-ray beam and θ is half of the scattering angle), $\vec{s} = (s_1, s_2, s_3)$ and $s_{12} = \left(s_1^2 + s_2^2\right)^{1/2}$ (the subscript 3 represents the direction along the shish axis), the scattering intensity I (s_{12}, s_3) of the shish-kebab structure can be expressed as follows:

$$I\left(s_{12},s_3\right) \sim K_s\left[\left\langle\left|A\left(s_{12},s_3\right)\right|^2\right\rangle_{D,T} - \left|\left\langle A\left(s_{12},s_3\right)\right\rangle_{D,T}\right|^2 + \left|\left\langle A\left(s_{12},s_3\right)\right\rangle_{D,T}\right|^2\left|Z_L\left(s_3\right)\right|^2\right] \quad (4)$$

In this equation, the scaling parameter, K_s, includes (1) a constant prefactor due to the electron density difference, $\Delta\rho^2 = (\rho_c - \rho_a)^2$, between crystalline ($\rho_c$) and amorphous phases ($\rho_a$), (2) a factor $\phi(1 - \phi)$, where ϕ is the crystalline volume fraction, and (3) a factor, $H_z^2 = \exp\left(-2\pi d_z^2 s^2\right)$, due to the finite density transition at the interface, and other approximation constants that are not known in calibration of absolute scattered intensity. In Equation 4, we choose a 1D paracrystalline lattice factor $|Z_L(s_3)|^2$ given by [26–28],

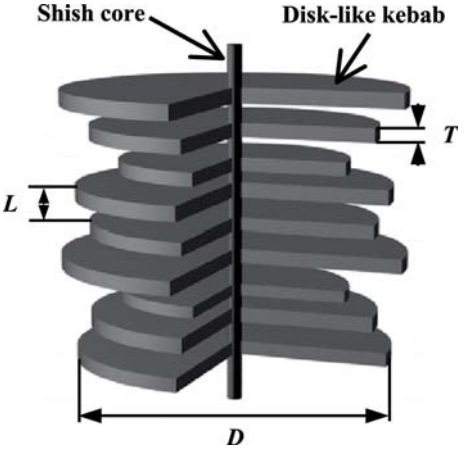

Fig. 7 The shish-kebab model for the SAXS analysis. Disks of diameter D and thickness T are arranged in a moderately periodic fashion with distances L. All lengths $X = D, T, L$ are assumed to be described by distributions $h(X)$ with center, $\overline{X}$ and standard deviation σ_X, and are assumed to be statistically independent. A sector has been cut out to enhance visibility

$$|Z_L(s_3)|^2 = \mathrm{Re}\,\frac{1 + H_L(s_3)}{1 - H_L(s_3)} \quad (5)$$

where $H_L(s_3)$ is the one-dimensional Fourier-transform of $h_L(L)$. The traditional choice for $h(L)$ would be a shifted Gaussian [29, 30],

$$h_L(L) = \left(2\pi\sigma_L^2\right)^{-1/2}\exp\left[-\frac{(L-\bar{L})^2}{2\sigma_L^2}\right] \tag{6}$$

However, if the stacking periodicity is highly disordered (i.e., σ_L is large) there will be an unreasonable tail of the distribution at negative values. Therefore, we chose the following Γ-distribution, which does not suffer from this problem [31].

$$h_L(L) = \frac{1}{\Gamma(v_L)L_0}\left(\frac{L}{L_0}\right)^{v_L-1}\exp\left(-\frac{L}{L_0}\right) \tag{7}$$

$$H_L(s_3) = (1-2\pi i L_0 s_3)^{-v_L} \tag{8}$$

where the parameters L_0 and v_L depend on the average value (center), $\bar{L}$, and standard deviation, σ_L, via $L_0 = \sigma_L^2/\bar{L}$ and $v_L = \bar{L}^2/\sigma_L^2$.

In Equation 4, $A(s_{12}, s_3)$ is the form factor describing the Fourier transform of the density distribution of a single disk (lamellae) of diameter, D, and thickness, T.

$$\begin{aligned} A(s_{12}, s_3) &= \frac{\pi D^2}{4}\frac{2J_1(\pi D s_{12})}{\pi D s_{12}}T\frac{\sin(\pi T s_3)}{\pi T s_3} \\ &\equiv \frac{\pi D^2}{4}A_2(Ds_{12})TA_1(Ts_3) \end{aligned} \tag{9}$$

where we have introduced the abbreviated notation A_1 and A_2, in which the index can be considered as a dimension (A_1 and A_2 are one- and two-dimensional, respectively). Because h_D and h_T are assumed to be statistically independent, their averages can be factorized:

$$\left|\langle A(s_{12}, s_3)\rangle_{D,T}\right| = \left\langle\frac{\pi D^2}{4}A_2(Ds_{12})\right\rangle_D \langle TA_1(Ts_3)\rangle_T \tag{10}$$

$$\left\langle|A(s_{12}, s_3)|^2\right\rangle_{D,T} = \left\langle\frac{\pi^2 D^4}{16}A_2^2(Ds_{12})\right\rangle_D \langle T^2A_1^2(Ts_3)\rangle_T \tag{11}$$

When the diameter (D) and thickness (T) are completely monodisperse, the first two terms in Equation 4 would cancel each other, leading to the familiar product of form factor and lattice factor.

A bell-shaped density distribution, which works well for both h_D and h_T, and for which the required averages can be calculated analytically, is given by ($X = D$ or T, respectively):

$$h_X(X) = \frac{2}{\Gamma(v_X)}\left(\frac{X}{X_0}\right)^{2v_X-1}\exp\left[-\left(\frac{X}{X_0}\right)^2\right] \tag{12}$$

with higher order moments as:

$$\begin{aligned} \langle X^n\rangle_X &= \frac{\Gamma\left(v_X+\frac{n}{2}\right)X_0^n}{\Gamma(v_X)} \\ \langle X\rangle_X &= \frac{\Gamma\left(v_X+\frac{1}{2}\right)X_0}{\Gamma(v_X)} \\ \langle X^2\rangle_X &= v_X X_0^2 \\ \langle X^4\rangle_X &= v_X(1+v_X)X_0^4 \end{aligned} \tag{13}$$

For a given center $\bar{X}$ with standard deviation σ_X, the parameters X_0 and v_X need to be evaluated by numerical iteration. The analytical averages, Eqs. 10 and 11, calculated for this distribution are listed in the appendix. Functions of this type have been used before in a different context in Ruland's group to model the fluctuation part of the scattering of spherical and cylindrical block-copolymer domains [31]. Equation 4 together with Equations 5–13 and the appendix provide a complete analytical solution for the SAXS of an oriented shish-kebab model according to the independent statistics model as described above.

The physical implications of the three parameters (D, T and L) and their standard deviations are as follows. The lateral lamellar size polydispersity, σ_D, would indicate the type of nucleation process. If the value of σ_D is small, which suggests that all lamellae have a similar lateral size (or they are nucleated at about the same time), then the nucleation condition may be instantaneous (i.e., athermal nucleation). If the value of σ_D is large, which suggests that the lamellae have a large distribution of the lateral size (or they are nucleated at different times), then the nucleation may be spontaneous (thermal nucleation). The value of σ_D has a profound effect on the resulting scattering features, such as the scattering intensity at low angles and the distinction of the interference maxima (scattering peak). Calculated 2D SAXS patterns using the shish-kebab model (Equation 9) at two different σ_D values (σ_D = 10 and σ_D = 50) and their corresponding surface plots are illustrated in Figure 8. It is seen that at the lower σ_D value (σ_D = 10), two distinct scattering maxima are seen along the meridional direction; whereas at the higher σ_D value (σ_D = 50), since the point reflection becomes broader and weaker, the intensity at low angle relatively increases and the interference maximum becomes diffuse. The scattering pattern calculated from the σ_D = 10 conditions resembles the typical SAXS pattern observed from well oriented semicrystalline polymers with uniform lamella diameters; while the scattering pattern calculated from the σ_D = 50 conditions resembles the 'meridional streak' pattern observed at the initial stages of crystallization under shear, as shown in Figure 6. The calculated linear intensity profiles along

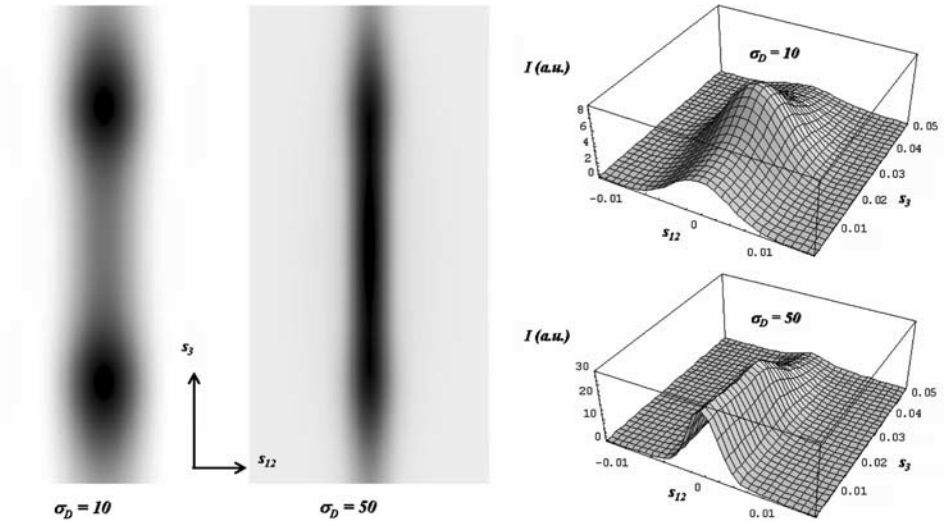

Fig. 8 Calculated 2D scattering patterns $I(s_{12}, s_3)$, and corresponding 2D profiles based on equation 6. $\overline{L} = 50$ nm, $\sigma_L = 15$, $\overline{T} = 15nm$, $\sigma_T = 7$, $\overline{D} = 100$ nm and σ_D as indicated. The displayed range extends to $s_{12} = 0.02$ nm^{-1} and $s_3 = 0.04$ nm^{-1}. Both images have been scaled for maximum contrast. A low lateral lamellar size polydispersity leads to a two-point pattern whereas increasing the lateral lamella size leads to increased scattering at small angles

the meridian at different σ_D values (from 10 to 80) are illustrated in Figure 9(a). Although the scattering profile becomes diffuse with the increase of σ_D, the interference maximum peak is always present.

An increase in the polydispersity of the lamellar thickness (σ_T) would also increase the overall density fluctuations, resulting in the production of strong scattering at small angles. The calculated linear intensity profiles along the meridian at different σ_T values are shown in Figure 9(b), which clearly show this effect. However, we believe that the σ_T value would not be too large at the initial crystallization stages under chosen experimental conditions (isothermal temperature), unless the lamellar thickness is governed by special thermodynamic considerations (such as isothermal thinning and isothermal thickening [32]). In the chosen PE systems of large chain polydispersity, the lamellar thickness should be near a thermodynamic variable, which varies only with temperature.

The variation of the lamellar stacking disorder (or the polydispersity of lamellar long period), σ_L, also affects the scattering profile, similarly to the effects of polydispersities in lamellar diameter and in thickness. The calculated linear intensity profiles along the meridian at different σ_L values are illustrated in Figure 9(c), which show that the scattered intensity at low angles also increases with the increasing σ_L value. It is interesting to note that, under the combined condition of large σ_L and large σ_T values (i.e., both polydispersities of the lamellar long period and the lamellar lateral size are large), the scattering interference maximum can disappear completely. The physical implication of the σ_L value would also indicate the type of the nucleation. Under spontaneous (sporadic) nucleation condition, the value of σ_L is expected to be large; whereas under instantaneous nucleation condition, the value of σ_L is expected to be small.

The above scattering treatment only considered the perfectly oriented shish-kebab structure. This is a reasonable approximation, since the shish-kebab structure generated under the intense shear flow should lead to a very small degree of misorientation. If the misorientation of the shish-kebab structure is a concern, it is straightforward to introduce preferred orientation into the model. In the scenario that the lamellar orientation is perfect and the lateral lamellar size is finite, then the lateral integral width, B_{12} of the streak-like scattering pattern at the meridian remains constant. The lateral stack size, $\langle D \rangle$, can be estimated as the reciprocal integral width using the following expression:

$$\frac{1}{\langle D \rangle^2} \equiv B_{12}^2 = \int_0^\infty I(s_{12}) 2\pi s_{12} ds_{12} / I(s_{12} = 0) \tag{14}$$

However if the orientation is finite, the lateral stack size, $\langle D \rangle$, becomes [33–35],

$$B_{obs}(s) = \frac{1}{\langle D \rangle \cdot s} + B_\phi \tag{15}$$

where B_{obs} represents the observed azimuthal integral width (radian) of the streak with the corresponding orientation distribution represented by the Lorentzian function, which gave the best fits to our experimental results; the slope, $1/\langle D \rangle$, is the reverse of the diameter; the intercept, B_ϕ, is the misorientation width. Equation 15 has been referred to as Ruland's streak method. This method is usually applied to analyze the equatorial streak. However, since it basically relies on separating two width contributions which, as a function of the radius, are constant and varying, respectively, the method could be applied to a meridional streak as well.

The analysis of the HDPE/LLDPE blend data using Equation 15 is shown in Figure 10. Herman's orientation

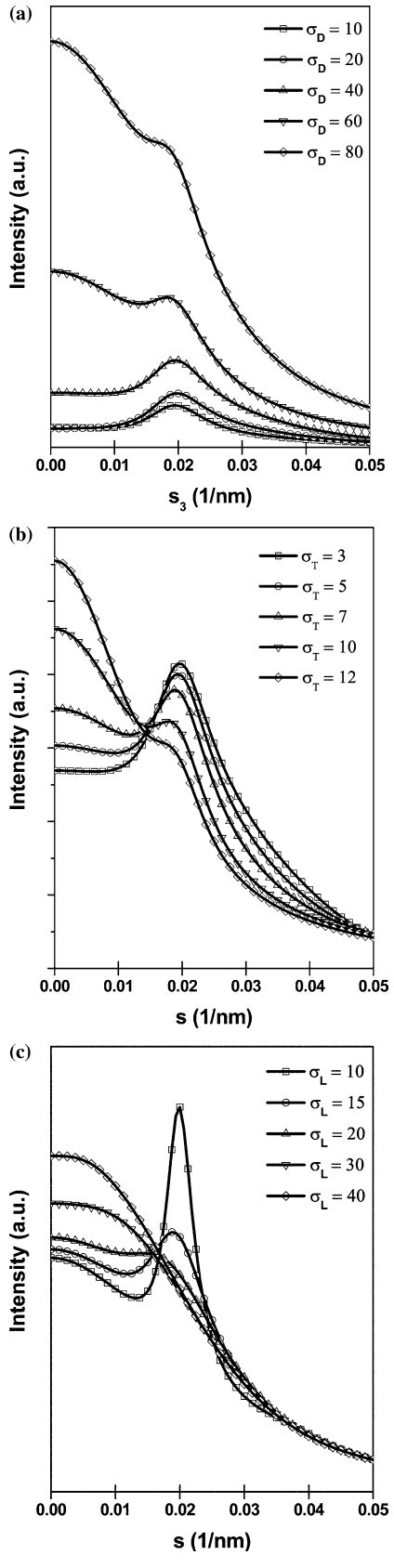

Fig. 9 **a** Calculated 1D scattering intensity, $I(0,s_3)$. $\overline{L} = 50$ nm, $\sigma_L = 15$, $\overline{T} = 15$ nm, $\sigma_T = 7$, $\overline{D} = 100$ nm and σ_D as indicated. **b** Calculated 1D scattering intensity, $I(0,s_3)$. $\overline{L} = 50$ nm, $\sigma_L = 15$, $\overline{T} = 15$ nm, $\overline{D} = 100$ nm, $\sigma_D = 50$ and σ_T as indicated. **c** Calculated 1D scattering intensity, $I(0,s_3)$. $\overline{L} = 50$ nm, $\overline{T} = 15$ nm, $\sigma_T = 7$, $\overline{D} = 100$ nm, $\sigma_D = 50$ and σ_L as indicated

function [36, 37] was introduced to calculate the orientation parameter and the misorientation angle from these extrapolated azimuthal profiles. Figure 11 illustrates the angle between the flow axis and the lamellar growth direction, $\phi_{S,L}$, as a function of crystallization time. The direction of interest is the flow direction; the angle between the flow direction and the direction normal to the lamellar surface is (90-$\phi_{S,L}$). In Figure 11, the orientation parameters are found to increase with time. This may be due to some cooperative interactions between the adjacent lamellae during growth, which lead to an improved orientation with time.

Results from the Shish-Kebab analysis and comparison with Ruland's streak method

Figure 12(a) shows the observed SAXS data at different crystallization time, t, and the fits using the shish-kebab model (Equation 4 with 6 parameters: L, T, D, σ_L, σ_T, and σ_D). Fitted results at selected times are summarized in Table 2. In Figure 12(a), the intensity profiles (I vs s) were averaged over a 10° sector on the meridian. We caution that the derived shish-kebab model is most appropriate to use in the initial stages of flow induced

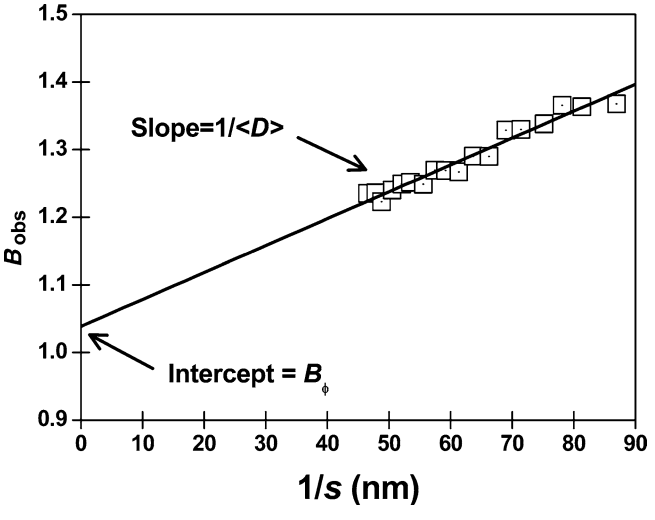

Fig. 10 The integral width (B_{obs}) versus the reverse of scattering vector (1/s) plot for HDPE/LLDPE blend based on Equation 15. The intercept (B_ϕ) represents the orientational integral width, and the slope represents the value of $1/\langle D \rangle$. Since the intensity became very weak at high s values, leading to large errors, we took only the slope of the intermediate s region ($0.011 < s < 0.022$ nm^{-1})

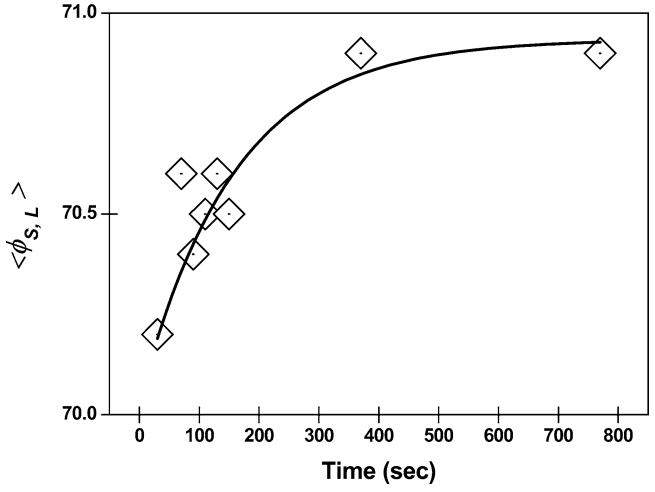

Fig. 11 The change of the average misorientation angle (with respect to the meridian) derived from the Herman's orientation function at different crystallization time

crystallization, where the experimental conditions generally agree with the assumptions of the model. In the later stages, where the kebab growth impingement or lamellar branching may occur, this model will no longer be suitable to use.

In Figure 12(a), at crystallization times lower than 30 s, the scattering profiles exhibit a faint but discernable first-order interference maximum; at crystallization times longer than 30 s (e.g. 50 s), the profiles exhibit strong scattering at the low s region, whereby the interference maximum peak becomes diffuse. At long crystallization times (e.g. 90 s), the meridional scattering profile becomes almost completely diffuse, unlike the typical patterns observed from oriented semicrystalline polymers. This suggests that the lamellar (kebab) stack is highly oriented with the axis pointing into the flow direction but having broad distributions in both long spacing and thickness in the flow-induced shish-kebab structure.

The changes of lamellar long period obtained from the shish-kebab model fit using Equation 4 and the reciprocal center of the scattering peak in the Is^2 profile, are compared in Figure 12(b). The long period value obtained from the shish-kebab model fit is consistently higher (by about 14 nm) than that from the position of the maximum. However, both curves showed exactly the same trend – a drastic increase in the initial stages of crystallization followed by a gradual decrease in the later stage of crystallization. This behavior can be explained as follows. The very early formed kebabs (< 60 s), initiated from certain shish, are probably densely packed with a relatively short long period. But the kebabs developed at later time (> 60 s) are loosely packed where new kebabs can be initiated at varying times. This mechanism, consistent with the assumption of spontaneous (sporadic) nucleation on the shish axis, would lead to a gradual

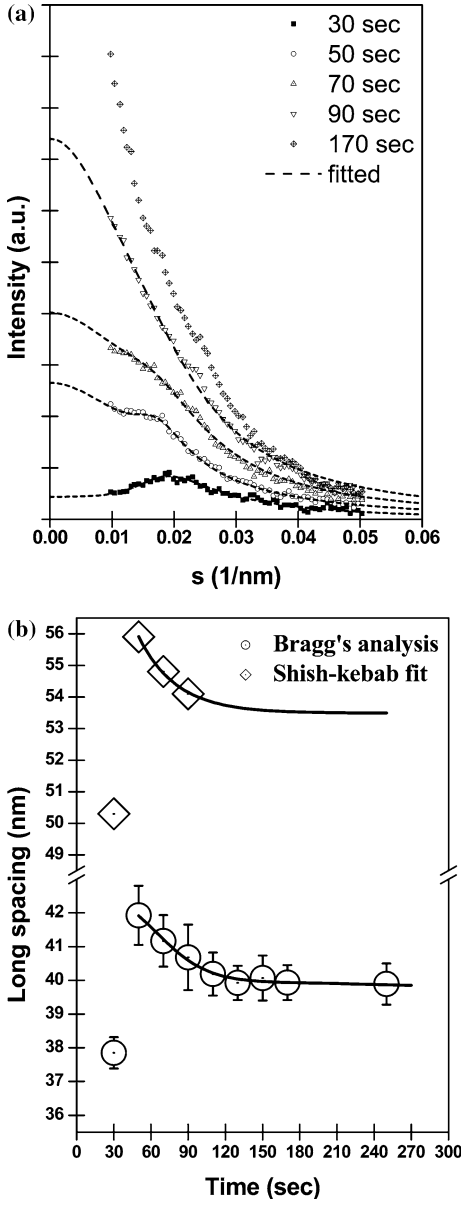

Fig. 12 a The experimental SAXS profile along the meridian (circularly averaged between ϕ = 85~95° to compensate the finite orientation) for HDPE/LLDPE under shear and the corresponding fits using the shish-kebab model (Equation 4). **b** The lamellar long period changes at different crystallization times for the HDPE/LLDPE blend determined from the shish-kebab model fits and from the Is^2 profiles (Lorentz corrected)

decrease in the average long period with increasing time. We believe that the decrease in long period is not due to the inter-lamellar impingement (so called interdigitation) [38], but due to the lamellar nucleation on the shish. This is because while the total crystallinity (determined from WAXD) in the HDPE/LLDPE blend under shear was low (less than 10% as shown in Figure 4), the linear crystallinity in the shish-kebab structure determined from

Table 2 Fitting results based on Equation 4 and experimental SAXS data for the HDPE/LLDPE blend, where L, T and D represent the lamellar long spacing, lamellar thickness and diameter of the disk-like lamellae, respectively, and σ_L, σ_T and σ_D are their standard deviations

Time (sec)	L(nm)	σ_L	T(nm)	σ_T	D(nm)	σ_D
30	50.3	18.1	12.5	6.5	95	11
50	55.9	18.9	12.9	8.9	156	84
70	54.8	21.5	12.7	9.2	185	99
90	54.1	25.9	12.4	10.5	269	170

SAXS was high ($\phi = T/L \approx 30\%$). This suggests that the shish-kebab entities are separately immersed in the matrix of amorphous chains, forming a dilute system, which was one of the assumptions of the model, and are not impinged with each other.

The time evolution of the kebab diameter determined from the Ruland's streak method and the shish-kebab model analysis of the meridional streak are compared in Figure 13. Results showed an excellent agreement. It was seen that the average kebab diameter increased rapidly at the initial crystallization stages (the crystallization time lower than 130 s) and reached a plateau value of about 26 nm afterwards. The dormant stage of the shish-kebab structure indicates that most of the crystallizable chains near the growth fronts of kebabs under this crystallization condition are probably consumed. Based on the diameter changes of kebabs obtained from the Ruland's streak method (Figure 13), the kebab growth rate, G ($=\mathrm{d}r/\mathrm{d}t$) where r and t being the radius of kebab and crystallization time, was calculated and results are shown in logarithmic scale in Figure 14. It is seen that the growth rate approximately followed the $\log G \propto -0.5 \log t$ relationship, which indicated that the kebab formation in HDPE/LLDPE blends was diffusion-controlled and probably under the conditions of sporadic (or spontaneous) nucleation (in free crystal growth condition, $G =$ constant) [24].

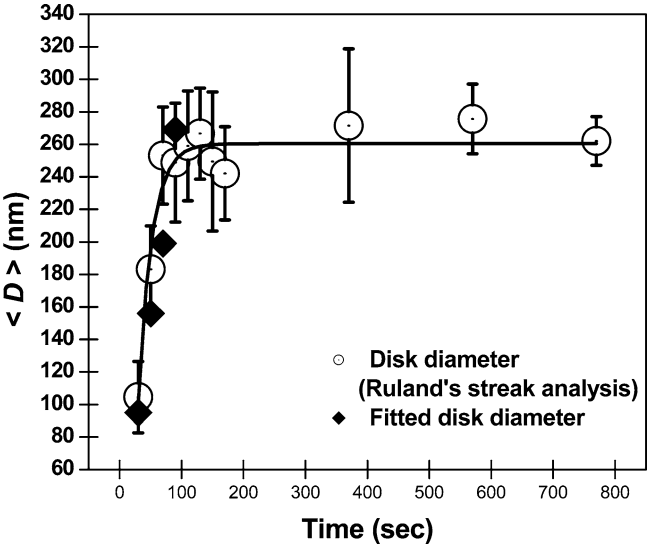

Fig. 13 The comparison of the diameter changes of disk-like lamellae (kebabs) for HDPE/LLDPE determined from the Ruland's streak method (Equation 15) and the shish-kebab model fits (Equation 4) of the meridional streak

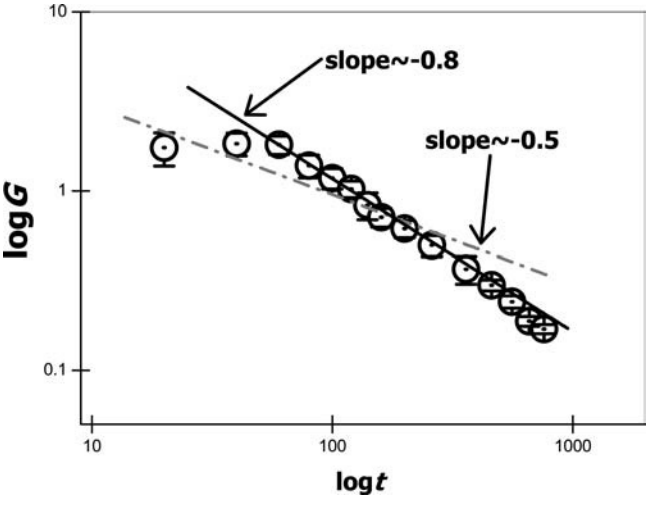

Fig. 14 The kebab growth rate (log G) as a function of time (log t). The dotted line represents the diffusion-controlled growth rate, log G˜−0.5 log t

Conclusion

The nature of flow-induced shish-kebab structure in polyethylene (HDPE/LLDPE) blends was examined by using synchrotron SAXS and WAXD techniques. The time-evolving features in the shish-kebab structure could be determined by the SAXS analysis using a model containing a thin central shish core and a moderately periodic arrangement of relatively large kebab disks with polydispersities of disk diameter, disk thickness and long period. Based on the Avrami analysis of the crystallinity from WAXD (Avrami constant ~ 2), the kebab growth was assumed to be two dimensional and under the conditions of sporadic nucleation and diffusion-controlled growth rate ($G \sim t^{-1/2}$). This assumption was confirmed by the parameter analysis (long period and disk diameter) using results from the model fit. The time evolution of the disk diameter extracted from the shish-kebab model analysis of the SAXS meridional streak was further compared with that from the Ruland's streak method, which showed excellent agreement between the two different methods.

Acknowledgement We wish to acknowledge the assistance of Drs. Igors Sics and Carlos A. Avila-Orta for synchrotron SAXS and WAXD experimental setup. The financial support of this work was provided by the National Science Foundation (DMR-0405432).

Appendix

The required averages in Equation 13 are given as follows (to simplify the notation we write v for v_X):

$$\left\langle \frac{\pi^{d/2}X^d}{2^d\Gamma(1+d/2)}A_d(Xs)\right\rangle_X = \frac{\pi^{d/2}\Gamma(v+d/2)X_0^d}{2^d\Gamma(v)\Gamma(1+d/2)} \times {}_1F_1\left(\begin{matrix}v+d/2\\1+d/2\end{matrix}\middle| -\frac{\pi^2X_0^2s^2}{4}\right)$$

$$\left\langle \frac{\pi^{d}X^{2d}}{4^d[\Gamma(1+d/2)]^2}A_d^2(Xs)\right\rangle_X = \frac{\pi^{d}\Gamma(v+d)X_0^{2d}}{4^d\Gamma(v)[\Gamma(1+d/2)]^2} \times {}_2F_2\left(\begin{matrix}(1+d)/2,d+v\\1+d/2,1+d\end{matrix}\middle| -\pi^2X_0^2s^2\right)$$

$$\langle TA_1(Ts_3)\rangle_T = \frac{\Gamma(v+1/2)T_0}{\Gamma(v)}{}_1F_1\left(\begin{matrix}v+1/2\\3/2\end{matrix}\middle| -\frac{\pi^2T_0^2s_3^2}{4}\right)$$

$$\left\langle \frac{\pi D^2}{4}A^2(Ds_{12})\right\rangle_D = \frac{\pi vD_0^2}{4}{}_1F_1\left(\begin{matrix}1+v\\2\end{matrix}\middle| -\frac{\pi^2D_0^2s_{12}^2}{4}\right)$$

$$\langle T^2A_1^2(Ts_3)\rangle_T = \left[1-{}_1F_1\left(\begin{matrix}v\\1/2\end{matrix}\middle|-\pi^2T_0^2s_3^2\right)\right]/\left(2\pi^2s^2\right)$$

$$\left\langle \frac{\pi^2D^4}{16}A_2^2(Ds_{12})\right\rangle_D = \frac{\pi^2v(1+v)D_0^4}{16}{}_2F_2\left(\begin{matrix}3/2,2+v\\2,3\end{matrix}\middle|-\pi^2D_0^2s_{12}^2\right)$$

where ${}_1F_1$ is the confluent hypergeometric function and ${}_2F_2$ is a generalized hypergeometric function. For the present purposes, both can be readily calculated from their ascending series, if no other computational implementation is available.

References

1. Keller A (1979) Faraday Discussions of the Royal Society of Chemistry 68:145
2. Hill MJ, Keller A (1969) J Macromol Sci (Phys) B3: 1531
3. Dukovski I, Muthukumar M (2003) J Chem Phys 118: 6648
4. Hu W, Frenkel D, Mathot VBF (2002) Macromolecules 35: 7172
5. Hobbs JK, Miles MJ (2001) Macromolecules 34: 353
6. Hobbs JK, Humphris ADL, Miles MJ (2001) Macromolecules 34: 5508
7. Liu T, Tjiu WC, Petermann J (2002) J Crystal Growth 243: 218
8. Liu T, Lieberwirth I, Petermann J (2001) Macromol Chem Phys 202: 2921
9. Kolnaar JWH, Keller A, Seifert S, Zschunke C, Zachmann HG (1995) Polymer36: 3969
10. Wu J, Schultz JM, Yeh F, Hsiao BS, Chu B (2000) Macromolecules 33: 1765
11. Somani RH, Hsiao BS, Nogales A, Srinivas S, Tsou AH, Sics I, Balta-Calleja FJ, Ezquerra TA (2000) Macromolecules 33: 9385
12. Somani RH, Hsiao BS, Nogales A, Fruitwala H, Srinivas S, Tsou AH (2001) Macromolecules 34: 5902
13. Somani RH, Yang L, Hsiao BS, Agarwal PK, Fruitwala HA, Tsou AH (2002) Macromolecules 35: 9096
14. Chu B, Hsiao BS (2001) Chem Rev 101: 1727
15. Yang L, Somani RH, Sics I, Hsiao BS, Kolb R, Fruitwala H, Ong C (2004) Macromolecules 37(13): 4845
16. de Gennes PG (1974) J Chem Phys 60: 5030
17. Seki M, Thurman DW, Oberhauser JP, Kornfield JA (2002) Macromolecules 35: 2583
18. Fetters LJ, Lohse DJ, Garcia-Franco CA, Brant P, Richter D (2002) Macromolecules 35: 10096
19. Fraser RDB, Macrae TP, Miller A, Rowlands RJ, Appl Cryst J (1976) 9: 81
20. Hoffman JD, Davis GT, Lauritzen JI (1976) Treatise on Solid State Chemistry. Hannay NB (ed), Plenum Press, New York, Vol 3:Chap 7
21. Hu S R, Kyu T, Stein RS (1987) Polym Sci Part B Polym Phys Ed 25: 71
22. Keller A, Kolnaar HWH (1997) Mater Sci Technol 18: 189
23. Avrami MJ (1939) Chem Phys 7: 1103
24. Schultz JM (2001) Polymer crystallization Oxford University Press Washington D C 2001: 176–187
25. Wang ZG, Hsiao BS, Sirota EB, Agarwal P, Srinivas S (2000) Macromolecules 33: 978–989
26. Hermans JJ (1944) Rec Trav Chim Pay-Bas 63: 211
27. Ruland W, Smarsly B (2004) J Appl Cryst 35: 624
28. Ruland W, Smarsly B (2004) J Appl Cryst 37: 565
29. Stribeck N (1993) J Phys IV 3: 507
30. Lech Gmachowski (2002) Colloids and Surfaces A Physicochemical and Engineering Aspects 201: 41
31. Wolff T (1994) Ph.D. Thesis, University of Marburg
32. Thünemann AF, Ruland W (2000) Macromolecules 33: 1848
33. Chen EQ, Lee SW, Zhang A, Moon BS, Mann I, Harris FW, Cheng SZD, Hsiao BS, Yeh F, Von Merrewell E, Grubb DT (1999) Macromolecules 32: 4784
34. Perret R, Ruland W (1969) J Appl Cryst 2: 209
35. Ruland W (1969) J Polym Sci Part C 28: 143
36. Wilchinsky ZM (1960) J Appl Phys 31: 1969
37. Ran S, Fang D, Zong X, Hsiao BS, Chu B, Cunniff PM (2001) Polymer 42: 1601
38. Hama H, Tashiro K (2003) Polymer 44: 2159

Progr Colloid Polym Sci (2005) 130: 127–139
DOI 10.1007/b107331
Published online: 3 June 2005

Norbert Stribeck
Peter Bösecke
Rüdiger Bayer
Armando Almendarez Camarillo

Structure transfer between a polymer melt and the solid state. Investigation of the nanostructure evolution in oriented polyethylene by means of continuous X-ray scattering

Abstract During the melting and crystallization of uniaxially oriented polyethylene small-angle X-ray scattering (SAXS) and wide-angle X-ray scattering (WAXS) patterns are recorded simultaneously and continuously, i.e. with high signal-to-noise ratio and a time resolution of 7 s. The multidimensional chord distribution function (CDF) is computed from each of the SAXS patterns and visualises the nanodomain structure of the material in physical space. Thus without application of a model a detailed and continuous multidimensional stream of data is obtained that reveals the mechanisms which govern melting and crystallization in the material studied. Finally the CDF is semi-quantitatively analysed as a function of the temperature programme.

We find that swarms of small crystalline blocks which are observed during the heating of the injection moulded rods are melting earlier than the extended lamellae. Directly after the last lamellae have vanished we quench to a crystallization temperature. No formation of blocky crystals is observed. Instead, before the beginning of crystallization, a mesophase separation into disentangled and entangled regions is indicated. Moreover, row structures of nuclei are observed coming and going. As long as these rows are oriented in fibre direction, the orientational memory of the melt is not erased. Crystallization starts in disentangled bundles of chain segments at the tips of knots (entanglement strands). Fast and continuous lamellar growth is observed. Most of the lamellae are positioned at random. Correlations between lamellae are limited to twins which are formed when lamellae grow at both ends of the same entanglement strand. Thereafter slow thickness growth of lamellae is observed, and in twins this growth is directed outwardly, away from the entanglement-rich amorphous zone between them. Only during this period the wide-angle X-ray scattering (WAXS) exhibits an increasing orientation of the crystals. At a high undercooling or after there is no space for lamellae any more, secondary crystals (blocks) are formed that are unoriented but placed in such a manner that correlations among them are high both in longitudinal and transversal direction.

Keywords Fibers · Polyethylene · SAXS · Crystallization · Melting

Dedicated to Prof. Dr. Wilhelm Ruland on the occasion of his 80th birthday

N. Stribeck (✉)
A. Almendarez Camarillo
Institut für Technische und Makromolekulare Chemie, Universität Hamburg, Bundesstr. 45, 20146 Hamburg, Germany
e-mail: Norbert.Stribeck@desy.de
Tel.: +49-40-42838-3615
Fax: +49-40-42838-6008

P. Bösecke
ESRF, 6 rue Jules Horowitz, B.P. 220, 38043 Grenoble Cedex 9, France

R. Bayer
Institut für Werkstofftechnik, Universität GH Kassel, Mönchebergstrasse 3, 34125 Kassel, Germany

Introduction

The mechanisms of structure transfer which are the basis of polymer crystallization have been studied in polymer science for several decades. Since industry has returned to the tailoring of bulk polymer materials, this field is back in the focus of scientific interest [1, 2, 3, 4, 5, 6, 7, 8]. Nevertheless, the views concerning the nanostructure evolution are still conflicting, because the experimental data collected so far are still incomplete. In this paper we propose and exercise a method that appears apt to narrow the mentioned gap and is resting on both in-situ experiments with high time resolution using oriented materials, and an advanced technique of data analysis.

Using imaging methods like atomic force microscopy (AFM) or scanning near-field optical microscopy (SNOM) it appears very difficult to in-situ monitor a structure transfer process executed under technical conditions with sufficient resolution corresponding to both time and space [9, 10, 11]. Utilising X-ray scattering, such experiments are possible, but the recorded data require mathematical evaluation, as long as it is not considered to apply simplified notions. Unfortunately a mathematical treatment is still frequently avoided, and thus the present state of science in the field of small-angle X-ray scattering (SAXS) is similar to the state of solid-state NMR before the multidimensional NMR was invented.

Since several years one of us is developing automated data evaluation methods for the SAXS aiming at the investigation of nanostructure evolution processes [12, 13, 14, 15]. Fundamental with respect to this development is the principle of late modelling which, for the field of SAXS and nanostructure analysis, has been pointed out early in the work of Ruland [16, 17, 18, 19, 20, 21]. According to this principle the interesting information concerning the structure is first extracted from the raw data, then visualised after an appropriate Fourier transformation, before, as the final step, modelling comes into play.

Such kind of investigations make substantially higher demands on the experiment than common SAXS studies carried out at synchrotrons with two-dimensional (2D) detectors. If the only goal is to document that a peak is emerging and moving, a SAXS setup at a less-advanced synchrotron, a typical sample-to-detector distance of 2 m and a small detector with few pixels is adequate. If a Fourier analysis is the aim, it is no longer sufficient to be able to recognise a peak close to the beam stop, the position of that equals a long period of 100 nm. Then, additionally information from the USAXS region is required, which has to be recorded with both high signal-to-noise (S/N) ratio and high spatial resolution on a large detector positioned in typical USAXS distance.

If, today, we combine sufficiently equipped synchrotron radiation facilities with both an advanced concept of analytics for the investigation of oriented polymer materials, it becomes possible to study the processes of structure transfer in two or three dimensions of physical space. Figuratively, we no longer interpret the fringe structure of a hologram, but shine light on it and describe the image that is flashing up. Recently we have already reported results of corresponding crystallization experiments [22, 23, 24], which have been carried out with a time resolution of 2 min at the Hamburg Synchrotron Laboratory (HASYLAB). Because of the coarse time pattern some basic questions concerning the mechanisms of melting and crystallization remained unanswered. We found, for example, not only lamellar crystals, but also distorted lattices from block-shaped ones, which are much less extended than the lamellae. Nevertheless, we were not able to enlighten the genesis of the latter. Alike we observed in our high S/N-data row structure nuclei before the first lamellae showed up; two minutes later there was nothing but a crowd of oriented lamellae placed at random positions. We postulated that the statistical placement should have been preceeded by a regular and long ranging "shish kebab"[25] structure. Now we present the results from an extended series of experiments that have been recorded at the European Synchrotron Radiation Facility (ESRF) in Grenoble, where time resolution was increased to 7 s at even higher S/N-ratio as compared to the earlier studies. Utilising such a fine time pattern at high data quality we are entering the new field of continuous and multidimensional investigation of nanostructure evolution, and thus achieve new vistas concerning the mechanisms that are governing the processing of polymer materials, as has already been pointed out in a short communication [26].

In order to record such data streams, a powerful X-ray source and two modern two-dimensional (2D) detectors are required. The concept of scattering pattern analysis developed by us utilises methods of image processing that have successfully been applied in medical technology for years. Combined we obtain a detailed image in physical space of the correlations among the surfaces of the crystalline domains. This image is the multidimensional chord distribution function (CDF) [14, 27, 28].

In particular during the period of nascent nanostructure the CDF is a favourable tool, because it perfectly discriminates the emerging structure (correlation peaks in the CDF) from the chaos (CDF vanishing everywhere). On the other hand, the interpretation of such weak pre-crystalline structures never seen before appears to be susceptible to misinterpretation to a considerable extent.

As here we report results of an in-situ study of polyethylene crystallization, we continue a series of papers [29, 30, 31] aiming at the advance of understanding structure transfer between a polymer melt and the solid state.

Experimental

Highly oriented polyethylene (PE) rods are prepared from commercial material, cautiously melt–annealed in a furnace, and finally crystallized in the synchrotron beam of an ultra small–angle X–ray scattering (USAXS) beam line. In the majority of the experiments orientation is preserved, although the nanostructure itself changes completely.

Commercial high-density, low-branched Ziegler-Natta type polyethylene is used for our experiments (Lupolen 6021 D, BASF, $M_W = 182$ kg/mol, $M_n = 25$ kg/mol, density 0.962 g/cm^3, melt index 0.2). In order to achieve high orientation, an equilibrated, low–temperature melt (160 °C) is injected into a cold mold. Maximum mold pressure is 444 MPa and final mold pressure 336 MPa after 180 s. In the differential scanning calorimetry (DSC) the material exhibits bimodal melting with peak maxima at 131°C and 141 °C.

As a result of this high-pressure injection-moulding (HPIM) process, rods of 10 cm length and a diameter of 6 mm are obtained. Inspection by the eye exhibits a core–shell structure with a core diameter of 2.5 mm. Samples for the present investigation are sectioned [32] from the shell of the rod using a low–speed diamond saw. In tests carried out during previous experiments [32] we ascertained fibre symmetry by comparing the scattering patterns before and after turning the samples by 90° about fibre axis and finding no difference.

The experiments are performed in the synchrotron beam line ID02 [33] of ESRF. The wavelength of the X-ray beam is 0.1 nm. USAXS images are collected by a two-dimensional position sensitive XRII–FReLoN (''X-Ray Image Intensifier, Fast Readout, Low Noise'') CCD detector developed at ESRF (driven in1024×1024 pixel mode of each $0.164 \times 0.164 mm^2$ 14 bit resolution). The sample–to–detector distance is set to 10 m.

Wide-angle X-Ray scattering (WAXS) is simultaneously recorded using a MCP-Sensicam CCD detector positioned [34, 35] at a short distance of the sample.

Samples of 2 mm thickness are mounted in a Mettler-Toledo FP82HT hot stage and subjected to a temperature programme. Temperature is measured using a separate thermo couple being in direct contact with the sample. USAXS exposure is varied during the experiment between 0.1 s and 3 s in order to always use the full linear range of the detector, i.e. in every image the most intense pixel is exposed to about 14000 counts. The incident beam is attenuated by a factor of 10 in order to keep the exposure in a reasonable range with respect to the available timers and counters. A minimum cycle time of 7 s between two snapshots provides for both control of exposure and data storage (4 s) of single snapshots. We use to start with an exposure of 0.3 s as soon as the material is reaching a temperature of 120°C, then decrease it to 0.1 s up to the moment when most of the material is melting. Thereafter we instantly increase to 3 s and finally slowly adjust to lower exposure. The CDFs presented in Fig. 2 are computed from scattering patterns which have been exposed for 3 s each.

The flexible concept of a general experiment control by small programme modules under Linux which communicate via pipes has been a crucial prerequisite for the ad-hoc implementation of the dynamic exposure control.

Data evaluation

A major problem concerning time-resolved 2D-experiments is the sifting and evaluation of the data flood. In 3 days we have accumulated 30 GB of data. In order to pre-evaluate the huge amount of scattering patterns we have adapted our evaluation programme to the actual local experimental conditions and have added a parameter tracking system. As a result, the most frequent action of the user is nothing but a mouse click that confirms the computed proposal concerning centre and alignment of the pattern. Utilising this procedure the pre-evaluation can be carried out in tolerable time. Thereafter the scattering images belonging to a series are automatically transformed to the multi-dimensional CDF of a nanostructured sample with fibre symmetry [14, 32, 22].

For the purpose of visualisation the CDFs are, in general, plotted in a logarithmic intensity scale. The obvious method to handle negative values is described upon request. For the plot an upper level of interest in the CDF is scaled to a value of 100. A mask eliminates all values below 0.1. The logarithm is taken. An inverted copy of the CDF is treated the same way and re-inverted. Both partial surfaces match and, ''glued together'', yield a continuous 3D surface in a logarithmic scale.

Concerning the next step, i.e. sifting of the CDF results, a manual survey has proven inapplicable. In order to take advantage of the continuous multi-dimensional data stream, adapted presentation tools have to be built in order to become able first to comprehend the dynamics of the process, and, second to properly describe it.

Therefore we have programmed animation tools. In the most simple case we choose a fixed viewpoint and scale, load one CDF after another from the hard disk, and display it on the computer screen. Such an animation cannot be controlled by the user, the built-in display quality of our data evaluation language pv-wave [36] is insufficient for our purpose, and we can only watch single 3D functions viewed from a single viewpoint. In order to improve the practical value of the animation we have rendered the data from each snapshot (USAXS, WAXS, CDF from two viewpoints) using a ray-tracing programme (PoVRay 3.1), have combined them in a composite image and, in the final step, have merged the series of composite images to make it a movie. Format conversions and image composition are carried out by the modules of the ImageMagick package. The movie is generated by transcode.

Ultimately, as the control functions of the programme mplayer are used to replay the movies, the essential phases and processes of nanostructure evolution become evident. All the programmes mentioned (except for pv-wave) are free software and have been developed by the community of Linux programmers.

The CDF of distorted structures

The structure evaluation method used in this report extracts the information on the samples nanostructure (i.e. a topology $\rho(r) \in [\rho_{cryst}, \rho_{amorph}]$ of phases with distinct densities) from two-dimensional (2D) SAXS

patterns with fibre symmetry. The CDF z (**r**) is an ''edge-enhanced autocorrelation function''—the autocorrelation of the gradient $\nabla\rho(\mathbf{r})$, or the Laplacian $\Delta\left(\rho^{*2}(\mathbf{r})\right)$ of Vonk's multidimensional correlation function [37] $\rho^{*2}(\mathbf{r})$. It shows peaks where ever there are domain surface contacts between domains in $\rho(\mathbf{r})$ and its displaced ghost as a function of ghost displacement.

Thus, compared to the correlation function $\rho^{*2}(\mathbf{r})$, the effect of the CDF is ''edge enhancement'', if we apply the terminology of the field of digital image processing. This means that for multi-phase systems the interpretation of the CDF is obvious, but from its mathematical definition it is not restricted to such systems and, therefore, can be applied to deliberate distributions of density $\rho(\mathbf{r})$ in space. However, in the latter case its interpretation may be difficult or even impossible.

If, in the sequel, we take the chance to as well interpret the distorted structures observed in the CDF of the cool polymer melt, then we apply a similar method of edge enhancement as astronomy when it is using the very Laplacian operator [38, 39], in order to visualise details in photographic images of the universe. Similar to our case, the mentioned images cannot be described by a small number of discrete phases. Nevertheless, the mathematical operator acts edge-enhancing and visualises details, which are difficult to find in the raw data. Admittedly, the interpretation of such details is to some extent speculative. On the other hand, there are several reasons encouraging us to publish our data and our interpretation:

1. We are reproducing the structural details in all experiments on this material during the last four years – and now even on a totally different instrument.
2. We are able to erase the observed details in the CDF by heating the melt to a higher temperature.
3. The danger that the features are artifacts which are generated by Fourier transformation of noisy data is much smaller now because of the very good S/N-ratio achieved at the ESRF beam line. Single adulterated scattering patterns are easily detected in the extended series due to the short cycle time between snapshots.
4. The reported measurements with high time resolution exhibit for the first time that an initially monotonous CDF feature first changes to form discrete peaks (i.e. a mesophase), before crystallization is starting.

Results

From the injected rod to the oriented melt

The nanostructure as reflected in the CDF

Our experiments start from highly oriented, HPIM-PE rods which, in a first step, are slowly melted. In contrast to an earlier paper [32] it now has become possible to record the structure transfer with high accuracy and quasi-continuously. Figure 1 shows three phases during the heating.

The presented CDF of the melting semicrystalline material describes the correlations among domain surfaces. In the present paper the functions are always scaled to a constant maximum amplitude, because we are focusing on the investigation of topology variations. In the left column (Fig. 1a) the typical triangular peaks of lamellar domains are observed with their surface normals oriented parallel to the fibre axis, as was already reported in previous work [32].

Figure 1b demonstrates the transitional stage between solid and melt. The corresponding movie clearly exhibits the regression of the lamellar structure which is accompanied by the emerging of a novel kind of structure, which is characterised by a narrow negative ridge on the meridian of the CDF. We address this feature by a row structure . It is worth to be noted that a ''shish'' made from a bundle of straightly extended chains would be characterised by two close, narrow and positive ridges extending on both sides of the meridian. The negative ridge can only be explained by a modulation of electron

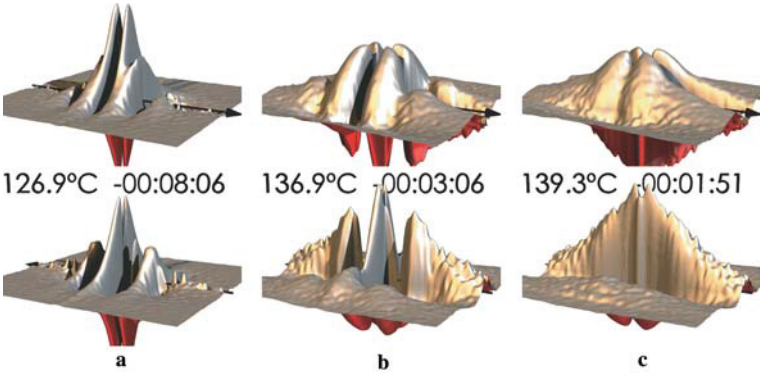

Fig. 1 Heating of HPIM–PE. The images show the CDF in a logarithmic intensity scale watched from a top viewpoint (top) and a bottom viewpoint (bottom), respectively. The fibre axis (meridian) is indicated by an arrow in the base plane. The clips represent an area of 300 nm × 300 nm. Times are computed with respect to the moment of quenching the melt

density, and the observed shape of the peak indicates a peculiar probability distribution of long periods according to an exponential fall off.

Outside the meridian we, additionally, observe strong and diffuse positive regions that, in the course of melting, are more and more veiling the lamellar peaks on the top face of the CDF. Fortunately the CDF shows a second and clear feature related to lamellae-shaped domains that is not veiled during the process of melting. If we turn the CDF upside down (Fig. 1b, bottom) the self-correlation peak of a lamellar system (cf. [14], Fig. 9) is found on the equator. In the plot it is almost looking like a triangle. During the melting process the width of this triangle is narrowing continuously. Thus the lamellae are melting continuously from their edges. There is little evidence of a subdivision process into blocks.

In a previous paper [22] we reported the results of a survey carried out at HASYLAB. A few minutes before melting a block structure (i.e. floes in planes with their normal parallel to the fibre direction) had sometimes been observed. Because of the outdated detector at beam line BW4 the evolution of this block structure could not be studied. In the experiments from the ESRF presented here we use only 10% of the incident intensity, adjust to a tenfold S/N–ratio and a 15 fold time resolution. Again we sometimes find modulations of the triangular peaks that indicate the presence of arranged blocks. Nevertheless, now the continuous stream of data reveals that such block structures vanish before the lamellae themselves start to melt, and that the observed blocks are less stable than the lamellae.

Admittedly, there is a feature observed during melting that we first took for an indication of a block structure during melting when we sifted through the images one by one. It is related to a negative ridge subdivided in three parts (Fig. 1b bottom) that is extending parallel to the meridian in a distance of 200 nm. Observing the corresponding videos it becomes clear that this feature does not grow in phase with the melting of the lamellae. Instead, it is correlated both to the four diffuse positive domain peaks that are veiling the lamellar triangles (Fig. 1b, top) and the sharp row structure on the meridian (Fig. 1b, bottom). Moreover, the discussed negative ridge is found outside the range of lamellae extension, and thus can hardly indicate a decomposition of lamellae.

The row structure

At the end of the melting we still observe a small bulge in equatorial direction indicating the presence of crystallites (''kebab''). Just when this bulge has vanished, the discrete WAXS has vanished as well. Nevertheless, the row structure is surviving the melting of the crystallites (Fig. 1c). In this phase of the melting there is no preferential distance between the row nuclei, else the meridional triangle should be subdivided into a sequence of peaks. If, moreover, the nuclei would show a rather uniform height (in fibre direction), then, in addition, we would expect discrete peaks pointing upwards on the meridian (in Fig. 1c, top). However, there we only find a diffuse positive region extending far out into space. The structural feature behind this CDF feature cannot be explained by the row structure itself. So, although this is only a poor approximation of structure with respect to the observed regime of a cool melt, let us use the notion of domains and answer the question, in which simple case we would observe a positive region in the CDF. The most simple explanation is some weak segregation in the melt, and in this case the positive signal $z(\mathbf{r}')$ at some displacement $\mathbf{r}'$ would measure the probability of finding a chord crossing a ''homogeneous'' domain of length and direction given by $\mathbf{r}'$. Prerequisite is that there are no correlations among the regions of segregation. The structure and its evolution shows that such segregation-domains are associated to the row structure and reach out into space. Therefore we call them ''row structure associated domains'', RADs. We recognise that the diffuse positive regions in the CDF are characterising a volume in correlation space that is governed by such RADs.

In Fig. 1c, top, an indentation on the equator reflects an aspect of memory concerning the lamellar structure of the precursor material: With respect to the beginning of a RAD its end is preferentially found in a distance A along fibre direction. A shrinks during the progress of melting, and the longitudinal extension of the RADs becomes more and more statistical. Finally, in the melt there is no preferential RAD extension any more. However, let us go back and, again, compare this image to Fig. 1b, top, where still a much stronger modulation of the RAD structure is observed. There a majority of the RADs is still restricted to regions whose extensions in fibre direction are given by the average amorphous thickness, A, in the lamellae stacks of the precursor injection moulded rod.

The ultimate orientation preserving structure of the melt

Figure 2 shows some of the CDFs recorded close to the melting point. Although the intensity of the row structure is decreasing by two orders of magnitude, its principal shape remains similar for a considerable period when the melt-annealing temperature of 140 °C is reached (Fig. 2a) (recent test measurements show that even after 20 min at 140 °C the basic topology remains unchanged). Nevertheless, during the period of constant temperature one feature of the topology is vanishing (Fig. 2b). It is related to the melting of the last lamellae, and the corresponding change of the diffuse scattering can hardly be detected during the course of the experiment.

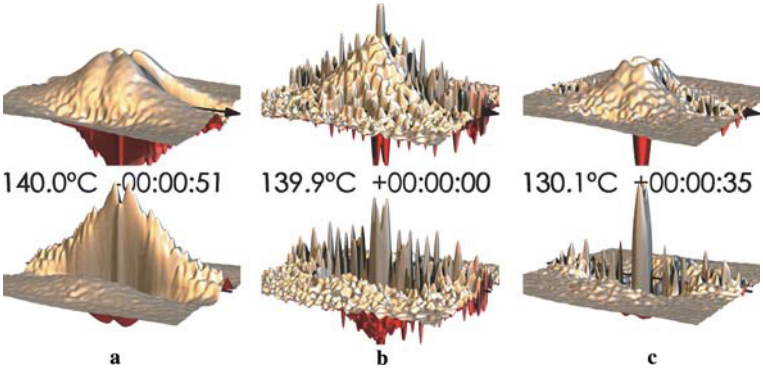

Fig. 2 The last phase of HPIM–PE melting and the beginning of quenching. The images show the CDF in a logarithmic intensity scale watched from a top viewpoint (top) and a bottom viewpoint (bottom), respectively. The fibre axis (meridian) is indicated by an arrow in the base plane. The clips represent an area of 300 nm × 300 nm. Times are computed with respect to the moment of quenching the melt

Because during our experiments we expected the ultimate orientation preserving structure to be destroyed after a long period of melt-annealing, we have only kept the samples at the melt-annealing temperature for 2 min, and thus sometimes have not reached the pure ultimate orientation preserving structure of the melt that is shown in Fig. 2b. In the other experiments we have got stuck in a densely populated row structure with a few isolated lamellae persisting (Fig. 2a). This difference has a consequence on the following process of crystallization that is reported in section ''Crystallization from the oriented melt''.

The ultimate orientation preserving structure is a sparse row structure (Fig. 2b) and exhibits on the meridian of the CDF a statistical ensemble of rows. Each row is made from nuclei of varying thickness but well-defined long period, and during the period of melt-annealing the thicknesses of the nuclei become more homogeneous, so that now positive *and* negative peaks show up, as is expected for a simple one-dimensional lattice of homogeneous nuclei. In the raw data scattering pattern the corresponding layer line is not directly observed, but the interference function (computed by projecting the scattering data and applying the Laplacian in reciprocal space) shows the feature. In addition, on the top face of the CDF we still observe the continuous and diffuse positive peak of pyramid shape that is characterising a very broad distribution of RADs (with the most probable chord of the RADs being an infinitesimally short one).

In the figure this pyramid is already slightly structured, and after it decomposes into single peaks of similar strength as those characterising the oriented row structure, an isotropic phase is observed during the following crystallization process. The orientation memory is lost. Nevertheless, as long as the oriented row structure is still observed on the meridian, the result of the following crystallization is a two-component material comprising both a highly oriented structure and an isotropic one [22].

In earlier work [32] on the melting of HPIM–PE we have reported discrete and regular undulations on the row structure ridge in the CDF based on experiments at HASYLAB. Because of the long exposure required in Hamburg we that time have integrated the pulsating row structure for 2 min, and this integration results in the undulations formerly observed.

In a short communication [26] the results concerning the structure formation during cooling and before the first crystallites show up are presented in combined SAXS/WAXS patterns and sketches of the nanostructure. Here we only summarise the results.

Now quenching the sparse row structure to the crystallization temperature we immediately observe a novel, now less extended nanostructure of RADs, from which a lamellar structure will grow that, again, is highly oriented. Due to the high time resolution we observe that the row structure itself is only a latent one. In our previous study [22] based on data accumulated with a coarse time resolution we had perpetuated the common notion that from a static row structure or a ''shish'' (bundle of extended chains) one-dimensional lattices of lamellae should have formed which (during the next two minutes needed for exposure) should have been overgrown by many secondary lamellae poured in between. Now we observe that the correlations among most of the nuclei stringed like beads on a chain are subjected to atrophy, and we speculate that the creation of a primary nucleus is going along with the generation of a harmonic sequence of only latent secondary nuclei that extend along the preferential direction of the polymer chains. A second possible explanation would be to assume that all the nuclei are converted into crystals, but that the crystal growth itself is destroying the correlated arrangement among them.

Discussion of the RAD structure

Up to this point we have described the development of the CDF in the vicinity of the melting point without modelling the RADs. We have observed that the lamellae do not disintegrate into blocks upon melting. Moreover we have found a nanostructure emerging that is made from a row structure and row-structure associated

domains. What kind of notions can we associate to these RADs? Certainly there must be some contrast in electron density between the RADs and a matrix phase in the melt.

We assume that the contrast observed is caused from a different degree of chain entanglement what the RADs and the matrix phase is concerned. If we write the pyramid shaped positive peak in the CDF as a chord distribution, $f_0(r_{12}, r_3)$, in correlation space described by the transverse coordinate r_{12} and the longitudinal coordinate r_3, the height f_0 may be associated to the probability to find the other end of the RAD chord at $(r_{12},\ r_3)$, and the identification of RADs with strands of entanglements or knots appears to be reasonable. Two observations make us assume that the RADs are entanglement strands and as such the precursors of the amorphous phase but not pre-crystals (bundles, nuclei). Firstly, there is another feature (the row structure) that appears to be related to nuclei in the melt. Secondly, as crystallization is starting later on, not the crystalline layers but the amorphous gaps are emerging from the RADs.

In the oriented melt the RAD peak is a pyramid with its maximum in the origin of correlation space. So most of the RADs are single entanglements. Nevertheless, some of the RADs reach out far into space and may be identified by the knot zones of the entangled network [30, 31]. In the most extended ultimate melt structure at the end of the melt-annealing period (Fig. 2b) the extension of the region governed by the RADs is more than 300 nm in longitudinal direction and 130 nm in transverse direction.

At each side of the central column in Figure 2 more solidified states of the melt are shown. Both in Figure 2a and in Fig. 2c there is no pyramid peak. Instead, the positive peak of the RADs appears indented both along the meridian and the equator. A "sofa cushion peak" exhibiting four lappets has replaced the pyramid. Thus at this stage of the crystallization process a domain structure is, for the first time undoubtedly observed. We interpret the observed change of the CDF from the pyramid to a sofa cushion shape as a mesophase separation process causing the merging of single entanglements and other RADs into an ensemble of better defined RADs of preferential size and orientation. The most probable RAD no longer is a single entanglement, but a strand extending under an oblique angle with respect to the fibre direction (meridian). As a result of melt solidification thus we observe a condensation of entanglements, and a mesophase separation into entanglement- or knot-strands [30, 31] and bundles [8] takes place. As a function of increasing solidification the relative probability of long-ranging strands is decreasing. It remains unanswered, if this effect is caused from a compression of existing knot strands or from the precipitation of additional and less extended strands.

Crystallization from the oriented melt

RADs and crystallization

Only 20 s after the RAD pyramid has been converted into the mentioned sofa cushion shape we observe the first crystals in the CDF (Fig. 3a). In the top view we detect the corresponding tip of the peak on the meridian exactly between two lappets of the RAD structure. Because of the strong RAD peaks we are unable to discriminate the shape of the crystals, but in the bottom view beneath we observe on the equator the sharp self-correlation ridge of lamellae sitting on the background of the RAD "sofa cushion". In comparison to the block shaped nuclei on the meridian that are still present at this early stage of crystallization it becomes clear that the first lamellae are not preceeded by ensembles of blocks arranged on planes. Shortly after that (Fig. 3b) the strength of the RAD feature on the equator has decreased, and the extended lamellae are now very clear. Inspecting the RAD peaks we observe that the lappets have become compressed and converted into thickness distributions of amorphous layers.

Primary crystallization of our polyethylene material is finished after the crystal lamellae have formed. We do not observe series of layer peaks that would be typical for a lattice of alternating crystalline and amorphous layers, and the only observed quartet of peaks related to non-crystalline structures is readily explained by a mechanism, in which crystalline layers are formed at both ends of the same entanglement strand (Fig. 4). We can discriminate the amorphous layers from the crystalline ones, because the maxima of their triangular peaks are displaced off the meridian. In the structure-ghost construction of CDF peaks this displacement is additionally required in order to perfectly match the bottom surface of one crystalline lamella on the top surface of its related twin. Because during the processing this shift is continuously emerging from the lateral tilt of the most probable

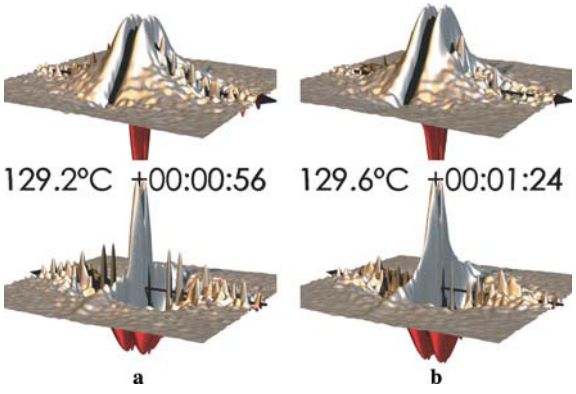

Fig. 3 Oriented crystallization of PE from the RAD structure

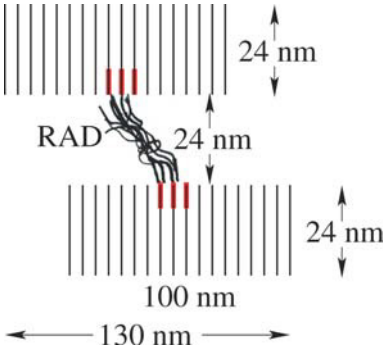

Fig. 4 Isothermal crystallization of PE at 130 °C. Sketch of the characteristic nanostructure of a lamellar twin as indicated by the CDF. The entity is showing two crystalline and one amorphous layer of almost equal thickness. At the tips of the RADs (row nuclei associated structure) primary nuclei are indicated, from which the twin lamellae have been grown

RAD, the RADs appear to have a chaperoning function for the formation of amorphous layers between correlated twin lamellae.

Bundles and knots, blocks and lamellae

In summary, before the start of crystallization we observe a phase separation into bundles and knots (RADs). To us it appears most probable that the phase separation is driven by the formation of bundles from parallelised polymer chains which are not yet crystalline, but crystallizable. A force generated by bundle growth might then cause the entanglement strands to become compressed and tilted. Because of the relatively low molecular mass of our material the knots do not percolate [30], and the crystallizable bundle phase is forming the matrix in the cool melt. Only if we were willing to define the average distance between the knots in transversal direction as some block extension, then the crystallization could be said to be preceeded by a block structure.

Crystal nuclei are supposed to predominantly emerge from the interface between knots and bundles, and this proposed mechanism is able to explain the observed association between the entanglement strands and the structure of row nuclei. The generation of a primary nucleus at an interface appears to induce the generation of a row of secondary nuclei, the whole row being a latent nanostructure only. Crystallization at low undercooling causes the first crystallites to rapidly and continuously grow into lamellar shape. Most probably during this process knots are circumvented and enclosed in the crystalline domain.

During crystallization at high undercooling we find that after a short period of time most of the domains are no longer lamellae. Instead, we observe planes tiled with blocky crystals (Fig. 5). The two CDFs in the figure show the situation 90 s after the start of isothermal crystallization at 130 °C (Fig. 5a) and 120 °C (Fig. 5b), respectively. The differences of the nanostructure are clear. At 130 °C we observe on the equator a strong intensity ridge that is decreasing monotonously as a function of distance (triangular peak). The observed discontinuity in the centre is an artifact resulting from the automatic data evaluation (background scattering correction). Crystallizing at 120 °C, the ridge is clearly modulated (i) and thus reveals oriented planes full of blocky crystals. Moreover, on the meridian we always observe a strong long period peak (j) emerging, as soon as blocks are becoming the predominant crystalline feature. This shows that only the blocks, i.e. the secondary crystallites, are seeking strong correlations (short-range order, lattice) with other domains, whereas the primary lamellae occupy volume without any relation to their neighbours (random car parking process) [22, 23, 24] – as long as the already mentioned formation of twins is disregarded.

Nanostructure evolution visualised in movies

The dynamics of nanostructure evolution during the crystallization as a function of different temperature profiles are most clearly visualised in sequences of 3D representations of the CDF that are collected in movies (http://www.chemie.uni-hamburg.de/tmc/stribeck/crys/). The principal steps of the crystallization from our oriented but quiescent melt are sketched in Fig. 6.

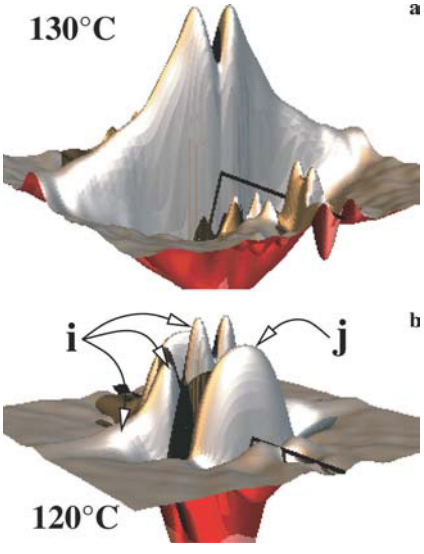

Fig. 5 Lamellae **(a)** and a plane tiled with blocks **(b)** are clearly discriminated in the CDF. View of the bottom face of the CDF in the range $|r_{12}|$, $|r_3| \leq 150$nm. The r_3–direction (meridian) is indicated by an arrow in the base plane. Both images show the structure during isothermal crystallization of PE 90 s after quenching

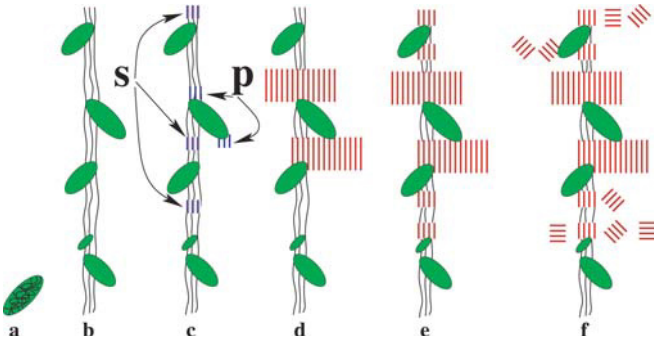

Fig. 6 Sketch of the principal steps of crystallization from a highly oriented, quiescent polyethylene melt as indicated from CDF-images generated from 2D–SAXS/WAXS image series accumulated during a continuous, simultaneous in-situ experiment. Knots (entanglement strands, (a)) are represented in a simplified manner by ellipses. The backbone (b) is a sequence of bundles and knots, not an extended chain crystal. When crystallization starts (c), primary nuclei (p) induce a row of latent secondary nuclei (s) arranged on a lattice along the backbone. Primary crystallization (d) results in extended lamellae grown from the primary nuclei only. Secondary crystallization starts (e) with the generation of rows of blocks, followed by (f) the crowding of virtual planes oriented perpendicular to the fibre direction by unoriented, block-shaped crystals

A semi–quantitative analysis of the nanostructure and its evolution for the different crystallization conditions from our experiments is presented in a following section.

The ultimate structure

Back at room temperature all samples show a two-component nanostructure made from both lamellae and blocks. The average lateral extension of the lamellae in the ultimate structure is lower (70 nm) than that observed directly after the beginning of the crystallization process (100 nm).

Fig. 7 shows the different ultimate structures which are obtained as a result of different temperature programmes.

In the ultimate structure the longitudinal correlation peak (next strongest peak on the meridian) has changed its character. The peak that has been rather narrow when it has started to emerge (correlation between two blocks in fibre direction) has become a broad triangle. This observation does not indicate that blocks have merged to form lamellae, but only that there is no 3D colloidal lattice. On the other hand, a structured arrangement within a single plane filled with blocks is clearly indicated by the satellites to the strongest peaks (cf. arrows in Figure 7f). In our cursory study reported recently [22] we crystallized at 127 °C, but found no longitudinal correlation among planes tiled with blocks. Instead, the longitudinal correlation was found to be restricted to rows of single blocks. From the former experiment we unfortunately have neither WAXS data nor data concerning the achieved structure of the annealed melt.

The shape of the satellites to the strongest peaks in the ultimate CDF is indicating the distribution of block sizes. Blocks are more uniform and bigger, if the material is quenched after isothermal crystallization (Fig. 7c,e). As well a crystallization at a low temperature that is, in general, favouring the formation of blocks provides for more uniform blocks (compare Fig. 7b with Fig. 7a).

If we crystallize for half an hour at a very low temperature (120 °C, Fig. 7b), the ultimate nanostructure is no longer a function of the cooling rate chosen.

The samples which have not completely been molten (Fig. 7a,c,f) exhibit their strongest peaks in the CDF extending on a straight line parallel to the equator. In contrast, the corresponding peaks of the samples which have been completely molten during melt-annealing (Fig. 7b,d,e) exhibit arc-shaped positive peaks. As revealed in the movies generated from the stream of X-ray data, the bending is the result of preferential directed thickness growth of twin lamellae during the isothermal phase, away from the nuclei at the tips of the tilted entanglement strands. Thus the central part from the set of three triangles is moving outward (thickness growth), whereas the outer triangles (amorphous zone in

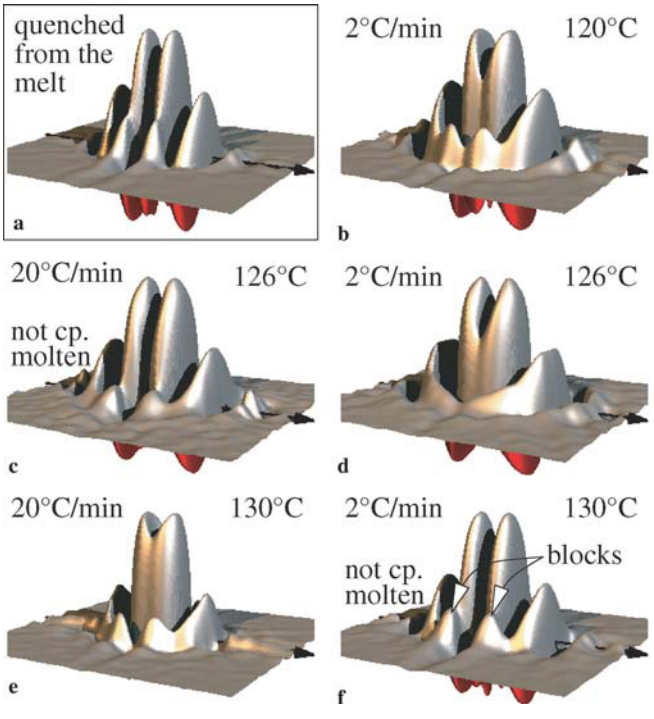

Fig. 7 Oriented crystallization of PE from the melt. Ultimate nanostructures as revealed in the CDF. The images show the top view of the CDF in the range $|r_{12}|$, $|r_3| \leq 150$nm. The r_3-direction (meridian) is indicated by an arrow in the base plane. Indicated are the crystallization parameters and, in addition, if the crystals were not completely molten during 2 min melt annealing at 140 °C

between) remain at almost the same position. An explanation for the different behaviour of the two kinds of samples appears to be obvious. If the memory of the sample is not only in the knots of the cool melt, but as well in remnant crystallites, lamellae grow from these unmelted crystallites, and a considerable fraction of the original lamellae is instantly restored.

Semi-quantitative evaluation of the domain structure

A complete evaluation of the high-resolution multidimensional data from our experiments would require novel concepts for data evaluation as well as a multidimensional modelling of the data to be developed. We do not have the means to surmount this task in a reasonable period of time. Nevertheless, even at this stage we can acquire more in-depth notions concerning the structure transfer between the melt and the solid state, if only we study the positions of the peak maxima in the CDF. Moreover, the results obtained by such analysis may result in hints concerning the answer to the question of how to design more advanced methods of data analysis.

In any case, a shortcoming of this semi-quantitative analysis is that it can only be applied to such peaks in the CDF which are sufficiently separated from each other. Most clearly this is the case for the crystallization at 130 °C. Here all the peaks that are of primary interest for the nanostructure are well-separated. For the materials crystallized at lower temperature this is no longer the case, and for analysis we have to pick clear peaks with a less direct meaning.

5.4.1 Isothermal crystallization at high temperature

Figure 8 shows the variation of nanostructure parameters as a function of time after quenching to 130 °C as determined from the positions of the peak maxima in the CDF. Only a fraction of the collected images have been subjected to this analysis. Cooling rate during quenching is 20 °C/min. Crystallization starts 35 s after leaving the melt-annealing temperature of 140 °C. During the first 100 s the most probable thickness of the crystallites in the ensemble (filled circles) is 24 nm. The most probable amorphous gap between twin lamellae (open circles) is rapidly decreasing from 30 nm to 23 nm. On this level it remains constant for 5 min. The most probable transversal offset of the crystalline lamellae from twins with respect to each other (diamonds) is initially continuously decreasing to 16 nm. Thereafter this parameter, as well, is constant for 5 min. During this first 5 min the stable crystalline domain is a fairly extended lamella (100 nm diameter). In the period between 2 min and 5 min we both observe a continuous increase of the most probable layer thickness to 27 nm and an increase of the crystal orientation in the WAXS pattern. During this period of crystallite thickness growth the distance between both the correlated lamellae is constant. Thus the semi-quantitative analysis now provides means to measure the phenomenon of directed thickness growth that has already been detected by inspection of the movies. In the image inset in Fig. 8 the proposed average stabilising primary knot (entanglement strand) is indicated between the two lamellae.

After the first 5 min the generation of blocky crystals (secondary crystallization) is starting in addition to the continued formation of lamellae. The average transversal offset in twins is considerably decreasing, then becomes more and more diffuse, and cannot be determined any more for crystallization periods >20 min. The most probable crystalline thickness (as measured in fibre direction) is once again increasing up to a value of 30 nm, but here we can no longer address this phenomenon by the term layer thickness growth because—as is exhibited by the 2D WAXS data measured simultaneously [26]—the blocky crystals are oriented at random.

During the final quenching after an isothermal phase of 30 min the average crystal extension decreases considerably and the nanostructure becomes heterogeneous to such an extent that the determination of most of the nanostructure parameters becomes insignificant.

Crystallization during quenching from the cool melt

Nanostructure is evolving in a different manner, if the material is cooled from the melt as fast as possible (20 °C/min). Fig. 9 presents the structural data retrieved from the peak maxima in the CDF. The first crystals are observed when the temperature has dropped to 130 °C. Down to a temperature of 118 °C

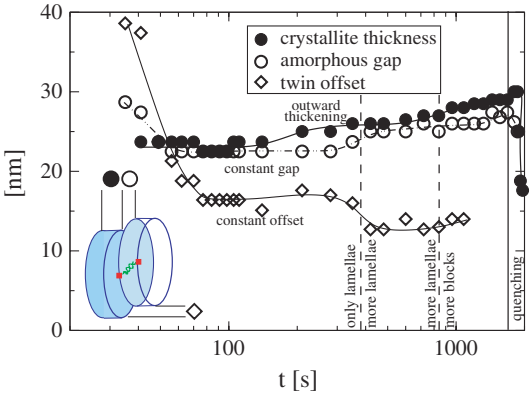

Fig. 8 Isothermal crystallization at 130 °C followed by quenching. Parameters of the nanostructure as determined from the maxima of the corresponding peaks in the CDF

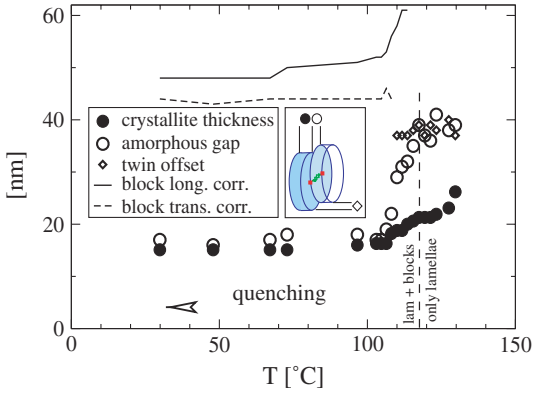

Fig. 9 PE crystallization during the quenching (20 °C/min) from the melt. Parameters of the nanostructure as determined from the maxima of the corresponding peaks in the CDF

we only observe the formation of lamellae; at lower temperatures blocky crystals are becoming predominant.

During the initial period the average layer thickness (filled circles) drops from 24 nm to 20 nm, where it pauses a while up to the time when the formation of blocky crystals is starting. Thereafter it decreases to 15 nm. The amorphous interlayers (open circles) and the transversal offset of twin lamellae (diamonds) are constantly high during the phase of layer generation. As soon as the formation of blocks is starting, the transversal offset cannot be determined any longer and the average amorphous thickness drops to the level of the extension of the secondary crystalline blocks. A longitudinal correlation (solid line) of blocks in the fibre direction is the first clear indication of block formation. Particularly distinct are the corresponding positive peaks on the positive face of the CDF. They characterise the distance from the ''upper'' end of a block to the ''lower'' end of its neighbour. Thus the value determined from the peak position is $L + b$, long period plus block extension in fibre direction. The corresponding value (solid line) drops from initially 60 nm to 50 nm and then remains at this lower level. For temperatures below 110 °C we as well find a transversal correlation among blocks (dashed line). According to the peak position the distance between neighbouring blocks in the (layer) plane is constant at 43 nm.

As expected, the average crystallite sizes are considerably smaller for the material that has been quenched from the melt as compared to the material discussed before (isothermally crystallized at a high temperature). Moreover, here there are less lamellae, and because of the quenching the block size distribution is relatively narrow. This causes the nanostructure made from arranged blocks to become particularly clear in the CDF of this material.

Isothermal crystallization at medium and low temperature

At medium (126 °C) and low (120 °C) crystallization temperature the semi-quantitative data analysis is more difficult than in the two cases discussed before, because a superposition of lamellar and block structure is observed almost from the beginning of the isothermal phase.

Thus during crystallization at 126 °C (Fig. 10) a slow decrease of the most probable crystallite thickness (filled circles) from 24 nm to 20 nm is observed, and the only other parameter that is easily accessible is the long period. At the beginning of crystallization two clear long periods (triangles) are found in the CDF, which merge 2 min after the quenching. In the beginning the long period is rapidly decreasing and indicates a predominantly statistical process of crystallite placing in the volume (''random car parking'' [23]). Only 5 min after the quenching the most probable structural parameters have reached their ultimate value. They even do not change during the quenching after the isothermal phase. From both the data accumulated at the ESRF and the earlier data from the cursory study at HASYLAB [22] we estimate the same lateral distance between two blocks from the same plane (45 nm).

If the melt is crystallized at 120 °C (Fig. 11), the decrease of the crystallite thickness from 24 nm to 20 nm is much faster than in the material crystallized at 126 °C. After only 2 min the satellite peaks of blocks arranged in planes (open triangles) are very clear. Initially the distance of the satellite peaks from the equator is somewhat longer than that of the central peak. This means that the extensions in fibre direction of the blocks arranged in planes are somewhat thicker than the most probable thickness of all crystallites. The reason may be the random orientation of crystal axes in the blocks. 4 min after the start of the crystallization there is no more difference.

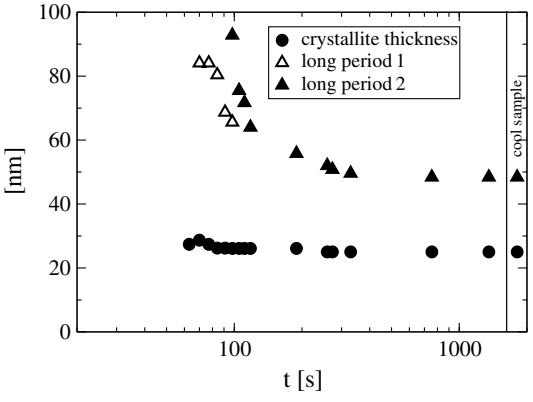

Fig. 10 Isothermal crystallization at 126 °C. Parameters of the nanostructure as determined from the maxima of the corresponding peaks in the CDF. The long periods are very weak during the first 10 min (little correlation among domains), and peak maxima of block arrangement cannot be determined

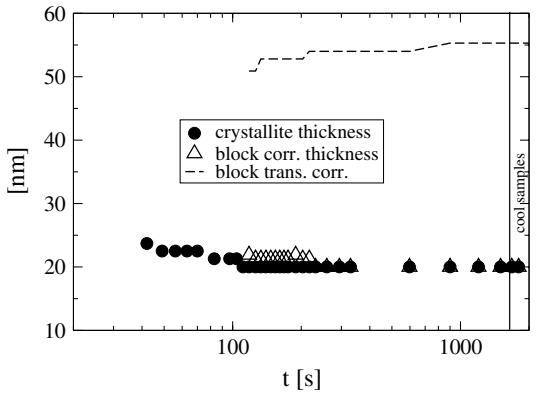

Fig. 11 Isothermal crystallization at 120 °C. Parameters of the nanostructure as determined from the maxima of the corresponding peaks in the CDF

While the long period is decreasing during crystallization, the average transverse distance between neighbouring blocks in a plane (dashed line) is slightly increasing from 50 nm to 55 nm. As well at this low crystallization temperature, the final cooling to ambient temperature has no effect on the average parameters of the nanostructure. Here, at the lowest crystallization temperature chosen, even the widths of the peaks and thus the widths of the distributions of the nanostructure parameters are neither changed by cooling nor by variation of the cooling rate.

Conclusions

In this paper we have shown that the analysis of X-ray data from polymer materials recorded with high resolution in time and space can be carried out in physical space. It results in a detailed, almost continuous data stream which reflects the evolution of nanostructure during materials processing. By application of this method we have been able to gain a rather detailed description and notion concerning the mechanisms that control the formation of crystals in our oriented polyethylene melt.

After a semi-quantitative analysis we, moreover have obtained curves describing the variation of nanostructure parameters during the crystallization processes investigated. We expect that similar studies will contribute to the understanding of the relationships between process control parameters and the features of the resulting nanostructure, in particular if the typical industrial production stages with respect to polymer materials processing like fibre spinning, extrusion, straining or annealing are set up at a modern synchrotron beam line, monitored continuously by 2D detectors, and finally analysed by advanced data evaluation procedures that incorporate the fields of scattering theory and digital image processing.

Even if the novel combination of experiment and analysis provides detailed insight into the mechanisms of nanostructure transfer, new limits of cognition become apparent. For example, we now would wish to be able to discriminate the continued growth of "early" crystals from the effects arising from the formation and growth of late crystals. In order to perform such investigations it would be desirable to minimise the volume integration of the scattering method down to a cross-section far below that of the presently available microfocus beams, or to advance an imaging method in a way that it can be used in-situ in a minimal invasive environment, similar to what already at this stage can be achieved by utilisation of X-rays.

Acknowledgement We thank the European Synchrotron Radiation Facility, Grenoble, for beam time granted in the frame of project SC 1396.

References

[1] Heck B, Hugel T, Iijima M, Sadiku E, Strobl G (1999) New J Phys 1:17.1
[2] Heck B, Hugel T, Iijima M, Strobl G (2000) Polymer 41: 8839
[3] Heeley EL, Maidens AV, Olmsted PD, Bras W, Dolbnya IP, Fairclough JPA, Terrill NJ, Ryan AJ (2003) Macromolecules 36: 3656
[4] Bras W, Dolbnya I, Detollenaere D, van Tol R, Malfois M, Greaves G, Ryan A, Heeley E (2003) J Appl Cryst 36: 791
[5] Somani RH, Yang L, Hsiao BH, Fruitwala H (2003) J Macromol Sci Part B Phys B42: 515
[6] Somani RH, Yang L, Hsiao BS, Agarwal PK, Fruitwala HA, Tsou AH (2002) Macromolecules 35: 9096
[7] Yamazaki S, Hikosaka M, Toda A, Wataoka I, Yamada K, Tagashira K (2003) J Macromol Sci Part B Physics B42: 499
[8] Allegra G, Meille SV (1999) Phys Chem Chem Phys 1: 5179
[9] Pearce R, Vancso GJ (1998) Polymer 39: 1237
[10] Hobbs JK, Humphris ADL, Miles MJ (2001) Macromolecules 34: 5508
[11] Humphris ADL, Hobbs JK, Miles MJ (2003) Appl Phys Lett 83: 6
[12] Stribeck N (1993) Colloid Polym Sci 271: 1007
[13] Stribeck N (2000) ACS Symp Ser 739: 41
[14] Stribeck N (2001) J Appl Cryst 34: 496
[15] Stribeck N (2002) Colloid Polym Sci 280: 254
[16] Ruland W (1971) J Appl Cryst 4: 70
[17] Perret R, Ruland W (1971) Colloid Polym Sci 247: 835

[18] Brämer R, Ruland W (1976) Makromol Chem 177: 3601
[19] Ruland W (1977) Colloid Polym Sci 255: 417
[20] Ruland W (1977) Colloid Polym Sci 255: 833
[21] Ruland W (1987) Macromolecules 20: 87
[22] Stribeck N, Almendarez Camarillo A, Cunis S, Bayer RK, Gehrke R (2004) Macromol Chem Phys 205: 1445
[23] Stribeck N (2004) Macromol Chem Phys 205: 1455
[24] Stribeck N, Almendarez Camarillo A, Bayer R (2004) Macromol Chem Phys 205: 1463
[25] Barham PJ, Keller A (1985) J Mater Sci 20: 2281
[26] Stribeck N, Bayer R, Bösecke P, Almendarez Camarillo A (2005) Polymer 46: 2579
[27] Stribeck N, Buzdugan E, Ghioca P, Serban S, Gehrke R (2002) Macromol Chem Phys 203: 636
[28] Stribeck N, Funari SS (2003) J Polym Sci Part B Polym Phys 41: 1947
[29] Bayer RK (1991) Colloid Polym Sci 269: 421
[30] Bayer RK, Liebentraut F, Meyer T (1992) Colloid Polym Sci 270: 331
[31] Bayer RK (1994) Colloid Polym Sci 272: 910
[32] Stribeck N, Bayer R, von Krosigk G, Gehrke R (2002) Polymer 43: 3779
[33] Narayanan T, Diat O, Bösecke P (2001) Nucl Instrum Methods Phys Res Sect A 467-468: 1005
[34] Bösecke P, Diat O (1997) J Appl Cryst 30: 867
[35] Urban V, Panine P, Ponchut C, Bösecke P, Narayanan T (2001) J Appl Cryst 36: 809
[36] pv-wave, version 7.5 (2001), Visual Numerics Inc., Boulder, Colorado
[37] Vonk CG (1979) Colloid Polym Sci 257: 1021
[38] Rosenfeld A, Kak AC (1982) Digital Picture Processing, vol. 1. Academic Press, London
[39] Haberäcker P (1989) Digitale Bildverarbeitung. Hanser, Munich

Progr Colloid Polym Sci (2005) 130: 140–148
DOI 10.1007/b107390
Published online: 3 June 2005

Francisco J. Baltá Calleja
Fernando Ania
Inés Puente Orench
Eric Baer
Anne Hiltner
Teresa Bernal
Sérgio S. Funari

Nanostructure development in multilayered polymer systems as revealed by X-ray scattering methods

Abstract The crystallization behaviour of semicrystalline polymers in structurally confined environments is becoming a topic of increasing interest in the area of soft condensed matter. In the present study *in-situ* wide angle (WAXS), small angle (SAXS) and ultra-small angle X-ray scattering (USAXS) experiments concerning the development of nanostructure in multilayered poly(ethylene terephthalate)/polycarbonate (PET/PC) films prepared by continuous layer-multiplying coextrusion are reported. These materials show up rather uniform laminates up to thousands of layers from the micrometer down to the nanometer range. USAXS profiles with the X-ray beam parallel to the nanolayered packing reveal the occurrence of scattering maxima corresponding to the PET/PC stacking periodicity. It is shown that the confined crystallization of PET from the glassy state, taking place between the amorphous layers of PC, is hindered when the thickness of the PET layers lies below the micrometer range. The obtained results indicate that for pure PET multilayers the appearance of the first WAXS and SAXS peaks occurs at much lower temperatures (~117°C) than when PET is confined between the PC layers (~132°C). In other words, the PET confinement delays the crystallization process. On the other hand, it is also shown that the long period of the crystal stacks within the semicrystalline PET layers increases with decreasing layer thickness while the degree of crystallinity becomes smaller. Results are highlighted on the basis of thinner multilayers giving rise to a smaller density of crystallites involving stacks that exhibit larger periodicities. Finally, the increasing lamellar orientation appearing within the PET layers with decreasing layer thickness is discussed.

Keywords Multilayered polymer systems · Nanostructure development · Cold crystallization · Confinement · Lamellar orientation · Small-angle X-ray scattering · Wide angle X-ray scattering

Dedicated to Prof. Dr. Wilhelm Ruland on occasion of his 80th birthday

F. J. Baltá Calleja (✉)
F. Ania · I. Puente. Orench
Instituto de Estructura de la Materia, CSIC, Serrano 119, 28006 Madrid, Spain
e-mail: embalta@iem.cfmac.csic.es

E. Baer · A. Hiltner · T. Bernal
Case Western Reserve University, 2100 Adelbert Road, Cleveland, Ohio 44106-7202, USA

S. S. Funari
Max-Planck Institute for Colloids and Surfaces, c/o HASYLAB, DESY, Notkestrasse 85, 22603 Hamburg, Germany

Introduction

Microlayer coextrusion has been developed as a new processing technique in which two or more polymeric materials are combined into a layered configuration, thereby controlling the architecture of the final product (1). Generally the synergistic combination of two or more materials in a layered structure can enhance the overall properties of the material. For instance in the case of metals like steel, the higher carbon content leads to the formation of a layered structure that increases the hardness of the material (2). The layered

structure of steel provides two property improvements: a toughness enhancement and a hardness increase. On the other hand, natural biological systems as diverse as cotton fibers, wood, tendon and even the lens of the human eye possess layered structures designed to meet a diverse spectrum of functional requirements (3–5). The multilayer film nanostructure in coextruded films of high-density polyethylene, confined between polystyrene (PS) layers, (6) and of ultrathin polypropylene (PP) layers alternating with PS in multilayer films (7) has been investigated using optical-, transmission electron- and atomic force microscopy, as well as X-ray scattering techniques (6, 7). Enhanced mechanical properties have been previously obtained in systems like PC/styrene acrylo nitrile (PC/SAN) microlayer composites with decreasing layer thickness (8). This has been attributed to the change in the deformation mechanism of the brittle SAN layers, from craze opening to shear yielding, as layer thickness decreases. Interaction between the crazes in the brittle layers and micro-shear-bands in the tough layers is the key to this change in mechanism (8). The basic aspects of microindentation in multilayered PET/PC films produced by continuous layer multiplying coextrusion have been recently reported (9). Experimental confirmation of the extension of the deformation field beneath the indenter, previously calculated by numerical methods, was presented. Results reveal that the most important parameter in determining the final hardness (H) of the multilayer films is the ratio of the indenter penetration depth to the thickness of the layers. The influence of the interphase on the H-values for samples with large number of layers is however rather small.

The aim of the present study is to report new results concerning the structure development of a semicrystalline polymer (PET) in a structurally confined environment (in between PC layers) by means of X-ray scattering techniques. Since the pioneering work of Keller and Baer (6), the study of the crystallization behaviour of semicrystalline polymers in structurally confined environments is a topic of increasing interest. Confined crystallization may occur in different polymer systems, including block copolymers (10–12), semicrystalline polymers with nano-fillers (13), free surfaces in thin films (14) and, in our case, multilayered films.

The paper is organized as follows: 1) we will show that nanostructure layering in PET/PC systems can be detected by ultra-small angle X-ray scattering (USAXS), 2) new results on microstructure development in confined PET/PC systems will be presented and the influence of temperature and layer thickness on the structure formation will be discussed and 3) the effect of confinement on crystallinity, lamellar orientation and long period will be illustrated.

Experimental

Materials

The coextrusion system used to prepare microlayered and nanolayered materials consists of two 1.9 cm single screw extruders with melt pumps, a coextrusion block, a series of layer multiplier elements and an exit die as described previously (5). From the feedblock, the two layers flow through a series of multiplying elements, each of these doubles the number of layers. In each element, the melt is first sliced vertically, then spread horizontally and finally recombined by stacking. An assembly of n multiplier elements produces an extrudate with the layer sequence $(AB)_x$ where x is equal to 2^n. Nanolayered structures with over 8000 layers have been successfully processed by this versatile coextrusion system. By varying the processing conditions, the final sheet or film thickness, the number of layers and the individual layer thickness can be precisely controlled down to the nanoscale. The materials used in our study using the multilayer co-extrusion method were PET (M&G Cleartuf 8004) and PC (Dow Calibre 200-10), both having molecular weights of about 30,000 and glass transition temperatures of 75 and 150°C respectively, experimentally measured by DSC. Multilayered composites with 8, 32, 256 and 1024 layers and PET/PC volume compositions of 100/0, 70/30, 50/50, 30/70 and 0/100 were used in this study. The number of layers, the volume composition and the film and layer thickness are collected in Table I. The PET thicknesses ranged between 50 nm and 32 μm. Figure 1 shows an optical micrograph of a typical 8-microlayered 50/50 PET/PC film with a regular layer thickness of about 60 μm viewed along the transverse direction. It is also shown the three reference directions of the film: the coextrusion or flow direction (F), the transverse direction (T) and the direction normal to the film (N). The initial multilayered materials were amorphous. Samples were annealed in vacuum for 25 minutes at four different temperatures: 100, 117, 132 and 150 °C. In this temperature range, it is known that only PET modifies its morphology as a result of cold crystallization. PC layers, in turn, undergo a densification due to a decrease in free volume (physical ageing).

Techniques

Ultra-small angle X-ray scattering (USAXS) experiments were performed at the beam-line BW4 in HASYLAB at the storage ring DORIS (DESY, Hamburg), to obtain the USAXS patterns of some nanolayered films (15). A wavelength of 0.138 nm (photon energy of 8.98 keV) and a sample-detector distance of 13.04 m were

Table 1 Number of layers and film and layer thicknesses for the nano and micro-layered samples of PET/PC

Name	PET/PC (%vol)	# Layers	Film Thickness (μm)	Layer Thickness PET/PC (μm)
M1	100/0	1024	76	0.07
M2	70/30	1024	76	0.1/0.05
M3	50/50	1024	76	0.07/0.07
M4	30/70	1024	76	0.05/0.1
M5	0/100	1024	76	0.07
M24	50/50	256	76	0.3/0.3
M23	50/50	256	254	1/1
M22	50/50	32	76	2.4/2.4
M21	50/50	32	254	8/8
M17	50/50	8	254	32/32

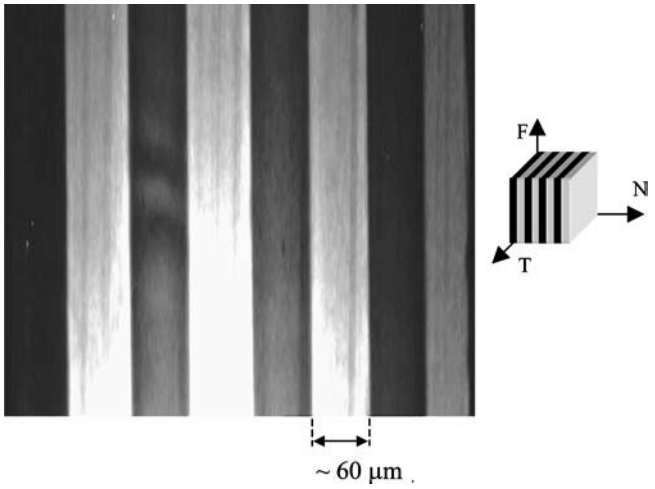

Fig. 1 Optical micrograph of a 8-microlayered 50/50 PET/PC film with layer thickness of about 60 μm. The sketch shows the reference directions

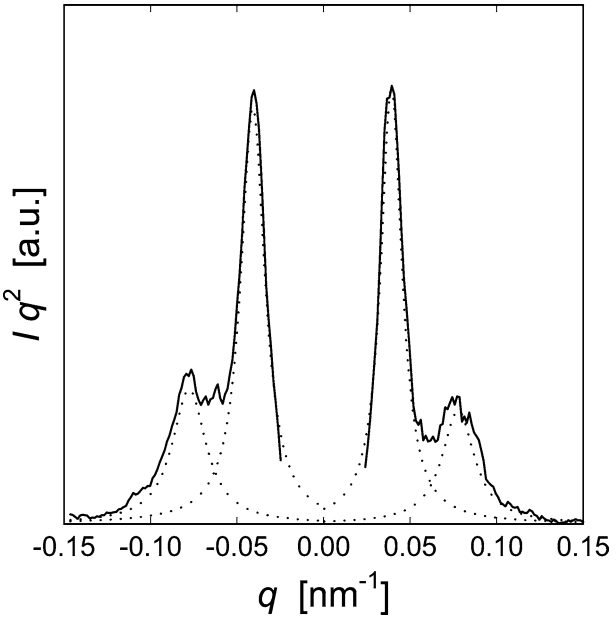

Fig. 2 USAXS intensity profile *vs* wave vector ($q = 4\pi\sin\theta\,/\lambda$) with the X-ray beam parallel to the nanolayered structure of a 70/30 PET/PC film (1024 layers) annealed at 180°C for 2 hours

chosen. A two dimensional 512 × 512 Gabriel detector with a spatial resolution of 390 μm per pixel was used. The nanolayered films were positioned with the X-ray beam parallel to the stacking of the layers (F or T directions). The long period was calculated from meridional cuts of the original patterns after background subtraction.

The WAXS and SAXS experiments were performed at the beam-line A2 in HASYLAB using a double-focusing camera, attached to the synchrotron radiation source (16). A wavelength of 0.150 nm (~8 keV) and a sample-SAXS detector distance of 2343 mm were used. Position calibration was performed using standards of PET and rat-tail tendon for WAXS and SAXS respectively. Simultaneous WAXS and SAXS patterns, with the films normal to the beam (N), were collected at room temperature during 300 s using linear position sensitive detectors. Data were corrected for fluctuations in intensity of the primary beam and detector responses. In order to investigate lamellar orientation, two dimensional SAXS experiments at room temperature, with the X-ray beam parallel to the layer stacks (F or T) were also performed. For this purpose, a MAR CCD detector which has an active area diameter of 165 mm (pixel size = 158 × 158 μm^2) was used.

Ultrathin sections (~70 nm) of the samples were cut along the N direction using an ultramicrotome and investigated in a Leo 912 transmission electron microscope (TEM).

Results and Discussion

Figure 2 illustrates the USAXS profile with the X-ray beam parallel to the nanolayered structure of a 70/30 PET/PC film (1024 layers having an alternating thickness of 100 and 50 nm, respectively) annealed at 180 °C for two hours and measured at room temperature. Several scattering maxima, that arise from the electronic density difference among alternating PET and PC layers, are observed. From the angular position of the maxima (first and second order) fitted to Lorentz profiles (dotted lines), an average spacing of about 160 nm is derived for the layer structure. This value agrees quite well with the nominal average separation between equivalent layers though it is somewhat smaller than the distance measured by TEM (Fig. 3). In the particular region shown in the figure, the distance between the centers of two consecutive light layers (PET) separated by a dark one (PC) is about 270 nm.

In Figure 4 the WAXS profiles, in the normal direction, of the initially amorphous pure PET (a) and

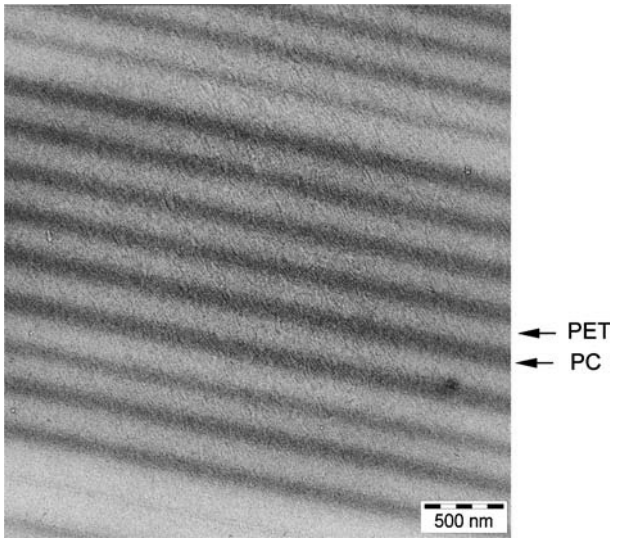

Fig. 3 Transmission electron micrograph of a 1024-nanolayered film of 70/30 PET/PC; thicknesses: 180 nm/90 nm

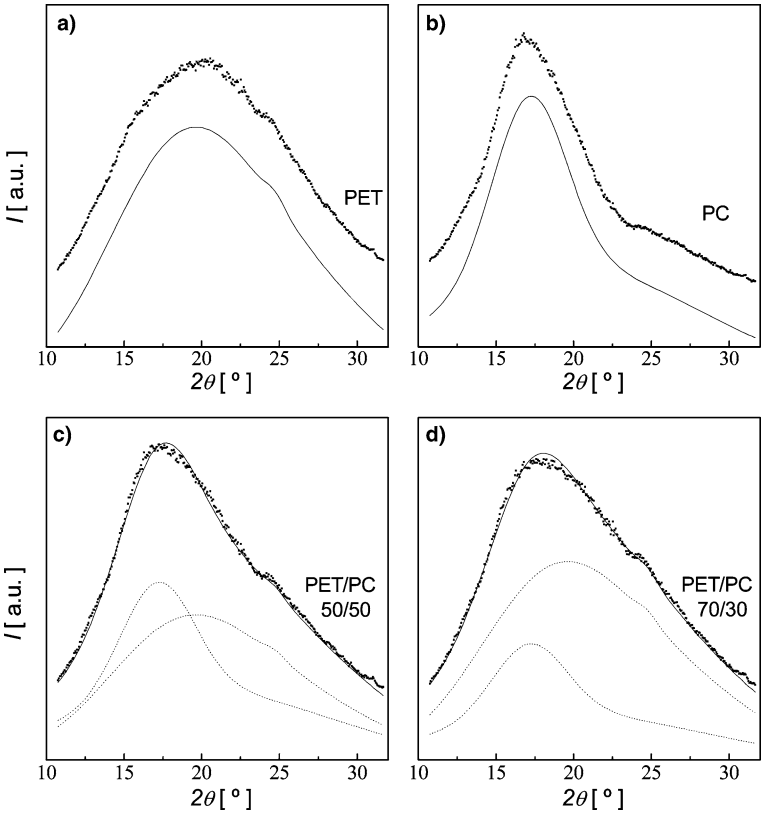

Fig. 4 Wide-angle X-ray diffraction patterns of 1024 layered films of: a) PET, b) PC and c) and d) PET/PC, before crystallization. For the PET/PC profiles, the separate contributions of PET and PC are shown as dotted lines

pure PC (b) multilayered samples are presented in comparison with the diffraction patterns of the also initially amorphous 50/50 (c) and 70/30 (d) PET/PC films. All these films are composed of 1024 layers. The best fits to the experimental scattering intensity, found for the amorphous halos of PET and PC, are shown as continuous lines in Figure 4a and 4b. For the sake of clarity the fitted curves are shifted downwards in Figure 4a and 4b. The weighted averages, according to the volume composition, of the above curves have been used for fitting the PET/PC amorphous profiles (continuous lines in 4c and 4d). In other words, the X-ray amorphous halos of the multilayered PET/PC systems can be decomposed into the separate contributions (dotted lines) of the PET and the PC components.

Figure 5 illustrates the variation of the WAXS pattern in N direction, with increasing annealing temperature, for a pure multilayered PET (a) and for a 50/50 PET/PC film with a layer thickness of 70 nm (b). Results for multilayered PET reveal the appearance of a three-dimensional crystalline structure at about $T = 117$ °C in close resemblance to previous WAXS data obtained during crystallization of bulk PET from the glassy state (17). The present results suggest that the layer boundaries of the multilayered films tend to disappear when processing the single polymer through melt coextrusion. However, for PET confined between layers of an immiscible polymer such as PC and with a PET layer thickness, h, of 70 nm, the crystalline peaks do not appear till a temperature of 132 °C; i.e., the confinement of PET delays the crystallization process. In addition, for each crystallization temperature, the total crystallinity level reached is smaller for the confined PET layers than for the pure PET annealed samples.

Figure 6 illustrates the evolution of the SAXS maximum with increasing temperature for the same non-confined PET (a) and confined PET/PC multilayers (b) as in Figure 5. In both cases it is observed that, the appearance of the SAXS maximum occurs at the same temperatures as those found for the crystalline peaks (117 °C and 132 °C, respectively). Previous studies for different polymers, including PET (18–20), have proved that there is a clear time delay between the appearance of SAXS and WAXS maxima. Accordingly, the appearance of density fluctuations during the induction period prior to crystallization has been proposed and the spinodal decomposition formalism for describing the kinetics of the ordering process has been used (21). It is evident that our present data do not show such a distinction due to the limited temperatures used and more detailed investigations concerning this point are in preparation. On the other hand, it is found that confinement induces a shift of the SAXS maximum towards smaller scattering angles.

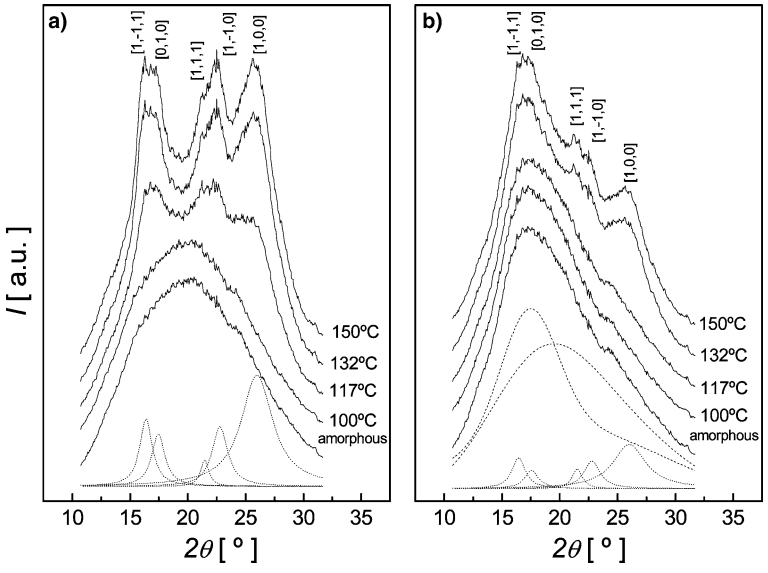

Fig. 5 Structure development from WAXS, in PET/PC systems, with increasing temperature: a) 100/0 and b) 50/50 with $h = 70$ nm. Crystallographic indices and separate contributions of the main diffraction peaks are shown

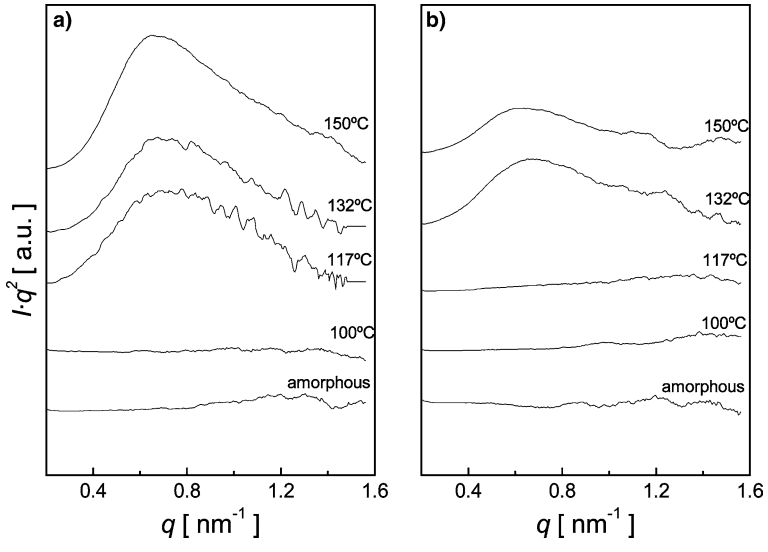

Fig. 6 Plot of normalized SAXS intensity *vs* q showing the nanostructure development in PET/PC systems with increasing temperature: a) 100/0 and b) 50/50 with $h = 70$ nm

From the above results we can compute the influence of confinement on the long period L and on crystallinity X_c. The long period was derived from the peak maximum of the SAXS patterns, after background subtraction and Lorentz correction. Taking into account that in the temperature range chosen, only PET changes its morphology, remaining PC in the glassy state, it is convenient to calculate the volume degree of crystallinity not referred to the whole sample but only to the PET content. Figure 7 illustrates the variation of PET volume crystallinity and long period as a function of PET layer thickness, h, for samples crystallized at different temperatures for 25 minutes. For each temperature, one observes a gradual $X_{c,PET}$ decrease with decreasing thickness (bottom), while the stacks of crystals within the crystallized PET layers show a clear long period increase as h decreases (top). On the other hand, both, L and $X_{c,PET,}$ increase with annealing temperature (T_A). The range of long periods (8.5–9.5 nm) and crystallinities (20–36%) found at high h values agrees well with previous data on amorphous PET films annealed at similar temperatures (22).

Furthermore, we have also shown that the degree of crystallinity follows a stepwise increase with crystallization temperature, at temperatures about 30°C above T_g (23). In case of confined PET between PC layers in the nm range (70 nm), higher temperatures (more than ten degrees) as seen in Fig. 8, are required to obtain a similar

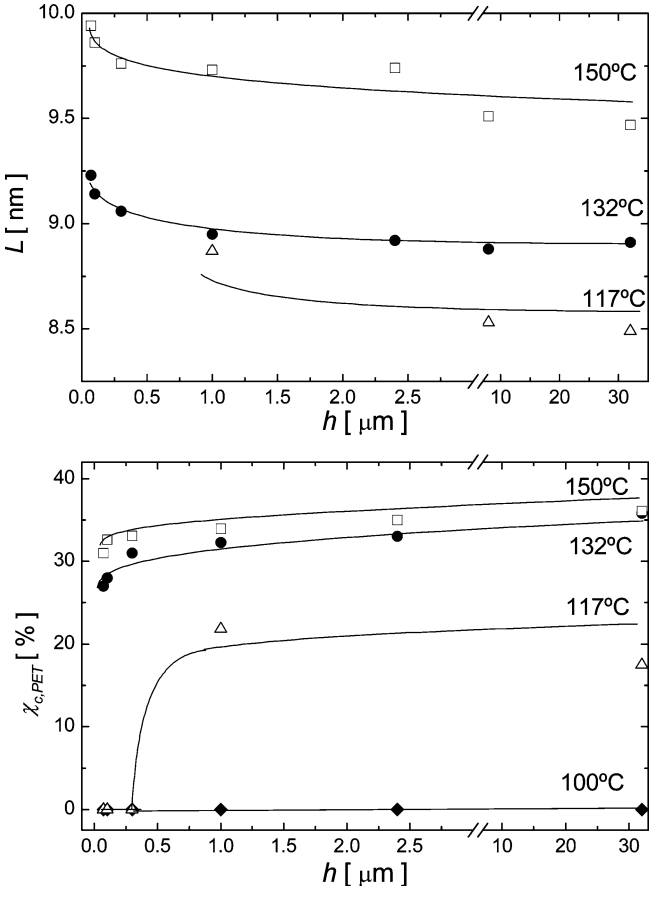

Fig. 7 Influence of PET layer thickness h on the long period L and PET crystallinity of PET/PC multilayers crystallized at different temperatures

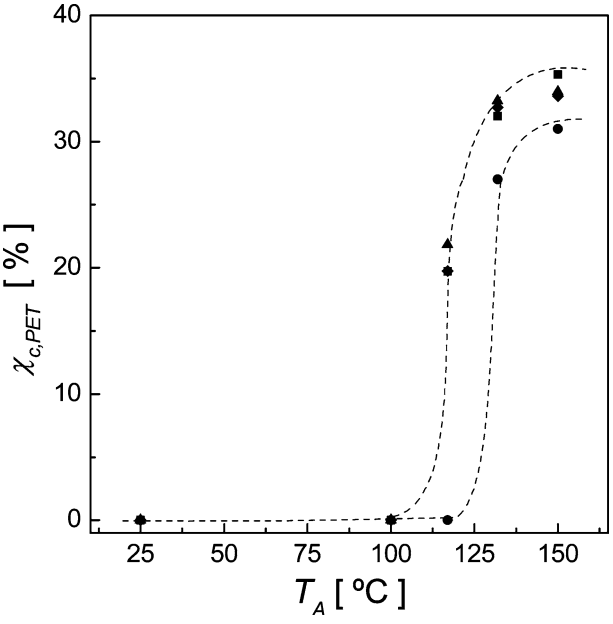

Fig. 8 Variation of PET crystallinity from WAXS with annealing temperature for multilayered PET/PC films having different PET layer thickness h: (■) 100/0, 70 nm; (▲) 50/50, 1 μm; (♦) 50/50, 32 μm and (●) 50/50, 0.07 μm

increase in crystallinity. Hence, it could be concluded that confinement also induces an increase in the crystallization temperature of PET.

We wish to examine next the influence of confinement on lamellar orientation Figure 9a illustrates the SAXS pattern in T direction for 50/50 multilayers with $h = 2.4$ μm, showing no orientation of the stacking periodicity. However, an equatorial streak, perpendicular to the packing planes of the layers is seen. For thinner 30/70 multilayers of h about 50 nm one observes an equatorial SAXS orientation corresponding to the stacks of oriented crystal lamellae superposed to a stronger equatorial streak (Fig. 9b). By plotting the scattering intensity I, at the maximum corresponding to the PET long period, as a function of azimuth angle φ, one observes the occurrence of two maxima at 0° and 180°, respectively (Fig. 10). Each maximum is clearly composed of the superposition from the two above mentioned contributions: 1) the equatorial streak (long dashed line) and 2) the equatorial scattering due to a weakly oriented lamellar PET structure (continuous line). The former probably arises from the presence of microvoids among adjacent layers (6).

Using the definition of orientation function f:

$$\mathbf{f} = \frac{\mathbf{3} < \mathbf{cos^2}\varphi > \mathbf{-1}}{\mathbf{2}}$$

where φ is the azimuth angle and $<\cos^2 \varphi>$ is defined in terms of the azimuthal intensity, I, one can calculate the value of f for different PET layer thicknesses. Fig. 11 shows how the orientation of the crystalline lamellae within the PET layer crystallized at two temperatures rapidly increases when the layer thicknesses become smaller than 0.5 μm. The values of f are slightly higher for the highest annealing temperature.

It is worth mentioning that SAXS patterns for the same materials in flow direction F show similar results as those in T direction. On the contrary, those patterns taken in normal direction N do not present any equatorial streaks and the scattering due to the PET lamellar structure is completely isotropic.

In summary, both, lamellar orientation and long period of the lamellar stacks within the PET layer, increase with decreasing layer thickness while the crystallinity within the layers diminishes with decreasing layer thickness (Fig. 7). The lamellae in confined PET are slightly oriented with the long axes parallel to the flow direction F.

In the light of the above results figure 12 schematically illustrates the occurrence of lamellar orientation as a

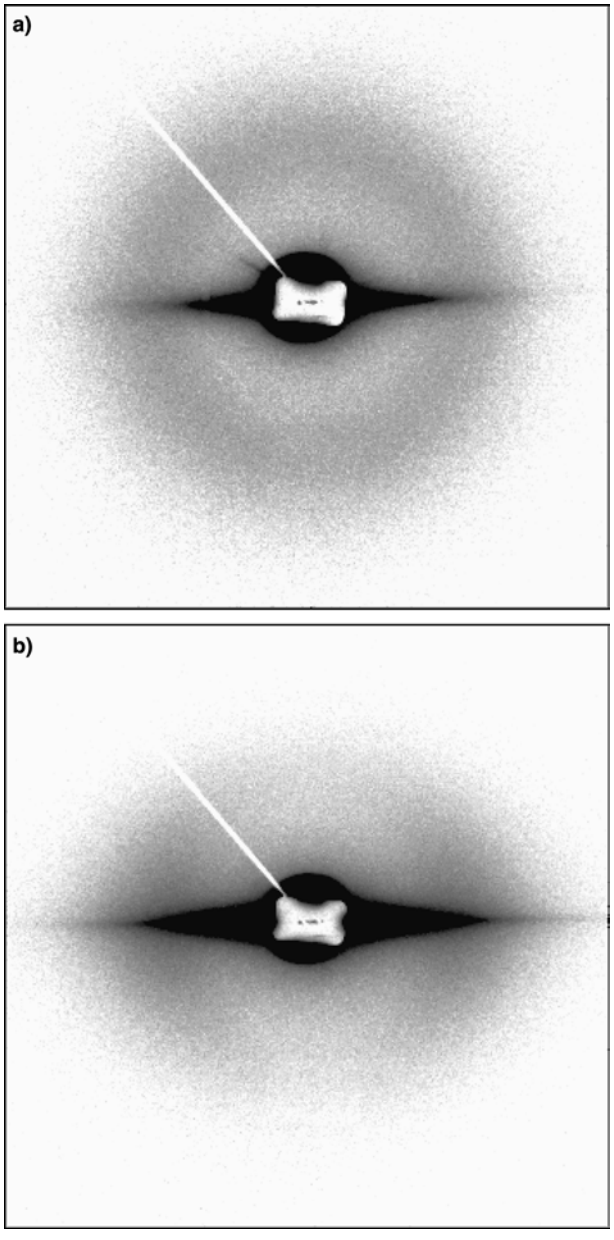

Fig. 9 Two-dimensional SAXS patterns in T direction for multilayered PET/PC films having a PET thickness of: a) $h = 2.4\ \mu m$ and b) $h = 50$ nm

result of confinement within PET layers while the number of crystals per unit volume is reduced. As a consequence, the stacking periodicities are larger within the confined layers (L_1) than in non-confined PET crystallized at the same temperature (L_2). The model suggests that those lamellae, close to the interlayers, are preferentially oriented with their basal surfaces parallel to the stacking planes of the layers. A decrease in the PET layer thickness, h, should consequently improve the level of lamellar orientation.

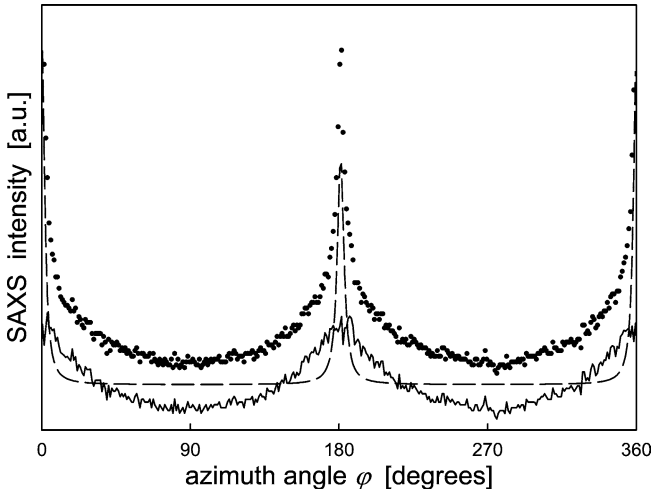

Fig. 10 Azimuthal SAXS intensity at the PET maximum for 30/70 PET/PC nanolayers with $h = 50$ nm. Experimental points are represented by dots. The continuous and the long dashed lines show the independent scattering due to the PET contribution and the equatorial streak, respectively

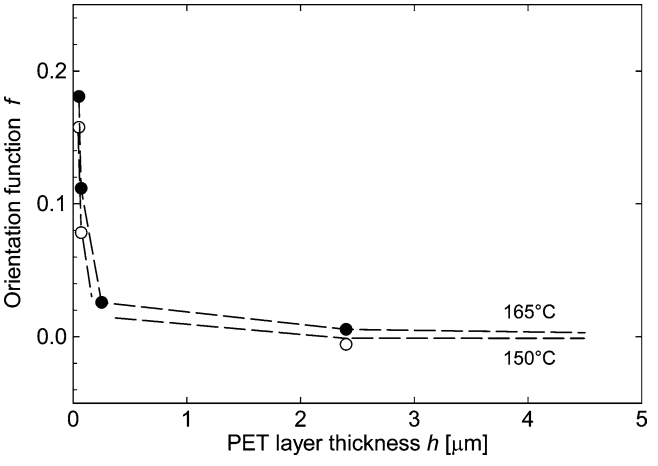

Fig. 11 Plot of the orientation function of multilayered PET/PC films *vs* layer thickness h

We are aware that the present results differ from the typical lamellar orientation found, for instance, in ultrathin PE layers confined between PS layers (6). In this system, lamellae were reported to be oriented with the long axes perpendicular to the flow direction F. Such a morphology arises from the epitaxial nature of crystallization and is related to the shish-kebab structures obtained under special conditions from flowing melts or solutions (6). However, in PP/PS nanolayers (7) as well as in (poly(ethylene oxide)-b-PS) diblock copolymers (12), in addition to a population of lamellae with homogeneous orientation (crystalline molecular chains parallel to the F direction), a new type of homeotropic

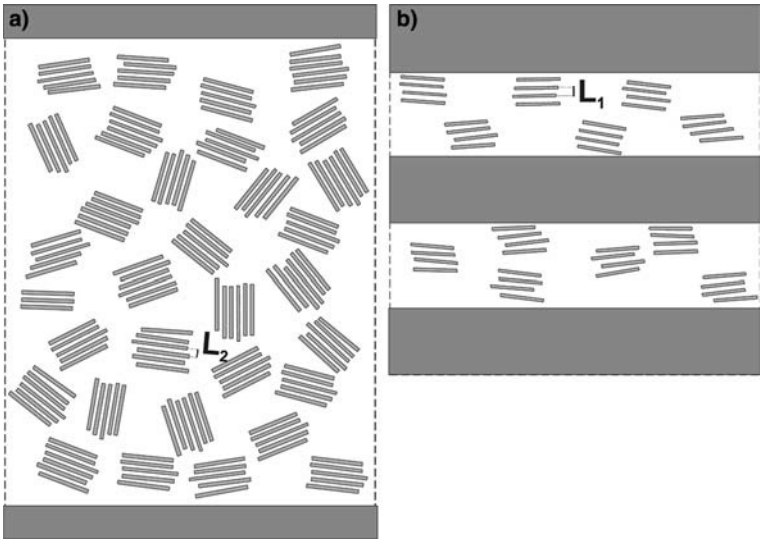

Fig. 12 Schematic model of PET crystallization in a) a thick layer ($h = 2.4\ \mu m$) and in a confined environment ($h = 70$ nm)

orientation (perpendicular to the former one) is observed, resembling that found in our multilayered system.

Conclusions

– The use of ultra-SAXS in the transverse direction T reveals the occurrence of scattering maxima corresponding to the PET/PC stacking periodicity.
– During crystallization from the glassy state the crystallization of PET, taking place between the amorphous layers of PC, is hindered when the thickness of the PET multilayers is confined below the micrometer range.
– The appearance of the first WAXS and SAXS peaks for non-confined PET occurs at much lower temperatures (~117 °C) than when PET is confined between the PC layers (~132 °C). In other words, the confinement of PET delays the crystallization process.
– The SAXS long period from the crystal stacks within the semicrystalline PET multilayers increases with decreasing layer thickness, while the degree of crystallinity becomes smaller. Results are highlighted on the basis of thinner multilayers, giving rise to a smaller density of crystals, involving oriented stacks parallel to the plane of the layers that exhibit larger periodicities.

Acknowledgements Grateful acknowledgement is due to the MEC, Spain (grant FIS2004-01331) for the generous support of this work. The IHP-Contract HPRI-CT-1999-00040 of the European Community funded the SAXS and WAXS measurements carried out at HASYLAB, DESY, Hamburg under project II-04-029 EC. One of us I.P.O., also acknowledges the support of the Formación de Personal Investigador program of MEC, Spain (grant BFM2000-1474). We wish to thank Prof. G.H. Michler and Mr. S. Henning for the facilities given to obtain the TEM micrograph shown in Figure 3 and to Ms. S. Cunis (HASYLAB) for her technical assistance during the USAXS measurements.

References

1. Baer E, Kerns J, Hiltner A (2000) Processing and Properties of Polymer Microlayered Systems. In: Cunha AM, Fakirov S (eds) Structure Development during Polymer Processing. Kluwer Academic Pub, Dordrecht
2. Wadsworth J, Kum DW, Sherby OD (1986) Metal Progress, p 61
3. Baer E, Hiltner A, Morgan R (1992) Physics Today October: 60
4. Baer E, Hiltner A, Keith HD (1987) Science 235: 1015
5. Mueller CD, Nazarenko S, Ebeling T, Hiltner A, Baer E (1997) Polym Eng Sci 37: 355
6. Pan SJ, Im J, Hill MJ, Keller A, Hiltner A, Baer E (1990) J Polym Sci Polym Phys B28: 1105
7. Jin Y, Rogunova M, Nowacki R, Piorkowska E, Galeski A, Hiltner A, Baer E (in press) J Polym Sci Polym Phys B
8. Ma M, Vijayan K, Im J, Hiltner A, Baer E (1990) J Mater Sci 25: 2039
9. Puente Orench I, Ania F, Baer E, Hiltner A, Bernal T, Baltá Calleja FJ (2004) Phil Mag 84: 1841
10. Loo YL, Register RA, Ryan AJ (2002) Macromolecules 35(6): 2365
11. Schmalz H, Knoll A, Müller AJ, Abetz V (2002) Macromolecules 35(27): 10004
12. Huang P, Zhu L, Guo Y, Ge Q, Jing AJ, Chen WY, Quirk RP, Cheng SZD, Thomas EL, Lotz B, Hsiao BS, Avila-Orta CA, Sics I (2004) Macromolecules 37(10): 3689

13. Yalcin B, Valladares D, Cakmak M (2003) Polymer 44: 6913
14. Durell M, Macdonald JE, Trolley D, Wehrum A, Jukes PC, Jones RAL, Walker CJ, Brown S (2002) Europhys Lett 58(6): 844
15. Puente Orench I, Ania F, Baltá Calleja FJ, Funari S, Baer E, Hiltner A, Bernal T (2002) HASYLAB-DESY Annual Report:p. 783
16. Puente Orench I, Ania F, Baltá Calleja FJ, Funari S, Baer E, Hiltner A, Bernal T (2003) HASYLAB-DESY Annual Report
17. Asano T, Dzeick-Pickuth A, Zachmann HG (1989) J Mater Sci 24: 1967
18. Imai M, Mori K, Mizukami T, Kaji K, Kanaya T (1992) Polymer 33: 4457
19. Ezquerra TA, López-Cabarcos E, Hsiao B, Baltá Calleja FJ (1996) Phys Rev E 4: 989
20. Ania F, Cagiao ME, Baltá Calleja FJ (1999) Polymer J 31: 735
21. Kaji K (2002) Structure Formation in PET during the Induction Period of Crystallization. In: Fakirov S (ed) Handbook of Thermoplastic Polyesters. Wiley-VCH: 225
22. Santa Cruz C, Stribeck N, Zachmann HG, Baltá Calleja FJ (1991) Macromolecules 24: 5980
23. Santa Cruz C, Baltá Calleja FJ, Zachmann HG, Stribeck N, Asano T (1991) J Polym Sci Polym Phys B29: 81

Progr Colloid Polym Sci (2005) 130: 149–158
DOI 10.1007/b107341
Published online: 3 June 2005

Geoffrey R. Mitchell
Sayant Saengsuwan
Sauvarop Bualek-Limcharoen

Evaluation of preferred orientation in multi-component polymer systems using x-ray scattering procedures

Abstract A new approach is presented for the decomposition of anisotropic x-ray scattering patterns from oriented multi-component samples into the scattering from each component. The method is based on the representation of an anisotropic scattering pattern by an orthogonal series of spherical harmonic functions. These functions may be written as the linear combination of the equivalent functions from the pure samples. This provides a route to separate the data from the multi-phase samples into the scattering from each phase. Complete 2-d scattering patterns for each phase can be reconstructed from the series of extracted spherical harmonics. The use of the spherical harmonics leads naturally to the evaluation of the levels of preferred orientation of each phase. The method is demonstrated using the scattering from molecular composite films based on isotactic polypropylene and a thermotropic liquid crystalline polyester. We show how the methodology may be applied to systems where the scattering from partially aligned samples of the pure components are available and to data where no other information is available.

Keywords Multi-phase materials · Molecular composites · Orientation parameters · Structural analysis · Wide angle x-ray scattering · Orientation distribution function

Dedicated to Professor Dr Wilhelm Ruland on the occasion of his 80th Birthday

G. R. Mitchell (✉) · S. Saengsuwan
JJ Thomson Physical Laboratory,
Department of Physics,
University of Reading, Reading,
RG6 6AF, UK
e-mail: g.r.mitchell@reading.ac.uk
Tel.: +44-118-378-8573
Fax: +44-118-975-0203

S. Bualek-Limcharoen · S. Saengsuwan
Department of Chemistry,
Faculty of Science,
Mahidol University, Rama 6 Road,
Bangkok, 10400, Thailand

Introduction

X-ray scattering techniques provide a powerful route to the quantitative analysis of preferred orientation in both crystalline and non-crystalline polymers [1, 2]. In particular, the use of x-ray scattering data enables the complete orientation distribution function to be evaluated. Although the quantitative procedures for samples such as fibres or other samples with uni-axial symmetry are relatively straightforward, natural complications arise with multi-component systems. For semi-crystalline samples containing both amorphous and crystalline phases, a variety of empirical approaches have been employed to separate the scattering from the two phases in order to evaluate the levels of preferred orientation, see for example [3]. The details of these approaches are very dependent on the characteristics of the structure of the sample and may need to vary from sample to sample even within a seemingly systematic series of samples. It is self-evident that such approaches will only work effectively when the components of the scattering can be clearly identified. This is often straightforward for highly aligned crystalline fibres but for other systems such as disordered polymers, liquid crystal polymers or materials with partial orientation, separation may be somewhat ambiguous.

In this contribution we develop a new approach which is particularly suited to the study of partially ordered polymers. We utilise a series of molecular composite samples [4] based on isotactic polypropylene blended with varying fractions of a thermotropic liquid crystal polymer to illustrate the procedures. Blending is widely

used to optimise the physical and chemical properties of polymer systems and the materials used in this study are typical of many such polymer mixtures in that there are two components with little mutual solubility leading to an essentially two phase structure.

The methodology developed in this contribution is based on the representation of a two-dimensional X-ray scattering pattern from a sample with uni-axial symmetry as a series of spherical harmonics. This representation allows the orientational dependence of the scattering to be separated from the variation that arises from the spatial correlations within the sample. As a consequence we are able to obtain the spherical harmonic functions for both the polypropylene and the liquid crystal polymer components of the X-ray scattering from the molecular composite. The complete scattering pattern for each of these components can be then obtained by summing the extracted harmonics and the necessary structural analysis carried out. In this work we focus on evaluation of the levels of preferred molecular orientation in each component.

Theory

We shall be concerned with the single elastically scattered X-ray intensity I ($|\underline{Q}|, \alpha$) from a sample with uni-axial symmetry where $|\underline{Q}| = 4\pi \sin\theta/\lambda$ with 2θ as the scattering angle, λ the incident wavelength and α the angle between the scattering vector $\underline{Q}$ and the symmetry axis of the sample.

We consider a two phase system containing a fraction x of a and 1-x of b. For a system in which the length scale of the phase separated structure is large compared with the length scale giving rise to the scattering, the total scattering I($|\underline{Q}|, \alpha$) can be written as the alegbraic sum of the scattering from the two components:

$$I\left(|\underline{Q}|, \alpha\right) = xI^{a}\left(|\underline{Q}|, \alpha\right) + (1-x)\left(I^{b}|\underline{Q}|, \alpha\right) \tag{1}$$

The scattering for a sample exhibiting a partial level of preferred orientation can be written as the convolution of the scattering for a perfectly aligned system $I^{0}(|\underline{Q}|, \alpha)$ with the orientation distribution function D(α):

$$I\left(|\underline{Q}|, \alpha\right) = I^{0}\left(|\underline{Q}|, \alpha\right) * D(\alpha) \tag{2}$$

The function D(α) describes the distribution of the structural units with respect to the symmetry axis of the sample.

If we express the intensity functions and the orientation distribution function in terms of a series of spherical harmonics, $I_{2n}(|\underline{Q}|)$, $I^{0}_{2n}(|\underline{Q}|)$ and D_{2n} we can write this convolution as [5–8]:

$$I_{2n}(|\underline{Q}|) = \left\{\frac{2\pi}{(4n+1)}\right\} D_{2n}\, I^{0}_{2n}(|\underline{Q}|), \alpha) \tag{3}$$

where $n = 0, 1, 2, 3 \ldots \infty$. Only the even terms of each series are required due to the inversion centre intrinsic to a X-ray scattering pattern for a non-absorbing sample. The components of each series can be obtained by:

$$I_{2n}(|\underline{Q}|) = (4n+1) \int_{0}^{\pi/2} I(|\underline{Q}|, \alpha) P_{2n}(\cos\alpha) \sin\alpha . d\alpha \tag{4}$$

and related expressions. The complete scattering pattern may be recovered by:

$$I(|\underline{Q}|, \alpha) = \sum_{2n=0}^{2n=\infty} I_{2n}(|\underline{Q}|) P_{2n}(\cos\alpha) \tag{5}$$

The value of this representation is that the effects of preferred orientation are separated from the dependence of the scattering on the spatial correlations. Eq. 3 underlines the fact that for samples with the same structure, the variation of the amplitudes of the spherical harmonics $I_{2n}(|\underline{Q}|)$ with $|\underline{Q}|$ are essentially the same, with a simple constant multiplier dependent on the level of preferred orientation. This observation is the basis of a wide-angle x-ray scattering based conformational analysis procedure developed for disordered polymers [8].

The orthogonal nature of the spherical harmonics in Eq. 4 means that for a multiple phase structure in which the scattering is additive, the resultant spherical harmonics will also be linear combinations of the harmonic functions for each phase. We can write:

$$I_{2n}(|\underline{Q}|) = xI^{a}_{2n}(|\underline{Q}|) + (1-x) I^{b}_{2n}(|\underline{Q}|) \tag{6}$$

where $I^{a}{}_{2n}(|\underline{Q}|)$ are the spherical harmonics for the pure phase. Combining Eq. 6 with 3 we can write more completely:

$$I_{2n}(|\underline{Q}|) = xI^{0a}_{2n}(|\underline{Q}|) D^{a}_{2n} \frac{2\pi}{4n+1} + (1-x) I^{0b}_{2n}(|\underline{Q}|) D^{b}_{2n} \frac{2\pi}{4n+1} \tag{7}$$

where $I^{0a}{}_{2n}(|\underline{Q}|)$ are the functions for the pure perfectly aligned phase. For a particular experimentally observed harmonic Eq. 7 reduces to:

$$I_{2n}(|\underline{Q}|) = k^{a}_{2n} I^{0a}_{2n}(|\underline{Q}|) + k^{b}_{2n} I^{0b}_{2n}(|\underline{Q}|) \tag{8}$$

where k_a and k_b are scaling constants with k_a given by

$$k^{a}_{2n} = xD^{a}_{2n} \frac{2\pi}{4n+1} \tag{9}$$

and k_b by a similar expression. Eq. 8 provides a route to the separation of the scattering into the contributions from each phase. We simply need a mechanism to identify the components within each 1-d function. There is considerable advantage in using information from the scattering patterns of the pure phases where this is available. Although such scattering patterns need to arise from samples with the same structure, it is not necessary for the level of preferred orientation to be the same. As emphasised above the variation of the harmonic function with $|\underline{Q}|$ does not depend, other than through a simple constant, on the orientation. This allows information from partially oriented samples to be used as "standards" in the separation and analysis. The process of separation is then a simple numerical fitting process. Moreover, since such processes are performed in the more straightforward environment of 1-d functions, rather than directly on the original 2-d patterns, there is a considerable gain in simplicity. It is also possible to use calculated curves from atomistic or analytical models as the base functions.

In the description of the levels of preferred orientation, it is convenient and conventional to work with normalised spherical harmonics $< P_{2n}(\cos\alpha) >$ [7]. The harmonic $< P_{2}(\cos\alpha) >$ is often referred to as the "Hermans orientation function" in the field of polymers or the "order parameter" in the context of liquid crystals; for perfect alignment $< P_{2}(\cos\alpha) > = 1.0$ and for a random or isotropic distribution $< P_{2}(\cos\alpha) > = 0$. The normalised functions are defined as [7]:

$$<P_{2n}(\cos\alpha)>=\frac{\int_0^{\pi/2} D(\alpha)P_{2n}(\cos\alpha)\sin\alpha.d\alpha}{2\pi\int_0^{\pi/2} D(\alpha)\sin\alpha\, d\alpha} \quad (10)$$

Such normalised orientation parameters can be obtained from the scaling constants in Eq. 9:

$$<P^a_{2n}\cos(\alpha)>=\frac{k^a_{2n}}{k^a_0}=\frac{D^a_{2n}}{D^a_0(4n+1)} \quad (11)$$

Alternatively we can obtain the numerical values of these orientation parameters from the extracted spherical harmonic functions using:

$$<P^a_{2n}\cos(\alpha)>=\frac{I^a_{2n}(|\underline{Q}|)}{I^a_0(|\underline{Q}|)(4n+1)P^m_{2n}(\cos\alpha)} \quad (12)$$

where $P^m_{2n}(\cos\alpha)$ are normalised coefficients which describe the scattering for a perfectly aligned sample [7]. The values will depend upon the particular structural feature and hence are in part Q dependent. For an *hk0* Bragg reflection the value of $P^m_2(\cos\alpha) = -0.5$, while for a meridional feature $P^m_2(\cos\alpha) = 1.0$ [7]. Eq. 12 represents a more generalised approach which can be used with any set of extracted spherical harmonic functions. For example, we will use this equation in the example below, as the base functions from the fully aligned pure samples required for the implementation of Eq. 11 are not available. Such base functions may be obtained from experiment or through from models. Eq. 12 may also be used in situations where the separation inherent in Eq. 8 has been performed using a peak fitting approach based on differing peak shapes, for example, as appropriate for crystalline and amorphous phases.

Experimental Procedures

Materials

Molecular composites were prepared from isotactic polypropylene (PP), (PRO-FAX 6631 HMC Polymer Co., Thailand) and a thermotropic liquid crystalline polymer (LCP), a random copolyester based on 80% *p*-hydroxy benzoic acid/20% ethylene terephalate (Rodrun LC5000 Unitika, Co., Japan) with fractions of LCP of 0.05, 0.08, 0.10, 0.15 w/w [4]. Each composite also contained a small amount (3% w/w) of a block copolymer compatibiliser, SEBS-g-MA. All materials were dried in a vacuum oven at 80 °C for at least 10 h before use.

The composites were formed by melt-blending the PP with various contents of LCP in a co-rotating twin screw extruder with the die temperature of 295 °C. The dried blend pellets were then fabricated as extruded films using a mini-extruder (die temperature of 295 °C) equipped with a cast film line. The draw ratio of the film (die gap to final film thickness) was ~30. The thickness of the resultant films was ~20μm Optical and scanning electron microscopy revealed that the morphology is essentially two phase at room temperature. The LCP is present in the form of highly extended droplets, with a minium length scale of ~μm[9]. Clearly the basic length scale condition required to treat the scattering from the molecular composite as the addition of the weighted components (Eq. 1) is fully satisfied.

Films containing only isotactic polypropylene were also prepared using the same procedure as used for the molecular composites described above.

A series of LCP samples were prepared for x-ray scattering by holding the original melt extruded pellets for specified periods of time up to 250 minutes at 285 °C. This allowed the initial high levels of molecular alignment to progressively relax providing a series of samples with different levels of preferred orientation.

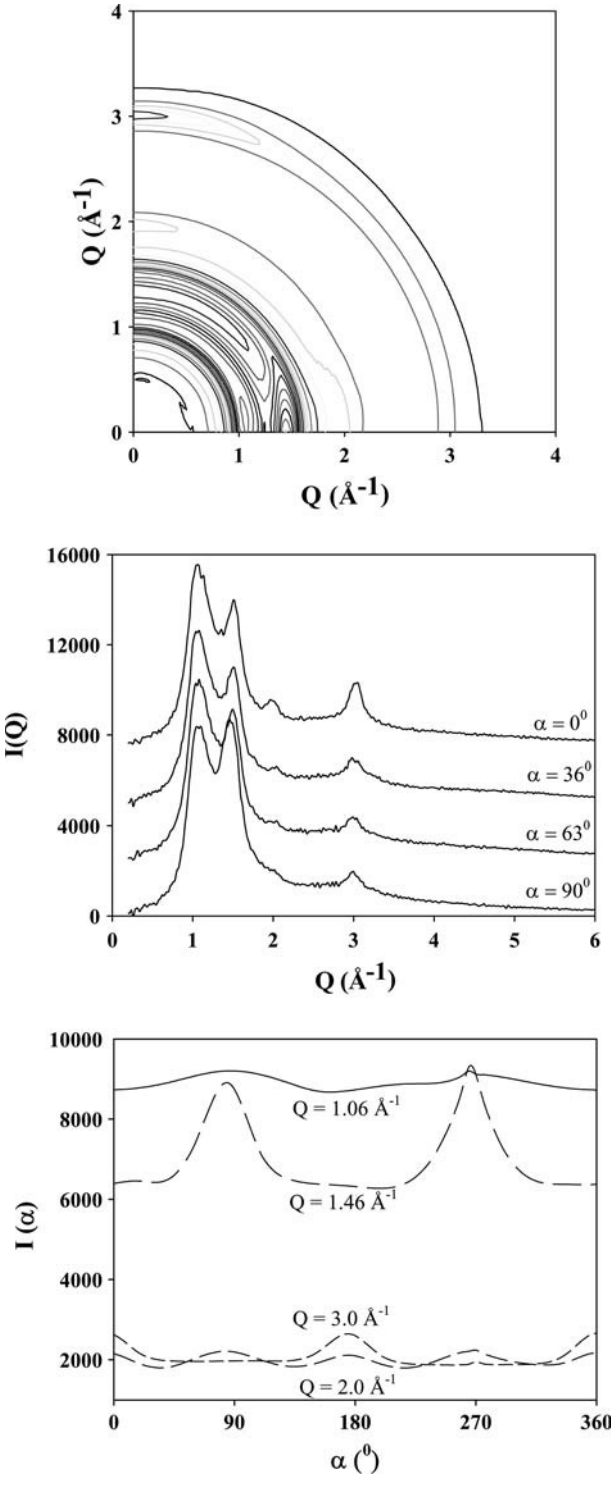

Fig. 1(a) Fully corrected and scaled 2-d scattering pattern $I(|\underline{Q}|, \alpha)$ for a drawn isotactic polypropylene film containing 15% w/w LCP, b) sections of the pattern in Fig. 1a taken at constant values of $\alpha = 0$,36,63 and 90 °C) sections of the pattern in Fig. 1a taken at fixed values of $|\underline{Q}| = 1.06$, 1.46, 2.0 and 3.0 Å^{-1}

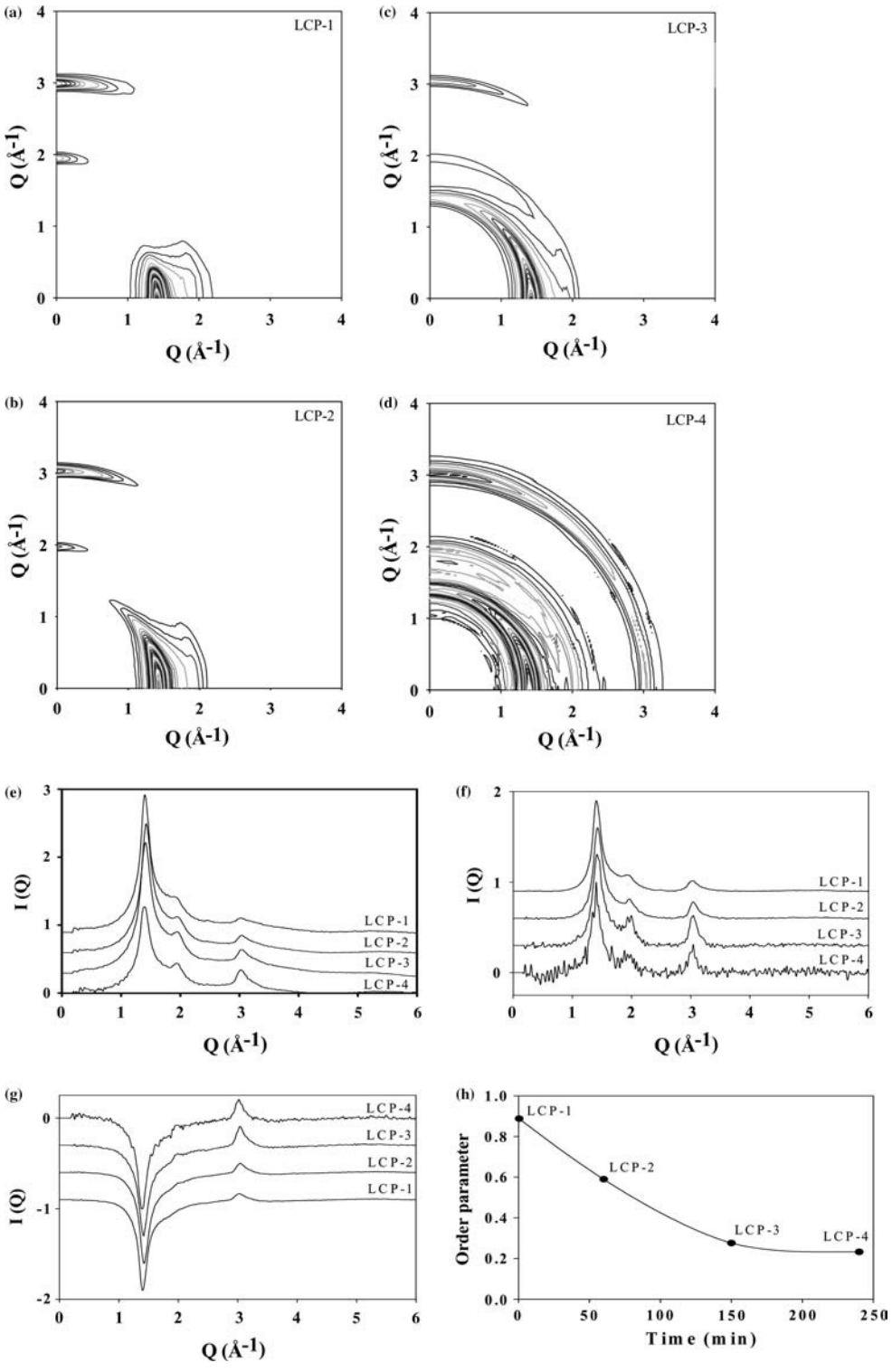

Fig. 2(a–d) Fully corrected and scaled 2–d scattering patterns of LCP samples prepared as described in the text with differing levels of preferred alignment; e-g the first three spherical harmonic components I_0, , I_2 , and I_4 derived from the patterns shown in Figs 2a–d; (h) a plot of the orientation parameter for each of the samples in Figs 2a–d plotted against the holding time during their preparation

X-ray scattering

Samples for x-ray scattering measurements were prepared by folding several layers of the film while retaining the relative orientation of the draw direction of each film. As a consequence the thickness of the samples used in the x-ray scattering measurement was $\sim$0.2 mm. The scattering data were obtained at room temperature using a 3-circle transmission diffractometer equipped with an incident-beam monochromator and pin-hole collimation operating in a symmetrically transmission mode. The X-ray source was a sealed X-ray tube with a copper target and stabilised power supply operating at 40kV and 40mA. The scattered intensity was measured with a scintillation

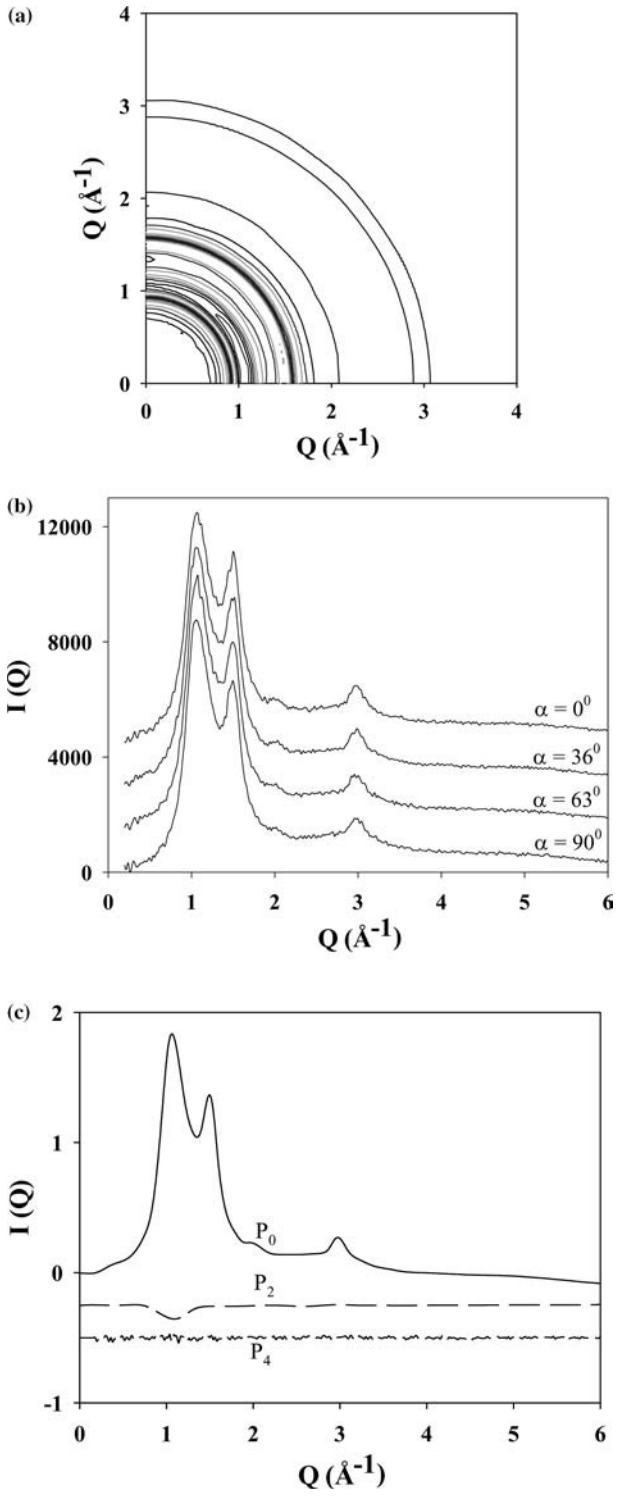

Fig. 3(a) The fully corrected and scaled 2-d scattering pattern for a drawn isotactic polypropylene film, (b) sections of the pattern in Fig. 3a taken at constant values of $\alpha = 0,36,63$ and 90° (c) the first three spherical harmonic functions I_0, , I_2 , and I_4 derived from the pattern shown in Fig. 3a

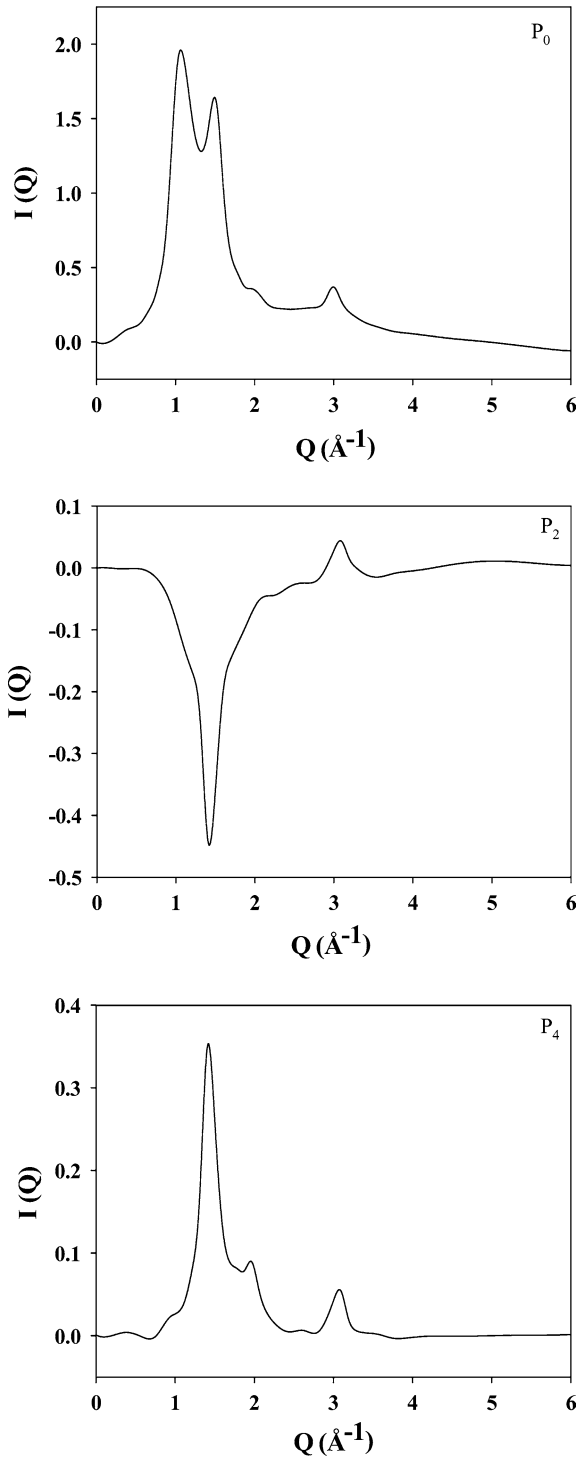

Fig. 4 The first three spherical harmonic functions (I_0, I_2 and I_4) for the pattern shown in Fig. 1a for the 15%wt LCP/PP molecular composite film

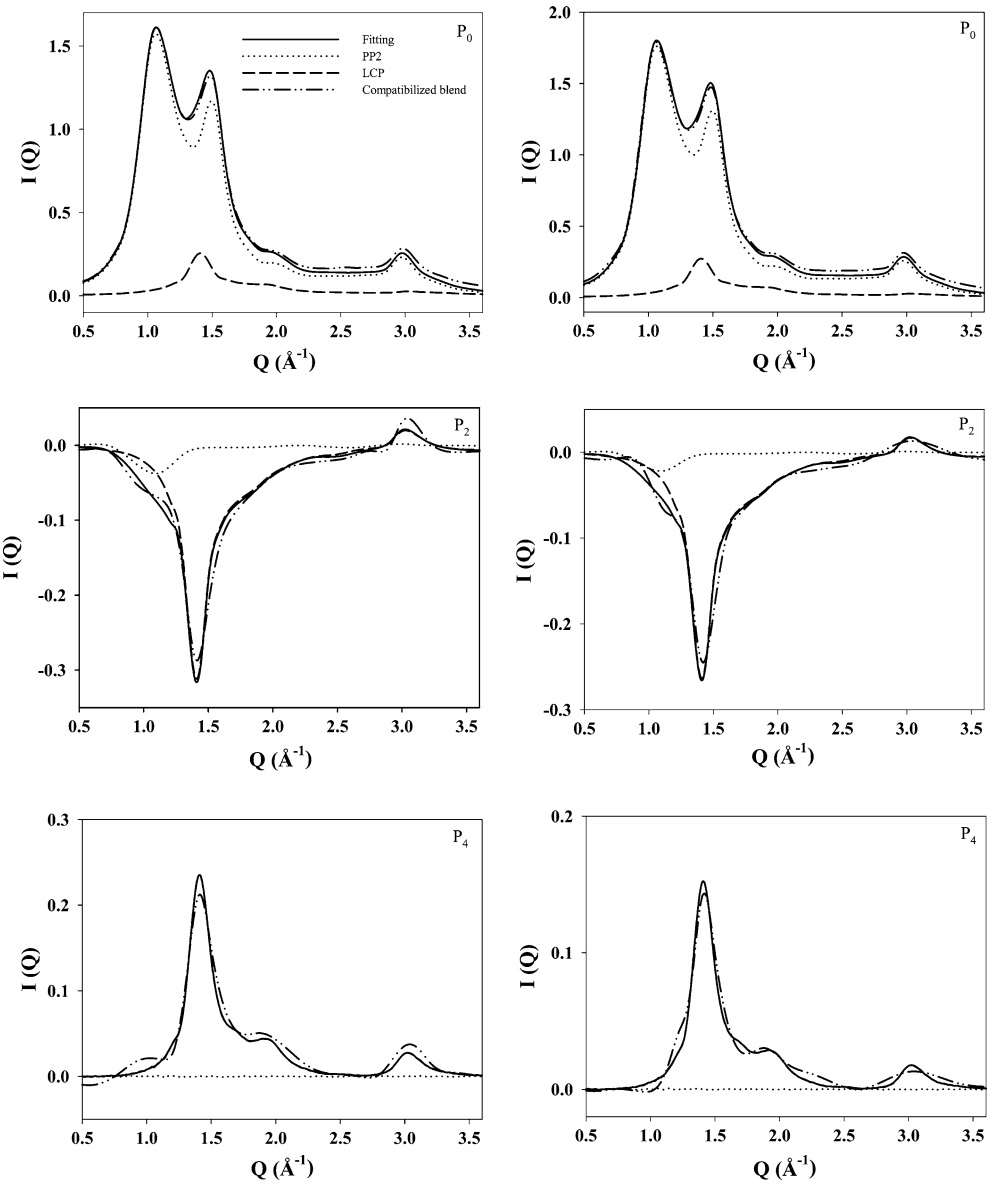

Fig. 5 First three spherical harmonic functions (I_0-I_4) derived from scattering data for drawn polypropylene films containing 10 wt% LCP with draw ratios of 30 (left-hand column) and 9 (right-hand column). The plots show the results of the fitting process described in the text. The key for each plot is shown in the figure

detector coupled with pulse height analysis. Intensity data were obtained for a grid of points as a function of $|Q|$ from 0.2–6.0 $Å^{-1}$ in steps of $\Delta Q = 0.02Å^{-1}$ and as a function of α from 0–90° in steps of $\Delta\alpha = 5°$. The count time for each grid point was set to provide an adequate signal to noise ratio, typically this was 10s.

Data analysis was performed using an in-house software package XESA [10] which was used to subtract the air and other background scattering, to make corrections for absorption, polarisation, multiple scattering and incoherent scattering and to scale the scattering to absolute (electron units) units [1, 8].

Method

Basic data

The experimental scattering data for PP/15%LCP, corrected for experimental aberrations and scaled to electron units are shown in Fig. 1a. The main features are two main intense peaks on the equator ($\alpha = 90°$) at $|Q| = 1.06$ and 1.46 $Å^{-1}$ and an intense peak on the meridional section at $|Q| = 3.0$ $Å^{-1}$. Each of these features exhibits some arcing, and it can be seen that the extent of the arcing of the peaks at $|Q| = 1.06$ and 3.0 $Å^{-1}$ is more than that of the peak at 1.46 $Å^{-1}$ suggesting different levels of anisotropy in the scattering data. Fig. 1b shows four sections through the data in Fig. 1a at values of $\alpha = 0$, 36, 63 and 90°. The scattering data at $\alpha = 0°$ belongs to the meridional section while at $\alpha = 90°$ belongs to the equatorial section. From Figure 1b, we can see more clearly the four peaks including the intense peaks at $|Q| = 1.06$ and 1.46 $Å^{-1}$ and the smaller features at $|Q| = 2.0Å^{-1}$ and 3.0 $Å^{-1}$. Close examination of the heights of the peaks in the various sections reveals a certain level of anisotropy.

This anisotropy is shown more clearly in sections taken at fixed values of $|Q|$ corresponding to the four peaks identified in Fig. 1 at $|Q| = 1.06$, 1.46, 2.0 and 3.0 $Å^{-1}$. These sections are presented in Fig. 1c. The marked level of anisotropy for the peak at $|Q| =$ 1.46 $Å^{-1}$ can now be clearly seen through the azimuthal variation of

the intensity. The features at $|\underline{Q}| = 1.06$, 2.0 and 3.0 $Å^{-1}$ exhibit smaller variations in intensity with the azimuthal angle. Note that these curves show an extended data range ie $\alpha = 0$ to 360° range to enable the azimuthal variation to be seen more easily.

Fig. 2a–d present the x-ray scattering patterns recorded for the series of LCP samples with different thermal treatment times. There are two main features in Fig. 2a; a peak on the equator at $|\underline{Q}| = 1.42$ $Å^{-1}$ which extends almost parallel to the meridian, and two peaks on the meridian at $|\underline{Q}| = 2.0$ and 3.0 $Å^{-1}$, which show slight arcing. These features are very similar to those reported for related liquid crystalline copolyesters [11]. The extent of arcing in these features in Fig. 2b,c,d increases as the initial high level of molecular anisotropy present in the extruded pellet relaxes with the increasing length of thermal treatment. We have used the azimuthal distribution of intensity at $|\underline{Q}| = 1.42$ $Å^{-1}$ to calculate the level of preferred orientation in this set of samples using the methodology described by Mitchell et al. [12]. This methodology is based on Eq. 12. The results of these calculations are plotted in Fig. 2h. There is, as expected, an exponential type decay in the level of preferred orientation.

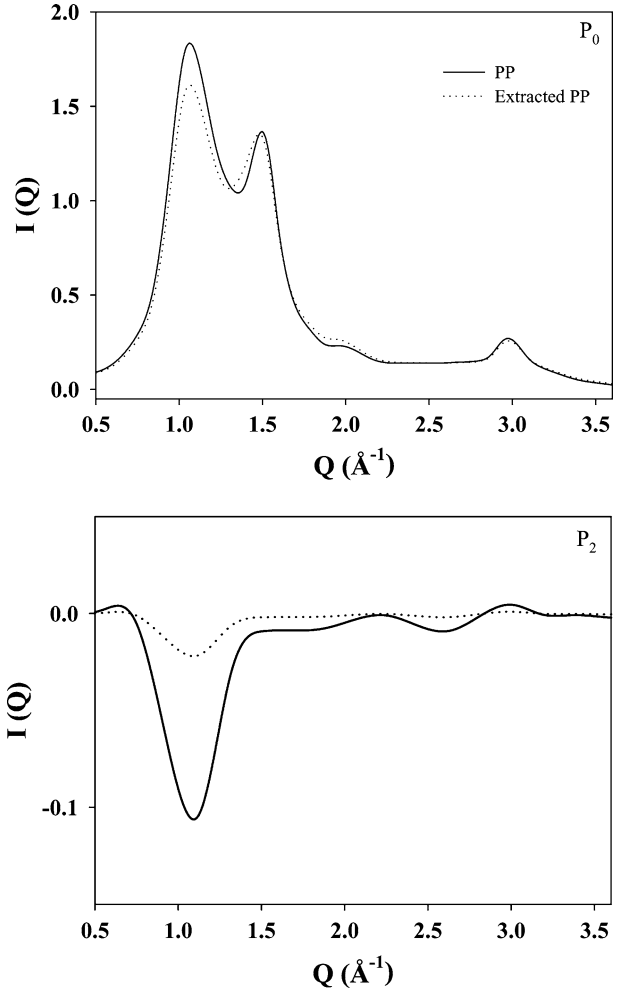

Fig. 6 Comparison between the first two spherical harmonic functions derived from the scattering pattern for the pure PP film and the PP component extracted from the data for a drawn polypropylene film containing 15%wt LCP shown in Fig. 1

We have used each of the four experimental scattering functions $I(|\underline{Q}|, \alpha)$ shown in Fig. 2a–2d to calculate the first three spherical harmonics $I_{2n}(|\underline{Q}|)$ for n = 0,1,2 as a function of $|\underline{Q}|$ and these are plotted in Fig. 2e,f,g. The functions for n = 1,2 have been scaled to exhibit principal peaks with similar heights to enable a more direct comparison. It can be seen that the characteristics of each set of spherical harmonics remain the same in terms of shape, peak positions and relative peak positions. However, the noise in the functions $I_{2n}(|\underline{Q}|)$ particularly for n = 2 increases with increasing thermal treatment time reflecting the reduction in anisotropy. These curves underline one of the key advantages of the spherical harmonic function representation, namely the separation of preferred orientation and structure. We see that although these samples exhibit very different levels of anisotropy , in fact the level of orientation varies by a factor of 4, the spherical harmonics for each pattern are essentially the same. This contrasts with the differences observed in the full x-ray scattering patterns. We will use the spherical harmonics calculated from the data shown in Figure 2a to fit the data from the molecular composite samples as will be described below.

Fig. 3a shows the x-ray scattering data for a PP film prepared using the same conditions as used to form the composite films. In comparison to the LCP patterns shown in Fig. 3, there is low level of anisotropy with a very extended arc on the equator at $|\underline{Q}| = 1.05$ $Å^{-1}$. Fig. 3b shows four sections through the data in Fig. 3a at values of $\alpha = 0$, 36, 63 and 90°. There are two intense peaks at $|\underline{Q}| = 1.05$ and 1.5 $Å^{-1}$, and weaker peaks at $|\underline{Q}| = 2.0$, 3.0 $Å^{-1}$. The peak positions reveal that the PP is present in the so-called "smectic" phase first observed by Natta et al. [13] and by later researchers [14, 15]. The presence of the "smectic" phase is related to the rapid cooling experienced by the thin films during the final drawing stage in the processing. The similarity of these sections underlines the limited level of anisotropy in this PP film. We have calculated the first three spherical harmonics components of the scattering data shown in Fig. 3a and these are plotted in Fig. 3c. In contrast to the spherical harmonics calculated for the LCP scattering patterns, those for the PP film for n = 1 or 2 are close to zero except for the peak in the $I_{2n}(|\underline{Q}|)$ function at $|\underline{Q}| = 1.05$ $Å^{-1}$. film. These spherical harmonics are used to fit those of the composite data. As we have already highlighted, these harmonic functions need to have been obtained for a sample with the same structure but not necessarily the same level of preferred orientation. For isotactic polypropylene samples, whether the α or smectic phases are formed depends on the cooling rate, so we prepared the drawn films of the pure polypropylene using the same processing procedure.

Decomposition

Fig. 4a–4c shows the first three spherical harmonics components derived from the data for the PP/15%LCP sample displayed in Figure 1a. We can recognise some features in these three harmonic functions from those shown in Figures 2 and 3 for the LCP and PP samples. Eq. 8 implies that the harmonics derived from the scattering patterns for the molecular composites will be linear combinations of the equivalent harmonic functions for the pure phases. This requires these base functions to have originated from a sample with the same structure. The use of the spherical harmonic representation means that any mismatch in peak shapes is due to structural differences, rather than orientational differences. The weightings of these combinations will depend on both the composition and the level of preferred orientation in each sample. Since we have used, as the base functions, spherical harmonics obtained from partially aligned samples, these weightings will be also reflect the level of anisotropy in the pure samples as well as in the level of preferred orientation in the blended samples. As a consequence we will use Eq. 12 rather than 11 to derive the orientation parameters for each phase in the composite.

We have used standard least-squares techniques to fit the spherical harmonic functions obtained from the pure samples to the equivalent functions obtained from the scattering for the composite samples. Fig. 5a – 5c show the results of this fitting process for the first three spherical harmonics components for the scattering from the PP/10%LCP film with a draw ratio of ~30, while Figs. 5d– 5f show the results for the harmonics for the scattering from the PP/10%LCP film with a draw ratio of ~9.3. Not surprisingly the PP component dominates in fitting the $I_0(|\underline{Q}|)$ function while the LCP component is most significant in the functions $I_{2n}(|\underline{Q}|)$ for n = 1, 2. Nevertheless, there are distinctive features in each curve which underline the efficacy of the procedure. Clearly the structure of the two components in the molecular composite is the same as that in the pure components. The spherical harmonic representation makes such deductions straightforward as well as providing a route to the evaluation of the level of preferred orientation.

Extracted components

Fig. 6a and 6b show the comparison between the first two spherical harmonics derived from the data for the pure PP sample and those extracted using the above procedure from the data for the PP2/10%LCP film with a draw ratio = 30. There is a reasonable agreement between these two sets of curves. The extracted spherical harmonic functions for each phase can be used to regenerate the complete scattering pattern using Eq. 5. The reconstructed 2d-patterns for both the extracted LCP and PP components of the scattering from the PP/10%LCP film with a draw ratio = 30 are shown in Figs. 7a and 7b. In addition, Figs. 7c and 7d show the equatorial and meridional sections of the reconstructed patterns. In principle, the reconstruction process (Eq. 5) involves an infinite series. Clearly for a highly anisotropic pattern a convergent series will require a large number of terms whilst for a system with a low level of anisotropy, a few terms will be sufficient. For this particular example we have followed two routes. The first is use a large number of terms, we found ~11 sufficient in the decomposition and fitting process. The second approach was to recognise that fewer terms are required for convergence for the PP component; we found 4 were sufficient. This enabled the PP component 2-d scattering pattern to be reconstructed and the equivalent LCP patterns was found by a simple difference. We found that both procedures gave equivalent patterns, those shown here were derived using the first approach with 11 terms.

The reconstructed 2-d scattering pattern for the LCP component shows an intense peak on the equator at $|\underline{Q}| = 1.42$ Å^{-1} with a shoulder at $|\underline{Q}| = 1.98$ Å^{-1} and a weaker peak at $|\underline{Q}| = 3.0$ Å^{-1}, with three peaks on the meridian at $|\underline{Q}| = 1.42$, 1.98 and 3.0 Å^{-1}. It can also be seen that the peak on the equator extends parallel to the meridional section reflecting the high level of preferred orientation in the LCP component. The reconstructed 2-d scattering pattern of the PP component is close to being isotropic but not quite as can be seen from the halo patterns and the equatorial and meridional sections. It is salutory to compare these extracted patterns with the type of patterns initially recorded, for example Fig. 1. It is difficult to imagine how we might have started to make such a separation using the original 2-d scattering patterns.

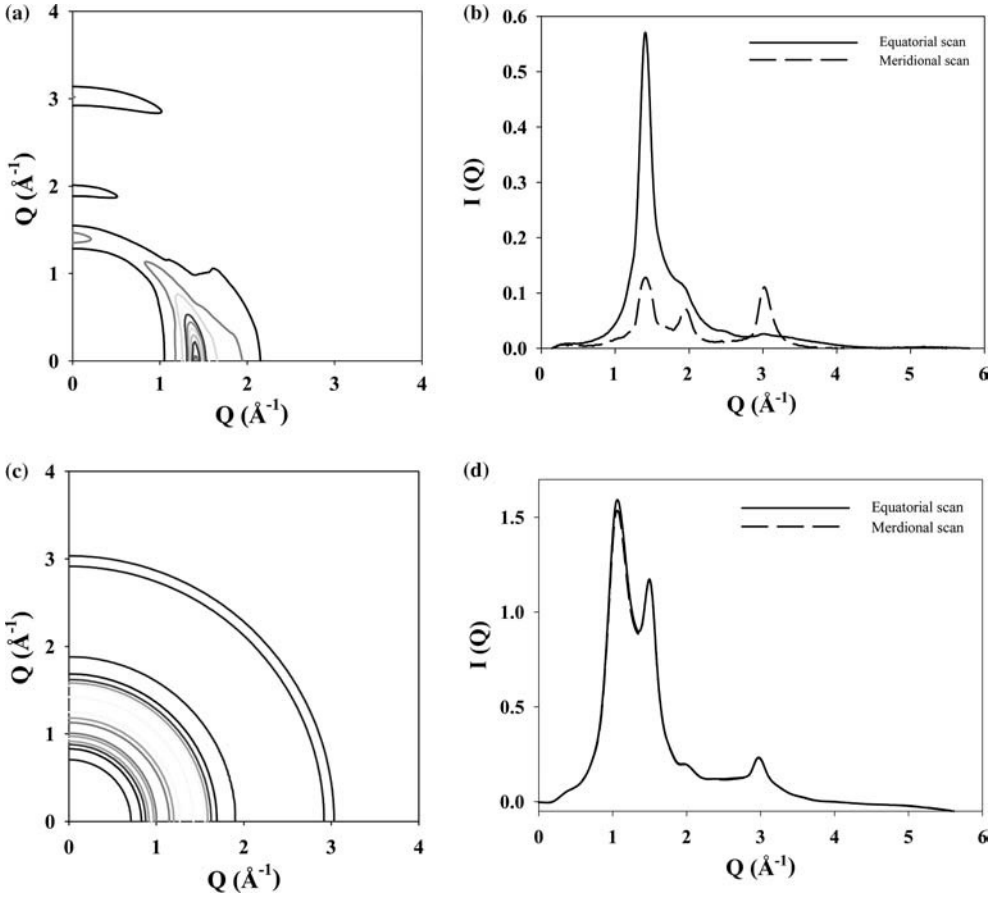

Fig. 7 The reconstructed patterns for the LCP (a) and PP(c) components extracted using the procedure described in the text for the scattering of a drawn polypropylene film sample containing 10 wt% LCP shown in Fig. 5; and sections taken at $\alpha = 0°$ and 90° of the patterns shown in Fig. 7a (LCP - b) and Fig. 7c (PP - d)

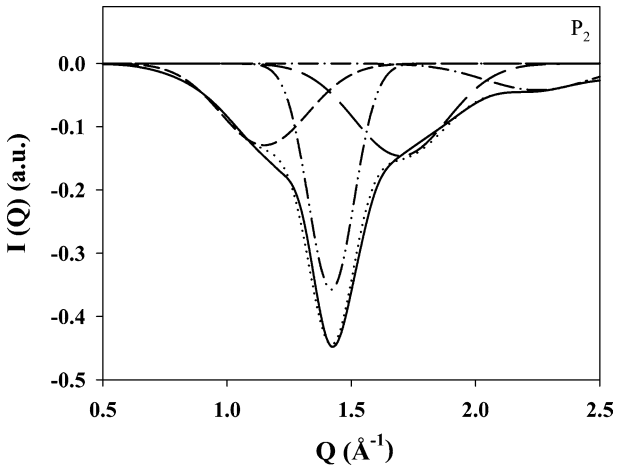

Fig. 8 An example of peak fitting applied to the spherical harmonics, I_2 derived from the data for a drawn polypropylene containing 15 wt% LCP shown in Figure 1 where the solid line is the experimental spherical harmonic, the broken line the result PP of the non-linear least squares fitting procedure; the other lines represent the individual Gaussian peaks as indicated on the figure

The overlapping nature of the features and the partial level of preferred orientation make any direct separation process fraught with difficulty. In contrast, the procedure described here using the spherical harmonics approach is straightforward and simple to apply.

The availability of the scattering patterns for each component of the composite makes analysis of the levels of preferred orientation particularly straightforward. The feature at $|\underline{Q}| = 1.48$ Å^{-1} which is most intense on the equator arises from correlations between chains [1] and the values of the appropriate model parameters and their dependence on the structure have been discussed in detail by Mitchell et al [12]. Using Eq. 12, the equatorial scattering feature at $|\underline{Q}| = 1.48$ Å^{-1} and a value of $P_2^m(\cos\alpha) = -0.5$, we obtain values for the orientation parameter $<P_2(\cos\alpha)>$ of 0.78 and 0.69 for the films of PP/10%LCP with draw ratios of 30 and 9.6. These are typical of values observed for films prepared from related LCPs [16]. Analysis of the PP component using the feature at $|\underline{Q}| = 1.05$ Å^{-1} as a hk0 reflection yields values of $<P_2(\cos\alpha)>$ for the PP component for both films of ~ 0.01.

Decomposition without pure phases

The approach described above has two stages, the first involves representing the 2-d scattering pattern as a series of 1-d functions. The second stage is the separation of the spherical harmonics into the contributions for each component. The 1-d nature of each function considerably simplifies the separation process. For isotropic samples, for example the measurement of crystallinity in semi-crystalline polymers, there are well established procedures for the separation of components based upon the shape of the peaks. Typically crystalline peaks are rather sharp whereas the amorphous component will exhibit rather broad peaks. Fig. 8 shows, as an example, this approach applied to the function $I_2(|\underline{Q}|)$ for the data obtained for the PP/15%LCP film shown in Fig. 1. A number of Gaussian peaks are fitted to the data using nonlinear least-squares techniques. The dominant LCP at $|\underline{Q}| \sim 1.4$ Å^{-1} is reproduced along with the PP component at $|\underline{Q}| \sim 1.1$ Å^{-1}. This suggests that peak fitting used in conjunction with the spherical harmonic description represents a useful method when the harmonics from aligned samples of the pure phases are not available or cannot be calculated [8]. Clearly the use of any other data is a considerable advantage, but Fig. 8 illustrates the potential for progress with an *ab-inito* approach and work is in hand to develop this approach.

Conclusions

We have introduced a methodology to evaluate the orientation parameters of anisotropic composite samples. We can represent the 2-d x-ray scattering patterns from the aligned samples as a series of spherical harmonic functions without loss of information. We show that each of these series of spherical harmonics is the linear combination of the equivalent functions for the pure aligned samples. The weighting factors depend on the composition and the levels of preferred orientation. If the harmonic functions for a perfectly aligned pure sample are available or can be calculated, the level of preferred orientation may be derived directly from the weighting factors. This requires such base functions to arise from a sample or model with the same structure. The spherical harmonic representation makes such comparison for patterns with differing levels of anisotropy a straightforward procedure. The orientation parameters can be easily obtained by analysis of the extracted functions. The complete scattering patterns for each component can also be reconstructed from the extracted spherical harmonic functions. We have demonstrated the efficacy of this new approach using the scattering data from a polypropylene/liquid crystalline polyester molecular composite. This type of sample with broad overlapping peaks and modest levels of anisotropy presents a challenging problem. We have shown that this new approach can succesfully cope with such challenges. It is clear that the availability of data from aligned samples of the pure components considerably simplifies the analysis process. We have shown that there is potential for an *ab-initio* approach for the more general problem. This methodology is not limited to wide-angle x-ray scattering patterns and there are clear possibilities and advantages of applying the same approach to the small-angle x-ray scattering patterns of multiphase samples and such work is in hand.

Acknowledgement The authors acknowledge the Thailand Research Fund for providing the RGJ-PhD scholarship (40-00107) for SS and the Postgraduate Education and Research Program in Chemistry at Mahidol University.

References

1. Mitchell GR (1989) in Comprehesive Polymer Science, Vol.1, Ch.31, ed. Allen, G.; Bevington, J., Pergamon Press Oxford pp 687–729
2. Roe R-J (2000) Methods of X-ray and neutron scattering in polymer science Oxford University Press, Oxford
3. Ran S, Zong X, Fang D, Hsiao BS, Chu B (2000) J. Appl. Cryst 33: 1031
4. Saengsuwan S, Mitchell GR, Bualek-Limcharoen S (2003) Polymer 44: 5951
5. Deas HD (1952) Acta Cryst 5: 542
6. Ruland W (1977) Colloid and Polymer Science 255: 57
7. Lovell R, Mitchell GR (1981) Acta Cryst A37: 135
8. Mitchell GR, Windle AH (1982) Colloid and Polymer Science 260: 754
9. Saengsuwan S, Bualek-Limcharoen S, Mitchell GR, Olley RH (2003) Polymer 44: 3407
10. Mitchell GR (2003) XESA Version 1.8 User Manual University of Reading, Reading UK
11. Shimoda T, Kimura T, Ito E (1997) Macromolecules 30: 5045
12. Mitchell GR, Windle AH (1988) in Developments in Crystalline Polymers-2, ed. D.C. Bassett, Elsevier, London, pp 115–175
13. Natta G, Corrandini P (1960) Nuovo Cimento Suppl 15: 40
14. Seguela R, Staniek E, Escaig B, Fillon B (1999) J. Appl Polymer Sci 71: 1873
15. Cohen Y, Saraf RF (2001) Polymer 42: 5865
16. Donald AM, Windle AH (1992) Liquid Crystalline Polymers Cambridge University Press Cambridge Chapters 7 & 8

Progr Colloid Polym Sci (2005) 130: 159–166
DOI 10.1007/b107332
Published online: 3 June 2005

Anton A. Apostolov
Ognian Samokovliyski
Stoyko Fakirov
Norbert Stribeck
Zlatan Denchev
Michel Evstatiev
Klaus Friedrich
Sergio S. Funari

Transcrystallisation with reorientation of polypropylene in drawn PET/PP and PA66/PP blends. Part 1. Study with WAXS of synchrotron radiation

Abstract Transcrystallisation induced by annealing in the polypropylene (PP) component of nanostructured polymer-polymer composites (NPC) was studied for two different polymeric fillers. In contrast to the typical narrow columnar transcrystalline regions around filler fibres in common glass-fibre reinforced PP, volume-filling transcrystallisation was observed for both of the polymer fillers, thus resulting in reorientation of the PP matrix crystals instead of an expected isotropisation. Two cold-drawn blends of PP with poly(ethylene terephthalate) (PET) or polyamide 66 (PA66), respectively, namely PET/PP and PA66/PP both in a ratio of 50/50 wt.% were investigated by means of wide-angle X-ray scattering (WAXS) of synchrotron radiation during heating, melting of only the low-melting component (PP) at 200 °C yielding an isotropic melt, and subsequent crystallisation upon cooling. A strong epitaxial effect of the persistent embedded microfibrillar component (PET or PA66) on the non-isothermal crystallisation behaviour of PP during its cooling to room temperature was found. The composites obtained after such thermal treatment represented anisotropic semi-crystalline nanocomposites, in which the PP crystallites were reoriented. The ultimate structure for the PET/PP blend exhibited crystals with their molecular axis tilted at approx. 49° with respect to their initial orientation (parallel to the fibre axis). In the PA66/PP blends the ultimate structure returned to the initial orientation of the PP chains parallel to the fibre axis, but with a broadened orientation distribution. Results of similar studies on other blends are reviewed.

Keywords Transcrystallisation · Blends · PET/PP · PA66/PP · Reorientation · Synchrotron radiation

Dedicated to Prof. Dr. Wilhelm Ruland on the occasion of his 80th birthday

A. A. Apostolov (✉)
O. Samokovliyski · S. Fakirov
M. Evstatiev
Laboratory on Structure and Properties of Polymers, University of Sofia, 1 J. Bourchier Blvd., 1164 Sofia, Bulgaria
e-mail: apostolov@onil.chem.uni-sofia.bg
Tel.: +359-2-8161-418
Fax: +359-2-962-5438

N. Stribeck
Institute of Technical and Macromolecular Chemistry, University of Hamburg, Bundesstr. 45, 20146 Hamburg, Germany

Z. Denchev
Department of Polymer Engineering, University of Minho, Campus Azurem, 4800–058 Guimarães, Portugal

K. Friedrich
Institute for Composite Materials (IVW GmbH), University of Kaiserslautern, Erwin-Schrœdinger Straße, 67663 Kaiserslautern, Germany

S. S. Funari
HASYLAB at DESY, Notkestr. 85, 22603 Hamburg, Germany

Introduction

Classical transcrystallisation and polypropylene composites

It is well known [1] that polypropylene (PP) is distinguished by its strong ability to form transcrystalline layers in its short-glass fibre reinforced composites. These transcrystalline layers represent columnar structures, grown in radial direction away from the central core fibre. Their radial extension is about several tenths of a micron. They can easily be observed in a polarised light microscope on thin cuts in longitudinal direction. It is noteworthy that at larger distance from the glass fibres the PP matrix crystallises completely isotropic. Outside the columnar transcrystalline structures there is no macroscopic preferred orientation of the polymer chains.

Conditions precedent to transcrystallisation

In general, transcrystallisation takes place if heterogeneous nucleation occurs with sufficiently high density along the fibre surface and the resulting crystal growth is restricted to the lateral direction. The transcrystallisation is a function of nucleating activity of the fibre surface and crystallisation kinetics of the resin matrix. A literature survey [2] states that the fibre surface tends to induce nucleation of matrix material under at least one of the following conditions: (i) a topographical match between the fibre and the matrix; (ii) a thermal conductivity mismatch between the fibre and the matrix; (iii) an extensional flow field developed by processing conditions, or (iv) a high surface free energy on the fibre.

Structures found in transcrystalline regions

Depending on the interaction mechanism between the reinforcing microfibrils and the surrounding matrix, literature reports various arrangements of structure. For instance, in cellulose/PP composites, the PP chains of the matrix are found to be parallel to the fibre axis [3]. The same arrangement dominates in some advanced polymer composites based on polyetherketoneketone and polyetheretherketone reinforced by carbon, Kevlar, or glass fibres [2].

In a detailed study on the interfacial interaction between Kevlar filaments and a polyamide 6 (PA6) matrix crystallised from the melt, two kinds of transcrystalline zones have been observed around the filament surface [4]. It has been confirmed by polarising light microscopy, microbeam X-ray diffraction, and transmission electron microscopy that the PA6 chains crystallise epitaxially. In this case the a* and a axes of PA6 are directed along the radius of the Kevlar filament in the interfacial and intermediate zones, respectively. The b* axis (molecular axis) and the c axis rotate around the a* or a axis [4].

In a more recent study [5] on aramid and carbon fibre reinforced PA66 composites, atomic force microscopy reveals radial regularity in the transcrystalline layer, relative to the fibre, and X-ray diffraction investigations of the isolated layer suggest that the polymer chain is oriented predominantly perpendicular to the fibre axis.

Moreover, Seth and Kempster [6] study blends of polyamide 11 (PA11) and PP. Different orientations of PP crystallites are reported in dependence on the PA11 content in the blend. The c-oriented unit cells predominate in the range 5–40% PA11, but a second mode of crystallisation with unit cell a-directions parallel to the FA occurs alongside the c-oriented mode. The third mode, with unit cell [101]-directions parallel to the FA appears to be present to some extent throughout the series, but only becomes significant in the blends with more than 40% PA11. The proportion of the third mode then increases with the amount of PA11 present [6]. It is suggested that the third orientation of PP crystallites is the result of epitaxy on portions of the PA11 fold surface at the interface between the two components [6]. The orientation of PP crystallites in the as obtained thread is found to depend on the amount of PA11 present, and no reorientation due to recrystallisation is reported in this paper [6].

New focus on transcrystallisation studies

The nucleation of a transcrystallised region on the reinforcing fibre is thought to be central to the improvement of some composite properties [7]. The contribution of these transcrystalline layers to the improvement of the adhesion between the matrix and the reinforcing component as well as their effect on the entire mechanical behaviour of PP-based glass-fibre reinforced composites is extensively studied[1]. Unfortunately, this is neither the case for the orientation of PP macromolecules with respect to the axis of the reinforcing fibres in the transcrystalline layers, nor for the effect of a variation of the substrate material (in the most common cases it consists of glass fibres) on this orientation.

Advanced tools for the study of transcrystallisation

The reason might be that the most common technique for determination of molecular orientation, the classical X-ray diffraction, is not applicable to a bulk PP composite that is organised as it is described above, because the scattering from the relatively thin transcrystalline layers is masked by the scattering from the relatively huge amount of the isotropically crystallised PP matrix.

An advanced X-ray study of thin longitudinal slices, on the other hand, requires a high spatial resolution, i.e. the use of microbeam X-ray diffraction as is reported on investigation of various polymorphic modifications of PP after deformation[8]. A different approach for examining the same problem is a time-resolved synchrotron radiation X-ray diffraction study starting from samples in which PP is in molten state, whereas the fibrous substrate is solid. Studying such samples during cooling by application of a technique that is able to register chain orientation in real time with short exposure and short cycle time between successive snapshots, should yield results concerning the evolution of epitaxial chain orientation during the very first stage of the crystallisation process, i.e., when the major fraction of the crystallised PP is found close to the oriented substrate where the interaction is strong.

Transcrystallisation with reorientation

In fact, this approach was explored some time ago on the system poly(ethylene terephthalate) (PET) melt-blended with polyamide 12 (PA12) and cold drawn [9]. After selective melting of the PA12 component at 220 °C, when the WAXS pattern indicated a completely isotropic amorphous halo and the PET reflections remained highly oriented, the subsequent cooling to room temperature lead to the quite unexpected result that the PA12 did not undergo isotropisation. During the cooling stage the major fraction of PA12 crystallised anisotropically, but did not preserve its original orientation, i.e., with the direction of the chains parallel to the drawing direction (i.e. the fibre axis, FA). Instead, the chains in the crystals turned perpendicular to FA. A process of transcrystallisation with reorientation [9] had been observed for the first time. A respective reorientation phenomenon upon temperature treatment was recently reported by Schmidt et. al. [10] resulting from analogous processing of a polyethylene/PP blend. It appears important to remind that the reported transcrystallisation with reorientation takes place on a highly crystalline polymeric microfibrillar substrate (PET or PP, respectively), as has been documented by means of scanning electron microscopy [11].

Nanostructured Polymer-polymer composites

As a matter of fact, both the last-mentioned systems PET/PA12 and polyethylene/PP belong to the class of nanostructured polymer composites (NPC) [11–15], in which the polymer matrix is reinforced by polymer nanostructures of microfibrillar type [11]. In contrast to the common glass-fibre reinforced composites where the polymer is melt-blended with fibres, the NPCs are prepared by melt-blending of two polymer components (distinguished by different melting temperatures), followed by cold drawing of the blend, aiming at a high degree of orientation. An essential step of the NPC manufacturing is the thermal treatment of the oriented blend at temperatures between the melting temperatures of the two blend components. This treatment results in melting of the lower melting component. Upon subsequent cooling we frequently have observed isotropisation, i.e. the melted component recrystallises, but not again in oriented state as proved by WAXS tests [12, 15]. In this way only preserving the microfibrillar nanostructure and orientation of the higher melting component, the NPC is produced.

Variation of the substrate

Taking into account two facts, namely the strong ability of PP to form transcrystalline layers in the fibre reinforced composites [1, 8] and the emerging technical possibility to study the very early crystallisation stages by means of two-dimensional X-ray scattering from synchrotron source in order to determine the chain orientation [9] it appears challenging to, as well, study the crystallisation behaviour of PP on a substrate representing highly oriented polymeric microfibrils. For this purpose two melt-blended, extruded, and cold-drawn materials were prepared, namely PET/PP and PA66/PP, where PA66 stands for polyamide 6.6.

Experimental

Commercial, engineering grade PET (Yambolen, Bulgaria), PA66 (Ultramid, BASF, Germany) and PP (Burgas, Bulgaria) were dried at 100 °C for 24 h. The blends PET/PP and PA66/PP were prepared in a ratio of 50/50 wt.% by extrusion in a Brabender single screw (30 mm diameter) extruder with a length-to-diameter ratio of 25 at 30–35 rpm. The temperature zones starting from the feed to the die were set to 210, 240, 270, 280, and 240 °C. The extrudate from the 2 mm capillary die was immediately quenched in a water bath at 15–18 °C. The threads were moved trough the bath by means of two rubber cylinders (60 mm diameter) rotating at a rate of about 90 rpm.

In the next step the blends were drawn in a tensile testing machine Zwick 1464 at room temperature and a strain rate of 80 mm/min to a draw ratio λ = 3.6–4.0, which resulted in a final diameter of about 1 mm, followed by annealing at 140 °C for 6 h with fixed ends in a vacuum oven.

WAXS patterns of these samples were obtained using synchrotron radiation from beamline A2 of HASYLAB in Hamburg, Germany. The sample-to-detector distance was set to approx. 150 mm. Diffraction patterns were registered on image plate. The exposure time was between 10 and 30 s. Scattering angle calibration was carried out by means of a PET standard. The observed reflections were identified with the aid of crystallographical data and scattering patterns from neat PP, PET, and PA66 samples [16–18].

In order to characterise the orientation of the PP crystallites before and after the recrystallisation, the azimuthal angle α_{hkl} of each reflection (*hkl*) on the respective pattern was measured. Bearing in mind that, before the recrystallisation, the PP-crystallites are oriented with the c–axis coinciding with FA, the indices of the plane perpendicular to the [001] direction were found after resorting to reference literature[19]. In order to find the orientation of the PP crystallites after the recrystallisation, the angles ρ_{hkl} between (*hkl*) and the plane normal to FA, characterising the new orientation, were calculated from the measured angles α_{hkl} and the Bragg's angle θ_{hkl} according to Cullity [20])

$$\cos \rho_{hkl} = \cos \theta_{hkl} \cos \alpha_{hkl}. \quad (1)$$

Searching for low-index planes to be perpendicular to the FA, theoretical values for α_{hkl} were calculated on the basis of the alpha-PP unit cell parameters (a = 6.65 Å, b = 20.96 Å, c = 6.5 Å; β = 99.33° [21]) by varying the corresponding indices until a satisfactory match between the measured and calculated values of α_{hkl} was found.

Results and discussion

Results are displayed in Figures 1 and 2 for the system PET/PP and in Figure 3 for the system PA66/PP. For

both blends WAXS patterns were taken during equivalent stages of the thermal processing. First, such patterns were recorded at room temperature (Figures 1a and 3a), followed by patterns taken at 200 °C (Figures 1b and 3b), i.e., well above the melting temperature of PP (171 °C). After cooling down to room temperature new patterns were taken (Figures 1c and 3c). Then a similar cycle was started, in which the PP was kept in the molten state for a longer period of time.

Figure 1a exhibits a very well expressed fibre texture for both components of the PET/PP blend in accordance with the expectation for a highly drawn and annealed blend of semicrystalline polymers. Several PP reflections are well distinguished. From the position and the number of reflections it is concluded that PP exists only in α-modification with its c-axis parallel to the FA. The same chain axis orientation is found for the PET component. Nevertheless, in Figure 1a the WAXS reflections arising from both components, PET and PP, overlap to a great extent. In Figure 1b, on the other hand, the PP is molten and only the PET reflections are observed. Thus, before studying the PP reflections in detail, we separated the two contributions to Figure 1a by a weighted subtraction of Figure 1b from Figure 1a after proper scaling. For this purpose we used the commercial scientific image processing tool *pv-wave*[22]. The result of this separation is shown in Figure 2a. Figure 2b was obtained in a similar way by

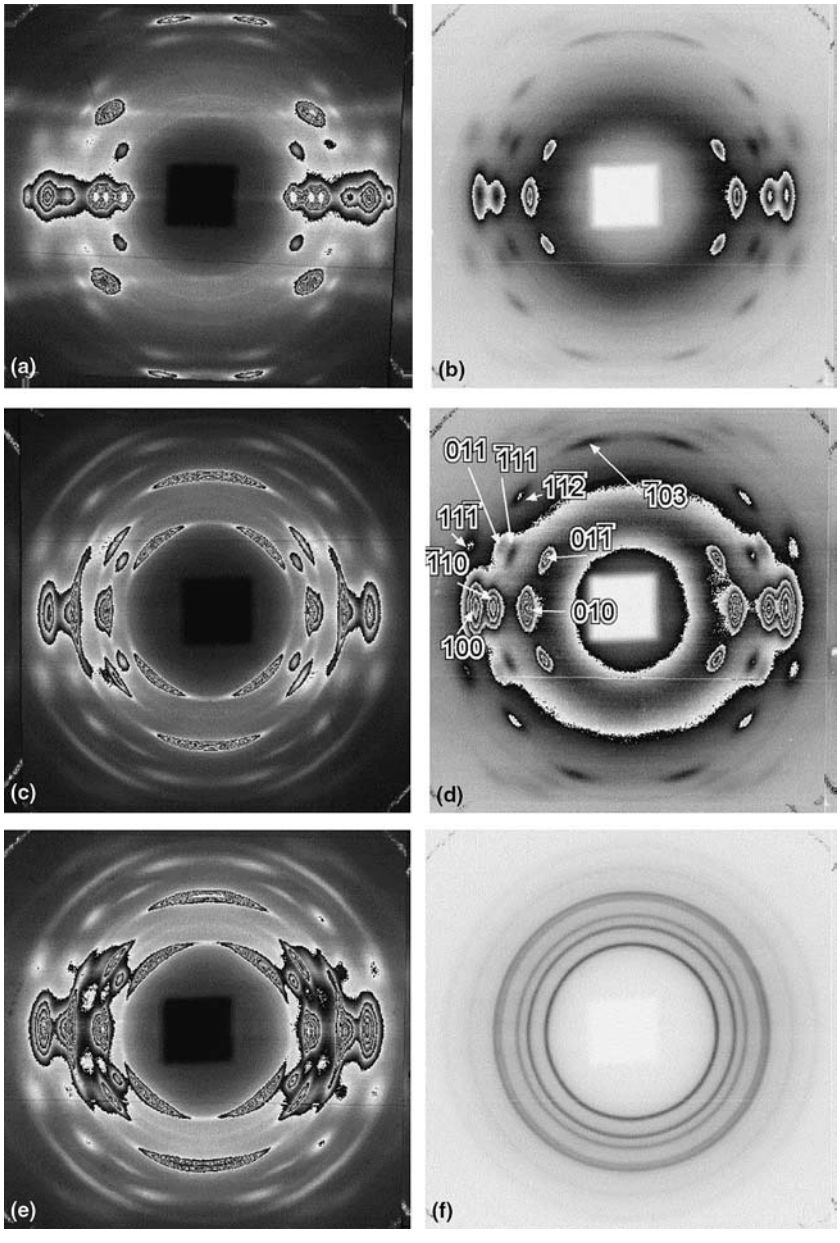

Fig. 1 Wide-angle X-ray scattering patterns of PET/PP blend: a) initial sample, pattern taken at room temperature, b) after 1 hour at 200 °C, pattern taken at 200 °C, c) after 1 hour at 200°C, pattern taken at 30°C, d) after 2 hours at 200 °C, pattern taken at 200 °C (Miller indices of PET indicated), e) after 2 hours at 200 °C, pattern taken at 30 °C and f) after 5 min at 280 °C, pattern taken at 30 °C. The fibre axis (FA) is vertical

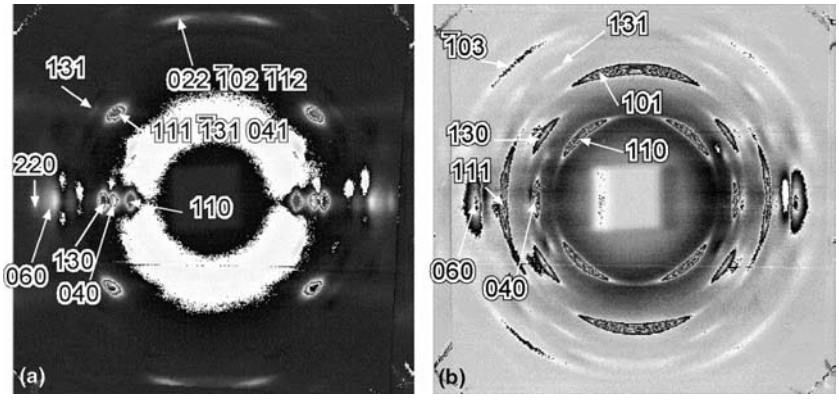

Fig. 2 Scattering patterns of PET/PP blend obtained by: a) subtraction of the scattering pattern taken at 200 °C (Figure 1b) from the scattering pattern taken at room temperature (Figure 1a); (b) subtraction of the scattering pattern taken at 200 °C (Figure 1b) from the scattering pattern taken at room temperature after melting at 200 °C (Figure 1c). Miller indices of α-PP are presented. The fibre axis (FA) is vertical

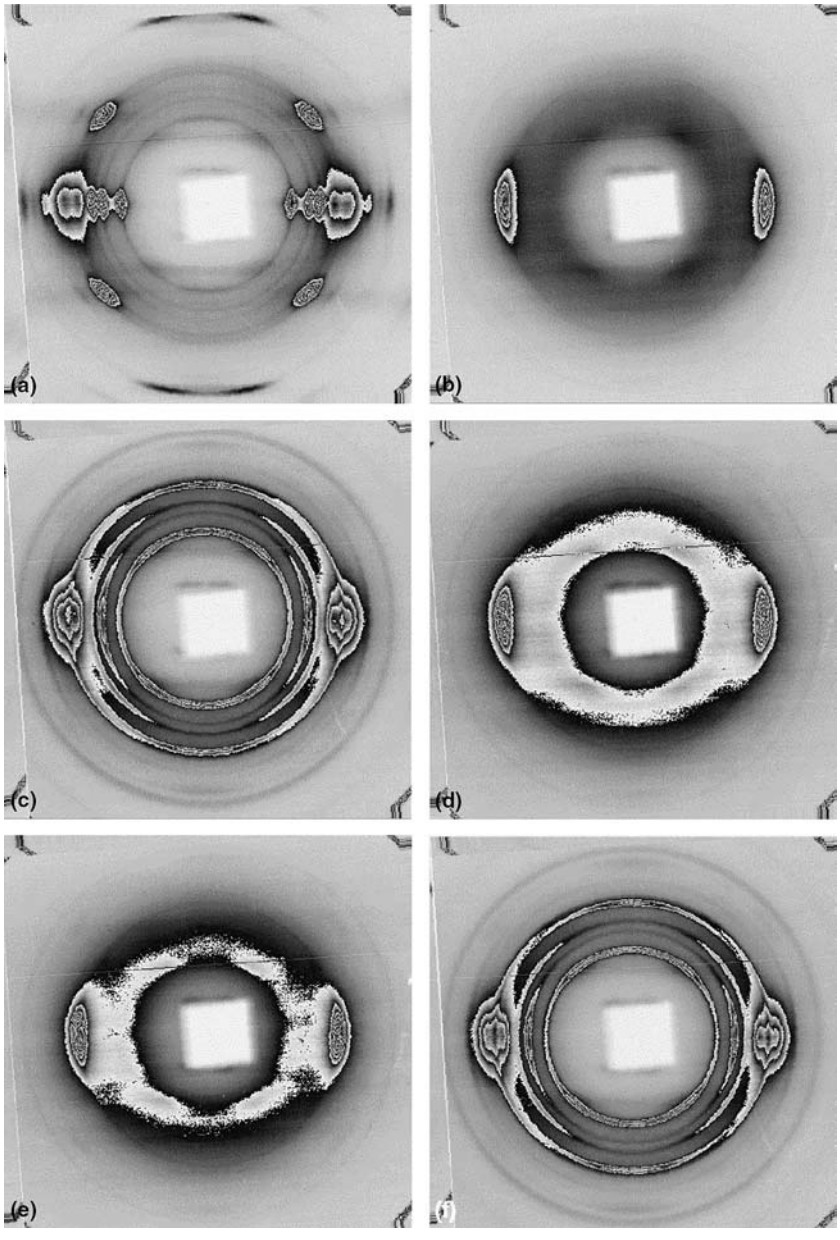

Fig. 3 Wide-angle X-ray scattering patterns of PA66/PP blend: a) initial sample, pattern taken at room temperature, b) after 1 min at 200 °C, pattern taken at 200 °C, c) after 1 min at 200 °C, pattern taken at 30 °C, d) after 10 min at 200 °C, pattern taken at 200 °C, Miller index of PA66 is presented, e) after 1 hour at 200 °C, pattern taken at 200 °C and f) after 1 hour at 200 °C, pattern taken at 30 °C. The fibre axis (FA) is vertical

subtracting the scattering pattern taken at 200 °C (Figure 1b) from the scattering pattern taken at room temperature after melting and recrystallisation (Figure 1c). Thus the separated patterns from Figure 2 exhibit the changes in the PP phase due to the applied melting/recrystallisation cycle.

Only in the subtracted pattern (Figure 2a) the position of the α-PP [10$\bar{6}$] reflection is detectable. Its position on the meridian is an independent direct support of the mentioned c-axis orientation of the PP crystallites, as deduced from the analysis of several strong reflections and the α-PP unit cell parameters [21].

In Figure 1b taken at 200 °C after melt annealing for 1 hour, one observes the fibre texture of only PET. The PP component forms an isotropic amorphous halo, i.e. the melt of PP is in perfect isotropic state.

After melting of PP at 200 °C and recrystallisation (Figure 1c) the PP reflections in the WAXS pattern taken at room temperature are quite different from those in the patterns already discussed. Taking into account that PP before cooling is in the molten state and does not show any orientation (Figure 1b) we expected formation of a more or less isotropic crystalline phase as a result of non-isothermal crystallisation during the cooling. Surprisingly, the distribution of PP reflections is rearranged (better seen in comparison between Figures 2a and 2b). Similar to two earlier reports on polymer-polymer composites [9, 10], again a transcrystallisation with reorientation with respect to the original orientation is observed.

By application of the fitting procedure described in the experimental section a satisfactory match between measured and calculated azimuthal angles, α_{hkl}, was found for a preferred crystallite orientation in which the (101) plane is oriented perpendicular to the FA. Using the crystallographic data of the planes (10$\bar{6}$), (101) and the indices of the zone axis [010] (according to [20]), an angle of 49° between FA and the chain direction of the recrystallised PP was computed. Compared to the first study of a blend (PET/PA12 [9]) in which reorientation was observed, we thus observe a different reorientation angle with the PET/PP blend.

This finding is manifested by the result of the next experiment during which the same sample was annealed for a longer time of 2 hours (Figure 1d), followed, again, by non-isothermal crystallisation during cooling to room temperature (Figure 1e). The scattering pattern shows the same features as that of Figure 1c, and the effects already described are even more pronounced.

It is worth mentioning that the majority of the two-component blends which are used for manufacturing of NPC behave in a different way if subjected to melting and crystallisation of the low-melting component. Generally, the latter crystallises without a macroscopic preferrential orientation. Based on WAXS patterns showing only Debye-Scherrer rings, this isotropisation process is well documented for the blends PET/PA6 [12], PET/PBT, [12] and PET/PBT/PA6 [12, 14], where PBT stands for poly(butylene terephthalate). However, it should be noted that from these observations one can hardly draw the conclusion that in the last-mentioned systems [12,14] transcrystallisation with reorientation is completely excluded, because for these blends the WAXS patterns were taken after very long melt annealing times (between 6 and 24 h). Moreover, the patterns were taken by means of a conventional X-ray source that does not allow real-time in-situ experiments. Obviously, in these cases the high crystallinity of the samples [11–15] may have a masking effect on the transcrystallisation with possible reorientation as already observed for the blend PET/PA12 [9].

The difference between both the classical fibre-reinforced materials [2, 4, 7] as well as the common NPCs [12, 14] on the one hand, and the reoriented transcrystalline materials both from earlier work [9, 10] as well as from the present study is notable. The results of the in-situ measurements indicate that in the second case the oriented crystallisation emanating from the PET microfibrils is propagating through almost the complete matrix volume before the usual spherulitic crystallisation is activated. There may be several reasons for the dominance of the orienting crystallisation process. The crystallisation emanating from the fibrillar inclusions may (i) start earlier (at lower undercooling) than the spherulitic growth, (ii) may propagate faster than the spherulite, (iii) may propagate at a constant high speed, if the common transcrystallisation was slowed down during its propagation (e.g. due to accumulation of defects). In order to investigate this competition of two crystallisation mechanisms, in-situ studies with novel two-dimensional detectors are required.

The assumption about the crucial role of oriented PET microfibrils for the crystallisation and orientation of the low-melting blend component can easily be checked by extinguishing them. For this purpose the blend was heated up to a temperature well above the melting temperature of PET. In Figure 1f the WAXS pattern taken at 30 °C is shown; after having kept the PET/PP blend at 280 °C for 5 min and having cooled the sample. One observes isointensity circles which are characteristic for the crystallites of the two homopolymers and demonstrate that both the components crystallise in isotropic state during cooling.

The results from the PA66/PP blend are somewhat different. The WAXS patterns are taken in the same way as in the previous case and are shown in Figure 3. In the patterns taken at 200 °C, where PP is molten, one observes an isotropic amorphous halo and crystalline reflections of only the semicrystalline PA66 oriented parallel to FA (Figures 3b, 3d and 3e). Thus up to this stage the evolution of the PA66/PP material is the same as that of PET/PP (Figure 1).

After the finalising non-isothermal crystallisation step, on the other hand, there are considerable differences. As compared to the data of the PET/PP material, the arc-shaped PP reflections in Figures 3c and 3f are much wider than the almost point-shaped reflections of the PET/PP material. Thus although we observe the return of an oriented PP matrix (reorientation) as well, the orientation distribution of the corresponding crystals is much wider for PA66/PP than in the case of PET/PP. This finding allows one to conclude that the orienting effect of PA66 fibrillar nanostructures on the crystallisation of PP from the melt is much weaker in comparison with PET.

Moreover, the positions of the returned PP reflections have not changed as compared to the initial cold-drawn thread (Figure 3a). Thus the PA66 induces oriented crystallisation of the isotropic PP melt with the chain axes, again, parallel to the chain axes of the PA66 filler fibrils.

Conclusions

The WAXS method utilised with synchrotron radiation offers the possibility to observe the initial stage of crystallisation and to draw important conclusions on this process as well as to gather detailed crystallographic information. Similarly to the previously studied cold drawn PET/PA12 blend [9] one observes in the present case a strong epitaxial effect of the nanostructures of microfibrillar type (PET) on the non-isothermal crystallisation behaviour of PP during its cooling from 200 °C to room temperature. Thus, the cold drawn and annealed blends of PET/PP and PA66/PP represent highly anisotropic crystalline structures. Finally, the observed orientation effect due to transcrystallisation with reorientation is more uniform in the system PET/PP in comparison to the PA66/PP system, which indicates a stronger epitaxial effect of the microfibrillar nanostructures of PET than that arising from the PA66 microfibrils.

Reviewing the results concerning the crystallisation in an isotropic polymer melt containing oriented embedded core filaments (different polymer microfibrils, glass fibres etc.) we have found competition between the isotropic crystallisation (spherulitic, three-dimensional, spreading from points in space) and the anisotropic transcrystallisation emanating from straight lines in space, namely the core filaments represented by the filler particles. Moreover, as the result of transcrystallisation we have found several variants of anisotropy. In order to understand both the process of competition and the mechanisms that control the formation of the different anisotropic structures the essential steps of NPC preparation should be studied in-situ in time-resolved studies. For such in-depth studies by means of synchrotron radiation modern two-dimensional CCD detectors are presently becoming available. Studies with a cycle time of 30 s should then be possible at almost every synchrotron source and yield WAXS patterns with sufficient accuracy even to carry out quantitative analyses of crystallite orientation distributions, ultimately using theoretical approaches devised in several papers of Ruland, e.g.[23–25]. If the results of corresponding studies would show that a continuous recording of structure evolution were necessary, high-brilliance synchrotron radiation sources are required. As a result of such studies one should finally become able to control the nanostructure formation during the physical NPC formation steps in order to manufacture advanced polymer materials. The wide spectrum of possibilities concerning the structure of NPCs can already be anticipated both based on the reviewed and the newly reported results.

Acknowledgements This study has been supported by the Bilateral Cooperation Programme between the University of Hamburg, Germany, and the University of Sofia, Bulgaria, which is funded by the DAAD (German Academic Exchange Service). We thank the Hamburg Synchrotron Radiation Laboratory (HASYLAB) for beam time granted in the frame of project II-01-041. M.E, K.F. and S.F. express their appreciation to Alexander von Humboldt Foundation for the partial support of this study through the Institute Partnership Program (Project no. 4584). S.F. would like to acknowledge the financial support of the Foundation for Research, Science and Technology of New Zealand making possible his stay at the Department of Mechanical Engineering and the Centre for Advanced Composite Materials of The University of Auckland, Auckland, New Zealand where this paper was finalised.

References

1. Varga J (1995) In: Karger-Kocsis J (ed.), Polypropylene: Structure, blends and composites, chap. 3, pp. 51–106, Chapman & Hall, London
2. Chen EJH, Hsiao BS (1992) Polym Eng Sci 32: 280
3. Felix J M, Gatenholm P (1994) J Mater Sci 29:3043
4. Kumamaru F, Oono T, Kajiyama T, Takayanagi M (1983) Polym Compos 4: 141
5. Klein N, Marom G, Wachtel E (1996) Polymer 37: 5493
6. Seth KK, Kempster CJE (1977) J Polym Sci Polym Symp 58: 297
7. Peacock JA, Hill B, Niel E, Barlow CY (1996) In: Ishida H, Koenig JL (eds.), Composite Interfaces. Proceedings of the ICCI-I, North-Holland, New York
8. Riekel C, Karger-Kocsis J (1999) Polymer 40: 541

9. Sapoundjieva D, Denchev Z, Evstatiev M, Stribeck N, Stamm M (1999) J Mater Sci 34: 3063
10. Schmidt P, Baldrian J, Ščudla J, Dybal J, Raab M, Eichhorn KJ (2001) Polymer 41: 5321
11. Evstatiev M, Nicolov N, Fakirov S (1996) Polymer 37: 4455
12. Evstatiev M, Fakirov S (1992) Polymer 33: 877
13. Fakirov S, Evstatiev M (1994) Adv Mater 6: 395
14. Fakirov S, Evstatiev M, Petrovich S (1993) Macromolecules 26: 5219
15. Fakirov S, Evstatiev M, Friedrich K (2002) In: Fakirov S (ed.), Handbook of Thermoplastic Polyesters, vol. 1, chap. 23, pp. 1093–1132, Wiley-VCH, Weinheim
16. Brandrup J, Immergut EH (eds.) (1999) Polymer Handbook. 4th edn., Wiley Interscience, New York, Chichester, Brisbane, Toronto, Singapore
17. Liu J, Geil PH (1997) J Macromol Sci Phys B36: 61
18. Radusch HJ, Stolp M, Androsch R (1994) Polymer 35: 3568
19. Henry NFM (ed.) (1969) International Tables for X-ray Crystallography, vol. 1. Symmetry Groups. 3rd edn., The Kynoch Press, Birmingham
20. Cullity BD (1978) Elements of X-ray Diffraction. 2nd edn., Addison-Wesley, Reading, Mass.
21. Clark ES (1996) In: Mark JE (ed.), Physical Properties of Polymers Handbook, vol. 67, AIP Press, Woodbury, New York
22. pv-wave, version 7.5 (2001), Visual Numerics Inc., Boulder, Colorado
23. Ruland W, Tompa H (1968) Acta Cryst A24: 93
24. Ruland W (1977) Colloid Polym Sci 255: 833
25. Ruland W, Smarsly B (2002) J Appl Cryst 35: 624

Progr Colloid Polym Sci (2005) 130: 167–173
DOI 10.1007/b107339
Published online: 3 June 2005

Marina Krumova
Goerg H. Michler
Michel Evstatiev
Klaus Friedrich
Norbert Stribeck
Stoyko Fakirov

Transcrystallisation with reorientation of polypropylene in drawn PET/PP and PA66/PP blends. Part 2. Electron microscopic observations on the PET/PP blend

Abstract In the present second part of the study it is shown that polymer microfibrils are able to promote transcrystallisation of the surrounding polymer matrix in agreement with the results of an X-ray study reported in the first part. Polymer blends (microfibrillar-reinforced composites, MFC) containing microfibrils of poly(ethylene terephthalate) (PET) in a matrix phase consisting of polypropylene (PP) were studied by means of transmission electron microscopy (TEM), scanning electron microscopy (SEM) and environmental scanning electron microscopy (ESEM) after melting and crystallisation of only the matrix phase polymer in an injection moulding process. Collective preferred orientation of layers was observed in the PP matrix in transcrystalline zones grown epitaxially from the PET microfibrils. With respect to these microfibrils the lamellar stacks are oriented in perpendicular direction. The range of collective layer orientation along the longitudinal direction of a microfibril was found to be very long. ESEM exhibits layers which appear to be stacked, two-dimensional spherulites with a diameter of several microns. TEM micrographs show a transcrystalline zone around the PET microfibrils containing stacked crystalline PP layers. The lateral extension of these zones is restricted to a region narrower (100–200 nm) than that observed in respective MFC fibre materials (cf. Part 1) in which the matrix phase polymer was molten and crystallised more slowly and under quiescent conditions. The differing results of ESEM and TEM concerning the extension of the transcrystalline zone can be explained on the basis of a complex model by Bassett (dominant crystallites close to the nucleating microfibril and subsidiary crystallites farther out). The addition of a compatibiliser to the PET/PP blend completely inhibits the formation of transcrystalline layers in samples with MFC structure.

Keywords Transcrystallisation · Lamellae · Blends · PET/PP · Electron microscopy

Dedicated to Prof. Dr. Wilhelm Ruland on the occasion of his 80th birthday

M. Krumova (✉) · G. H. Michler
Halle-Wittenberg,
Martin-Luther-University,
06099 Halle (Saale), Germany
E-mail: marina.krumova@iw.uni-halle.de
Tel.: +49- 3461-462558
Fax: +49-3461-462535

M. Evstatiev
Laboratory on Polymers,
University of Sofia, 1164 Sofia,
Bulgaria

K. Friedrich
Institute for Composite Materials (IVW GmbH), University of Kaiserslautern,
67663 Kaiserslautern, Germany

N. Stribeck
Institute of Technical and Macromolecular Chemistry,
University of Hamburg, Bundesstr. 45, 20146 Hamburg, Germany

S. Fakirov
Department of Mechanical Engineering and Centre for Advanced Composites Materials of The University of Auckland,
Private Bag 92019, Auckland,
New Zealand

S. Fakirov
Laboratory on Polymers,
University of Sofia, 1164 Sofia, Bulgaria

Introduction

Whenever a polymeric material or a blend of several polymers is first partially molten and then recrystallised, the newly forming crystals may grow epitaxially from the conserved entities. This so-called transcrystallisation process has a considerable effect on the bonding between the afore molten matrix phase and the conserved entities, and therefore on materials properties[1]. In the first part of this study [2] the transcrystallisation phenomenon was discussed in detail. It was shown that it is an important characteristic feature of all polymer composites, partic-

ularly those reinforced with such kind of fibres that show a considerable nucleating power concerning the matrix crystallisation. In our studies the required fibres are prepared in a process starting from co-extrusion of two polymers with different melting temperature that finally results in microfibrillar reinforced composites (MFC). The MFC represent a new type of polymer-polymer composite where the isotropic matrix is reinforced with microfibrils of another polymer [3–7].

Fibres blended into a polymer matrix may nucleate matrix material crystallisation and thus induce peculiar crystalline morphologies in the surrounding zone, which are different from the morphology in the bulk [1]. Such a zone is called ''transcrystalline layer''. An early electron microscopic study on polypropylene (PP) [8] evidenced columns of crystalline and amorphous layers around a ''central linear thread'' with long periods of 12–14 nm. This ''shish-kebab'' structure (in which two components of a polymer–polymer blend are discriminated not by their chemical structure but by extremely different molecular weight) is, in fact, nothing but a transcrystalline morphology. In a later paper [9] the same group studied the propagation of crystallisation from ''linear instead of point-nuclei'' emerging from high molecular weight polyethylene (PE) fibres immersed in linear low-density polyethylene. Concerning the diameter of the transcrystalline zone around the central fibre they proposed that ''accumulation of rejected species ahead of the growth envelope'' should lead to the breakdown of correlated crystal growth that is typical for the transcrystalline zone. The basic principle of this idea was already put forward in an early paper of Bassett and Patel [10] which states that during growth front propagation at first ''dominant lamellae'' are formed, which are followed by imperfect crystallites in ''subsidiary lamellae''. An *in-situ* X-ray study of polymer crystallisation that supports such an idea of two crystallisation mechanisms can be found elsewhere in this special issue [11], and another paper [12] from this special issue is devoted to *in situ* X-ray studies of shish-kebab crystallisation in PE-blends similar to the ones used by Bassett [9]. The goal of all these efforts is the tailoring of the properties of thermoplastic materials after understanding their complicated issues of structure and processing. Detailed insight concerning these interrelationships is progressively achieved by means of newly developed advanced equipment (e.g. Environmental scanning electron microscopy (ESEM) or synchrotron radiation).

Transcrystallisation takes place in the matrix component whenever heterogeneous nucleation occurs with sufficiently high density along the fibre surface. In this way, the resulting crystal growth is restricted to the lateral direction, away from the microfibrillar core. Transcrystallisation is a function both of the nucleating activity of the fibre surface, and of the crystallisation kinetics of the matrix resin. The phenomenon is well known for the case of polymer composites that are either reinforced by carbon fibre or surface-treated glass fibre [13] and has also been observed in composites in which the reinforcement is based on polymeric fibres like cellulose [14], Kevlar [15] and others [16].

For such polymer-polymer composites complete melting of all blend components and subsequent crystallisation should lead to an isotropic material in which the crystallites of both components are oriented at random. This behaviour has been demonstrated in part 1 [2] by means of wide-angle X-ray scattering (WAXS) for the drawn blend poly(ethylene terephthalate) (PET) / PP (40/60 by wt.). It was found that after melting the blend at 280 °C completely, the subsequent non-isothermal crystallisation during the cooling down to room temperature (RT) takes place in an isotropic manner, i.e. the initially very high uniaxial orientation of both the PET and the PP is totally lost. Quite different is the situation when an intermediate melting temperature (200°C) is chosen, and thus only the lower melting component (PP) of the blend is molten. According to the WAXS data, then its non-isothermal crystallisation takes place with a well-expressed preferential orientation of crystallites (under an average angle of 49°) with respect to the initial orientation direction (fibre axis, FA). Thus this phenomenon may be called a ''transcrystallisation with reorientation'', as it has already been well documented for the system PET/polyamide 12 (PA12) [17].

For the last-mentioned drawn PET/PA12 blend it must be stressed that the WAXS patterns have been taken continuously during the cooling down, and the crystallisation has thus been followed in real-time. From the series of scattering patterns it has been concluded [17] that for this material the crystallisation with reorientation takes place only at the very first stages of crystallisation, i.e. during the period in which the predominant fraction of already crystallised PA12 material is found close to the un-molten PET microfibrils, whereas the later stages of crystallisation are proceeding in the bulk and are producing randomly oriented crystals, the Debye-Scherrer rings of which are increasingly masking the arc-shaped reflections from the minor volume fraction occupied by the transcrystalline material.

This situation was later confirmed on the system PET/low density polyethylene (LDPE). By means of transmission electron microscopy (TEM) on stained thin sections the transcrystalline morphology was resolved on a lamellar level [18]. The TEM observations demonstrated that close to the PET microfibrils the PE lamellae are not only parallel to each other, but also oriented perpendicular to the microfibrils surface in contrast to the bulk, where the lamellae are oriented at random [18, 19].

These observations were recently supported by those of Li et al. [20] who reported similar results for samples of PET/isotactic polypropylene (iPP) characterised also by a MFC-structure although obtained in a slightly different way (slit dye extrusion with hot drawing [21]).

Coming back to the results on PET/PP reported in Part 1 [2] it should be stressed that the WAXS patterns have been taken in a "*post mortem*" mode, i.e. after the completion of the crystallisation process. For this reason, starting from the reported results [2], it is hardly possible to derive reliable conclusions regarding the stage of the crystallisation process when this well-documented reorientation of crystallites takes place. Some useful information in this respect can be obtained from TEM analysis on stained thin sections, where the arrangement of the PP lamellae can be identified as a function of their distance from the PET microfibrils. In fact, this task is the goal of this second part of our systematic study on the transcrystallisation phenomenon in oriented polymer blends and systems distinguished by a MFC structure.

Experimental

Materials

Microfibrillar reinforced composites for this investigation were prepared from PET, iPP and a compatibiliser. The compatibiliser used was ethylene glycidyl methacrylate (E-GMA) (type Lotader AX 8840, a commercial product of Atochem, France). Recycled material from PET bottles (type FR 65, with a melting temperature (T_m) range of 236–252 °C, supplied by Rethmann Plano GmbH, Germany) was used as the reinforcing component. The matrix-component iPP was provided by Basell, Germany (type Novolen with melt flow index 5). The blends PET/iPP were prepared in a 40/60 wt ratio. Compatibiliser content was varied between 0 and 9 wt.-%.

MFC manufacturing comprised melt blending of the two immiscible blend components at high temperature and extrusion in a co-rotating twin-screw extruder, followed by a fibrillation process achieved by cold drawing. The highly drawn filaments were chopped and, finally, converted to "dog bone" test specimens via injection moulding (Kloeckner Feromatik FM20) under industrially relevant conditions. During this stage the maximum processing temperature was 200 °C.

Characterisation techniques

Scanning electron microscopy (SEM)

SEM observations were performed on a JEOL JSM 5400 SEM with an accelerating voltage of 20 kV. As-drawn samples were fractured in liquid nitrogen for observation of their surface. Part of these samples was treated with boiling xylene, a selective solvent for PP, in order to remove this component. All the samples were coated with a thin gold layer prior the SEM analysis.

Environmental scanning electron microscopy (ESEM)

A FEG XL30 Philips ESEM was used for morphological observation of the injection moulded samples. Flat surfaces were prepared by cutting the samples at −100 °C along the injection moulding direction. A wet mode at 0.2 Torr water pressure and accelerating voltage of 15 kV was chosen for the observation. The signal was recorded using a detector for backscattered electrons.

Transmission electron microscopy (TEM)

For the TEM observations a JEM 2010 JEOL microscope at 200 kV accelerating voltage was used. Ultrathin sections of 80 nm thickness were cut by means of an ultramicrotome "Leica Ultracut UCT" after staining the bulk sample in RuO_4 vapour overnight.

Results and discussion

MFC without compatibiliser

Figure 1 shows SEM micrographs reflecting the blend morphology after each of the first two essential stages of MFC manufacturing – the melt-blending in an extruder and the subsequent cold-drawing step imprinting orientation of the two blend components.

The picture on Figure 1a is obtained from the cryofracture of the as-extruded PET/PP blend. The typical morphology for a well homogenised blend of two immiscible polymers is observed, characterised by spherical particles with diameters of several microns (average around 5 μm).

Figure 1b shows PET microfibrils obtained via selective dissolution of PP (by boiling xylene) from a

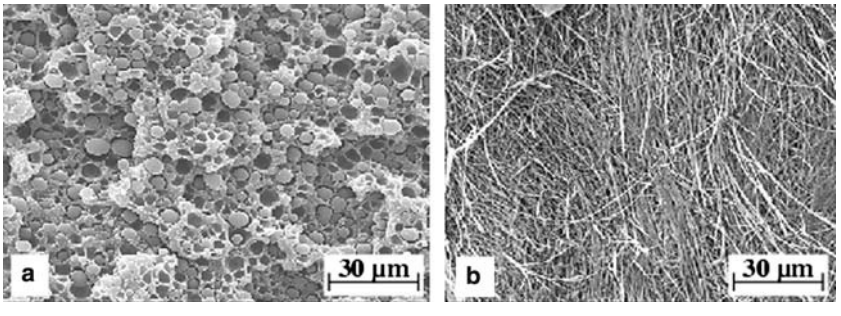

Fig. 1 SEM micrographs of: a) cryofracture of PET/PP blend (40/60 by wt.) after melt blending and extrusion, b) PET microfibrils obtained via selective dissolution of PP from the same PET/PP blend

drawn PET/PP blend. One observes excellent microfibrils with diameters between 1 and 3 μm and a length of several hundreds of microns (almost no fibril ends are observed). Such microfibrillar morphology is well documented for various drawn polymer blends [3–7,18–24] and injection [22] or compression [23,24] moulded samples with MFC structure. In this new class of polymer-polymer composites [3–7, 18–24] they not only play the role of the reinforcement, but also express their ability to induce transcrystallisation of the respective matrix polymer (PA12 [17], LDPE [18, 19], iPP [20]).

Figure 2 is an ESEM micrograph which shows the morphology of the MFC after the final processing step (injection moulding) at a similar magnification as Figure 1. The PET microfibrils appear bright in the surrounding PP matrix. As compared to Figure 1 however, their shape is altered as a result of this last processing step. Although the majority of the PET microfibrils are aligned in the direction of the melt flow during injection moulding (vertical), some of the microfibrils are not. Thus after cutting parallel to this direction and taking a micrograph they either appear as bright short lines or even as dots only.

It is known that exposure of semicrystalline polymers to electron beam provokes radiation-induced changes in the structure [25], e.g. mass loss, chain break or cross-linking in the amorphous phase. As a result, contrast enhancement is frequently observed in spherulites as a function of radiation dose, thus increasing the visibility of the lamellar morphology. The fact that the ESEM does not require the coverage of the sample with a thin metal layer offers the opportunity to *in situ* observe the varying contrast of the semicrystalline PP morphology as a function of radiation dose.

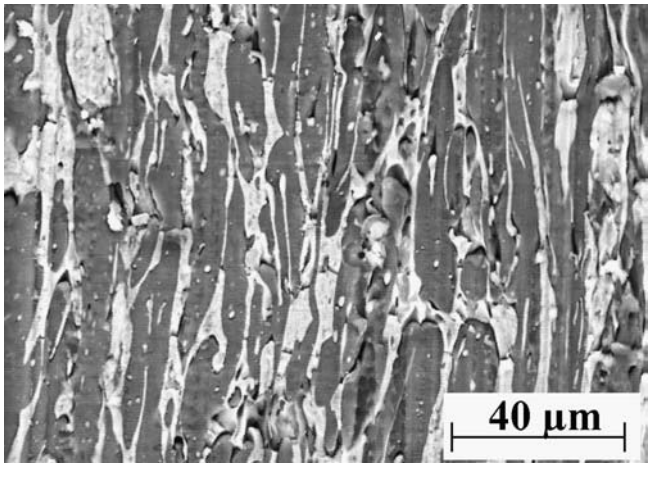

Fig. 2 ESEM micrograph of injection moulded PET/PP blend (40/60 by wt.) sample with MFC structure. The observed surface is obtained via cryo-cutting along the injection moulding direction (vertical)

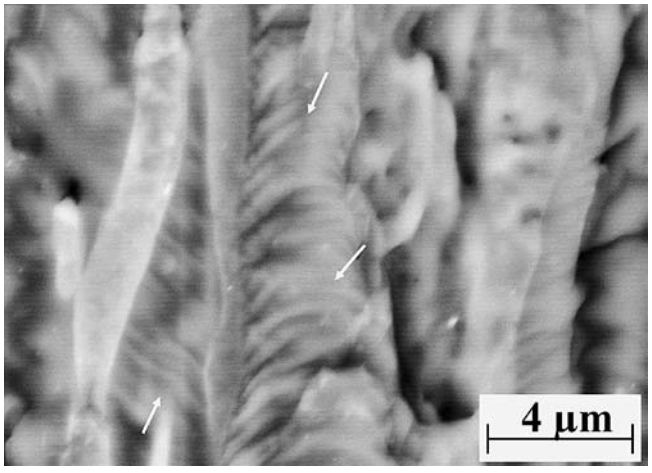

Fig. 3 ESEM micrograph of the same sample according to Figure 2 after irradiation. Some of the column forming layers are marked by arrows

As shown in Figure 3, after a short irradiation in the electron beam, well-defined columns built from stacked "two-dimensional spherulites" (which are supposed to contain high amounts of lamellae of crystalline PP) with an average diameter of 1–4 μm can be distinguished around the PET fibrils. The formation of such structures can be attributed to collective oriented growth of PP crystallites away from the PET fibrils into the thermoplastic matrix, thus forming some kind of transcrystalline zone. For PP such morphology has early been evidenced by Monks et al. [8]. The growing crystalline PP layers, built up along the PET fibrils, impinge upon one another and cannot develop to larger dimensions. This situation is well-known and repeatedly documented by polarising light microscopy particularly for fibre reinforced PP [1, 13, 14, 16, 26].

A much higher magnification is possible, if ultra-thin stained sections are studied in a TEM instrument. The TEM micrograph in Figure 4 exhibits the organisation of the crystalline entities on a much finer level. Here the crystalline lamellae of the PP matrix are resolved. The bright regions in the micrograph represent cross-sections of PET microfibrils. In the PP matrix close to these regions the crystalline lamellae are extending more or less in radial direction away from the PET surface, whereas far from the microfibrils (in the bulk) the layer orientation appears to be no longer correlated to the surface normal of the microfibrils and resembles the typical morphology of α–iPP bulk material. The fact that the transcrystalline layers obviously are not covering the PET microfibrils completely on all sides may result from the irregular shape of the fibrils and from the cutting, which is not everywhere strictly perpendicular to the fibril axis.

Figure 5 represents a detail of the transcrystalline structure as observed in the TEM at a higher magnifi-

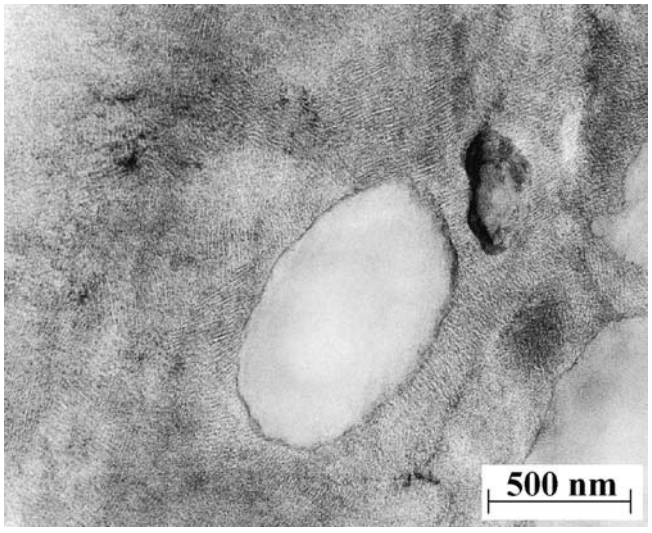

Fig. 4 TEM micrograph of a stained ultra thin section (perpendicular to the orientation direction) of injection moulded PET/PP (40/60 by wt.) blend sample with a MFC structure

cation. One can clearly see that the individual PP crystalline lamellae closest to the PET microfibril are both oriented strongly parallel to each other and at the same time perpendicular to the microfibril surface. In cases when two microfibrils lie close to each other, the PP lamellae are again arranged parallel to each other and perpendicular to the both surfaces as observed in many cases (not shown in Figure 5). In all the cases the average thickness of the individual lamellae is about 8–10 nm and the width (thickness) of the transcrystalline layer is 100–200 nm.

Not only samples from the final MFC material were investigated by SEM and TEM, but also samples taken after different earlier stages of the MFC preparation process. Even immediately after the first stage (blend melt-extrusion) transcrystalline PP layers were found at the surface of some of the PET spheres. The latter look very similar to those presented on the TEM micrograph of Figures 4 and 5. Obviously, the conditions prevailing during cooling down to RT after the melt blending lead to formation of transcrystalline layers around the PET spheres. During cold drawing, i.e. the next step of MFC preparation, these transcrystalline formations on the PET-PP phase boundary are destroyed. As already discussed, transcrystallisation again takes place, when the blend is cooling down from the intermediate temperature after injection moulding (cf. Figures 4 and 5).

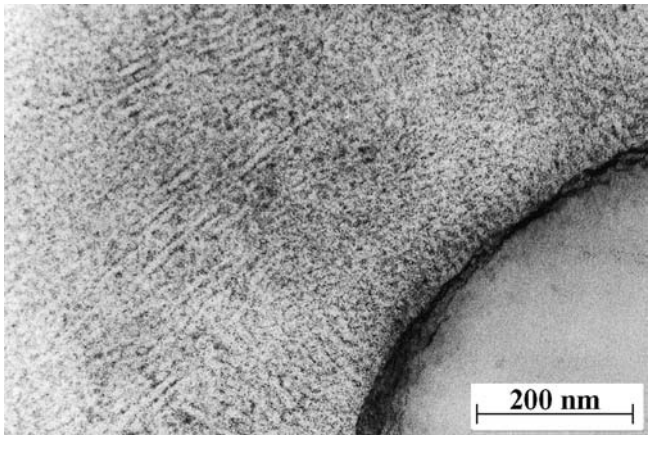

Fig. 5 Detail of the lamellar structure in the PP matrix. TEM micrograph on ultrathin section

MFC with compatibiliser

Figure 6 shows the TEM micrograph of a PET/PP/E-GMA composite 40/54/6 containing 6 wt.-% of the compatibiliser E-GMA. A reduction of the average diameter of the PET fibrils to 1 μm is observed [27] and, what is more striking, in comparison to Figure 4, no transcrystalline zones with lamellae preferentially extending away from the microfibrils are found. Even in a magnified image (Fig. 7) the thin layer of oriented "dominant" lamellae [10] that are clearly visible in the material without compatibiliser (compare to Fig. 5) is not present on the microfibril surface if compatibiliser is present. A small–angle X–ray scattering (SAXS) study [28] during drawing (between 0 and 10% relative deformation) of PET/PP drawn blends containing various amounts of compatibiliser demonstrates the effect of compatibiliser on the MFC nanostructure. An

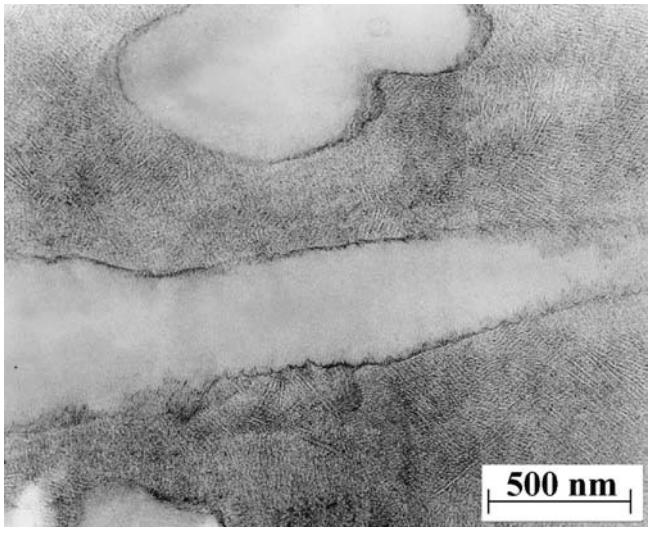

Fig. 6 Injection moulded PET/PP/E-GMA (40/54/6 by wt.) material containing compatibiliser. TEM micrograph of a stained ultra thin section (perpendicular to the orientation direction) of blend sample with MFC structure

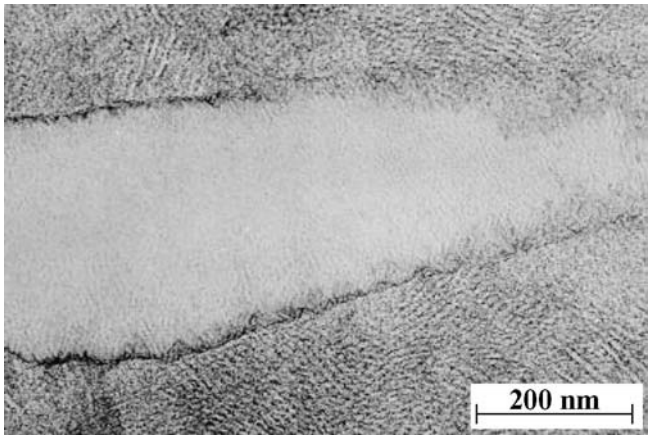

Fig. 7 Injection moulded PET/PP/E-GMA (40/54/6 by wt.) material containing compatibiliser. Detail of the typical lamellar structure close to the PET microfibrils. TEM micrograph on ultrathin section

extended equatorial streak (void scattering) is typical for the PET/PP blends without compatibiliser. The PET/PP/E-GMA blends show equatorial scattering as well, but the reflection is much shorter, much higher, and by more than an order of magnitude less intense. Thus the few holes generated in the blend during cold drawing are needle-shaped for the material without compatibiliser, whereas they are shorter, wider and less pronounced for the material containing compatibiliser. This result supports the expected role of the compatibiliser, namely that it is enriched in the interphase between the two blend components where it changes the delamination behaviour of the components during cold drawing.

The suggested interpretation of these SAXS and electron microscopic data [27] assumes that the PET microfibrils (particularly after the isotropisation of the second blend component, the PP in the present case) are coated by a thin layer of the added compatibiliser. The latter prevents the direct contact between PET and PP and thus suppresses the epitaxial as well as the nucleating effect of the PET microfibrils on the PP crystallisation, i.e. transcrystalline layers can not be formed and the crystallisation of PP even in the very close proximity to the microfibrils surface is performed in the same way as in the PP matrix far from the microfibril surfaces.

Transcrystalline structure and materials processing

In Part 1 of this study the material, at the beginning of the last MFC processing step, is a fibre in which the PET microfibrils are excellently oriented. Then the quiescent PP matrix is molten, and during the following and relatively slow cooling stage the transcrystalline nanostructure is formed. Our WAXS results show that, obviously, under these conditions the epitaxial nucleation of the PP is very efficient, and as a result the transcrystalline PP crystallites are able to interfuse a considerable fraction of the matrix volume before the ordinary bulk crystallisation sets in.

The measured reorientation effect of the PP matrix crystallites in the MFC fibre material even requires a second prerequisite. Not only must the epitaxially nucleated crystallites be able to interfuse the matrix volume, but also must the PET microfibrils be well-oriented, so that the orientation of the crystallites with respect to their local microfibrils will lead to an observable global orientation in the PP phase. In general, such kind of macroscopic orientations of crystal lamellae or microfibrils cause peculiar materials properties, as e.g. in the well-established hard elastic materials [29, 30]. For a systematic study of orientation distributions in transcrystalline MFC materials as a function of the processing parameters appropriate methods have been developed by Ruland [31–33].

Concerning the materials investigated here in Part 2 of the study, the PP matrix is molten as well, but thereafter the material is injection moulded. Caused from the melt flow some preferential orientation of the embedded PET microfibrils is established, and during the quenching in the mould the observed transcrystalline nanostructure is formed. Its constricted transcrystalline zones can be explained, if it is assumed that the advantage of epitaxial nucleation with respect to nucleation in the bulk is decreased as a result of the considerable undercooling of the PP melt which is rapidly established in the moulding process. In this way the rather thin (around 100 nm) transcrystalline layers found by the TEM analysis on stained thin sections can be explained.

Conclusions

The obtained results show that polymer microfibrils of PET are able to promote transcrystallisation also in a polypropylene matrix. This is similar to the already reported cases of PET/PA12 [17] and PET/PE [18–20] blends. Using TEM on stained ultra thin sections one can observe the alignment of the crystalline lamellae in the proximity of the microfibril's surface. In addition, imaging with backscattered electrons in ESEM gives excellent possibilities for investigation of the "spherulitic" morphology at an intermediate scale – over the resolution limit of the light microscopy.

Thus each of the utilised structure investigation methods is recognising different aspects of the transcrystalline structure. The ESEM exhibits that an oriented growth front propagation away from the line nucleus may reach out into the matrix for several microns, even if

(as shown in the TEM micrographs) the oriented and stacked "dominant" [10] crystalline lamellae are only found in a zone that is not wider than a few hundred nanometres. Moreover, in the WAXS patterns transcrystallisation is indirectly detected based on preferred orientation of the growing matrix crystals. A first study [11] indicates that the distorted "subsidiary" [10] crystals are oriented at random. Under this assumption WAXS data should be compared to the data from TEM rather than to the ESEM results.

Comparing the MFC fibres of Part 1 with the MFC injection-moulded parts investigated here, different characteristics of the transcrystalline nanostructure and its orientation with respect to the main axis of the specimen are found. The observed differences exhibit that the importance of the process control for the specificity of the transcrystalline structure should not be underestimated.

Acknowledgements This study has partly been supported by the Bilateral Cooperation Program between the University of Hamburg, Germany, and the University of Sofia, Bulgaria, which is funded by the DAAD (German Academic Exchange Service). M.E, K.F. and S.F. express their appreciation to Alexander von Humboldt Foundation for the partial support of this study through the Institute Partnership Program (Project no. 4584). One of us (S.F.) would like to acknowledge the financial support of the Foundation for Research, Science and Technology of New Zealand making possible his stay at the Department of Mechanical Engineering and the Centre for Advanced Composite Materials of The University of Auckland, Auckland, New Zealand where is Part 1 of this paper was finalised. The SEM observations were performed with an instrument donated by the Alexander von Humboldt Foundation to the Faculty of Chemistry of the Sofia University, Sofia, Bulgaria.

References

1. Folkes MJ (1995) In: Karger-Kocsis J (ed.), Polypropylene: Structure, blends and composites, chap. 10, pp. 340–370, Chapman & Hall, London
2. Apostolov A, Samokovlijski O, Fakirov S, Stribeck N, Denchev Z, Evstatiev M, Friedrich K, Funari SS (2005) Progr Coll Polym Sci 130: 159
3. Evstatiev M, Fakirov S (1992) Polymer 33: 877
4. Fakirov S, Evstatiev M (1994) Adv Mater 6: 395
5. Fakirov S, Evstatiev M, Friedrich K (2000) In: Paul DR, Bucknall CD (eds.), Polymer Blends, vol. 2, chap. 33, p. 455, J. Wiley & Sons, New York
6. Fakirov S, Evstatiev M, Friedrich K (2002) In: Fakirov S (ed.), Handbook of Thermoplastic Polyesters, vol. 2, chap. 23, pp. 1093–1132, Wiley-VCH, Weinheim
7. Evstatiev M, Nicolov N, Fakirov S (1996) Polymer 37: 4455
8. Monks AW, White HM, Bassett DC (1996) Polymer 37: 5933
9. Janimak JJ, Bassett DC (1999) Polymer 40: 459
10. Bassett DC, Patel D (1994) Polymer 35: 1855
11. Stribeck N, Bösecke P, Bayer R, Almendarez Camarillo A (2005) Progr Coll Polym Sci 130: 127
12. Keum JK, Burger C, Hsiao BS, Somani R, Yang L, Kolb R, Chen H, Lue CT (2005) Progr Colloid Polym Sci 130: 114
13. Chen EJH, Hsiao BS (1992) Polym Eng Sci 32: 280
14. Verpoest L, Desaeger M, Keunings R (1990) In: Ishida H (ed.), Proc. of ICCM-4: Controlled interphases in composite materials, pp. 653–666, Elsevier, New York
15. Felix JM, Gatenholm P (1994) J Mater Sci 29: 3043
16. Assouline E, Wachtel E, Grigull S, Lustiger A, Wagner HD, Marom G (2001) Polymer 42: 6231
17. Sapoundjieva D, Denchev Z, Evstatiev M, Stribeck N, Stamm M (1999) J Mater Sci 34: 3063
18. Friedrich K, Ueda E, Kamo H, Evstatiev M, Krasteva B, Fakirov S (2002) J Mater Sci 37: 4299
19. Fakirov S, Kamo H, Evstatiev M, Friedrich K (2004) J Macromol Sci Phys 43: 775
20. Li ZM, Li LB, Shen KZ, Yang W, Huang R, Yang MB (2004) Macromolecul Rapid Commun 25: 553
21. Li ZM, Yang MB, Lu A, Feng JM, Huang R (2002) Mater Lett 56: 756
22. Evstatiev M, Fakirov S, Krasteva B, Friedrich K, Covas JA, Cunha AM (2002) Polym Eng Sci 42: 826
23. Friedrich K, Evstatiev M, Fakirov S, Evstatiev O, Ishii M, Harass M (2005) Compos Sci Technol 65: 107
24. Evstatiev M, Fakirov S, Friedrich K (2004) In: Friedrich K, Fakirov S, Zhang Z (eds.), Polymer Composites: From Nano- to Macroscale, p. in press, Springer, Boston
25. Grubb DT (1974) J Mater Sci 9: 1715
26. Felix JM, Gatenholm P (1994) J Mater Sci 29: 3043
27. Krumova M, Michler GH, Evstatiev M, Friedrich K, Fakirov S (2003) In: Proc. of PC2003: Polymer Crystallization, Linz, Austria
28. Stribeck N, Evstatiev O, Boyanova M, Almendarez Camarillo A, Fakirov S, Friedrich K, Cunis S, Gehrke R (2003) Hasylab Ann Rep 1: 953
29. Noether HD (1979) Intern J Polymeric Mater 7: 57
30. Sprague BS (1973) J Macromol Sci Phys B8: 157
31. Ruland W (1969) J Polym Sci Part C 28: 143
32. Perret R, Ruland W (1969) J Appl Cryst 2: 209
33. Ruland W, Smarsly B (2002) J Appl Cryst 35: 624

Progr Colloid Polym Sci (2005) 130: 174–175

AUTHOR/TITLE INDEX

Progr Colloid Polym Sci (2005) 130: 176

KEY WORD INDEX